論文 / 著書情報
Article / Book Information

題目(和文)	
Title(English)	Modeling Ecological and Physical Processes in Blue Carbon Ecosystems: Biomass Dynamics and Hydrodynamics-Sediment Transport
著者(和文)	吉開仁哉
Author(English)	Masaya Yoshikai
出典(和文)	学位:博士(工学), 学位授与機関:東京工業大学, 報告番号:乙第4197号, 授与年月日:2024年2月29日, 学位の種別:論文博士, 審査員:中村 隆志,神田 学,木内 豪,高木 泰士,中村 恭志
Citation(English)	Degree:Doctor (Engineering), Conferring organization: Tokyo Institute of Technology, Report number:乙第4197号, Conferred date:2024/2/29, Degree Type:Thesis doctor, Examiner:,,,,
学位種別(和文)	博士論文
Type(English)	Doctoral Thesis

Modeling Ecological and Physical Processes in Blue Carbon Ecosystems: Biomass Dynamics and Hydrodynamics-Sediment Transport

A Dissertation Submitted to Tokyo Institute of Technology
In Partial Fulfillment of the Requirements for the Degree of
Doctor of Philosophy by Publication (“RONPAKU”)

Masaya Yoshikai

September 2023

Abstract

This thesis presents modeling works on biomass dynamics and hydrodynamics-sediment transport in blue carbon ecosystems with a specific focus on seagrass meadows and mangrove forests. Chapters 2–3 introduce innovative models for the biomass dynamics of seagrass meadows and mangrove forests. Chapters 4–6 investigate the complex flow-vegetation interactions in mangrove forests, and integrate the impact of mangroves on flow in a hydrodynamic model. Chapters 7–8 present case studies that apply the developed hydrodynamic model and highlight the vital role of mangrove forests in retaining sediments and soil organic carbon. Overall, this thesis advances our understanding of the ecological and physical processes governing blue carbon dynamics, providing a solid foundation for modeling the blue carbon dynamics under the impacts of climate change.

Summary

Blue carbon ecosystems, including mangrove forests, seagrass meadows, and salt marshes, are coastal vegetation ecosystems renowned for their remarkable capacity to sequester carbon. They store a large amount of carbon, often referred to as “blue carbon”, particularly in their soil. Carbon sequestration in the soil of these ecosystems is governed by two key processes – the internal supply of organic carbon through biomass production and turnover (the “ecological process”), and trapping of particulate organic carbon hydrodynamically transported from external systems via fluvial and tidal processes (the “physical process”). However, our understanding of these processes is limited, which hampers our understanding of the dynamics of blue carbon under the impact of climate change. This thesis focuses on modeling biomass dynamics and hydrodynamics-sediment transport particularly in seagrass meadows and mangrove forests towards a better understanding of the ecological and physical processes shaping the blue carbon dynamics.

Chapters 2–3 address a better understanding of biomass dynamics of seagrass meadows and mangrove forests. Chapter 2 presents a new seagrass growth model driven by a coupled hydrodynamic-biogeochemical model. This model is applied to a seagrass meadow in the Philippines, which has been impacted by the unregulated mariculture activities in adjacent areas. The model successfully reproduces the distribution of above-ground seagrass biomass for two co-existing species. It highlights the impact of high nutrient loads on underwater light and seagrass growth rates and a potential of recovery of seagrass meadows through mariculture regulation. In Chapter 3, a new mangrove growth model is developed and applied to a mangrove forest in Japan. This model incorporates a plant hydraulic module to consider the soil salinity control on plant water uptake and its linkage to photosynthesis and nutrient uptake. The model shows a remarkable performance in predicting the patterns in forest structures composed of two co-existing species across the soil salinity gradient. It unveils the roles of salinity and tree competition in shaping the forest structures, and identifies crucial plant traits.

Chapters 4–6 address a better understanding of hydrodynamics-sediment transport in mangrove forests, with a specific focus on the flow-vegetation interaction of *Rhizophora* mangroves, characterized by their complicated above-ground root structures (prop root systems). Chapter 4 extensively investigates the morphological structures of the prop root systems by collecting data from 156 trees in Indonesia, the Philippines, and Japan. This research establishes an allometric relationship between root structures and stem diameter and develops an empirical model for predicting *Rhizophora* root structures, demonstrating an excellent fit with the collected data. In Chapter 5, a detailed measurement of hydrodynamics

in a planted *Rhizophora* mangrove forest is presented. This includes quantifying the drag force exerted by the mangroves and estimating the drag coefficient of *Rhizophora* mangroves in the field for the first time. This research demonstrates a reasonable prediction of drag using the obtained drag coefficient and the empirical *Rhizophora* root model. Chapter 6 formulates and implements the impact of *Rhizophora* mangroves on flow in a hydrodynamic model. It incorporates the empirical *Rhizophora* root model, which enables the forest-scale simulation of hydrodynamics without rigorous measurements of root structures. The model's reasonable performance in predicting mean flow and turbulence in *Rhizophora* mangrove forests is verified using data from previous studies.

Chapters 7–8 feature two case studies applying the developed hydrodynamic model to investigate sediment transport processes in mangrove forests. In Chapter 7, the model is applied to a riverine mangrove forest in the Philippines. The results reveal that the increased hydraulic resistance of the mangrove forest significantly attenuates flow within the forest, leading to retention of sediments. When the effect of mangroves on flow is deactivated in the model, a substantial loss of sediments occurs due to soil erosion. Chapter 8 extends the model to consider the effect of mangroves on wave damping. It assesses the impact of typhoon events on sediment loss in a mangrove forest. The model demonstrate that mangroves effectively dissipate wave energy, regulating sediment loss. It also suggests that as typhoon intensity rises, sediment loss increases nonlinearly. However, the loss of mangroves has a far more significant impact on sediment erosion than an increase in typhoon intensity. These results underscore the vital role of mangrove forests in retaining sediments and thus soil organic carbon. Altogether, this thesis advances our understanding of ecological and physical processes in blue carbon ecosystems, providing a solid foundation for modeling the blue carbon dynamics under the impacts of climate change.

Acknowledgements

First of all, I would like to express my sincere appreciation to my advisor Prof. Kazuo Nadaoka for his continuous support and encouragement on this study. I am very grateful for him offering an opportunity to pursue research life through being a researcher in the BlueCARES Project. Though it has been hard to complete the requirement of the PhD degree by publications, I appreciate this long-term period that I could devote myself to research and develop my skill and interests. I feel very lucky for this. I especially appreciate his mind of involving people in research. I was able to meet many people and learn many things because of it.

I also deeply thank Dr. Takashi Nakamura for supporting and encouraging my study. He has always given me inspiration and guided me to the right direction when I felt lost along the way in the study. Due to his diverse expertise, he served as my role model of an excellent researcher. He has taught me how to model the environment and ecosystems as well as the spirit of being a modeler. I am confident as a modeler and as a researcher because of my advisors.

I owe a special thanks to my collaborators especially of BlueCARES Project. To mention a few, I have been fortunate to work with Dr. Rempei Suwa and Dr. Raghab Ray. Having many fieldworks and discussion with them expanded my interests and perspective in ecology and biogeochemistry in mangrove ecosystems aside from physical aspects. I thank Dr. Ariel Blanco and Dr. Eugene Herrera for their support on the fieldworks and modeling works and for their friendship. I also thank my collaborators/friends of the Japan, Philippines, Indonesia, Malaysia, and the UK. I really hope to continue the collaboration with them.

I thank the former members of Nadaoka Laboratory and the former and the present members of Nakamura Laboratory.

Thank you, Dr. Charissa Ferrera, for your support.

Finally, I would like to thank Dr. Julia Mullarney for generaously offering me a position as a postdoctoral research fellow and to continue doing research on what I am interested in together with great researchers, even though I have not been conferred with the PhD degree yet.

Thank you very much. Cheers.

Table of Contents

List of Figures

List of Tables

Chapter 1: General introduction

Mangrove forests, seagrass meadows, and salt marshes are vegetation habitats that grow in coastal wetlands. Mangroves are woody plants that grow in intertidal areas in tropical and subtropical regions. Seagrasses are grass-type plants that can be found in shallow coastal areas in temperate to tropical regions. Salt marshes are also grass-type plants but grow in intertidal areas in temperate regions. These vegetation habitats are known to store a large amount of organic carbon in their biomass and/or in their soil, called “blue carbon”, and are therefore often referred to as “blue carbon ecosystems” (Nellemann et al., 2009). Blue carbon ecosystems show high carbon sequestration rate, especially in their soil, more than other ecosystems (Fig. 1.1). They have been thus gaining significant attentions in terms of global warming mitigation (Donato et al., 2011; Fourqurean et al., 2012; Taillardat et al., 2018; Temmink et al., 2022). The frequent or constant inundation of their soil by tides regulates microbial activities to decompose organic matters. This partially explains why the soil of blue carbon ecosystems are efficient in sequestrating organic carbon and can show large carbon stock in their soil in disproportional to their biomass amount.

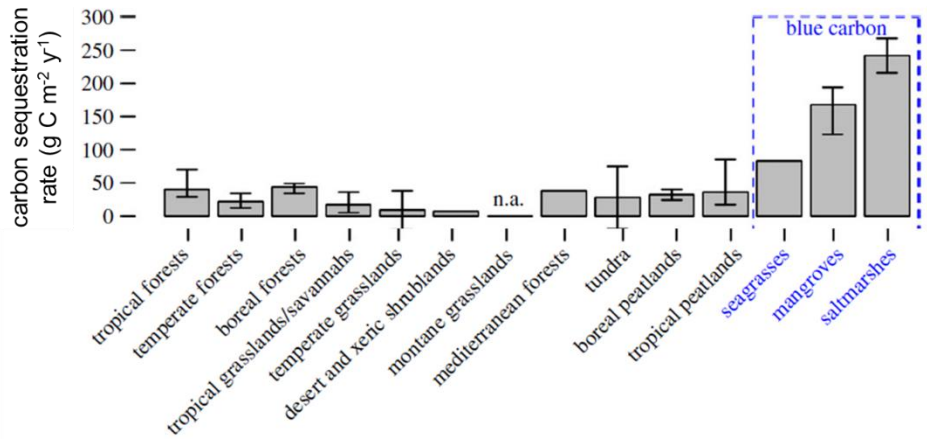

Figure 1.1. Compilation of carbon sequestration rate in various ecosystems by Taillardat et al. (2018). The figure is adapted from Taillardat et al. (2018).

There are two major sources of organic carbon stored in the soil of the blue carbon ecosystems – autochthonous carbon and allochthonous carbon (Woodroffe et al., 2016). The autochthonous carbon refers to the carbon internally produced in the blue carbon ecosystems and then being stored in the soil. We call the process of autochthonous carbon sequestration as “biological feedback” of the blue carbon ecosystems. On the other hand, the allochthonous carbon refers to the carbon externally derived and transported to the soil of blue carbon ecosystems by water flow through the continuum of terrestrial-river-ocean. We call the process

of allochthonous carbon sequestration as “biogeomorphic feedback” of the blue carbon ecosystems. Several studies have shown that the allochthonous carbon can account for a significant fraction of the total carbon stored in the blue carbon ecosystems (Sasmito et al., 2020; Suello et al., 2022; Temmink et al., 2022; Fig. 1.2). The presence of biogeomorphic feedback in addition to the biological feedback explains why blue carbon ecosystems exhibit the highest sequestration rates among ecosystems (Temmink et al., 2022).

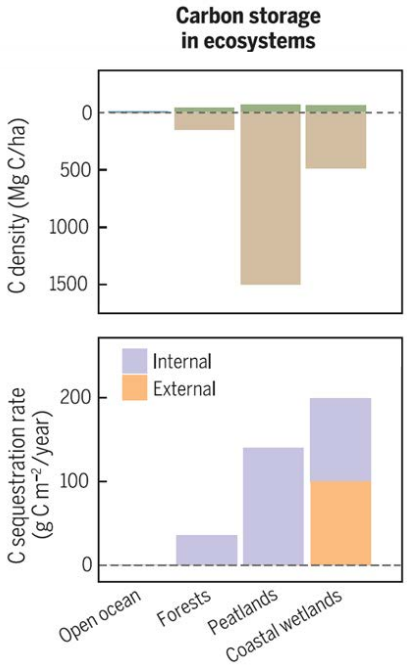

Figure 1.2. Compilation of carbon density and sequestration rate in the world’s major carbon-storing ecosystems by Temmink et al. (2022). The figure is adapted from Temmink et al. (2022).

The biological feedback occurs through the supply of biomass products of blue carbon ecosystems to their soil which involves the processes such as photosynthesis, biomass production, litterfall, and fine root turnover. Figure 1.3 shows an example of a compilation of global data on the major carbon pathways in mangrove forests by Alongi (2014). While the study unraveled how the biological feedback drives carbon sequestration in mangrove forests, there still is a significant knowledge gap on how the environmental stresses could affect these pathways. This gap leads to the significant uncertainty in the estimation of the future carbon pathways in mangrove forests under climate change. This knowledge gap also applies to the seagrass meadows and salt marshes. In order to understand the impact of climate change on the dynamics of blue carbon, first we need to understand the response of the blue carbon ecosystems’ biomass dynamics to environmental stresses.

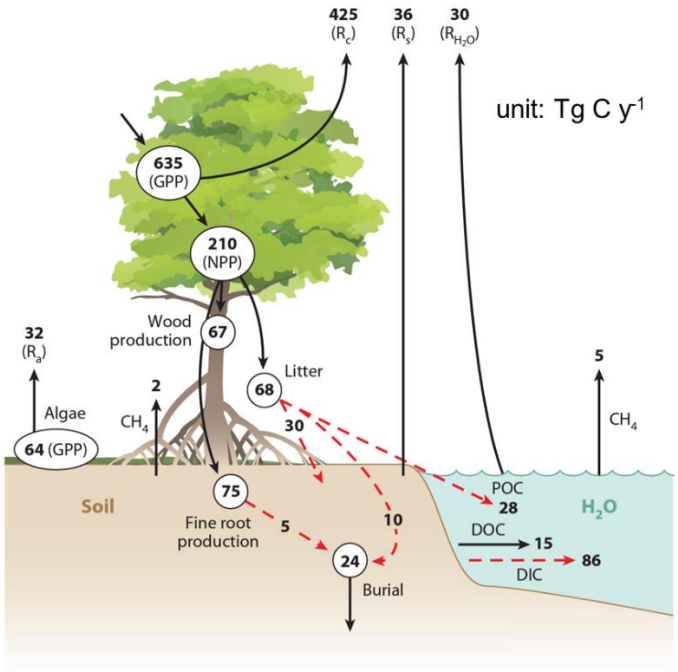

Figure 1.3. Compilation of the major pathways of carbon flow through the world's mangrove ecosystems by Alongi (2014). The figure is adapted from Alongi (2014).

The biogeomorphic feedback occurs largely due to the flow-vegetation interaction. The coastal vegetation habitats slow down the water flow and attenuate waves by exerting drag force (Mazda et al., 1997; Nepf, 1999; Temmerman et al., 2005). This creates conditions preferable for sediment deposition and retention, which is otherwise resuspended and flowed away (Xu et al., 2022; Fig. 1.4). This process is sometimes called "sediment trapping". By promoting sedimentation, the blue carbon ecosystems affect landforms in a long-term (and thus referred to as "biogeomorphic feedback"). Some of the suspended sediments transported to the blue carbon ecosystems are in the form of particulate organic carbon originated from external systems – allochthonous carbon, which may significantly contribute to the carbon sequestration function of the blue carbon ecosystems (Temmink et al., 2022). However, the insights into the biogeomorphic feedback are largely limited. This can be inferred from Fig. 1.3 of the compilation of the major carbon pathways in mangrove ecosystems by Alongi (2014) which lacks the information on carbon flux transported from external systems through the hydrodynamics. In order to understand how the biogeomorphic feedback controls the carbon sequestration in the blue carbon ecosystems, first we need to understand the hydrodynamics-sediment transport in the blue carbon ecosystems.

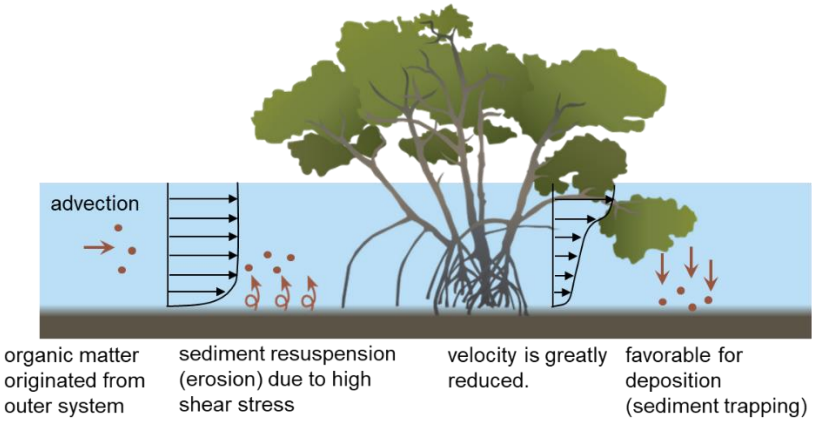

Figure 1.4. Schematic of flow-vegetation interaction promoting sedimentation in a mangrove forest.

Based on the above-mentioned knowledge gap on the biological feedback and biogeomorphic feedback in the blue carbon dynamics, this study aims to better understand the biomass dynamics and the hydrodynamics-sediment transport in the blue carbon ecosystems. These results would take a step forward in our understanding of blue carbon sequestration rate and its dynamics. This study was conducted as a part of a project "Comprehensive Assessment and Conservation of Blue Carbon Ecosystems and Their Services in the Coral Triangle (Blue CARES)" led by Prof. Kazuo Nadaoka (Tokyo Institute of Technology) in collaboration with the Philippines and Indonesia counterparts. Due to the absence of salt marshes in the study sites of the project, this study focusses on the seagrass meadows and mangrove forests only. This study specifically aims at modeling of the biomass dynamics and hydrodynamics-sediment transport – an ecological and physical process controlling the blue carbon dynamics. These models would serve as a first step in developing an integrated and comprehensive blue carbon dynamics model which can be used to predict how blue carbon dynamics responds to the stressors such as climate change and human activities (e.g., land conversion).

This study is presented as follows. In Chapter 2 and 3, the novel models for biomass dynamics of seagrass meadows and mangrove forests are presented, respectively, for a better understanding of the biological feedback (Fig. 1.5). For biogeomorphic feedback, however, hydrodynamics and sediment transport in seagrass meadows have already been investigated by many studies (e.g., Nepf, 1999; Lightbody & Nepf, 2006; Hansen & Reidenbach, 2017; Zhu et al., 2021) and the models have been established (e.g., Temmerman et al., 2005; Marsooli et al., 2016; Nardin et al., 2016; Beudin et al., 2017). In contrast, the hydrodynamics and sediment transport in mangrove forests have been relatively unexplored. Specifically, the insights into the hydrodynamics-sediment transport in *Rhizophora* mangrove forests, one of the most dominant mangrove genera in the world (Friess et al., 2019), are largely limited. This

is mainly because of the lack of insights into the complex structures of the above-ground root systems and their impacts on hydrodynamics. Consequently, no model has been established yet to predict the hydrodynamics in *Rhizophora* mangrove forests. Therefore, the following chapters (Chapter 4–6) are dedicated to the modeling of hydrodynamics in the *Rhizophora* mangroves. Specifically, in Chapter 4, modeling of the above-ground root system structures is addressed, and in Chapter 5, results from a detailed field measurement of flow in a *Rhizophora* mangrove forest is presented (Fig. 1.5). Then, in Chapter 6, a novel hydrodynamic model incorporating the impacts of *Rhizophora* mangroves on flow is presented by implementing the insights obtained from Chapter 4 and 5. After that, two examples of the application of the developed model for the hydrodynamics and sediment transport in mangrove forests are presented in Chapter 7 and 8. Finally, a summary of the insights obtained from this study is presented in Chapter 9.

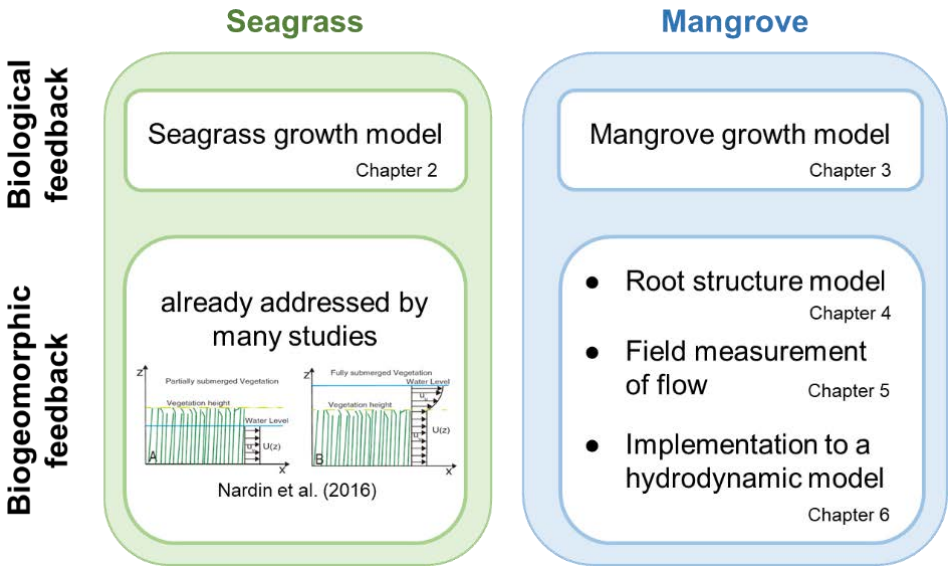

Figure 1.5. Diagram of the contents of Chapter 2–6 addressing the modeling of biological feedback and biogeomorphic feedback in seagrass meadows and mangrove forests.

1.1 References

Alongi, D. M. (2014). Carbon cycling and storage in mangrove forests. Annual review of marine science, 6, 195-219. https://doi.org/10.1146/annurev-marine-010213-135020.

Beudin, A., Kalra, T. S., Ganju, N. K., & Warner, J. C. (2017). Development of a coupled wave-flow-vegetation interaction model. Computers & Geosciences, 100, 76–86. https://doi.org/10.1016/j.cageo.2016.12.010.

Donato, D. C., Kauffman, J. B., Murdiyarso, D., Kurnianto, S., Stidham, M., & Kanninen, M. (2011). Mangroves among the most carbon-rich forests in the tropics. Nature geoscience, 4(5), 293-297. https://doi.org/10.1038/ngeo1123.

Fourqurean, J. W., Duarte, C. M., Kennedy, H., Marbà, N., Holmer, M., Mateo, M. A., ... & Serrano, O. (2012). Seagrass ecosystems as a globally significant carbon stock. Nature geoscience, 5(7), 505-509. https://doi.org/10.1038/ngeo1477.

Friess, D. A., Rogers, K., Lovelock, C. E., Krauss, K. W., Hamilton, S. E., Lee, S. Y., ... & Shi, S. (2019). The state of the world's mangrove forests: past, present, and future. Annu. Rev. Environ. Resour, 44(1), 89–115. https://doi.org/10.1146/annurev-environ-101718-033302.

Hansen, J. C., & Reidenbach, M. A. (2017). Turbulent mixing and fluid transport within Florida Bay seagrass meadows. Advances in Water Resources, 108, 205-215. https://doi.org/10.1016/j.advwatres.2017.08.001.

Lightbody, A. F., & Nepf, H. M. (2006). Prediction of velocity profiles and longitudinal dispersion in salt marsh vegetation. Limnology and oceanography, 51(1), 218–228. https://doi.org/10.4319/lo.2006.51.1.0218.

Marsooli, R., Orton, P. M., Georgas, N., & Blumberg, A. F. (2016). Three-dimensional hydrodynamic modeling of coastal flood mitigation by wetlands. Coastal Engineering, 111, 83–94. https://doi.org/10.1016/j.coastaleng.2016.01.012.

Mazda, Y., Wolanski, E., King, B., Sase, A., Ohtsuka, D., & Magi, M. (1997). Drag force due to vegetation in mangrove swamps. Mangroves and salt marshes, 1, 193-199. https://doi.org/10.1023/A:1009949411068.

Nardin, W., Edmonds, D. A., & Fagherazzi, S. (2016). Influence of vegetation on spatial patterns of sediment deposition in deltaic islands during flood. Advances in Water Resources, 93, 236–248. https://doi.org/10.1016/j.advwatres.2016.01.001.

Nellemann, C., Corcoran, E., Duarte, C. M., Valdés, L., De Young, C., Fonseca, L., and Grimsditch, G. (2009) :Bluecarbon: a rapid response assessment, United Nations Environment Programme, GRID-Arendal, ISBN978-82-7701-060-1.

Nepf, H. M. (1999). Drag, turbulence, and diffusion in flow through emergent vegetation. Water resources research, 35(2), 479–489. https://doi.org/10.1029/1998WR900069.

Sasmito, S. D., Kuzyakov, Y., Lubis, A. A., Murdiyarso, D., Hutley, L. B., Bachri, S., ... & Borchard, N. (2020). Organic carbon burial and sources in soils of coastal mudflat and mangrove ecosystems. Catena, 187, 104414. https://doi.org/10.1016/j.catena.2019.104414.

Suello, R. H., Hernandez, S. L., Bouillon, S., Belliard, J. P., Dominguez-Granda, L., Van de Broek, M., ... & Temmerman, S. (2022). Mangrove sediment organic carbon storage

and sources in relation to forest age and position along a deltaic salinity gradient. Biogeosciences, 19(5), 1571–1585. https://doi.org/10.5194/bg-19-1571-2022.

Taillardat, P., Friess, D. A., & Lupascu, M. (2018). Mangrove blue carbon strategies for climate change mitigation are most effective at the national scale. Biology letters, 14(10), 20180251. https://doi.org/10.1098/rsbl.2018.0251.

Temmerman, S., Bouma, T. J., Govers, G., Wang, Z. B., De Vries, M. B., & Herman, P. M. J. (2005). Impact of vegetation on flow routing and sedimentation patterns: Three-dimensional modeling for a tidal marsh. Journal of Geophysical Research: Earth Surface, 110(F4). https://doi.org/10.1029/2005JF000301.

Temmink, R. J., Lamers, L. P., Angelini, C., Bouma, T. J., Fritz, C., van de Koppel, J., ... & van der Heide, T. (2022). Recovering wetland biogeomorphic feedbacks to restore the world's biotic carbon hotspots. Science, 376(6593), eabn1479. https://doi.org/10.1126/science.abn1479.

Woodroffe, C. D., Rogers, K., McKee, K. L., Lovelock, C. E., Mendelssohn, I. A., & Saintilan, N. 529 (2016). Mangrove Sedimentation and Response to Relative Sea-Level Rise. Annual Review of 530 Marine Science, 8(1), 243–266. https://doi.org/10.1146/annurev-marine-122414-034025.

Xu, Y., Esposito, C. R., Beltrán-Burgos, M., & Nepf, H. M. (2022). Competing effects of vegetation density on sedimentation in deltaic marshes. Nature communications, 13(1), 1–10. https://doi.org/10.1038/s41467-022-32270-8.

Zhu, Q., Wiberg, P. L., & Reidenbach, M. A. (2021). Quantifying Seasonal Seagrass Effects on Flow and Sediment Dynamics in a Back-Barrier Bay. Journal of Geophysical Research: Oceans, 126(2), e2020JC016547. https://doi.org/10.1029/2020JC016547.

Chapter 2: Modeling seagrass bed dynamics under environmental impacts of intensive mariculture activities in Bolinao and Anda, the Philippines

2.1.1 Abstract

This study assessed the estuarine-scale dynamics of mixed seagrass beds in Bolinao and Anda coastal areas in the Philippines, where seagrass beds have declined primarily due to eutrophication-induced degradation of light environment caused by unregulated mariculture activities in the adjacent areas. A seagrass model, driven by a coupled hydrodynamic-biogeochemical model, was developed and applied to the two-dominant species in the area – *Thalassia hemprichii* and *Enhalus acoroides*, and validated using observed spatial seagrass shoot density. The results showed the degradation of light environment in the seagrass beds, especially near mariculture areas, due to advective fluxes of water with high phytoplankton biomass and high nutrients from fish farms. The seagrass model driven by the reproduced water quality showed high reproducibility of seagrass above-ground biomass distribution of the two co-existing species, with R^2 values of 0.78 and 0.60 for *T. hemprichii* and *E. acoroides*, respectively. Scenario analysis was conducted to examine the effectiveness of individual- and inter-municipality mariculture management (e.g., regulating fish feed input) in improving the light environment and facilitating the recovery of seagrasses. Results showed that the light environment could be significantly enhanced by an inter-municipality scheme compared to individual efforts of Bolinao and Anda municipalities, since their waters are interconnected through hydrodynamics. In conjunction with the improvement of light conditions, the recovery in seagrass abundance is most significant under the cooperative management scheme, thus highlighting its effectiveness.

2.1.2 Introduction

Seagrasses are known to be highly productive plants (Duarte et al., 2010). They provide

a wide range of ecosystem services such as nursery grounds for many juvenile fishes and invertebrates, thus supporting fishery production (Bertelli and Unsworth, 2014; Unsworth et al., 2018), and as a major sink of atmospheric CO_2 to mitigate global warming (Nellemann et al., 2009; Fourqurean et al., 2012). However, seagrasses have been in decline worldwide, with their disappearance recently accelerating at a rate of 110 km^2 yr^{-1} due to increased anthropogenic pressures (Waycott et al., 2009). Eutrophication and sediment loading as well as coastal development are typically the most common and significant causes of seagrass decline (Orth et al., 2006; Burkholder et al., 2007; Brun et al., 2008; Waycott et al., 2009; Govers et al., 2014; Evans et al., 2018). As a result, there are increases in phytoplankton biomass and suspended solids in the water, and epiphyte biomass on seagrass leaves (Dennison et al., 1993; Ralph et al., 2007). This increase in particulate matter leads to a reduction of light availability – the most critical water quality parameter for seagrass growth (Waycott et al., 2005; Collier et al., 2012). However, as shown by the cases in Europe, seagrass ecosystems may recover after implementing management actions to improve water quality conditions (de los Santos et al., 2019). The need to take such countermeasures for seagrass ecosystem conservation is especially urgent in Southeast Asian coasts where seagrass species diversity is the highest in the world (Short et al., 2011), and where many local communities rely directly on coastal resources for their food and livelihood (Añabieza et al., 2010; Cruz-Trinidad et al., 2011; Quiros et al., 2018). This region, unfortunately, is also where many seagrass habitats face threats from rapid coastal development.

Seagrass habitats along the coasts of the municipalities of Bolinao and Anda in the northwest Philippines also experience the said stressors brought about by coastal development. Bolinao and Anda waters are characterized by two distinct features: a reef area and a mariculture area (Fig. 2.1). Extensive and abundant mixed seagrass beds with high species richness are located in the reef area (Varmaat et al., 1995; Bach et al., 1998). On the other hand, the mariculture area is known as one of the most intensive milkfish (*Chanos chanos*) culture production in the country, which started in 1995 (Verceles et al., 2000). The mariculture industry is operated by the local government of Bolinao and Anda, with the total number of fish-rearing structures at 351 and 588 in January 2014, respectively (Ferrera et al., 2016; Fig. 2.1d), and where the mean sizes of fish pens and cages are 5280 and 310 m^2, correspondingly. Uneaten feeds and fish excretions attributed to intensive fish feeding in a large number of fish-rearing structures have resulted in sediments enriched in organic matter (Holmer et al., 2002, 2003). Nutrient inputs due to decomposition of organic matter led to eutrophic waters, red tides, and hypoxia in this area (Ferrera et al., 2016). This degradation of water quality has resulted in the recurrence of fish kills (San Diego-McGlone et al., 2008; Escobar et al., 2013). The eutrophic waters have also affected the adjacent mixed seagrass bed ecosystem to some extent. Tanaka et al. (2014) studied the recent state of water quality

and seagrass bed conditions at four sites and compared with data from 1995 (Bach et al., 1998) when mariculture has just started (Fig. 2.1c). They found increases in chlorophyll-a (Chl-a) by a factor of 8 to 17, and the associated reduction in underwater light at three sites located adjacent or inside the mariculture area (Sites 2, 3, and 4 in Tanaka et al. (2014); Fig. 2.1d). The seagrass species richness has drastically deteriorated at the three sites. Specifically, seagrasses disappeared at a site in the mariculture area (Site 4 in Tanaka et al. (2014); Fig. 2.1d) where seagrasses used to be present in 1995 (Bach et al., 1998). Macrofaunal communities and bivalves in seagrass beds have also been affected relative to their distance from the mariculture area (Leopardas et al., 2016; Morimoto et al., 2017). These studies highlight the need for regulation in order to achieve sustainable mariculture as suggested by several studies (Yap et al., 2004; Azanza et al., 2005; San Diego-McGlone et al., 2008; Gecek and Legovic, 2010; Escobar et al., 2013; Ferrera et al., 2016), and to prevent further degradation and promote restoration of seagrass beds. However, previous assessments of mariculture impacts on seagrasses in the area were limited to a few sites (Tanaka et al., 2014; Leopardas et al., 2016). Thus, significant gaps in our knowledge on estuarine-scale assessment remain, including the extent to which eutrophic waters from mariculture activities spread over seagrass beds through hydrodynamic processes, and how these eutrophic waters have negatively impacted the seagrasses.

Seagrasses are subject to environmental variables that vary in space and time. The response of coastal ecosystems to environmental variables are usually nonlinear, and current conditions of an ecosystem may be the cumulative result of its sequential responses to the environment. Therefore, an estuarine-scale assessment of seagrass bed dynamics requires information of seagrass abundance with time-series data of environmental variables at many points covering wide area of the seagrass bed, as well as data from the source of pollution such as a mariculture area. However, it is difficult to obtain such data through discrete field surveys only. A way to address this difficulty is through the development of a numerical simulation model that can explicitly reproduce the spatiotemporal dynamics of environmental variables and ecosystem responses (Nakamura et al., 2018). Several seagrass models have been proposed to simulate biological processes such as photosynthesis and respiration according to environmental variables including light, nutrient concentrations, and water temperature (Verhagen and Nienhuis, 1983; Bach, 1993; Bocci et al., 1997; Cerco and Moore, 2001; Elkalay et al., 2003; Plus et al., 2003; Carr et al., 2012; Baird et al., 2016). However, most of the modeling studies have focused on seasonal dynamics of seagrasses in the temperate region (Verhagen and Nienhuis, 1983; Bach, 1993; Bocchi et al., 1997; Elkalay et al., 2003; Plus et al., 2003; Carr et al., 2012). Studies to assess seagrass responses to anthropogenic impacts in an estuarine-scale are limited (Cerco and Moore, 2001; Baird et al., 2016). In addition, most of the existing seagrass models have been limited to mono-specific

seagrass beds application, thus, they do not account for interspecies competition for light, which may be important in mixed seagrass beds (Williams, 1987; Duarte et al., 2000) like in the case for Bolinao and Anda. Only Baird et al. (2016) developed a model for the assessment of an estuarine-scale dynamics of a mixed seagrass bed with two species by taking account of the shading effects of taller canopy species on the shorter canopy species. However, the accuracy of the spatial distribution of seagrass biomass was somewhat low, probably due to the low accuracy of the reproduced environmental variables by the hydrodynamic-biogeochemical model. Thus, to our knowledge, an estuarine-scale assessment of anthropogenic impacts on mixed seagrass bed dynamics has not been achieved.

In this study, we aimed at an estuarine-scale assessment of the dynamics of two dominant seagrass species – *Thalassia hemprichii* and *Enhalus acoroides* – through the development of a hydrodynamic-biogeochemical model and a seagrass model for a mixed seagrass bed in Bolinao and Anda coastal areas, which have been exposed to anthropogenic impacts due to mariculture. Unlike in Baird et al. (2016), the seagrass canopy compartment in the water was partitioned to multiple layers, and irradiance and photosynthetic rate of each species were calculated at each canopy layer. This approach makes it possible to compute the seagrass production rate of each species influenced by shading effects in mixed seagrass beds with more than two coexisting species, an approach necessary to assess the dynamics of seagrass species richness. With the developed model, we focused particularly on reproducing eutrophication and the associated light reduction underwater, and on assessing the dynamics of seagrass abundance under the reproduced environmental conditions. We also examined the effectiveness of individual- and inter-municipality mariculture management for improving the light environment and facilitating the recovery of seagrasses.

2.2 Materials and Methods

2.2.1 Study site

Our study sites are the Bolinao and Anda coastal areas located in Lingayen Gulf in the northwest Philippines (Fig. 2.1a, b). Here, most seagrasses are found in the reef area located around Santiago Island (Fig. 2.1c). Among the stations used by Tanaka et al. (2014) (Fig. 2.1c), Site 1 is still pristine and has high species richness, while the seagrass beds at Sites 2 and 3 have declined since the introduction of intensive milkfish mariculture in 1995. No seagrass was seen in Site 4 where seagrass beds were observed in 1995 (Tanaka et al., 2014). *T. hemprichii* and *E. acoroides* are the two dominant seagrass species in the area (Vermaat et al., 1995; Tanaka et al., 2014), which was also seen in other mixed seagrass beds

in Southeast Asia (Vermaat et al., 1995). These species are characterized by their larger shoots and higher longevity than other seagrass species (Duarte 1991; Vermaat et al., 1995). Specifically, *E. acoroides* has the largest leaves among tropical seagrasses (100.78 cm^2 of leaf surface on average: Duarte 1991), which gives this species an advantage in terms of light acquisition (Vermaat et al., 1995).

The mariculture area in Bolinao and Anda is found in a shallow enclosed bay connected to the outer sea in the north and Tambac Bay in the south via small channels (Fig. 2.1c, d). Mariculture of milkfish is done using fish cages placed in areas where water depth is >8 m, and fish pens where depth is shallower (<4 m) (Ferrera et al., 2016).

The spatial gradient in light attenuation seen in 1995 was attributed to siltation mainly from the rivers in Tambac Bay (Bach et al., 1998). Upon comparison of water quality between 1995 and 2012 at the four sites in Bach et al. (1998) and Tanaka et al. (2014), respectively, the particulate inorganic matter (PIM) concentrations were significantly lower in 2012. However, light attenuation was higher in 2012 at sites located adjacent to or inside the mariculture area due to increased levels of particulate organic matter (POM) and Chl-a (Tanaka et al., 2014).

The study area has two pronounced seasons – a wet season and a dry season. The wet season occurs from June to September and is characterized by heavy rainfall and a prevailing southwest wind, while the dry season is from November to March and is characterized by less precipitation and a prevailing northeast wind. Two major rivers – Bani River and Alaminos River with 17,000 ha and 21,100 ha of watershed areas, respectively, flow into Tambac Bay, supplying a large amount of freshwater, especially during the wet season.

The tides in this area are mixed and mainly diurnal, and the range is up to around 1.1 m. The tides provide the main circulation force in the area (Gecek and Legovic 2010).

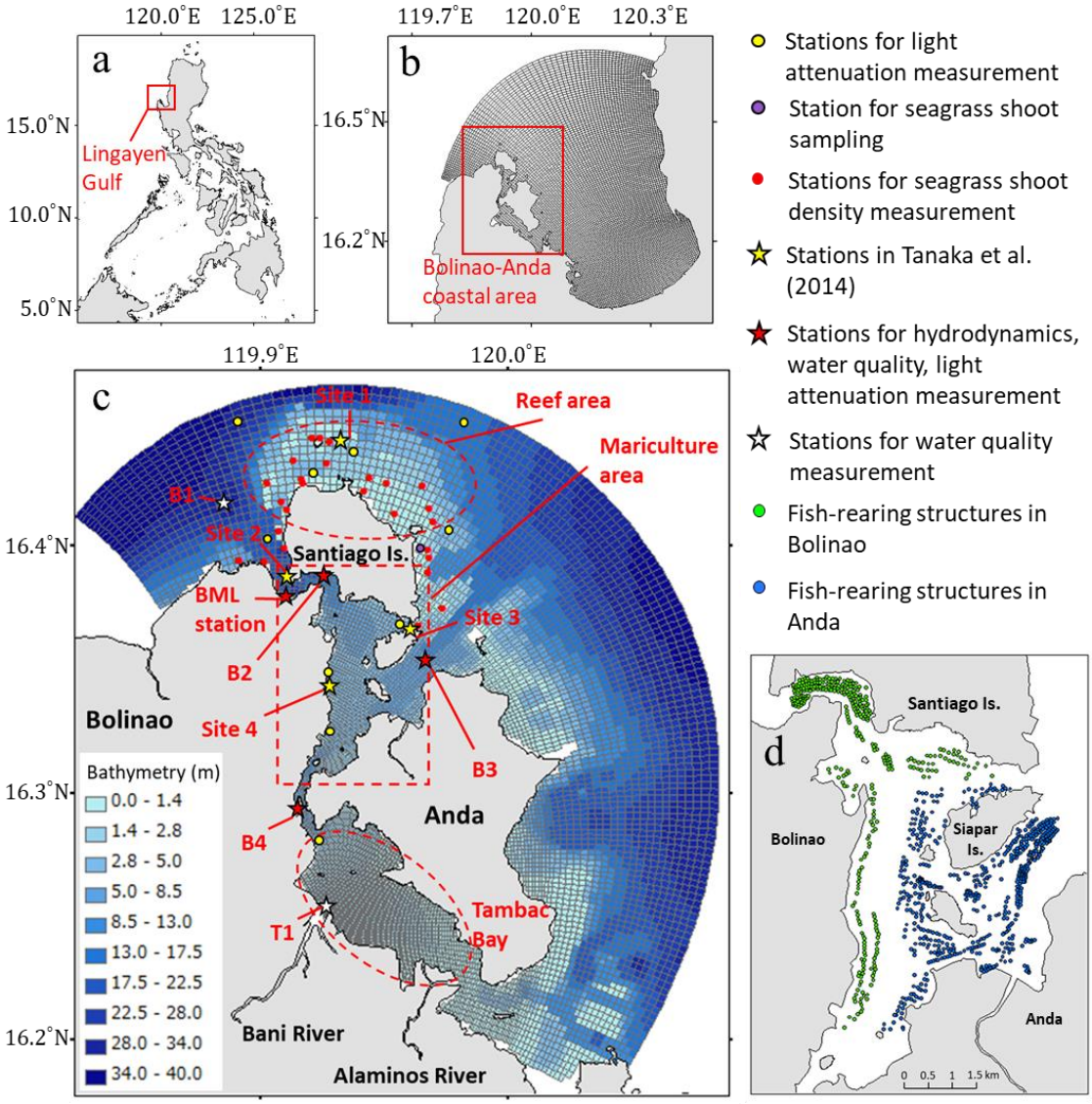

Figure 2.1. (a) Location of Lingayen Gulf, (b) computational domain for the gulf-scale hydrodynamic model, (c) the Bolinao-Anda coastal area – computational domain for the coupled hydrodynamic-biogeochemical model and seagrass model, stations for field surveys, and stations in Tanaka et al. (2014), (d) location of fish-rearing structures of Bolinao and Anda, based on Ferrera et al. (2016). The "B" stations arbitrarily refer to the stations in Bolinao, the "T" station pertains to the station in Tambac Bay, and the "BML" station indicates the station in front of Bolinao Marine Laboratory (BML). The coordinates of the stations are provided in Table S2.1.

2.2.2 Field surveys

2.2.2.1 Estimation of light attenuation coefficient

Vertical profiling of down-welling photosynthetically active radiation (PAR) and chlorophyll-a (Chl-a) was done using a water quality profiler (AAQ-RINKO, JFE-Advantech, Japan). Surface water was sampled in the Bolinao and Anda coastal area for suspended solids (SS) using a Niskin water sampler in September 2014. The stations where measurements were taken included the mariculture area, reef area, and outer sea to capture a wide range of water quality conditions (Fig. 2.1c). Light attenuation coefficient (k_d; m^{-1}) values at the near-surface water were estimated based on light attenuation from the water surface to a depth of 1 m using the following model (Dennison et al., 1993):

$$k_d = \frac{\ln(E_0/E_z)}{z} \quad (2.1)$$

where E_z is the down-welling PAR (μmol photons m^{-2} s^{-1}) at depth z (m), and E_0 is the down-welling PAR just below the sea surface.

Water samples for SS were immediately filtered through pre-weighed 47 mm glass fiber filters (GF/F, Whatman GE Healthcare Life Sciences, England). The filters were rinsed with distilled water to remove salts. Upon returning to the laboratory, the filters were dried in an oven at 80 °C for 24 h and weighed to obtain their dry weight. SS concentrations were determined using the dry weight of the filtered material divided by the water volume used for filtration.

To characterize k_d from Chl-a and SS in the area, multiple regression was done using k_d as the dependent variable and Chl-a and SS as the independent variables. The empirical model of k_d obtained was then incorporated into a three-dimensional hydrodynamic-biogeochemical model, which is described in the next section.

2.2.2.2 Seagrass shoot sampling and dry weight measurement

Seagrass shoot sampling was conducted in the east coast of Santiago Island in October 2018 (Fig. 2.1c) using a sampling design adapted from Kim et al. (2016). There were fifteen sampling plots with at least 25 m distance between each plot. In one sampling plot, four 0.5 m × 0.5 m quadrats were randomly placed with at least 10 m distance between quadrats. Within a quadrat, two shoots of every species were randomly collected carefully to avoid leaf or tissue loss. In total, 94 and 82 shoot samples were obtained for *T. hemprichii* and *E. acoroides*, respectively. The shoots were then stored in air tight plastic bags and brought to the laboratory. Epiphytes attached to seagrass blades were removed and below-ground tissue was snipped-off. Seagrass shoots were then dried in an oven at 60 °C for 72 hours and weighed to obtain their dry weight. The mean dry weight per shoot was then used to estimate the above-ground biomass of each species from the shoot density data (Tanaka et al., unpublished data) collected extensively in the seagrass beds in Bolinao and Anda (see section 2.2.6).

2.2.2.3 Three-dimensional hydrodynamic-biogeochemical model

A framework for model analysis was established in order to assess the impact of fish food input on seagrass bed ecosystem (Fig. 2.2). A coupled model using Delft3D, a three-dimensional hydrodynamic model (Deltares, 2014a), and Delwaq, a biogeochemical model (Deltares, 2014b), were used to reproduce the circulation of coastal waters and the impacts of fish-food derived waste load on water quality. The computational domain of the model is shown in Fig. 2.1c. The grid has nine vertical layers in the σ-coordinate with non-orthogonal grid in the horizontal plane. The grid resolutions are approximately 150 m in the mariculture area, 80 m in Tambac Bay, and 300 m in the reef area.

The hydrodynamic model was driven by water level at the open boundary, meteorological forcing (e.g., wind, solar radiation, air temperature), and freshwater inputs from the rivers flowing into Tambac Bay, mostly during the wet season. The water level at the boundary was given by offline nesting from a Lingayen Gulf-scale hydrodynamic model (Fig. 2.1b) driven by a global tidal model NAO.99b (Matsumoto et al., 2000). Data for atmospheric conditions were obtained from a weather station installed in the area (16.42877°N, 119.94983°E). For freshwater discharge, assumed values were inputted based on observed hydrodynamic conditions with which the model agreed, in particular for salinity. The validation results of the hydrodynamic model were provided in Fig. S2.3 and Note S.2.2 in the Supplementary Information.

The biogeochemical model was configured to simulate the dynamics of nutrients (nitrate, ammonium, ortho-phosphate, and silicate), phytoplankton, particulate organic matter (POM), particulate inorganic matter (PIM), dissolved organic matter, and dissolved oxygen (DO) (See Note S2.2 for the detailed description). The fish-food derived waste load attributed to uneaten food and fish feces was modeled as POM to be discharged at the surface layer as point sources. Information about the amount of fish food supplied to a fish structure per day was obtained from an interview survey in 2014 with local mariculture farmers as respondents (Table S2.2). Relative nutrient contents of fish food and ratio of waste load to fish food given were determined based on Magdaong (2008) and Holmer et al. (2002) (Table S2.2). The waste load rate at the individual grid cell was then determined by multiplying the waste load rate from a fish-rearing structure and the number of fish-rearing structures in a grid cell, assuming fixed rates of waste load at each fish-rearing structure. Due to lack of available data, a constant concentration of PIM throughout the year was assumed to be discharged from river waters to coastal waters (Table S2.3). The simulated light intensity at the height of the seagrass canopy top was then provided to the multi-layer irradiance distribution model for the

mixed seagrass canopy (Fig. 2.2). The simulated nutrient levels near the bottom of an individual grid cell was provided to the seagrass model as driving factors of seagrass growth (Fig. 2.2). The connections of the hydrodynamic-biogeochemical model with the irradiance distribution model and seagrass growth model were one-way (Fig. 2.2); thus no feedback processes of seagrass nutrient uptake, photosynthesis, respiration, and detritus inputs to water quality were considered in the present modeling framework. The validation results of the biogeochemical model were provided in Fig. S2.4 and Note S2.2.

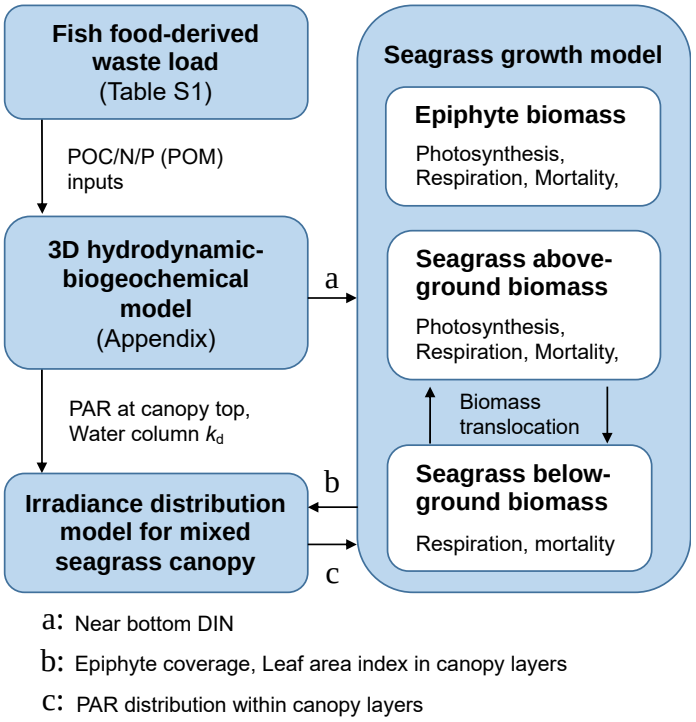

Figure 2.2. Model analysis framework.

2.2.2.4 Seagrass bed dynamics

Aside from light attenuation within the water column, which is a function of water quality, the three-dimensional architecture of seagrass canopy that may significantly influence light environment within canopy (Enriquez and Pantoja-Reyes 2005; Hedley and Enriquez 2010; Hedley et al., 2014) was considered in the model. To compute the species-specific light availability in a mixed seagrass bed with different leaf height among species, a multi-layer irradiance distribution model for mixed seagrass canopy was used, similar to the model of irradiance distribution in Zimmerman (2003) but without considering light scattering.

The change in seagrass biomass was computed using the seagrass growth model (Fig. 2.2) at an hourly time step. The model includes processes such as photosynthesis, respiration, and mortality. The model has three state-variables, these are seagrass above-ground biomass, below-ground biomass, and attached epiphyte biomass for each seagrass species, all

expressed in mmol C m^{-2} ground. The light intensity used for photosynthesis computation is provided by the multi-layer irradiance distribution model. Then the feedback of epiphyte biomass density and leaf area index at each layer is provided to the multi-layer irradiance distribution model for computation of light intensity within the canopy at the next time step. The two dominant species in the area – *T. hemprichii* and *E. acoroides* – were selected as target species to be included in the model. The model computed biomass changes in both species simultaneously. The parameters of the models are summarized in Table 2.1.

Table 2.1. Parameters and values used in the seagrass model. Values in parenthesis indicate the range of literature values.

Symbol	Description	Value		Unit
Seagrass related parameters		*T. hemprichii* (s = 1)	*E. acoroides* (s = 2)	
$Absl_s$	Leaf absorbance of PAR[a]	0.78	0.81	-
$\sin\theta_s$	Sine of leaf bend nadir angle[k]	0.25	0.47	-
$d_{1,s}$	Parameter of shallow water depth effects on mortality[k]	0.0	8.10	-
$d_{2,s}$	Parameter of shallow water depth effects on mortality[k]	0.0	19.16	m^{-1}
$E_{k,s}$	Saturation PAR[b]	180	110	µmol photons m^{-2} s^{-1}
$f_{below,s}$	Fraction biomass below-ground[c]	0.84 (0.62 – 0.93)	0.78 (0.69 – 0.91)	-
$K_{din,s}$	Half saturation concentration of DIN[k]	0.20	0.25	µmol L^{-1}
l_s	Leaf length[d]	0.08	0.5	m
$M_{l,s}$	Mortality rate of above-ground biomass[e]	0.025 (0.0013 – 0.05)	0.0006 (0.0006 – 0.0147)	day^{-1}
$M_{r,s}$	Mortality rate of below-ground biomass[f]	0.0015	0.0006	day^{-1}
$P_{max,s}$	Maximum photosynthetic rate[b]	0.207	0.097	day^{-1}
$R_{l,s}$	Leaf respiration rate[b]	0.028	0.018	day^{-1}
$R_{r,s}$	Root respiration rate[k]	0.003	0.009	day^{-1}
$\tau_{tran,s}$	Translocation rate[k]	0.11	0.03	day^{-1}
Epiphyte related parameters				
A_e	PAR absorption coefficient of epiphytes[h]	0.0015		m^2 $mmol^{-1}$ C
E_{ke}	Saturation PAR for epiphytes[i]	183		µmol photons m^{-2} s^{-1}
$K_{din,e}$	Half saturation concentration of DIN for epiphytes[k]	0.25		µmol L^{-1}
P_{emax}	Maximum photosynthetic rate of epiphytes[j]	0.344		day^{-1}
R_e	Epiphyte respiration rate[j]	0.06		day^{-1}
s_{e1}	Parameter of density saturation limitation for epiphytes	340		mmol C m^{-2}
s_{e2}	Parameter of density saturation limitation for epiphytes[k]	0.1		m^2 $mmol^{-1}$ C

[a] Purvaja et al. (2020)
[b] Agawin et al. (2001)
[c] Calibrated within the range reported by Fortes et al. (2012)
[d] Vermaat et al. (1995)
[e] Calibrated within the range reported by Duarte (1991) and Vermaat et al. (1995)

[f] Duarte (1991)
[g] Estimated from Duarte (1991) and Vermaat et al. (1995)
[h] Bulthuis et al. (1983)
[i] Plus et al. (2003)
[j] Klumpp et al. (1992)
[k] Calibrated

2.2.2.4.1 Multi-layer irradiance distribution model for mixed seagrass canopy

The descriptions on the geometric representation of seagrass leaves, vertical layering of the mixed seagrass canopy for the submerged condition and the partially exposed condition are summarized in the Supplementary Information (Note S2.1). The graphical descriptions are shown in Fig. S2.1. Epiphyte biomass colonizing each species is variable in the canopy layers. Epiphyte biomass density at canopy layer i for a species ($De_{s,i}$, mmol C m^{-2} leaf) is given by

$$De_{s,i} = EB_{s,i}/LAI_{s,i} \quad (2.2)$$

where $EB_{s,i}$ is the epiphyte biomass attached on the leaves of the species at layer i (mmol C m^{-2} ground) and $LAI_{s,i}$ is layer leaf area index of the species (m^2 leaf m^{-2} ground). Here and hereafter, "s" denotes species, where 1 is *T. hemprichii* and 2 is *E. acoroides*. Epiphyte biomass density is zero ($De_{s,i}$ = 0) when there is no seagrass biomass of the species in the layer. See Note S2.1 for the calculation of leaf area index from above-ground biomass.

Light is absorbed by the epiphyte, seagrass leaves, and water at each layer. Light absorption by epiphyte and seagrass leaves in a layer is related to the projected leaf area of the species in the layer ($Al_{s,i}$, m^2 leaf m^{-2} ground) (Baird et al., 2016) and epiphyte biomass density, $De_{s,i}$ (Bulthuis and Woelkerling, 1983; Drake et al., 2003), where $Al_{s,i} = LAI_{s,i} \sin\theta_s$ and θ_s is leaf nadir angle of the species (see also Note S2.1). If down-welling PAR at the upper boundary of layer i is given as $E_{d,i}$ (μmol photons m^{-2} ground s^{-1}), the PAR that transmitted the layer i and reached the layer i+1 ($E_{d,i+1}$) is calculated as

$$E_{d,i+1} = E_{d,i} exp\left(-Canopyk_{d,i} - k_d dz\right) \quad (2.3)$$

where $Canopyk_{d,i}$ is light attenuation coefficient of seagrass leaves and epiphytes in layer i (dimensionless), k_d is light attenuation coefficient of water column (m^{-1}) as described in Section 2.2.2, and *dz* is layer thickness (*dz* = 0.01 m). $Canopyk_{d,i}$ is calculated as

$$Canopyk_{d,i} = \sum_{s=1}^{2}\left(Absl_s + Abse \times De_{s,i} - Absl_s \times Abse \times De_{s,i}\right)Al_{s,i} \quad (2.4)$$

where $Absl_s$ is leaf absorbance of PAR of the species (dimensionless), *Abse* is PAR absorption coefficient of epiphytes (m^2 leaf mmol^{-1} C). The expression $Absl_s \times Abse \times De_{s,i}$ is subtracted in Eq. (2.4) to account for the effects of the overlaid distribution of epiphytes on the seagrass leaves in the layer, i.e. the light passing through the seagrass leaves in the layer is not influenced by epiphyte light absorption.

The incident PAR that is used for seagrass and epiphyte photosynthesis computation in a layer is affected by the leaf bend nadir angle (θ_s) and is calculated after the computation of irradiance distribution described above. In a layer i, epiphytes acquire PAR ahead of seagrasses. The incident PAR for the photosynthesis of epiphyte attached on leaves of a species ($E_{ince,s,i}$, μmol photons m^{-2} s^{-1}) is then calculated as

$$E_{\mathrm{ince,s,i}} = E_{\mathrm{d,i}} \sin\theta_{\mathrm{s}} \quad (2.5)$$

and the incident PAR for the photosynthesis of the seagrass species ($E_{incl,s,i}$, μmol photons m^{-2} s^{-1}) following epiphyte light absorption is calculated as

$$E_{\mathrm{incl,s,i}} = E_{\mathrm{ince,s,i}}\left(1 - Abse \times De_{\mathrm{s,i}}\right) \quad (2.6)$$

For the partially-exposed condition of leaves due to very shallow waters, $E_{d,1}$ corresponds to the PAR at the water surface, and θ = 90 degrees at the top layer (air-water interface). See also the Note S2.1 in the Supplementary Information.

2.2.2.4.2 Seagrass growth model

Seagrass above-ground biomass is controlled by photosynthesis, leaf respiration, mortality, and biomass translocation between above- and below-ground parts. The change in species-specific above-ground biomass (LB_s, mmol C m^{-2}) is governed by the equation

$$\frac{dLB_{\mathrm{s}}}{dt} = P_{\mathrm{n,s}} - M_{\mathrm{l,s}}\left(1 + f_{\mathrm{d,s}}\right)LB_{\mathrm{s}} - \gamma_{\mathrm{s}} \quad (2.7)$$

where $P_{n,s}$ (mmol C m^{-2} day^{-1}) is net production rate, $M_{l,s}$ (day^{-1}) is mortality rate of above-ground biomass, $f_{d,s}$ (dimensionless) is a factor of the influence of shallow water depth on above-ground mortality, and γ_s (mmol C m^{-2} day^{-1}) is biomass translocation rate between above- and below-ground of each species. The below-ground biomass is controlled by root respiration, mortality, and biomass translocation with above-ground biomass. The equation for the change in species-specific below-ground biomass (RB_s, mmol C m^{-2}) is

$$\frac{dRB_{\mathrm{s}}}{dt} = -R_{\mathrm{r,s}}RB_{\mathrm{s}} - M_{\mathrm{r,s}}RB_{\mathrm{s}} + \gamma_{\mathrm{s}} \quad (2.8)$$

where $R_{r,s}$ (day^{-1}) is root respiration rate, and $M_{r,s}$ (day^{-1}) is mortality rate of below-ground biomass.

Species-specific net production rate at canopy layer i ($P_{n,s,i}$, mmol C m^{-2} day^{-1}) is computed from the hyperbolic tangent function that represents a production-irradiance (P-I) curve (Jassby and Platt, 1976) with additional nutrient limitation function, and subtraction of leaf respiration rate

$$P_{\mathrm{n,s,i}} = \left[P_{\mathrm{max,s}} f_{\mathrm{n,s}} \tanh\left(\frac{E_{\mathrm{incl,s,i}}}{E_{\mathrm{k,s}}}\right) - R_{\mathrm{l,s}}\right] LB_{\mathrm{s,i}} \quad (2.9)$$

where $P_{max,s}$ is maximum photosynthetic rate (day^{-1}), $E_{k,s}$ is saturation PAR (μmol photons m^{-2} s^{-1}), $f_{n,s}$ is a factor of nutrient limitation on production (dimensionless), $R_{l,s}$ is leaf respiration

rate (day^{-1}), and $LB_{s,i}$ is above-ground biomass at layer i (mmol C m^{-2}) of a species. Species-specific nutrient limitation, $f_{n,s}$, is given by the Michaelis-Menten equation

$$f_{n,s} = \frac{DIN_w}{K_{din,s} + DIN_w} \quad (2.10)$$

where DIN_w (μmol L^{-1}) is concentration of dissolved inorganic nitrogen (DIN) in near-bottom water, and $K_{din,s}$ (μmol L^{-1}) is species-specific half saturation concentration of DIN. Although the seagrass beds in Bolinao and Anda coastal area have been impacted by eutrophication-induced light reduction (Tanaka et al., 2014), this function was introduced to consider possible nutrient limitation in pristine seagrass beds in the area (Agawin et al., 1996; Terrados et al., 1999a). The Bolinao and Anda coastal area is a nitrogen-limited environment in terms of Redfield stoichiometry (Ferrera et al., 2016); thus, only nitrogen availability represented by DIN was considered in this model. One assumption here is that nutrient availability is represented by the simulated DIN concentration in the near-bottom waters, despite the ability of seagrasses to take up nutrients from both their leaves and roots (Stapel et al., 1996). This assumption was made due to the difficulties in accurately simulating nutrient concentrations in sediment pore water in the present hydrodynamic-biogeochemical model. Species-specific net production rate per unit ground area ($P_{n,s}$, mmol C m^{-2} day^{-1}) is calculated by vertically integrating the profile of net production rate

$$P_{n,s} = \sum_i P_{n,s,i} \quad (2.11)$$

Background mortality rates were defined both for the above- and below-ground biomass (Eq. (2.7), (2.8)). Above-ground mortality rates may be enhanced by emergence stress when water depth is very shallow (Tanaka and Nakaoka, 2004; Unsworth et al., 2012). These effects may be significant for the distribution of *E. acoroides*, which is characterized by tall leaves (Unsworth et al., 2012). *E. acoroides* was rarely observed growing in very shallow waters in Bolinao and Anda, with few exceptions. Therefore the effect of emergence stress has been included in the model, in particular for *E. acoroides*, using the same formulation introduced in Verhagen and Nienhuis (1983) in the expression

$$f_{d,s} = d_{1,s} exp(-d_{2,s} z) \quad (2.12)$$

where $d_{1,s}$ (dimensionless) and $d_{2,s}$ (m^{-1}) are species-specific parameters of shallow water depth effects on mortality, and z (m) is water depth. Translocation of biomass between above- and below-ground parts (γ_s, mmol C m^{-2} day^{-1}) was modeled following Baird et al. (2016), which assumes that seagrass has a fixed optimal ratio of above- and below-ground biomass

$$\gamma_s = \left(f_{below,s} - \frac{RB_s}{LB_s + RB_s}\right)(LB_s + RB_s)\tau_{tran,s} \quad (2.13)$$

where $f_{below,s}$ (fraction) and $\tau_{tran,s}$ (day^{-1}) are species-specific optimal fraction of below-ground biomass and translocation rate, respectively.

Epiphyte biomass is controlled by photosynthesis, respiration, and seagrass above-ground mortality, hence loss of seagrass leaves leads to loss of epiphyte biomass attached to

the leaves. The changes of epiphyte biomass attached on the leaves of a species ($EB_{s,i}$, mmol C m^{-2}) at layer i is then given by

$$\frac{dEB_{s,i}}{dt} = P_{ne,s,i} - M_{l,s}\left(1 + f_{d,s}\right)EB_{s,i} \quad (2.14)$$

where $P_{ne,s,i}$ is epiphyte net production at layer i (mmol C m^{-2} day^{-1}). Spatial limitation on epiphyte production ($f_{se,s,i}$, dimensionless) was assumed as in Elkalay et al. (2003) and was calculated based on epiphyte biomass density at a specific layer

$$f_{se,s,i} = \frac{1}{1+exp\left[s_{e2}\left(De_{s,i} - s_{e1}\right)\right]} \quad (2.15)$$

where s_{e1} (mmol C m^{-2} leaf) and s_{e2} (m^2 leaf $mmol^{-1}$ C) are parameters of epiphyte biomass density saturation. Nutrient limitation on epiphyte production (f_{ne}, dimensionless) was calculated using the same equation as for seagrass (Eq. (2.10)). Epiphyte net production ($P_{ne,s,i}$, mmol C m^{-2} day^{-1}) attached on each seagrass species was formulated using almost the same equations as for seagrass

$$P_{ne,s,i} = \left[P_{emax} f_{se,s,i} f_{ne} \tanh\left(\frac{E_{ince,s,i}}{E_{ke}}\right) - R_e\right] EB_{s,i} \quad (2.16)$$

where P_{emax} is epiphyte maximum photosynthetic rate (day^{-1}), E_{ke} is saturation PAR intensity for epiphytes (μmol photons m^{-2} s^{-1}), and R_e is epiphyte respiration rate (day^{-1}). The effect of temperature on seagrass and epiphyte production (Perez and Romero, 1992), was not considered in this study; this is because the area is in a tropical region with small temperature variations throughout the year (27.8°C ± 2.1°C, based on the continuous monitoring data from September 2011 to September 2012 in the area).

2.2.2.5 Model configuration

To reproduce the environmental conditions that are driving factors for seagrass bed dynamics, the hydrodynamic-biogeochemical model was run for a two-year period, February 2012 to February 2014. The first year was for the spin-up of the hydrodynamic-biogeochemical model, and the second year was for driving the seagrass model. At every grid cell, the initial condition of the seagrass biomass was set to 2000 mmol C m^{-2}, 4000 mmol C m^{-2} for above- and below-ground biomass, respectively, both for *T. hemprichii* and *E. acoroides*. The initial condition of epiphyte attached on each seagrass species in each layer was set as 5 mmol C m^{-2} at every grid cell.

If seagrass biomass was extinct due to low productivity in a grid cell, 50 mmol C m^{-2} of biomass was added for both above- and below-ground for their possible recovery at any time. Likewise, 1 mmol C m^{-2} of biomass for epiphyte attached on the seagrass species in a layer was added when it was extict in a grid cell. The seagrass model was then run until the growth rates reached a steady-state in every grid cell. Because the seagrass model required a longer computational period (around 10 years) to reach steady-state than the hydrodynamic-

biogeochemical model, the simulated one-year water quality was repeatedly given to the seagrass model. The simulated steady-states of seagrasses were then assumed to be the current condition of seagrass biomass distribution in the area, although the seagrass beds here may not be in steady-states and could be undergoing degradation. This assumption was made because there was no available data on temporal variations in seagrass biomass in the area following the introduction of the mariculture industry.

2.2.2.6 Model validation

The parameter values of the seagrass model were determined from literatures when available (Table 2.1). When the values are unknown or the reported values have certain ranges, the values of the parameters were determined in order to fit the simulated spatial distribution of the steady-state above-ground biomass with the data as described below.

The field data used for model validation was collected at 23 stations in the reef area (Fig. 2.1c) from February to March 2014 (Tanaka et al., unpublished data). The seagrass properties measured by Tanaka et al. were species composition and shoot densities of each species and substrate type. To estimate the above-ground biomass from shoot density, mean dry weight per shoot data of each species (see Section 2.2.2) were used. Literature values for carbon content in seagrass leaves (Duarte 1990) were used for converting the unit dry weight to carbon molar density. Above-ground biomass (mmol C m^{-2}) was then estimated by multiplying shoot density (shoots m^{-2}) with mean biomass per shoot (mmol C $shoot^{-1}$).

Three stations, where corals and rocks comprised more than 30% cover, were removed from the dataset used for model validation because this may affect seagrass biomass distribution in addition to any environmental impacts of adjacent mariculture activities. Site 4 from Tanaka et al. (2014) (Fig. 2.1c) was added to the comparison as a reference station with no seagrass habitat. The computed seagrass above-ground biomass distribution in a steady-state was then compared with the field data-estimated above-ground biomass distribution.

After the model validation, sensitivity analysis of the seagrass above-ground biomass to the seagrass model parameters was performed. Sensitivity analysis of the water quality and the seagrass above-ground biomass to the biogeochemical model parameters was likewise performed. The detailed description of the analyses and results are provided in Note 2. 3 in the Supplementary Information.

2.2.2.7 Scenario analysis

The responses of seagrass bed ecosystems to the implementation of mariculture management were assessed by changing the amount of fish-food derived waste load inputted

to the hydrodynamic-biogeochemical model and examining the changes on the results of seagrass growth simulation (Fig. 2.2). Three scenarios were examined. Scenario 1 represents the case where fish feed amount was reduced by 25% at the fish-rearing structures in the Bolinao area only (the green dots in Fig. 2.1d). Scenario 2 represents the case where fish feed amount was reduced by 25% at the fish-rearing structures in the Anda area only (the blue dots in Fig. 2.1d). Scenario 3 represents the case where fish feed amount was reduced by 25% in both Bolinao and Anda (the green and the blue dots in Fig. 2.1d) through an inter-municipal cooperation scheme. Although the present model is not capable of predicting the mariculture production with the regulation, given the high feed conversion ratio (FCR ~ 2.5; the ratio of the amount of feed needed to grow 1 kg of fish; Ferrera et al. (2016)), reducing fish feeding by 25% may still be reasonable for the mariculture industry. For the initial condition of the scenario analyses, the distribution of seagrass biomass in a steady-state generated by the procedure in Section 2.2.5 was given. If the seagrass and epiphyte biomass were extinguished in a grid cell after the procedure in Section 2.2.5, a certain biomass was added in the grid cell for the extinguished variables for the possible recovery during the scenario; the same procedure done in Section 2.2.5. The water quality in February 2013 generated in Section 2.2.5, which is the condition after the one-year hydrodynamic-biogeochemical model spin-up, was used as the initial condition for the water quality simulation. Then, the effects of one-year mariculture management applied from February 2013 to February 2014 on seagrass bed ecosystems were examined.

2.3 Results

2.3.1 Water quality and k_d

The k_d values in the water column of the mariculture area ranged from 0.78 to 2.50, higher than those in the reef area and the outer sea (Fig. 2.3a, b). The k_d values showed positive linear relationships with both SS and Chl-a, with coefficients of determination R^2 = 0.40 and 0.68 having p-values < 0.02 and < 0.0005, respectively (Fig. 2.3a, b). The correlation between SS and Chl-a was weak with R^2 = 0.20 (Fig. 2.3c). Based on the multiple linear regression analysis involving k_d as a dependent variable and SS and Chl-a as independent variables, k_d was expressed using the following equation:

$$k_d = 0.028 \times SS + 0.050 \times \text{Chl-a} + 0.215 \quad (2.17)$$

where the units of SS and Chl-a are mg L^{-1} and μg L^{-1}, respectively. The k_d derived from field measurement and the k_d estimated from SS and Chl-a using Eq. (2.17) showed significant relationship (R^2 = 0.77) (Fig. 2.3d).

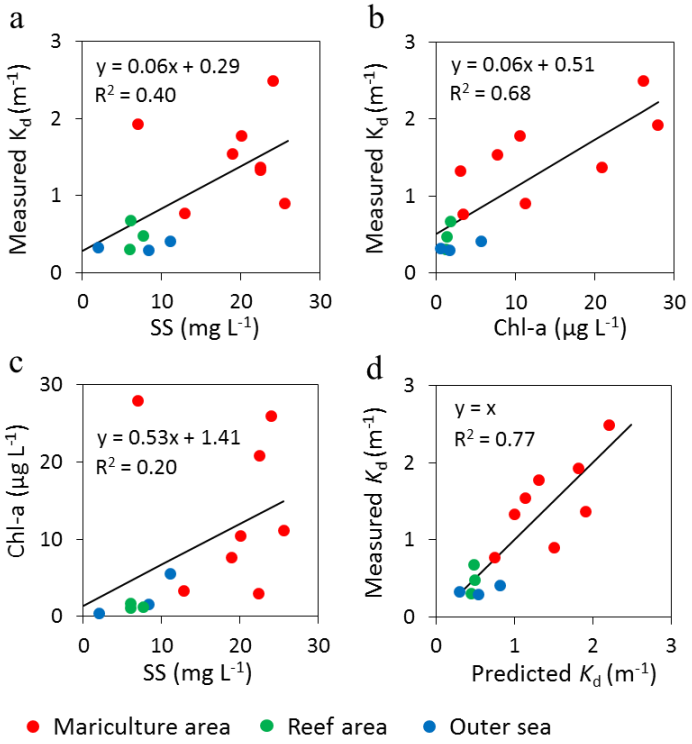

Figure 2.3. Relationships between measured k_d and (a) SS, (b) Chl-a; (c) relationship between SS and Chl-a; and (d) comparison of measured k_d and predicted k_d using Eq. (2.17).

2.3.2 Spatial patterns of simulated water quality

To assess the spatial gradients of the impacts of mariculture on water quality, one-year averaged DIN, Chl-a, and k_d in the surface water, and light intensity at the seabed relative to the surface were mapped (Fig. 2.4). The validation results of the biogeochemical model were provided in Fig. S2.3 and Note S2.2 as described in Section 2.2.3. The model showed high concentrations of DIN and Chl-a in the mariculture area ranging from 4 - 11 µmol L^{-1} and 10 - 17 µg L^{-1}, respectively (Fig. 2.4a, b). Consequently, k_d values in the mariculture area were elevated mainly by the high Chl-a, and were higher than the reef area or the outer sea (Fig. 2.4c). Advected water from the mariculture area, with high concentrations of DIN and Chl-a, affected the southeastern part of the reef area (near Site 3) (Figs. 4a, b). Light intensity at the seabed relative to the water surface was generally higher in the reef area due to the low k_d values and shallow water depth (Fig. 2.4d). In contrast, light intensity in the mariculture area was generally low even in shallow areas due to high k_d values. For instance, the computed one-year averaged relative light intensity was only 25% near Site 4 with water depth of 1.6 m (Fig. 2.4d).

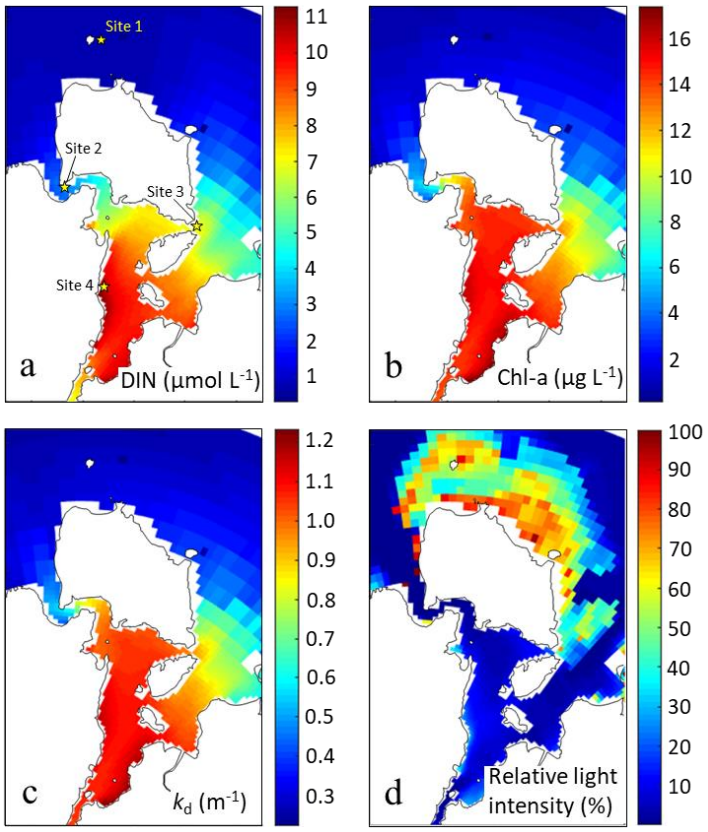

Figure 2.4. Spatial distribution of simulated one-year averaged (a) DIN, (b) Chl-a, (c) k_d at surface waters, and (d) light intensity at the seabed relative to the surface. Leaf shading effects are not reflected in (d). The locations of Site 1-4 in Tanaka et al. (2014) are shown in (a).

2.3.3 Comparison between observed and simulated seagrass above-ground biomass

Mean values of measured shoot biomass were 280 ± 140 mg shoot^{-1} and 2280 ± 680 mg shoot^{-1} for *T. hemprichii* and *E. acoroides*, respectively. These values were used to estimate the above-ground biomass from shoot density measured at the 23 stations in the area (Fig. 2.1c). The simulated spatial patterns of above-ground biomass of *T. hemprichii* and *E. acoroides* in steady states were then compared with the estimated above-ground biomass at the 24 stations (including Site 4).

Using the parameter values shown in Table 2.1, the model showed relatively good agreement with the field data for both *T. hemprichii* and *E. acoroides* (R^2 = 0.78 and 0.60, respectively), suggesting that the model was acceptable for reproducing the general spatial patterns of these species in the area (Fig. 2.5).

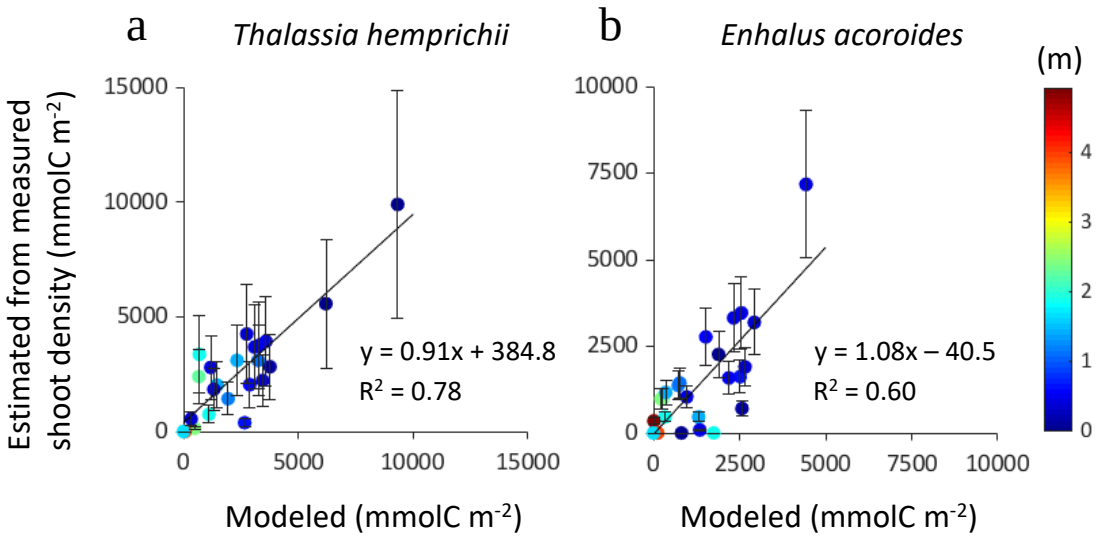

Figure 2.5. Comparison of modeled above-ground biomass and estimated above-ground biomass from measured shoot density of (a) *T. hemprichii*, and (b) *E. acoroides*. Error bars are attributed to standard deviation of shoot biomass from the pooled samples. The color of the dots represents water depth at each station.

2.3.4 Spatial distribution of simulated seagrass biomass

The spatial distribution of above-ground biomass of *T. hemprichii* and *E. acoroides* in a steady-state, as predicted by the seagrass model under the current conditions of environmental stress caused by mariculture activities, is given in Fig. 2.6. The model showed the widespread growth of both species in the reef area. On the other hand, the simulated biomass for both species in the southeastern part of the reef area, located near the mariculture area, was low (Fig. 2.6). While most of the mariculture area was predicted as the area with no seagrass biomass due to low light intensity, the model predicted some areas with very low biomass of *T. hemprichii* (57 ~ 68 mmol C m^{-2}) where the water is shallow (1.2 ~ 1.3 m). There were no areas in the mariculture area where *E. acoroides* grew in the model. By comparing the simulated biomass distributions of the two-species, *E. acoroides* showed limited coverage and relatively lower biomass (Fig. 2.6).

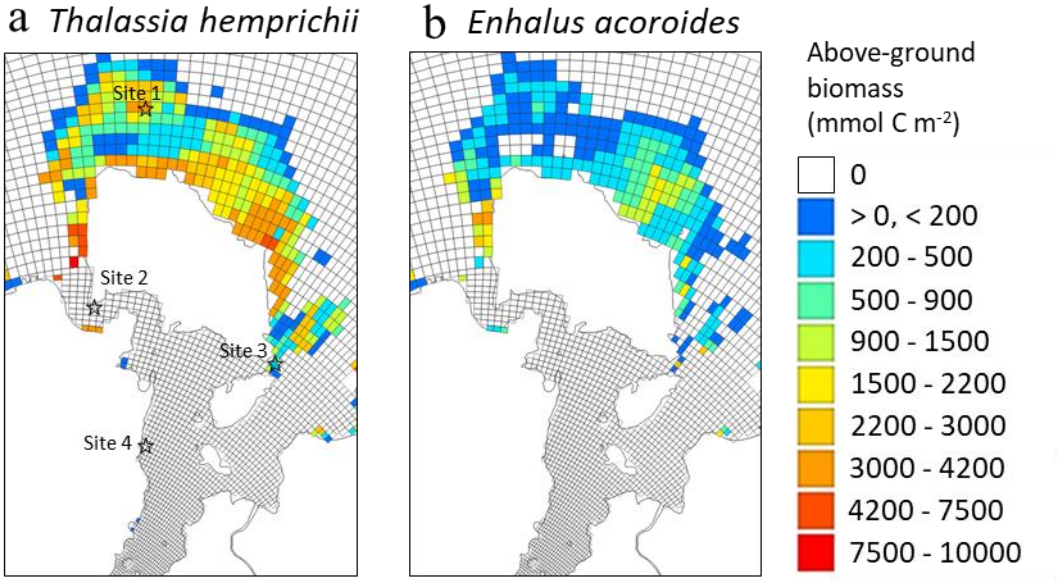

Figure 2.6. Spatial distribution of simulated above-ground biomass of (a) *T. hemprichii* and (b) *E. acoroides* in steady states under the current conditions of environmental stress caused by mariculture activities. The locations of Site 1-4 in Tanaka et al. (2014) are shown in (a).

2.3.5 Scenario analysis

Scenario analysis showed decreases in Chl-a and increases in light intensity at the seabed in the mariculture area and some parts of the reef area, especially near Site 3, following one-year mariculture management (Fig. 2.7). In Scenario 1, water quality improved the most in the mariculture area of Bolinao, with some improvement in Anda. Similarly, in Scenario 2, water quality improved the most in the mariculture area of Anda and extending to some areas in Bolinao. Scenario 3 showed more considerable improvement in water quality than Scenarios 1 and 2. The decrease or increase in values of Chl-a and light intensity, respectively, in Scenario 3 was almost twice than those in Scenarios 1 and 2.

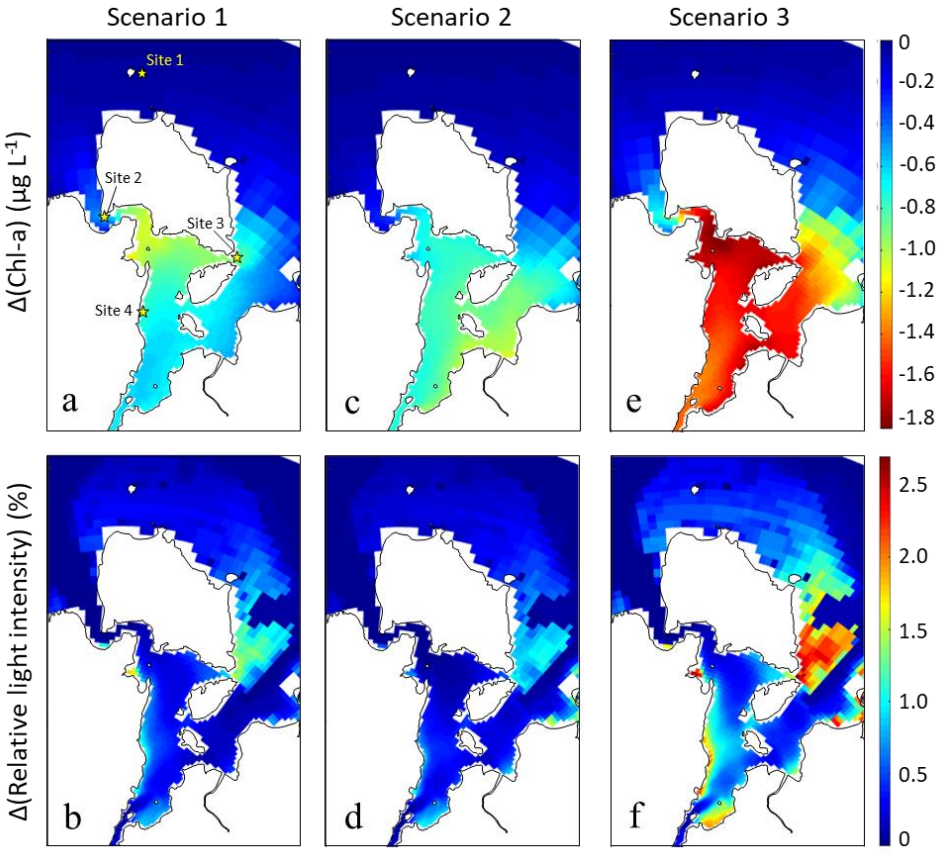

Figure 2.7. Spatial distribution of the relative decreases and increases of simulated one-year averaged Chl-a and light intensity at the seabed in (a, b) Scenario 1, (c, d) Scenario 2, and (e, f) Scenario 3, compared to those shown in Fig. 2.4. Leaf shading effects are not reflected in the figures of relative light intensity (b, d, and f). The locations of Site 1-4 in Tanaka et al. (2014) are shown in (a).

The one-year seagrass growth simulation under different water quality conditions as simulated in Scenarios 1, 2, and 3 showed increases in the above-ground biomass of *T. hemprichii* in a wide area of the reef, but for *E. acoroides* this was limited (Fig. 2.8). Similar to the trends seen in water quality improvement, the area where biomass increased the most for both species was the seagrass bed located near the mariculture area, where seagrasses have degraded after the intensification of the mariculture industry (Tanaka et al., 2014). While the increased ratios of biomass of *T. hemprichii* in Scenario 1 and 2 were almost the same, the increased ratio of biomass in Scenario 3 was nearly twice those of Scenarios 1 and 2 at the area near Site 3. The biomass of *T. hemprichii* in the mariculture area predicted in Section 2.3.4 (Fig. 2.6a) also showed an increase as large as the area near Site 3 due to the improved light environment. The eastern and southeastern parts of the reef area showed increases in biomass of *E. acoroides*, but some areas in the northern and the western parts of the reef area showed small decreases in biomass especially under Scenarios 1 and 3 (Fig. 2.8b, f). Unlike

T. hemprichii, there were no areas where *E. acoroides* recovered in the mariculture area in all the scenarios.

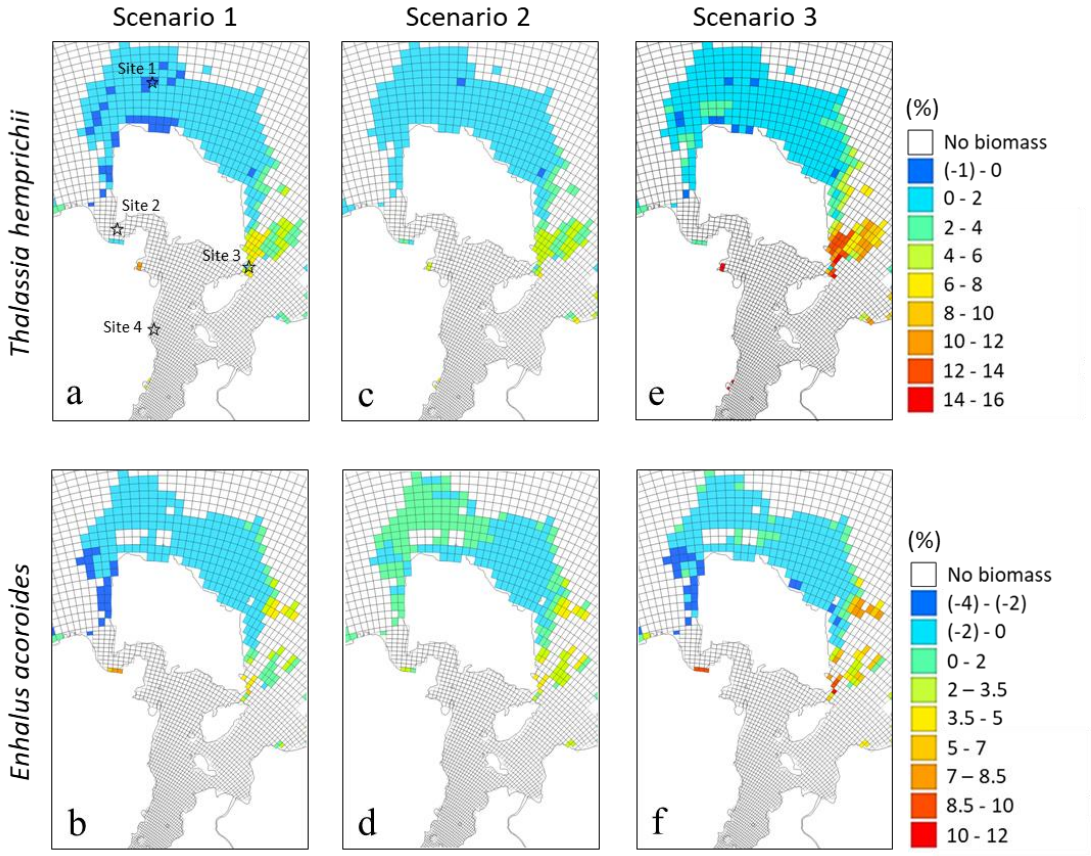

Figure 2.8. Spatial distribution of increase ratios of above-ground biomass of *T. hemprichii* and *E. acoroides* relative to those shown in Fig. 2.6, after one-year seagrass growth simulation under water quality simulated in (a, b) Scenarios 1, (c, d) 2, and (e, f) 3. The locations of Site 1-4 in Tanaka et al. (2014) are shown in (a).

2.4 Discussion

2.4.1 Evaluation of the model

In order to assess the seagrass bed dynamics under the environmental impact of intensive mariculture activities, an appropriate reproduction of the spatiotemporal dynamics of water quality is needed. The primary cause of degradation of seagrass beds may be a reduced-light environment attributed to eutrophication-induced increase in phytoplankton biomass and organic matter, such as uneaten fish food and fish feces in the mariculture area (Tanaka et al., 2014), along with the advective flux from the mariculture area to the reef area

through hydrodynamics. The transport of eutrophic waters to the reef area may contribute to the production of phytoplankton and epiphytes in the seagrass beds, resulting in the reduction of light intensity at the seabed. Based on field data, the light environment in the area was mostly affected by phytoplankton biomass (Fig. 2.3). Therefore, important processes to reproduce were eutrophication and enhanced phytoplankton production caused by excessive fish feeding, and the hydrodynamics that generate the spatial gradients of water quality in the area. The hydrodynamic model applied for this area where the circulation is primarily driven by tides (Gecek and Legovic, 2010), accurately reproduced the tidal currents at the three channels connecting the mariculture area to the outer sea and Tambac Bay (Fig. S2.3b-d). The freshwater flux from Tambac Bay to the mariculture area was also well reproduced (Fig. S2.3e). Hence, the reproduction of overall spatiotemporal variations of hydrodynamics in the area was deemed acceptable. The overall trends in temporal dynamics of Chl-a and DIN in the mariculture area were also well reproduced by the simulation, although there were some discrepancies between simulated and observed values (Fig. S2.4). Comparing the simulated one-year averaged DIN and Chl-a at BML station (Fig. 2.1c) with those reported in Ferrera et al. (2016), the model somewhat underestimated the one-year averaged DIN (2.8 μmol L^{-1} in the model, Fig. 2.4a, and 5.0 μmol L^{-1} in Ferrera et al. (2016)). Still, the value of simulated one-year averaged Chl-a (4.0 μg L^{-1}, Fig. 2.4b) was close to that in Ferrera et al. (2016) (5.5 μg L^{-1}). The spatial distribution of simulated one-year averaged Chl-a and k_d (Fig. 2.4b, c), which are the water quality parameters that have changed the most since 1995 (Tanaka et al., 2014), was consistent with the spatial pattern as measured by Tanaka et al. (2014). Therefore, we consider the accuracy of the current hydrodynamic-biogeochemical model to be acceptable for assessing the environmental impacts on seagrass beds.

By providing the simulated water quality parameters to the seagrass growth simulation as driving factors, the model predicted the spatial distribution of above-ground biomass of *T. hemprichii* and *E. acoroides* with R^2 values of 0.78 and 0.60, respectively (Fig. 2.5). To our knowledge, this would be the first study that achieved such accuracy for the spatial distribution of above-ground biomass of two coexisting species. This observation suggests that the model has reached the practical use level for assessing the dynamics of a mixed seagrass bed ecosystem influenced by spatial gradients in water quality created by intensive mariculture activities (Fig. 2.4). The model also showed its potential to reproduce the dynamic responses of seagrasses to the combined effects of time-varying physicochemical variables (Fig. S2.5 and Note S2.4). These results suggest the advantage of using the model over observations, with regards to the assessment of spatiotemporal dynamics of seagrass beds on an estuarine-scale under the impacts of intensive mariculture activities.

The light intensity in seagrass canopies was computed using a multi-layer model and the leaf shading effects on photosynthetic rates were explicitly taken into account in this study.

Thus, the model also accounts for the species competition for light with different species-specific leaf heights. This approach makes it possible to assess the light environment in seagrass canopies and associated species-specific photosynthetic rates in mixed seagrass beds with more than two coexisting species, which are commonly observed in tropical Southeast Asian coasts (Ooi et al., 2011). Therefore, the model has the potential to assess the changes in species richness in seagrass beds under a reduced light environment associated with water quality degradation, like in the case of Bolinao and Anda.

However, the current model, which did not take into consideration the feedback of seagrass nutrient uptake to the sediment and water compartments, holds some limitations, specifically in reproducing the seagrass nutrient availability. Nevertheless, the spatial distribution of above-ground biomass of the two-dominant species – *T. hemprichii* and *E. acoroides* – was successfully reproduced using the current model (Fig. 2.5). This is because the seagrass beds in Bolinao and Anda have been under the impacts of eutrophication from mariculture activities, hence they may not be nutrient limited. Also, *T. hemprichii* and *E. acoroides* are characterized by large below-ground biomass and deep penetration of roots in the sediment compared to other small species (Duarte et al., 1998), which gives them an advantage in terms of interspecies competition for resources below-ground. With the current model that is not possible to simulate the interspecies competition for resources below-ground, it may still be difficult to reproduce the biomass distribution of species other than *T. hemprichii* and *E. acoroides*.

The sensitivity analysis for the seagrass growth model parameters described in Note S2.3 also highlighted the limitations of the model in terms of the reproduction of the seagrass nutrient availability. This is seen in the high sensitivity of the model results to the below-ground related parameters such as f_{below}, R_r, and τ_{tran} (Table S2.4). In the current model, the seagrass growth rate gets significantly lowered as below-ground biomass fraction (f_{below}) or root respiration rate (R_r) increases, and vice versa. This is because the seagrass growth is dependent on only above-ground biomass (photosynthetic capacity) in the model, and the effects of coupled dynamics of photosynthesis (above-ground) and nutrient uptake (below-ground) on the seagrass growth have not been considered. In an actual condition, the larger fraction of below-ground biomass could be in favor of seagrass growth in nutrient-poor environment (Ferguson et al., 2016). Conversely, the larger fraction of above-ground biomass, which increases the photosynthetic capacity, may accelerate the seagrass growth rate in a nutrient-rich environment, but the whole-plant nutrient demand also increases at the same time. Thus it may be eventually limited by the nutrient availability and/or nutrient uptake ability before it is constrained by the self-shading effects. The current model can be improved by two-way coupling of seagrass model and hydrodynamic-biogeochemical model, which explicitly simulates the seagrass nutrient uptake process, to make the model more robust so

that it can be applied to the various seagrass species in different environmental conditions. Further research on seagrass below-ground root architecture, nutrient uptake ability of roots and leaves, and nutrient assimilation is needed to realize such model development.

Another factor to be improved could be the accurate inputs of sediment discharge from rivers in the model, which was not verified in this study due to lack of data. Although the major factor affecting the light environment in the area is Chl-a (Fig. 2.3; Tanaka et al., 2014), the primary factor affecting seagrass distribution in 1995 was siltation from the rivers in Tambac Bay (Bach et al., 1998). Furthermore, reducing conditions of the sediment may be one of the factors affecting seagrass distribution (Terrados et al., 1999b). This may be significant, especially in and near the mariculture area where the long-term operation may have altered the sediment conditions (Holmer et al., 2002, 2003; Ferrera et al., 2016). The predicted biomass of *T. hemprichii* at the shallow waters in the mariculture area (Fig. 2.6a) and its increase in the scenarios (Fig. 2.8a, c, and e) may have been overestimated in this regard. The spatial extent of reduced sediments in the area and the effects of sediment conditions on seagrass establishment, growth, and species-specific response must be quantified and modeled in future studies for more precise assessment of the impacts of intensive mariculture activities on adjacent seagrass beds.

A fixed optimal biomass ratio (f_{below}) between the above- and below-ground was assumed in this study, as in other seagrass models (Elkalay et al., 2003; Plus et al., 2003; Carr et al., 2012; Baird et al., 2016). However, it is known that the seagrass above-ground to below-ground biomass ratio varies with environmental factors such as depth, light intensity, and nutrients, to maintain a favorable carbon balance (Ferguson et al., 2016). The ratio can also vary with species, due to interspecific variations in photosynthesis and respiration balance (Tanaka and Nakaoka, 2007). In fact, Fortes et al. (2012) reported a higher above- to below-ground biomass ratio of *T. hemprichii* near the mariculture area, and a lower ratio with increased distance from the mariculture area. There were more complex variations in the ratio with *E. acoroides*. Elucidation of mechanisms and modeling of such dynamics are needed, in particular for assessing the role of seagrass beds as “blue carbon sinks” through the carbon-trapping function of their leaves, and the direct supply of below-ground detritus (Samper-Villarreal et al., 2016; Oreska et al., 2018; Tanaya et al., 2018).

2.4.2 Impacts of intensive mariculture activities

Based on the results of the hydrodynamic-water quality simulation, it was revealed that the effects of mariculture reached the eastern parts of the reef area (Fig. 2.4). The most impacted seagrass beds were in the southeastern part of the reef (near Site 3), which is most adjacent to the mariculture area. Consequently, the simulated biomass of the two seagrass

species in this area was sparse compared to other parts of the reef area (Fig. 2.6). There had been some seagrass beds in the year 1995 in the mariculture area at least at Site 4, but they had disappeared by the year 2012 due to water quality degradation (Tanaka et al., 2014). The model suggested that there were no suitable areas for seagrass growth in the mariculture area, except for some areas with very shallow waters (Fig. 2.6), due to the low light intensities as shown by the high k_d values (Fig. 2.4c, d), which is consistent with the observations of Tanaka et al. (2014).

Scenario analysis predicted that decreases in Chl-a concentrations to a certain level could be expected following one year of mariculture management (Fig. 2.7a, c, e). Such improvement in water quality is due to a reduction in the accumulation rate of organic matter derived from uneaten or undigested fish food and fish excretions. This result means there is decreased rate of nutrients released, for instance, from the sediments, which is one of the sources of eutrophication in the area (Ferrera et al., 2016). In conjunction with a decrease in Chl-a concentrations, the relative light intensities increased in shallow waters in the mariculture area and some seagrass beds adjacent to the mariculture area in all scenarios, suggesting that cutting the amount of feeding input is an effective way to improve the light conditions in those areas (Fig. 2.7b, d, f). When comparing the scenarios, the level of decreases in Chl-a concentrations and increases in relative light intensities were rather limited in Scenarios 1 and 2. It is noteworthy that water quality in the mariculture area significantly improved in Scenario 3, even in Bolinao compared with Scenario 1, and in Anda compared with Scenario 2. The improvement in light intensities in Scenario 3 was also higher than in Scenarios 1 and 2. These results clearly indicate that the waters in the area are interconnected across Bolinao and Anda municipalities through hydrodynamics, thus waters in the area are affected not only by the adjacent local mariculture activities but also mariculture activities in the whole area. Integrated Coastal Zone Management (ICZM) is a crucial process for the improvement of coastal water quality in areas where environmental stresses are spatially connected through hydrodynamics (Yamamoto et al., 2019). The results presented here demonstrate the importance of an integrated management scheme for the case of mariculture in Bolinao and Anda.

Similar to the trends in water quality improvement predicted for mariculture regulation, significant increases in seagrass above-ground biomass (up to 16 % increase for *T. hemprichii*, and up to 12 % increase for *E. acoroides* in Scenario 3) can be expected at the southeastern part of the reef area which is adjacent to the mariculture area (Fig. 2.8). While Scenario 1 and 2 showed almost the same increase ratio in the seagrass above-ground biomass of *T. hemprichii*, Scenario 3 showed significantly higher increases than those in Scenarios 1 and 2 in the seagrass beds (Fig. 2.8). This highlights the effectiveness of interconnected mariculture management between the two municipalities, which is important for ecosystem conservation.

Compared to the biomass distribution of *T. hemprichii*, the model predicted a limited area and lower biomass of *E. acoroides* distribution (Fig. 2.6). Responses of *E. acoroides* to the improved water quality were relatively weaker, and there were some areas that showed slight decreases in above-ground biomass due to decreased nutrient levels from mariculture regulation (Fig. 2.8b, d, and f). This may be because the growth rate of *E. acoroides* is slower (Agawin et al., 1996; 2001), and nutrient demand is higher (Agawin et al., 1996) than other species. This result somehow agrees with the implication of the results by Tanaka et al. (2014), indicating that there may be a beneficial aspect of nutrient loading from mariculture for the growth of *E. acoroides* in the area. On the other hand, SGD may be a significant source of nutrients for seagrass beds in the area (Senal et al., 2014). The scenario analysis using the present model, which did not include SGD fluxes, may have underestimated the effects of mariculture management on seagrass beds.

Site 4, a former seagrass bed in the mariculture area, is one of the areas where water quality improved the most following mariculture management (Fig. 2.7), but was still not suitable for seagrass growth in terms of photosynthesis-respiration balance (Fig. 2.8). In addition to improvements in water quality, improvements in sediment conditions may also be needed for the recovery of seagrass beds at this site, as stated in Section 2.4.1. Further investigations through field surveys, laboratory experiments, and modeling studies on the effects of sediment are needed for a more quantitative assessment of possible recoveries of seagrasses, especially for areas undergoing anthropogenic impacts.

The importance of implementing a joint cooperative management system for Bolinao and Anda to regulate excessive feeding and the number of fish-rearing structures has been stressed in previous studies aimed at realizing a sustainable mariculture industry (Ferrera et al., 2016; Sugimoto et al., 2016). The results of the scenario analysis in the present study highlight the importance of such management for improving the water quality in the mariculture area. Furthermore, the results presented here expand the perspective of its importance to the conservation of the adjacent seagrass ecosystem.

2.5 References

Agawin, N.S.R., Duarte, C.M., Fortes, M.D., 1996. Nutrient limitation of Philippine seagrasses (Cape Bolinao, NW Philippines): in situ experimental evidence. Mar. Ecol. Prog. Ser. 138, 233–243.

Agawin, N.S.R., Duarte, C.M., Fortes, M.D., Uri, J.S., Vermaat, J.E., 2001. Temporal changes in the abundance, leaf growth and photosynthesis of three co-occurring Philippine seagrasses. J. Exp. Mar. Biol. Ecol. 260, 217–239.

Añabieza,M., Pajaro, M., Reyes, G., Tiburcio, F., Watts, P., 2010. Philippine alliance of fisherfolk: ecohealth practitioners for livelihood and food security. EcoHealth 7, 394–399.

Azanza, R.V., Fukuyo, Y., Yap, L.G., Takayama, H., 2005. Prorocentrum minimum bloom and its possible link to a massive fish kill in Bolinao, Pangasinan, Northern Philippines. Harmful Algae 4, 519–524.

Bach, H.K., 1993. A dynamic model describing the seasonal variations in growth and the distribution of eelgrass (*Zostera marina* L.) I. Model theory. Ecol. Model. 65, 31–51.

Bach, S.S., Borum, J., Fortes, M.D., Duarte, C.M., 1998. Species composition and plant performance of mixed seagrass beds along a siltation gradient at Cape Bolinao, the Philippines. Mar. Ecol. Prog. Ser. 174, 247–256.

Baird, M.E., Adams, M.P., Babcock, R.C., Oubelkheir, K., Mongin, M., Wild-Allen, K.A., Skerratt, J., Robson, B.J., Petrou, K., Ralph, P.J., O'Brien, K.R., Carter, A.B., Jarvis, J.C., Rasheed, M.A., 2016. A biophysical representation of seagrass growth for application in a complex shallow-water biogeochemical model. Ecol. Model. 325, 13–27.

Bertelli, C.M., Unsworth, R.K.F., 2014. Protecting the hand that feeds us: seagrass (*Zostera marina*) serves as commercial juvenile fish habitat. Mar. Pollut. Bull. 83, 425–429.

Bocci, M., Coffaro, G., Bendoricchio, G., 1997. Modelling biomass and nutrient dynamics in eelgrass (*Zostera marina* L.): applications to the Lagoon of Venice (Italy) and Øresund (Denmark). Ecol. Model. 102 (1), 67–80.

Brun, F.G., Olive, I., Malta, E., Vergara, J.J., Hernandez, I., Perez-Llorens, J.L., 2008. Increased vulnerability of *Zostera noltii* to stress caused by low light and elevated ammonium levels under phosphate deficiency. Mar. Ecol. Prog. Ser. 365, 67–75.

Bulthuis, D.A., Woelkerling, W.J., 1983. Biomass accumulation and shading effects of epiphytes on leaves of the seagrass, *Heterozostera tasmanica*, in Victoria, Australia. Aquat. Bot. 16, 137–148.

Burkholder, J.M., Tomasko, D.A., Touchette, B.W., 2007. Seagrasses and eutrophication. J. Exp. Mar. Biol. Ecol. 350 (1–2), 46–72.

Carr, J.A., D'Odorico, P., McGlathery, K.J., Wiberg, P.L., 2012. Stability and resilience of seagrass meadows to seasonal and interannual dynamics and environmental stress. J. Geophys. Res. 117, G01007.

Cerco, C.F., Moore, K., 2001. System-wide submerged aquatic vegetation model for Chesapeake Bay. Estuaries 24, 522–534.

Collier, C.J., Waycott, M., McKenzie, L.J., 2012. Light thresholds derived from seagrass loss in the coastal zone of the northern Great Barrier Reef, Australia. Ecological Indicators. 23, 211–219.

Cruz-Trinidad, A., Geronimo, R.C, Cabral, R.B., Aliño, P.M., 2011. How much are the Bolinao-Anda coral reefs worth? Ocean and Coastal Management 54, 696–705.

Deltares, 2014a. Delft3D-FLOW: Simulation of multi-dimensional hydrodynamic flows and transport phenomena, including sediments — User Manual, version: 3.15.34158, Delft, Netherlands.

Deltares, 2014b. D-Water Quality: Versatile water quality modelling in 1D, 2D or 3D systems including physical, (bio)chemical and biological processes - User Manual, version 4.99.34158, Delft, Netherlands.

Dennison, W.C., Orth, R.J., Moore, K.A., Stevenson, J.C., Carter, V., Kollar, S., Bergstrom, P.W., Batiuk, R.A., 1993. Assessing water quality with submersed aquatic vegetation: habitat requirements as barometers of Chesapeake Bay health. BioScience 43, 86–94.

des los Santos, C.B., Krause-Jensen, D., Alcoverro, T., Marbà, N., Duarte, C.M., et al., 2019. Recent trend reversal for declining European seagrass meadows. Nat. Commun. 10, 3356.

Drake, L.A., Dobbs, F.C., Zimmerman, R.C., 2003. Effects of epiphyte load on optical properties and photosynthetic potential of the seagrasses *Thalassia testudinum* Banks ex König and *Zostera marina* L. Limnol. Oceanogr. 48(1, Part 2), 456–463.

Duarte, C.M., 1990. Seagrass nutrient content. Mar. Ecol. Prog. Ser. 67, 201–207.

Duarte, C.M., 1991. Allometric scaling of seagrass form and productivity. Mar. Ecol. Prog. Ser. 77, 289–300.

Duarte, C.M., Marba, N., Gacia, E., Fourqurean, J.W., Beggins, J., Barron, C., Apostolaki, E.T., 2010. Seagrass community metabolism: assessing the carbon sink capacity of seagrass meadows. Global Biogeochem. Cycles. 24, GB4032. doi: 10.1029/2010GB003793.

Duarte, C.M., Merino, M., Agawin, N.S.R., Uri, J., Fortes, M.D., Gallegos, M.E., Marba, N., Hemminga, M.A., 1998. Root production and belowground seagrass biomass. Mar. Ecol. Prog. Ser. 171, 97–108.

Duarte, C.M., Terrados, J., Agawin, N.S.R., Fortes, M.D., 2000. An experimental test of the occurrence of competitive interactions among SE Asian seagrasses. Mar. Ecol. Prog. Ser. 197, 231–240.

Elkalay, K., Frangoulis, C., Skliris, N., Goffart, A., Gobert, S., Lepoint, G., Hecq, J.-H., 2003. A model of the seasonal dynamics of biomass and production of the seagrass *Posidonia oceanica* in the Bay of Calvi (Northwestern Mediterranean). Ecol. Model. 167, 1–18.

Enriquez, S., Pantoja-Reyes, N.I., 2005. Form-function analysis of the effect of canopy morphology on leaf self-shading in the seagrass *Thalassia testudinum*. Oecologia 145, 235–243.

Escobar, M.T.L., Sotto, L.P.A., Jacinto, G.S., Benico, G.A., San Diego-McGlone, M.L., Azanza, R.V., 2013. Eutrophic conditions during the 2010 fish kill in Bolinao and Anda, Pangasinan, Philippines. J. Environ. Sci. Manag. 29-35 (Special Issue 1-2013).

Evans, S.M., Griffin, K.J., Blick, R.A.J., Poore, A.G.B., Vergés, A., 2018. Seagrass on the brink: Decline of threatened seagrass *Posidonia australis* continues following protection. PLoS ONE 13(4): e0190370. https://doi.org/10.1371/journal.pone.0190370

Ferguson, A.J.P., Gruber, R.K., Orr, M., Scanes, P., 2016. Morphological plasticity in *Zostera muelleri* across light, sediment, and nutrient gradients in Australian temperate coastal lakes. Mar. Ecol. Prog. Ser. 556, 91–104.

Ferrera, C.M., Watanabe, A., Miyajima, T., San Diego-McGlone, M.L., Morimoto, N., Umezawa, Y., Herrera, E., Tsuchiya, T., Yoshikai, M., Nadaoka, K., 2016. Phosphorus as a driver of nitrogen limitation and sustained eutrophic conditions in Bolinao and Anda, Philippines, a mariculture-impacted tropical coastal area. Mar. Pollut. Bull. 105, 237–248.

Fortes, M.D., Go, G.A., Bolisay, K., Nakaoka, M., Uy, W.H., Lopez, M.R., Leopardas, V., Leriorato, J., Pantallano, A., Paciencia Jr., F., Watai, M., Honda, K., Edralin, M., 2012. Seagrass response to mariculture-induced physico-chemical gradients in Bolinao, northwestern Philippines. Proceedings of the 12th international Coral Reef Symposium, Cairns, Australia, 9-13 July 2012.

Fourqurean, J.W., Duarte, C.M., Kennedy, H., Marbà, N., Holmer, M., Mateo, M.A., et al., 2012. Seagrass ecosystems as a globally significant carbon stock. Nat. Geosci. 5, 505–509. doi: 10.1038/ngeo1477.

Gecek, S., Legovic, T., 2010. Towards carrying capacity assessment for aquaculture in the Bolinao Bay, Philippines: A numerical study of tidal circulation. Ecol. Model. 221 (10), 1394–1412.

Govers, L.L., Lamers, L.P.M., Bouma, T.J., de Brouwer, J.H.F., van Katwijk, M.M., 2014. Eutrophication threatens Caribbean seagrasses – An example from Curaçao and Bonaire. Mar. Pollut. Bull. 89, 481–486.

Hedley, J., Enriquez, S., 2010. Optical properties of canopies of the tropical seagrass *Thalassia testudinum* estimated by a three-dimensional radiative transfer model. Linmol. Oceanogr. 55(4), 1537–1550.

Hedley, J., McMahon, K., Fearns, P., 2014. Seagrass canopy photosynthetic response is a function of canopy density and light environment: a model for *Amphibolis griffithii*. PLoS ONE 9(10), e111454.

Holmer, M., Duarte, C.M., Heilskov, A., Olesen, B., Terrados, J., 2003. Biogeochemical conditions in sediments enriched by organic matter from net-pen fish farms in the Bolinao area, Philippines. Mar. Pollut. Bull. 46, 1470–1479.

Holmer, M., Marba, N., Terrados, J., Duarte, C.M., Fortes, M.D., 2002. Impacts of milkfish (*Chanos chanos*) aquaculture on carbon and nutrient fluxes in the Bolinao area, Philippines. Mar. Pollut. Bull. 44, 685–696.

Jassby, A.D., Platt, T., 1976. Mathematical formulation of the relationship between photosynthesis and light for phytoplankton. Limnol. Oceonogr. 21, 540–547.

Kim, J.Y., Im, R.Y., Do, Y. Kim, G.-Y., Joo, G.-J., 2016. Above-ground biomass estimation of tuberous bulrush (*Bolboschoenus planiculmis*) in mudflats using remotely sensed multispectral image. Ocean Sci. J. 51, 151–158.

Klumpp, D.W., Salita-Espinosa, J.S., Fortes, M.D., 1992. The role of epiphytic periphyton and macroinvertebrate grazers in the trophic flux of a tropical seagrass community. Aquat. Bot. 43, 327–349.

Leopardas, V., Honda, K., Go, G.A., Bolisay, K., Pantallano, A.D., Uy, W., Fortes, M.D, Nakaoka, M., 2016. Variation in macrofaunal communities of sea grass beds along a pollution gradient in Bolinao, northwestern Philippines. Mar. Pollut. Bull. 105, 310–318.

Magdaong, E., 2008. Modeling Residence Time and Aquaculture Waste Dispersal. MSc Thesis, University of the Philippines.

Matsumoto, K., Takanezawa, T., Ooe, M., 2000. Ocean tide models developed by assimilating TOPEX/POSEIDON Altimeter Data into hydrodynamical model: a global model and a regional model around Japan. Journal of Oceanography 56, 567–581.

Morimoto, N., Umezawa, Y., San Diego-McGlone, M.L., Watanabe, A., Siringan, F.P., Tanaka, Y., Regino, G.L., Miyajima, T., 2017. Spatial dietary shift in bivalves from embayment with river discharge and mariculture activities to outer seagrass beds in northwestern Philippines. Mar Biol 164, 84. https://doi.org/10.1007/s00227-016-3063-z

Nakamura, T., Nadaoka, K., Watanabe, A., Yamamoto, T., Miyajima, T., Blanco, A.C., 2018. Reef-scale modeling of coral calcification responses to ocean acidification and sea-level rise. Coral Reefs 37, 37–53.

Nellemann, C., et al., 2009. Blue Carbon. A Rapid Response Assessment. United Nations Environment Programme (GRID-Arendal, 2009).

Ooi, J.L.S., Kendrick, G.A., Van Niel, K.P., Affendi, Y.A., 2011. Knowledge gaps in tropical Southeast Asian seagrass systems. Estuar. Coast. Shelf Sci. 92, 118–131.

Oreska, M.P.J., Wilkinson, G.M., McGlathery, K.J., Bost, M., McKee, B.A., 2018. Non-seagrass carbon contributions to seagrass sediment blue carbon. Limnol. Oceanogr. 63, S3–S18.

Orth, R.J., Carruthers, T.J.B., Dennison, W.C., Duarte, C.M., Fourqurean, J.W., Heck Jr., K.L., Hughes, A.R., Kendrick, G.A., Kenworthy, W.J., Olyarnik, S., Short, F.T., Waycott, M., Williams, S.L., 2006. A global crisis for seagrass ecosystems. Bioscience 56, 987–996.

Perez, M., Romero, J., 1992. Photosynthetic response to light and temperature of the seagrass *Cymodocea nodosa* and the prediction of its seasonality. Aquat. Bot. 43, 51–62.

Plus, M., Chapelle, A., Menesguen, A., Deslous-Paoli, J.-M., Auby, I., 2003. Modelling seasonal dynamics of biomasses and nitrogen contents in a seagrass meadow (*Zostera noltii Hornem*.): application to the Thau lagoon (French Mediterranean coast). Ecol. Model. 161, 213–238.

Purvaja, R., Ganguly, D., Hariharan, G., Arumugam, K., Ramesh, R., 2020. In situ photosynthetic activities and associated biogeochemical changes in three tropical seagrass species. Front. Earth. Sci. 8, 467540.

Quiros, T.E.A.L., Beck, M.W., Araw, A., Croll, D.A., Tershy, B., 2018. Small-scale seagrass fisheries can reduce social vulnerability: a comparative case study. Ocean and Coastal Management 157, 56–67.

Ralph, P.J., Durako, M.J., Enriquez, S., Collier, C.J., Doblin, M.A., 2007. Impact of light limitation on seagrasses. J. Exp. Mar. Biol. Ecol. 350, 176–193.

Samper-Villarreal, J., Lovelock, C.E., Saunders, M.I., Roelfsema, C., Mumby, P.J., 2016. Organic carbon in seagrass sediments is influenced by seagrass canopy complexity, turbidity, wave height, and water depth. Limnol. Oceanogr. 61, 938–952.

San Diego-McGlone, M.L., Azanza, R.V., Villanoy, C.L., Jacinto, G.S., 2008. Eutrophic waters, algal bloom and fish kill in fish farming areas in Bolinao, Pangasinan, Philippines. Mar. Pollut. Bull. 57, 295–301.

Senal, M.I.S., Jacinto, G.S., San Diego-McGlone, M.L., Siringan, F., Zamora, P., Soria, L., Cardenas, M.B., Villanoy, C., Cabrera, O., 2011. Nutrient inputs from submarine groundwater discharge on the Santiago reef flat, Bolinao, Northwestern Philippines. Mar. Pollut. Bull. 63, 195–200.

Short, F.T., Polidoro, B., Livingstone, S.R., Carpenter, K.E., Bandeira, S., Bujang, J.S., Calumpong, H.P., Carruthers, T.J.B., Coles, R.G., Dennison, W.C., Erftemeijer, P.L.A., Fortes, M.D., Freeman, A.S., Jagtap, T.G., Kamal, A.H.M., Kendrick, G.A., Kenworthy, J.W., La Nafie, Y.A., Nasution, I.M., Orth, R.J., Prathep, A., Sanciangco, J.C., van Tussenbroek, B., Vergara, S.G., Waycott, M., Zieman, J.C., 2011. Extinction risk assessment of the world's seagrass species. Biol. Conserv. 144, 1961–1971. http://dx.doi.org/10.1016/j.biocon.2011.04.010.

Stapel, J., Aarts, T.L., van Duynhoven, B.H.M., de Groot, J.D., van den Hoogen, P.H.W., Hemminga, M.A., 1996. Nutrient uptake by leaves and roots of the seagrass *Thalassia*

hemprichii in the Spermonde Archipelago, Indonesia. Mar. Ecol. Prog. Ser. 134, 195–206.

Sugimoto, A., San Diego-McGlone, M.L., Paciencia, F., Milan, S.P., Tomas, E.T., Ramirez, C.C., Echavez, A., Gabatin, J., Fortes, M.D., Nadaoka, K., 2016. Comanagement for aquaculture: Suggestions from a comparative study between two major production areas of milkfish in the Philippines. Journal of Applied Aquaculture. doi:10.1080/10454438.2016.120971.

Tanaka, Y., Go, G.A., Watanabe, A., Miyajima, T., Nakaoka, M., Uy, W.H., Nadaoka, K., Watanabe, S., Fortes, M.D., 2014. 17-year change in species composition of mixed seagrass beds around Santiago Island, Bolinao, the northwestern Philippines. Mar. Pollut. Bull. 88, 81–85.

Tanaka, Y., Nakaoka, M., 2004. Emergence stress and morphological constraints affect the species distribution and growth of subtropical intertidal seagrasses. Mar Ecol. Prog. Ser. 284, 117–131.

Tanaka, Y., Nakaoka, M., 2007. Interspecific variation in photosynthesis and respiration balance of three seagrasses in relation to light availability. Mar. Ecol. Prog. Ser. 350, 63–70.

Tanaya, T., Watanabe, K., Yamamoto, S., Hongo, C., Kayanne, H., Kuwae, T., 2018. Contributions of the direct supply of belowground seagrass detritus and trapping of suspended organic matter to the sedimentary organic carbon stock in seagrass meadows. Biogeosciences 15, 4033–4045.

Terrados, J., Agawin, N.S.R., Duarte, C.M., Fortes, M.D., Kamp-Nielsen, L., Borum, J., 1999a. Nutrient limitation of the tropical seagrass *Enhalus acoroides* (L.) Royle in Cape Bolinao, NW Philippines. Aquat. Bot. 65, 123–139.

Terrados, J., Duarte, C.M., Kamp-Nielsen, L., Agawin, N.S.R., Gacia, E., Lacap, D., Fortes, M.D., Borum, J., Lubanski, M., Greve, T., 1999b. Are seagrass growth and survival constrained by the reducing conditions of the sediment? Aquat. Bot. 65, 175–197.

Unsworth, R.K.F., Nordlund, L.M., Cullen-Unsworth, L.C., 2018. Seagrass meadows support global fisheries production. Conservation Letters, e12566. doi: 10.1111/conl.12566.

Unsworth, R.K.F., Rasheed, M.A., Chartrand, K.M., Roelofs, A.J., 2012. Solar radiation and tidal exposure as environmental drivers of *Enhalus acoroides* dominated seagrass meadows. PLoS ONE 7(3), e34133. doi:10.1371/journal.pone.0034133.

Verceles, L.F., Talaue-McManus, L., Aliño, P.M., 2000. Participatory monitoring and feedback system: an important entry towards sustainable aquaculture in Bolinao, Northern Philippines. Science Diliman 12(2), 78–87.

Verhagen, J.H.G., Nienhuis, P.H., 1983. A simulation model of production, seasonal changes in biomass and distribution of eelgrass (*Zostera marina*) in lake Grevelingen. Mar. Ecol. Prog. Ser. 10, 187–195.

Vermaat, J.E., Agawin, N.S.R., Duarte, C.M., Fortes, M.D., Marba, N., Uri, J.S., 1995. Meadow maintenance, growth and productivity of a mixed Philippine seagrass bed. Mar. Ecol. Prog. Ser. 124, 215–225.

Waycott, M., Duarte, C.M., Carruthers, T.J.B., Orth, R.J., Dennison, W.C., Olyarnik, S., Calladine, A., Fourqurean, J.W., Heck Jr., K.L., Hughes, A.R., Kendrick, G.A., Kenworthy, W.J., Short, F.T., Williams, S.L., 2009. Accelerating loss of seagrasses across the globe threatens coastal ecosystems. Proc. Natl. Acad. Sci. U.S.A. 106, 12377–12381.

Waycott, M., Longstaff, B.J., Mellors, J., 2005. Seagrass population dynamics and water quality in the Great Barrier Reef region: A review and future research directions. Mar. Pollut. Bull. 51, 343–350.

Williams, S.L., 1987. Competition between the seagrasses *Thalassia testudinum* and *Syringodium filiforme* in a Caribbean lagoon. Mar. Ecol. Prog. Ser. 35, 91–98.

Yamamoto, T., Malingin, M.A.C.L., Pepino, M.M., Yoshikai, M., Campos, W., Miyajima, T., Watanabe, A., Tanaka, Y., Morimoto, N., Ramos, R., Pagkalinawan, H., Nadaoka, K., 2019. Assessment of coastal turbidity improvement potential by terrigenous sediment load reduction and its implications on seagrass inhabitable area in Banate Bay, central Philippines. Sci. Total Environ. 656, 1386–1400.

Yap, L.G., Azanza, R.V., Talaue-McManus, L., 2004. The community composition and production of phytoplankton in fish pens of Cape Bolinao, Pangasinan: a field study. Mar. Pollut. Bull. 49, 819–832.

Zimmerman, R.C., 2003. A biooptical model of irradiance distribution and photosynthesis in seagrass canopies. Limnol. Oceanogr. 48(1, part 2), 568–585.

Supporting Information for Chapter 2

Note S2.1. Geometric representation of seagrass canopy layers

To compute the irradiance distribution within a mixed seagrass canopy, the leaf length and leaf bend nadir angle were assumed as fixed parameters for simplicity. It was also assumed that the blade shapes are straight under the water. The leaf height of each species (h_s, m) is then given by

$$h_s = l_s \cos\theta_s \quad \text{(S1)}$$

where l_s is the leaf length (m), and θ_s is the leaf bend nadir angle (Fig. S2.1a), and "s" denotes species, where 1 is *Thalassia hemprichii* and 2 is *Enhalus acoroides*. Seagrass canopy was divided into multi-layers with a uniform thickness *dz* = 0.01m. The layers were numbered from the canopy top to the ground (Fig. S2.1b). It was assumed that above-ground biomass of each species is evenly distributed from the leaf top (h_s) to the ground. If the above-ground biomass in layer i of a species is given as $LB_{s,i}$ (mmol C m^{-2} ground), the layer leaf area index of the species ($LAI_{s,i}$, m^2 leaf m^{-2} ground) is calculated as

$$LAI_{s,i} = LB_{s,i}/LAR_s \quad \text{(S2)}$$

where LAR_s is leaf area ratio of the species (m^2 leaf $mmol^{-1}$ C). *LAR* for each species was estimated from leaf dimension, leaf biomass in Vermaat et al. (1995), and biomass carbon contents in Duarte (1990), which were calculated as 2701 and 2198 (m^2 leaf $mmol^{-1}$ C) for *T. hemprichii* and *E. acoroides*, respectively. The projected leaf area of a species in a layer ($Al_{s,i}$, m^2 leaf m^{-2} ground) is calculated as

$$Al_{s,i} = LAI_{s,i} \sin\theta_s \quad \text{(S3)}$$

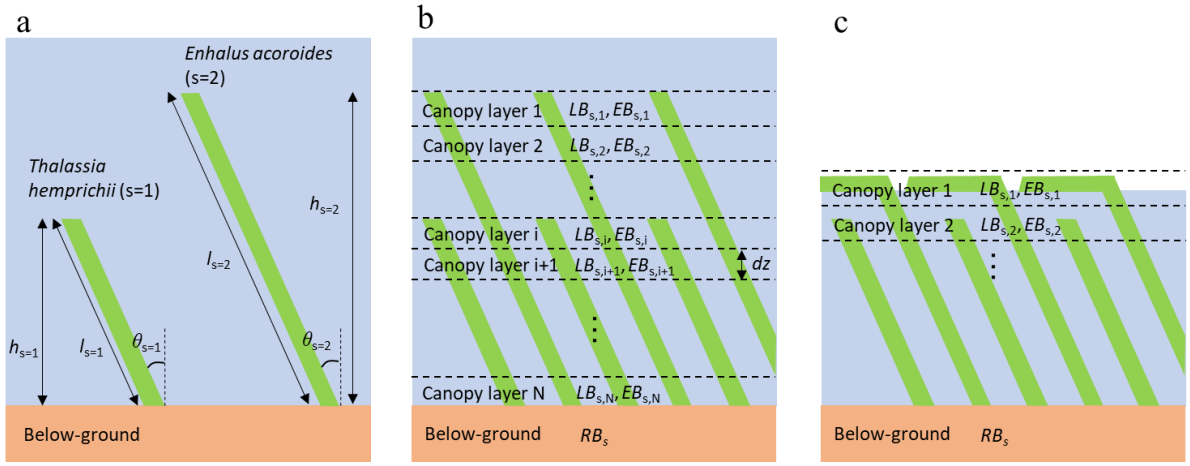

Figure S2.1. (a) Geometric representation of seagrass leaves, (b) vertical layers of mixed seagrass canopy with layer variables of species-specific above-ground biomass ($LB_{s,i}$),

epiphyte biomass attached on the respective species ($EB_{s,i}$), and species-specific below-ground biomass (RB_s) for the submerged condition, and (c) the partially exposed condition.

Note S2.2. Three-dimensional hydrodynamic-biogeochemical model

Biogeochemical model configuration

Delwaq, a biogeochemical model used in this study, is a generic biogeochemical model that simulates biogeochemical processes in waters and sediments by solving advection-diffusion-reaction equation for various substances (Smits and Beek, 2013; Deltares, 2014). Delwaq has many options for substances and processes to be simulated, thus users have to configure the processes and state variables to model individually. The schematic diagram of our model configuration for the Bolinao-Anda coastal area is shown in Fig. S2.2. The water quality in the mariculture area has become eutrophic due to nutrients from decomposition of organic matter (e.g., uneaten fish food and feces due to excessive mariculture activities) in the water and sediment (Holmer et al., 2002, 2003; Ferrera et al., 2016). Therefore, the sediment compartment was vertically partitioned to seven layers to simulate the organic matter accumulation and decomposition processes.

Particulate organic carbon (POC), nitrogen (PON), and phosphorus (POP) were divided into four different substances according to their decomposition speeds. POC/N/P1 represents the fast decomposing detritus fraction, POC/N/P2 the moderately slow decomposing detritus fraction, POC/N/P3 the slow decomposing fraction, and POC/N/P4 the refractory fraction (Fig. S2.2). Mineralization rates of these substances at 20 ℃ were set as 0.288, 0.0576, and 0.00192 (day^{-1}) for fast, moderately slow, and slow classes, respectively. The decomposed detritus goes to inorganic nutrients, and to slower decomposing class, and dissolved organic matter (DOC/N/P). Particulate organic matter (POC/N/P or POM) is supplied from unconsumed fish food and fish feces as waste load input from the fish-rearing structures, and dead phytoplankton biomass (Fig. S2.2). The amount of fish food given in a fish-rearing structure a day, the ratio of waste load input in the forms of unconsumed food and fish feces to fish food given, and their nutrient contents are shown in Table S2.2. The relative contents of fast, moderately slow, and slow detritus are assumed to be 80%, 10%, and 10% for fish food, and 39%, 21%, and 40% for fish feces, respectively, based on a laboratory experimental study of fish food and feces decomposition (Sakami et al., 2010).

Phytoplankton was divided to diatom and algae (non-diatom) (Fig. S2.2). The changes in their biomass are governed by net production, respiration, and mortality. When phytoplankton dies, a certain proportion of biomass goes into inorganic nutrients through

autolysis without any influence on dissolved oxygen (DO). The rest of biomass goes into fast (POC/N/P1) and moderately slow decomposing detritus (POC/N/P2). Nitrate (NO3), ammonium (NH4), ortho-phosphate (PO4), and silicate (Si) were configured in the nutrient dynamics in the area (Fig. S2.2). The changes in their concentrations are governed by autolysis and uptake by phytoplankton, and mineralization of particulate organic matter. NH4 and NO3 are also affected by nitrification and denitrification depending on the DO concentration. The changes in DO are governed by net production of phytoplankton, and oxygen consumption by mineralization and nitrification (Fig. S2.2). Particulate inorganic matter (PIM) was also configured in the model, supplied from Bani and Alaminos Rivers as point sources.

Mass exchange of dissolved substances across the sediment-water interface is modeled as dispersion flux. These fluxes include the return fluxes of nutrients to the water column and the sediment oxygen consumption flux (Deltares, 2014). Mass exchange of particulate substances occurs as a result of settling and resuspension. The settling flux is proportional to its concentration and settling velocity. The resuspension flux (E) is computed using the following equation:

$$\mathrm{E} = \mathrm{M} \times \left(\frac{\tau_b}{\tau_c} - 1\right) \qquad \text{(S4)}$$

where the unit of E is (g m^{-2} day^{-1}), M is the first-order resuspension flux (g m^{-2} day^{-1}), τ_b is the bed shear stress (Pa), and τ_c is the critical shear stress (N m^{-2}) (Deltares, 2014). The resuspension flux of the individual particulate substance is then computed from the weight fractions in the sediment.

Field survey for model inputs and validation

Surface water sampling was conducted at B1, B2, B3, B4, and T1 (Fig. 2.1d) in March 2013. After transporting the samples to the laboratory, nutrient concentrations were determined using a QuAAtro 2-HR Nutrient AutoAnalyzer (SEAL Analytical Ltd., Germany and BLTEC K.K., Japan). Duplicated sediment cores were sampled using acrylic pipes by SCUBA diving at B2, B3, B4, and T1 in September 2013. 30 cm^3 of the top 5 cm of each core sample was centrifuged and the nutrient concentrations of the extracted pore water were analyzed. Another core sample was oven-dried at 60 ℃, and bulk density was determined by dividing the dry weight by its original volume.

In addition to water sampling and sediment core sampling, time series of flow velocity (using Infinity-EM, JFE Advantech, Japan), salinity and temperature (using Infinity-CTW, JFE Advantech) at the near bottom were measured at B2, B3, and B4. Time-series of DO (using Infinity-DOW, JFE Advantech), turbidity and Chl-a (using Infinity-CLW, JFE Advantech) were measured at B2 and B4. Water level was also measured at B2 with a pressure sensor (HOBO

water level logger, Onset Computer Corporation, USA). Vertical profiling of water quality was periodically done using AAQ-RINKO water quality profiler (JFE Advantech) for salinity and water temperature at B4.

Model setup (initial conditions)

The determined nutrient concentrations from water sampling at B1 and T1, and the averaged nutrient concentrations of B2, B3, and B4 were used in the reef and offshore areas, Tambac Bay, and the mariculture area, respectively as initial conditions of water quality for February 2012 in the biogeochemical model (Table S2.3). Due to lack of data on the vertical profile of water quality during this sampling period, vertically uniform conditions were assumed. This assumption could be acceptable given the vertically homogeneous waters in the dry season (November to March) (Ferrera et al., 2016).

The measured pore water quality and bulk density at T1, and the averaged measured pore water quality and bulk density of B2, B3, and B4 were used in Tambac Bay and the mariculture area, respectively as initial conditions of sediment pore water quality and bulk density (Table S2.3). Due to lack of data on the reef and the offshore areas, assumed values of sediment pore water quality and bulk density were used as initial conditions (Table S2.3). For the initial conditions of the relative contents of POC and PON in sediments, values measured in the mariculture area by Holmer et al. (2002) were used for the mariculture area, and assumed values were used for Tambac Bay, offshore, and reef area due to absence of available data (Table S2.3).

Model setup (point sources and boundary conditions)

For river water discharged as point source, water quality obtained at T1 by sampling in September 2011 was used for both Bani and Alaminos River due to lack of data. Constant concentration of water quality parameters was assumed throughout the year (Table S2.3). An assumed constant value was given to the inorganic suspended solids concentrations of Bani and Alaminos River waters (Table S2.3). The value was based on the averaged turbidity (7.09 FTU) measured at T1 from September 2011 to November 2011 and turbidity-suspended solids relationship obtained at the Bani River by water sampling (Blanco et al., unpublished data). The sediment was assumed to be fine silt (φ = 3 μm), and the settling velocity was calculated based on Stokes' law formula. Also, constant water quality was assumed at the open boundary throughout the year, and the same values used as the initial conditions for the reef and offshore areas were given as boundary conditions.

Model validation

Figure S2.3 shows the comparison of observed and simulated hydrodynamic parameters such as water level, flow velocity, salinity, and temperature at B2, B3, and B4. Figure S2.4a - e shows the comparison of observed and simulated DO and Chl-a at B2 and B4. Regular water sampling data at BML station from Ferrera et al. (2016) was also used for validation of temporal variations of DIN (Fig. S2.2.4f).

Table S2.1. Location of stations for light attenuation measurement, seagrass shoot sampling, hydrodynamics, and water quality measurement.

Station	Latitude (°N)	Longitude (°E)
Stations for light attenuation measurement		
L1	16.36767	119.95900
L2	16.35037	119.93943
L3	16.28358	119.92172
L4	16.32718	119.93131
L5	16.43282	119.91561
L6	16.43668	119.94173
L7	16.40400	119.97419
L8	16.47570	119.89792
L9	16.47230	120.01012
Station for seagrass shoot sampling		
S1	16.39731	119.96744
Stations for hydrodynamics, water quality, light		
B2	16.38687	119.92661
B3	16.35431	119.96543
B4	16.30489	119.91742
BML	16.38248	119.91280
Stations for water quality measurement		
B1	16.41356	119.89120
T1	16.25757	119.92666

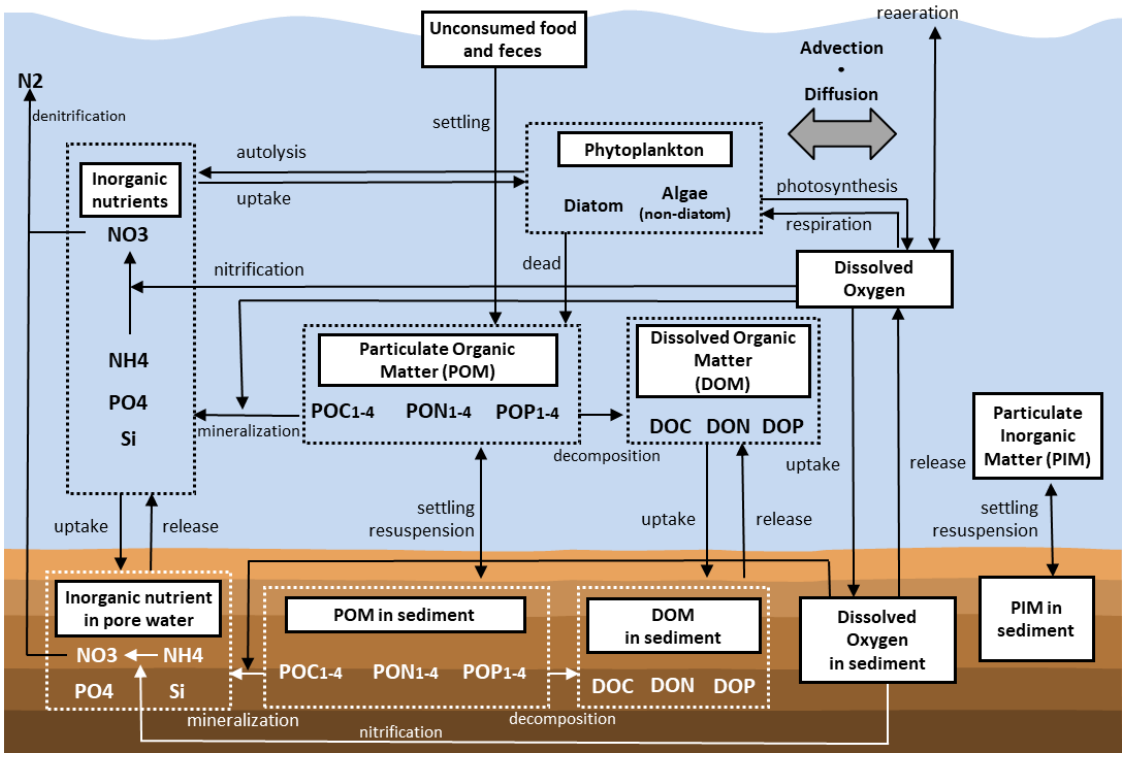

Figure S2.2. Schematic diagram of the biogeochemical model for the Bolinao-Anda coastal area.

Table S2.2. Amount of fish food given in a fish-rearing structure per day, ratio of waste load input in the form of unconsumed food and fish feces to fish food given, and their nutrient contents.

Fish food given in a fish-rearing structure (kg day^{-1})	Form of fish food to be inputted as waste load	Ratio of waste load input to fish food given (kg kg^{-1})	Relative nutrient content		
			Carbon (% DW)	Nitrogen (% DW)	Phosphorus (% DW)
2470[a]	Unconsumed food	0.2[b]	40.7[c]	4.1[c]	1.0[c]
	Fish feces	0.3[b]	20.0[b]	4.0[b]	1.6[b]

[a] From an interview survey in 2014
[b] From Magdaong (2008)
[c] From Holmer et al. (2002)

Table S2.3. Values used for the initial condition and point source in the biogeochemical model.

		DO	NH4	NO3	PO4	Si	POC	PON	POP	Chl-a	PIM	Bulk density
		mg L^{-1}	µmol L^{-1}	µmol L^{-1}	µmol L^{-1}	µmol L^{-1}	µmol L^{-1} (water) % DW (sediment)	µmol L^{-1} (water) % DW (sediment)	µmol L^{-1} (water) % DW (sediment)	µg L-1 (water) % DW (sediment)	mg L-1 (water) % DW (sediment)	g cm^{-3}
Initial condition												
Reef and offshore	Water	6.4	0.1	0.34	0.08	2.52	7.9[a]	1.38[a]	0.06[e]	1.92[b]	0[e]	
	Sediment	3[e]	250[e]	0.26[e]	73[e]	142[e]	1.1[e]	0.17[e]	0.003[e]	0[e]	98.73[e]	1.3[e]
Mariculture area	Water	4.4	8.05	1.26	2.06	4.42	53.16[a]	8.44[a]	0.14[e]	27.64[b]	0[e]	
	Sediment	1[e]	500	0.5	73	190	7.28[c]	0.58[c]	0.2[c]	0[e]	91.94[e]	0.65
Tambac Bay	Water	7.88	1.74	0.43	1.46	8.36	51.34[a]	7.55[a]	0.14[e]	39.8[b]	0[e]	
	Sediment	3[e]	250	0.26	26	142	5.3[c]	0.84[c]	0.014[e]	0[e]	93.85[e]	1.3
Point source												
River water		5.2	9.81	6.59	1.68	192	32[a]	4.4[a]	0[e]	2.93[b]	7.08[d]	

[a] Observed, but assumed fraction of POC1 (85%) and POC2 (15%) was given.

[b] Observed, but assumed composition of diatom (75%) and algae (25%) was given.

[c] From data reported by Holmer et al. (2002), and fraction of POC1 (15%) and POC2 (85%) was assumed.

[d] Assumed based on averaged turbidity at T1 from September 2011 to November 2011 and turbidity-suspended solids relationship for Bani River.

[e] Assumed.

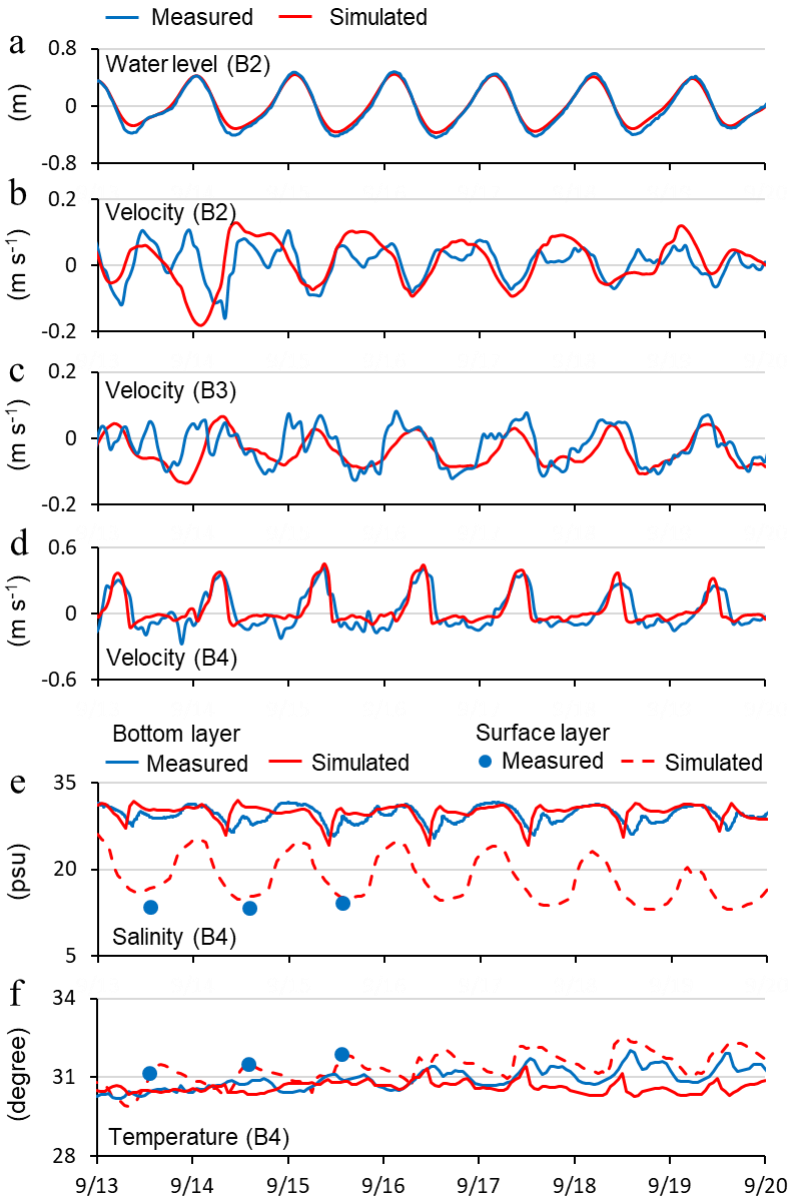

Figure S2.3. Comparison of measured and simulated time series (a) water level at B2; near-bottom flow velocity at the major axis at (b) B2, (c) B3, (d) B4; (e) surface and bottom salinity at B4; and (f) temperature at B4. The azimuths of the major axes from north at B2, B3, and B4 are 127°, 46°, and 25°, respectively. Positive values of the velocity represent water fluxes from the outer sea or Tambac Bay to the mariculture area, and negative values represent the opposite fluxes. In (e) and (f), the measured and simulated bottom salinity and temperature are shown in bold lines. The simulated surface salinity and temperature are shown in red dashed lines. The data from periodic measurement of surface salinity and temperature using a water quality profiler are shown as blue circular dots.

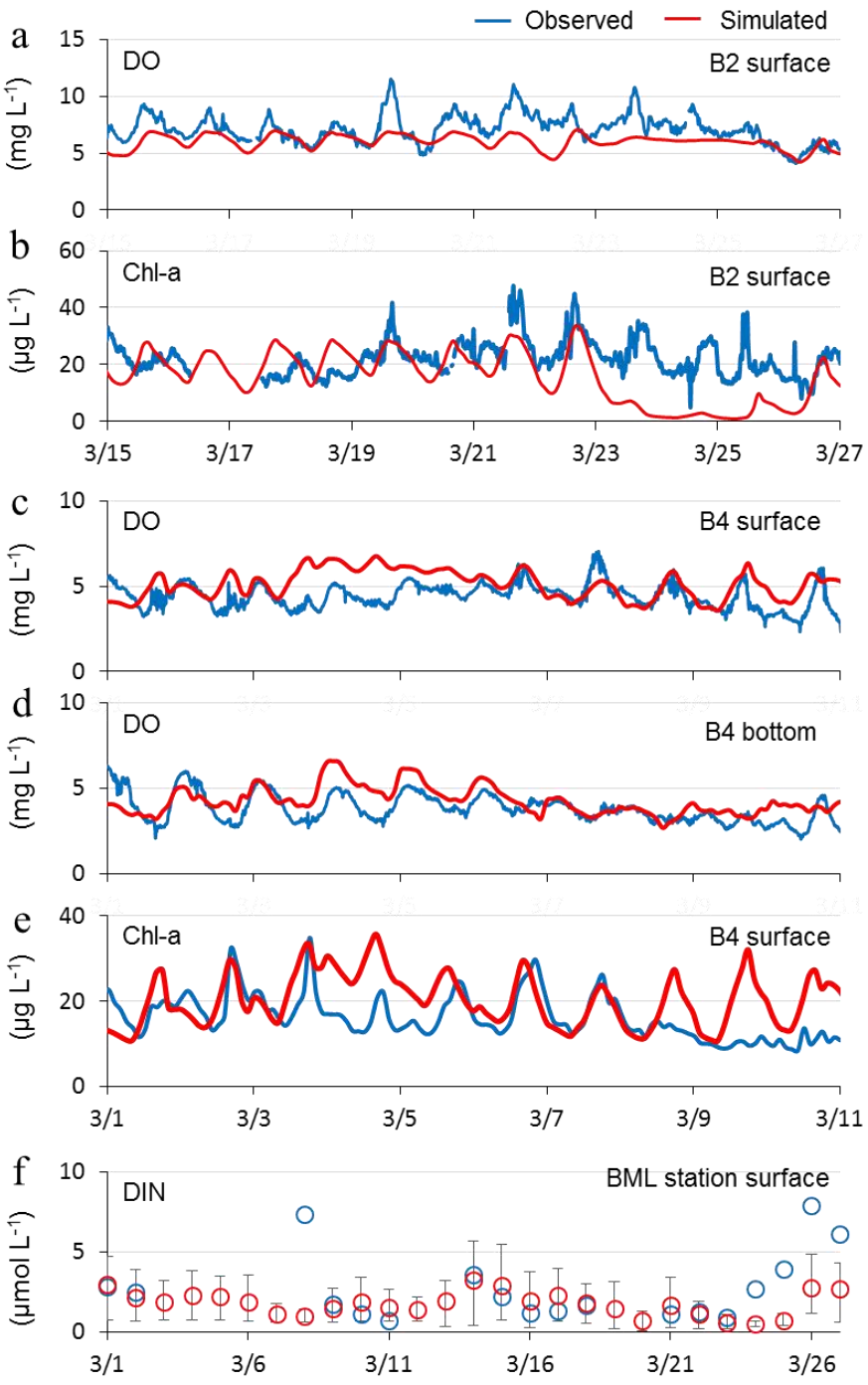

Figure S2.4. Comparison of observed and simulated time series of (a) surface DO and (b) Chl-a at B2; (c) surface DO, (d) bottom DO and (e) surface Chl-a at B4; and (f) surface DIN concentrations at BML station. DIN data were based on regular water sampling at the station (Ferrera et al., 2016) and shown in blue circular dots. The red circular dots and bars show daily means and ranges of simulated surface DIN.

Note S2.3. Sensitivity analysis of the seagrass growth and biogeochemical model parameters

Seagrass growth model parameters

Sensitivity of the seagrass biomass to the seagrass growth model parameters was examined. The parameters which were used for the model calibration were selected as the target parameters for the analysis. We increased or decreased the value of each target paramter shown in Table 2.1 by 50 %, then run the seagrass growth model until growth rates reached a steady-state in every grid cell – the same procedure done in Section 2.2.5. Then, the change ratios of the total above-ground biomass of each species in the computational area to the original values which correspond to Fig. 2.6 were examined. Because the seagrass species (*T. hemprichii* and *E. acoroides*) interact with each other in the model through the shading effects, we changed the parameter value for each species one by one to examine the sensitivity of the above-ground biomass of the two species. The results are summarized in Table S2.4.

The results showed that the increase in the sine of leaf bend nadir angle of *T. hemprichii* ($\sin\theta_1$) increased the above-ground biomass of *T. hemprichii* (LB_1) by 2.05 because it increases the incident PAR for the photosynthesis of this species as suggested by Eqs. (2.5) and (2.6). Likewise, the decrease in $\sin\theta_1$ decreased LB_1 by 0.37. The changes in $\sin\theta_1$ did not significantly affect the above-ground biomass of the other species – *E. acoroides* (LB_2). On the other hand, the increase in $\sin\theta_2$ increased LB_2 by 1.53. However, this increase in LB_2 significantly reduced LB_1 by 0.49 due to the shading of *E. acoroides* enhanced by the increased above-ground (leaf) biomass and inclined leaves, which consequently increased the projected leaf area of this species. Similarly, the decrease in $\sin\theta_2$ decreased LB_2 by 0.29, which resulted in the significant increase in LB_1 by 1.83. These results indicate that *T. hemprichii* could be significantly influenced by the changes in *E. acoroides* above-ground biomass and the leaf bend nadir angle through the shading effects, while *E. acoroides* is not likely affected by *T. hemprichii*.

Seagrass above-ground biomass was most sensitive to the parameter fraction of below-ground biomass (f_{below}). The decrease of $f_{below,1}$ increased LB_1 by 4.86, and the decrease of $f_{below,2}$ increased LB_2 by 6.60, with maximum values of 16,800 and 12,600 mmol C m^{-2} for LB_1 and LB_2, respectively. While the increases in LB are quite large for both species, these maximum values of LB_1 and LB_2 correspond to 611 g DW m^{-2} and 398 g DW m^{-2}, respectively, which are below the maximum value of the reported seagrass above-ground biomass (Vieira et al., 2018). Thus, it is considered that the seagrass growth is well constrained by the self-

shading effects in the model. The large increases in *LB* are because the decrease of this parameter value – f_{below} reduces the below-ground root respiration demand and increases the photosynthetic capacity (above-ground biomass). Similarly, the seagrass above-ground biomass was sensitive to parameters that affect root respiration demand, such as root respiration rate (R_r) and biomass translocation rate between the above- and below-ground parts (τ_{tran}).

The sensitivity of *E. acoroides* to half saturation concentration of DIN (K_{din}) is higher than *T. hemprichii* that may reflect the higher nutriend demand of *E. acoroides* (Agawin et al., 1996). The changes of epiphyte-related parameters also affect seagrass above-ground biomass. For example, the decrease of half saturation concentration of DIN for epiphyte ($K_{din,e}$) increased the epiphyte biomass density, which decreased *LB* of both species. On the other hand, the increase of $K_{din,e}$ decreased the epiphyte biomass density for both species, which increased *LB* of *E. acoroides*; whereas *LB* of *T. hemprichii* decreased due to the enhanced shading effects by *E. acoroides*. This suggests that *T. hemprichii* may be more sensitive to the shading effects by *E. acoroides* than shading by epiphytes.

Biogeochemical model parameters

Sensitivity of the seagrass biomass to the biogeochemical model paramaters was also examined. The parameters selected for the analysis were summarized in Table S2.5. The change of phytoplankton mortality rate (*Phy_mort*) affects the input amount of dead phytoplankton to POM (Fig. S2.2). Phytoplankton maximum production rate (*Phy_pmax*) and respiration rate (*Phy_resp*) affect the phytoplankton photosynthesis and respiration amount. These phytoplankton-related parameters also affect the phytoplankton nutrient uptake, and nutrient release (autolysis) by the dead phytoplankton. The maximum nitrification rate (*nit*) affects the nitrification rate, which affect the NH4, NO3, and DO concentrations in water column and sediment layers (Fig. S2.2). Mineralization rate of particulate organic matter (*min*) affects decomposition and mineralization of POM in water column and sediment layers, which also affect nutrient release rate by POM mineralization and the associated oxygen consumption and denitrification rates (Fig. S2.2). Dispersion coefficient for solute in sediment (*diff*) affects the dispersion of dissolved nutrients, DO, and DOM in sediment layers, and the exchanges (uptake and release) between the water and sediment interface (Fig. S2.2). Critical shear stress for resuspension (*cr_tau*) affects resuspension flux of POM and PIM.

The biogeochemical model parameters were increased or decreased by 50 %, respectively, and the hydrodynamic-biogeochemical model was run for each parameter change for a two-year period – the first year for the spin-up of the hydrodynamic-biogeochemical model, and the second year for driving the seagrass model – the same

procedure done in Section 2.2.5. The increase of *min* by 50 % caused numerical instability in the model, thus the increase in the value was down-regulated by 30 %. The seagrass model was then run using the respective simulated water quality until the growth rate reached a steady-state as done in Section 2.2.5. The simulated one-year averaged water quality at the surface layer (SS, DO, DIN, Chl-a, and k_d) was spatially averaged over the mariculture area and the reef area, and was compared to that of the original simulated water quality which corresponds to Fig. 2.4. The change ratios of the spatially averaged water quality for each parameter change are summarized in Table S2.6. The change ratios of the simulated total above-ground biomass of each seagrass species in the computational area driven by the respective simulated water quality to the ones shown in Fig. 2.6 were also shown in Table S2.6.

The results showed that water quality and seagrass biomass are most sensitive to phytoplankton-related parameters (*Phy_mort*, *Phy_pmax*), while the effects of phytoplankton respiration (*Phy_resp*) were not as significant (Table S2.6). Phytoplankton mortality rate (*Phy_mort*) and maximum production rate (*Phy_pmax*) directly affects phytoplankton biomass as seen in the changes in Chl-a, which is the most critical parameter for the light environment in the Bolinao and Anda coastal area (Fig. 2.3). The decrease of *Phy_pmax* by 50 % made the phytoplankton photosynthesis rate below the respiration rate that extinguished the phytoplankton biomass during the simulation. The changes in phytoplankton biomass affects the nutrient uptake, autolysis, photosynthesis, and respiration amounts as seen in the changes in DIN and DO. The amounts of dead phytoplankton that enter the pool of POM (Fig. S2.2) also changed, thus SS – expressed as the sum of PIM and POM – was also affected to an extent. Primarily due to the changes in Chl-a, the light environment represented as k_d is also largely influenced. Although the change ratios of the water quality in the reef area were not as high as the mariculture areas, the changed light environment and nutrient concentrations in the reef area significantly affected the seagrass above-ground biomass of both species.

The parameter that significantly affected the water quality and seagrass biomass next to *Phy_mort* and *Phy_pmax* was critical shear stress for resuspension (*cr_tau*). The decrease in *cr_tau* promotes resuspension as seen in the increase in SS. Due to the exposure of the resuspended POM to oxygen in the water column, the decomposition of POM associated with DO consumption and nutrient release by mineralization occurs especially in the mariculture area, which significantly lowered and raised DO and DIN, respectively. Chl-a decreased due to the lowered phytoplankton production caused by the resuspension-induced turbidity. As a result of the increased SS and the decreased Chl-a, k_d value increased in the mariculture area and also in the reef area. Due to the degraded light environment, above-ground biomass of *T. hemprichii* decreased by 7 %. On the other hand, while the reduced light is the factor affecting

E. acoroides, the above-ground biomass of this species did not change much probably due to the benefit of the increased DIN.

Similarly, the increase in the value *cr_tau* regulates resuspension, thus SS decreased. Chl-a then showed slight increase due to increased phytoplankton production rate. Due to the combined effects of the increased nutrient uptake by phytoplankton and the decreased mineralization rate of POM in the water column by the regulation of the resuspension, DIN decreased by 10 % in the mariculture area. k_d values also changed with the slight decrease in the mariculture area and the reef area although the changes in the seagrass biomass were not significant for both species.

Another important parameter that affects water quality and seagrass growth may be mineralization rate (*min*). The decrease in *min* regulates the mineralilzation of POM and the associated nutrient release both in the water column and sediment layers. The decrease in the mineralization of POM in the sediment layers reduces nutrient efflux from the sediment to the water column through solute diffusion. The decrease in the mineralization of POM in the water column directly reduces the nutrient inputs to the water column. As a result of decreased DIN, Chl-a decreased in the mariculture area and the reef area. The slight increase in SS may be due to the increased POM in the water column by the lowered decomposition rate of POM. k_d values decreased at both areas, then the above-ground biomass of both species increased with slightly larger increase of *T. hemprichii* than *E. acoroides*. The increase in *min* by 30 % did not largely affect the water quality and the seagrass biomass. This may indicate that most of POM in the water column and the sediment layers, especially the fast decomposing detritus fraction (POC/N/P1), underwent decomposition process already using the current parameter value setting shown in Table S2.5; thus, the increase in *min* did not cause significant relative increase in the decomposition of POM.

Table S2.4. Results of the sensitivity of the seagrass above-ground biomass and epiphyte biomass density to the seagrass growth model parameters, which are shown as the change ratios of the total above-ground biomass and epiphyte biomass density to the parameter changes in the computational area. The left-hand side values indicate the results from the parameter increased by 50 % while the right-hand side values in the parentheses indicate the results from the parameter decreased by 50 %. The bold numbers indicate change ratios larger than 50 %.

Parameters	**Above-ground biomass**		**Epiphyte biomass density**	
	LB_1 (*T. hemprichii*, s = 1)	LB_2 (*E. acoroides*, s = 2)	EB_1 / LAI_1	EB_2 / LAI_2
$\sin\theta_1$	**2.05** (**0.37**)	0.97 (1.03)	**2.29** (**0.34**)	0.98 (1.00)
$\sin\theta_2$	**0.49** (**1.83**)	**1.53** (**0.29**)	**0.13** (**1.73**)	1.18 (0.68)

$d_{1,2}$[a]	1.06 (0.91)	0.96 (1.06)	1.06 (0.94)	1.00 (1.00)
$d_{2,2}$[a]	0.95 (1.11)	1.03 (0.92)	0.99 (1.06)	1.00 (1.00)
$f_{below,1}$[b]	- (**4.86**)	- (0.88)	- (**0.41**)	- (0.95)
$f_{below,2}$[b]	- (**0.03**)	- (**6.60**)	- (**0.03**)	- (**0.41**)
$K_{din,1}$	0.62 (**1.74**)	1.01 (0.98)	1.06 (0.97)	1.01 (1.00)
$K_{din,2}$	**1.82** (**0.29**)	**0.37** (**3.00**)	1.29 (0.75)	1.04 (0.88)
$M_{l,1}$	0.86 (1.15)	1.01 (0.99)	0.96 (1.10)	1.00 (1.00)
$M_{l,2}$	1.15 (0.80)	0.85 (1.20)	1.12 (0.90)	1.01 (0.99)
$R_{r,1}$	0.55 (**1.74**)	1.02 (0.97)	1.14 (0.94)	1.01 (0.99)
$R_{r,2}$	**1.72** (**0.21**)	**0.35** (**3.09**)	1.43 (**0.32**)	1.03 (0.79)
$\tau_{tran,1}$	0.79 (**1.73**)	1.01 (0.97)	1.06 (0.96)	1.00 (0.99)
$\tau_{tran,2}$	**1.82** (**0.16**)	**0.40** (**3.92**)	**2.04** (**0.33**)	1.04 (0.67)
$K_{din,e}$	0.65 (0.74)	**1.59** (0.55)	**0.24** (**4.45**)	0.58 (**2.09**)
s_{e1}	1.39 (0.54)	**0.48** (**1.97**)	**1.79** (**0.20**)	**1.58** (**0.40**)
s_{e2}	1.03 (0.91)	0.98 (1.08)	1.03 (0.90)	1.02 (0.94)

[a] The sensitivity of the shallow water depth effects on mortality of *T. hemprichii* ($d_{1,s=1}$, $d_{2,s=1}$) was not examined because the effects were introduced only for *E. acoroides* in the model.
[b] The sensitivity of the increase of $f_{below,s}$ by 50 % was not examined because it will exceed the value "1.0".

Table S2.5. Biogeochemical model parameters examined in the sensitivity analysis. The parameter values which were used to reproduce the water quality in the Bolinao and Anda coastal areas are also shown.

Parameter	Description	Unit	Used values
Phy_mort	Phytoplankton mortality rate at 20 ℃	day^{-1}	0.25 for Diatom, 0.35 for Algae
Phy_pmax	Phytoplankton maximum production rate	day^{-1}	4.6 for Diatom, 3.6 for Algae
Phy_resp	Phytoplankton respiration rate at 20 ℃	day^{-1}	0.035 for Diatom, 0.053 for Algae
nit	Maximum nitrification rate at 20 ℃	g N m^{-3} day^{-1}	0.1
min	Mineralization rate of particulate organic matters	day^{-1}	0.288 for fast, 0.0576 for moderate slow, 0.00192 for slow decomposing organic matters
diff	Dispersion coefficient for solute in sediment	m^2 day^{-1}	0.0005
cr_tau	Crtical shear stress for resuspension	N m^{-2}	0.1

Table S2.6. Sensitivity of water quality and seagrass biomass to the biogeochemical parameters shown in Table S2.5. The change ratios of the spatially averaged values over the mariculture area and the reef area for the simulated one-year averaged water quality at the surface layer are shown. The change ratios of the simulated total above-ground biomass of each seagrass species are also shown. SS (suspended solids) denotes the sum of PIM and POM. The shaded cells indicate change ratios larger than 10 %.

Examined parameter		**Water quality**										**Seagrass above-ground biomass**	
		Mariculture area					Reef area						
		SS	DO	DIN	Chl-a	k_d	SS	DO	DIN	Chl-a	k_d	*T. hemprichii*	*E. acoroides*
Phy_mort	+ 50 %	0.82	0.87	2.00	0.42	0.57	0.86	0.98	1.78	0.52	0.78	1.13	1.55
	– 50 %	0.98	1.08	0.35	1.74	1.52	0.95	1.01	0.42	1.67	1.29	0.49	0.41
Phy_pmax	+ 50 %	1.2	1.11	0.36	1.29	1.26	1.21	1.02	0.41	1.26	1.16	0.52	0.38
	– 50 %	0.51	0.77	2.69	0.01	0.25	0.5	0.95	2.53	0.03	0.55	1.75	3.40
Phy_resp	+ 50 %	0.95	0.98	1.09	0.90	0.92	0.95	1.00	1.07	0.92	0.96	1.05	1.06
	– 50 %	1.06	1.02	0.91	1.11	1.08	1.06	1.00	0.93	1.09	1.04	0.94	0.94
nit	+ 50 %	0.99	0.99	0.97	0.98	0.98	0.99	1.00	0.98	0.98	0.99	1.01	1.00
	– 50 %	1.02	1.01	1.04	1.03	1.03	1.02	1.00	1.03	1.03	1.01	0.99	1.00
min[a]	+ 30 %	0.96	1.00	1.02	1.05	1.02	0.96	1.00	1.02	1.05	1.02	0.99	0.99
	– 50 %	1.06	1.00	0.90	0.85	0.93	1.07	1.00	0.90	0.86	0.94	1.06	1.03
diff	+ 50 %	1.03	1.00	1.05	1.06	1.05	1.03	1.00	1.03	1.05	1.02	0.98	0.99
	– 50 %	0.97	1.00	0.94	0.94	0.94	0.97	1.00	0.95	0.94	0.97	1.01	1.00
cr_tau	+ 50 %	0.87	1.02	0.90	1.04	0.97	0.82	1.00	0.95	1.02	0.98	1.01	1.00
	– 50 %	1.81	0.87	1.86	0.79	1.16	2.51	0.99	1.44	0.85	1.12	0.93	1.00

[a] The increase of *min* was down-regulated by 30 % to avoid numerical instability in the model.

Note S2.4. Temporal variations of simulated water quality and seagrass production

Extracted as an example and shown in Fig. S2.5 are the temporal variations of computed water depth, surface water quality, surface and bottom PAR, and net production of *T. hemprichii* at Site 3 (see Fig. 2.1c for the location of Site 3). The computed water quality showed diurnal variations, and PAR reaching the seabed was affected by a combination of factors including tide, k_d, and surface PAR fluctuations. The net production rate was affected by temporal variations in PAR at the seabed, which also showed diurnal fluctuations, leading to dynamic changes in seagrass biomass (Fig. S2.5d).

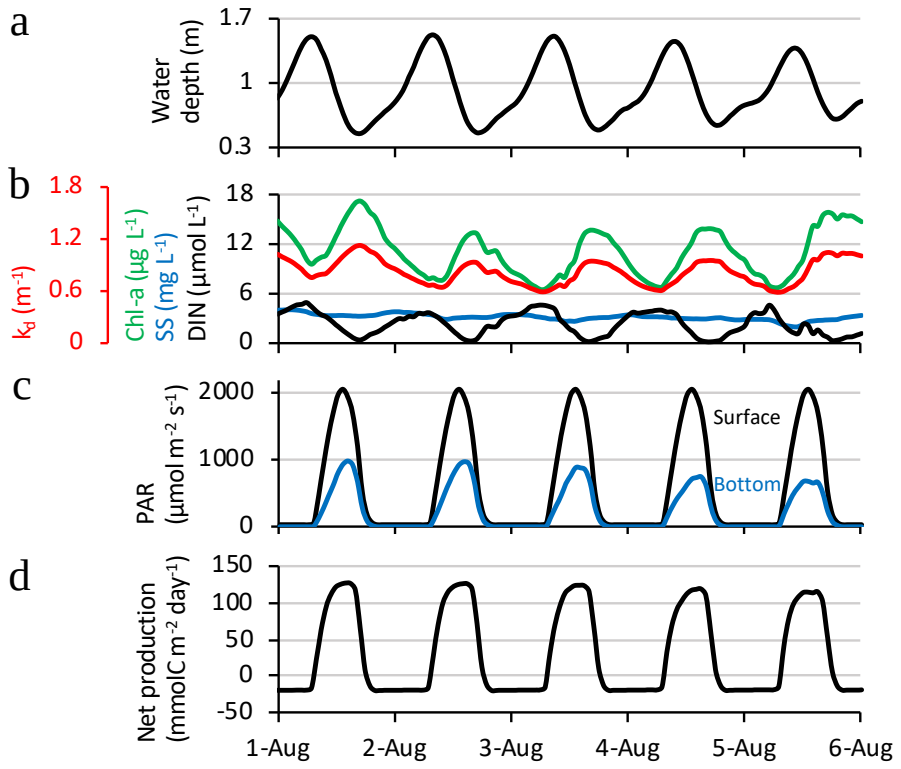

Figure S2.5. Time series of computed (a) water depth, (b) DIN, SS, Chl-a, k_d at the surface, (c) PAR at the surface and bottom, and (d) net production of *T. hemprichii* at Site 3.

References for the Supporting Information

Agawin, N.S.R., Duarte, C.M., Fortes, M.D., 1996. Nutrient limitation of Philippine seagrasses (Cape Bolinao, NW Philippines): in situ experimental evidence. Mar. Ecol. Prog. Ser. 138, 233–243.

Deltares, 2014. D-Water Quality: Versatile water quality modelling in 1D, 2D or 3D systems including physical, (bio)chemical and biological processes - User Manual, version 4.99.34158, Delft, Netherlands.

Duarte, C.M., 1990. Seagrass nutrient content. Mar. Ecol. Prog. Ser. 67, 201–207.

Ferrera, C.M., Watanabe, A., Miyajima, T., San Diego-McGlone, M.L., Morimoto, N., Umezawa, Y., Herrera, E., Tsuchiya, T., Yoshikai, M., Nadaoka, K., 2016. Phosphorus as a driver of nitrogen limitation and sustained eutrophic conditions in Bolinao and Anda, Philippines, a mariculture-impacted tropical coastal area. Mar. Pollut. Bull. 105, 237–248.

Holmer, M., Duarte, C.M., Heilskov, A., Olesen, B., Terrados, J., 2003. Biogeochemical conditions in sediments enriched by organic matter from net-pen fish farms in the Bolinao area, Philippines. Mar. Pollut. Bull. 46, 1470–1479.

Holmer, M., Marba, N., Terrados, J., Duarte, C.M., Fortes, M.D., 2002. Impacts of milkfish (*Chanos chanos*) aquaculture on carbon and nutrient fluxes in the Bolinao area, Philippines. Mar. Pollut. Bull. 44, 685–696.

Magdaong, E., 2008. Modeling Residence Time and Aquaculture Waste Dispersal. MSc Thesis, University of the Philippines.

Sakami, T., K. Abo, Takaashi, T., 2010. Laboratory studies on oxic and anoxic decomposition of fish food and feces. Nippon Suisan Gakkaishi. 76, 933–937 (in Japanese).

Smits, J.G.C., Beek, J.K.L., 2013. ECO: A generic eutrophication model including comprehensive sediment-water interaction. PLoS ONE 8(7), e68104.

Vermaat, J.E., Agawin, N.S.R., Duarte, C.M., Fortes, M.D., Marba, N., Uri, J.S., 1995. Meadow maintenance, growth and productivity of a mixed Philippine seagrass bed. Mar. Ecol. Prog. Ser. 124, 215–225.

Vieira, V.M.N.C.S., Lopes, I.E., Creed, J.C., 2018. The biomass–density relationship in seagrasses and its use as an ecological indicator. BMC Ecol 18, 44.

Chapter 3: Predicting mangrove forest dynamics across a soil salinity gradient using an individual-based vegetation model linked with plant hydraulics

3.1.1 Abstract

In mangrove forests, soil salinity is one of the most significant environmental factors determining forest distribution and productivity as it limits plant water uptake and carbon gain. However, salinity control on mangrove productivity through plant hydraulics has not been investigated by existing mangrove models. Here we present a new individual-based model linked with plant hydraulics to incorporate physiological characterization of mangrove growth under salt stress. Plant hydraulics was associated with mangroves' nutrient uptake and biomass allocation apart from water flux and carbon gain. The developed model was performed for two-coexisting species – *Rhizophora stylosa* and *Bruguiera gymnorrhiza* – in a subtropical mangrove forest in Japan. The model predicted that the productivity of both species was affected by soil salinity through downregulation of stomatal conductance. Under low soil salinity conditions (< 28‰), *B. gymnorrhiza* trees grew faster and suppressed the growth of *R. stylosa* trees by shading that resulted in a *B. gymnorrhiza*-dominated forest. As soil salinity increased, the productivity of *B. gymnorrhiza* was significantly reduced compared to *R. stylosa*, that led to an increase in biomass of *R. stylosa* despite the enhanced salt stress (> 30‰). These predicted patterns in forest structures across soil salinity gradient remarkably agreed with field data, highlighting the control of salinity on productivity and tree competition as factors that shape the mangrove forest structures. The model reproducibility of forest structures was also supported by the predicted self-thinning processes, which likewise agreed with field data. Aside from soil salinity, seasonal dynamics in atmospheric variables (solar radiation and temperature) was highlighted as factors that influence mangrove productivity in a subtropical region. This physiological principle-based improved model has the potential to be extended to other mangrove forests in various environmental settings, thus contributing to a better understanding of mangrove dynamics under future global climate change.

3.1.2 Introduction

Mangrove forests grow in intertidal zones in tropical and subtropical regions (Giri et al., 2011) and store a large amount of carbon (C) especially in their soil, commonly referred to as “blue carbon”. It has roughly four times higher ecosystem-scale carbon stock than other forest ecosystems (Donato et al., 2011), characterizing them as globally important C sinks (Mcleod et al., 2011; Alongi, 2014; Taillardat et al., 2018; Sharma et al. 2020), therefore playing an important role in climate change mitigation. However, mangrove forests have declined worldwide; at least 35% of the mangrove forests had disappeared in the 1980s and 1990s predominantly because of deforestation due to conversion to aquaculture ponds, rice fields, urban development and palm oil plantations (Friess et al., 2019). Deforestation has been continuing until now particularly in Southeast Asia with a recent estimate of mangrove loss rates between 0.11%–0.70% (Friess et al., 2019, 2020). The loss of mangrove soil C through mineralization following deforestation has been of concern as a source of carbon emission to the atmosphere in addition to the loss of C sequestration capacity (Atwood et al., 2017; Sharma et al. 2020; Adame et al., 2021). To facilitate effective mangrove conservation, management, and restoration, a better understanding of C sequestration rates and the soil C dynamics, hence mangrove blue C dynamics, under different environmental conditions and climate change are urgently needed.

While the mangrove soil C dynamics are complex and involve physical, biogeochemical, and ecological processes (Kristensen et al., 2008; Alongi, 2014; Bukoski et al. 2020) that still remains poorly understood, one of the most important variables determining soil C dynamics may be related to mangrove productivity. Mangroves supply their products, such as leaf litter and dead roots to the soil C pool (Kristensen et al., 2008; Alongi, 2014; Ouyang et al., 2017) which are closely related to forest structural variables such as canopy height and above-ground biomass (AGB) (Saenger and Snedaker, 1993; Komiyama et al., 2008). Such autochthonous C accounts for a significant amount of total soil C in mangrove forests (Xiong et al., 2018; Sasmito et al., 2020). Therefore, the aim of this study is to successfully quantify and predict the biomass dynamics and growth processes of mangroves in different environmental conditions. These results would take a step forward in our understanding of mangrove C sequestration rate and soil C dynamics.

Although data and insights on mangrove AGB distributions in relation to environmental variables have recently increased (Simard et al., 2019; Rovai et al., 2015, 2021), there is still no established way to predict the dynamics of mangrove AGB in the changing environmental conditions. Generally, ecosystem’s response to environmental variables is nonlinear, and

biomass dynamics is cumulatively affected by nonlinear response. Therefore, predicting the effect of one environmental variable on mangrove biomass dynamics is difficult if based only from the monitoring data on mangroves' biomass, which are exposed to the effects of multiple environmental variables. This makes the assessment of environmental impacts on mangrove biomass dynamics challenging if datasets from only the field-based monitoring approach are used.

The dynamic vegetation model (DVM) simulates vegetation or forest growth based on physiological principles that includes processes such as tree competition, establishment, and mortality (Fisher et al., 2017). This model could be a way to overcome the limitation of field-based approach and predict mangrove biomass dynamics under multiple environmental variables. Various DVMs (e.g., big-leaf, cohort-based, individual-based) have been developed mainly for terrestrial ecosystems and have successfully reproduced the dynamics of various forests in the temperate, tropical, and boreal regions (Fisher et al., 2017). Recently, DVMs have advanced in physiological expression of stomatal conductance under water stress, by incorporating a plant hydraulic model that explicitly solves plant water flux (Bonan et al., 2014; Xu et al., 2016; Li et al., 2021). Recent studies also identified plant hydraulics as a critical factor that determines the plants' biomass allocation pattern to leaves, stem, and roots (Magnai et al., 2000; Trugman et al., 2019b; Portkay et al., 2021), the variations of which could drive a significant variation in plant productivity (Trugman et al., 2019a).

In mangrove forests, the salt in soil porewater (soil salinity) is one of the significant environmental factors that determine the mangroves' distribution, productivity, structure, and zonation pattern (Ball and Farquhar, 1984; Clough and Sim, 1989; Sobrado, 2000; Ball, 2002; Suarez and Medina, 2005; Suwa et al., 2009; Barr et al., 2013; Nguyen et al., 2015). Therefore, it is essential to properly represent the effects of soil salinity on mangrove growth considering species differences in the tolerance of salinity in order to accurately predict the mangrove biomass dynamics. Soil salinity imposes highly negative water potential in the substrate, making the water acquisition energetically challenging for plants, which acts in a similar way to water stress (Reef and Lovelock, 2015). With this perspective, the theoretical works of Perri et al. (2017, 2019) demonstrated the importance of considering the plant hydraulics for predicting the photosynthetic and transpiration rates under salt stress. However, although there are several individual-based DVMs for mangroves (e.g., FORMAN by Chen and Twilley, 1998, Kiwi by Berger and Hildenbrandt, 2000, mesoFON by Grueters et al., 2014, and BETTINA by Peters et al., 2014), no model yet has considered salinity control role in photosynthesis and transpiration through plant hydraulics, suggesting a room for improvement in the physiological representation of the mangrove biomass dynamics under the impacts of soil salinity. It is expected that the nutrient uptake rate is also affected by soil salinity through

the regulated transpiration rate (Simunek and Hopmans, 2009), making nutrient availability as one of the key factors controlling mangrove growth especially under high soil salinity conditions (Lovelock et al., 2004, 2006a, 2006b; Feller et al., 2007; Reef et al., 2010). Nonetheless, the modeling studies have not explicitly considered the role of nutrient uptake in mangrove growth.

Here we hypothesized that the individual-based DVM incorporating plant hydraulic traits can reasonably predict mangrove biomass, structure, and species zonation pattern across a soil salinity gradient without empirical expression of the soil salinity influence on mangrove productivity. Such model would advance the understanding of mangrove biomass dynamics under multiple environmental stresses, which ultimately influence the mangrove soil carbon dynamics. To test the hypothesis and contribute to the improvement of the physiological representation of mangrove growth specifically under soil salinity impacts, we developed a new individual-based DVM for the mangrove forest. The developed model is based on a terrestrial individual-based DVM – the SEIB-DGVM (Spatially-Explicit Individual-Based Dynamic Global Vegetation Model, Sato et al., 2007). We added a plant hydraulic model to SEIB-DGVM and coupled it with the photosynthetic model to consider the impacts of soil salinity on the mangrove water uptake and carbon gain. We also explicitly considered the role of nutrient uptake on biomass dynamics. Furthermore, a novel biomass allocation scheme linked with plant hydraulics and resource uptake rate was introduced as the mangroves' strategy to cope with salt stress and enhance the rate of production. We tested the developed model and determined the reproducibility of forest structures (e.g., species composition, biomass) in a subtropical mangrove forest in Japan with two coexisting species (*Rhizophora stylosa* and *Bruguiera gymnorrhiza*).

3.2 Materials and Methods

3.2.1 Study site

Our study site for the model application is an estuarine mangrove of the Fukido River (Fukido mangrove forest) in Ishigaki Island, Japan (Fig. 3.1, 24° 20' S, 124° 15' E). The site is characterized as a subtropical region. According to the climatological normal data obtained by the Japan Meteorological Agency, the annual-mean air temperature is 24.5 ℃, with a monthly average of 29.6 ℃ in July and 18.9 ℃ in January (see also Fig. 3.4). The mean monthly precipitation is 142 mm in July and 135 mm in January. Four small rivers (R1 – R4) flow into the Fukido mangrove forest, while the river R2 has two outlets (Fig. 3.1c). The mean discharge

rates of the rivers in October 2012 were less than 0.03 m^3 s^{-1} for R1, R3, and R4 and around 0.05 m^3 s^{-1} for R2 (Mori et al., unpublished data). The tide is semi-diurnal with the highest and lowest amplitude of 1.8 m and 0.8 m, respectively (Egawa et al., 2021).

The site is vegetated by two species, *R. stylosa* and *B. gymnorrhiza*. The trees of *R. stylosa* dominated the sea-ward zone, especially areas close to the river mouth (Fig. 3.1c) while *B. gymnorrhiza* dominated the landward zone. The species *R. stylosa* is classified as a relatively salt-tolerant species while *B. gymnorrhiza* is classified as a less salt-tolerant but shade-tolerant species (Putz and Chan, 1986; Sharma et al. 2012; Reef et al., 2015). According to Ohtsuka et al. (2019), the Fukido mangrove forest is a mature and intact mangrove forest designated as natural protection area by Ishigaki City, where distinct disturbances to the mangroves have not occurred since at least 1977 based on aerial photograph analysis.

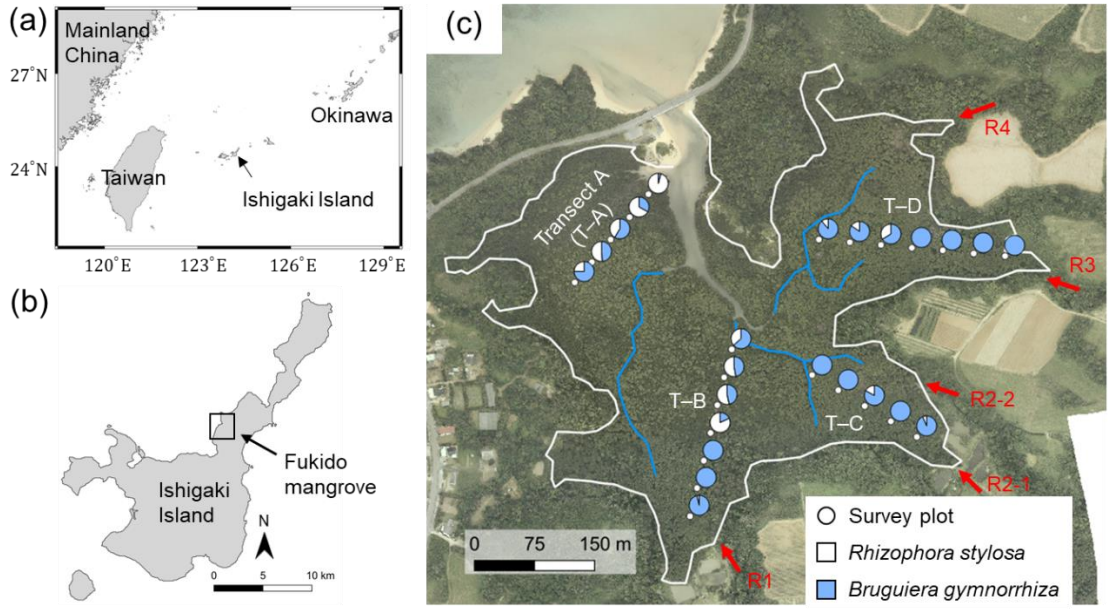

Figure 3.1. (a) Location of Ishigaki Island, (b) location and (c) aerial photo of the study site – Fukido mangrove forest. The white line in panel (c) indicates the boundary of mangroves and other land covers where mangroves are assumed to inhabit the areas of elevation < 1.0 m + mean sea level, which was delineated based on a LiDAR-derived digital elevation model (DEM). The blue lines indicate small creeks. The circular makers indicate survey plots' locations along with four transects (T–A to T–D), while the pie charts indicate species composition in each plot. The red arrows indicate outlets of rivers flowing into the mangrove forest (R1 to R4). The aerial photo and DEM products were obtained from Asia Air Survey Co. Ltd., Japan. Shorelines are from Global Shelf-consistent, Hierarchical, High-resolution Shorelines (GSHHG).

3.2.2 Field data collection

We used the tree census data of the Fukido mangrove forest shown in Suwa et al. (2021) to assess model performance. The tree census data were collected from the survey plots established along four transects (T–A, T–B, T–C, and T–D), shown in Fig. 3.1c. The details of the survey protocol are described in Suwa et al. (2021). The stem biomass of individual trees (M_S, g) was estimated from a common mangrove allometric equation proposed by Komiyama et al. (2005), which was validated with various mangrove species:

$$M_S = 70\rho[(\mathrm{DBH}/100)^2 H]^{0.931} \quad (3.1)$$

where ρ is the wood density (g cm^{-3}), DBH is the stem diameter at breast height (m) divided by 100 for the unit conversion from meter to centimeter, and H is the tree height (m). However, tree height data were occasionally absent at some plots, especially along T–C and T–D, and in such cases, the tree height was estimated using a DBH-H allometric relationship (Supporting Information Fig. S3.1a and b). The AGB at each plot (Mg ha^{-1}) was then calculated from the estimated stem biomass.

The crown diameter was also measured for some selected trees, besides the data shown in Suwa et al. (2021). The trees for crown measurement were randomly selected at each transect. The diameters parallel and perpendicular to the transect line were measured for each tree, and the crown diameter (D_{crown}, m) was represented by the average of the values from the two directions. Totally, crowns of 81 trees of *R. stylosa* and 103 trees of *B. gymnorrhiza* were measured (Supplementary materials Fig. S3.1 c and d).

Soil salinity and porewater dissolved inorganic nitrogen concentration (DIN) were also measured at each plot as environmental drivers of mangrove production. Soil samples were collected by inserting a PVC pipe into the soil at each plot, and soil porewater was extracted from the surface 10 cm soil sample. The porewater samples were kept frozen and brought to the laboratory for analysis. Salinity of the porewater (soil salinity) was measured using a salinity meter (PAL-SALT, ATAGO Co. Ltd., Japan) while DIN concentrations were measured using a QuAAtro 2-HR (SEAL Analytical Ltd., Germany and BLTEC K.K., Japan). These measurements were conducted from August to September 2013. The summary of the environmental and vegetation variables at each plot is provided in Table S3.1.

3.2.3 Model description

The mangrove growth model was formulated based on an individual-based model, SEIB-DGVM (Sato et al., 2007). The forest dynamics was represented by a 30 m × 30 m computational domain. In this domain, the irradiance distribution, tree establishment, death, and changes in plant morphology subsequent to growth were simulated (Sato et al., 2007). A

feature of SEIB-DGVM is that it explicitly solves the effects of shading by neighboring trees on the light acquisition. The SEIB-DGVM thus provides the advantage in describing tree competition for light more than the other types of DVMs such as big-leaf or cohort-based models (Fisher et al., 2017). In SEIB-DGVM, the crown of each tree is represented by a cylindrical-shaped object divided by 0.1 m-thick crown layers to account for the within-crown vertical variability in irradiance distribution. It is assumed that leaf biomass is evenly distributed in the crown layers.

Originally, the SEIB-DGVM defines four biomass pools – leaf, trunk, fine root, and stock (non-structural storage pool); the trunk includes both the above-ground stem and the below-ground coarse root (Sato et al., 2007). In this study, we considered the stem and coarse root separately to explicitly consider the role of coarse root turnover in the biomass dynamics (Castaneda-Moya et al., 2011; Adame et al., 2014). Additionally, we added a new biomass pool – the above-ground root, especially for *Rhizophora* species whose above-ground root, or "prop root", could account for nearly 60% of their AGB (Nishino et al., 2015; Vinh et al., 2019).

The original SEIB-DGVM does not have a plant hydraulic module and the effects of soil water on stomatal conductance were empirically parameterized. It also does not account for plant nutrient uptake; thus, the plant growth depends solely on photosynthesis. The biomass allocation is modeled based on scaling law (Trugman et al., 2019a). In this study, these processes that control plant growth were almost entirely modified to describe mangrove growth under salt stress (Fig. 3.2). The following sections explain the modification of the SEIB-DGVM for this study related to plant hydraulics. Other modifications to the SEIB-DGVM are summarized in Note S3.3–3.4.

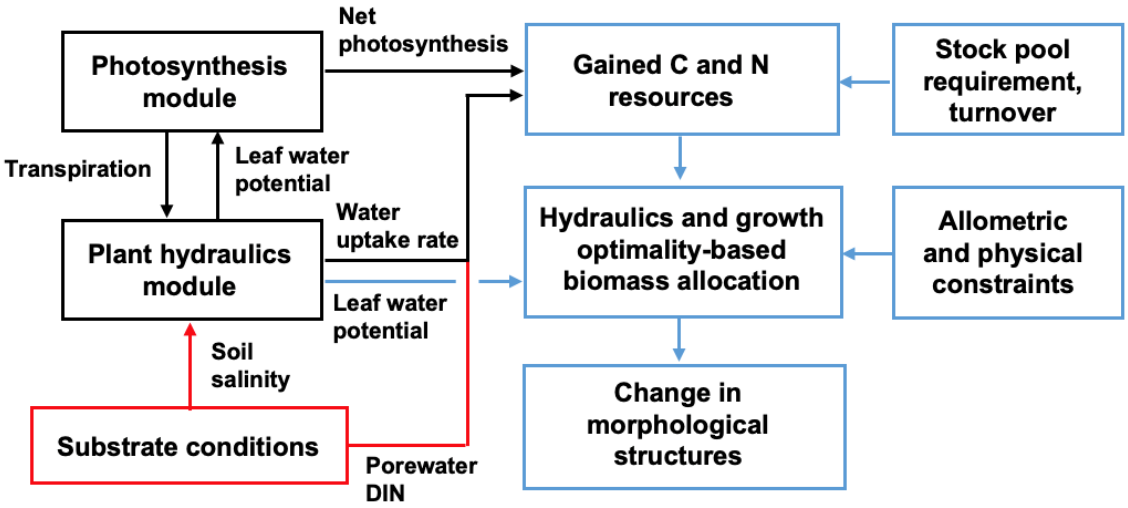

Figure 3.2. The model framework newly added to SEIB-DGVM for describing mangrove growth. The red box and arrows indicate the substrate conditions given in the model. The

black boxes and arrows indicate processes computed in the hourly time steps while the blue ones are for the daily time step.

3.2.3.1 Inclusion of plant hydraulic module

The plant hydraulic module implemented in this study is primarily based on the model developed by Xu et al. (2016) in a soil-plant-atmosphere continuum scheme. Here we describe essential processes in the plant hydraulic module which will be related to the new biomass allocation model in the next section.

The plant water uptake rate (≈ sap flow rate (J_{sap}, kg H_2O tree^{-1} s^{-1})) is calculated as

$$J_{\mathrm{sap}} = \frac{\Psi_{\mathrm{s}} - \Psi_{\mathrm{l}} - \Psi_{\mathrm{h}}}{R_{\mathrm{whole}}} \quad (3.2)$$

where R_{whole} is the whole-plant hydraulic resistance (MPa s tree kg^{-1} H_2O) and Ψ_s and Ψ_l are the soil and leaf water potential (MPa), respectively; the $\Psi_h = \rho_w g H 10^{-6}$, which is the gravitational water potential drop from the ground to the crown (MPa), where ρ_w is the water density (kg m^{-3}) and g is the gravitational acceleration (m s^{-2}). The parameter Ψ_s can be expressed as a sum of the matric potential and osmotic potential (Ψ_π, MPa). The parameter Ψ_π can be expressed as the difference in the osmotic potential between the soil and plant, which is linearly related to soil salinity and the partial uptake of the salt by mangroves represented by the salt filtration efficiency, ε (fraction) (Perri et al., 2017). Here, a constant water temperature value (25 ℃) was used to compute Ψ_π; however, note that sensitivity of Ψ_π to change in temperature is significantly small compared to salinity. Alternatively, the matric potential is negligibly small compared to Ψ_π in mangrove forests where the soil is usually water-saturated due to frequent tidal flooding (Perri et al., 2017). The parameter R_{whole} can be expressed as the sum of the root to stem hydraulic resistance (R_{root}) and the stem to leaf hydraulic resistance (R_{stem}), both expressed in (MPa s tree kg^{-1} H_2O). The parameter R_{root} is given by:

$$R_{\mathrm{root}} = \frac{R_{\mathrm{r}}}{M_{\mathrm{FR}}} \quad (3.3)$$

where R_r is the fine root hydraulic resistance per unit biomass (MPa s g kg^{-1} H_2O) and M_{FR} is the fine root biomass (g tree^{-1}). The parameter R_{stem} is given by:

$$R_{\mathrm{stem}} = \frac{a_1 H}{K_{\mathrm{sap}} A_{\mathrm{sap}}} \quad (3.4)$$

where, a_1 is the correction factor for tree height (H) to water path length, K_{sap} is the stem hydraulic conductivity per unit sapwood area (kg H_2O m m^{-2} sapwood s^{-1} MPa^{-1}), and A_{sap} is the sapwood area of a tree (m^2 sapwood tree^{-1}), which is calculated from the DBH and diameter ratio of the heartwood relative to the entire stem (β_{heart}, Table 3.1; Trugman et al.,

2019b). The parameter K_{sap} can be expressed as a product of saturated xylem conductivity ($K_{sap,sat}$) and a factor representing the effect of xylem cavitation (Xu et al., 2016):

$$K_{\mathrm{sap}} = K_{\mathrm{sap,sat}} \left(1 + \left(\frac{\Psi_{\mathrm{l}}}{P_{50}}\right)^{a_2}\right)^{-1} \quad (3.5)$$

where P_{50} (MPa) is the water potential at which 50% of the xylem conductivity is lost and a_2 is an empirical parameter (dimensionless). The change in leaf water potential is governed by the equation:

$$\frac{\mathrm{d}\Psi_{\mathrm{l}}}{\mathrm{d}t} = \frac{J - T_{\mathrm{whole}}}{C_{\mathrm{p}} LA} \quad (3.6)$$

where T_{whole} is the whole-plant transpiration rate (kg H_2O tree^{-1} s^{-1}), LA is the whole-plant leaf area (m^2 leaf tree^{-1}), and C_p is the plant capacitance (kg H_2O m^{-2} leaf MPa^{-1}). The parameter T_{whole} is calculated by vertically integrating the product of the leaf-level transpiration rate and the leaf area in each crown layer. The leaf-level transpiration and photosynthetic rates and stomatal conductance are calculated using a leaf flux model of Bonan et al. (2014), where the stomatal conductance is estimated from an optimization approach of Cowan and Farquhar (1977) using the marginal water use efficiency ($\lambda = \Delta A_n/\Delta E$, where λ is the optimal water use efficiency (WUE), and A_n and E are the leaf net photosynthetic rate and the transpiration rate, respectively) and regulated by Ψ_l. See Note S3.4 for the detailed calculations of A_n and E, and the linkage to Ψ_l.

The processes for transpiration, photosynthesis, plant water uptake, and change in leaf water potential were computed in hourly time step (Fig. 3.2). Overall, high salinity increases sensitivity of the leaf water potential to plant transpiration (Eqs. (3.2), (3.6)), which in turn may cause stomatal closure even with a low transpiration rate. It also increases the optimal WUE value leading to lower stomatal conductance (Ball and Farquhar, 1984; Clough and Sim, 1989; Barr et al., 2014; Perri et al., 2019), thereby lowering the photosynthetic and transpiration rates.

3.2.3.2 Inclusion of hydraulics and growth optimality-based biomass allocation

The biomass allocation occurs at the daily time step in the new biomass allocation scheme introduced in this study (Fig. 3.2). At each time step, four variables were considered for biomass allocation of individual trees – the daily C (C_{grow}, g C tree^{-1} day^{-1}) and N (N_{grow}, g N tree^{-1} day^{-1}) resources that can be used for tree growth, the daily minimum leaf water potential ($\Psi_{l,daymin}$, MPa), and the midday photosynthetically active radiation (PAR) at the crown top (PAR_{top}, μmol photon m^{-2} s^{-1}). The C_{grow} and N_{grow} were computed from the daily C and N uptake rates, where N uptake rate was calculated by multiplying the porewater DIN

concentration and plant water uptake rate (See Note S3.5 for the detail). Biomass was allocated according to these variables to optimize the plant hydraulics and enhance the uptake rate of growth-limiting resource (C or N) under the constraints summarized in Table 3.1. Allometric and physical constraints were considered for H and D_{crown} (Fig. 3.3a–d, see Note S3.1 for the derivation of the allometric constraints).

Table 3.1. Parameters constraining plant morphology, biomass proportion, and stoichiometry. *R. s* = *R. stylosa*, *B. g* = *B. gymnorrhiza*.

Type of constraint	Symbol	Description	Related portion	Units	*R. s*	*B. g*	Source
Morphological structure	H_{max}	Maximum tree height relative to stem diameter	Tree height	m	a		Field data
	H_{con}	Physical constraint on tree height	Tree height	m	b		
	D^*_{crown}	Maximum crown diameter relative to stem diameter	Crown diameter	m	c		Field data
	$D_{crown,con}$	Physical constraint on crown diameter	Crown diameter	m	b		
	DBH_{max}	Species-specific maximum stem diameter	Stem diameter	m	0.25	0.45	Field data
	β_{heart}	Diameter ratio of heartwood relative to entire stem	Sapwood cross-sectional area	–	0.15	0.15	Sato et al. (2007)
Biomass pool	$dLAI_{max}$	Maximum leaf area index per 1 m vertical height	Leaf biomass	m^{-1}	0.8	0.8	Estimated from Clough et al. (1997)
	β_{stock}	Target C and N in stock pool relative to stem	C and N in stock pool	–	0.05	0.05	Assumed
	β_{FR}	Target fine root biomass relative to coarse root	Fine root and coarse root biomass	–	0.2	0.2	Literature survey[d]
	β_{AR}	Target prop root biomass ratio relative to stem	Above-ground biomass of *Rhizophora* species	–	e		Yoshikai et al. (2021)
Stoichiometry	CN_l	C/N ratio in leaf tissue	Leaf	g C g^{-1} N	47	47	Tanu et al. (2020)
	CN_w	C/N ratio in woody tissue	Stem, above-ground root, coarse root	g C g^{-1} N	280	280	Alongi (2003), Alongi et al. (2004)
	CN_r	C/N ratio in fine root tissue	Fine root	g C g^{-1} N	103	103	Alongi (2003)

a. Derived from DBH-H_{max} relationship. See Note S3.1 and Fig. S3.1 for details.
b. Computed in the model. See Fig. 3.3c-d.
c. Derived from DBH-D^*_{crown} relationship. See Note S3.1 and Fig. S3.1 for details.
d. Average of values reported in Tamooh et al. (2008), Castañeda-Moya et al. (2011), Adame et al. (2014), Robertson et al. (2016), and Muhammad-Nor et al. (2019).
e. Estimated from prop root allometry in Fukido mangrove forest. See Fig. S3.3.

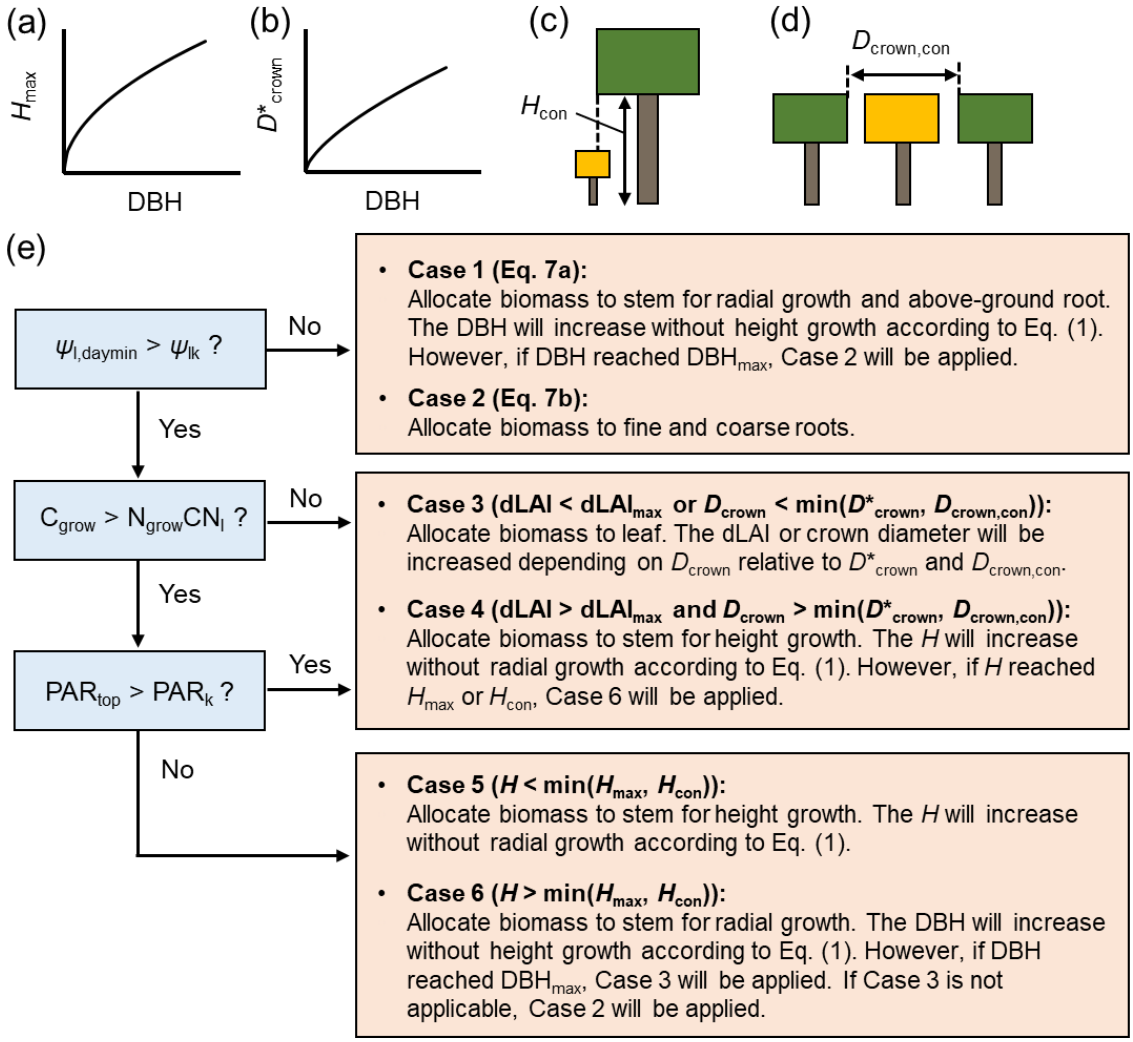

Figure 3.3. Schematics of (a, b) allometric and (c, d) physical constraints on tree height (H_{max}, H_{con}) and crown diameter (D^*_{crown}, $D_{crown,con}$), where the H_{con} and $D_{crown,con}$ in panels (c) and (d) are for the tree with crown filled by yellow color, and (e) newly added biomass allocation scheme to SEIB-DGVM. See Note S3.1 for the derivation of allometric constraints from field data.

The parameters C_{grow} and N_{grow} are allocated to the respective biomass pools in a scheme shown in Fig. 3.3. We applied the concept that plants keep their favorable hydraulic conditions throughout the growth periods by adjusting the morphological structures (Magnai et al., 2000). In this regard, we introduced a parameter Ψ_{lk} – the critical leaf water potential (MPa) – at which plants aim to maintain their leaf water potential (note that Ψ_{lk} is different from

$\Psi_{l,min}$ at which plants close the stomata). It was then considered that when $\Psi_{l,daymin}$ fell below Ψ_{lk}, the plant tries to reduce R_{whole} by allocating biomass to either the fine root, or stem, which reduces R_{whole} more effectively (Case 1 and 2 in Fig. 3.3; note that decreases in R_{stem} and R_{root} were expressed by negative value):

$$M_{S,t} = M_{S,t-1} + dM_S \qquad if\ \frac{dR_{root}}{dM_{FR}} > \frac{dR_{stem}}{dM_S} \tag{3.7a}$$

$$M_{FR,t} = M_{FR,t-1} + dM_{FR} \qquad if\ \frac{dR_{root}}{dM_{FR}} < \frac{dR_{stem}}{dM_S} \tag{3.7b}$$

where $M_{FR,t}$ and $M_{S,t}$ are the fine root and stem biomass (g tree^{-1}) at time step t (day), and dM_{FR} and dM_S are the daily biomass increment potential of fine root and stem (g tree^{-1} day^{-1}), respectively, which are limited by either of C_{grow} and N_{grow} and represented as:

$$dM_{FR} = \frac{1}{C_M} \times \min\left[C_{grow}(1 - F_{gr})(1 - F_{CR,C}), N_{grow}(1 - F_{CR,N})CN_r\right] \tag{3.8a}$$

$$dM_S = \frac{1}{C_M} \times \min\left[C_{grow}(1 - F_{gr})(1 - F_{AR}), N_{grow}(1 - F_{AR})CN_w\right] \tag{3.8b}$$

where, C_M is the carbon mass per unit dry weight in plant tissue (g C g^{-1} DW), F_{gr} is the growth respiration fraction, $F_{CR,C}$ and $F_{CR,N}$ are the fractions of C_{grow} and N_{grow}, respectively, to be allocated to the coarse root to realize β_{FR} (target fine root biomass relative to coarse root; Table 3.1), F_{AR} is the fraction of the resources to be allocated to the above-ground root to realize β_{AR} (target prop root biomass relative to stem; Table 3.1, also see Fig. S3.3) which was determined from an allometric model using DBH obtained in our study site by Yoshikai et al. (2021), and CN_r and CN_w are the CN ratios in fine root and woody tissue (g C g^{-1} N), respectively, that convert the unit of N_{grow} to C_{grow}. In Eq. (3.7), the dR_{root}/dM_{FR} is calculated from Eq. (3.3), while the dR_{stem}/dM_S is calculated from:

$$\frac{dR_{stem}}{dM_S} = \frac{dA_{sap}}{dM_S} \times \frac{dR_{stem}}{dA_{sap}} \tag{3.9}$$

where dA_{sap}/dM_S is obtained from Eq. (3.1) by calculating the increase of DBH with stem biomass increment dM_S without height growth, and dR_{stem}/dA_{sap} is given from Eqs. (3.4), (3.5) where $\Psi_{l,daymin}$ is used in Eq. (3.5). It should be noted that the variables $\Psi_{l,daymin}$, C_{grow}, and N_{grow} change with various factors including atmospheric and substrate variables and tree competition, and no absolute optimal biomass proportion achieves the condition $dR_{root}/dM_{FR} = dR_{stem}/dM_S$ throughout the computational period. Also, due to the different CN ratios in fine root and woody tissues, the increment in stem biomass (dM_S) with a unit N resource is greater than that of the fine root biomass (dM_{FR}) under N-limited conditions (Eq. (3.8), Table 3.1).

Alternatively, if plants are not stressed by the lowered leaf water potential ($\Psi_{l,daymin} > \Psi_{lk}$), the resources are allocated to a plant organ that effectively increases the uptake rate of either C or N, limiting the growth rate. Under N-limited conditions, plants allocate biomass to the leaves to increase whole-plant transpiration capacity, which increases N uptake rate nearly proportionally (as suggested by Eq. (S3.22)) (Case 3 in Fig. 3.3); this is considering that the

limited uptake of N is due to the small transpiration rate rather than water uptake regulation by hydraulic resistance. The increase in leaf biomass increases either D_{crown} and dLAI (leaf area index per 1 m vertical height) depending on the crown diameter constraints (D^*_{crown} and $D_{crown,con}$, see Note S3.6 for the details). However, if the increase in leaf biomass is inhibited by $dLAI_{max}$ (maximum dLAI; Table 3.1) and crown diameter constraints, the resources are allocated to the stem for height growth, which in turn will make a new crown layer and eventually allow further leaf accommodation (Case 4 in Fig. 3.3). Under a C-limited condition, the limited C uptake rate may be attributed to low light availability or small whole-plant leaf area. In this regard, we introduced a criterion PAR_k, where the photosynthetic rate is reduced by half of the light-saturated photosynthetic rate, allowing the assumption that the limited C uptake rate is due to low light availability if PAR_{top} is lower than PAR_k. In this case, the resources are allocated to the stem for height growth to acquire better light conditions under tree competition (Case 5 or 6 in Fig. 3.3); otherwise, the resources are allocated for an increase in leaf area (Case 3 or 4 in Fig. 3.3). Lastly, the residual C_{grow} or N_{grow} after the biomass allocation is allocated to the stock pool.

3.2.4 Simulation configuration

The model was applied to the Fukido mangrove forest to test its performance in reproducing the forest structural variables (species composition, mean DBH, and AGB). The model was forced with atmospheric variables (air temperature, relative humidity, atmospheric pressure, wind speed, and cloud fraction) and substrate conditions (soil salinity and porewater DIN). Direct and diffused solar radiation and longwave radiation were calculated in SEIB-DGVM from the given variables such as cloud fraction, air temperature, and latitude (Sato et al., 2007). The atmospheric variables for the Fukido mangrove forest given to the model were derived from a global reanalysis product JRA-55 (Kobayashi et al., 2015). For long-term simulation (i.e. more than 100 years), the yearly atmospheric variation in 2013, a year when the field-data collection was conducted, was repeatedly given in the simulation.

Simulations with different soil salinity, or the “salinity gradient simulation”, which varied from 18‰ to 36‰ with 2‰ intervals, were conducted to reproduce the forest structural variables across a soil salinity gradient. For the porewater DIN, a spatially averaged DIN (average of DIN measured at the survey plots: 200 μmol L^{-1}) was given to the model as the representative value of the porewater DIN in this forest. In each simulation, soil salinity and the porewater DIN were set as constant due to lack of data and model on the temporal variations in substrate conditions. We also conducted “plot-wise simulation”, or the simulation for each survey plot, by giving the measured soil salinity and porewater DIN at each plot. Note

that the results shown in this manuscript are from the “salinity gradient simulation”; the results of the “plot-wise simulation” is provided in Fig. S3.5 in the Supporting Information and discussed later.

The initial condition was set as bare land (no vegetation) for all simulations. Tree establishment occurs at 1 m × 1 m grid-cells at yearly time step according to light condition at the forest floor and a parameter of establishment probability ($P_{establish}$, m^{-2} $year^{-1}$) prescribed for each species (Sato et al., 2007). The species that will establish at a grid-cell is determined according to a fraction of total biomass of each species in the computational domain such that a species occupying a larger fraction has a higher probability of establishment. On the other hand, it is sometimes randomly determined by a probability Est_{random}, where the value of Est_{random} was set to 0.05 in this study. This corresponds to Scenario 4 in the tree establishment scheme in SEIB-DGVM (see Sato, 2015 for the details). We followed Sato et al. (2007) for the initial conditions (tree morphology and biomass proportion) of the established trees.

The SEIB-DGVM uses stochastic models for the processes of tree establishment and mortality, and for this reason the result of a simulation varies every time. In this regard, we conducted ensemble simulations (20 runs) for each soil salinity in the “salinity gradient simulation” and extracted the general trends.

The model parameter settings related to plant hydraulics and productivity are summarized in Table 3.2. Other minor model parameters are summarized in Table S3.2. The parameter values for the two-species in the Fukido mangrove forest, *R. stylosa* and *B. gymnorrhiza*, were determined based on literatures. If the data for a focal species was unavailable from the literature, the data from the genus or family was applied. Some parameter values were adapted from other mangrove genus or terrestrial ecosystems, and in this case, the same value was given to the two species (Table 3.2). The values of two plant hydraulic trait parameters – Ψ_{lk} (critical leaf water potential) and β_0 (sensitivity of marginal WUE to leaf water potential in Eq. (S3.21), see Note S3.3) – were calibrated to reproduce the AGB and mean DBH of each species across the soil salinity gradient.

Fukido mangrove forest’s age is unknown, which makes the comparison between the model and field-data difficult. However, considering that it is an old and mature forest intact at least since 1977 (Ohtsuka et al., 2019), we assumed that the forest structural variables of the Fukido mangrove forest are in steady states. We conducted long-term simulations for 450 years with this assumption, and extracted the modeled DBH and AGB in steady states (> 300 years) and compared them with the field data.

Lastly, we performed sensitivity analysis of the plant hydraulic trait parameters (ε, P_{50}, Ψ_{lk}, and β_0) to see the relative importance of each parameter in reproducing the observed pattern of the forest structure, specifically AGB, across the soil salinity gradient. We changed

the value of a target parameter of one species (either *R. stylosa* or *B. gymnorrhiza*) to the one determined for the other species which is shown in Table 3.2, and run the "salinity gradient simulation". Note that to examine the sensitivity to Ψ_{lk}, we changed the values of Ψ_{lk} and $\Psi_{l,min}$ to keep the buffer between the two parameter values. Also, to save on computational cost, we run only one simulation for each sensitivity test instead of the ensemble approach described above. Model sensitivities are shown in Fig. S3.6.

Table 3.2. Model parameters related to plant hydraulics and productivity.

Symbol	Description	Units	*R. s*	*B. g*	Source
ρ	Wood density	g cm^{-3}	0.84	0.76	Zanne et al. (2009)
SLA	Specific leaf area	cm^2 g^{-1}	45	71	Sharma et al. (2012)
ε	Salt filtration efficiency	Fraction	0.90[a]	0.99	Reef and Lovelock (2015)
R_r	Fine root hydraulic resistance	MPa s g kg^{-1} H_2O	2220[b]	2220[b]	Bonan et al. (2014)
K_{sap}	Stem hydraulic conductivity	kg H_2O m m^{-2} sapwood s^{-1} MPa^{-1}	1.44[a]	1.13	Melcher et al. (2004), Jiang et al. (2017)
P_{50}	Water potential at which 50% of xylem conductivity is lost	MPa	-4.4[a]	-8.2	Melcher et al. (2004), Jiang et al. (2017)
a_2	Empirical parameter shaping xylem vulnerability	–	4.5[a]	4.6	Melcher et al. (2004), Jiang et al. (2017)
C_p	Plant capacitance	kg H_2O m^{-2} leaf MPa^{-1}	0.045[b]	0.045[b]	Bonan et al. (2014)
$\Psi_{l,min}$	Minimum leaf water potential	MPa	-4.5[a,c]	-4.0[c]	Hao et al. (2009), Lovelock et al. (2006), Deshar et al. (2008)
Ψ_{lk}	Critical leaf water potential	MPa	-3.9	-3.4	Calibrated
$V_{cmax,25}$	Maximum carboxylation rate at 25 ℃	μmol CO_2 m^{-2} s^{-1}	50[d]	50	Estimated from Ball et al. (1988)
λ_0	Reference marginal water use efficiency in Eq. (S3.21)	μmol CO_2 mol^{-1} H_2O	250	250	Assumed
β_0	Sensitivity of marginal water use efficiency to leaf water potential in Eq. (S3.21)	MPa^{-1}	-0.4	-0.6	Calibrated
TO_l	Leaf turnover rate	day^{-1}	0.0024	0.0019	Sharma et al. (2012)
TO_{cr}	Coarse root turnover rate	day^{-1}	0.0003[e]	0.0003[e]	Castañeda-Moya et al. (2011)
TO_{fr}	Fine root turnover rate	day^{-1}	0.001[e]	0.001[e]	Castañeda-Moya et al. (2011)
NRE	Nitrogen resorption efficiency	fraction	0.85	0.85[f]	Lin et al. (2010)

a. Value for *Rhizophora magle*
b. The value used for terrestrial forest ecosystem was applied due to lack of information.
c. The minimum of the reported values was adopted.

d. Value for *Rhizophora apiculata*
e. The average value of data in Castañeda-Moya et al. (2011) was adopted.
f. Value for *Rhizophora stylosa*

3.3 Results

3.3.1 Modeled seasonal and diurnal dynamics

Seasonal variations in atmospheric forcing variables and modeled species-specific gross photosynthetic rate (P_g) and transpiration (T) normalized by the leaf area index (LAI) and midday ($\Psi_{l,midday}$) and predawn ($\Psi_{l,predawn}$) leaf water potential are shown in Fig. 3.4. The modeled variables were from one of the ensemble simulations with soil salinity set as 30‰. The model demonstrated strong seasonality in photosynthesis and transpiration primarily due to seasonality in solar radiation and air temperature. The model predicted the peak of P_g/LAI in June with values ~ 5.1 and 4.9 g C m^{-2} day^{-1} for *R. stylosa* and *B. gymnorrhiza*, respectively, and the peak in T/LAI in July–Sep with values ~ 1.07 and 0.85 mm day^{-1} for each species, respectively. The P_g/LAI and T/LAI were predicted to be depressed during winter (December–February) with values ~ 3.0 g C m^{-2} day^{-1} for both species and ~ 0.43 and 0.36 mm day^{-1} for each species, respectively. We compared the modeled leaf-level P_g with the field-estimated values in the Fukido mangrove forest by Okimoto et al. (2007). Their measurements were conducted in an area where the LAI is 1.55, the same LAI as the one shown in Fig. 3.4d; thus, the effects of LAI on leaf-level P_g could be eliminated for comparison. Although the modeled P_g/LAI of both species are slightly lower than the one obtained by Okimoto et al. (2007) (~ 1.0 g C m-2 day^{-1}), especially from June to August, overall, the model agreed well with their results.

The midday leaf water potential showed seasonal variations as with photosynthesis and transpiration (Fig. 3.4f). Due to the partial salt uptake of *R. stylosa* (as indicated by the lower ε value of this species, Table 3.2) that alleviates the osmotic potential difference between the soil and plant, the predawn leaf water potential of *R. stylosa* was constantly higher than that of *B. gymnorrhiza* (Fig. 3.4f). *Rhizophora stylosa* also showed larger magnitude of leaf water potential reduction at midday during summer compared to *B. gymnorrhiza*, and higher leaf-level transpiration rate, correspondingly (Fig. 3.4e and f). During winter, due to the lowered transpiration rate, the leaf water potential reduction at midday was resultantly alleviated compared to summer.

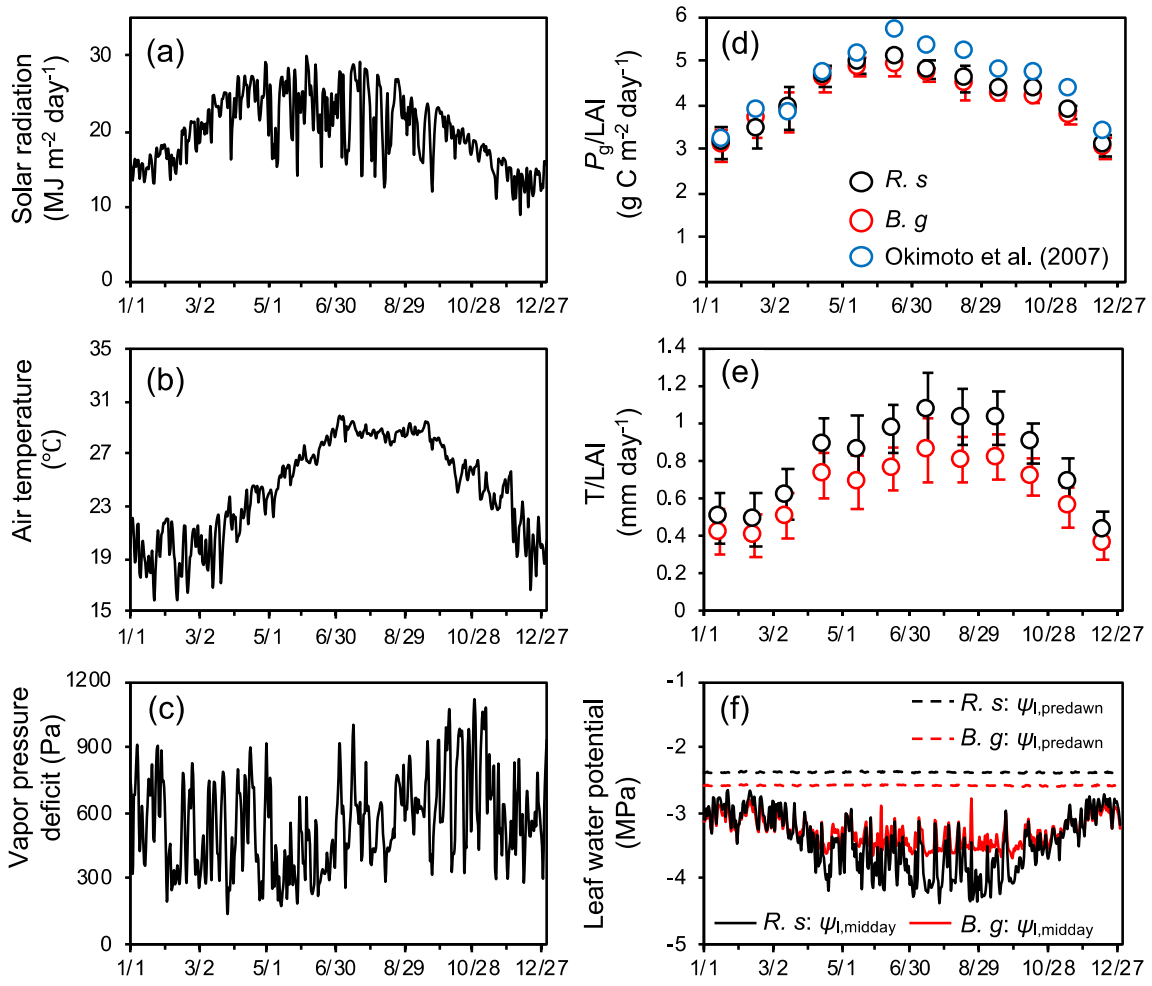

Figure 3.4. Seasonal variations in atmospheric forcing variables: (a) solar radiation, (b) air temperature, and (c) vapor pressure deficit (VPD), and modeled seasonal dynamics: (d) monthly mean and standard deviation of species-specific gross photosynthetic rate (P_g, g C m^{-2} ground day^{-1}), (e) transpiration (T, mm day^{-1}) normalized by leaf layer index (LAI, m^2 leaf m^{-2} ground) of the respective species, and (f) midday ($\Psi_{l,midday}$) and predawn ($\Psi_{l,predawn}$) leaf water potential of each species. *R. s* = *R. stylosa*, *B. g* = *B. gymnorrhiza*. Solar radiation is expressed as daily sum while air temperature and VPD are expressed as daily mean. Leaf water potential shown is the median value of individuals. Here, the modeled dynamics were from a simulation of soil salinity set as 30‰, and the results of a year when LAI reached 1.55 were shown. At this time, the LAI of *R. stylosa* and *B. gymnorrhiza* were 0.87 and 0.68, respectively. In panel (d), seasonal variations in P_g/LAI measured by Okiomoto et al. (2007) are also shown as reference, the data of which are from an area with LAI = 1.55 in Fukido mangrove forest in 2000–2001.

Diurnal variations of the simulated photosynthesis, transpiration, and leaf water potential of the two species during summer and winter under two different salinity conditions

(30 ‰ and 24 ‰) are shown in Fig. 3.5. Compared to salinity 24 ‰, both species showed significantly lowered leaf-level transpiration rates under salinity 30 ‰ especially during summer (Fig. 3.5b and e), suggesting downregulation of stomatal conductance under high soil salinity conditions. On the other hand, the decrease in leaf-level photosynthetic rates were not significant (Fig. 3.5a and d). The leaf water potential during night-time was lower when soil salinity was 30 ‰ compared to conditions when salinity was 24 ‰, due to the different osmotic potential in soil porewater. The leaf water potential, however, showed almost the same levels at midday during summer, which were close to the values of Ψ_{lk} determined for each species (Fig. 3.5c, Table 3.2). The reduction in leaf water potential to the level of Ψ_{lk} suggests the role of dynamic biomass allocation, which adjusts the whole-tree transpiration demands and hydraulic conductivity, in constraining the leaf water potential dynamics (Fig. 3.3). In contrast, the diurnal dynamics in leaf water potential during winter showed similar magnitude of reduction of the water potential at midday between the two soil salinity conditions (Fig. 3.5f).

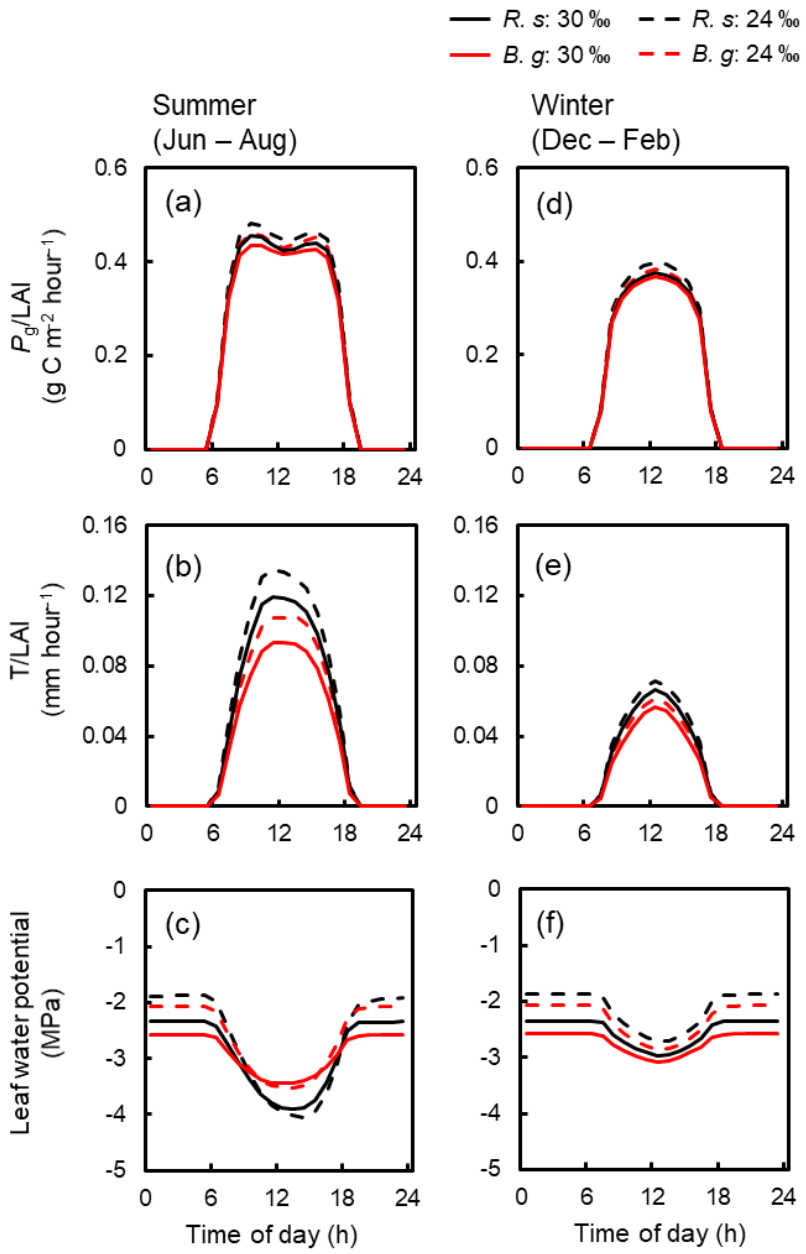

Figure 3.5. Simulated averaged diurnal variations in (a, d) photosynthesis and (b, e) transpiration of *R. stylosa* (*R. s*) and *B. gymnorrhiza* (*B. g*) normalized with LAI of the respective species, and (c, f) leaf water potential of the two species for summer (June–August) and winter (December–February) under two soil salinity conditions (30 ‰ and 24 ‰). The variations under soil salinity 30 ‰ correspond to the results shown in Fig. 3.4. The variations under soil salinity 24 ‰ are from the results of a year that showed the same LAI (1.55). The diurnal variations in leaf water potential were derived based on the median value of individuals.

3.3.2 Modeled biomass dynamics under different soil salinity

Figure 3.6 shows the changes in the forest structures for over 200 years under different soil salinity conditions, 20‰, 24‰, 30‰, and 34‰, from one of the ensemble simulations (the present-day average soil salinity of the survey plots is 28 ‰). The time-series results of AGB, LAI, and mean DBH of the two species are shown in Fig. 3.7. Trees with DBH < 0.05 m were not accounted for in the calculation of the mean DBH because it is sensitive to the presence of small trees. Overall, the model demonstrated the significant influence of soil salinity on species composition and forest structure.

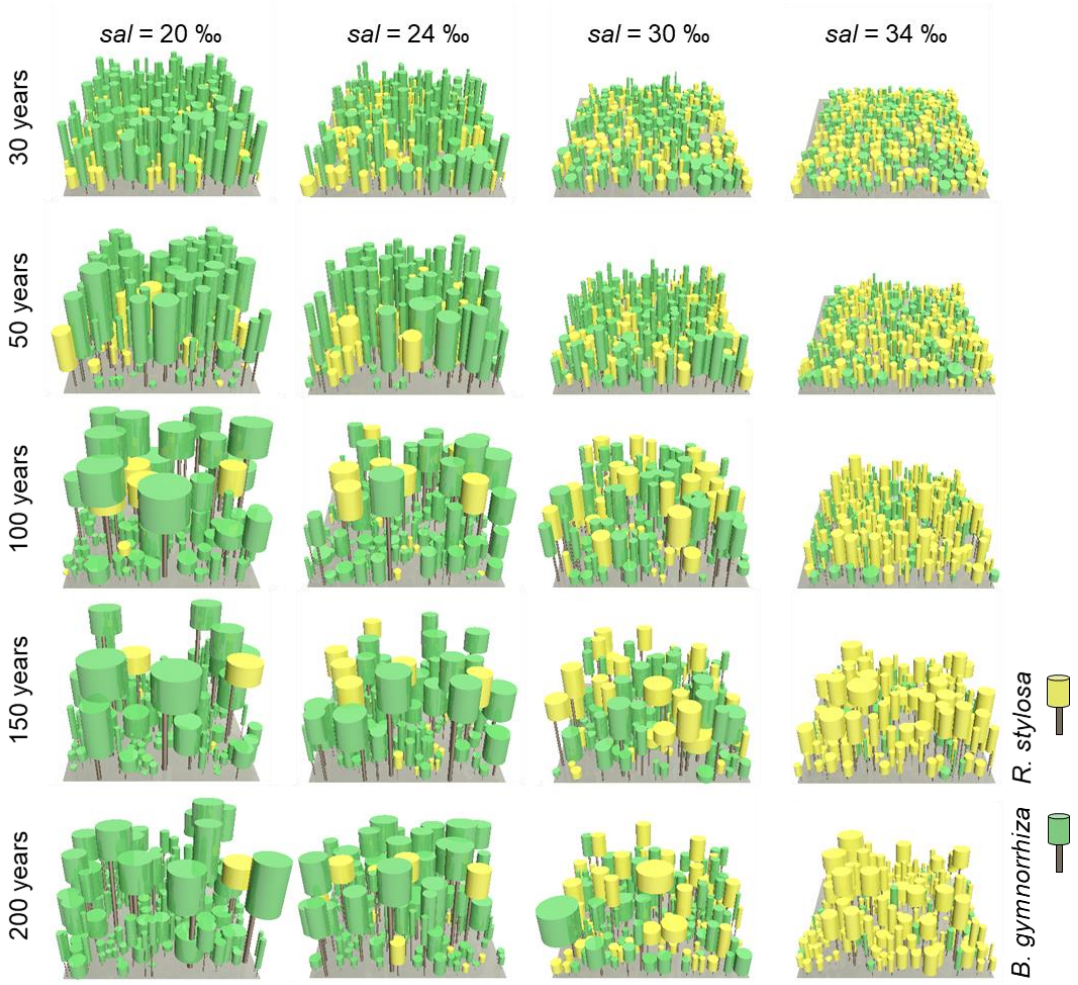

Figure 3.6. Visualization of forest structures over 200 years under different soil salinity (*sal*), 20, 24, 30, and 34‰, taken from one of the ensemble simulations. The brown-colored objects represent the stem while the yellow- and green-colored objects represent the crowns of *R. stylosa* and *B. gymnorrhiza*, respectively. The forest floor shown is the 30 m × 30 m-wide computational domain.

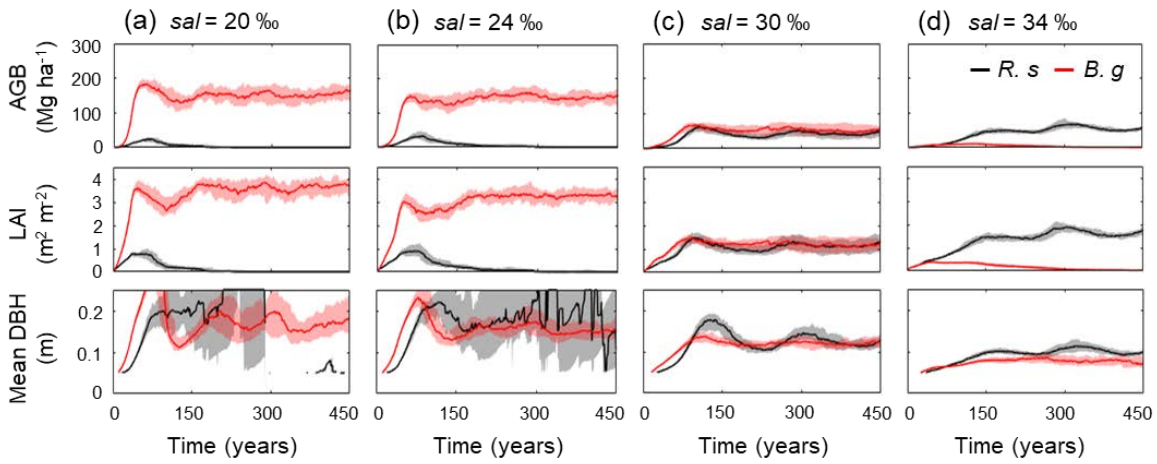

Figure 3.7. Temporal dynamics in above-ground biomass (AGB), leaf area index (LAI), and mean diameter at breast height (DBH) of *R. stylosa* (*R. s*) and *B. gymnorrhiza* (*B. g*) in four soil salinity conditions (a) 20‰, (b) 24‰, (c) 30‰, and (d) 34‰. Note that trees with DBH < 0.05 m were not included in the calculation of mean DBH. Solid lines show median and shading the 90-th percentile from ensemble simulations.

The model predicted that *B. gymnorrhiza* dominates over *R. stylosa* when soil salinity is 20‰ or 24‰ (Fig. 3.7a–b). Under soil salinity of 20‰, the AGB of *B. gymnorrhiza* exponentially increased up to 200 Mg ha^{-1} after 60 years since the initial condition. It slightly decreased after that, and was kept almost constant at 175 Mg ha^{-1} after 150 years. The LAI of this species showed almost the same trend with AGB while the mean DBH showed fluctuation especially in the first 200 years (Fig. 3.7a). The sudden decrease in the mean DBH is attributed to the onset of formation of forest gaps resulting from deaths of large *B. gymnorrhiza* trees that promoted the establishment of small trees (Fig. 3.6). After the decrease in the mean DBH, it gradually increased again and saturated at 0.17 m (Fig. 3.6a). Alternatively, the AGB and LAI of *R. stylosa* were significantly lower than *B. gymnorrhiza* with its peak at only 25 Mg ha^{-1} and 1 m^2 m^{-2}, respectively. This can also be seen in the decreasing number of *R. stylosa* trees subsequent to forest growth (Fig. 3.6). In contrast to AGB and LAI, the mean DBH of *R. stylosa* reached around 0.2 m after 75 years, as large as that of *B. gymnorrhiza* in steady state (Fig. 3.7a). This suggest that some *R. stylosa* trees can grow until mature conditions (see also Fig. 3.6), while trees of this species with DBH > 0.05 m disappeared in all ensemble simulations after 300 years (Fig. 3.7a). The trees of *R. stylosa* sometimes emerge due to the random factor in the establishment process, but most of the trees did not grow more than DBH of 0.05 m in the canopy of *B. gymnorrhiza*.

The trend in forest growth under 24‰ salinity was similar to that of 20‰ (Fig. 3.6, Fig. 3.7b), but showed a slightly lower and higher peak for *B. gymnorrhiza* and *R. stylosa*, respectively, of the AGB, LAI, and mean DBH. This suggests decreased productivity of *B.*

gymnorrhiza compared to soil salinity 20‰, and increased productivity of *R. stylosa* albeit the increase in soil salinity. The survival rate of *R. stylosa* was higher than the results for 20‰, resulting in the high mean DBH of this species throughout the simulation period (Fig. 3.7b).

When the soil salinity was 30‰, the AGB of *B. gymnorrhiza* significantly decreased compared to the results for salinities 20‰ and 24‰, becoming equivalent to those of *R. stylosa* (Fig. 3.7c). The LAI and mean DBH also showed a significant decrease, suggesting significantly lowered productivity of *B. gymnorrhiza*. The AGB and LAI of *R. stylosa* significantly increased compared to the results for 20‰ and 24‰, but the mean DBH significantly decreased.

The model predicted that *B. gymnorrhiza* cannot grow well at soil salinity 34‰, and that *R. stylosa* dominates under this salinity condition (Fig. 3.6, Fig. 3.7d). Despite the further decrease in AGB, LAI, and mean DBH of *B. gymnorrhiza*, those of *R. stylosa* showed almost the same level for these parameters at soil salinity 30‰.

3.3.3 Comparison between modelled and field-measured forest structural variables

Figure 3.8 shows the field-measured and modeled mean DBH and AGB of *R. stylosa* and *B. gymnorrhiza* across the soil salinity gradient. The field data clearly showed the effects of soil salinity on forest structural variables – decrease in mean DBH for both species, and decrease in AGB of *B. gymnorrhiza* but increase in AGB of *R. stylosa* with increasing soil salinity. The model reproduced well the said patterns across the soil salinity gradient and the values are within or close to the field-data variations (Fig. 3.8). The change in species composition is also well-reproduced, suggesting that the model can reproduce the forest structural variables across the soil salinity gradient.

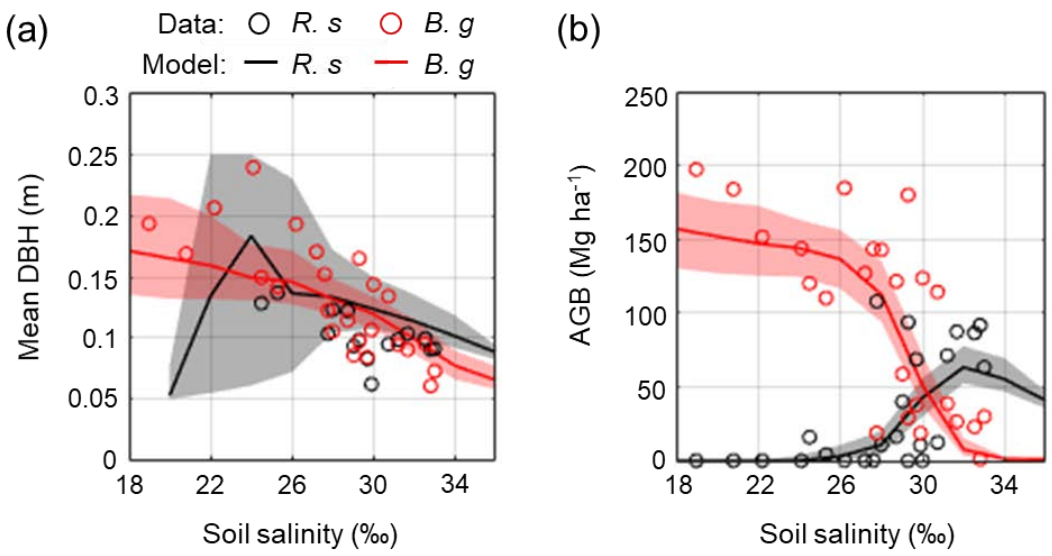

Figure 3.8. Comparison of field-measured and modeled (a) mean DBH and (b) AGB of *R. stylosa* and *B. gymnorrhiza* along with soil salinity gradient. From each ensemble simulation, modeled mean DBH and AGB in steady states (> 300 years) were extracted and pooled for all ensembles, and the median (solid line) and the 90-th percentile (shading) of the pooled samples were shown. Note that trees with DBH < 0.05 m were not included in the calculation of the mean DBH.

Figure 3.9 shows the field-measured and modeled relationship of tree density and mean individual stem biomass. Although there are some discrepancies between the model and field data especially for conditions soil salinity > 30‰, the model reproduced the overall pattern of the field data.

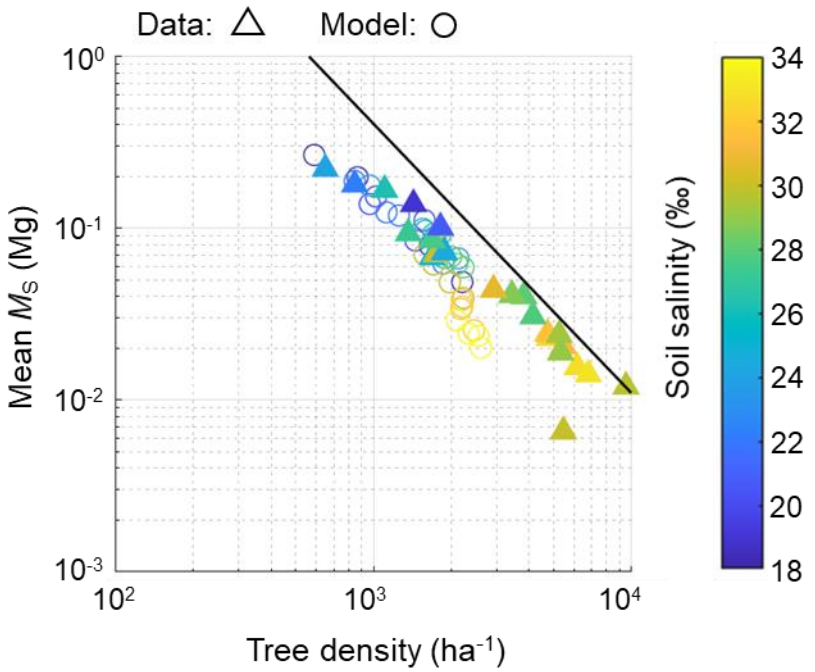

Figure 3.9. The relationship of tree density and mean individual stem biomass (M_S). Triangles show field data while circles show modeled values from one of the ensemble simulations with different soil salinity settings (from 18‰ to 34‰ with 2‰ increments) plotted from 300–450 years (with interval of 50 years), which is in steady states in terms of forest structural variables (see Fig. 3.7). Note that trees with DBH < 0.05 m were not counted in calculating tree density and mean M_S. The line represents the full density curve proposed by Tabuchi et al. (2013): $y = 20389x^{-1.567}$.

3.4 Discussion

3.4.1 Model performance

Forest growth is influenced by leaf-level and whole-plant CO_2, water and nutrient fluxes, and forest-scale tree competition, which are all interconnected. The leaf-level fluxes were simulated using a well-established stomatal optimization scheme with the marginal WUE linked with leaf water potential (Bonan et al., 2014; Xu et al., 2016). The model predicted the distinct seasonal dynamics in photosynthesis and transpiration as well as leaf water potential in the Fukido mangrove forest (Figs. 3.4 and 3.5). The modeled seasonal variations in leaf-level photosynthesis (P_g/LAI) agreed well with the one measured by Okimoto et al. (2007) in this forest (Fig. 3.4d). Although there are no data on the seasonal variations in transpiration in this forest, studies on other subtropical mangrove forest, such as the Everglades National

Park, Florida (Barr et al., 2014), and China (Liang et al., 2019) that incorporated the eddy-covariance approach also showed strong seasonality in transpiration, similar to the one predicted for the Fukido mangrove forest in this study (Fig. 3.4e). The evapotranspiration rate normalized by LAI in the Everglades measured by Barr et al. (2014) was 0.4–1.2 mm day^{-1}, which is close to the variation of the modeled T/LAI in the Fukido mangrove forest (Fig. 3.4e). These results suggest that the model produced realistic seasonal dynamics for transpiration in the Fukido mangrove forest.

Tree growth was driven by C and N uptake rates in the developed model resulting from the leaf-level and the whole-plant CO_2 and water fluxes. The modeled growth rates at a soil salinity condition where *B. gymnorrhiza* is the dominant species (*sal* < 28‰) showed close values to the ones measured by Ohtsuka et al. (2019) at a *B. gymnorrhiza*-dominated site in the Fukido mangrove forest (Fig. S3.4). This suggests that the model also reasonably predicted the growth rate of each species in addition to the leaf-level CO_2 and water fluxes.

This model also showed reasonable reproducibility of the self-thinning process arising from tree competition. This was inferred from the decrease in tree density with increase in individual tree biomass patterns based on the agreement of the measured and modeled tree density-mean M_S relationship, except for those with soil salinity > 30‰ (Fig. 3.9). An exponent value close to -3/2 was obtained, similar to what is observed in the Fukido mangrove forest (Suwa et al., 2021; Fig. 3.9) and in many mangrove forests as well (e.g., Analuddin et al., 2009; Deshar et al., 2012; Khan et al., 2013; Tabuchi et al., 2013; Azman et al. 2021). This was achieved by implementing the species-specific morphological traits especially the DBH-D^*_{crown} relationship (Fig. 3.3b, see also Note S3.1 and Fig. S3.1). The underestimation trend of modeled tree density at high soil salinity (> 30‰) where *R. stylosa* starts to dominate (Fig. 3.9) may be attributed to the inaccurate representation of the crown morphological trait of this species, which generally gives larger D^*_{crown} compared to observed values (see Note S3.1 and Fig S3.1c). Basically, the crown diameters of individuals determine the tree accommodation spaces, and therefore the overestimated crown diameter may have resulted to the underestimation of the tree density. Crown size representation could be a factor that drives a large part of the uncertainty in DVMs (Meunier et al., 2021). Nevertheless, the data are remarkably scarce in the case of mangroves. The morphological traits of crown size should be investigated in future studies for more realistic representation of mangroves' tree competition and forest dynamics in the model. It is also important to note that some variables of model prediction such as LAI, shoot/root biomass ratio, morphological plasticity in accordance to changes in environmental variables (as shown in Fig. S3.7), and leaf water potential dynamics have not been validated due to lack of data, and future research is needed to address these aspects.

Overall, this is first modeling study to introduce detailed physiological and mechanistic representations of the mangrove forest growth controlled by photosynthesis, water and nutrient (represented by DIN) uptake, tree competition, and achieved good as well as comprehensive reproducibility of mangrove growth processes. The remarkable agreement of modeled forest structures with field data across a soil salinity gradient validated our hypothesis – individual-based DVM incorporating plant hydraulic traits can reasonably predict mangrove growth processes under salt stress without empirical expression of the soil salinity influence on mangrove productivity. However, the model still does not account for the plant-to-soil feedback through water uptake, which has been identified by a mangrove growth-groundwater flow coupled model (Bathmann et al., 2021) as an important factor affecting both mangrove and substrate conditions (soil salinity). Alternatively, the said model also demonstrated that the forest structural variable and soil salinity dynamics could reach steady states after some time from the initial condition, a setting that is considered to describe the Fukido mangrove forest (Ohtsuka et al., 2019). Our modeling results, which did not include the plant-to-soil feedback, therefore may be valid only for the steady states and still holds uncertainty in the developmental stage. This further implies that model application may be limited only to mature mangrove forests, and further model improvement is needed for its application to forests during the developmental stage (after plantation) or during the recovery stage (after disturbances such as typhoons and deforestation).

3.4.2 Soil salinity and interspecific competition shaping the forest structural variables

Overall, the model explained that the changes in mean DBH and AGB of the two coexisting species with change in soil salinity are due to the difference in their salt tolerance and interspecific competition (Figs. 3.7–3.8). While the model predicted the contrasting changes of AGB of the two species, both species showed decrease in productivity with increase in soil salinity as seen in the monotonic decrease in DBH (Figs. 3.7–3.8). This decrease in productivity can be partly explained by the downregulation of stomatal conductance under high soil salinity conditions (Fig. 3.5). In addition, the changes in the biomass allocation pattern that increased the allocation to the stem and roots relative to leaves with increase in soil salinity have influenced productivity (Fig. S3.7) – a pattern that reduced the whole-plant photosynthesis and transpiration and increased the carbon (through the stem and root respiration and root turnover) and nitrogen (through the root turnover) cost relative to the unit leaf area. It should be noted that such morphological plasticity with changes in soil salinity predicted by the model qualitatively agrees with the implications by other studies (e.g.,

Suwa et al., 2008, 2009; Vovides et al., 2014; Nguyen et al., 2015; Chatting et al., 2020), but future studies are needed for quantitative and systematic validation.

The sensitivity analysis of the plant hydraulics trait parameters provided some insights into the different salt tolerance of the two species that shaped the forest structures along the soil salinity gradient (Fig. S3.6). For example, it showed the substantial contribution of the partial salt uptake of *R. stylosa*, represented by the lower ε, to the salt tolerance of this species (Fig. S3.6a) at the possible expense of higher P_{50} value (Table 3.2, Fig. S3.6c and d), which is considered as the coordinated functional traits (Jiang et al., 2017). The model showed highest sensitivity to the parameters ψ_{lk} and $\psi_{l,min}$ (Figs. S3.6e and f), suggesting that the mangroves' capacity to reduce the leaf water potential is one of the most important functional traits characterizing their salt tolerance, as suggested by Reef and Lovelock (2015). The response of AGB to changes in ψ_{lk}, a parameter controlling biomass allocation pattern, also indicates the substantial impact of biomass allocation dynamics influenced by salinity on plant productivity. On the other hand, the model showed minimal sensitivity to β_0 (Figs. S3.6g–h). While the higher stomatal conductance of *R. stylosa* than *B. gymnorrhiza* (as shown in Figs. 3.4–3.5) qualitatively agreed with the implications by Clough and Sim (1989) and Reef and Lovelock (2015), the model results suggested that the choice of -0.6 for β_0 already leads to efficient stomatal openings for photosynthesis compared to the case of -0.4 for β_0 (Table 3.2). This may explain the small variations in the simulated leaf-level photosynthetic rates between the two species and among the different soil salinity levels (Figs. 3.4–3.5). Understanding the mangroves' stomatal behavior relative to soil salinity and covariation of leaf water potential and photosynthesis have not been well established from field data (Perri et al., 2019). Further field-based research and data implementation to the model are needed for better and more reliable representation of mangroves' stomatal conductance and associated regulation of photosynthesis under salt stress.

The model specifically predicted that *B. gymnorrhiza* competes over *R. stylosa* when soil salinity is favorably low for the growth of *B. gymnorrhiza* (sal < 28‰), an observation that is consistent with our field data and the data from other mangrove forests (Putz and Chan, 1986; Enoki et al., 2014). This result may be attributed to the following model parameter settings based on literature – higher wood density (ρ), smaller specific leaf area (SLA), and higher leaf turnover rate (TO_l) of *R. stylosa* than *B. gymnorrhiza* (Table 3.2). Higher ρ indicates the requirement of higher biomass increase for the height or radial growth of the stem. Smaller SLA and higher TO_l indicate the higher requirement of C and N to produce new leaf tissues or to keep the same amount of leaves, i.e. the need of *R. stylosa* for more C and N resources for growth compared to *B. gymnorrhiza*. The biomass requirement of prop roots, which lowers the biomass allocation to the stem (Fig. S3.3), and the smaller D^*_{crown} of *R. stylosa* compared to

B. gymnorrhiza (Fig. S3.1c–d) may also have contributed to the former's lower growth rate. Consequently, *B. gymnorrhiza* grew faster and suppressed the growth of *R. stylosa* by severe shading (Figs. 3.6–3.7). The higher growth rate of *B. gymnorrhiza* compared to *R. stylosa* at relatively low salinity conditions agrees with the study by Jiang et al. (2019).

Interestingly, our model was able to simulate unique conditions not previously reported by other modeling works. For instance, the model predicted that *R. stylosa* trees could grow until the mature conditions under the canopy of *B. gymnorrhiza*-dominated forest provided the chance of favorable light conditions, resulting in the high mean DBH but low AGB of this species at relatively low soil salinity (~ 24‰) (Figs. 3.6–3.7). Simulating this kind of process may only be possible through the individual-based approach with calculations of detailed irradiance distribution as done by the SEIB-DGVM in this study. Alternatively, the model predicted the significantly lowered growth rate of *B. gymnorrhiza* at high soil salinity condition (*sal* > 30‰) where *B. gymnorrhiza* cannot grow until mature conditions, which resulted in the low AGB and small mean DBH of this species. This reduced the suppression of *B. gymnorrhiza* on *R. stylosa* and generated the *Rhizophora stylosa*-dominated forest (Figs. 3.6–3.7). Despite the abundant population of *R. stylosa*, the sizes of individuals were relatively small due to high salt stress, and resulted in the high AGB but small mean DBH of this species.

3.4.3 Effects of other factors and further model improvement

Besides soil salinity, this study highlighted the importance of atmospheric variables as important drivers controlling mangrove production. This is seen in the photosynthesis-transpiration seasonal dynamics with peak during summer (June–September) and depression during winter (November–March) (Fig. 3.4) that none of the previous mangrove modeling studies has examined yet. The model predicted winter depression primarily due to low solar radiation and air temperature. Specifically, low air temperature (< 20 ℃) significantly reduced photosynthetic capacity – the maximum carboxylation rate and the maximum electron transport rate (Aspinwall et al., 2021); this, in turn, decreased the marginal WUE ($\Delta A_n/\Delta E$), leading to the downregulation of stomatal conductance, a behavior of mangroves' stomata observed under low temperature conditions (Akaji et al., 2019; Aspinwall et al., 2021). This resulted in the depression of photosynthesis and transpiration during this season. The significance of atmospheric control on stomatal conductance and associated dynamics in winter compared to salinity control is also highlighted in the similar magnitude of reduction of the leaf water potential at midday between the different soil salinity conditions in this season compared to summer (Fig. 3.5c and f). Such winter depression lowers the production of mangroves in subtropical regions, and may be differentiated from tropical mangroves in terms

of productivity. This could be a key factor in explaining and predicting the latitudinal gradients in mangroves' structural variables such as canopy height and AGB with the highest values at the equatorial region (Saenger and Snedaker, 1993; Simard et al., 2019; Rovai et al., 2021).

The model gave significantly better prediction of the AGB spatial distribution when the spatially averaged DIN concentrations were applied to the substrate condition compared to plot-wise DIN values (Fig. S3.5, "plot-wise simulation"). This suggests that N availability was better represented by the spatially averaged value in this study. Porewater DIN in mangrove forests is highly heterogeneous horizontally (Inoue et al., 2011) and vertically (Kristensen et al., 1998; Lee et al., 2008) even in very small scales such as 10 cm. The DIN measured from one soil core sample might not have captured the representative value at each plot due to such heterogeneity. Differences in the predicted AGB between the two cases highlight nutrient availability in affecting mangrove production and biomass dynamics in this forest. Therefore, an appropriate representation of nutrient availability is critical for accurate prediction of mangrove production. More detailed measurement of porewater nutrient concentrations in space and time is needed for a more reliable model prediction, and future works will account for this aspect. Similarly, future works should consider biogeochemical processes which control nutrient dynamics in the substrate. For example, the porewater of the Fukido mangrove forest is rich in ammonia compared to nitrate (Table S3.1), contrary to the groundwater flowing into this forest, which is rich in nitrate (Mori et al., unpublished data). This suggests that biogeochemical processes, such as mineralization of organic matter, N fixation, and denitrification (Reef et al., 2010) are important drivers controlling nutrient dynamics in the forest, which ultimately affects soil organic matter dynamics. These factors should therefore be taken into consideration in future works as one of the plant-to-soil feedbacks in addition to water uptake processes.

3.5 Concluding remarks

This manuscript presents a new individual-based model modified from SEIB-DGVM for a better physiological representation of mangrove growth under the impact of soil salinity. The plant hydraulics was incorporated and linked with the plant production process (C and N uptake) and biomass allocation. The developed model showed high reproducibility of the complex nonlinear patterns in species composition and forest structural variables in a subtropical mangrove forest shaped across a soil salinity gradient without empirical parameterizations of soil salinity influence on mangrove productivity. While there are still some important processes to be accounted for to further improve the model (e.g., plant-to-soil

feedback and soil biogeochemical processes), the physiologically-improved model predicted the various key ecological processes such as seasonal dynamics in photosynthesis and transpiration, interspecific competition, and self-thinning process, together with forest structure. Thus, including plant hydraulic traits that incorporates species differences in the ability to deal with salinity is critical and adequate for predicting the dominant dynamics in mangrove forests. Although the model has been tested using only two species in one site, owing to its physiological principles that do not hold empirical expressions of influences of environmental variables on mangrove productivity, it can be potentially extended to other mangrove species in various environmental settings. Therefore, it may contribute to predicting how the mangrove biomass dynamics will respond to future changes in global climate.

3.6 References

Adame, M. F., Connolly, R. M., Turschwell, M. P., Lovelock, C. E., Fatoyinbo, T., Lagomasino, D., Goldberg, L. A., Holdorf, H., Friess, D. A., Sasmito, S. D., Sanderman, J., Sievers, M., Buelow, C., Kauffman, J. B., Bryan-Brown, D., and Brown, C. J.: Future carbon emissions from global mangrove forest loss. Glob. Change Biol., 27(12), 2856–2866, 2021.

Adame, M. F., Teutli, C., Santini, N. S., Caamal, J. P., Zaldívar-Jiménez, A., Hernández, R., and Herrera-Silveira, J. A.: Root biomass and production of mangroves surrounding a karstic oligotrophic coastal lagoon. Wetlands, 34(3), 479–488, 2014.

Akaji, Y., Inoue, T., Tomimatsu, H., and Kawanishi, A.: Photosynthesis, respiration, and growth patterns of *Rhizophora stylosa* seedlings in relation to growth temperature. Trees, 33(4), 1041–1049, 2019.

Alongi, D. M.: Carbon cycling and storage in mangrove forests. Annu. Rev. Mar. Sci., 6, 195–219, 2014.

Alongi, D. M., Clough, B. F., Dixon, P., and Tirendi, F.: Nutrient partitioning and storage in arid-zone forests of the mangroves *Rhizophora stylosa* and *Avicennia marina*. Trees, 17(1), 51–60, 2003.

Alongi, D. M., Wattayakorn, G., Tirendi, F., and Dixon, P.: Nutrient capital in different aged forests of the mangrove *Rhizophora apiculata*. Bot. Mar., 47(2), 116–124, 2004.

Analuddin, K., Suwa, R., and Hagihara, A.: The self-thinning process in mangrove Kandelia obovata stands. J. Plant Res., 122(1), 53–59, 2009.

Aspinwall, M. J., Faciane, M., Harris, K., O'Toole, M., Neece, A., Jerome, V., Colón, M., Chieppa, J., and Feller, I. C.: Salinity has little effect on photosynthetic and respiratory

responses to seasonal temperature changes in black mangrove (*Avicennia germinans*) seedlings. Tree Physiol., 41(1), 103–118, 2021.

Atwood, T. B., Connolly, R. M., Almahasheer, H., Carnell, P. E., Duarte, C. M., Lewis, C. J. E., Irigoien, X., Kelleway, J. J., Lavery, P. S., Macreadie, P. I., Serrano, O., Sanders, C. J., Santos, I., Steven, A. D. L., and Lovelock, C. E.: Global patterns in mangrove soil carbon stocks and losses. Nat. Clim. Change, 7(7), 523–528, 2017.

Azman, M. S., Sharma, S., Shaharudin, M. A. M., Hamzah, M. L., Adibah, S. N., Zakaria, R. M., and MacKenzie, R. A.: Stand structure, biomass and dynamics of naturally regenerated and restored mangroves in Malaysia. Forest. Ecol. Manag., 482, 118852, 2021.

Ball, M. C.: Interactive effects of salinity and irradiance on growth: implications for mangrove forest structure along salinity gradients. Trees, 16(2), 126–139, 2002.

Ball, M., Cowan, I. R., and Farquhar, G. D.: Maintenance of leaf temperature and the optimisation of carbon gain in relation to water loss in a tropical mangrove forest. Funct. Plant Biol., 15(2), 263–276, 1988.

Ball, M. C. and Farquhar, G. D.: Photosynthetic and stomatal responses of two mangrove species, *Aegiceras corniculatum* and *Avicennia marina*, to long term salinity and humidity conditions. Plant Physiol., 74(1), 1–6, 1984.

Barr, J. G., DeLonge, M. S., and Fuentes, J. D.: Seasonal evapotranspiration patterns in mangrove forests. J. Geophys. Res-Atmos., 119(7), 3886–3899, 2014.

Barr, J. G., Engel, V., Fuentes, J. D., Fuller, D. O., and Kwon, H.: Modeling light use efficiency in a subtropical mangrove forest equipped with CO 2 eddy covariance. Biogeosciences, 10(3), 2145–2158, 2013.

Bathmann, J., Peters, R., Reef, R., Berger, U., Walther, M., and Lovelock, C. E.: Modelling mangrove forest structure and species composition over tidal inundation gradients: The feedback between plant water use and porewater salinity in an arid mangrove ecosystem. Agr. Forest Meteorol., 308, 108547, 2021.

Berger, U. and Hildenbrandt, H.: A new approach to spatially explicit modelling of forest dynamics: spacing, ageing and neighbourhood competition of mangrove trees. Ecol. Model., 132(3), 287–302, 2000.

Berger, U., Rivera-Monroy, V. H., Doyle, T. W., Dahdouh-Guebas, F., Duke, N. C., Fontalvo-Herazo, Hildenbrandt, H., Koedam, H., Mehlig, N., Piou, C., and Twilley, R. R.: Advances and limitations of individual-based models to analyze and predict dynamics of mangrove forests: A review. Aquat. Bot., 89(2), 260–274, 2008.

Bonan, G. B., Williams, M., Fisher, R. A., and Oleson, K. W.: Modeling stomatal conductance in the earth system: linking leaf water-use efficiency and water transport along the soil–plant–atmosphere continuum. Geosci. Model Dev., 7(5), 2193–2222, 2014.

Bukoski, J. J., Elwin, A., MacKenzie, R. A., Sharma, S., Purbopuspito, J., Kopania, B., Apwong, M., Poolsiri, R., and Potts, M. D.: The role of predictive model data in designing mangrove forest carbon programs. Environ. Res. Lett., 15(8), 084019, 2020.

Castañeda-Moya, E., Twilley, R. R., Rivera-Monroy, V. H., Marx, B. D., Coronado-Molina, C., and Ewe, S. M.: Patterns of root dynamics in mangrove forests along environmental gradients in the Florida Coastal Everglades, USA. Ecosystems, 14(7), 1178–1195, 2011.

Chatting, M., LeVay, L., Walton, M., Skov, M. W., Kennedy, H., Wilson, S., and Al-Maslamani, I.: Mangrove carbon stocks and biomass partitioning in an extreme environment. Estur. Coast. Shelf S., 244, 106940, 2020.

Chen, R. and Twilley, R. R.: A gap dynamic model of mangrove forest development along gradients of soil salinity and nutrient resources. J. Ecol., 86(1), 37-51, 1998.

Clough, B. F., Ong, J. E., and Gong, W. K.: Estimating leaf area index and photosynthetic production in canopies of the mangrove *Rhizophora apiculata*. Mar. Ecol. Prog. Ser., 159, 285–292, 1997.

Clough, B. and Sim, R. G.: Changes in gas exchange characteristics and water use efficiency of mangroves in response to salinity and vapour pressure deficit. Oecologia, 79(1), 38–44, 1989.

Cowan, I. R. and Farquhar, G. D.: Stomatal function in relation to leaf metabolism and environment, in: Integration of Activity in the Higher Plant, edited by: Jennings, D. H., Cambridge University Press, Cambridge, 471–505, 1977.

Deshar, R., Sharma, S., Mouctar, K., Wu, M., Hoque, A. T. M. R., and Hagihara, A.: Self-thinning exponents for partial organs in overcrowded mangrove *Bruguiera gymnorrhiza* stands on Okinawa Island, Japan. Forest Ecol. Manag., 278, 146–154, 2012.

Deshar, R., Suwa, R., and Hagihara, A.: Leaf water potential of two mangrove species in different seasons and salinity conditions on Okinawa Island, Japan. Mangrove and Wetland Ecosystem, 6, 85–97, 2008.

Donato, D. C., Kauffman, J. B., Murdiyarso, D., Kurnianto, S., Stidham, M., and Kanninen, M.: Mangroves among the most carbon-rich forests in the tropics. Nat. geosci., 4(5), 293–297, 2011.

Egawa, R., Sharma, S., Nadaoka, K., and MacKenzie, R. A.: Burrow dynamics of crabs in subtropical estuarine mangrove forest. Estur. Coast. Shelf S., 252, 107244, 2021.

Enoki, T., Yasuda, K., and Kusumoto, B.: Aboveground net primary production and stand dynamics of mangroves along a river on Iriomote Island, southwestern Japan. Tropics, 23(3), 91–98, 2014.

Feller, I. C., Lovelock, C. E., and McKee, K. L.: Nutrient addition differentially affects ecological processes of *Avicennia germinans* in nitrogen versus phosphorus limited mangrove ecosystems. Ecosystems, 10(3), 347–359, 2007.

Fisher, R. A., Koven, C. D. anderegg, W. R., Christoffersen, B. O., Dietze, M. C., Farrior, C. E., Holm, J. A., Hurtt, G. C., Knox, R. G., Lawrence, P. J., Lichstein, J. W., Longo, M., Matheny, A. M., Medvigy, D., Muller-Landau, H. C., Powell, T. L., Serbin, S. P., Sato, H., Shuman, J. K., Smith, B., Trugman, A. T., Viskari, T., Verbeeck, H., Weng, E., Xu, C., Xu, X., Zhang, T., and Moorcroft, P. R.: Vegetation demographics in Earth System Models: A review of progress and priorities. Glob. Change Biol., 24(1), 35–54, 2018.

Friess, D. A., Rogers, K., Lovelock, C. E., Krauss, K. W., Hamilton, S. E., Lee, S. Y., Lucas, R., Primavera, J., Rajkaran, R., and Shi, S.: The state of the world's mangrove forests: past, present, and future. Annu. Rev. Env. Resour., 44, 89–115, 2019.

Friess, D. A., Yando, E. S., Abuchahla, G. M., Adams, J. B., Cannicci, S., Canty, S. W., Cavanaugh, K. C., Connolly, R. M., Cormier, N., Dahdouh-Guebas, F., Diele, K., Feller, I. C., Fratini, S., Jennerjahn, T. C., Lee, S. Y., Ogurcak, D. E., Ouyang, X., Rogers, K., Rowntree, J. K., Sharma, S., Sloey, T. M., and Wee, A. K.: Mangroves give cause for conservation optimism, for now. Curr. Biol., 30(4), R153–R154, 2020.

Giri, C., Ochieng, E., Tieszen, L. L., Zhu, Z., Singh, A., Loveland, T., Masek, J., and Duke, N.: Status and distribution of mangrove forests of the world using earth observation satellite data. Global Ecol. Biogeogr., 20(1), 154–159, 2011.

Grueters, U., Seltmann, T., Schmidt, H., Horn, H., Pranchai, A., Vovides, A. G., Peter, R., Vogt, J., Dahdouh-Guebas, F., and Berger, U.: The mangrove forest dynamics model mesoFON. Ecol. Model., 291, 28–41, 2014.

Hao, G. Y., Jones, T. J., Luton, C., Zhang, Y. J., Manzane, E., Scholz, F. G., Bucci, S. J., Cao, K-F., and Goldstein, G.: Hydraulic redistribution in dwarf *Rhizophora mangle* trees driven by interstitial soil water salinity gradients: impacts on hydraulic architecture and gas exchange. Tree Physiol., 29(5), 697–705, 2009.

Inoue, T., Nohara, S., Takagi, H., and Anzai, Y.: Contrast of nitrogen contents around roots of mangrove plants. Plant Soil, 339(1), 471–483, 2011.

Jiang, G. F., Goodale, U. M., Liu, Y. Y., Hao, G. Y., and Cao, K. F.: Salt management strategy defines the stem and leaf hydraulic characteristics of six mangrove tree species. Tree Physiol., 37(3), 389–401, 2017.

Jiang, Z., Guan, W., Xiong, Y., Li, M., Chen, Y., and Liao, B.: Interactive effects of intertidal elevation and light level on early growth of five mangrove species under *Sonneratia apetala* Buch. Hamplantation canopy: Turning monocultures to mixed forests. Forests, 10(2), 83, 2019.

Khan, M. N. I., Sharma, S., Berger, U., Koedam, N., Dahdouh-Guebas, F., and Hagihara, A.: How do tree competition and stand dynamics lead to spatial patterns in monospecific mangroves?. Biogeosciences, 10(4), 2803–2814, 2013.

Kobayashi, S., Ota, Y., Harada, Y., Ebita, A., Moriya, M., Onoda, H., Onogi, K.,, Kamahori, H., Kobayashi, C., Endo, H., Miyaoka, K., and Takahashi, K.: The JRA-55 reanalysis: General specifications and basic characteristics. Journal of the Meteorological Society of Japan. Ser. II, 93(1), 5–48, 2015.

Komiyama, A., Ong, J. E., and Poungparn, S.: Allometry, biomass, and productivity of mangrove forests: A review. Aquat. Bot., 89(2), 128–137, 2008.

Komiyama, A., Poungparn, S., and Kato, S.: Common allometric equations for estimating the tree weight of mangroves. J. Trop. Ecol., 21(4), 471–477, 2005.

Kristensen, E., Bouillon, S., Dittmar, T., and Marchand, C.: Organic carbon dynamics in mangrove ecosystems: a review. Aquat. Bot., 89(2), 201–219, 2008.

Kristensen, E., Jensen, M. H., Banta, G. T., Hansen, K., Holmer, M., and King, G. M.: Transformation and transport of inorganic nitrogen in sediments of a southeast Asian mangrove forest. Aquat. Microb. Ecol., 15(2), 165–175, 1998.

Lee, R. Y., Porubsky, W. P., Feller, I. C., McKee, K. L., and Joye, S. B.: Porewater biogeochemistry and soil metabolism in dwarf red mangrove habitats (Twin Cays, Belize). Biogeochemistry, 87(2), 181–198, 2008.

Li, L., Yang, Z. L., Matheny, A. M., Zheng, H., Swenson, S. C., Lawrence, D. M., Barlage, M., Yan, B., McDowell, N. G., and Leung, L. R.: Representation of Plant Hydraulics in the Noah - MP Land Surface Model: Model Development and Multiscale Evaluation. J. Adv. Model. Earth Sy., 13(4), e2020MS002214, 2021.

Liang, J., Wei, Z., Lee, X., Wright, J. S., Cui, X., Chen, H., and Lin, G.: Evapotranspiration Characteristics Distinct to Mangrove Ecosystems Are Revealed by Multiple - Site Observations and a Modified Two - Source Model. Water Resour. Res., 55(12), 11250–11273, 2019.

Lin, Y. M., Liu, X. W., Zhang, H., Fan, H. Q., and Lin, G. H.: Nutrient conservation strategies of a mangrove species *Rhizophora stylosa* under nutrient limitation. Plant Soil, 326(1), 469–479, 2010.

Lovelock, C. E., Ball, M. C., Choat, B., Engelbrecht, B. M., Holbrook, N. M., and Feller, I. C.: Linking physiological processes with mangrove forest structure: phosphorus deficiency

limits canopy development, hydraulic conductivity and photosynthetic carbon gain in dwarf *Rhizophora mangle*. Plant Cell Environ., 29(5), 793–802, 2006a.

Lovelock, C. E., Ball, M. C., Feller, I. C., Engelbrecht, B. M., and Ling Ewe, M.: Variation in hydraulic conductivity of mangroves: influence of species, salinity, and nitrogen and phosphorus availability. Physiol. Plantarum, 127(3), 457–464, 2006b.

Lovelock, C. E., Feller, I. C., McKee, K. L., Engelbrecht, B. M., and Ball, M. C.: The effect of nutrient enrichment on growth, photosynthesis and hydraulic conductance of dwarf mangroves in Panama. Funct. Ecol., 18(1), 25–33, 2004.

Magnani, F., Mencuccini, M., and Grace, J.: Age - related decline in stand productivity: the role of structural acclimation under hydraulic constraints. Plant Cell Environ., 23(3), 251–263, 2000.

Manzoni, S., Vico, G., Katul, G., Fay, P. A., Polley, W., Palmroth, S., and Porporato, A.: Optimizing stomatal conductance for maximum carbon gain under water stress: a meta - analysis across plant functional types and climates. Funct. Ecol., 25(3), 456–467, 2011.

Mcleod, E., Chmura, G. L., Bouillon, S., Salm, R., Björk, M., Duarte, C. M., Lovelock, C. E., Schlesinger, W. H., and Silliman, B. R.: A blueprint for blue carbon: toward an improved understanding of the role of vegetated coastal habitats in sequestering CO_2. Front. in Ecol. Environ., 9(10), 552–560, 2011.

Melcher, P. J., Goldstein, G., Meinzer, F. C., Yount, D. E., Jones, T. J., Holbrook, N. M., and Huang, C. X.: Water relations of coastal and estuarine *Rhizophora mangle*: xylem pressure potential and dynamics of embolism formation and repair. Oecologia, 126(2), 182–192, 2001.

Meunier, F., Krishna Moorthy, S. M., Peaucelle, M., Calders, K., Terryn, L., Verbruggen, W., Liu, C., Saarinen, N., Origo, N., Nightingale, J., Disney, M., Malhi, Y., and Verbeeck, H.: Using terrestrial laser scanning to constrain forest ecosystem structure and functions in the Ecosystem Demography model (ED2.2), Geosci. Model Dev. Discuss. [preprint], https://doi.org/10.5194/gmd-2021-59, in review, 2021.

Muhammad-Nor, S. M., Huxham, M., Salmon, Y., Duddy, S. J., Mazars-Simon, A., Mencuccini, M., Meir, P., and Jackson, G.: Exceptionally high mangrove root production rates in the Kelantan Delta, Malaysia; An experimental and comparative study. Forest Ecol. Manag., 444, 214–224, 2019.

Nguyen, H. T., Stanton, D. E., Schmitz, N., Farquhar, G. D., and Ball, M. C.: Growth responses of the mangrove *Avicennia marina* to salinity: development and function of shoot hydraulic systems require saline conditions. Ann. Bot-London, 115(3), 397–407, 2015.

Nishino, Y., Fujimoto, K., Ryuichi, T., Hirata, Y., Ono, K., Taniguchi, S., Ogawa, T., and Lihpai, S.: Estimation of aboveground biomass in a *Rhizophora stylosa* forest with densely developed prop roots in Pohnpei Island, Federated States of Micronesia. Mangrove Science, 9, 17–25, 2015.

Ohtsuka, T., Tomotsune, M., Suchewaboripont, V., Iimura, Y., Kida, M., Yoshitake, S., Kondo, M., and Kinjo, K.: Stand dynamics and aboveground net primary productivity of a mature subtropical mangrove forest on Ishigaki Island, south-western Japan. Regional Studies in Marine Science, 27, 100516, 2019.

Okimoto, Y., Nose, A., Katsuta, Y., Tateda, Y., Agarie, S., and Ikeda, K.: Gas exchange analysis for estimating net CO2 fixation capacity of mangrove (*Rhizophora stylosa*) forest in the mouth of river Fukido, Ishigaki Island, Japan. Plant Prod. Sci., 10(3), 303–313, 2007.

Ouyang, X., Lee, S. Y., and Connolly, R. M.: The role of root decomposition in global mangrove and saltmarsh carbon budgets. Earth-Sci. Rev., 166, 53–63, 2017.

Perri, S., Katul, G. G., and Molini, A.: Xylem–phloem hydraulic coupling explains multiple osmoregulatory responses to salt stress. New Phytol., 224(2), 644–662, 2019.

Perri, S., Viola, F., Noto, L. V., and Molini, A.: Salinity and periodic inundation controls on the soil - plant - atmosphere continuum of gray mangroves. Hydrol. Process., 31(6), 1271–1282, 2017.

Peters, R., Vovides, A. G., Luna, S., Grüters, U., and Berger, U.: Changes in allometric relations of mangrove trees due to resource availability–A new mechanistic modelling approach. Ecol. Model., 283, 53–61, 2014.

Potkay, A., Trugman, A. T., Wang, Y., Venturas, M. D., Anderegg, W. R., Mattos, C. R., and Fan, Y.: Coupled whole - tree optimality and xylem hydraulics explain dynamic biomass partitioning. New Phytol., 230(6), 2226–2245, 2021.

Putz, F. E. and Chan, H. T.: Tree growth, dynamics, and productivity in a mature mangrove forest in Malaysia. Forest Ecol. Manag., 17(2–3), 211–230, 1986.

Reef, R., Feller, I. C., and Lovelock, C. E.: Nutrition of mangroves. Tree Physiol., 30(9), 1148–1160, 2010.

Reef, R. and Lovelock, C. E.: Regulation of water balance in mangroves. Ann. Bot-London, 115(3), 385–395, 2015.

Robertson, A. I. and Alongi, D. M.: Massive turnover rates of fine root detrital carbon in tropical Australian mangroves. Oecologia, 180(3), 841–851, 2016.

Rovai, A. S., Riul, P., Twilley, R. R., Castañeda - Moya, E., Rivera - Monroy, V. H., Williams, A. A., Simard, M., Cifuentes-Jara, M., Lewis, R. R., Crooks, S., Horta, P. A., Schaeffer-Novelli, Y., Cintrón, G., Pozo-Cajas, M., and Pagliosa, P. R.: Scaling mangrove

aboveground biomass from site - level to continental - scale. Global Ecol. Biogeogr., 25(3), 286–298, 2016.

Rovai, A. S., Twilley, R. R., Castañeda - Moya, E., Midway, S. R., Friess, D. A., Trettin, C. C., Bukoski, J. J., Stovall, A. E. L., Pagliosa, P. R., Fonseca, A. L., Mackenzie, R. A., Aslan, A., Sasmito, S. D., Sillanpää, M., Cole, T. G., Purbopuspito, J., Warren, M. W., Murdiyarso, D., Mofu, W., Sharma, S., Hong Tinh, P., and Riul, P.: Macroecological patterns of forest structure and allometric scaling in mangrove forests. Global Ecol. Biogeogr., 30(5), 1000–1013, 2021.

Saenger, P. and Snedaker, S. C.: Pantropical trends in mangrove above-ground biomass and annual litterfall. Oecologia, 96(3), 293–299, 1993.

Sasmito, S. D., Kuzyakov, Y., Lubis, A. A., Murdiyarso, D., Hutley, L. B., Bachri, S., Friess, D. A., Martius, C., and Borchard, N.: Organic carbon burial and sources in soils of coastal mudflat and mangrove ecosystems. Catena, 187, 104414, 2020.

Sato, H., Itoh, A., and Kohyama, T.: SEIB–DGVM: A new Dynamic Global Vegetation Model using a spatially explicit individual-based approach. Ecol. Model., 200(3–4), 279–307, 2007.

Sato, H.: SEIB-DGVM v2.80 online description document (http://seib-dgvm.com), 2015.

Sharma, S., Kamruzzaman, M., Hoque, A. R., and Hagihara, A.: Leaf phenological traits and leaf longevity of three mangrove species (Rhizophoraceae) on Okinawa Island, Japan. J. Oceanogr., 68(6), 831–840, 2012.

Sharma, S., MacKenzie, R. A., Tieng, T., Soben, K., Tulyasuwan, N., Resanond, A., Blate, G., and Litton, C. M.: The impacts of degradation, deforestation and restoration on mangrove ecosystem carbon stocks across Cambodia. Sci. Total Environ., 706, 135416, 2020.

Simard, M., Fatoyinbo, L., Smetanka, C., Rivera-Monroy, V. H., Castañeda-Moya, E., Thomas, N., and Van der Stocken, T.: Mangrove canopy height globally related to precipitation, temperature and cyclone frequency. Nat. Geosci., 12(1), 40–45, 2019.

Šimůnek, J. and Hopmans, J. W.: Modeling compensated root water and nutrient uptake. Ecol. Model., 220(4), 505–521, 2009.

Sobrado, M. A.: Leaf photosynthesis of the mangrove *Avicennia germinans* as affected by NaCl. Photosynthetica, 36(4), 547–555, 2000.

Suárez, N. and Medina, E.: Salinity effect on plant growth and leaf demography of the mangrove, *Avicennia germinans* L. Trees, 19(6), 722–728, 2005.

Suwa, R., Analuddin, K., Khan, M. N. I., and Hagihara, A.: Structure and productivity along a tree height gradient in a *Kandelia obovata* mangrove forest in the Manko Wetland, Okinawa Island, Japan. Wetl. Ecol. Manag., 16(4), 331–343, 2008.

Suwa, R., Deshar, R., and Hagihara, A.: Forest structure of a subtropical mangrove along a river inferred from potential tree height and biomass. Aquat. Bot., 91(2), 99–104, 2009.

Suwa, R., Rollon, R., Sharma, S., Yoshikai, M., Albano, G. M. G., Ono, K., Adi, N. S., Ati, R. N. A., Kusumaningtyas, M. A., Kepel, T. L., Maliao, R. J., Primavera-Tirol, Y. H., Blanco, A. C., and Nadaoka, K.: Mangrove biomass estimation using canopy height and wood density in the South East and East Asian regions. Estur. Coast. Shelf S., 248, 106937, 2021.

Tabuchi, R. and Unyavejchewin, S. B.: Development of mangrove stands in Southeast Asia: with special reference to the west coast of the Malay Peninsula. Global Environ. Res, 215–221, 2013.

Taillardat, P., Friess, D. A., and Lupascu, M.: Mangrove blue carbon strategies for climate change mitigation are most effective at the national scale. Biol. Letters, 14(10), 20180251, 2018.

Tamooh, F., Huxham, M., Karachi, M., Mencuccini, M., Kairo, J. G., and Kirui, B.: Below-ground root yield and distribution in natural and replanted mangrove forests at Gazi bay, Kenya. Forest Ecol. Manag., 256(6), 1290–1297, 2008.

Tanu, F. Z., Asakura, Y., Takahashi, S., Hinokidani, K., and Nakanishi, Y.: Variation in Foliar δ15N Reflects Anthropogenic Nitrogen Absorption Potential of Mangrove Forests. Forests, 11(2), 133, 2020.

Trugman, A. T. anderegg, L. D., Sperry, J. S., Wang, Y., Venturas, M., and Anderegg, W. R.: Leveraging plant hydraulics to yield predictive and dynamic plant leaf allocation in vegetation models with climate change. Glob. Change Biol., 25(12), 4008–4021, 2019a.

Trugman, A. T. anderegg, L. D., Wolfe, B. T., Birami, B., Ruehr, N. K., Detto, M., Bartlett, M. K., and Anderegg, W. R.: Climate and plant trait strategies determine tree carbon allocation to leaves and mediate future forest productivity. Glob. Change Biol., 25(10), 3395–3405, 2019b.

Vinh, T., Marchand, C., Linh, T. V. K., Vinh, D. D., and Allenbach, M.: Allometric models to estimate above-ground biomass and carbon stocks in *Rhizophora apiculata* tropical managed mangrove forests (Southern Viet Nam). Forest Ecol. Manag., 434, 131–141, 2019.

Vovides, A. G., Vogt, J., Kollert, A., Berger, U., Grueters, U., Peters, R., Lara-Domínguez, A. L., and López-Portillo, J.: Morphological plasticity in mangrove trees: salinity-related changes in the allometry of *Avicennia germinans*. Trees, 28(5), 1413–1425, 2014.

Xiong, Y., Liao, B., and Wang, F.: Mangrove vegetation enhances soil carbon storage primarily through in situ inputs rather than increasing allochthonous sediments. Mar. Pollut. Bull., 131, 378–385, 2018.

Xu, X., Medvigy, D., Powers, J. S., Becknell, J. M., and Guan, K.: Diversity in plant hydraulic traits explains seasonal and inter - annual variations of vegetation dynamics in seasonally dry tropical forests. New Phytol., 212(1), 80–95, 2016.

Yoshikai, M., Nakamura, T., Suwa, R., Argamosa, R., Okamoto, T., Rollon, R., Basina, R., Primavera-Tirol, Y. H., Blanco, A. C., Adi, N. S., and Nadaoka, K.: Scaling relations and substrate conditions controlling the complexity of *Rhizophora* prop root system. Estur. Coast. Shelf S., 248, 107014, 2021.

Zanne, A.E., Lopez-Gonzalez, G., Coomes, D.A., Ilic, J., Jansen, S., Lewis, S. L., Miller, R.B., Swenson, N.G., Wiemann, M.C., Chave, J., and Lopez-Gonzalez, G.: Global Wood Density database. http://hdl.handle.net/10255/dryad.235, 2009.

Supporting Information for Chapter 3

Note S3.1. Derivation of species-specific morphological traits

Tree height (H, m) and crown diameter (D_{crown}, m) of individual trees were constrained in the mangrove growth model using the field data-derived species-specific morphological traits. The H of individuals usually obeys allometric scaling relationship expressed as

$$H = \beta_H \mathrm{DBH}^{\alpha} \quad \text{(S3.1)}$$

where β_H is the normalization term, α is the scaling exponent, and DBH is the diameter at breast height (m) (West et al., 2009). However, mangroves probably show some flexibility in the DBH-H relationship depending on environmental variables such as soil salinity (Peters et al., 2014). Figure S3.1a–b shows the compilation of DBH-H data from Fukido mangrove forest for the two species, and indeed the data showed some variabilities of H relative to DBH especially for relatively large trees (DBH > 0.1 m). To allow flexibility in the DBH-H relationship but to constrain it within the observed range, we derived two allometric relationships for H – DBH-maximum tree height (H_{max}) and DBH-minimum tree height (H_{min}) relationships – as follows. We first binned H data with the DBH width of 0.01 m for *Rhizophora stylosa* and 0.02 m for *Bruguiera gymnorrhiza*, where the choice of different binning widths was attributed to the different data densities in bins between the two species. Maximum and minimum H were then extracted for each bin, and were fitted to Eq. (S3.1) to obtain DBH-H_{max} and DBH-H_{min} relationships, respectively. Here, we removed from the fitting some binned data that could be outliers to avoid under- or overestimation of H_{max} and H_{min}. Additionally, we derived the general allometric relationship of DBH-H for each species by fitting all the data to Eq. (S3.1). This relationship was used to estimate H of trees whose H was not measured in the field as described in the Section 3.2.2. The fitted curves are shown in Fig. S3.1a–b.

The parameter D_{crown} also usually follows an allometric scaling relationship, where the scaling exponent is often assumed to be 2/3 based on a metabolic scaling theory (West et al., 2009; Shenkin et al., 2020):

$$D_{\mathrm{crown}} = \beta_{\mathrm{crown}} \mathrm{DBH}^{2/3} \quad \text{(S3.2)}$$

where β_{crown} is the normalization term for crown diameters. However, crown structures are significantly influenced by tree competition, resulting in variability of D_{crown} (Pretsch, 2014; Jucker et al., 2015). Here, we assumed that the crown diameter of the allometric ideal trees (D^*_{crown}) follows Eq. (S3.2), where we refer to allometric ideal as the condition where the crown expansion is not influenced by local competition. We derived the coefficient β_{crown} of D^*_{crown} for the two species using a similar approach of deriving DBH-H_{max} relationships. For *B. gymnorrhiza*, the data of D_{crown} were binned with DBH width of 0.02 m, and the maxima in bins

of DBH < 0.1 m were extracted. The maxima were assumed to represent D^*_{crown} and were fitted to Eq. (S3.2) to derive β_{crown} (Fig. S3.1d). We removed the maxima of DBH > 0.1 m from fitting because of less certainty in the representation of D^*_{crown} for large trees due to data scarcity compared to smaller trees. Alternatively, D_{crown} of *R. stylosa* showed significantly different trend from *B. gymnorrhiza* – none of the measured D_{crown} exceeded 2.0 m, which implies the strong influence of local competition for this species. Therefore, we supplemented the data with D_{crown} from two different mangrove forests in the Philippines and Indonesia (see Note S3.2 for the details). Specifically, supplemented data for large trees (DBH > 0.1 m) were from relatively open canopy forests, thus it is more probable that the data represent D^*_{crown}. Note that the supplemented data used are from *R. apiculata* and *R. mucronata*, which are so far the only available data on the crown diameter of *Rhizophora* species, and may apply to *R. stylosa*. After combining the data from Fukido mangrove and other two sites, we binned the data with DBH width of 0.02 m, and the maxima were fitted to Eq. (S3.2) to estimate β_{crown} for *R. stylosa* (Fig. S3.1c); some maxima that could be outliers were removed from the fitting.

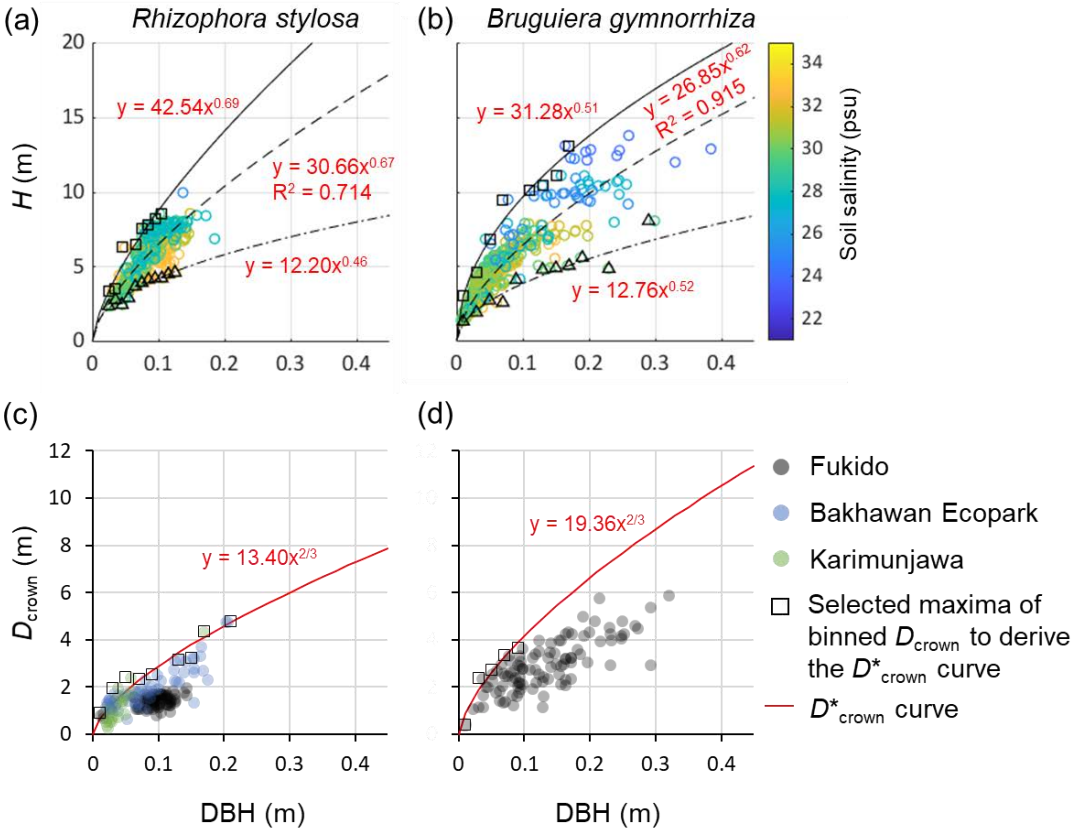

Figure S3.1. Field data-derived morphological traits of *Rhizophora stylosa* and *Bruguiera gymnorrhiza*. (a–b) DBH-tree height (H) relationships and (c–d) DBH-crown diameter (D_{crown}) relationships of the two species in Fukido mangrove forest. In panels (a–b), the solid and dot-dash lines indicate DBH-maximum height (H_{max}) and DBH-minimum height (H_{min}) relationships,

respectively, while the rectangular and triangular markers indicate the maxima and minima of selected bins used for the derivation of DBH-H_{max} and DBH-H_{min} relationships, respectively. The dashed lines indicate the general allometric relationship of DBH-*H*. In panel (c), the supplemented data from *R. apiculata* and *R. mucronata* in Bakhawan Ecopark and Karimunjawa, and *R. stylosa* in Fukido were used.

Note S3.2. Supplementary data on crown diameters

Supplementary measurements of crown diameter for the genus *Rhizophora* were conducted in a planted mangrove forest in Bakhawan Ecopark, Panay Island, Philippines and a dwarf mangrove forest in Karimunjawa Island, Central Java, Indonesia. In Bakhawan Ecopark, ~10- (11.7195°N, 122.3927°E), ~20- (11.7180°N, 122.3892°E), and ~30-year-old forests (11.7180°N, 122.3911°E) were selected so that the measurement will have a wide range in tree size variability. In each forest, 20 trees were randomly selected, and the crown diameters were measured using the same protocol as described in Section 3.2.2. The forests are mix of *R. apiculata* and *R. mucronata* stands, and sampled trees cover diameters at breast height (DBH) of ~0.05 m, 0.05–0.13 m, and 0.1–0.2 m at ~10-, ~20-, and ~30-year-old forests, respectively. Photographs of the canopy taken by looking upward are shown in Fig. S3.2a–c. The canopy of ~10- and ~20-year-old forests are closed while the canopy of ~30-year-old forest is relatively open. The mangrove forest in Karimunjawa Island is a mix of natural and planted stands of *R. apiculata* and *R. mucronata*. The canopy is completely open; thus, no influence of competition is expected (Fig. S3.2d). The sampled trees cover DBH of 0.02–0.17 m.

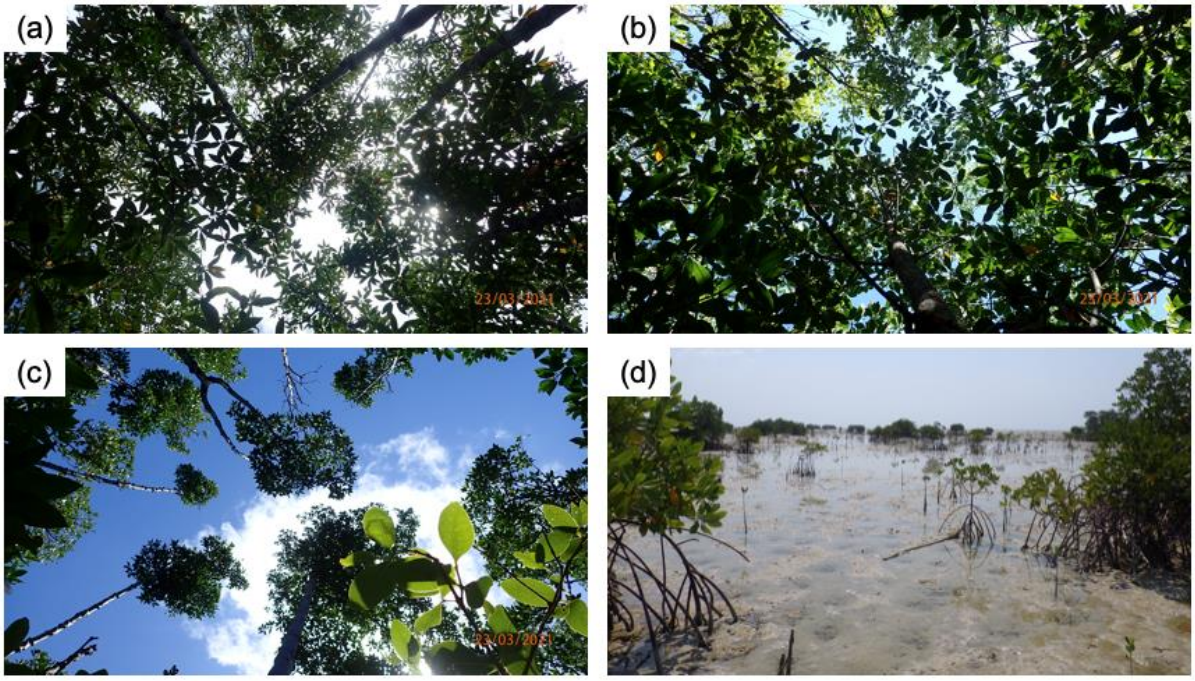

Figure S3.2. Upward-looking view of canopies in (a) ~10-, (b) ~20-, and (c) ~30-year-old forests in Bakhawan Ecopark, and (d) view of a dwarf mangrove forest in Karimunjawa Island.

Note S3.3. Minor modification of processes in SEIB-DGVM

Tree establishment

The computational domain is divided into 1 m × 1 m grid-cells, and the establishment of a tree is simulated at each grid-cell at yearly time step according to establishment probability and some criteria. The original SEIB-DGVM defines criteria of climate conditions for the establishment to reproduce the global vegetation distribution (Sato et al., 2007). However, the site of model application in this study is small and the spatial variations in atmospheric variables are not expected, thus such criteria were not considered in this study. Therefore, the environmental factor that affects the establishment is only annual-mean midday photosynthetically active radiation at the forest floor in a grid-cell (PAR_{floor}). If $PAR_{floor} > PAR_{min}$, the grid-cell has the potential of new establishment of a species, where PAR_{min} is the minimum PAR_{floor} required to establish the species. If several species satisfied this condition, the species that will establish in the grid cell is determined according to the fraction of total biomass of each species in the computational domain such that the dominant species has a higher probability of establishment. Simultaneously, it is sometimes randomly selected with a probability Est_{random}, where the value of Est_{random} was set as 0.05 in this study. This corresponds to Scenario 4 in the tree establishment scheme in SEIB-DGVM (see Sato, 2015 for the detail).

Then, the determined species establishes at the grid cell with a probability $P_{establish}$ (m^{-2} $year^{-1}$).

Mortality

Mortality occurs at a yearly time step in SEIB-DGVM. Mortality is usually modeled as a sum of growth efficiency mortality ($mort_{greff}$, $year^{-1}$) and background mortality ($mort_{bg}$, $year^{-1}$) in dynamic vegetation models. Additionally, SEIB-DGVM introduced heat stress- or cold stress-induced mortality to describe global vegetation distribution (Sato et al., 2007), but these additional factors were not considered in this study for the same reason as the establishment. The SEIB-DGVM also defines the maximum age that trees can survive, but it was also not considered in this study due to the uncertainty in the longevity of mangroves. Also, the formulation of growth-efficient mortality was replaced with the following equation which is used as such in Sitch et al. (2003) and Thum et al. (2019):

$$mort_{\mathrm{greff}} = \frac{k1_{\mathrm{mort\_greff}}}{1+k2_{\mathrm{mort\_greff}} \times eff_{\mathrm{growth}}} \quad \text{(S3.3)}$$

where $k1_{mort\_greff}$ ($year^{-1}$) and $k2_{mort\_greff}$ (m^2 leaf year g^{-1} Dry Weight) are parameters and eff_{growth} (g DW m^{-2} leaf $year^{-1}$) is the net primary production minus tissue turnover per unit leaf area which is described as

$$eff_{\mathrm{growth}} = \frac{NPP-TO}{LA} \quad \text{(S3.4)}$$

where *NPP* is the annual net primary production (g DW $tree^{-1}$ $year^{-1}$), *TO* is the annual whole-plant turnover demand (g DW $tree^{-1}$ $year^{-1}$), and *LA* is the whole-plant leaf area (m^2 leaf $tree^{-1}$). The equation was replaced because the original equation in SEIB-DGVM has a parameter with a physically complicated unit.

In this study, we introduced additional mortality that is related to salt stress ($mort_{salt}$, $year^{-1}$). As described in Section 3.2.3.2, if a tree is stressed by salt, the tree adjusts plant hydraulics from the sapwood area or root biomass (Eq. (3.7)). Consequentially, *H* of the tree could go below the DBH-H_{min} curve shown in Fig. S3.1a–b, depending on salt stress. In such a case, the tree was regarded as “salt-stressed tree” and high mortality was given. In this study, $mort_{salt}$ was set to 0.3 for salt-stressed trees and 0.0 for non-stressed trees. Then, the mortality of a tree (f_{mort}, $year^{-1}$) is calculated by adding each mortality factor:

$$f_{\mathrm{mort}} = \min\left(mort_{\mathrm{greff}} + mort_{\mathrm{bg}} + mort_{\mathrm{salt}}, 1.0\right) \quad \text{(S3.5)}$$

Maintenance respiration

In SEIB-DGVM, a parameter called the specific respiration rate per unit nitrogen in the plant tissue at 15.0 ℃ (*RM*, g DW g^{-1} N day^{-1}) is used to calculate the maintenance respiration rate of each tree organ. However, for the leaf respiration, we used the dark respiration rate

per unit area at 25 ℃ ($R_{d,25}$, μmol C m^{-2} s^{-1}) instead of *RM*, which is a common parameter for leaf respiration rate. For the temperature response of $R_{d,25}$, a function used in Kumarathunge et al. (2019) (also see Note S3.4) was used. For maintenance respiration of other organs, the parameters RM_W and RM_{FR} (respiration rate per unit biomass at 15.0 ℃, g DW g^{-1} DW day^{-1}) for woody organ and fine root, respectively, were used instead of *RM* to adopt literature values. Temperature response of maintenance respiration of these organs was kept the same as in the original SEIB-DGVM. Likewise, as in the original SEIB-DGVM, if the whole-plant gross primary production (g C $tree^{-1}$ day^{-1}) is insufficient for satisfying the whole-plant demand of maintenance respiration, the deficit is supplemented from the stock carbon pool.

Crown layer purge

In SEIB-DGVM, trees purge the bottom crown layer at yearly time step depending on the balance between resource gain and maintenance cost of the layer. Here, the resource gain of the layer is expressed using leaf-level net primary photosynthesis rate at the layer ($Crown_{C\_gain}$, g C m^{-2} leaf day^{-1}), while the maintenance cost ($Crown_{C\_cost}$, g C m^{-2} leaf day^{-1}) is expressed using:

$$Crown_{\mathrm{C\_cost}} = \frac{TO_l \times C_M}{SLA \times 10^{-4}} \quad \text{(S3.6)}$$

where TO_l is the leaf turnover rate (day^{-1}), C_M is the carbon mass per unit dry weight in plant tissue (g C g^{-1} DW), *SLA* is the specific leaf area (cm^2 leaf g^{-1}), and the multiplication of 10^{-4} is for unit conversion of *SLA*.

In this study, nitrogen (N) uptake was also considered in addition to carbon uptake by photosynthesis, which emerges as an additional need for the consideration of gain and cost balance for N. The N uptake by a crown layer ($Crown_{N\_gain}$, g N m^{-2} leaf day^{-1}) is expressed as:

$$Crown_{\mathrm{N\_gain}} = T_{\mathrm{layer}} \times \mathrm{DIN} \times \frac{14}{1000} \quad \text{(S3.7)}$$

where T_{layer} is the leaf-level transpiration rate at the bottom layer (mm day^{-1}), DIN is the dissolved inorganic nitrogen concentration in porewater (mol N m^{-3}), and the multiplication of 14/1000 is for unit conversion. The N cost by the layer ($Crown_{N\_cost}$, g N m^{-2} leaf day^{-1}) is expressed as:

$$Crown_{\mathrm{N\_cost}} = \frac{TO_l \times C_M \times (1 - NRE)}{SLA \times CN_l} \quad \text{(S3.8)}$$

where CN_l is the C/N ratio in the leaf (g C g^{-1} N), and *NRE* is the nitrogen resorption efficiency (fraction). A tree purges the crown layer if the annual mean of $Crown_{C\_gain}$ or $Crown_{N\_gain}$ is less than $Crown_{C\_cost}$ or $Crown_{N\_cost}$, respectively.

Note S3.4. Leaf flux model

Leaf temperature and transpiration

Leaf temperature and transpiration rates are calculated at each crown layer of each tree using the equations presented by Bonan et al. (2014); these are summarized below.

The leaf energy balance can be written by equating the net radiation ($R_{n,i}$, W m^{-2}) to the sum of sensible heat flux (H_i, W m^{-2}) and latent heat flux ($\lambda_w E_i$, W m^{-2}) at each crown layer, where the symbol "*i*" indicates crown layer index here and hereafter:

$$R_{n,i} = H_i + \lambda_w E_i \quad \text{(S3.9)}$$

where λ_w (J mol^{-1}) is the latent heat of vaporization of water and E_i is leaf transpiration rate at crown layer *i* (mol m^{-2} s^{-1}). The sensible heat flux H_i is represented as:

$$H_i = 2c_p(T_{l,i} - T_a)g_{bh,i} \quad \text{(S3.10)}$$

where c_p is the specific heat of air at constant pressure (J mol^{-1} K^{-1}), $T_{l,i}$ is the leaf temperature (K), T_a is the air temperature (K), and $g_{bh,i}$ is the boundary layer conductance for heat (mol m^{-2} s^{-1}). The parameter $g_{bh,i}$ is a function of leaf size (d_l, m) and wind speed. Here, wind speed profile within the canopy is calculated from a model proposed by Barnard and Bauerle (2016) by approximating a horizontally uniform canopy structure. Latent heat flux is given by:

$$\lambda_w E_i = \frac{c_p}{\gamma}(e_{l,i} - e_a)g_{v,i} \quad \text{(S3.11)}$$

where γ is the psychrometric constant (Pa K^{-1}) given by $\gamma = c_p P_a/\lambda_w$ with P_a atmospheric pressure (Pa), $e_{l,i}$ the leaf vapor pressure (Pa), e_a the air vapor pressure (Pa), and $g_{v,i}$ the conductance for water vapor (mol m^{-2} s^{-1}) expressed as a series of stomatal conductance ($g_{s,i}$, mol m^{-2} s^{-1}) and boundary layer conductance ($g_{bv,i}$, mol m^{-2} s^{-1}) with $g_{v,i} = 1/(g_{s,i}^{-1} + g_{bv,i}^{-1})$. The parameter $g_{bv,i}$ is a function of leaf size and wind speed, similar to $g_{bh,i}$. It is assumed that the water vapor pressure in the stomatal pore is saturated; therefore $e_{l,i}$ is a function of leaf temperature $T_{l,i}$. Here, once the value of $g_{s,i}$ is given, the values of $T_{l,i}$ and $E_{l,i}$ were determined from Eqs. (S3.9)–(S3.11).

Leaf photosynthesis

Leaf photosynthesis is calculated using the biochemical model of Farquhar et al. (1980), which was adapted by the leaf flux model of Bonan et al. (2011) and (2014). The equations are summarized below.

The net leaf photosynthesis rate at a crown layer *i* ($A_{n,i}$, μmol CO_2 m^{-2} s^{-1}) is given by:

$$A_{n,i} = \min(A_{c,i} - A_{j,i}) - R_d \quad \text{(S3.12)}$$

$$A_{c,i} = \frac{V_{cmax}(c_{i,i} - \Gamma_*)}{c_{i,i} + K_c(1 + o_i/K_o)} \quad \text{(S3.13)}$$

$$A_{j,i} = \frac{J_i(c_{i,i} - \Gamma_*)}{4c_{i,i} + 8\Gamma_*} \quad \text{(S3.14)}$$

where $A_{c,i}$ and $A_{j,i}$ (μmol m^{-2} s^{-1}) are the Rubisco carboxylation-limited and RuBP-regeneration-limited photosynthetic rates, respectively, R_d is the leaf respiration rate (μmol m^{-2} s^{-1}), $c_{i,i}$ is the intercellular CO_2 concentration (μmol mol^{-1}), Γ_* is the CO_2 compensation point (μmol mol^{-1}), V_{cmax} is the maximum rate of Rubisco activity (μmol m^{-2} s^{-1}), o_i is the intercellular O_2 concentration (209 mmol mol^{-1}), K_c (μmol mol^{-1}) and K_o (mmol mol^{-1}) are the Michaelis-Menten coefficients of Rubisco activity for CO_2 and O_2 respectively, and J_i is the electron transport rate at a crown layer i (μmol m^{-2} s^{-1}), which is related to absorbed PAR at the layer (APAR$_i$, μmol photon m^{-2} s^{-1}); these are described as:

$$\theta_{\mathrm{PSII}} J_i^2 - (I_{\mathrm{PSII}} + J_{\max}) J_i + I_{\mathrm{PSII}} J_{\max} = 0 \quad \text{(S3.15)}$$

$$I_{\mathrm{PSII}} = 0.5(1-f)\mathrm{APAR}_i \quad \text{(S3.16)}$$

where θ_{PSII} is the curvature for electron transport (0.7), I_{PSII} is the PAR absorbed by PS II (μmol photon m^{-2} s^{-1}), f is a fraction of PAR absorbed by non-photosynthetic materials (0.15), and J_{max} is the maximum electron transport rate (μmol m^{-2} s^{-1}). In Eqs. (S3.12)–(S3.15), the parameters V_{cmax}, J_{max}, R_d, Γ_*, K_c, and K_o vary with leaf temperature, thus the values may vary within crown layers. Following Kumarathunge et al. (2019), the values and temperature responses of Γ_*, K_c, and K_o were adapted from Bernacchi et al. (2001) and Medlyn et al. (2002), respectively. The temperature response of V_{cmax} and J_{max} are given by the peaked Arrhenius function:

$$k_1(T_v) = k_{25} \times \exp\left[\frac{E_a(T_v - 298.15)}{298.15 R T_v}\right] \frac{1+\exp\left(\frac{298.15\Delta S - H_d}{298.15 R}\right)}{1+\exp\left(\frac{T_v \Delta S - H_d}{T_v R}\right)} \quad \text{(S3.17)}$$

while the temperature response of R_d is given by:

$$k_2(T_v) = k_{25} \times \exp\left[\frac{E_a(T_v - 298.15)}{298.15 R T_v}\right] \quad \text{(S3.18)}$$

where $k_1(T_v)$ and $k_2(T_v)$ are the process rates at a given temperature, T_v (K), k_{25} is the process rate at 25 ℃, R is the universal gas constant (J K^{-1} mol^{-1}), E_a is the activation energy (J mol^{-1}), H_d is the deactivation energy (J mol^{-1}), and ΔS is the entropy term (J K^{-1} mol^{-1}).

Gas exchange is regulated by the diffusion process between the atmosphere and the leaf through the stomata. The net photosynthesis rate $A_{n,i}$ can also be expressed using the diffusive rate given by:

$$A_{n,i} = \frac{(c_a - c_{i,i})}{1.4 g_{bv,i}^{-1} + 1.6 g_{s,i}^{-1}} \quad \text{(S3.19)}$$

where c_a is the atmospheric CO_2 concentration (μmol mol^{-1}), $c_{i,i}$ is the intercellular CO_2 concentration (μmol mol^{-1}), $g_{s,i}$ and $g_{bv,i}$ are the stomatal conductance and boundary layer conductance for water vapor (mol m^{-2} s^{-1}), respectively, and the factor 1.4 and 1.6 are for adjusting the diffusivity of CO_2 compared with H_2O for the boundary layer and stomatal conductance (Bonan, 2019). The value of $A_{n,i}$ can then be obtained once the value of $g_{s,i}$ is given by equating Eqs. (S3.12) and (S3.19).

Stomatal conductance optimization

The leaf transpiration rate, temperature, and photosynthetic rate at a crown layer depend on stomatal conductance at the layer. Here, the stomatal conductance at a layer, $g_{s,i}$, is estimated from the optimization theory. The theory assumes that plants regulate stomatal conductance to keep the marginal water use efficiency (WUE) constant (Cowan and Farquhar, 1977), which has been used in the models of Bonan et al. (2014) and Xu et al. (2016). The stomatal conductance is optimized at each crown layer to achieve the condition:

$$\frac{\mathrm{d}A_{\mathrm{n},i}}{\mathrm{d}g_{\mathrm{s},i}} - \lambda \frac{\mathrm{d}E_i}{\mathrm{d}g_{\mathrm{s},i}} = 0 \quad \text{(S3.20)}$$

where λ is the Lagrangian multiplier of the optimization problem representing optimal WUE. This is a condition that indicates that the further opening of stomata does not yield a sufficient carbon gain per unit water loss, characterized by λ (Bonan et al., 2014). We followed Bonan et al. (2014) for the numerical solution of $g_{s,i}$. The value of λ increases as leaf water potential (Ψ_l, MPa) declines, as shown by a meta-analysis of Manzoni et al. (2011), where the increased λ generally leads to the regulation of stomatal conductance, resulting in decreased A_n and E. Then, following Xu et al. (2016), λ is determined at daily time step considering predawn leaf water potential ($\Psi_{l,predawn}$, MPa):

$$\lambda = \lambda_0 \exp\left(\beta_0 \Psi_{\mathrm{l,predawn}}\right) \quad \text{(S3.21)}$$

where λ_0 is the value of optimal WUE when there is no stress imposed by the decreased leaf water potential, and β_0 is an empirical parameter representing stomatal sensitivity. Additionally, when Ψ_l falls below a species-specific minimum value given by $\Psi_{l,min}$, the model simulates stomatal closure to prevent further decrease in Ψ_l that may cause xylem cavitation (Bonan et al., 2014).

Note S3.5. Daily C and N resources for tree growth

From the plant hydraulics module coupled with the photosynthesis module described in the section 3.2.3.1 and Note S3.4, the daily C (C_{gain}, g C tree^{-1} day^{-1}) and N (N_{gain}, g N tree^{-1} day^{-1}) uptake rates were calculated, where N_{gain} is given by:

$$\mathrm{N_{gain}} = J_{\mathrm{sap,day}} \times \mathrm{DIN} \times \frac{14}{\rho_{\mathrm{w}}} \approx T_{\mathrm{whole,day}} \times \mathrm{DIN} \times \frac{14}{\rho_{\mathrm{w}}} \quad \text{(S3.22)}$$

where, $J_{sap,day}$ and $T_{whole,day}$ are the daily sap flow and whole-plant transpiration rates (kg tree^{-1} day^{-1}), DIN is the dissolved inorganic nitrogen concentration in the porewater (mol N m^{-3}), ρ_w is water density (kg m^{-3}), and the factor 14 is for unit conversion of N from molar to gram concentration. Although the sap flow and whole-plant transpiration rates may differ at a short time step (e.g., hourly), these are equivalent at relatively a long time scale (e.g., daily); therefore, $J_{sap,day} \approx T_{whole,day}$. The C_{grow} (daily C resources that can be used for tree growth, g C

tree^{-1} day^{-1}) was calculated from C_{gain} using the following steps: subtraction for the whole-plant woody and root maintenance respiration and C cost for turnover compensation after accounting for growth respiration, and subtraction/addition of C deficit/surplus in the stock pool from the target value characterized by a parameter β_{stock} (Table 3.1). Likewise, N_{grow} (daily N resources that can be used for tree growth, g N tree^{-1} day^{-1}) was calculated from N_{gain} by subtraction of N cost for turnover compensation, the addition of N resorbed from the senescent leaves characterized by a parameter *NRE* (Table 3.1), and subtraction/addition of N deficit/surplus in the stock pool from the target value. Suppose C_{gain} or N_{gain} is insufficient for compensating the respiration (only for C_{gain}) and turnover cost, the deficit is supplemented from the stock pool, where the growth respiration is accounted for in the case of C compensation for the turnover cost.

Note S3.6. Crown diameter expansion

When biomass is allocated to leaves in a tree, the model simulates the increase of crown area or leaf area index (LAI) of the tree, depending on the crown morphology at a specific time. We considered that plants preferentially increase crown area rather than LAI to increases their occupied space if the expansion of crown diameter (D_{crown}) is not inhibited by allometric (D^*_{crown}) or physical ($D_{crown.con}$) constraints. The crown diameter expansion is also beneficial in terms of plant productivity because the increase in LAI attenuates radiation within the crown more rapidly, decreasing the photosynthetic and transpiration rates per unit leaf area.

If an increase in leaf biomass is given by dM_L (g leaf tree^{-1} day^{-1}) and the crown diameter expansion is not inhibited ($D_{crown} < \min(D^*_{crown}, D_{crown,con})$), the tree expands its crown by keeping the same LAI as follows:

$$\frac{M_L}{A_{crown}} = \frac{M_L + dM_L}{A_{crown} + dA_{crown}} \quad \text{(S3.23)}$$

where A_{crown} is the crown area, and dA_{crown} is the increase in crown area due to crown diameter expansion. Crown diameter after the expansion is then calculated from the value (A_{crown} + dA_{crown}).

Table S3.1. Summary of environmental and vegetation variables at survey plots. AGB = above-ground biomass, DBH = diameter at breast height, *R.s* = *Rhizophora stylosa*, *B.g* = *Bruguiera gymnorrhiza*. The names of transects are indicated as A–D while plots along a transect line are numbered from the nearest creek to landward (Fig. 3.1c).

Plot	Soil salinity (psu)	Porewater NH_4^+ (μmol L^{-1})	Porewater NO_3^- (μmol L^{-1})	Porewater DIN (μmol L^{-1})	AGB (Mg ha^{-1}), *R.s*	AGB (Mg ha^{-1}), *B.g*	Mean DBH (m), *R.s*	Mean DBH (m), *B.g*
A1	32.8	190	21	212	92	1	9.1	6.1
A2	32.53	219	31	250	87	23	9.9	9.5
A3	33.0	238	22	260	63	30	9.1	7.3
A4	29.7	49	5	54	69	38	8.3	8.4
A5	29.9	69	8	76	10	19	6.2	10.7
B1	31.2	154	5	159	71	39	9.9	9.5
B2	31.7	272	7	279	87	26	10.4	9.1
B3	29.3	293	8	302	94	29	9.8	9.7
B4	27.8	124	4	129	108	19	10.3	12.2
B5	27.2	83	4	87	0	127	-	17.0
B6	24.1	98	9	107	0	144	-	23.9
B7	25.3	119	26	145	4	110	13.7	14.2
C1	29.3	115	6	121	0	180	-	16.5
C2	30.0	143	11	154	0	124	-	14.4
C3	24.5	186	20	206	16	120	12.8	15.0
C4	27.6	242	29	272	0	143	-	15.2
C5	31.7	262	20	283	11	143	12.3	10.5
D1	28.7	233	15	249	16	122	12.2	11.4
D2	30.7	247	18	265	12	114	9.5	13.4
D3	29.0	290	20	311	40	59	9.3	8.6
D4	26.2	181	9	190	0	185	-	19.3
D5	19.0	183	8	191	0	197	-	19.4
D6	22.2	167	11	178	0	152	-	20.6
D7	20.8	312	19	332	0	184	-	16.9

Table S3.2. Summary of model parameters not shown in Table 3.2.

Symbol	Description	Units	R. s	B. g	Source
C_M	Carbon mass per unit dry weight in plant tissue	g C g^{-1} DW	0.45	0.45	Alongi (2003)
a_1	Correction factor for tree height to water path length	–	1.2	1.2	Xu et al. (2016)
F_{gr}	Growth respiration fraction	Fraction	0.25	0.25	Arora (2002)

PAR_{min}	Minimum PAR_{floor} required for establishment	μmol photon m^{-2} s^{-1}	100	100	
$P_{establish}$	Establishment probability	m^{-2} $year^{-1}$	0.1	0.1	
k_{1mort_greff}	Mortality parameter in Eq. (S3.3)	$year^{-1}$	0.1	0.1	
k_{2mort_greff}	Mortality parameter in Eq. (S3.3)	m^2 leaf year g^{-1} DW	0.03	0.03	
$mort_{bg}$	Background mortality rate	$year^{-1}$	0.007	0.007	Fisher et al. (2010)
RM_W	Maintenance respiration rate of woody organ at 15 ℃	g DW g^{-1} DW day^{-1}	6.5×10^{-5}	6.5×10^{-5}	Vinh et al. (2019)
RM_{FR}	Maintenance respiration rate of fine root at 15 ℃	g DW g^{-1} DW day^{-1}	4.3×10^{-3}	4.3×10^{-3}	Lovelock et al. (2006)
$R_{d,25}$	Dark leaf respiration rate at 25 ℃	μmol C m^{-2} s^{-1}	1.2	1.2	Aspinwall et al. (2021)
$J_{max,25}$	Maximum electron transport rate at 25 ℃	μmol C m^{-2} s^{-1}	1.54 × $V_{cmax,25}$		Aspinwall et al. (2021)
E_{aV}	Activation energy of the maximum rate of Rubisco activity (V_{cmax})	J mol^{-1}	108200	108200	Aspinwall et al. (2021)
E_{aJ}	Activation energy of the maximum electron transport rate (J_{cmax})	J mol^{-1}	73100	73100	Aspinwall et al. (2021)
E_{aR}	Activation energy of the dark leaf respiration rate (R_d)	J mol^{-1}	46400	46400	Bonan et al. (2014)
H_{dV}	Deactivation energy of V_{cmax}	J mol^{-1}	200000	200000	Kumarathunge et al. (2019)
H_{dJ}	Deactivation energy of J_{cmax}	J mol^{-1}	200000	200000	Kumarathunge et al. (2019)
ΔS_V	Entropy of V_{cmax}	J K^{-1} mol^{-1}	655	655	Aspinwall et al. (2021)
ΔS_J	Entropy of J_{cmax}	J K^{-1} mol^{-1}	655	655	Aspinwall et al. (2021)
d_l	Leaf dimension	m	0.1	0.1	

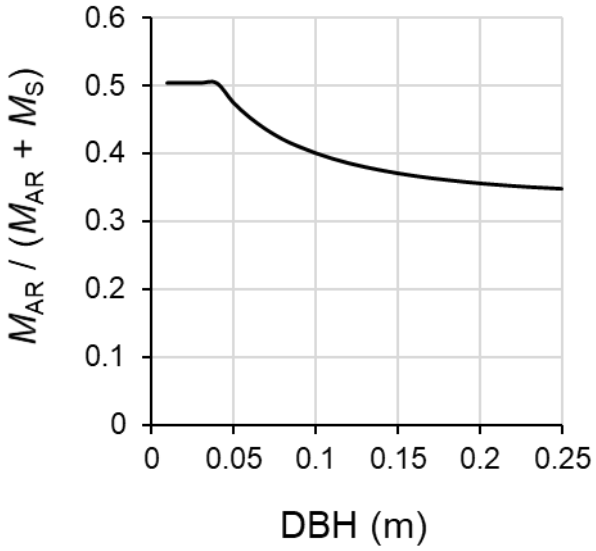

Figure S3.3. Example of prop root allometry in Fukido mangrove forest. The parameter M_{AR} is above-ground root (prop root) biomass, and M_S is stem biomass. The parameter M_S was calculated from the diameter at breast height (DBH), tree height (H), and wood density (ρ) using Eq. (3.1); H was calculated from the general allometric relationship shown in Fig. S3.1a. The prop root biomass was calculated by multiplying the prop root volume and ρ; the prop root volume was estimated from DBH and prop root diameter using the empirical model developed for Fukido mangrove forest in Yoshikai et al. (2021). Here, the prop root diameter was set as 0.03 m based on field data. For trees with DBH < 0.03 m, the value computed for the tree with DBH = 0.03 m was applied. Note that H does not always follow the general allometric relationship in the simulation, therefore the prop root biomass fraction may vary from the one shown here.

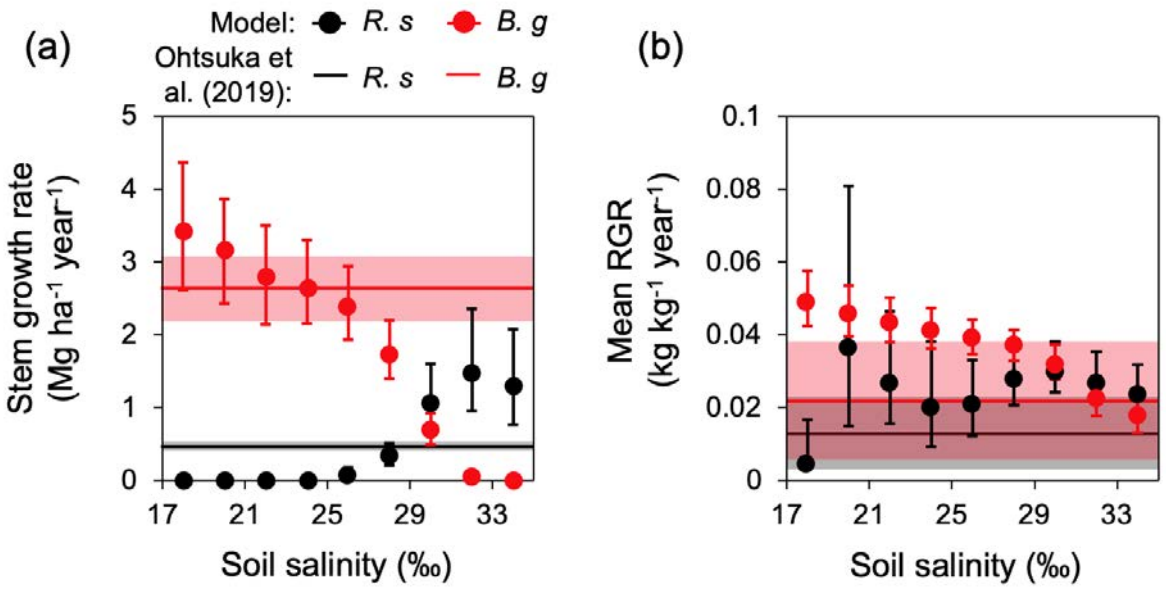

Figure S3.4. (a) Stem growth rate and (b) mean individual relative growth rate (RGR) of *R. stylosa* (*R. s*) and *B. gymnorrhiza* (*B. g*) along the soil salinity gradient. From each ensemble simulation, the modeled stem growth rate and mean RGR in steady states (> 300 years) were extracted and pooled for all ensembles, and the mean (circle marker) and standard deviation (error bar) values of the pooled samples were shown. The line and shade show the mean and standard deviation of data measured by Ohtsuka et al. (2019) in a *B. gymnorrhiza*-dominated site in Fukido mangrove forest.

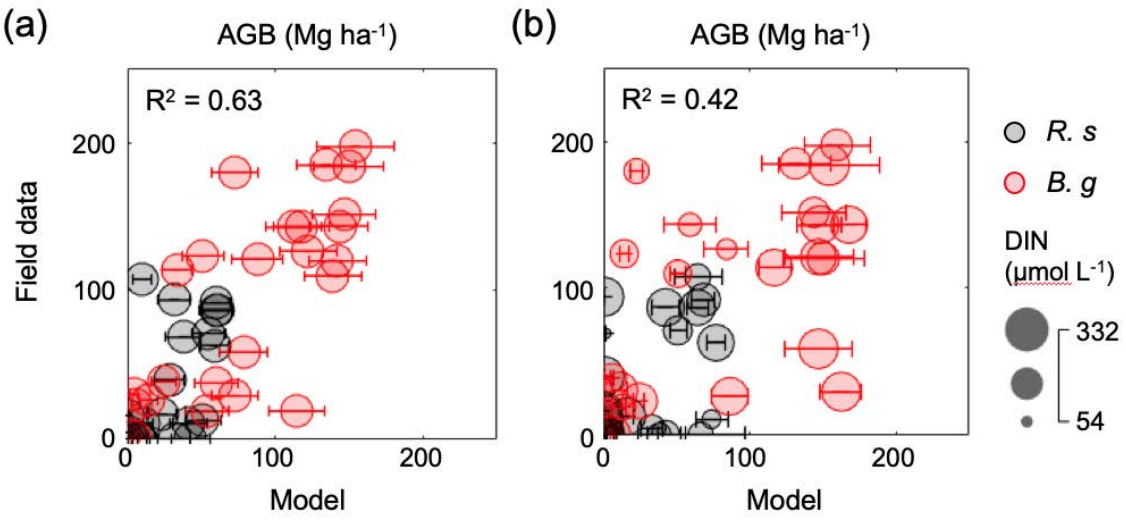

Figure S3.5. Results of “plot-wise simulation”. Comparison of modeled and field-measured AGB at survey plots in Fukido mangrove forest, where panel (a) is a case where spatially averaged DIN (200 μmol L^{-1}) was given while panel (b) is a case where plot-wise DIN is given.

The results shown are from one simulation, where modeled AGB in steady states (> 300 years) was extracted and the median (circles) and the 90-th percentile (bars) were shown.

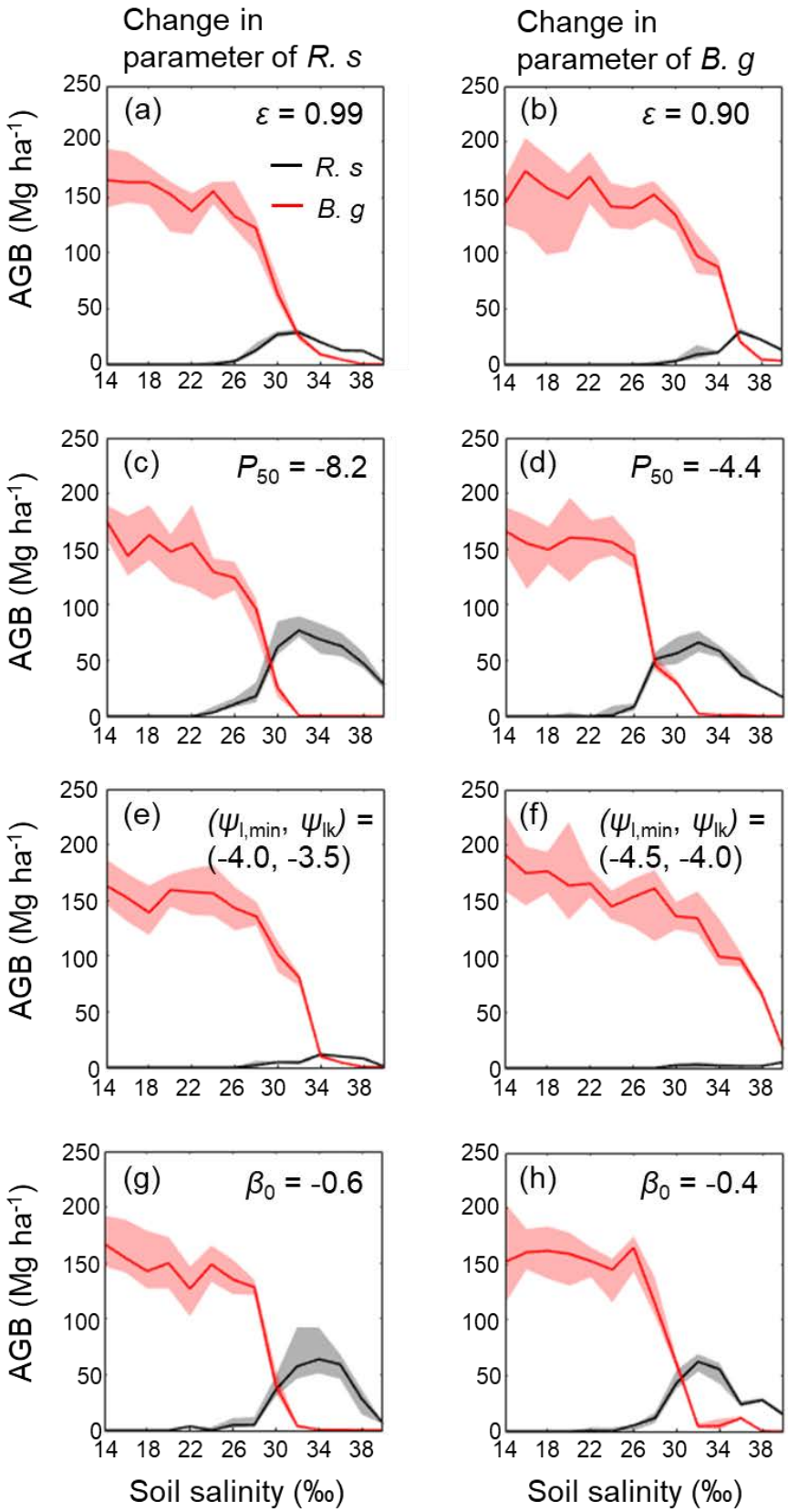

Figure S3.6. Sensitivity of above-ground biomass (AGB) of *R. stylosa* (*R. s*) and *B. gymnorrhiza* (*B. g*) across a soil salinity gradient to changes in parameter values of plant hydraulic traits: sensitivity to (a, b) salt filtration efficiency (ε), (c, d) water potential at which 50% of xylem conductivity is lost (P_{50}), (e, f) critical leaf water potential (Ψ_{lk}) and minimum leaf water potential ($\Psi_{l,min}$), and (g, h) sensitivity of marginal water use efficiency to leaf water potential (β_0). Sensitivities were examined by changing a value of one species (*R. s* or *B. g*) to the one determined for the other species shown in Table 3.2. Median (solid line) and 90-th percentile (shading) of AGB in steady states (> 300 years) are shown; the results are from one simulation without the ensemble approach, which caused some fluctuations in AGB along the soil salinity gradient.

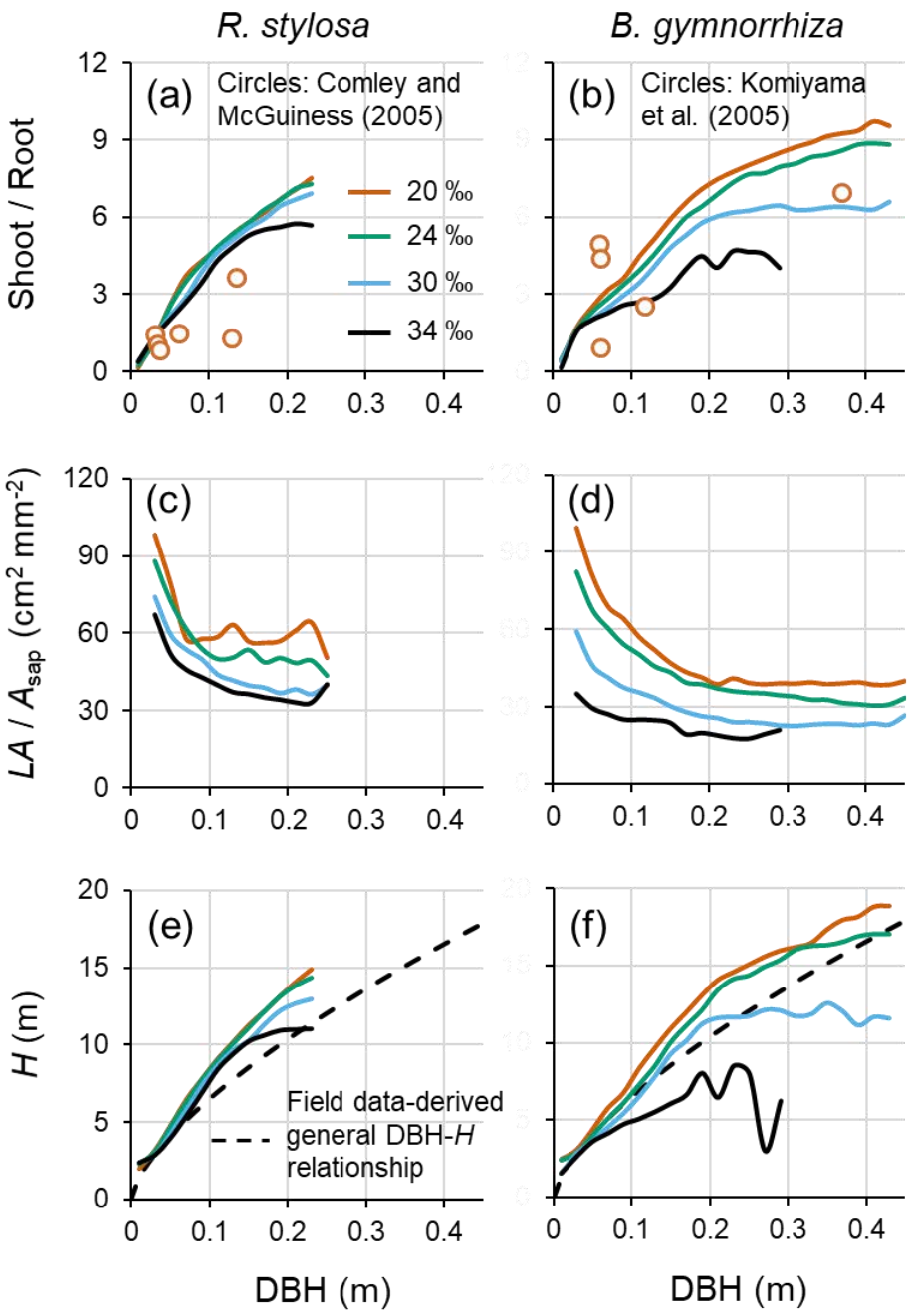

Figure S3.7. Modeled relationships of (a, b) shoot/root biomass ratio, (c, d) whole-plant leaf area (*LA*)/sapwood (A_{sap}) ratio, and (e, f) tree height (*H*) with DBH under different soil salinity conditions. From each ensemble simulation result from 300–450 years, which is in steady states in terms of forest structural variables, the modeled individual trees' variables were extracted every 10 years. The extracted samples were pooled for all ensemble simulations. The pooled samples were then binned with DBH width of 0.02 m, and the median value in each bin was shown. Here, the shoot biomass refers to the sum of stem and leaf biomass, and the root biomass refers to the sum of coarse and fine root biomass. Note that the above-ground root biomass (of *R. stylosa*) is not included in the shoot biomass both in the model

result and the data of Comley and McGuiness (2005). Also, note that Komiyama et al. (2005) data include *B. gymnorrhiza* and *B. sexangla*. See Note S3.1 and Fig. S3.1 for field-data derived general DBH-*H* relationship details.

References for the Supporting Information

Alongi, D. M., Clough, B. F., Dixon, P. and Tirendi, F.: Nutrient partitioning and storage in arid-zone forests of the mangroves *Rhizophora stylosa* and *Avicennia marina*. Trees, 17(1), 51–60, 2003.

Arora, V.: Modeling vegetation as a dynamic component in soil-vegetation-atmosphere transfer schemes and hydrological models. Rev. Geophys., 40(2), 3–1, 2002.

Aspinwall, M. J., Faciane, M., Harris, K., O'Toole, M., Neece, A., Jerome, V., Colón, M., Chieppa, J. and Feller, I. C.: Salinity has little effect on photosynthetic and respiratory responses to seasonal temperature changes in black mangrove (*Avicennia germinans*) seedlings. Tree Physiol., 41(1), 103–118, 2021.

Barnard, D. M. and Bauerle, W. L.: Seasonal variation in canopy aerodynamics and the sensitivity of transpiration estimates to wind velocity in broadleaved deciduous species. J. Hydrometeorol., 17(12), 3029–3043, 2016.

Bernacchi, C. J., Singsaas, E. L., Pimentel, C., Portis, A. R. Jr., and Long, S. P.: Improved temperature response functions for models of Rubisco-limited photosynthesis. Plant Cell Environ., 24: 253–259, 2001.

Bonan, G. B.: Climate change and terrestrial ecosystem modeling. Cambridge, UK; New York, NY: Cambridge University Press, 2019.

Bonan, G. B., Lawrence, P. J., Oleson, K. W., Levis, S., Jung, M., Reichstein, M., Lawrence, D. M., and Swenson, S. C.: Improving canopy processes in the Community Land Model version 4 (CLM4) using global flux fields empirically inferred from FLUXNET data. J. Geophys. Res- Biogeo., 116(G2), 2011.

Bonan, G. B., Williams, M., Fisher, R. A., and Oleson, K. W.: Modeling stomatal conductance in the earth system: linking leaf water-use efficiency and water transport along the soil–plant–atmosphere continuum. Geosci. Model Dev., 7(5), 2193–2222, 2014.

Comley, B. W. and McGuinness, K. A.: Above-and below-ground biomass, and allometry, of four common northern Australian mangroves. Aust. J. Bot., 53(5), 431–436, 2005.

Cowan, I. R. and Farquhar, G. D.: Stomatal function in relation to leaf metabolism and environment, in: Integration of Activity in the Higher Plant, edited by: Jennings, D. H., Cambridge University Press, Cambridge, 471–505, 1977.

Fisher, R., McDowell, N., Purves, D., Moorcroft, P., Sitch, S., Cox, P., Huntingford, C., Meir, P. M., and Ian Woodward, F.: Assessing uncertainties in a second - generation dynamic vegetation model caused by ecological scale limitations. New Phytol., 187(3), 666–681, 2010.

Jucker, T., Bouriaud, O., and Coomes, D. A.: Crown plasticity enables trees to optimize canopy packing in mixed-species forests. Funct. Ecol., 29(8), 1078–1086, 2015.

Komiyama, A., Poungparn, S., and Kato, S.: Common allometric equations for estimating the tree weight of mangroves. J. Trop. Ecol., 21(4), 471–477, 2005.

Kumarathunge, D. P., Medlyn, B. E., Drake, J. E., Tjoelker, M. G., Aspinwall, M. J., Battaglia, M., Cano, F. J., Carter, K. R., Cavaleri, M. A., Cernusak, L. A., Chambers, J. Q., Crous, K. Y., De Kauwe, M. G., Dillaway, D. N., Dreyer, E., Ellsworth, D. S., Ghannoum, O., Han, Q., Hikosaka, K., Jensen, A. M., Kelly, J. W. G., Kruger, E. L., Mercado, L. M., Onoda, Y., Reich, P. B., Rogers, A., Slot, M., Smith, N. G., Tarvainen, L., Tissue, D. T., Togashi, H. F., Tribuzy, E. S., Uddling, J., Vårhammar, A., Wallin, G., Warren, J. M., and Way, D. A.: Acclimation and adaptation components of the temperature dependence of plant photosynthesis at the global scale. New Phytol., 222: 768–784, 2019.

Lovelock, C. E., Ruess, R. W., and Feller, I. C.: Fine root respiration in the mangrove *Rhizophora mangle* over variation in forest stature and nutrient availability. Tree Physiol., 26(12), 1601–1606, 2006.

Manzoni, S., Vico, G., Katul, G., Fay, P. A., Polley, W., Palmroth, S., and Porporato, A.: Optimizing stomatal conductance for maximum carbon gain under water stress: a meta-analysis across plant functional types and climates. Funct. Ecol., 25(3), 456–467, 2011.

Medlyn, B. E., Dreyer, E., Ellsworth, D., Forstreuter, M., Harley, P. C., Kirschbaum, M. U. F., Roux, X. Le, Montpied, P., Strassemeyer, J., Walcroft, A., Wang, K., and Loustau, D: Temperature response of parameters of a biochemically based model of photosynthesis. II. A review of experimental data. Plant Cell Environ., 25(9), 1167–1179, 2002.

Ohtsuka, T., Tomotsune, M., Suchewaboripont, V., Iimura, Y., Kida, M., Yoshitake, S., Kondo, M., and Kinjo, K.: Stand dynamics and aboveground net primary productivity of a mature subtropical mangrove forest on Ishigaki Island, south-western Japan. Regional Studies in Marine Science, 27, 100516, 2019.

Peters, R., Vovides, A. G., Luna, S., Grüters, U., and Berger, U.: Changes in allometric relations of mangrove trees due to resource availability–A new mechanistic modelling approach. Ecol. Model., 283, 53–61, 2014.

Pretzsch, H.: Canopy space filling and tree crown morphology in mixed-species stands compared with monocultures. Forest Ecol. Manag., 327, 251–264, 2014.

Sato, H.: SEIB-DGVM v2.80 online description document (http://seib-dgvm.com), 2015.

Sato, H., Itoh, A., and Kohyama, T.: SEIB–DGVM: A new Dynamic Global Vegetation Model using a spatially explicit individual-based approach. Ecol. Model., 200(3–4), 279–307, 2007.

Shenkin, A., Bentley, L. P., Oliveras, I., Salinas, N., Adu-Bredu, S., Marimon-Junior, B. H., Marimon, B. S., Peprah, T., Choque, E. L., Trujillo Rodriguez, L., Clemente Arenas, E. R., Adonteng, C., Seidu, J., Passos, F. B., Reis, S. M., Blonder, B., Silman, M., Enquist, B. J., Asner, G. P., and Malhi, Y.: The influence of ecosystem and phylogeny on tropical tree crown size and shape. Frontiers in Forests and Global Change, 3, 109, 2020.

Sitch, S., Smith, B., Prentice, I. C., Arneth, A., Bondeau, A., Cramer, W., Kaplan, J. O., Levis, S., Lucht, W., Sykes, M. T., Thonicke, K., and Venevsky, S.: Evaluation of ecosystem dynamics, plant geography and terrestrial carbon cycling in the LPJ dynamic global vegetation model. Glob. Change Biol., 9: 161–185. https://doi.org/10.1046/j.1365-2486.2003.00569.x, 2003

Thum, T., Caldararu, S., Engel, J., Kern, M., Pallandt, M., Schnur, R., Yu, L., and Zaehle, S.: A new model of the coupled carbon, nitrogen, and phosphorus cycles in the terrestrial biosphere (QUINCY v1. 0; revision 1996). Geosci. Model Dev., 12(11), 4781–4802, 2019.

Vinh, T. V., Allenbach, M., Joanne, A., and Marchand, C.: Seasonal variability of CO_2 fluxes at different interfaces and vertical CO_2 concentration profiles within a *Rhizophora* mangrove forest (Can Gio, Viet Nam). Atmos. Environ., 201, 301–309, 2019.

West, G. B., Enquist, B. J., and Brown, J. H.: A general quantitative theory of forest structure and dynamics. Proc. Natl. Acad. Sci. U.S.A. 106, 7040–7045, 2009.

Xu, X., Medvigy, D., Powers, J. S., Becknell, J. M., and Guan, K.: Diversity in plant hydraulic traits explains seasonal and inter - annual variations of vegetation dynamics in seasonally dry tropical forests. New Phytol., 212(1), 80–95, 2016.

Yoshikai, M., Nakamura, T., Suwa, R., Argamosa, R., Okamoto, T., Rollon, R., Basina, R., Primavera-Tirol, Y. H., Blanco, A. C., Adi, N. S., and Nadaoka, K.: Scaling relations and substrate conditions controlling the complexity of Rhizophora prop root system. Estur. Coast. Shelf S., 248, 107014, 2021.

Chapter 4: Measurement and modeling of *Rhizophora* mangrove above-ground root system

4.1.1 Abstract

The complex structures of the prop root system of the mangrove genus *Rhizophora* attenuate storm surges and tsunamis and promote sedimentation. While quantification of the mangrove's drag force is essential for assessing the mangroves' ability to reduce the risk of disaster and vulnerability to rising sea-level, the projected area of prop root system having multiple orders of prop roots (e.g., first-, second-, and third-order prop roots, where the root order indicates the level of branching from the stem) are still unexplored. To contribute to the quantitative evaluation of the mangrove's drag force, we investigated the vertical profile of whole-tree prop root projected area and the number of prop roots of 156 trees sampled from Indonesia, the Philippines, and Japan. Our results showed that prop roots above the first-order contribute up to 80 % of the whole-tree prop root projected area, highlighting the importance of the presence of second-, third-, and even higher-order prop roots on the drag force exerted by mangroves. Based on field data, an empirical model for the prop root system, described by a scaling factor (S), and maximum and minimum root heights (HR_{max}, HR_{min}), was developed by assuming that the size distribution of prop roots follows a constant scaling factor S. S and HR_{max} showed significant correlations with stem diameter at breast height suggesting the scaling relations in the prop root system. The model, which employs the site- and species-specific regression models for S and HR_{max}, reproduced the vertical distribution of the number of prop roots – a good predictor of the prop root projected area – with reasonable accuracy. However, the site- and species-specific scaling relations are highly variable depending on the environment, suggesting morphological plasticity in the prop root system. *Rhizophora* trees that grow on a shallow sediment layer (around 0.1 m thickness) tend to produce more prop roots compared with those on a thicker sediment layer suggesting a morphological response of the prop root system to increase below-ground root biomass where below-ground root development is physically constrained. Multivariate analysis indicated that hard substrate also possibly contributes to higher complexity of prop root system. However, prediction of the site- and species-specific scaling relations from these environmental variables still needs to be

improved. Further research is needed to explain the mechanisms of morphological response of prop root systems to environmental gradients and to establish a generalized model for predicting the prop root system in various environments.

4.1.2 Introduction

Mangroves grow in intertidal zones in tropical and subtropical regions (Giri et al., 2011) and are known to form complex structures in their above-ground roots, as seen in the “prop root system” of the *Rhizophora* species (Tomlinson, 2016; Fig. 4.1). They exert a drag force that greatly affects tidal flow in mangrove areas (Furukawa et al., 1997; Mazda et al., 2005; Horstman et al., 2015; Chen et al., 2016), which can play a crucial role in reducing the risk of natural disasters, such as storm surges (Zhang et al., 2012; Montgomery et al., 2019) and tsunamis (Yanagisawa et al., 2009; Husrin et al., 2012; Ismail et al., 2012; Strusinska-Correia et al., 2013). The water flow attenuated by the drag force also enhances sediment deposition in mangrove areas (Furukawa et al., 1997; Horstman et al., 2015; Willemsen et al., 2016) as well as trapping sediments on the vegetation surface (Chen et al., 2018), thereby characterizing mangrove areas as depositional sites (Adame et al., 2010; Lovelock et al., 2015a). Sediment accretion, accelerated by its interaction with geomorphological characteristics, is considered as a key process of mangroves in adapting to rising sea-level (Krauss et al., 2014; Lovelock et al., 2015b; Woodroffe et al., 2016). Therefore, quantification of the mangroves’ drag force is essential for assessing the mangroves’ ecosystem service to reduce the risk of disaster and vulnerability to rising sea-level. The drag effects have been examined in an increasing number of recent studies in terms of field measurements (Horstman et al., 2014; Chen et al., 2016; Mullarney et al., 2017), laboratory flume experiments (Zhang et al., 2015; Maza et al., 2017, 2019; Shan et al., 2019), and numerical simulations (Zhang et al., 2012; Horstman et al., 2015).

The drag force per fluid mass caused by mangroves can be described as

$$F_D = \frac{1}{2} C_D A_f U^2 \tag{4.1}$$

where C_D is the drag coefficient, A_f is the total projected area of the submerged vegetation per unit volume, and U is the depth-averaged flow velocity (Chen et al., 2016; Maza et al., 2017). This equation suggests that the architectural traits of mangroves represented by A_f control the drag force within this type of forest. However, field data on above-ground roots’ morphological properties is very limited despite its importance for assessing the mangroves’ drag effects. This applies to the prop root system – above-ground roots of *Rhizophora* species (Fig. 4.1), the most dominant mangrove species in the Asia-Pacific region (Ong et al., 2004), which is

likely to exhibit the highest drag among mangrove species (Krauss et al., 2003; Horstman et al., 2014). Mazda et al. (1997) and Horstman et al. (2014, 2015) measured the representative A_f of the mangrove forests with *Rhizophora* species stands by measuring parameters such as the number of prop roots and their diameters. However, their results cannot generalize the morphology of the prop root system because A_f is influenced by tree density, and the number of prop roots in a tree may also differ among individual trees. A_f is also significantly influenced by tides because the projected area of submerged prop roots changes with the changes in water depth, thus, the information on vertical profile of prop root projected area is important. A model that predicts the vertical profile of whole-tree prop root projected area is therefore highly needed to effectively estimate A_f in mangroves with *Rhizophora* species stands.

Only Ohira et al. (2013) and Mendez-Alonzo et al. (2015) extensively measured the scaling relations in the morphology of the prop root system of *Rhizophora* species. Ohira et al. (2013) especially made efforts in developing an empirical model to predict the morphology of the prop root system from stem diameter at breast height (DBH) for the purpose of application to studies on mangrove drag effects. Such empirical model allows us to estimate A_f (which is very laborious to measure in the field) simply by measuring tree density and individual tree DBH. However, the model developed by Ohira et al. (2013) is limited to first-order (primary) prop roots (which emerge from the stem), whereas the prop root system of *Rhizophora* species is composed of multiple orders of prop roots, such as second-, third-, and fourth-order prop roots, branching from the first-, second-, and third-order, respectively (Fig. 4.1). The branching of prop roots continues until near the ground. The model by Ohira et al. (2013), which only accounts for first-order prop roots, may therefore largely underestimate A_f, especially when the water level becomes low, because the errors due to the branching of prop roots cumulatively propagate from the top of the prop root system to the bottom. This raises a question regarding the model's applicability to the studies on mangrove drag effects.

Figure 4.1. *Rhizophora* prop root system with multiple orders of roots. Photos were taken in the Fukido River mangrove forest (site Fuk in Table 4.1).

Mangroves also exhibit morphological plasticity according to environmental gradients. For example, Vovides et al. (2014) showed that mangrove tree stems tend to be less slender than the usual stem width and have wider crowns in relation to DBH with increasing soil (pore-water) salinity, the osmotic effects of which significantly regulate the resource uptake of mangroves in below-ground (Peters et al., 2014). The availability of resources below-ground also changes the mangrove carbon allocation to above- and below-ground (Castaneda-Moya et al., 2011, 2013). At a micro-scale, mangrove roots tend to proliferate in decomposing roots and old root channels that are characterized as nutrient-rich microsites in nutrient-poor sediments (Mckee, 2001). However, the relationships between environmental variables and morphology of prop root system have not been well investigated. Only Mendez-Alonzo et al. (2015) demonstrated that prop root architecture has a role in addressing loads from the above-ground structure of the tree in the typically unstable substrate on which the trees of *Rhizophora* species grow, but morphological plasticity in the prop root system has not been verified. Species variation may also be needed to be taken into consideration as a factor controlling the morphology of prop root system as seen in the species-specific allometric relationships in mangroves' above- and below-ground biomass (Clough and Scott, 1989; Komiyama et al., 2008).

If *Rhizophora* species respond to environmental conditions with morphological plasticity in the prop root system, the limitation in the resources below-ground for plant production could lead to the increase of the number of prop roots since the number of prop roots anchoring the ground is directly related to the fine root biomass (Wilkens et al., 2018). Hence, the prop root system may become more complex with increasing soil salinity, which is a regulator of resource uptake below-ground. If the below-ground root development is physically constrained by a very shallow sediment layer, resource uptake of plants in below-ground may also be regulated, which may also lead the morphological plasticity. On the other hand, less stable substrate may require more stability on the prop root system, which may result in higher complexity of the prop root system.

In this study, we aimed to extend the scaling relations in the morphological structures of first-order prop roots found by Ohira et al. (2013) to the whole-tree prop root system having multiple orders of prop roots. Because measuring the whole-tree prop root projected area is a very laborious fieldwork, we hypothesized that the vertical distribution of the number of prop roots (which is relatively easy to measure) would be a good predictor of the vertical profile of the whole-tree prop root projected area. After validating this hypothesis, we developed an empirical model to predict the vertical distribution of the number of prop roots. We also

hypothesized that *Rhizophora* species show morphological plasticity in their prop root system, depending on environmental variables. In this regard, we set up several study sites from Japan, the Philippines, and Indonesia, and measured the morphology of prop root system with environmental variables. Among the measured *Rhizophora* species (*Rhizophora apiculata*, *Rhizophora mucronata*, and *Rhizophora stylosa*), we targeted *R. apiculata* and *R. mucronata*, the prop root systems of which were measured at several environmental conditions, for comparing the differences in prop root morphology with corresponding environmental variables. The measured parameters were soil salinity (as a regulator of resource uptake below-ground), and sediment thickness (as a physical constraint of below-ground root development that also may regulate resource uptake), and surface sediment hardness (as an indicator of stability of the substrate). A multivariate analysis was then conducted to test if the scaling relations of the two *Rhizophora* species (*R. apiculata and R. mucronata*) can be predicted from the environmental variables.

4.2 Materials and Methods

4.2.1 Study sites

Study sites were selected from mangrove areas in Japan, the Philippines, and Indonesia (Fig. 4.2). Detailed locations of measurements, the conditions of the mangroves, sediment type, and information on the sampled trees are summarized in Table 4.1. The conditions of some of these can be seen in Fig. S4.1 in the Supporting Information. The coordinates in Table 4.1 show the locations of environmental variable measurements, and the trees for the prop root system measurement were selected within approximately 60 m of the locations. Among the eight study sites, Fuk is located in a subtropical region in Japan, while the other sites are located in tropical regions of the Philippines and Indonesia.

Fuk is a natural mangrove forest located near the mouth of the Fukido River in Ishigaki Island, Japan (Fig. 4.2). It is a pristine, mature forest that is densely vegetated by two dominant species, *R. stylosa* and *Bruguiera gymnorrhiza* (Sharma et al., 2014). The measurement was conducted near the coast, in an area dominated by *R. stylosa*.

Bak1, Bak2, Bat, and Kii are located in the Aklan province of Western Visayas, Panay Island, the Philippines (Fig. 4.2). Among them, Bak1 and Bak2 are in a replanted mangrove forest (known locally as Bakhawan Ecopark) at the mouth of the Aklan River. The plantation was started in the early 1990s in a mudflat, where over-exploitation of mangrove timber had occurred (Duncan et al., 2016). The dominant species at both sites is *R. apiculata*. Bak1 is a

relatively young mangrove forest (~ 17 years old) compared to Bak2 (~ 30 years old). Bat is a planted mangrove forest with mono-specific stands of *R. mucronata* and *R. apiculata* (~ 20 years old) located inside Batan Bay. *R. apiculata* stands are relatively younger than *R. mucronata* at this site as they were planted later than *R. mucronata* trees. Kii is a mix of natural and planted riverine mangrove forest located in Ibajay, Aklan Province, known locally as KII Ecopark. While mixed-species stands cover most of the mangrove area, the measurement was conducted at planted mono-specific stands of *R. mucronata* near the river mouth.

Mar and Ber are located around the Berau Continental Shelf in East Kalimantan, Indonesia (Fig. 4.2). The Berau River supplies large amount of freshwater and sediment to the continental shelf (Buschman et al., 2012). Ber is a natural mangrove forest fringing a mudflat formed by sediment deposition from the Berau River. According to Renema (2006), the substrate is sand with more than 5 m depth. It is dominated by *Sonneratia alba* and fewer small *R. mucronata* and *R. apiculata* stands with DBH ranging from 0.02 m to 0.04 m. Mar is a natural mangrove forest with mono-specific stands of *R. mucronata* fringing an island in the lagoon surrounded by Maratua Island. The trees are somewhat larger than those in Ber, but DBH range was limited up to 0.08 m. The mangroves are formed on a thin mud layer on a reef flat. Kar is a dwarf mangrove forest of *R. mucronata* and *R. apiculata* formed on a reef flat along the coasts of Karimunjawa Island and Kemujan Island, central Java, Indonesia (Fig. 4.2). The DBH of the measured trees is between 0.016 and 0.043 m. The sediment predominantly consists of carbonate sand.

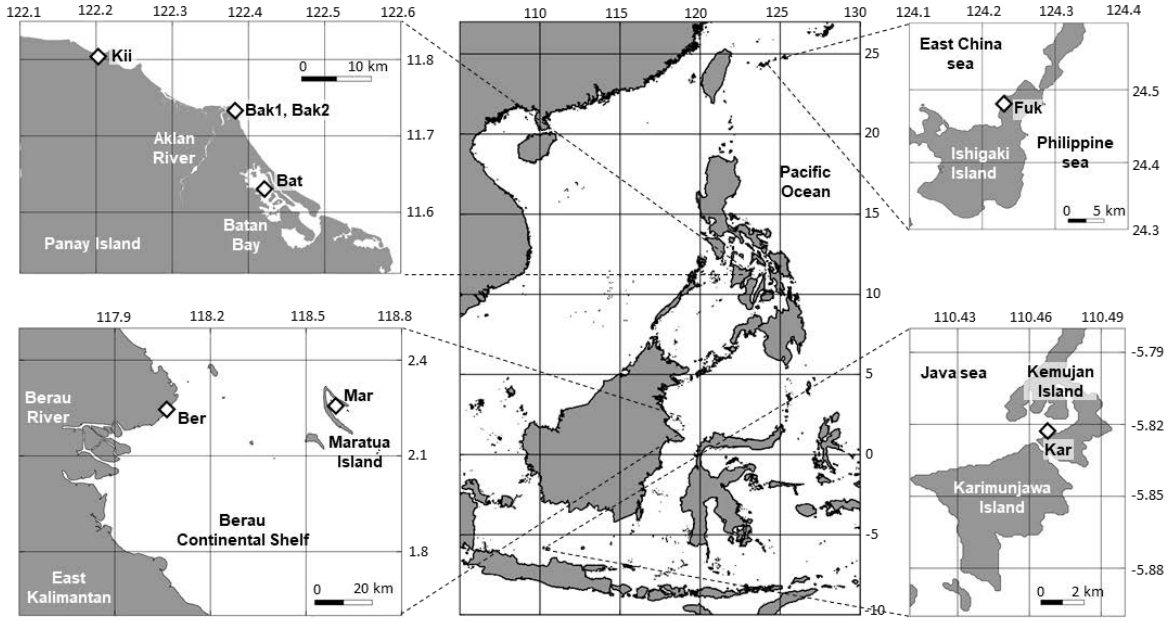

Figure 4.2. Diamond symbols indicate the locations of the study sites.

Table 4.1. Summary of study sites. Coordinates indicate the locations of environmental variable measurements. R. st = *Rhizophora stylosa*, R. a = *Rhizophora apiculata*, R. m =

Rhizophora mucronata, R. sp = *Rhizophora* species, S. a = *Sonneratia alba*. HR_k, L_k, θ_k, and Φ_k stand for height, horizontal distance, angle, and diameter of k-th root, respectively. See Fig. 4.3 for the graphical description. DBH and HT stand for diameter at breast height and tree height, respectively.

Site (Country)	Latitude (N) / Longitude (E)	Mangrove condition	Sediment type	Dominant species	Measured species	Measured parameters	Number of sampled trees (DBH range of sampled trees)
Fuk (Japan)	24.48626 N 124.22962 E	• riverine mangrove forest • natural stands	sandy clay	R. st	R. st	HR_k, L_k, θ_k, Φ_k, DBH	22 (0.023 - 0.143 m)
Bak1 (The Philippines)	11.71794 N 122.38919 E	• riverine mangrove forest • planted and young stands (~ 17 years) • formed on a tidal flat	clay	R. a	R. a	HR_k, L_k, θ_k, Φ_k, DBH, HT	13 (0.046 - 0.105 m)
Bak2 (The Philippines)	11.71802 N 122.39112 E	• riverine mangrove forest • planted and mature stands (~ 30 years) • formed on a tidal flat	clay	R. a	R. a	HR_k, DBH, HT	40 (0.019 - 0.185 m)
Bat (The Philippines)	11.63545 N 122.41884 E	• fringe mangrove forest • planted stands (~ 20 years)	sand	R. a, R. m	R. a, R. m[a]	HR_k, DBH, HT	25 (0.035 - 0.16 m)
Kii (The Philippines)	11.80697 N 122.19832 E	• fringe mangrove forest • planted stands	sandy clay	R. m	R. m	HR_k, DBH, HT	23 (0.030 - 0.065 m)
Mar (Indonesia)	2.25833 N 118.60209 E	• fringe mangrove forest • natural stands • formed on a reef flat	clay	R. m	R. m	HR_k, DBH, HT	6 (0.041 - 0.078 m)
Ber (Indonesia)	2.24181 N 118.06499 E	• fringe mangrove forest • natural stands • formed on a tidal flat	sandy clay	S. a	R. sp[b]	HR_k, DBH, HT	6 (0.022 - 0.041 m)
Kar (Indonesia)	-5.82319 N 110.46470 E	• dwarf mangrove forest • mix of natural and planted stands • formed on a reef flat	sand	R. a, R. m	R. a, R. m	HR_k, θ_k, DBH, HT	21 (0.016 – 0.043 m)

[a] The data covers both R. a and R. m, but species identification for all the measured trees was not conducted.
[b] The inhabiting *Rhizophora* species are R. a and R. m, but species identification for the measured trees was not conducted.

4.2.2 Field survey

4.2.2.1 Prop root projected area

The prop root projected area measurements were done in Fuk and Bak1 from August to November in 2018. In total, 22 and 13 trees were sampled from Fuk and Bak1, respectively. Those trees were sampled to ensure a wide range of tree sizes as much as possible. Following Ohira et al. (2013), we measured four prop root parameters: height (*HR*), horizontal distance (*L*), angle (θ), and diameter (Φ) (Fig. 4.3). Then, the length of each prop root was estimated by approximating it as a quadratic curve (See Ohira et al., 2013 for the formulations of the approximation). The projected area of each prop root was then estimated by multiplying the prop root length and the diameter. We measured these geometric parameters for all prop roots from one sampled tree to estimate the whole-tree prop root projected area, compared Ohira et al. (2013), which was limited to only first-order (primary) prop roots.

The prop root projected area of the submerged parts changes with the changes in the tidal level, therefore, the vertical profile of the whole-tree prop root projected area is necessary to calculate the drag force by prop root system. For this reason, the prop root system was partitioned into vertical layers of 0.1 m thickness (Fig. 4.3), and the total prop root projected area in each vertical layer (A_i, m^2, where i denotes the number of vertical layer) was calculated for each sampled tree. Note that the azimuth angle of prop roots to water flow direction was not considered, therefore, the total prop root projected area is the sum of the individual prop root projected area from the side view.

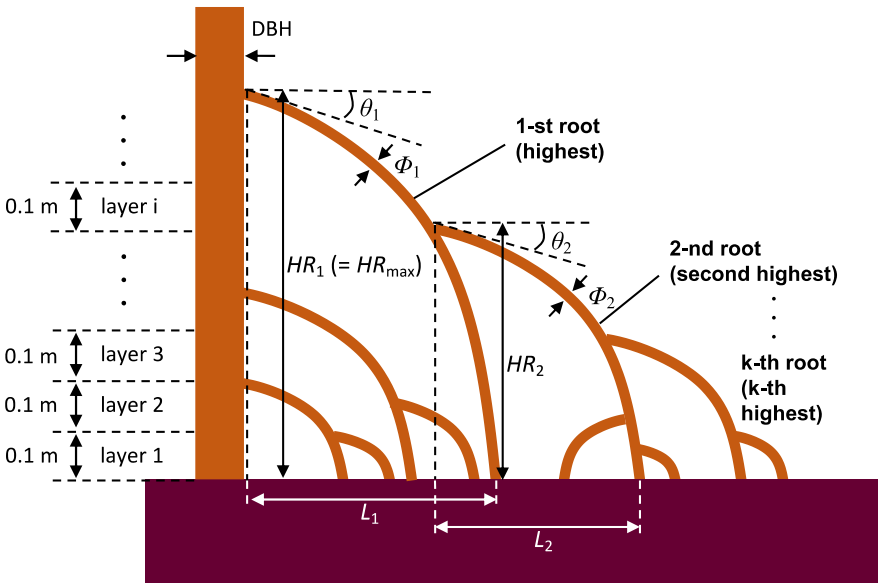

Figure 4.3. Vertical layering of the prop root system, numbering of individual prop roots, and geometric parameters of prop roots (HR_k: height, L_k: horizontal distance, θ_k: angle, Φ_k: diameter of k-th root), and stem (DBH: diameter at breast height) measurement. The figure shows the measured parameters for first and second roots only as an example. Note that not all parameters were measured at all study sites. See Table 4.1 for measured parameters at each site.

4.2.2.2 Number of prop roots in vertical layers

At Bak2, Bat, Kii, Mar, and Ber, instead of measuring the four prop root parameters, we only measured the height of prop roots (*HR*). At Kar, *HR* was measured along with the root diameter (Φ) (Table 4.1). The measurements were conducted from February to March in 2019. As with the measurement done in Fuk and Bak1, *HR* was measured for all prop roots from one sampled tree. When a prop root emerges upward, its maximum height was also measured along with the height at the point where the prop root emerges.

The number of sampled trees were 40 in Bak2, 25 in Bat, 23 in Kii, 6 in Mar, 6 in Ber, and 21 in Kar. As in Fuk and Bak1, the sampled trees were selected to have wide tree size range as much as possible. The number of prop roots in each vertical layer (N_i, where i denotes the number of vertical layer) was then obtained from the height data of prop roots by counting the number of prop roots at each vertical layer (e.g. add one to the layers N_1 - N_i if a prop root emerges at layer i downward), for each tree in all the study sites, including Fuk and Bak1. For the prop roots that emerge upward, the upward part was counted separately from the downward part for the number of prop roots in the layers where the upward part exists. Note that at sites Bat and Ber where *R. apiculata* and *R. mucronata* are coexisting, species identification for all the sampled tree was not conducted. A supplemental field survey was conducted at Bat in this regard in February 2020 with species identification, and the data obtained in this survey were used in the result section 4.3.4 to 4.3.6 to account for the effects of species variation on the prop root system. See Note S4.1 in the Supporting Information for the details in this field data collection.

4.2.2.3 Other tree parameters

The stem diameter at 130 cm height (DBH) was measured with a diameter tape for all trees sampled for prop root measurement to relate the morphology of the prop root system to the tree size. When prop roots in a tree exceed 130 cm height, the diameter above the highest prop root was measured. Tree height was also measured using a laser range finder (Leica DISTO D810) as supporting information.

4.2.2.4 Environmental variables

Soil salinity, sediment thickness, and surface sediment hardness were measured at each site as environmental variables that may affect prop root system morphology. Sediment porewater was extracted using a Rhizon sampler (Rhizosphere Research Products), and the extracted porewater's salinity was measured using a refractometer. Sediment thickness was measured with tools for a cone penetration test (KS-159, Kansaikiki Inc.). Surface sediment hardness was measured using a Yamanaka-type soil hardness tester (No. 351-B, Fujiwara Scientific Company, Japan). Soil hardness measured with this tool has a positive correlation with the penetration resistance measured by a cone penetrometer (Ebato 2020), which reflects the combined shear and compressive characteristics of the sediment.

4.2.3 Empirical model for prop root system

Based on the count of prop roots in each vertical layer of the prop root system obtained from field surveys, an empirical model was developed as a predictor of the vertical profile of the whole-tree prop root projected area. In the model, prop roots are numbered, in the order of root height, from highest to lowest in a whole-tree prop root system; the first root refers to the highest root, the second root refers to the second-highest, and k-th root refers to the k-th-highest root (Fig. 4.3). The model then assumes that the height ratio of the k-th root and (k + 1)-th root is constant in the whole-tree prop root system:

$$\frac{HR_{\mathrm{k+1}}}{HR_{\mathrm{k}}} = S \tag{4.2}$$

where HR_{k} and $HR_{\mathrm{k+1}}$ are the height of the k-th and (k + 1)-th root (m), and S is the scaling factor (-) ranging from 0 to 1. Note that the height ratio of k-th and (k + 1)-th root could be the ratio of roots coming from different branches. If the height of the first root (HR_1: hereafter denoted as HR_{max}), which is the maximum root height in a prop root system, is given, the height of the k-th root can be calculated as

$$HR_{\mathrm{k}} = HR_{\mathrm{max}} S^{(\mathrm{k}-1)}. \tag{4.3}$$

The minimum root height is determined by a critical height (HR_{min}, m). If the t-th root is the one with the minimum height in a prop root system, t is the largest integer number that satisfies

$$HR_{\mathrm{t}} = HR_{\mathrm{max}} S^{(\mathrm{t}-1)} \geq HR_{\mathrm{min}}. \tag{4.4}$$

In this way, heights of prop roots in a tree can be modeled from the parameters HR_{max}, S, and HR_{min}. The number of modeled prop roots in each vertical layer is then predicted by counting the number of modeled prop roots in each vertical layer. In this model, S is the parameter that controls the complexity of prop roots. Under the fixed values of HR_{max} and HR_{min}, the number

of prop roots in a tree increases as the value of *S* increases toward 1, which implies more 1-st order (primary) roots and/or more branching of prop roots (higher order roots).

The model was applied to all the sampled trees from all study sites, to see if the model could effectively predict the number of roots in the vertical layers for each tree. Among the three model parameters, HR_{max} and HR_{min} were measured in the field for all sampled trees. While HR_{max} varied widely depending on tree size (see the result section 4.3.4), no significant correlations between HR_{min} and tree size were obtained from all sites, and the variations in HR_{min} were small with a mean value of 0.062 ± 0.039 m (n = 156 trees). Therefore, the measured values for HR_{max}, and the median value of HR_{min}, which was 0.05 m, as a constant, were given to all sampled trees for the prediction using the model. We chose the median value (0.05 m) for HR_{min} because this value gave the highest accuracy for the comparison of the measured and modeled vertical distribution of the number of prop roots for all sampled trees (see Fig. 4.6 for the results). The values of *S* were determined for the individual tree by searching the optimum value (optimized *S*), with which the modeled number of prop roots in the vertical layer fits best with the field measured number of prop roots.

4.2.4 Regression analysis for scaling relations in the prop root system

To test if the prop root system can be expressed as a function of DBH, regression analyses, which employ the optimized *S* or the measured HR_{max} as dependent variables and DBH as an independent variable, were performed. We fitted the following power function for the optimized *S* for each species at each study site:

$$S = 1 - \alpha \mathrm{DBH}^{\alpha_1} \quad (4.5)$$

where α is a constant, and α_1 is the scaling exponent; the unit of DBH is meter. The value '1' in this equation represents the asymptotic maximum value of *S*. For HR_{max}, the following equation was fitted for each species at each study site following Ohira et al. (2013) and Mendez-Alonzo et al. (2015):

$$HR_{\max} = \beta_1 \mathrm{DBH} + \beta \quad (4.6)$$

where β_1 and β are the slope and intercept terms, respectively. Note that for site Bat, data from the field survey in February 2020 described in the Supporting Information was used to obtain the species-specific relationships of *R. apiculata* and *R. mucronata*, respectively. Also, note that for site Ber, where *R. apiculata* and *R. mucronata* are coexisting, the regression analyses were done without distinguishing species as species identification was not done for the measured trees at this site. Therefore, the results of the analyses for Ber represent the relationships which may implicitly include the effects of species variation.

4.2.5 Multivariate analysis for the scaling factor

We tested if the coefficients of the model for S (Eq. (4.5)) can be predicted from the measured environmental variables and species variation. After log-transformation, Eq. (4.5) can be written as

$$\log(1-S) = \alpha_0 + \alpha_1 \log(\mathrm{DBH}) \quad (4.7)$$

where α_1 and α_0 are slope and intercept term, respectively, and $\alpha_0 = \log(\alpha)$. Here and hereafter, log denotes common logarithm. Eq. (4.7) has two parameters – the slope α_1 and the intercept α_0; however, it was turned out that they have a linear relationship, which can be described as

$$\alpha_1 = \gamma_1 \alpha_0 + \gamma \quad (4.8)$$

where γ_1 and γ are the slope and intercept terms, respectively (see result section 4.3.6 and Fig. S4.3). Then, Eq. (4.7) can be expressed with a single parameter α_0:

$$\log(1-S) = \alpha_0 + f(\alpha_0) \log(\mathrm{DBH}) \quad (4.9)$$

where α_0 is a parameter that controls the site- and species-specific scaling relation in the prop root system. This equation indicates that once the value of α_0 is determined for a species in a site, S values of trees with various DBH can be predicted for the species in the site. Then, by substituting S values computed by Eq. (4.9) into Eqs. (4.3) and (4.4), the heights of prop roots in a tree, and the number of prop roots in each vertical layer can be predicted. The value of α_0 was determined for each species at each site by searching for the optimum value (optimized α_0), that minimizes the total error between the measured and modeled number of prop roots in the vertical layers for all sampled trees. Here, the measured values for HR_{max} and a constant value (0.05 m) for HR_{min} were used in Eqs. (4.3) and (4.4). As in section 4.2.4, data from the field survey in February 2020 described in the Supporting Information was used for site Bat to obtain the values of α_0 optimized for each coexisting species at the site. Also, the optimization of α_0 for site Ber was done without distinguishing species that may implicitly include the effects of species variation.

We considered that the parameter α_0 depends on environmental variables (soil salinity, sediment hardness, and sediment thickness) and species variation. The following models for α_0 were tested:

$$\alpha_0 = a_{sal} sal + a_{spe} spe + b \quad (4.10)$$

$$\alpha_0 = a_{har} har + a_{spe} spe + b \quad (4.11)$$

$$\alpha_0 = a_{th1}\left(1 - e^{(-a_{th2} th)}\right) + a_{spe} spe + b \quad (4.12)$$

$$\alpha_0 = a_{sal} sal + a_{har} har + a_{spe} spe + b \quad (4.13)$$

$$\alpha_0 = a_{sal} sal + a_{th1}\left(1 - e^{(-a_{th2} th)}\right) + a_{spe} spe + b \quad (4.14)$$

$$\alpha_0 = a_{har} har + a_{th1}\left(1 - e^{(-a_{th2} th)}\right) + a_{spe} spe + b \quad (4.15)$$

$$\alpha_0 = a_{sal} sal + a_{har} har + a_{th1}\left(1 - e^{(-a_{th2} th)}\right) + a_{spe} spe + b \quad (4.16)$$

where a_{sal}, a_{har}, a_{th1}, a_{th2}, a_{spe}, and b are coefficients, and *sal*, *har*, *th*, *spe* are soil salinity (‰), sediment hardness (kg cm^{-2}), sediment thickness (m), and *Rhizophora* species index, respectively. The use of saturation-type exponential function for *th* is because the below-ground biomass of *Rhizophora* species tends to be concentrated in the first 40 cm of the sediment layer (Tamooh et al., 2008; Xiong et al., 2017), and the effects on the below-ground root development of the substrate with more than 40 cm thickness, were not expected. The parameter *spe* was treated as a categorial parameter, and the values of *spe* for *R. mucronata* and *R. apiculata* were set as 0.0 and 1.0, respectively. Among the measured species in this study, *R. mucronata* and *R. apiculata* are the only species with scaling relations compared among sites or within a site. We therefore limited the application of the models to the two species – *R. mucronata* and *R. apiculata* – and excluded the data for *R. stylosa* which was measured only at site Fuk, and the data from site Ber where the species identification for the measured trees was not done.

Differences between models were evaluated based on the predictability of the values of α_0 optimized for each species at each site (optimized α_0) using the coefficient of determination (R^2) and Akaike's information criterion (AIC), *i.e.* the lowest AIC indicates the best model in terms of model fit and number of parameters. We also compared the models with R^2 based on the modeled *S* for all sampled trees (except data for *R. stylosa* and data from site Ber) computed using Eq. (4.9) with the optimized *S* values, and the modeled numbers of prop roots in the vertical layers for all sampled trees (except data for *R. stylosa* and data from site Ber) computed using Eqs. (4.3), (4.4), and (4.9) with the data. Here again, the measured values for HR_{max} and a constant value (0.05 m) for HR_{min} were used in Eqs. (4.3) and (4.4).

4.3 Results

4.3.1 Contribution of first-order roots to whole-tree prop root projected area

The fraction of the projected area of first-order (primary) roots to the whole-tree prop root projected area was plotted against DBH for 22 and 13 trees measured in Fuk and Bak1, respectively (Fig. 4.4). The fraction decreased as DBH increased at both sites due to the increase in the branching of prop roots. For trees with DBH larger than 0.11 m in Fuk, the contribution of first-order roots to the whole-tree prop root projected area was only 20 %.

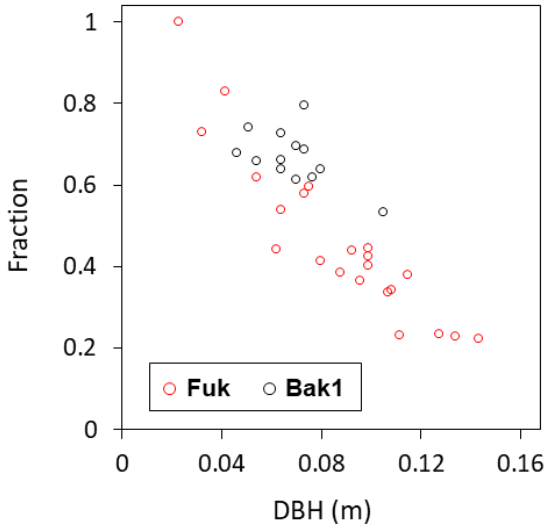

Figure 4.4. A comparison of DBH and a fraction of the projected area of first-order (primary) prop roots to the whole-tree prop root projected area. Data are from 22 and 13 trees in sites Fuk and Bak1, respectively.

4.3.2 Comparison between the number of prop roots and projected area

The number of prop roots in vertical layers was significantly correlated with the prop root projected area in the vertical layers for all sampled trees in Fuk and Bak1 (Fig. 4.5). The relationship at both sites can be expressed with a common linear equation with intercept fixed at zero:

$$A_{\mathrm{i}} = 0.0043 N_{\mathrm{i}} \quad (4.17)$$

with R^2 = 0.9632, where A_{i} and N_{i} are the prop root projected area (m^2) and the number of prop roots in vertical layer i, respectively. This suggests that the vertical profile of prop root projected area can be estimated accurately from the vertical distribution of the number of prop roots.

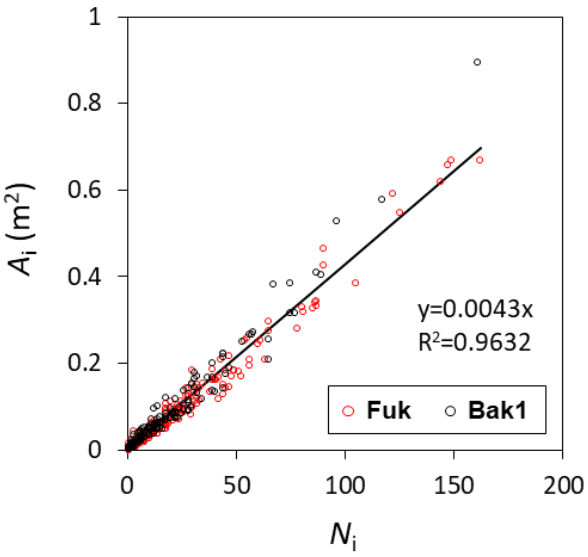

Figure 4.5. A comparison of the number of prop roots and projected area in vertical layers; "i" indicates the layer number shown in Fig. 4.3. All vertical layers with prop roots for all sampled trees in Fuk and Bak1 are used in the plot.

4.3.3 Comparison between the measured and modeled number of prop roots

It was generally observed that the number of prop roots increases from the top of the prop root system to the ground in the form of a power function (Fig. S4.2). With the measured values for HR_{max}, a constant value for HR_{min}, and the S values optimized for the individual trees, the model reproduced the vertical distribution of prop roots well. Comparison of measured and modeled vertical distribution of the number of prop roots for some selected trees is provided in Fig. S4.2 of the Supporting Information as an example of the model performance. When the measured and modeled number of prop roots in all vertical layers where prop roots exist for all sampled trees were compared, it showed a high correlation with R^2 = 0.9489 (Fig. 4.6). The highest observed number of prop roots in a vertical layer was 309 (Fig. 4.6), which was the data for the bottom layer (layer 1 in Fig. 4.3) of a *R. mucronata* tree with DBH = 0.16 m in site Bat.

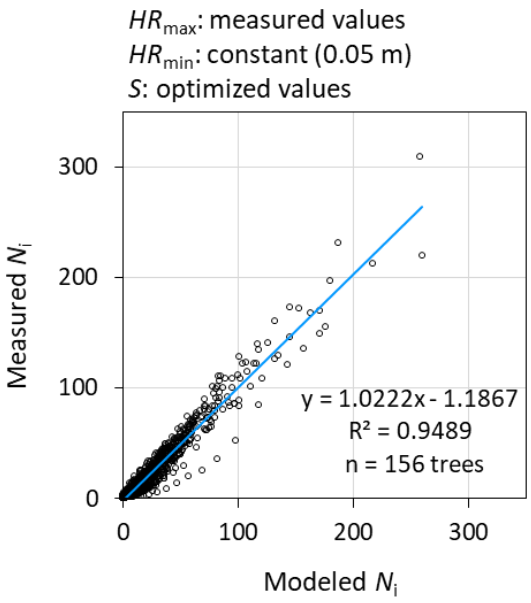

Figure 4.6. A comparison of the measured and modeled number of prop roots in vertical layers; "i" indicates the layer numbers shown in Fig. 4.3. All vertical layers with prop roots for all sampled trees (n = 156) were used in the plot. To predict N_i, measured values of HR_{max}, a constant value of 0.05 m for HR_{min}, and optimized values for S were used for individual trees.

4.3.4 Scaling relations in the prop root system

Values of *S*, optimized for the individual trees, were compared with DBH for each species at each study site (Fig. 4.7). Note that the values of the logarithms of (1 - *S*) and DBH were plotted in Fig. 4.7. The regression model for *S* for each species at each site fitted to Eq. (4.5) is also shown in Fig. 4.7. In general, *S* increases as DBH increases, indicating that trees with larger DBH tend to produce more prop roots than trees with smaller DBH. The significant correlations between the logarithms of (1 - *S*) and DBH were found for all species at all sites. At Kar, the values of the log-transformed (1 - *S*) showed more significant relationships with the log-transformed tree height than with DBH, with R^2 = 0.915 and 0.776 for *R. mucronata* and *R. apiculata*, respectively. The relationships for *R. mucronata* and *R. apiculata* are expressed as follows, respectively:

$$\log(1-S) = -2.67\log(TH) - 0.69 \quad (4.18)$$

$$\log(1-S) = -1.78\log(TH) - 1.09 \quad (4.19)$$

where *TH* is the tree height (m). This may indicate that tree height is a better indicator for the scaling relations in prop root system for dwarf mangroves where the size variations in DBH are quite small (Table 4.1). When the relationships for *R. mucronata* and *R. apiculata* coexisting in a site were compared, the values of (1 - *S*) of *R. apiculata* tend to be slightly

lower than *R. mucronata* as observed in Bat and Kar (Fig. 4.7). However, the site differences in the scaling relations for a species are more significant than the interspecific differences in a site. For example, based on the regression model for log-transformed (1 - *S*) and DBH for *R. apiculata* (Fig. 4.7), the value of *S* for a tree with DBH of 0.1 m in Bak2 is 0.919 while the values of *S* for trees with the same DBH in Bak1 and Bat are 0.972 and 0.970, respectively, and *S* values for trees in Kar with the same DBH could be more than 0.99.

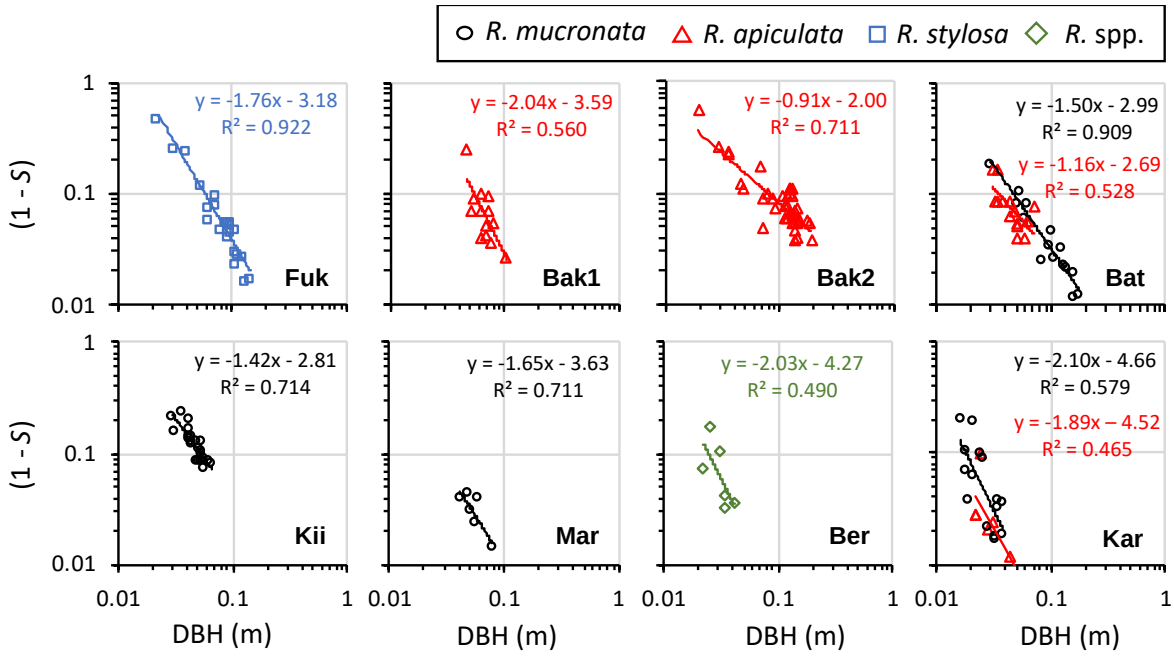

Figure 4.7. The scaling relations of optimized *S* and DBH for each species at each study site. The equations in the plots are for the relationships between log-transformed (1 - *S*) and DBH fitted to Eq. (4.5). The data for Ber is from a mixed forest of *R. mucronata* and *R. apiculata* stands, but species identification for the measured trees was not conducted. The data for Bat is from the field survey in February 2020 described in the Supporting Information for obtaining species-specific relationships at the site.

Another parameter of the empirical model for the prop root system, HR_{max}, is correlated linearly with DBH for each species at each site (Fig. 4.8), which is consistent with the findings by Ohira et al. (2013) and Mendez-Alonzo et al. (2015). However, the range of R^2 values for the correlations for each species at each study site is from 0.008 in Mar to 0.772 in Bak1, which indicates relatively weak correlations compared with the relationships between *S* and DBH. Similar to the case of *S*, the relationships between HR_{max} and DBH vary significantly, depending on the sites.

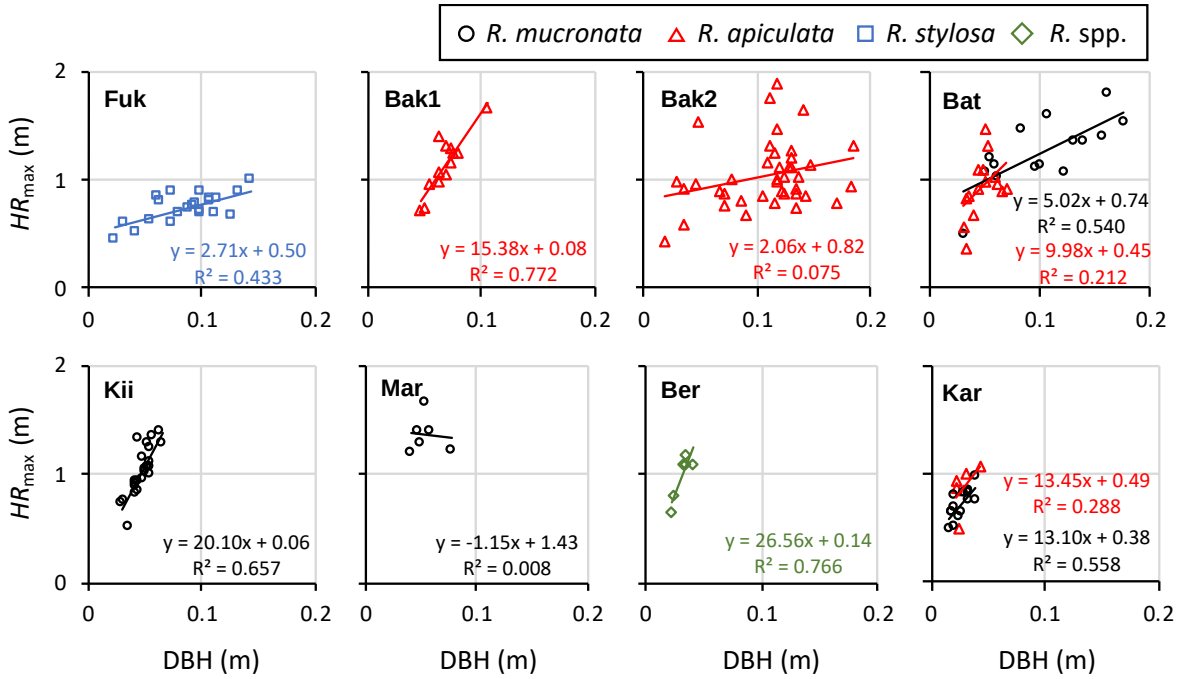

Figure 4.8. The scaling relations of HR_{max} and DBH for each species at each study site. The equations in the plots are for the relationships between HR_{max} and DBH fitted to Eq. (4.6). As in Fig. 4.7, the data for Ber is from a mixed forest of *R. mucronata* and *R. apiculata* stands. The data for Bat is from the field survey in February 2020 described in the Supporting Information for obtaining species-specific relationships at the site.

4.3.5 Site- and species-specific model of prop root system

The model for prop root system (Eqs. (4.3) and (4.4)) was applied to all sampled trees again by employing the site- and species-specific regression models for S (Eq. (4.5)) and HR_{max} (Eq. (4.6)). Two different parameter settings were tested: 1) a case using the measured values for HR_{max}, a constant value for HR_{min}, and the site- and species-specific regression models for S, and 2) a case using the site- and species-specific regression models for HR_{max} and S with a constant value for HR_{min}. When the modeled number of prop roots in the vertical layers were compared with the measured values for all sampled trees as in Fig. 4.6, both cases showed high correlations (Fig. 4.9) although the values of R^2 were lower than that in Fig. 4.6, which used the measured and optimized values for HR_{max} and S, respectively. By comparing the two cases in Fig. 4.9, the case that used the site- and species-specific regression models for HR_{max} (case 2) showed lower value of R^2 than in the case which employed the measured values for HR_{max} (case 1), but the difference was not significant, suggesting that S is the most critical parameter for reproducing the prop root system.

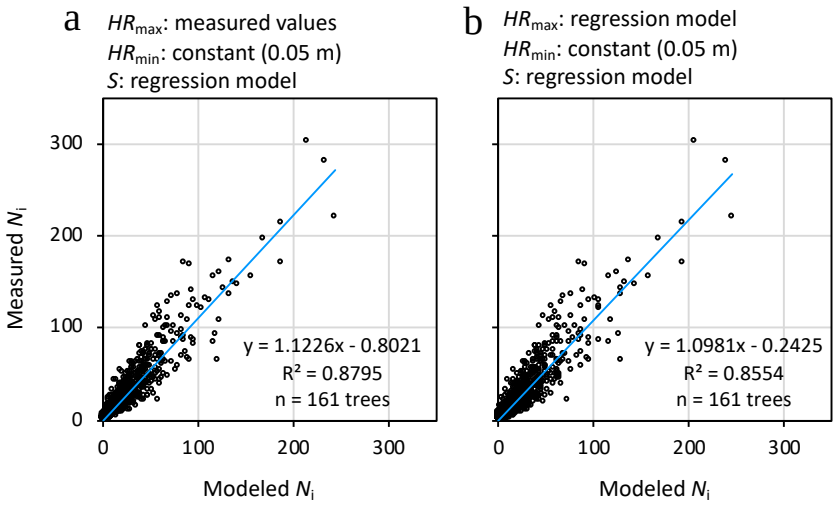

Figure 4.9. Similar to Fig. 4.6, but with a different parameter setting – the case that used (a) measured values for HR_{max}, a constant value for HR_{min}, and regression models for S, and (b) the case that used regression models for HR_{max} and S, and a constant value for HR_{min}. Note that for the trees in site Bat, the data from the field survey in February 2020 described in the Supporting Information is used, which is consistent with the data plotted in Figs. 4.7 and 4.8. This is the reason why the total number of the sampled trees is different from the one in Fig. 4.6. Also, because only the total number of prop roots, which corresponds to the number of prop root in layer 1 (see Fig. 4.3), was measured in the field survey in February 2020, the modeled number of prop roots in layer 1 was plotted with the data for site Bat.

4.3.6 Relationship between the scaling relation and environmental variables

Environmental variables measured at each study site can be seen in Fig. 4.10 and Table S4.1. Soil salinity ranged from 26 ‰ in Bak2 to 40 ‰ in Kii. The sediment thickness at Mar and Kar is around 0.1 m while other sites have sediment layer of more than 0.8 m thickness. Bak2 and Bat have the deepest sediment layer among the study sites except for Ber. Sediment thickness was not measured in Ber since the sediment layer is deeper than 5 m of the length of the tool used. Surface sediment hardness ranged from 0.4 kg cm^{-2} in Bak2 to 35.8 kg cm^{-2} in Ber. In general, sediment hardness was low (0.4 – 6.3 kg cm^{-2}) where the substrate is clay (Bak1, Bak2, and Mar), and was high (14.7 – 35.8 kg cm^{-2}) where the substrate is sandy clay (Fuk, Kii, and Ber) or sand (Bat and Kar).

Based on the site- and species-specific regression models for the relationship between log-transformed (1 – S) and DBH shown in Fig. 4.7, a significant relationship between the coefficients α_0 and α_1 in Eq. (4.7) was found (Fig. S4.3). Eq. (4.8), an equation for the

relationship between α_0 and α_1, can then be expressed using the following equation with R^2 = 0.8168:

$$\alpha_1 = 0.4192\alpha_0 - 0.2067. \quad (4.20)$$

The values of α_0 optimized for each species at each study site are shown in Fig. 4.10, where smaller value of α_0 produces larger value of *S* at a given DBH. With the optimized α_0, the *S* values computed using Eqs. (4.7) and (4.20) for all sampled trees showed a strong relationship with the optimized *S* values shown in Fig. 4.7 with R^2 = 0.790 (Table 4.2). The vertical distributions of the number of prop roots for all sampled trees were reasonably reproduced with R^2 = 0.873 (Table 4.2). These results suggest that the optimized α_0 well represents the site- and species-specific characteristics of the scaling relation in the prop root system.

It was observed that the optimized α_0 values of *R. mucronata* and *R. apiculata* significantly vary among sites even if the species is the same (Fig. 4.10a). On the other hand, *R. mucronata* and *R. apiculata* in the same environment showed similar values of α_0 as seen in Bat and Kar, with slightly lower α_0 values of *R. apiculata* than those of *R. mucronata* (Fig. 4.10a). When the optimized α_0 values were compared with the environmental variables using the Eqs. (4.10) – (4.12) that include the term for species variations, no significant correlations were found in the relationships of α_0 with soil salinity and sediment hardness (Fig. 4.10b and c). However, a strong relationship was found between α_0 and sediment thickness in the form of a saturation-type exponential function (Eq. (4.12)) with R^2 = 0.784 (p = 0.003; Fig. 4.10d).

The results of the multivariate analysis for the scaling factor are summarized in Table 4.2. Among the tested models (Eqs. (4.10) – (4.16)), the model with sediment thickness and hardness as the environmental variables (Eq. (4.15)) was the best parsimonious model for the optimized α_0 based on AIC values, and showed the highest accuracy both for the optimized *S* values and the number of prop roots in vertical layers (Table 4.2).

The slopes and intercepts of the site- and species-species regression models for the relationships between HR_{max} and DBH shown in Fig. 4.8 were compared with the environmental variables, but no significant relationship was found both for the slope (R^2 < 0.35, p > 0.12; plots not shown) and intercept (R^2 < 0.08, p > 0.49; plots not shown).

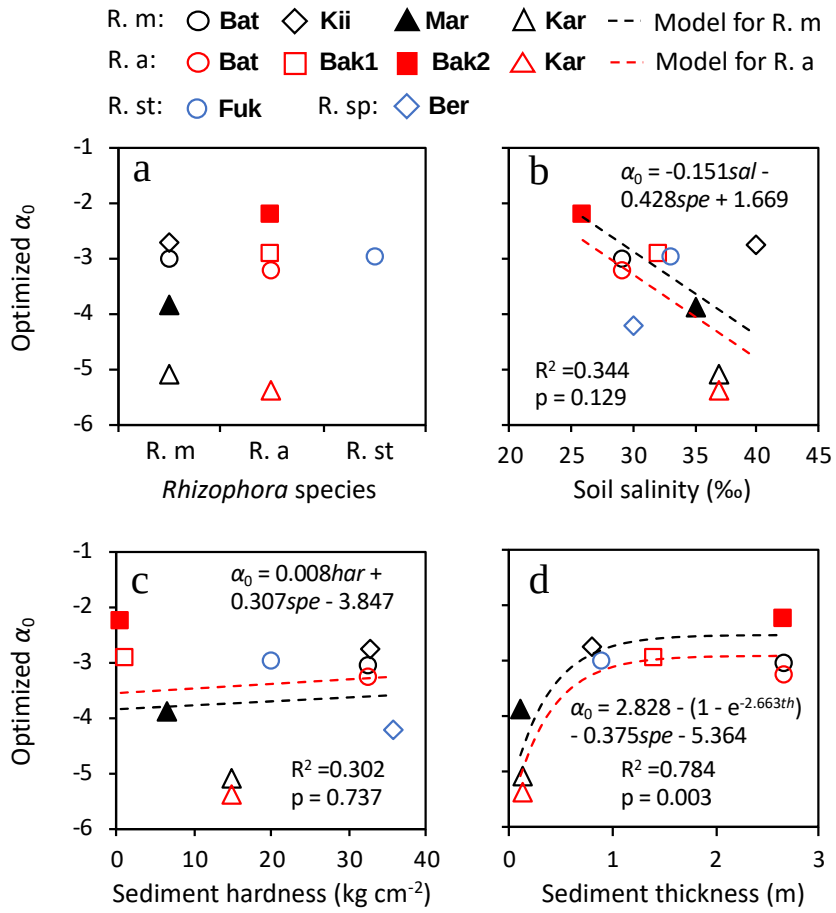

Figure 4.10. (a) Interspecific comparison of α_0 optimized for each species at each site (optimized α_0), and the relationships of optimized α_0 with (b) soil salinity, (c) sediment hardness, and (d) sediment thickness. The equations show the best fit of Eqs. (4.10) – (4.12), and the R^2 and p values are from the comparisons between the modeled and optimized α_0. The parameter *spe* was treated as a categorial parameter, and the values of *spe* for *R. mucronata* and *R. apiculata* were set as 0.0 and 1.0, respectively. See Table 4.2 for the results of other models (Eqs. (4.13) – (4.16)). Note that the data from Fuk and Ber were not included in the models (see section 4.2.5 for the reason). The value of Ber is not shown in optimized α_0-sediment thickness relationship since sediment thickness was not recorded at this site. R. m = *Rhizophora mucronata*, R. a = *Rhizophora apiculata*, R. st = *Rhizophora stylosa*, R. sp = *Rhizophora* species.

Table 4.2. Summary of multivariate models for scaling factor (*S*) with the coefficients. The values in parenthesis mean the standard error of the coefficient. Akaike's information criterion (AIC) and coefficient of determination (R^2) for α_0 optimized for each species at each study site (n = 8, excluding the data from Fuk and Ber), R^2 for *S* optimized for each individual tree (n = 133 trees, excluding trees sampled in Fuk and Ber) and number of prop roots in all vertical layers with prop roots for all sampled trees except the ones sampled in Fuk and Ber (n = 133

trees) are shown (see section 4.2.5 for the reason of exclusion of Fuk and Ber from the models). NA: not applicable.

Model	Coefficients								Optimized α_0		Optimized S	Number of prop roots in vertical layers
	α_0	α_1	a_{sal}	a_{har}	a_{th1}	a_{th2}	a_{spe}	b	AIC	R^2	R^2	R^2
Model with optimized α_0												
Eq. (4.9)	[1]	[2]	NA	NA	NA	NA	NA	NA			0.790	0.873
Model with environmental effects												
Eq. (4.10)	[3]	[2]	-0.151 (0.095)	NA	NA	NA	-0.43 (0.87)	1.67 (3.41)	23.3	0.344	0.332	0.245
Eq. (4.11)	[3]	[2]	NA	0.0079 (0.0385)	NA	NA	0.31 (1.01)	-3.85 (1.06)	26.5	0.002	0.138	0.245
Eq. (4.12)	[3]	[2]	NA	NA	2.83 (1.09)	2.66 (3.56)	-0.38 (0.55)	-5.36 (1.26)	15.4	0.784	0.586	0.443
Eq. (4.13)	[3]	[2]	-0.151 (0.106)	0.0068 (0.0350)	NA	NA	-0.36 (1.03)	1.51 (3.88)	24.2	0.349	0.312	0.262
Eq. (4.14)	[3]	[2]	-0.039 (0.245)	NA	2.83 (6.18)	3.78 (28.11)	3.78 (28.11)	-4.16 (3.39)	16.0	0.794	0.591	0.475
Eq. (4.15)	[3]	[2]	NA	-0.030 (0.019)	3.47 (1.49)	3.22 (3.93)	-0.73 (0.52)	-5.21 (1.57)	11.6	0.882	0.747	0.640
Eq. (4.16)	[3]	[2]	-0.011 (0.242)	-0.030 (0.025)	3.52 (5.34)	3.66 (20.37)	-0.74 (0.64)	-4.94 (3.42)	12.5	0.882	0.745	0.639

[1] Value of α_0 optimized for each species at each study site was used. The values can be seen in Fig. 4.10.

[2] Computed from Eq. (4.20).

[3] Computed from the equation shown in the 'Model' column.

4.4 Discussion

4.4.1 Model reproducibility of the complex structures of prop root system

While there have been several studies that investigated *Rhizophora* prop root morphology (Mazda et al., 1997; Ohira et al., 2013; Horstman et al., 2014, 2015; Mendez-Alonzo et al., 2015), this is the first study to investigate the morphological structures of whole-tree prop root system with multiple orders of prop roots (up to sixth-order). The first-order roots are dominant in the whole-tree prop root projected area of small trees, with DBHs less than 0.05m in Fuk and Bak1 (Fig. 4.4). However, the contribution rate of the first-order roots to the

whole-tree prop root projected area decreased significantly down to around 20 % in Fuk as DBH increases, due to the emergence of a significant number of branching of prop roots. This clearly indicates the significance of the second, third, and even higher-order roots for the whole-tree prop root projected area, especially for medium to large size trees with DBH > 0.05 m. The number of prop roots increases in the form of a power-function toward the ground (Fig. S4.2) suggesting that the prop root system is more complex in the lower portion. Therefore, when the water level fluctuation in mangrove areas is considered, the significance of the prop roots above the first-order for the submerged prop root projected area per unit volume is further enhanced by the decreasing water level. The prop root morphology model developed by Ohira et al. (2013) that accounts for only first-order roots may have largely underestimated the projected area of submerged prop roots in this regard. It may have further led to underestimation of the drag force exerted by whole *Rhizophora* trees studied by Maza et al. (2017, 2019), who used their model. Prop roots above the first-order should be considered for future studies on mangrove drag effects.

Based on the measurement of the prop root projected area in Fuk and Bak1, the significant relationships between the number of prop roots and projected area in vertical layers were found (Fig. 4.5), which validates the hypothesis that the vertical distribution of the number of prop roots is a good predictor of the vertical profile of prop root projected area, thus reducing measurement efforts. The equation for the relationship (Eq. (4.5)) indicates that the averaged projected area of one prop root in vertical layers can be considered uniform with an area of 0.0043 m^2. Given the average root diameter, Φ, is 0.030 ± 0.009 m, the average length of prop roots in a layer is 0.143 m, which corresponds to -44.3 degree of root angle in the layer.

The prop root system model (Eqs. (4.3) and (4.4)) that uses a parameter – scaling factor (S) successfully reproduced the vertical distribution of the number of prop roots (Fig. 4.6 and Fig. S4.2). This suggests that the approximation of the prop root system with S is appropriate. S can be considered as an indicator of the complexity of the prop root system. As expected, the value of S increased as the DBH increased (Fig. 4.7), indicating that a larger tree tends to have a more complex prop root system. The values of S optimized for individual trees are significantly correlated with DBH for each species at each site. This suggests that the scaling relations between DBH and first-order (primary) roots shown in Ohira et al. (2013) can be extended to the whole-tree prop root system, including prop roots above the first-order. Compared with the relationships between DBH and S, the correlations between DBH and HR_{max} tend to be lower and highly variable (Fig. 4.8), but comparable to the correlations shown by Ohira et al. (2013) and Mendez-Alonzo et al. (2015). The use of the site- and species-specific regression models for HR_{max} instead of the measured values in the prop root system model did not largely affect the results of the prop root vertical distribution (Fig. 4.9), and the

modeled distribution of prop roots by the model using the site- and species-specific regression models for S and HR_{max} agreed with the observed distribution in acceptable accuracy (R^2 = 0.855, Fig. 4.9b). Therefore, we propose the model to use the site- and species-specific regression models for S and HR_{max}, and a constant value for HR_{min}, for predicting the prop root system for the purpose of minimizing the number of parameters.

The proposed model predicts that the number of whole-tree prop roots is expressed as a form of power function of DBH, which agrees well with the observation (Fig. S4.4). From the modeled vertical distribution of the number of prop roots, and the relationship between the number of prop roots and projected area (Fig. 4.5; Eq. (4.17)), the whole-tree prop root projected area can also be expressed as a form of power function of DBH, which agrees with the observation (Fig. S4.5). These results suggest allometric relations in the complexity of prop root system, which is consistent with the allometric relations in the prop root biomass shown by Ong et al. (2014), Comley and McGuiness (2005), and Van Vinh et al. (2019).

4.4.2 The effects of substrate conditions on prop root system complexity

In this study, strong scaling relations in the prop root system complexity (represented by S) were found for each species at each site, but these significantly vary among sites (Fig. 4.7). Although site-specific scaling relations are common in mangrove above-ground biomass (Smith and Whelan, 2006; Estrada et al., 2014; Osland et al., 2014; Van Vinh et al., 2019), the site variations in prop root system complexity seem much larger. For example, in Kar, which has the highest S value among the study sites, more than 100 prop roots were observed in *R. apiculata* trees with DBH = 0.03 m, while only 9 - 10 prop roots were observed in trees of the same species with the same DBH in Bak2 (Fig. S4.4). While the optimized S values of *R. apiculata* tend to be slightly higher than *R. mucronata* in the same site as seen in Bat and Kar (Fig. 4.7), the differences in the scaling relations among sites could be much significant for each species (Fig. S4.6 and b). This suggests that species dependency may be less important for the scaling relations in S than the environmental variables for the two species.

The site and species-specific relations for S were well expressed by Eq. (4.9) with a single parameter α_0 – intercept term of the regression models for S, that were optimized for each species at each study site (Table 4.2). This result suggests that the value of α_0 represents the site- and species-specific scaling relations in S. While the optimized α_0 did not show significant correlations with soil salinity and sediment hardness, it did with sediment thickness in the form of saturation-type exponential function (Fig. 4.10). This suggests that the site- and species-specific scaling relations in S were mostly explained by sediment thickness, such that

mangroves inhabiting thin sediment layers tend to have more complex prop root system. Generally, the below-ground root biomass of mangroves is concentrated at depths of 0 - 40 cm, then decreases with soil depth (Komiyama et al., 2000; Tamooh et al., 2008; Castaneda-Moya et al., 2011; Xiong et al., 2017; Ha et al., 2018); *Rhizophora* species also have similar patterns (Tamooh et al., 2008; Xiong et al., 2017). Therefore, shallow sediment layers in Mar and Kar, where the thickness is around 0.1 m, may act as a physical constraint for below-ground root development, which, in turn, may regulate resource uptake from below-ground. It is well known that mangroves have plasticity in biomass allocation above- and below-ground depending on the environments (Sherman et al., 2003; Lovelock, 2008; Naidoo, 2009; Voivides et al., 2014). Under limited nutrient conditions, mangroves invest more biomass below-ground to compensate for the limited resources below-ground (Castaneda-Moya et al., 2011, 2013; Cormier et al., 2015). Such strategies may also be reflected in prop root system complexity by increasing the number of prop roots anchoring the ground to increase the fine root biomass in the limited space underground (Wilkens et al., 2018).

The physical constraints of the sediment layer on root development may be less important in other study sites where the sediment thickness is more than 0.4 m. However, Bak2 showed significantly lower S values for grown trees and higher α_0 value than the other sites (Figs. 4.7 and 4.10). Bak2 has the lowest soil salinity (26 ‰), implying the influence of groundwater in sediment that often has high nutrient concentrations. Therefore, grown trees with a large below-ground biomass and a deep root penetration depth may be able to uptake groundwater at this site. Hayes et al. (2019) showed that the mangroves' accessibility to groundwater enhances above-ground growth but does not enhance below-ground growth, which may also decrease S relative to DBH. Quantification of below-ground root biomass, root penetration depth, amount of resources belowground, such as water and nutrients, and mangrove groundwater use is required for further investigation of the mechanisms generating the site variations in the scaling relations in the prop root system.

While inclusion of soil salinity as a parameter in the model with sediment thickness for α_0 (Eq. (4.14)) did not affect the accuracies for the optimized α_0 and the number of prop roots in the vertical layers, inclusion of sediment hardness (Eq. (4.15)) significantly improved the accuracies (Table 4.2). AIC values for optimized α_0, and R^2 values both for optimized S and number of prop roots in vertical layers suggest that this model (Eq. (4.15)) is the best parsimonious model (Table 4.2). The coefficients of sediment hardness – α_{har} was negative in the model (Table 4.2). This indicates that trees on hard substrate tend to have somewhat lower α_0 values, which leads to more complex prop root system, contrary to our expectation. However, in terms of stability of the above-ground part of tree, dynamic loads from hydrodynamic force by tidal flow or waves may also be a factor in addition to the stability of

the substrate, because mangroves inhabit intertidal zones where trees and sediments are under the influences of tidal flow and waves (Mazda et al., 1997, 2005; Horstman et al., 2015; Chen et al., 2016). For example, the substrates with low sediment hardness indicating unstable substrate conditions are usually muddy (clay; Table 4.1) where the hydrodynamic loads from tidal flow and waves are expected to be small. Conversely, the substrates with high sediment hardness indicating stable substrate conditions are usually sandy (sandy clay or sand; Table 4.1) where the hydrodynamic loads may be larger. The effects of dynamic loads from the tidal flow and waves should be therefore taken into account in addition to the stability of substrate in future studies on the morphological plasticity in the prop root system.

Ber, a forest where *R. mucronata* and *R. apiculata* are coexisting, is an exceptional site in the relationship between optimized α_0 and sediment thickness, where the sediment thickness is more than 5 m (Renema, 2006), but α_0 at this site is the second lowest among the study sites after Kar (Fig. 4.10b and c). This may be related to interspecific competition. *S. alba* trees dominate Ber's forest, and *Rhizophora* trees are located where the ground is intensively covered by pneumatophores (Fig. S4.1e), which implies competition for below-ground resources, such as water and nutrients (Pranchai et al., 2018). The occupancy of the ground with a high density of pneumatophores may also interfere with the root development of *Rhizophora* trees below-ground, which may further lead to limited resource uptake. These factors may have caused *Rhizophora* trees to produce more prop roots anchoring the ground and increase the below-ground root biomass above the *Sonneratia* trees' root system horizontally radiating below-ground.

Another model parameter, maximum root height (HR_{max}), showed significant relationships with DBH for each species at most of the study sites (Fig. 4.8), similar to *S*. While the two coexisting *Rhizophora* species – *R. apiculata* and *R. mucronata* at a site show similar scaling relations in HR_{max} as seen in Bat and Kar (Fig. 4.8), the differences in the scaling relations among sites were not clear unlike the case of *S*, when the data from the different sites were plotted together for both species (Fig. S4.6c and d). This suggests that the site variations in the regression models of DBH-HR_{max} relationship may be attributed to allometric trajectory, where the comparison of scaling relations between the forests with different age/tree sizes is the reason of the site variations (Weiner, 2004). The slopes and intercepts of the regression models for the relationships between HR_{max} and DBH shown in Fig. 4.8 did not show any significant correlation with the measured environmental variables ($R^2 < 0.35$, $p > 0.12$ for slope and $R^2 < 0.08$, $p > 0.49$ for intercept). Thus, it is still not clear whether environmental variables could affect the relationships between HR_{max} and DBH. However, Rollon et al. (2017) found changes in HR_{max} following subsidence-induced sea-level rise, which may be related to aeration. Maximum tidal height and the inundation period may need

to be investigated considering the aeration function of prop roots in future studies for explaining the site variations.

4.4.3 Application of the prop root system model

The empirical model for prop root system proposed in this study has the potential to provide information on the vertical profile of prop root projected area, which is needed to estimate the drag force in mangroves. The novelty in the model is its ability to predict the vertical distribution of prop root system, including the prop roots above the first-order, which is not possible with the model by Ohira et al. (2013). As the complexity of the prop root increases in the form of a power-function of DBH (Fig. S4.4 and S4.5), the model is particularly useful for estimating the prop root structure of big trees, which are very laborious to measure in the field. Using the relationships between DBH and tree height (Suwa et al., 2009; Mendez-Alonzo et al., 2015), the spatial distribution of prop root morphological structures may be mapped from high-resolution remotely-sensed data, such as airborne LiDAR (Fatoyinbo et al., 2018) and unmanned aerial systems (Zhu et al., 2019). This may realize spatially explicit drag modeling in mangroves, although it is still limited to *Rhizophora* species.

The data showed that the scaling relations for S – the most critical model parameter – significantly vary depending on environments (Fig. 4.7; Fig. 4.10). Although the multivariate model that includes parameters or terms on the effects of environmental variables and species variation may have the potential to predict the scaling relations in various sites, there are still several limitations as follows. In this study, only *R. mucronata* and *R. apiculata* were tested, thus the application of the multivariate model may be limited to these two species only. Although the data suggested that the effect of species variation is less important compared to the effect of environmental variables for these species, the data from only two sites with the two coexisting species (Bat and Kar) were tested for the effect of species variation. The model also seems to work less well for mixed forests of *Rhizophora* species and other mangrove species as suggested by the data from Ber. Most of the sampled trees were less than 10 cm DBH, and there is no data for trees with DBH more than 20 cm, whereas *Rhizophora* species could attain more than 20 cm DBH, hence the validity of the model to larger trees is uncertain. Also, the accuracy of the multivariate model for predicting the number of prop roots in the vertical layers is not sufficiently high (R^2 = 0.640; Table 4.2) compared to the model with α_0 optimized for each species at each site (R^2 = 0.873; Table 4.2), suggesting the difficulty in accurately deriving the site- and species-specific scaling relations from the environmental variables measured in this study. Furthermore, factors controlling the scaling relations in HR_{max} are still unclear. Therefore, applying the prop root system model to other sites or species still

needs knowledge of scaling relations specific to the sites and the species, which requires fieldwork. While the relationships between DBH and HR_{max} are relatively easy to obtain in the field, the optimum *S* values for individual trees were derived after the numbers of prop roots in vertical layers were obtained in the field, as described in the section 4.2.3, which are relatively laborious works. A simple method for effectively estimating the *S* values for individual trees in the field may help with fast development of the site- and species-specific scaling relations. In this regard, we suggest measuring the maximum root height (HR_{max}) and the total number of prop roots for individual trees in the field, and derive the *S* values from the following equation, which is a rearrangement of Eq. (4.4):

$$\log S = \frac{\log HR_{\min} - \log HR_{\max}}{t-1} \quad (4.21)$$

where t is the total number of whole-tree prop roots. This equation gives *S* with very close values to the optimized values of *S* for individual trees (Fig. 4.11a), and the prop root model that used measured values for HR_{max}, a constant value for HR_{min}, and *S* values derived from Eq. (4.21) produced the vertical distribution of the number of roots with good accuracy (Fig. 4.11b). The proposed method should reduce the amount of fieldwork required to obtain the site- and species-specific scaling relations and contribute to the knowledge collection of the scaling relations of various species at various sites with environmental gradients, which is a key component to establishing a universal model for predicting the prop root system.

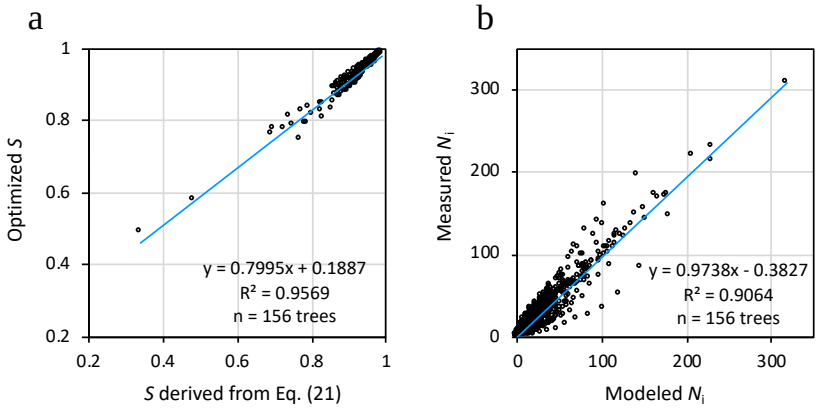

Figure 4.11. (a) A comparison of *S* optimized for individual trees and *S* derived from Eq. (4.21), and (b) a comparison similar to Fig. 4.6, but with different parameter settings. Measured values for HR_{max}, a constant value (0.05 m) for HR_{min}, and *S* values derived from Eq. (4.21) are used for the model.

4.5 Conclusions

In this study, we investigated the morphological structures of the prop root system with multiple orders of prop roots. The results show that first-order (primary) roots contribute to 20 %, at lowest, for the whole-tree prop root projected area, highlighting the importance of the presence of second, third, and even higher-order prop roots. Therefore, these prop roots above the first-order may contribute greatly to the drag force exerted by mangroves. We proposed a model to predict the vertical distribution of the number of prop roots composed of three parameters: scaling factor (S), maximum root height (HR_{max}), and minimum root height (HR_{min}). The model well reproduced the vertical structure of the prop root system for the 156 sampled trees. S, the most critical parameter describing the complexity of prop root system, and HR_{max} showed significant correlations with DBH, but the relationships significantly vary among sites. Site- and species-specific regression models for S and HR_{max} successfully reproduced the vertical profile of prop root structure with reasonable accuracy. The site variations in the scaling relations in S were mostly explained by sediment thickness among the measured environmental variables – soil salinity, sediment hardness, and thickness, suggesting the physical constraints of below-ground root development in a shallow sediment layer (around 0.1 m thickness), which promotes prop root production anchoring the ground to increase below-ground biomass. Multivariate analysis indicated that hard substrate also contributes to the higher complexity of prop root system albeit contrary to our expectation, implying the need for investigating the effects of hydrodynamic loads on the morphology of prop root system. The accessibility to groundwater or inter-specific competition for below-ground resources may also be the reasons for site differences in the scaling relations, where sediment thickness is unlikely to constrain below-ground root development, although it has not been verified in this study. Further research is needed to elucidate the mechanisms of morphological plasticity in prop root system.

4.6 References

Adame, M.F., Neil, D., Wright, S.F., Lovelock, C.E., 2010. Sedimentation within and among mangrove forests along a gradient of geomorphological settings. Estuar. Coast Shelf Sci. 86, 21–30.

Buschman, F. A., Hoitink, A. J. F., de Jong, S. M., Hoekstra, P., Hidayat, H., and Sassi, M. G., 2012. Suspended sediment load in the tidal zone of an Indonesian river. Hydrol. Earth Syst. Sci., 16, 4191–4204, https://doi.org/10.5194/hess-16-4191-2012.

Castañeda-Moya, E., Twilley, R.R., Rivera-Monroy, V.H., Marx, B.D., Coronado-Molina, C., Ewe, S.M., 2011. Patterns of root dynamics in mangrove forests along environmental gradients in the Florida Coastal Everglades, USA. Ecosystems 14, 1178–1195.

Castañeda-Moya, E., Twilley, R.R., Rivera-Monroy, V., 2013. Allocation of biomass and net primary productivity of mangrove forests along environmental gradients in the Florida Coastal Everglades, USA. For. Ecol. Manag. 307, 226–241.

Chen, Y., Li, Y., Cai, T., Thompson, C., and Li, Y., 2016. A comparison of biohydrodynamic interaction within mangrove and saltmarsh boundaries. Earth Surf. Process. Landforms 41: 1967– 1979. doi: 10.1002/esp.3964.

Chen, Y., Li, Y., Thompson, C., Wang, X., Cai, T., Chang, Y., 2018. Differential sediment trapping abilities of mangrove and saltmarsh vegetation in a subtropical estuary. Geomorphology 318, 270–282.

Clough, B.F., Scott, K., 1989. Allometric relationships for estimating above-ground biomass in six mangrove species. For. Ecol. Manag. 27 (2), 117–127.

Comley, B.W.T., McGuinness, K.A., 2005. Above and below ground biomass, and allometry of four common northern Australian mangroves. Aust. J. Bot. 53, 431-436.

Cormier, N., Twilley, R.R., Ewel, K.C., Krauss, K.W., 2015. Fine root productivity varies along nitrogen and phosphorus gradients in high-rainfall mangrove forests of Micronesia. Hydrobiologia 750, 69–87.

Duncan, C., Primavera, J.H., Pettorelli, N., Thompson, J.R., Loma, R.J.A., Koldewey, H.J., 2016. Rehabilitating mangrove ecosystem services: a case study on the relative benefits of abandoned pond reversion from Panay Island, Philippines. Mar. Pollut. Bull. 109, 772–782. https://doi.org/10.1016/j.marpolbul.2016.05.049.

Ebato, M., 2020. Evaluation of soil hardness in paddy fields by cone penetrometer as a simple soil physical diagnosis method. Agricultural Information Research 29 (1), 24-39.

Estrada, G.C.D., Soares, M.L.G., Santos, D.M.C., Fernandez, V., de Almeida, P.M.M., de Medeiros Estevam, M.R., Machado, M.R.O., 2014. Allometric models for aboveground biomass estimation of the mangrove *Avicennia schaueriana*. Hydrobiologia 734, 171e185.

Fatoyinbo, T., Feliciano, E.A., Lagomasino, D., Lee, S.K., Trettin, C., 2018. Estimating mangrove aboveground biomass from airborne LiDAR data: a case study from the Zambezi River delta. Environ. Res. Lett. 13, 12.

Furukawa, K., Wolanski, E., Mueller, H., 1997. Currents and sediment transport in mangrove forests. Estuar. Coast. Shelf Sci. 44, 301–310.

Giri, C., Ochieng, E., Tieszen, L., Zhu, Z., Singh, A., Loveland, T., et al., 2011. Status and distribution of mangrove forests of the world using earth observation satellite data. Global Ecology and Biogeography, 20, 154–159.

Ha, T.H., Marchand, C., Aimé, J., Dang, H.N., Phan, N.H., Nguyen, X.T., Nguyen, T.K.C., 2018. Belowground carbon sequestration in a mature planted mangroves (Northern Viet Nam). For. Ecol. Manag. 407, 191–199.

Hayes, M.A., Jesse, A., Welti, N., Tabet, B., Lockington, D., Lovelock, C.E., 2019. Groundwater enhances above - ground growth in mangroves. J Ecol. 107: 1120–1128.

Horstman, E.M., Dohmen-Janssen, C.M., Narra, P.M.F., Van den Berg, N.J.F., Siemerink, M., Hulscher, S.J.M.H., 2014. Wave attenuation in mangroves: a quantitative approach to field observations. Coast. Eng. 94, 47–62.

Horstman, Dohmen-Janssen, C.M., Bouma, T.J., Hulscher, S.J.M.H., 2015. Tidal-scale flow routing and sedimentation in mangrove forests: combining field data and numerical modelling. Geomorphology 228, 244–262.

Husrin, S., Strusinska, A., Oumeraci, H., 2012. Experimental study on tsunami attenuation by mangrove forest. Earth, Planets Sp. 64, 973–989.

Ismail, H., Abd Wahab, A.K., Alias, N.E., 2012. Determination of mangrove forest performance in reducing tsunami run-up using physical models. Nat. Hazards 63, 939–963.

Komiyama, A., Havanond, S., Srisawatt, W., Mochida, Y., Fujimoto, K., Ohnishi, T., Ishihara, S., Miyagi, T., 2000. Top/root biomass ratio of a secondary mangrove (*Ceriops tagal* (Perr.) CB Rob.) forest. For. Ecol. Manag. 139 (1–3), 127–134.

Komiyama, A., Ong, J.E., Poungparn, S., 2008. Allometry, biomass, and productivity of mangrove forests: A review. Aquat. Bot. 89, 128–137.

Krauss, K.W., Cahoon, D.R., Allen, J.A., 2003. Differential rates of vertical accretion and elevation change among aerial root types in Micronesian mangrove forests. Estuar. Coast Shelf S. 56, 251–259.

Krauss, K.W., McKee, K.L., Lovelock, C.E., Cahoon, D.R., Saintilan, N., Reef, R., Chen, L., 2014. How mangrove forests adjust to rising sea level. New Phytol. 202, 19–34.

Lovelock, C.E., 2008. Soil respiration and belowground carbon allocation in mangrove forests. Ecosystems 11, 342-354.

Lovelock, C.E., Adame, M.F., Bennion, V., Hayes, M., Reef, R., Santini, N., Cahoon, D.R., 2015a. Sea level and turbidity controls on mangrove soil surface elevation change. Estuar. Coast. Shelf Sci. 153, 1–9.

Lovelock, C.E., Cahoon, D.R., Friess, D.A., Guntenspergen, G.R., Krauss, K.W., Reef, R., Rogers, K., Saunders, M.L., Sidik, F., Swales, A., Saintilan, N., Thuyen, L.X., Triet, T.,

2015b. The vulnerability of Indo-Pacific mangrove forests to sea-level rise. Nature 526, 559–563.

Maza, M., Adler, K., Ramos, D., Garcia, A., Nepf, H., 2017. Velocity and drag evolution from the leading edge of a model mangrove forest. J. Geophys. Res. 122 (11), 9144–9159.

Maza, M., Lara, J.L., Losada, I.J., 2019. Experimental analysis of wave attenuation and drag forces in a realistic fringe *Rhizophora* mangrove forest. Adv. Water Resour. 131, 103376.

Mazda, Y., Wolanski, E., King, B., Sase, A., Ohtsuka, D., Magi, M., 1997. Drag force due to vegetation in mangrove swamps. Mangroves Salt Marshes 1, 193–199.

Mazda, Y., Kobashi, D., Okada, S., 2005. Tidal-scale hydrodynamics within mangrove swamps. Wetl. Ecol. Manag. 13, 647–655.

McKee, K.L., 2001. Root proliferation in decaying roots and old root channels: a nutrient conservation mechanism in oligotrophic mangrove forests? J Ecol. 89, 876-887.

Mendez-Alonzo, R., Moctezuma, C., Ordonez, V.R., Angeles, G., Martinez, A.J., LopezPortillo, J., 2015. Root biomechanics in *Rhizophora mangle*: anatomy, morphology and ecology of mangrove's flying buttresses. Ann Bot 115, 833–840.

Montgomery, J.M., Bryan, K.R., Mullarney, J.C, Horstman, E.M., 2019. Attenuation of storm surges by coastal mangroves. Geophys. Res. Lett. 46:2680–2689.

Naidoo, G., 2009. Differential effects of nitrogen and phosphorus enrichment on growth of dwarf *Avicennia marina* mangroves. Aquat. Bot. 90, 184–190

Ohira, W., Honda, K., Nagai, M., Ratanasuwan, A., 2013. Mangrove stilt root morphology modelling for estimating hydraulic drag in tsunami inundation simulation. Trees 27, 141–148.

Ong, J.E., Gong, W.K., Wong, C.H., 2004. Allometry and partitioning of the mangrove, *Rhizophora apiculata*. For. Ecol. Manag. 188 (1–3), 395–408.

Osland, M.J., Day, R.H., Larriviere, J.C., From, A.S., 2014a. Aboveground allometric models for freeze-affected black mangroves (*Avicennia germinans*): equations for a climate sensitive mangrove-marsh ecotone. PLoS One 9, e99604.

Peters, R., Vovides, A.G., Luna, S., Grueters, U., Berger, U., 2014. Changes in allometric relations of mangrove trees due to resource availability – a new mechanistic modelling approach. Ecol. Modell. 283, 53–61.

Pranchai, A., Jenke, M., Vogt, J., Grueters, U., Yue, L., de Menezes, M.M., Wagner, S., Berger, U., 2018. Density-dependent shift from facilitation to competition in a dwarf *Avicennia germinans* forest. Wetlands Ecol. Manage. 26: 139.

Renema, W., 2006. Habitat variables determining the occurrence of large benthic foraminifera in the Berau area (East Kalimantan, Indonesia). Coral Reefs 25, 351–359.

Rollon, R.N., Villamayor, B.M.R., Oropesa, L.J.B., Samson, M.S., 2017. Prop root production response of planted Rhizophora to abrupt subsidence-induced sea level rise. Ocean & Coast. Manag. 142, 198-208.

Shan, Y., Liu, C., Nepf, H., 2019. Comparison of drag and velocity in model mangrove forests with random and in-line tree distributions. J. Hydrol. 568, 735-746.

Sharma, S., Yasuoka, J., Nakamura, T., Watanabe, A., Nadaoka, K., 2014. The role of hydroperiod, soil moisture and distance from the river mouth on soil organic matter in Fukido Mangrove Forest, Ishigaki Island, Japan. In Proceeding of the International Conference on Advances in Applied Science and Environmental Engineering.

Sherman, R.E., Fahey, T.J., Martinez, P., 2003. Spatial patterns of biomass and aboveground net primary productivity in a mangrove ecosystem in the Dominican Republic. Ecosystems 6, 384–398.

Smith III, T.J., Whelan, K.R.T., 2006. Development of allometric relations for three mangrove species in South Florida for use in the Greater Everglades Ecosystem restoration. Wet. Ecol. Manage. 14, 409–419.

Strusińska-Correia, A., Husrin, S., and Oumeraci, H., 2013. Tsunami damping by mangrove forest: a laboratory study using parameterized trees. Nat. Hazards Earth Syst. Sci., 13, 483–503, https://doi.org/10.5194/nhess-13-483-2013.

Suwa, R., Deshar, R., Hagihara, A., 2009. Forest structure of a subtropical mangrove along a river inferred from potential tree height and biomass. Aquat. Bot. 91, 99–104.

Tamooh, F., Huxham, M., Karachi, M., Mencuccini, M., Kairo, J.G., Kirui, B., 2008. Belowground root yield and distribution in natural and replanted mangrove forests at Gazi bay Kenya. For. Ecol. Manage. 256 (6), 1290–1297.

Tomlinson, P.B., 2016. The Botany of Mangroves. Cambridge University Press, Cambridge.

Van Vinh, T., Marchand, C., Linh, T.V.K., Vinh, D.D., Allenbach, M., 2019. Allometric models to estimate above-ground biomass and carbon stocks in *Rhizophora apiculata* tropical managed mangrove forests (Southern Viet Nam). For. Ecol. Manage. 434, 131–141.

Vovides, A.G., Vogt, J., Kollert, A., Berger, U., Grueters, U., Peters, R., Lara-Domínguez, A.L., López-Portillo, J., 2014. Morphological plasticity in mangrove trees: Salinity-related changes in the allometry of *Avicennia germinans*. Trees 28, 1413–1425.

Weiner, J., 2004. Allocation, plasticity and allometry in plants. Perspectives in Plant Ecology, Evolution and Systematics 6, 207-215.

Wilkens, J.F., Huth, F., Berger, U., Devlin, D., Popow, F., Wagner, S., 2018. Spatial explicit distribution of individual fine root biomass of *Rhizophora mangle* L. (red mangrove) in South Florida. Wetlands Ecology and Management 26: 775–788.

Willemsen, P.W.J.M., Horstman, E.M., Borsje, B.W., Friess, D.A., Dohmen-Janssen, C.M., 2016. Sensitivity of the sediment trapping capacity of an estuarine mangrove forest. Geomorphology 273, 189–201.

Woodroffe, C.D., Rogers, K., McKee, K.L., Lovelock, C.E., Mendelssohn, I.A., Saintilan, N., 2016. Mangrove sedimentation and response to relative sea-level rise. Ann. Rev. Mar. Sci. 8, 243–266.

Xiong, Y., Liu, X., Guan, W., Liao, B., Chen, Y., Li, M., Zhong, C., 2017. Fine root functional group based estimates of fine root production and turnover rate in natural mangrove forests. Plant Soil 413, 83–95. https://doi.org/10.1007/s11104-016-3082-z.

Yanagisawa, H., Koshimura, S., Goto, K., Miyagi, T., Fumihiko, I., Ruangrassamee, A., Charlchai, T., 2009. The reduction effects of mangrove forest on a tsunami based on field surveys at Pakarang Cape, Thailand and numerical analysis. Estuar. Coast Shelf Sci. 81, 27-37.

Zhang, K., Liu, H., Li, Y., Xu, H., Shen, J., Rhome, J., Smith, T.J., 2012. The role of mangroves in attenuating storm surges. Estuar. Coast Shelf Sci. 102–103, 11–23. https://doi.org/10.1016/j.ecss.2012.02.021.

Zhang, X., Chua, V.P., Cheonf, H.F., 2015. Hydrodynamics in mangrove prop roots and their physical properties. J. Hydro-environ. Res. 9, 281–294.

Zhu, X., Hou, Y., Weng, Q., Chen, L., 2019. Integrating UAV optical imagery and lidar data for assessing the spatial relationship between mangrove and inundation across a subtropical estuarine wetland. ISPRS J. Photogramm. Remote Sens. 149, 146–156.

Supporting Information for Chapter 4

Note S4.1. Supplementary data collection at site Bat

Field survey for obtaining the species-specific relationship of the scaling factor (S) and the maximum root height (HR_{max}) with DBH was conducted at site Bat in February 2020 for supplementing the data collected at this site in February to March in 2019. We sampled 15 trees both for *Rhizophora apiculata* and *Rhizophora mucronata* at the same location as the field survey in 2019. DBH, maximum root height (HR_{max}), minimum root height (HR_{min}), and total number of prop roots in a tree were measured for each sampled tree. The S values for the individuals were then derived using Eq. (4.21). The data were used for obtaining the relationships of S and HR_{max} with DBH for *R. apiculata* and *R. mucronata* at this site (Figs. 4.7 and 4.8), and subsequent analyses (Figs. 4.9 and 4.10; Table 4.2). The data were also used for the comparison of relationships of S and HR_{max} with DBH among sites for *R. apiculata* and *R. mucronata* (Fig. S4.6).

Table S4.1. Summary of environmental variables at the study sites. While the environmental variables were measured at one location at each site, sediment thickness and hardness were measured at several points (n =13) in Kar, and the averaged values were considered as the representative values at the site. This was because the mangroves at Kar were formed on reef flat that might have rough surface, and variations in sediment thickness and hardness even within the area of measurement were expected.

Site	Sediment thickness (m)	Soil salinity (‰)	Surface sediment hardness (kg cm^{-2})
Fuk	0.9	33	20.0
Bak1	1.4	32	1.2
Bak2	2.65	26	0.4
Bat	2.65	29	32.4
Kii	0.8	40	32.6
Mar	0.1	35	6.3
Ber	Not measured	30	35.8
Kar	0.12 ± 0.08 (n = 13)	37	14.7 ± 4.0 (n = 13)

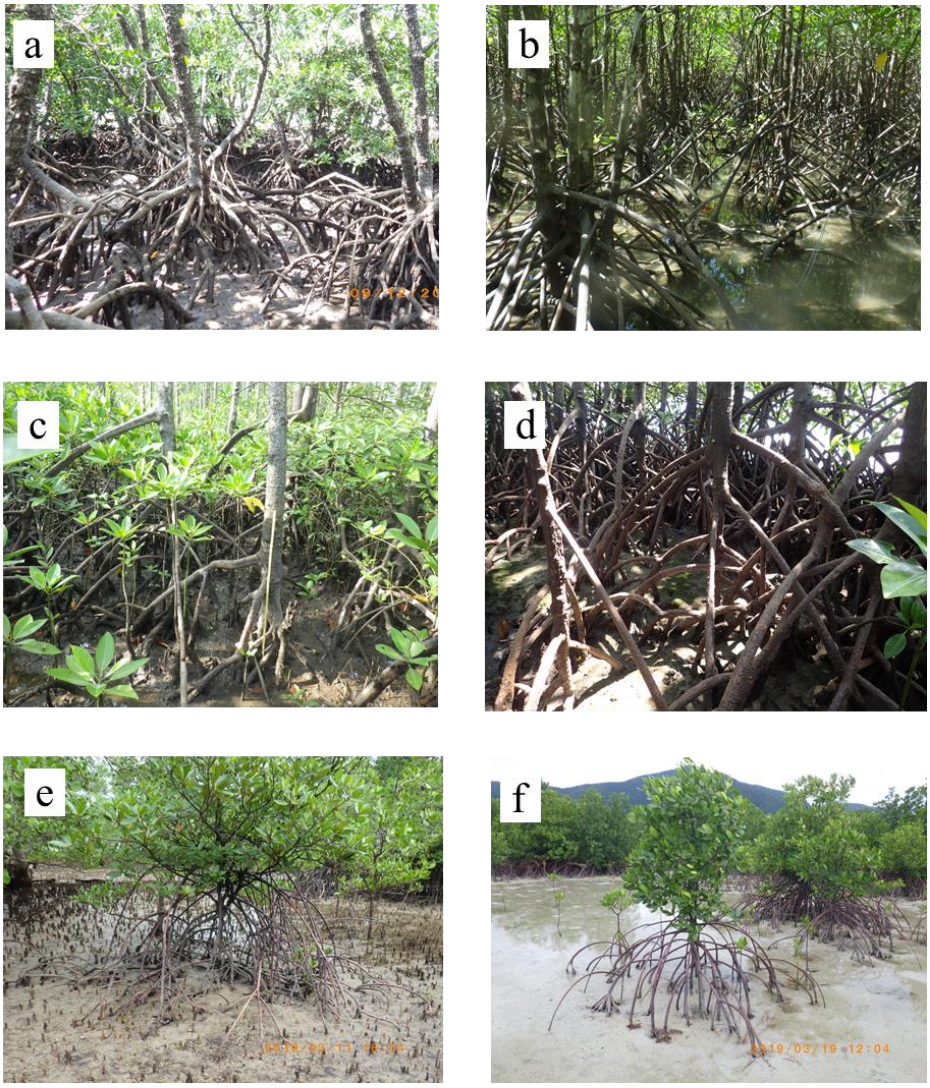

Figure S4.1. Mangrove forest at (a) Fuk, (b) Bak1, (c) Bak2, (d) Bat, (e) Ber, and (f) Kar. Photos of Kii and Mar were not taken.

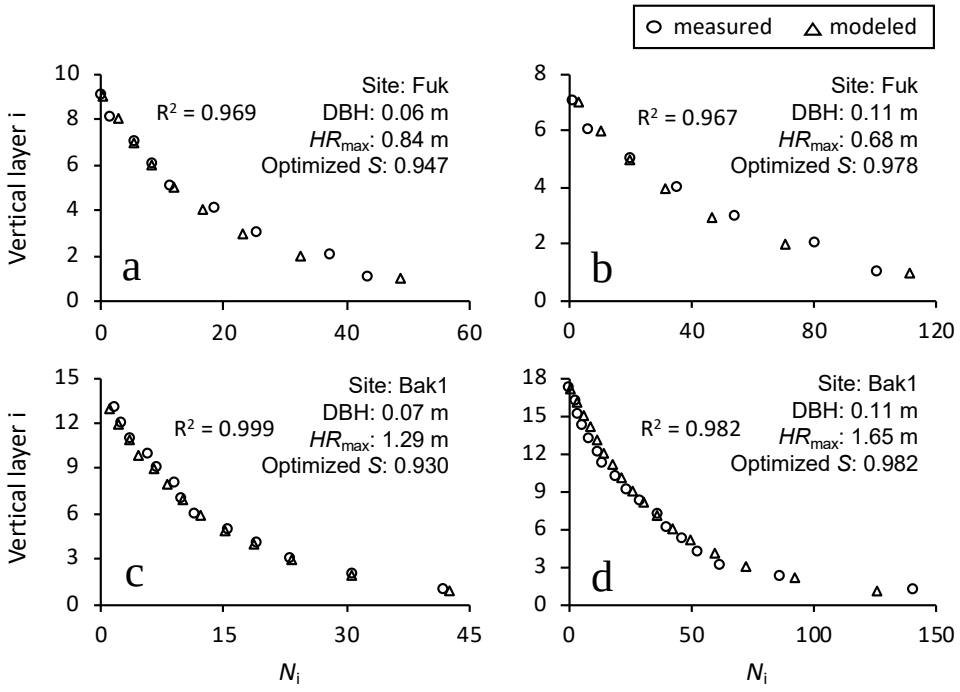

Figure S4.2. A comparison of measured and modeled vertical distribution of the number of prop roots (N_i) for selected trees from (a, b) Fuk and (c, d) Bak1. The measured values for HR_{max}, a constant value for HR_{min} (0.05 m), and the optimized values for S are used to predict N_i for individual trees.

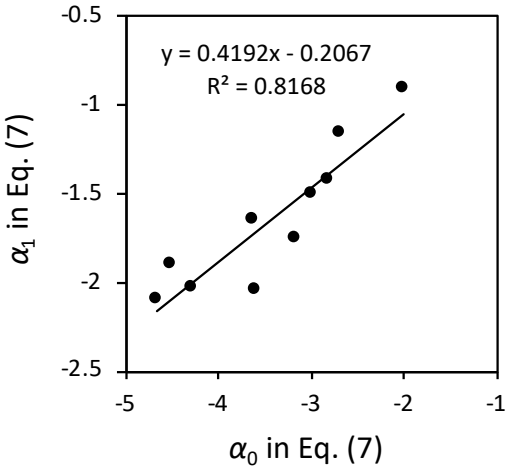

Figure S4.3. Relationship between the coefficients α_0 and α_1 in Eq. (4.7). The values of the coefficients are from the site- and species-specific regression models for the relationships between log-transformed (1 – S) and DBH shown in Fig. 4.7.

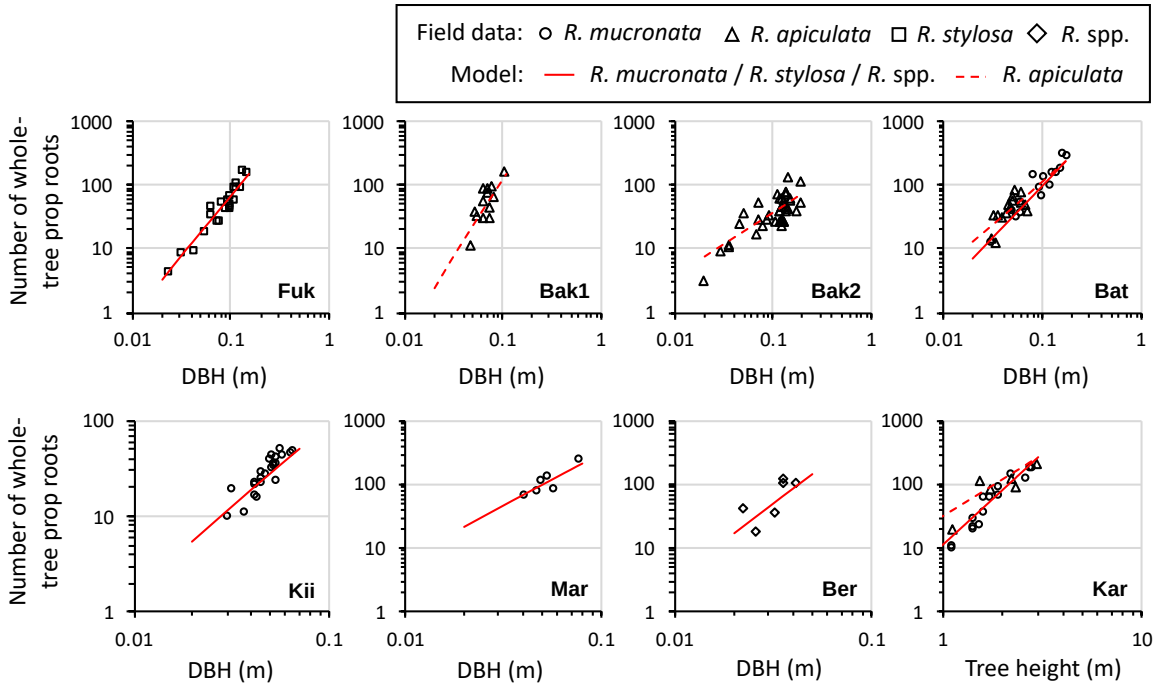

Figure S4.4. A comparison of the measured and modeled number of whole-tree prop roots. The markers indicate the field data, and the solid or dotted lines indicate the modeled values. The modeled values are derived from Eq. (4.4). A constant value (0.05 m) for HR_{min}, and the site- and species-specific regression models for S and HR_{max} shown in Fig. 4.7 and Fig. 4.8, respectively, are used for the modeled values. Note that the number of whole-tree prop roots at Kar is plotted according to tree height because it showed a higher correlation than with DBH.

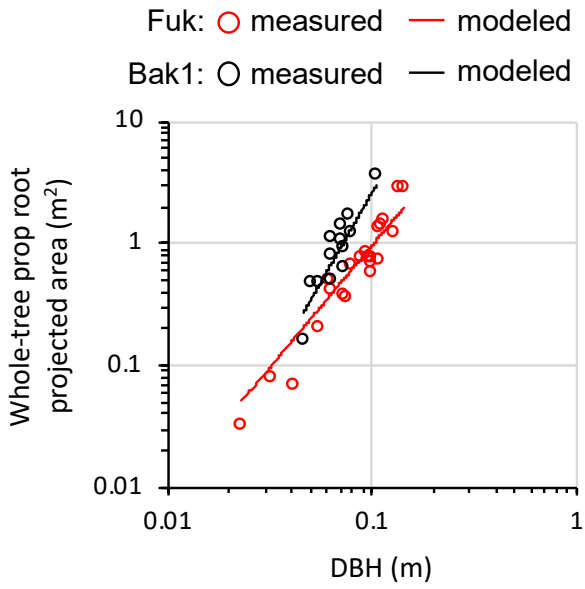

Figure S4.5. A comparison of the measured and modeled whole-tree prop root projected area. Data are from 22 and 13 trees in Fuk and Bak1, respectively. The circle markers indicate the

measured values, and the lines indicate the modeled values. The number of prop roots in the vertical layers was predicted using a constant value for HR_{min}, and the regression models for S and HR_{max} shown in Fig. 4.7 and Fig. 4.8, respectively. Then the modeled number of prop roots was multiplied by 0.0043, as shown in Eq. (4.17), to estimate the whole-tree prop root projected area.

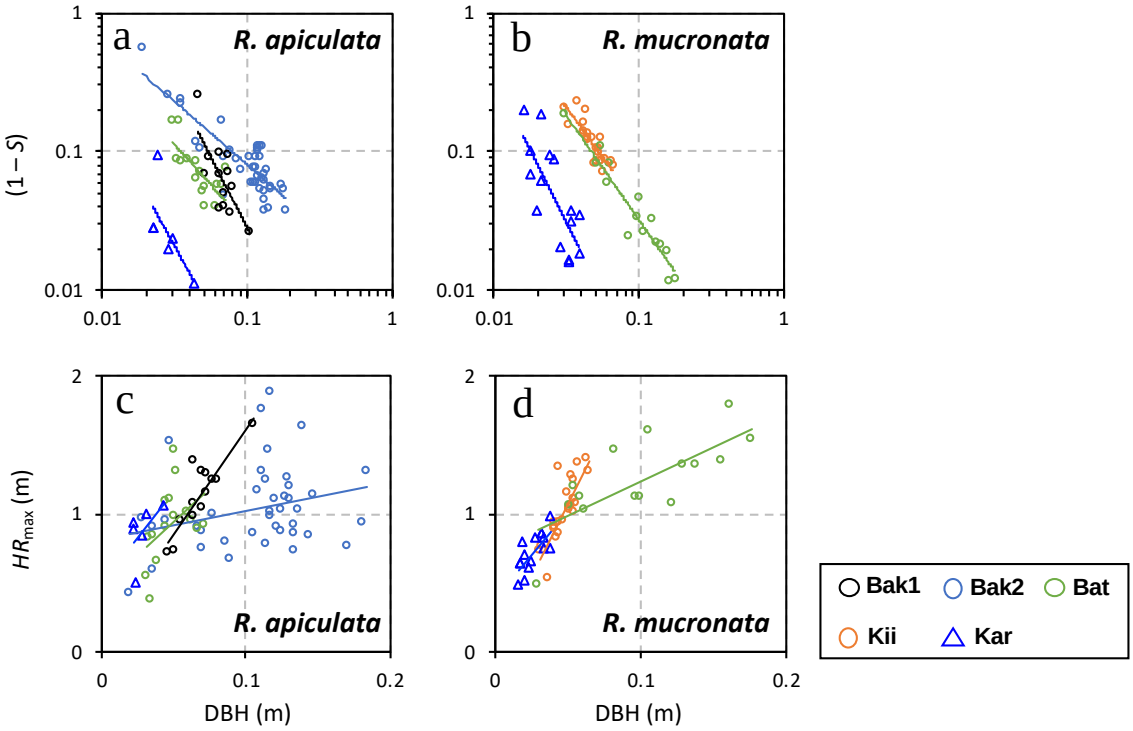

Figure S4.6. Comparison of relationships of (a, b) S and (c, d) HR_{max} with DBH among sites for *R. apiculata* and *R. mucronata*.

Chapter 5: Field measurement and prediction of drag in a planted *Rhizophora* mangrove forest

5.1.1 Abstract

Drag effects of mangrove forests with complex root systems modulate flow and substance transport and promote sedimentation, all of which are linked to mangroves' ecosystem services (e.g., coastal protection, trapping of suspended organic carbon) and resilience (e.g., vertical accretion relative to sea-level rise). Previous flume studies proposed a predictive model of drag by *Rhizophora* mangrove forests based on the quadratic drag law using two parameters–drag coefficient (C_D) and vegetation projected area density (a). However, its general applicability to mangrove forests in the field has not been tested. To fill this knowledge gap, this study quantified drag in a 17-year-old planted *Rhizophora* mangrove forest using comprehensive measurements of hydrodynamics and vegetation morphology. The site showed a much higher value for a than the conditions assumed in previous flume studies, mainly due to root branching and high tree density. We found that despite the much higher vegetation complexity, the derived C_D was 1.0 ± 0.2 for tide-driven currents, consistent with previous flume studies. By using the mean value of derived C_D (1.0), we confirmed that the quadratic drag model expresses well the field-measured drag. We also showed that the value of parameter a can be predicted by only two vegetation parameters (stem diameter and tree density) using an empirical *Rhizophora* root model, and confirmed the successful prediction of drag from these vegetation parameters and the derived C_D. This provides insights into effectively implementing the drag model in hydrodynamic models for better representation of flow, transport, and geomorphic dynamics in mangrove forests.

5.1.2 Introduction

Mangroves are one of the coastal vegetation ecosystems that grow in intertidal areas in tropical and subtropical regions (Giri et al., 2011). They are characterized by complicated patterns of above-ground root systems (Ezcurra et al., 2016; Tomlinson, 2016) that

substantially attenuate flow and wave energy and provide coastal protection (Furukawa et al., 1997; Horstman et al., 2014; Menéndez et al., 2018, 2020). Through the drag effects, they also modulate flow and substance transport, prevent erosion, and promote sedimentation of inorganic and organic matters (Adame et al., 2010; Chen et al., 2016, 2018; Bryan et al., 2017; Best et al., 2022), all of which are linked to various mangroves' ecosystem services and resilience. For instance, mangrove forests trap and accumulate organic carbon transported from outer systems (Sasmito et al., 2020; Suello et al., 2022), contributing to mangroves' characteristic as globally important carbon sink (Donato et al., 2011; Taillardat et al., 2018; Sharma et al., 2020). Mangroves' geomorphic evolution driven by sedimentation and below-ground organic matter production is considered as a key process of adaptation to threats due to sea-level rise (Krauss et al., 2014; Rogers et al., 2014; Saintilan et al., 2020; Xie et al., 2020).

Despite the valuable ecosystem services provided by mangroves, they have declined globally predominantly due to deforestation (Friess et al., 2019). Rigorous evaluation of the mangroves' ecosystem services and resilience is needed to facilitate mangrove conservation, management, and restoration (Macreadie et al., 2022). However, our understanding of the drag effects of mangrove forests remains limited, despite their central role in the physical processes that regulate the mechanisms behind the ecosystem services they provide. This is especially true for the case of *Rhizophora* mangroves that form complex root systems known as "prop root system" (Ong et al., 2004), which in itself is a challenging task to quantify. Thus, the primary motivation of this study is the quantification and prediction of the drag effects of *Rhizophora* mangrove forests – one of the most dominant mangrove genera in the Asia-Pacific region and is often used for mangrove plantation (Primavera and Esteban, 2008; Friess et al., 2019).

Recently, several studies have conducted flume experiments using model *Rhizophora* trees to characterize the flow and drag in *Rhizophora* mangrove forests (Zhang et al., 2015; Maza et al., 2017; Shan et al., 2019). They showed that the model based on the quadratic drag law with the spatial average of streamwise depth-averaged velocity or cross-sectional mean velocity ($\langle U \rangle$, m s^{-1}) can express well the drag exerted by mangroves (vegetation drag), where angle brackets denote the spatial average of velocity that smooths over the velocity heterogeneity due to vegetation obstacles. Note that this manuscript refers to velocities as temporally averaged ones unless specified. This can be written as a spatial average as (Nepf, 2012; Xu and Nepf, 2021)

$$F_{veg,model} = \frac{1}{2}\frac{C_D}{1-\varphi} A\langle U\rangle|\langle U\rangle| \quad \text{where} \quad A = \int_0^h a(z)dz \tag{5.1}$$

where $F_{veg,model}$ is the modeled vegetation drag per bed area (m^2 s^{-2}), C_D is the vegetation drag coefficient, φ is the solid volume fraction occupied by vegetation, and A is the submerged

vegetation projected area per bed area (m^2 m^{-2}), calculated by vertically integrating the vegetation projected area density a (m^2 m^{-3}) for a water column with depth h (m). Here, C_D values around 1 have been obtained in flows with Reynolds numbers (Re) high enough to ensure turbulent wakes (Re > 120; Shan et al., 2019).

The drag model, Eq. (5.1), with suggested C_D values may move forward our understanding of the physical process of mangroves' ecosystem service and resilience (i.e., transport, sedimentation, and geomorphic evolution) once it is implemented in coastal hydrodynamic models (Cao et al., 2021). However, the root systems of the model *Rhizophora* trees examined by previous flume experiments were rather simple to adequately represent the actual mangrove forests in the field that have complicated root systems. Hence, the applicability of the insights obtained by previous flume experiments to mangrove forests with complicated root systems is still uncertain, suggesting the need to investigate the applicability of the drag model in the field. To date, only a few studies have quantified vegetation drag in field mangrove forests. Mullarney et al. (2017) and Horstman et al. (2021) quantified drag from pressure gradients by measuring water level differences along transects, however, C_D was not derived because the parameter a was not quantified. Only Mazda et al. (1997) obtained field estimates of C_D by putting additional efforts in measuring vegetation morphology for a. The derived C_D showed high variability ranging from 0.4 to more than 10 in tide-driven currents where turbulent wakes are usually expected, which contradicts the results of laboratory-based studies. However, their estimates of C_D were based on velocity measured at a single point while derivation of C_D requires velocity profiling as indicated in Eq. (5.1). Also, the measurement of vegetation morphology was rather limited in terms of sampling number to obtain the representative (or spatially averaged) value of a in more than 100-m long transects. Thus, the reliability of the derived C_D is questionable, and we concluded that the drag model, Eq. (5.1), has not been adequately tested in field mangrove forests yet.

The feasibility of the drag model, which is attributed to parameter a in Eq. (5.1), also needs to be established. This parameter is labor-intensive to obtain in the field because it is significantly influenced by tree density and individual tree morphology and could be highly heterogeneous horizontally and vertically. Therefore, implementing the drag model in coastal hydrodynamic models is challenging, especially in a forest-scale simulation (but see Horstman et al., 2015 and Willemsen et al., 2016). In fact, numerical modeling studies often parameterize mangrove drag effects in the bed roughness parameter without accounting for the spatial heterogeneity of vegetation morphological structures (Li et al., 2012, 2014; Zhang et al., 2012; Menéndez et al., 2020; Gijsman et al., 2021); this results in an inaccurate representation of the physical process.

Here, we aim to examine the following: 1) Is the drag model, Eq. (5.1), applicable to real *Rhizophora* mangrove forests? 2) Can drag be predicted from limited vegetation parameters rather than measuring the labor-intensive parameter, ***a***, in Eq. (5.1), so that the realistic drag effects of *Rhizophora* mangrove forests can be feasibly implemented in the hydrodynamic models? To answer these questions, a comprehensive data set on hydrodynamics and vegetation morphology needed for testing the drag model was collected for the first time in the field to fill the knowledge gap between the model- and field-mangrove forests. To reduce the uncertainty in obtaining the representative (or spatially-averaged) information on hydrodynamics and vegetation structures (***a***), we selected a planted *Rhizophora* mangrove forest having relatively homogeneous structural complexity as a site for drag quantification. Unlike in previous studies, we shortened the transect length used for drag quantification down to 30 m to obtain the value for ***a*** with high reliability from a limited number of measurements of the vegetation morphology. Lastly, we applied the *Rhizophora* root morphological model developed in Yoshikai et al. (2021a) as a predictor of the parameter ***a***, and examined the predictability of drag in the forest using the predicted values of ***a***.

5.2 Materials and Methods

5.2.1 Study site overview and transect setting

This study was conducted in a planted mangrove forest (locally known as Bakhawan Ecopark) found at the mouth of Aklan River in the province of Aklan, Panay Island, Philippines (Fig. 5.1a, b). We chose 17-year-old (as of 2018) *Rhizophora apiculata* stands as the drag measurement site (Fig. 5.1c, d). The site is characterized by well-developed above-ground root systems, and uniformly sized and evenly distributed trees. Here, the trees were planted following a 1.5 m × 1.5 m spacing rule. The canopy is closed and sheltered from winds. This is also the site where the morphological structures of above-ground roots were investigated in Yoshikai et al. (2021a) (referred to as site Bak1). The tide in the region is semi-diurnal with the highest amplitude at 2.0 m. The flows in the forest and creeks are basically tide-driven and sheltered from waves by a sandbar (Fig. 5.1b).

A 30-m long transect along the major flow direction (A–B: Fig. 5.1c) was set with a reference tree located at the center of the transect. Afterwards, the *x*-coordinate was defined to align with the direction of mean flow during ebb tide (the major axis is shown in Fig. 5.2d), the *y*-coordinate oriented laterally, and the *z*-coordinate oriented vertically with z = 0 m at the bed. The *x*-coordinates of A and B were defined as x_1 and x_2, respectively.

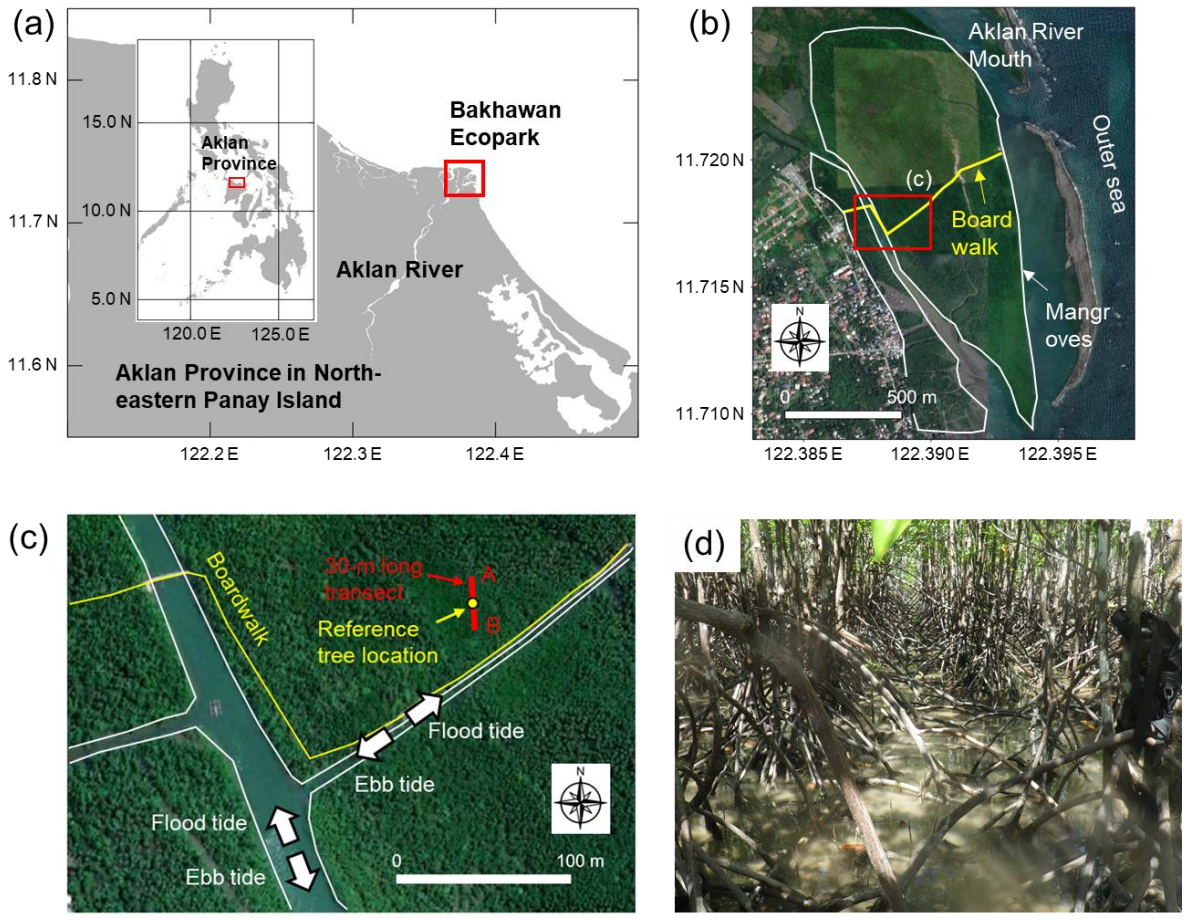

Figure 5.1. (a) Location of the study site – Bakhawan Ecopark in Aklan province, Panay Island, Philippines; (b) satellite images (Google Earth) of Bakhawan Ecopark (red box indicates the measurement site), (c) locations of transect A–B and the reference tree for drag measurement; and (d) photo of the drag measurement site taken near the reference tree. Shoreline data (as shown in panel "(a)") are from the Global Self-consistent, Hierarchical, High-resolution Geography (GSHHG) database.

5.2.2 Measurement of vegetation variables

To obtain the value of the spatially averaged vegetation projected area density, a (m^2 m^{-3}), the morphological structures of above-ground roots and stems around the reference tree were extensively measured from September 13–18, 2018. Data on some trees, including the reference tree, are shown in Yoshikai et al. (2021a). Ten additional trees were compiled and added for a total of 23 trees for this study. The information on the locations of the measured trees are provided in Fig. 5.2a. Some information on the vegetation parameters is provided in Table 5.1.

Table 5.1. Vegetation and topography information at the study site.

Parameter	Unit	Value
Forest age	years	17
Tree density (n_{tree})	trees m^{-2}	0.36
Number of measured trees (N_{tree})	trees	23
Mean and standard deviation of DBH	m	0.066 ± 0.013
DBH range of measured trees	m	0.045–0.105
DBH of the reference tree	m	0.076
Mean and standard deviation of maximum root height (HR_{max})	m	1.16 ± 0.27
Mean root diameter	m	0.03
Scaling parameter (α in Eq. (5.9))	m^{-1}	$10^{-3.59}$
Scaling parameter (α_1 in Eq. (5.9))	–	–2.04
Scaling parameter (β in Eq. (5.9))	m	0.08
Scaling parameter (β_1 in Eq. (5.9))	–	15.38
Critical height (HR_{min} in Eq. (5.10))	m	0.01
Root angle of approximated root shape (θ_l in Eq. (5.11))	degree	–34.5
Ground level at A relative to near the reference tree	m	0.045
Ground level at B relative to near the reference tree	m	–0.049

As described in Yoshikai et al. (2021a, b), four parameters of roots were measured; these are height (HR, m), horizontal distance (L, m), angle relative to horizontal axis at a point where a root emerges (θ, degree), and diameter (D_{root}, m) (see Fig. S5.1 for graphical description of these parameters). We also recorded root order (branching level from the stem) to characterize the significance of root branching to the total vegetation projected area. Then, following Ohira et al. (2013), the shape of each root projected from the mean flow direction was estimated with quadratic curve approximation as

$$z = -\frac{HR+L\tan\theta}{L^2}\left(\frac{y}{\cos\psi}\right)^2 + (\tan\theta)\left(\frac{y}{\cos\psi}\right) + HR \quad (5.2)$$

where ψ is the azimuth angle of root to the mean flow direction; here, y = 0 at the location where a root emerges from a stem or another root, i.e., the position of y-axis varies for each root. Because the azimuth root angles were not measured, a random number for ψ was given for each root in the range $0° \le \psi < 90°$ using the random number generator in MATLAB. The

projected area of one root can be estimated by multiplying D_{root} with the root length provided by Eq. (5.2). Similarly, root volume can be estimated from these parameters. By summing the projected areas of all roots in a tree per vertical height, *dz* (m), the whole-tree root projected area per *dz*, $a_{root,i}(z)$ (m tree^{-1}, here and hereafter; *i* denotes tree index), is obtained; a value 0.01 m was used for *dz* throughout this manuscript.

The stem diameter at 1.3 m height was also measured for the 23 trees. When the root in a tree exceeds the 1.3 m height, the diameters above the highest root were measured. Here, the *R. apiculata* trees have multiple stems, where one tree has 3–7 stems. We defined the measured diameter of the main stem as DBH (diameter at breast height) of a tree, which is a standard parameter in forestry that characterizes tree size (e.g., Suwa et al., 2021) and was used in the subsequent analysis of vegetation morphology. Some stems branched from other stems, and in such cases, the height of the branching point was also measured. Then, the whole-tree stem projected area per *dz*, $a_{stem,i}(z)$ (m tree^{-1}), was estimated by approximating it as a patch of cylinders with vertically uniform diameters whose stem density varies with height depending on the branching of the stems.

Three-dimensional point clouds of the measurement site were obtained using a hand-held GeoSLAM Horizon laser scanner (GeoSLAM Ltd., Nottingham, UK) for the purpose of site visualization (Fig. 5.2a). From the point clouds, locations of trees were identified, and tree density of the site, n_{tree} (tree m^{-2}), was computed from the visualized tree locations (Table 5.1).

From the derived parameters $a_{root,i}$, $a_{stem,i}$, and n_{tree}, the vertical profile of the parameter *a* was calculated as

$$a(z) = \frac{n_{tree} \sum_{i=1}^{N_{tree}} \left(a_{root,i}(z) + a_{stem,i}(z) \right)}{N_{tree}} \tag{5.3}$$

where N_{tree} is the number of measured trees (Table 5.1). Here, due to the randomness in the azimuth angle in Eq. (5.2), the estimated value of *a* has some uncertainties. In this regard, the value of *a* was computed repeatedly for 20 times, and the median value was taken as the representative value of *a* in the area.

5.2.3 Measurement of hydrodynamic variables

The measurement of hydrodynamic variables for drag quantification was conducted on September 10 and 11, 2018, which were spring tide conditions. A pressure sensor (U20L-04, Onset Computer Corporation, USA), four electromagnetic velocity meters (EM; Infinity-EM, JFE Advantech, Japan), and one Acoustic Doppler Velocimeter (ADV; Nortek Vector, Norway) were deployed around the reference tree (Fig. 5.2a) for the two-days measurement. The EMs were deployed to measure the near-bed (5 cm above the bed) velocities behind (P1), in front (P3), and at the sides (P2, P4) of the reference tree relative to the flow direction during ebb

tide (Fig. 5.2a, b). The ADV was deployed around 3 m away from the reference tree in a downward-looking orientation (Fig. 5.2a, c), where the center of the sampling volume was placed at 5 cm above the bed for bed drag quantification (Pope et al., 2006). The ADV was set to collect data with 16 Hz for 1 minute (960 samples) every 10 minutes, while the EMs were set to collect data at 1 Hz for 30 seconds with the same interval. The pressure sensor was set to collect data on the water depth near the reference tree (h_{ref}) every 10 minutes. Using data from the deployed EMs, it was confirmed that the flows had a distinct axis and did not rotate during the tidal cycles (Fig. 5.2d).

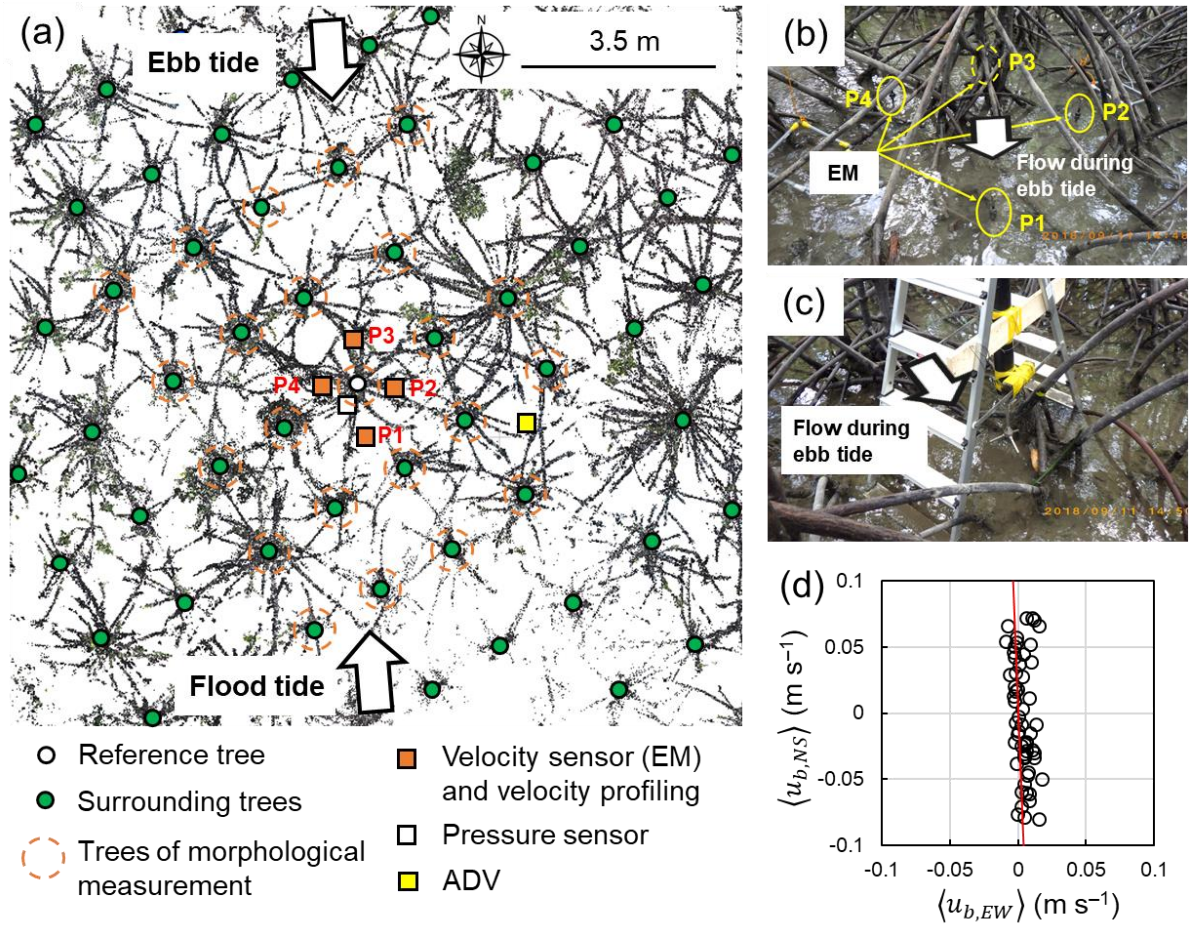

Figure 5.2. Visualization of the drag measurement set-up: (a) top view of LiDAR point clouds around the reference tree with information on the locations of measured trees and deployed sensors (The point clouds shown were cropped at heights between 0.1–1.7 m for a better visualization of the root systems); photos of (b) velocity sensors (EM) deployed near the bed around the reference tree (P1–P4) and (c) deployed ADV; and (d) near-bed spatially averaged horizontal flow velocities of the eastern ($\langle u_{b,EW} \rangle$) and northern ($\langle u_{b,NS} \rangle$) components indicating the major axis (red line) obtained by averaging the velocities from the four EMs.

Vertical profiling of flow velocity was conducted at the four locations around the reference tree (P1–P4; Fig. 5.2) to obtain the cross-sectional mean velocity near the reference tree ($\langle U_{ref} \rangle$) synchronized with the data collection by the deployed sensors. An electro-magnetic current meter equipped with a pressure sensor (AEM213-DA, JFE Advantech) was slowly moved (~1.0 cm s^{-1}) from the water surface to the bottom while collecting data at 1 Hz. When the water became shallower than around 20 cm, a propeller velocimeter (CR-11, Cosmo Riken, Japan) was used for the profiling instead of the AEM213-DA, the small propeller (~ 2 cm diameter) of which is well-suited to profile shallow waters. In this case, the flow velocities along the transect (x-axis) at the surface, middle, and bottom layers were measured at the four locations around the reference tree.

The water level differences between the transect ends A and B, $\Delta\eta$ (m), were measured during ebb tides using the water leveling method. We used this method because the usual pressure sensors were not expected to accurately detect the small water level differences across the 30-m long transect. A schematic of the measurement setup is shown in Fig. 5.3a. The method is based on the principle that the water level at both ends of a conduit will equalize based on atmospheric pressure. Plastic tubes (inner and outer diameters: 6 and 8 mm, respectively) were placed between the transect ends A and B, and at B vertically as shown in Fig. 5.3a, b. The connectivity of the water within the tubes was assured by removing any trapped air when the ground is submerged on a measurement day, so that the water levels at A ($\eta(x_1)$) and B ($\eta(x_2)$) were made visible at B (Fig. 5.3c). We then measured $\Delta\eta$ during ebb tides using a caliper with 0.1 mm resolution every 10 minutes, synchronized with the timing of data collection of other hydrodynamic parameters (Fig. 5.3c). The $\Delta\eta$ was recorded as 0 mm when the water level difference was too small to measure even though the waters were flowing.

The water depths at A, B, and near the reference tree were measured manually when the water was still at high tide (i.e., uniform water levels). From these water depths, the ground levels at A and B relative to the site near the reference tree were calculated (Table 5.1).

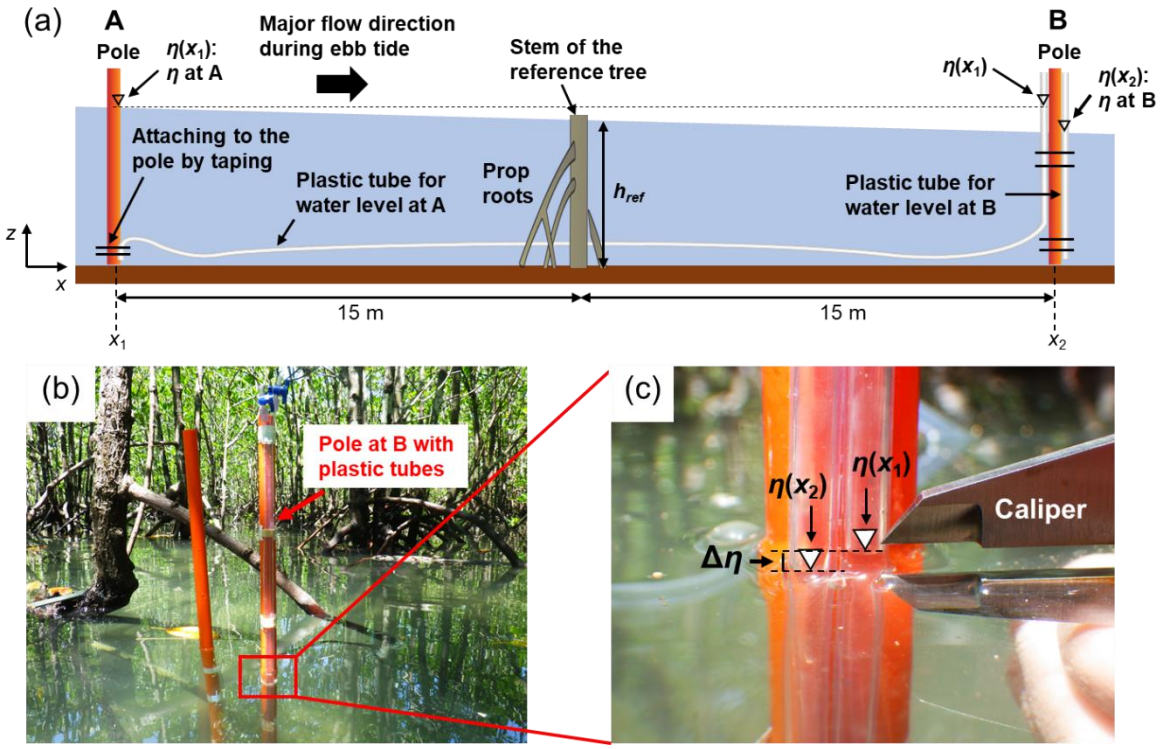

Figure 5.3. Water level difference measurement: (a) schematic diagram of setup; photos of (b) the pole set at B; and (c) a close view of the plastic tubes attached to the pole showing the water level difference ($\Delta\eta$) between A and B. The η is the water level (m), and h_{ref} is the water depth near the reference tree (m). Note that the schematic is not drawn to scale and the ground level slope is not depicted in the diagram.

5.2.4 Data processing and bed drag estimation

To obtain the streamwise temporal mean flow velocity profile, the instantaneous velocities along the *x*-axis, which were measured by the AEM213-DA, were binned using 0.05-m depth-intervals and averaged in each bin. The cross-sectional mean velocity near the reference tree, $\langle U_{ref} \rangle$, was calculated by averaging the mean velocities in the bins (or layers, in the case of data from the propeller velocimeter) of the four locations (P1–P4), based on the assumption that the average of the four locations represents the spatial average in the area. To check the validity of this assumption, a particle tracking velocimetry (PTV) survey was conducted around the reference tree in March 2019. See Note S5.1 and Fig. S5.2 for the details.

The bed drag, F_{bed} (m^2 s^{-2}), was quantified from the measured Reynolds stress provided by the ADV data (see Note S5.2 for the details). A bed drag coefficient (C_{bed}) was then determined by fitting the measured F_{bed} and $\langle U_{ref} \rangle$ in following equation of the quadratic drag law (Biron et al., 2004)

$$F_{bed} = C_{bed}\langle U_{ref}\rangle\left|\langle U_{ref}\rangle\right| \quad (5.4)$$

where the value of C_{bed} was determined as 4.2×10^{-3} with $R^2 = 0.55$ (see Note S5.2 and Fig. S5.3). This equation was used to compute the bed drag in the subsequent analyses.

5.2.5 Estimation of vegetation drag and drag coefficient

Drag by vegetation was quantified from the depth-averaged momentum balance. The inertial terms were significantly small compared to the pressure gradient (more than 20 times smaller), and thus they were neglected as done in other works (Nepf, 1999; Mullarney et al., 2017; Monismith et al., 2019; Horstman et al., 2021). The momentum balance can be then reduced to

$$g\frac{d\eta}{dx} = -\frac{F_{veg,obs}}{h} - \frac{F_{bed}}{h} \quad (5.5)$$

where g is the gravitational acceleration (m s^{-2}), h is the water depth (m), and $F_{veg,obs}$ is the vegetation drag (m^2 s^{-2}) quantified from field data. To account for the water depth variations along the transect attributed to the ground elevation slope, we assumed that the water flux is conserved between the transect, $\langle U(x,\ t)\rangle h(x,\ t) = \langle U_{ref}(t)\rangle h_{ref}(t)$ so that $\langle U(x,\ t)\rangle = \langle U_{ref}(t)\rangle h_{ref}(t)/h(x,\ t)$, where $\langle U_{ref}\rangle$ and h_{ref} are the cross-sectional mean velocity and water depth near the reference tree, respectively, and the bed slopes between A–reference tree and B–reference tree are constant. Then, following Lentz et al. (2017), Eq. (5.5) can be rearranged by horizontally integrating between A (x_1) and B (x_2) as

$$\langle F_{veg,obs}\rangle_x(x_2 - x_1) = -g\Delta\eta\int_{x_1}^{x_2} h\,dx - \langle F_{bed}\rangle_x(x_2 - x_1) \quad (5.6)$$

where the angle bracket with subscript "x" denotes the spatial average between the transect ends A–B and $\langle F_{bed}\rangle_x(x_2 - x_1) = C_{bed}\int_{x_1}^{x_2}\langle U\rangle|\langle U\rangle|\,dx$. This equation gives estimates of the mean vegetation drag between the transect, $\langle F_{veg,obs}\rangle_x$. Similarly, by assuming that the value of C_D does not vary between the ends of the transect, integration of the drag model Eq. (5.1) between x_1 and x_2 yields

$$\langle F_{veg,model}\rangle_x(x_2 - x_1) = \frac{1}{2}C_D\int_{x_1}^{x_2}\frac{A\langle U\rangle|\langle U\rangle|}{1-\varphi}dx \quad (5.7)$$

The value of C_D was derived by equating Eqs. (5.6) and (5.7) for each measurement.

5.2.6 Prediction of drag using a *Rhizophora* root model

The *Rhizophora* root model developed in Yoshikai et al. (2021a) was applied as a predictor of a in the drag model, Eq. (5.1). This model basically predicts the vertical distribution of root density per tree and has successfully predicted the complex root morphological

structures in various *Rhizophora* mangrove forests (Yoshikai et al., 2021a). The model assumes that the following equation applies for any root in the root system of a tree

$$HR_k = HR_{max} S^{(k-1)} \quad (5.8)$$

where HR_k and HR_{max} are the root heights (m) of the k^{th} highest and the highest root in a root system, respectively (Fig. S5.1), and S is a scaling factor. The parameters S and HR_{max} can be expressed as functions of DBH, and thus, HR_k is a function of DBH as

$$HR_k = (\beta_1 \mathrm{DBH} + \beta)(1 - \alpha \mathrm{DBH}^{\alpha_1})^{(k-1)} \quad (5.9)$$

where β, β_1 and α, α_1 are the scaling parameters for HR_{max} and S, respectively. The values of these parameters for our study site were derived in Yoshikai et al. (2021a) (Table 5.1). Similarly, if the t^{th} highest root is the one with the minimum height in a root system, t is the largest integer number that satisfies

$$HR_t = (\beta_1 \mathrm{DBH} + \beta)(1 - \alpha \mathrm{DBH}^{\alpha_1})^{(t-1)} \geq HR_{min} \quad (5.10)$$

where HR_{min} is the critical height (m) to be given as a model parameter. In this study, we assigned 0.01 m to HR_{min}, based on the average of the minimum root height of sampled trees. From Eqs. (5.9) and (5.10), the vertical variation of root density per dz in a tree is modeled.

To compute the root projected area from the modeled root density, an empirical relationship of $n_{root,i}(z)$ and $a_{root0,i}(z)$ provided in Fig. S5.4 was used, where $n_{root,i}(z)$ is the number of roots per dz in tree i (root m^{-1} tree^{-1}), and $a_{root0,i}(z)$ is the root projected area per dz with zero azimuth angles (m tree^{-1}). The strong linear relationship between $n_{root,i}(z)$ and $a_{root0,i}(z)$ suggests that, assuming a uniform root diameter, the individual roots can be approximated by a single linear shape, thereby reducing the number of parameters of root shape from Eq. (5.2) as:

$$z = (\tan \theta_l) \left(\frac{y}{\cos \psi} \right) + HR \quad (5.11)$$

where θ_l is the root angle of the approximated linear root shape. If Eq. (5.11) is applied, the slope of the $n_{root,i}(z)$ and $a_{root0,i}(z)$ relationship stands for $D_{root}dz/\sin(-\theta_l)$. By applying the average root diameter (D_{root} = 0.03 m; Table 5.1), the value of the root angle θ_l was determined as –34.5° for our study site (Fig. S5.4a; Table 5.1). As with the field data, random numbers were given to the root azimuth angle ψ in Eq. (5.11) for each root, and likewise, the model value of a was obtained from the ensemble calculations; the observed value was used for $a_{stem,i}(z)$, which can be easily measured in the field. The modeled a was then used in Eq. (5.7) for prediction of the drag exerted in the measurement site. Lastly, we tested the use of θ_l determined for another mangrove forest in Ishigaki Island, Japan (site Fuk in Yoshikai et al., 2021a; Fig. S5.4b) for drag prediction to quantify the sensitivity to this parameter, which demands the determination of values of the labor-intensive parameters $n_{root,i}(z)$ and $a_{root0,i}(z)$.

5.3 Results

5.3.1 Vegetation parameters

Figure 5.4 shows the vertical profile of the spatially averaged vegetation projected area density, *a*, with component-specific projected areas of the 1st order root, higher order root, and stem. The variations in *a* attributed to the random factor of root azimuth angle (Eq. (5.2)) were negligibly small (i.e., less than 2% of the value shown in Fig. 5.4); thus, these variations were not considered in the subsequent results. The slightly lower projected area of stems at the lower portion (z < 0.3 m) is attributed to the branching of stems. The parameter *a* showed significant vertical variation and the root is clearly the dominant factor affecting the value of *a* compared to the stem. While 1st order roots showed a moderate increase in their projected area towards the bed, the higher order roots showed a drastic increase below 0.3 m height, reaching almost twice of the 1st order near the bed (z < 0.1 m). Consequently, the value of *a* exhibited a nearly exponential increase with decreasing height and reached 1.06 m^{-1} near the bed (black solid line in Fig. 5.4). The vegetation solid volume fraction (φ) showed the same depth-variation as *a*, with a maximum value of 0.025 near the bed (Fig. S5.5).

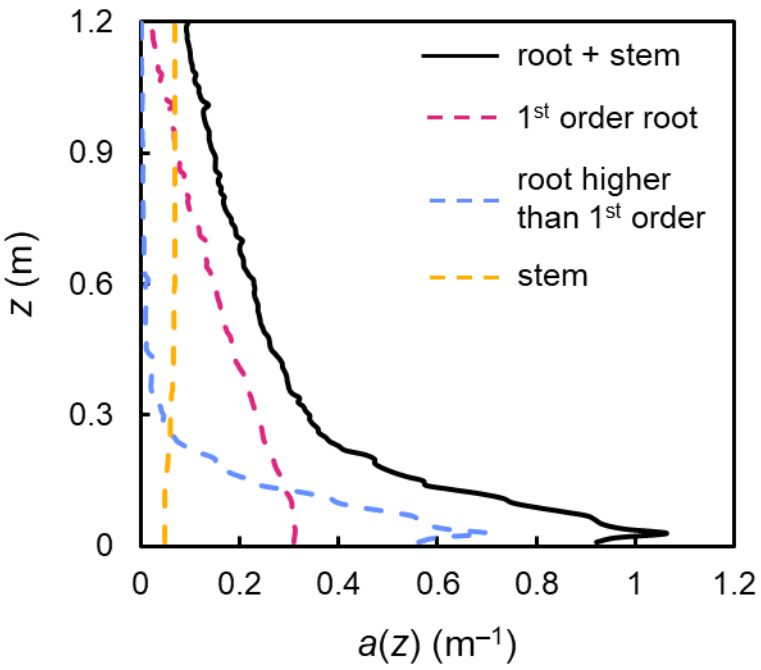

Figure 5.4. Vertical profile of spatially averaged vegetation projected area density (*a*, m^{-1}). The values of *a* were calculated with 0.01 m vertical resolution. The black solid line shows the median values of *a* from ensemble calculations (N = 20) while the red, blue, and yellow dashed lines show the projected area density of 1st order root (median values from ensemble

calculations), higher order root (median values from ensemble calculations), and stem, respectively.

5.3.2 Measured flow velocity and drag force

Figure 5.5 shows the time-series of measured hydrodynamic variables on September 10 and 11, 2018. Note that some data on $\langle U_{ref} \rangle$ and $\Delta\eta$ are absent due to instrument problems and measurement setup maintenance, therefore the number of transect mean vegetation drag measurements $\langle F_{veg,obs} \rangle_x$ is smaller than those of $\langle U_{ref} \rangle$ or $\Delta\eta$ (Fig. 5.5). The $\langle U_{ref} \rangle$ was generally around 1.5 times larger than the velocities measured at 5 cm above bed by EM sensors but became comparable when the water depth decreased ($h_{ref} < 0.2$ m). While these patterns were consistent during the two-days measurement, the $\langle U_{ref} \rangle$ on September 10, 14:00, was smaller than the velocity from EM sensors, possibly due to an unreliable measurement of $\langle U_{ref} \rangle$ using the propeller velocimeter (Fig. 5.5b).

The variations of the measured $\Delta\eta$ were 1.2–11.4 mm (Fig. 5.5c, g). The $\Delta\eta$ increased as water depth decreased. Accordingly, the vegetation drag per water volume $\langle F_{veg,obs} \rangle_x / h_{ref}$ showed an increase with decreasing water depth (Fig. 5.5d, h). The bed drag per water volume $\langle F_{bed} \rangle_x / h_{ref}$ was significantly smaller than the vegetation drag $\langle F_{veg,obs} \rangle_x / h_{ref}$, more than 15 times smaller during most of the measurement time.

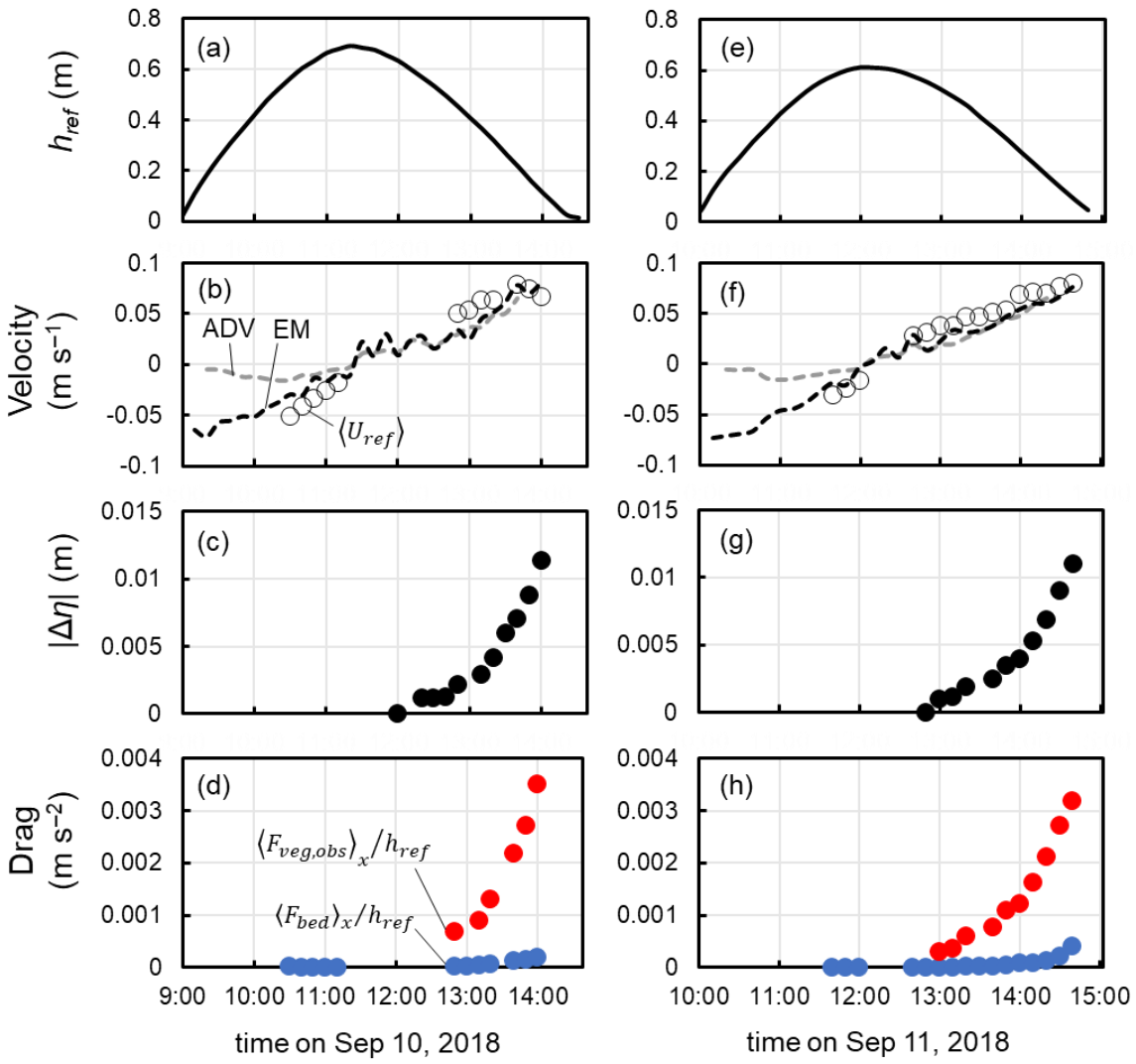

Figure 5.5. Time-series measurements on September 10 and 11, 2018, respectively, of (a, e) water depth near the reference tree (h_{ref}); (b, f) flow velocity (ADV-measured velocity (at 5 cm above the bed), average of EM-measured velocities (at 5 cm above the bed), and cross-sectional mean velocity $\langle U_{ref} \rangle$ near the reference tree provided by the velocity profiling); (c, g) water level difference between the ends of transect A–B ($\Delta\eta$); and (d, h) transect mean bed $\langle F_{bed} \rangle_x$ and vegetation $\langle F_{veg,obs} \rangle_x$ drag divided by h_{ref}. The angle bracket with subscript "x" denotes spatial average between A–B. The values for $\langle F_{bed} \rangle_x$ were given by Eq. (5.4).

Figure 5.6 shows the composite of velocity profile normalized by spatially averaged velocity at z = 0.1 m ($\langle u_{0.1} \rangle$) for the two-days measurement. The local velocity profiles (u_p) normalized by $\langle u_{0.1} \rangle$ showed some variations depending on the measurement locations (P1–4) (Fig. 5.6a). Overall, the flow velocities measured at the sides of the reference tree (P2, P4) were generally higher than the front (P3) or back (P1) of the tree, but these differences were more notable at z > 0.25 m. The velocities were greatly attenuated below 0.25-m height and

showed smaller variations among the locations. The profile of the spatially averaged velocity ($\langle u \rangle$) also showed a significant decrease below 0.25 m (Fig. 5.6b), corresponding to a significant increase in a (Fig. 5.4). The profile of $\langle u \rangle$ normalized by $\langle u_{0.1} \rangle$ showed agreement with the profile of $\sqrt{a_{0.1}/a(z)}$, a theoretical predictor of spatially averaged velocity profile (red line in Fig. 5.6b) derived by Lightbody and Nepf (2006), where $a_{0.1}$ is the value of a at 0.1 m above the bed (see Lightbody and Nepf, 2006 for the detail).

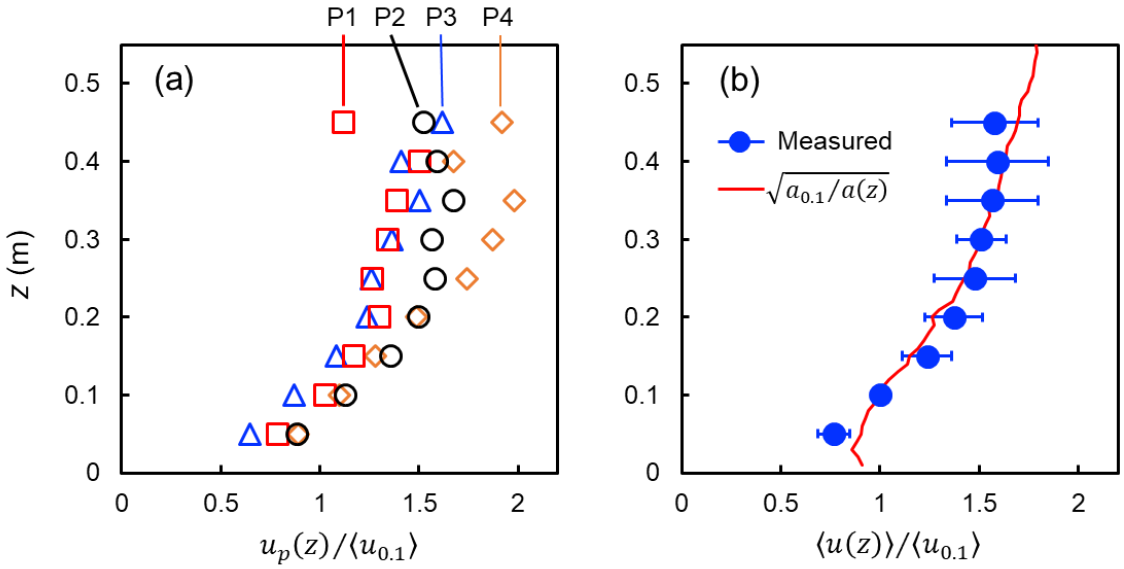

Figure 5.6. Vertical profile of streamwise horizontal velocity: (a) local velocity measured at P1–P4 (u_p) normalized by the spatial average (P1–P4) of velocity at 0.1 m above the bed ($\langle u_{0.1} \rangle$); and (b) spatial average of velocity ($\langle u \rangle$) normalized by $\langle u_{0.1} \rangle$ (markers) with a predictor of $\langle u(z) \rangle/\langle u_{0.1} \rangle$ (red line), where $a_{0.1}$ is the spatially averaged vegetation projected area density at 0.1 m above the bed. The normalized velocities shown are the mean values of the different velocity measurements during the two-days measurement and the horizontal bars in panel "(b)" indicate the standard deviation.

5.3.3 Drag coefficient and application of the drag model

The transect mean of cross-sectional mean velocity squared $\langle U^2 \rangle_x$ and vegetation drag averaged for unit water volume $\langle F_{veg,obs} \rangle_x / h_{ref}$ showed significant correlation (R^2 = 0.870), but separate line fittings for h_{ref} > 0.3 m and h_{ref} < 0.3 m exhibited different line slopes (Fig. 5.7a). Initially, we assumed the conserved water flux ($\langle U_{ref} \rangle h_{ref}$) across the transect, and therefore the transect mean of $\langle U \rangle$, $\langle U \rangle_x$, is given from $\langle U \rangle_x (x_2 - x_1) = \langle U_{ref} \rangle h_{ref} \int_{x_1}^{x_2} h^{-1} dx$. Note that the data taken on September 11, 14:00, was excluded from the line fitting as the data of $\langle U_{ref} \rangle$ may not be accurate (see Fig. 5.5b). Instead, the $\langle U^2 \rangle_x$ and drag averaged for unit vegetation

projected area $\langle F_{veg,obs}\rangle_x/\langle A\rangle_x$ showed higher correlation (R^2 = 0.901), and separate line fittings did not show significant difference in the line slopes (Fig. 5.7b).

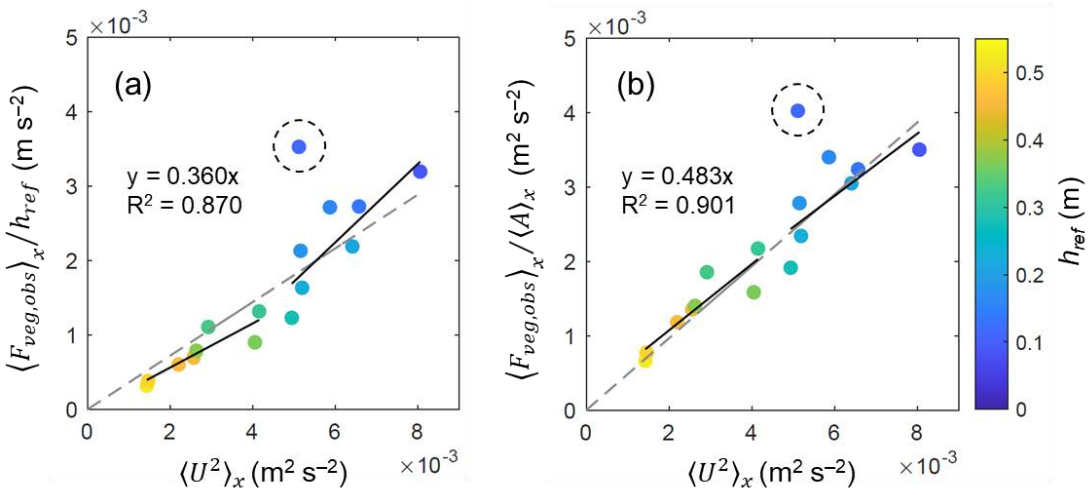

Figure 5.7. Comparison of the velocity squared with (a) transect mean vegetation drag $\langle F_{veg,obs}\rangle_x$ averaged for unit water volume and (b) for unit vegetation projected area. The parameter $\langle A\rangle_x$ is transect-mean total submerged vegetation projected area per ground area ($m^2\ m^{-2}$). The bracket with subscript "*x*" denotes spatial average between the ends of transect A–B. The gray dashed line indicates linear fit with intercept fixed at zero while the black lines indicate linear fit for h_{ref} > 0.3 m and h_{ref} < 0.3 m, respectively; the data enclosed by the dashed circle (data for September 11, 14:40) was excluded from the line fitting.

The value of C_D derived for each measurement using Eqs. (5.6) and (5.7) is shown in Fig. 5.8; a mean value and standard deviation of 1.01 ± 0.18 were obtained. The derived C_D showed close values to the results obtained in laboratory-based studies of Zhang et al. (2015), Maza et al. (2017), and Shan et al. (2019). The Reynolds number, *Re*, defined using the mean root diameter D_{root} as length scale, suggests the presence of the fully turbulent structures of root-generated wakes (> 1,000) and the derived C_D showed no dependence on *Re*. The C_D also did not show dependence on water depth (Fig. 5.8).

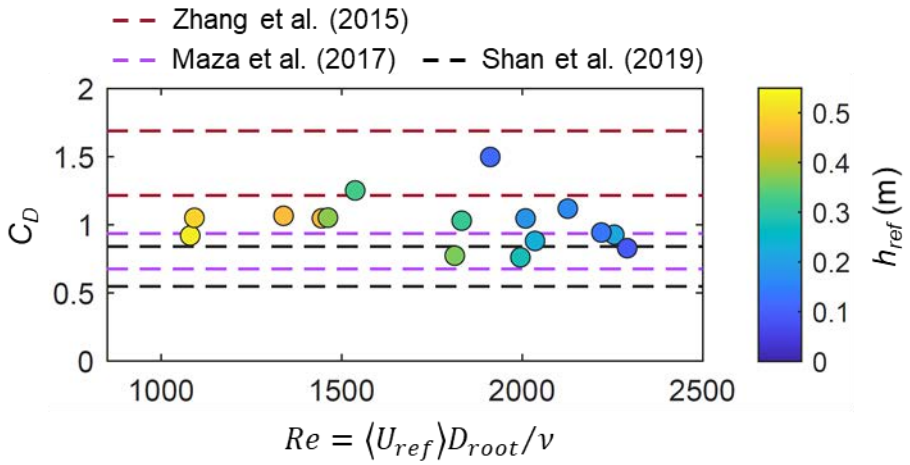

Figure 5.8. Drag coefficient (C_D) estimated for each hydrodynamic measurement and plotted against the Reynolds number (*Re*). The *Re* is defined by mean root diameter (D_{root}) as length scale and *v* for kinematic viscosity. The ranges of C_D obtained by flume experiments of Zhang et al. (2015), Maza et al. (2017), and Shan et al. (2019) (including both in-line and random tree distributions) are also shown. The *Re* defined by D_{root} in Zhang et al. (2015) is 360–720, and 314 in Shan et al. (2019). For Maza et al. (2017), the C_D range shown is the one derived in well-developed flow conditions with *Re* = 234–309, below which the dependence of C_D on *Re* was diminished.

Given the independent trend of C_D from *Re* and water depth and the small variations of the obtained values, it was inferred that C_D can take a constant value in the studied mangrove forest regardless of the timing of tidal cycles. The vegetation drag was then computed as model estimates using Eq. (5.7), a rearrangement of the drag model Eq. (5.1), with the mean C_D value (1.0) and the measured *a* profile shown in Fig. 5.4. The result showed a strong resemblance with the observations (near-unity correlation, R^2 = 0.86) for the vegetation drag averaged for unit water volume (Fig. 5.9).

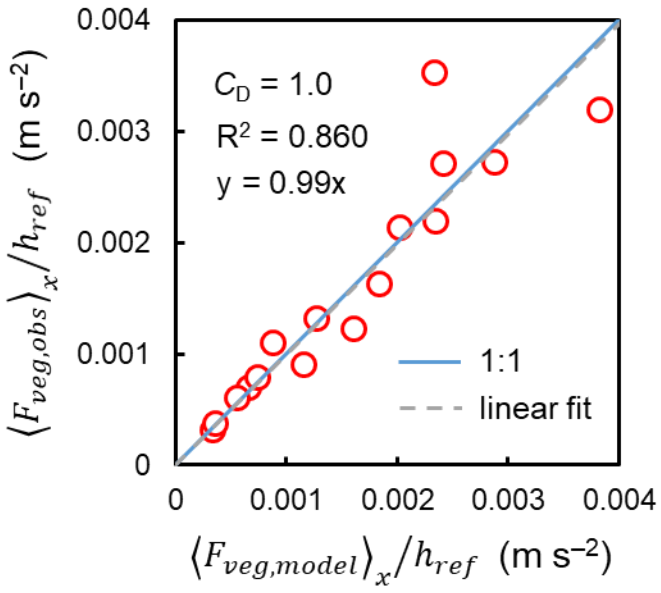

Figure 5.9. Comparison of measured and modeled vegetation drag. The modeled values were given by Eq. (5.7), a rearrangement of Eq. (5.1) with C_D = 1.0, and the measured profile for *a* shown in Fig. 5.4.

5.3.4 Prediction of drag using the Rhizophora root model

The *Rhizophora* root model predicted well the overall vertical profile of *a* composed of multiple order roots (Fig. 5.10a). This was achieved using a parameter setting for the root angle of approximated linear root shape θ_l = –34.5°, a value determined for the Bakhawan Ecopark study site (Fig. S5.4a). The modeled vegetation drag computed with the modeled *a* and C_D = 1.0 showed good agreement with the measured drag with a slope of 1.06 and R^2 = 0.84 of the linear fitted line (Fig. 5.10b). The use of θ_l value obtained in another mangrove forest (–41.9°; Fig. S5.4b) resulted in the underestimation of *a* due to the steeper angle of the approximated root shape (Eq. (5.11)) specifically at the lower part (z < 0.3 m) (Fig. 5.10c). Due to the underestimation of *a*, the predicted vegetation drag also showed an underestimated trend with a fitted line slope of 1.18, while the R^2 value did not significantly differ compared to when θ_l = –34.5° (Fig. 5.10d).

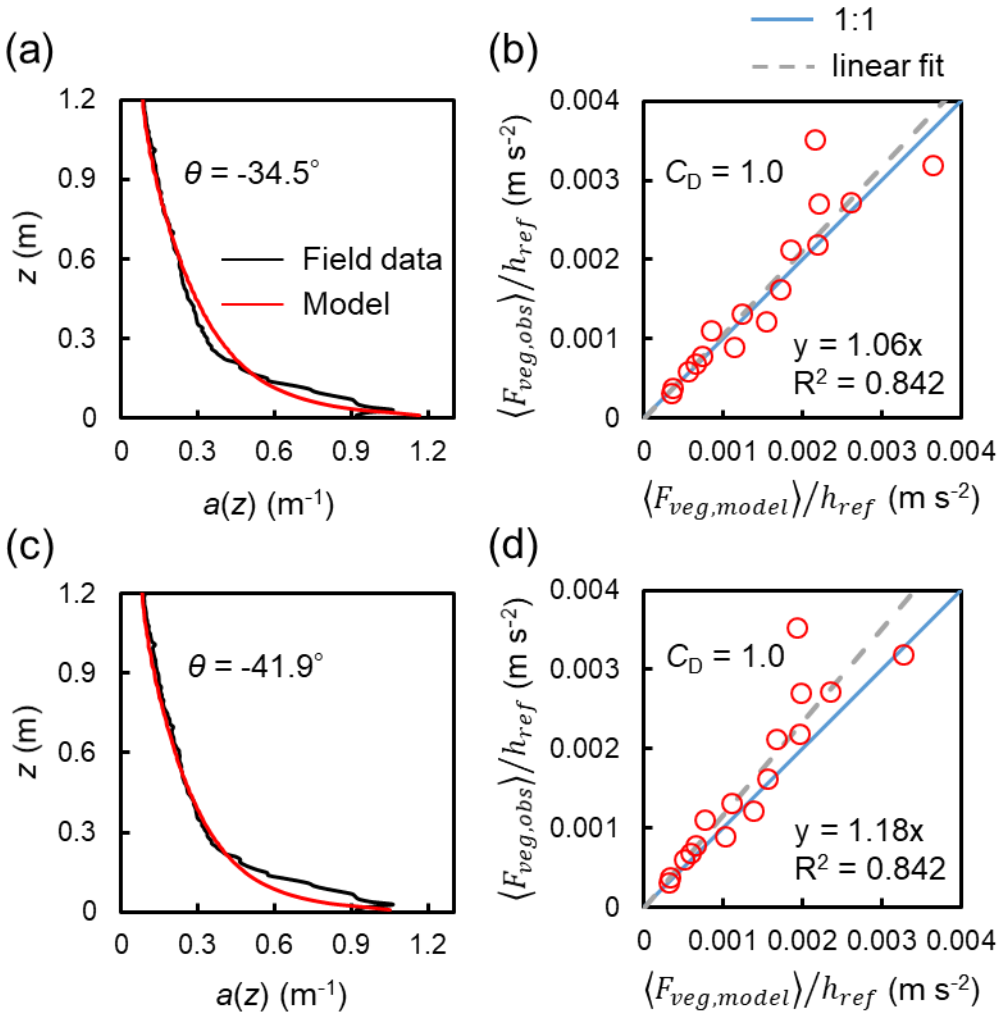

Figure 5.10. Comparisons of field-measured and modeled (a, c) *a* and (b, d) vegetation drag using the parameter settings of the root angle of approximated linear root shape θ_l = –34.5° and θ_l = –41.9°, respectively. The parameter setting θ_l = –34.5° is the value derived for the study site (see Fig. S5.4a) while θ_l = –41.9° is the value obtained from another mangrove forest (Fukido mangrove forest; Fig. S5.4b).

5.4 Discussion

5.4.1 Flow and drag in the studied field mangrove forest

The data presented here is the first to link the vegetation and hydrodynamic parameters in an actual *Rhizophora* mangrove forest. It showed a significant impact of the complex morphological structures of *Rhizophora* trees (Fig. 5.4) on flow structure (Fig. 5.6) and drag (Figs. 5.5 and 5.7). The normalized local velocity ($u_p/\langle u_{0.1}\rangle$) showed larger spatial

variations at higher elevation (z > 0.25 m) compared to lower elevation (Fig. 5.6a). Generally, roots are more clumped around the stem at the higher part of the root system, making for areas with low root blockage at the sides of the tree (P2, P4; Fig. 5.1d). The relatively higher velocity at P2 and P4 may be due to flow redistribution to the low blockage area (Maza et al., 2017), and the lower velocity at P1 or P3 may be due to the influence of wakes generated by roots and stems or velocity deceleration upstream of the clumped roots (Chen et al., 2012). Roots are spread widely at the lower part of the root system (Méndez-Alonzo et al., 2015; Fig. 5.1d) making a relatively uniform root distribution, which may explain the smaller spatial variations of velocity at lower elevations.

The profile of normalized velocity averaged for P1–P4 ($\langle u \rangle$) showed a good agreement with the theoretical model of Lightbody and Nepf (2006), which predicts the profile of spatially averaged velocity in vegetation with vertically-varying frontal area (Fig. 5.6b). The agreement of $\langle u \rangle$ normalized with $\langle u \rangle$ at z = 0.1 m with the model that only uses the profile of a normalized with a at z = 0.1 m as explanatory variable emphasizes the significant influence of vegetation morphology on flow structures in the studied mangrove forest. This agreement also implies the validity of the assumption that the velocity averaged for P1–P4 represents the spatially averaged velocity.

One key feature observed in the field mangrove forest is the depth dependence of drag per water volume as seen in Fig. 5.7a. The different slopes of the relationship between $\langle U^2 \rangle_x$ and $\langle F_{veg,obs} \rangle_x / h_{ref}$ depending on the water depth indicate the enhancement of vegetation drag per water volume relative to flow velocity when the water depth decreased. This may be considered the result of the vertical variation of the parameter a, leading to increased depth-averaged vegetation projected area to exert drag per unit water volume as the water depth decreases (Fig. 5.4). This highlighted the difference of drag characteristics in *Rhizophora* mangrove forests from an array of vertical emergent cylinders and the difficulty in parameterizing mangrove drag effects in roughness parameters such as Manning's roughness coefficient and Chezy coefficient (Li et al., 2012, 2014; Zhang et al., 2012). Interestingly, the depth dependence observed in the relationship between $\langle U^2 \rangle_x$ and $\langle F_{veg,obs} \rangle_x / h_{ref}$ was not evident when the $\langle U^2 \rangle_x$ was compared with $\langle F_{veg,obs} \rangle_x / \langle A \rangle_x$ (Fig. 5.7b), suggesting that the drag exerted per unit vegetation area solely depends on the square of flow velocity. This signifies that the quadratic drag law is applicable to the studied field mangrove forest.

5.4.2 Applicability of the drag model in the field mangrove forest

The spatially uniform distribution of the *Rhizophora* trees with the same age at the site investigated in this study resembles a setting that previous laboratory-based studies have

examined using model mangroves (Zhang et al., 2015; Maza et al., 2017; in-line distribution configuration in Shan et al., 2019). A notable difference between the field and model mangrove forest is the complexity of the root system. For instance, while the *Rhizophora* tree models used in Maza et al. (2017) and Shan et al. (2019) had only 1st order roots, we observed a significant contribution of the higher order roots to the projected area (Fig. 5.4). The tree density at our study site (0.36 m^{-2}; Table 5.1) was also higher than the conditions assumed in the previous flume experiments (e.g., 0.07 m^{-2} in Maza et al., 2017 in field-scale). Consequently, the spatially averaged vegetation projected area density, a, in our study site exhibited a much higher value than the conditions examined by flume experiments (nearly 10 times higher near the bed than the one in Maza et al., 2017). Yet, the vegetation complexity in this forest is not exceptional in terms of individual root system morphology (Yoshikai et al., 2021a, b) and spatially averaged vegetation projected area in other natural mangrove forests (Horstman et al., 2015; Norris et al., 2017).

Previous laboratory-based studies for flows in *Rhizophora* mangrove forest showed C_D values around 1 at Re high enough to ensure turbulent wakes (Zhang et al., 2015; Maza et al., 2017; Shan et al., 2019). Interestingly, the C_D derived for the studied field mangrove forest also showed values around 1.0 without dependence on Re (> 1,000) (Fig. 5.8), close to the ones obtained for the artificial laboratory model mangroves despite the complicated root systems that field mangroves have. This value also agrees with the value (1.0) which is typically used for the drag coefficient of other types of vegetation (e.g., seagrass) at high Re (Nepf, 2012; Kalra et al., 2017; Moki et al., 2020; Cao et al., 2021). The independence of C_D on water depth is consistent with the results of Maza et al. (2017), and Xu and Nepf (2020) who investigated drag exerted by a salt marsh plant *Typha* with vertically varying frontal area. The good agreement of the modeled drag using the mean value of obtained C_D (1.0) and observed drag verifies that Eq. (5.1) is a good model for predicting drag in real mangrove forests. The flow and drag in *Rhizophora* mangrove forests have been investigated mainly through flume experiments (Zhang et al., 2015; Maza et al., 2017; Shan et al., 2019). Our results provide the first evidence of the applicability of the drag model to field mangrove forests, the morphological complexities of which have not been well represented by flume experiments. Furthermore, given that observed vegetation projected area (Fig. 5.4) is much higher than the conditions assumed in the flume experiments, our results suggest that *Rhizophora* mangrove forests could have larger drag effects than what was shown by flume experiments. There may also be additional drag effects at the relatively rough vegetation surface (i.e., tree barks) compared to artificial mangrove models in previous flume experiments often made of plastic/metals; this effect, however, is difficult to isolate from our results. Although not in our site, the possible presence of biofouling fauna may provide additional drag in this effect

(Liénard et al., 2016). The significance of the contribution of surface friction to the total drag around natural vegetation remains uncertain and needs to be addressed in the future studies.

This study used spatially averaged equations (Eqs. (5.1), (5.4)–(5.7)) for deriving C_D. Therefore, the estimates of C_D could be significantly biased by the error in measuring the cross-sectional mean flow velocity, $\langle U \rangle$. While it is challenging to obtain the true value of cross-sectional mean velocity and assess the measurement error, we refer to the results of the PTV survey conducted around the reference tree (Note S5.1, Fig. S5.2). The results suggest that the velocity averaged for the four locations (P1–P4) deviates 10% to 20% from the PTV-estimated spatially averaged velocity. This deviation leads to C_D error estimates of 20% to 35%, which are close to the variations of the derived C_D values (Fig. 5.8). Thus, we consider that the derived C_D in the field mangrove forest may have errors of approximately 20–35% and the variations of the obtained C_D are attributed to the errors in measuring the cross-sectional mean flow velocity.

It should be noted that these results are for planted *Rhizophora* mangrove forests with uniform tree distribution and size and with vegetation complexity up to a = 1.06 m^{-1} and φ = 0.025 near the bed (Figs 5.4 and S5.4). Some factors which were not considered in this study may be significant for drag specifically in natural mangrove forests. For instance, some flume experiments showed elevated drag coefficient values for flows through high vegetation solid volume fraction (e.g., $\varphi > 0.15$) due to enhanced inertial drag effects (Tanino and Nepf, 2008; Liu et al., 2020; Gijón Mancheño et al., 2021). Although this may not be the case for our study site, Mazda et al. (1997) reported high solid volume fraction with such level in natural *Rhizophora* mangrove forests (φ = 0.1–0.3). Shan et al. (2019) investigated drag in model *Rhizophora* mangrove forests with in-line and random tree distributions, and demonstrated down to 23 % lower drag coefficients for in-line distributions than random distributions at high tree density conditions (> 0.1 m^{-2} in field-scale). This was because trees of in-line distribution tended to be located within the wake zones of upstream trees, experiencing diminished flow velocity, thereby lowering the drag. However, we noticed that such conditions could change with flow direction; in fact, trees in our site are not necessarily located just downstream of a tree (see Fig. 5.2a), thus it is uncertain whether the drag coefficient derived in this study reflects such effect or can be applied to natural *Rhizophora* mangrove forests (usually in random distribution). Also, it is not particularly rare in natural mangrove forests that the *Rhizophora* trees inhabit with other mangrove genera (e.g., *Avicennia* and *Bruguiera*) which have different root morphological structures (Horstman et al., 2015; Yoshikai et al., 2022), and flow and drag characteristics in such conditions are still uncertain. Additional investigations in natural mangrove forests are therefore needed to consider these aspects.

5.4.3 Implications for representing mangrove drag effects in hydrodynamic models

Representing mangrove drag effects using Eq. (5.1) in hydrodynamic models has been challenging because of the need for information on vegetation morphology for the parameter a, which is labor-intensive to obtain in the field. This study showed that a can be estimated from limited vegetation parameters (stem diameter and tree density) by using the *Rhizophora* root model of Yoshikai et al. (2021a). This model is valid for complicated root systems composed of multiple order roots, and accurately predicted the vertical profile of a in our study site (Fig. 5.10a). The good agreement of the modeled drag using the field-derived $C_D \approx 1$ and the predicted a with the measured drag (Fig. 5.10b) suggests that the drag in *Rhizophora* mangrove forests in the field can now be predicted once the input parameters as well as the site- or species-specific scaling parameters (α, α_1, β, β_1) of the *Rhizophora* root model are given. Note that we observed slight vertical variations in the stem projected area density attributed to stem branching (~0.02 m^{-1}; Fig. 5.4). However, these variations account for only 2.5 % of the submerged vegetation projected area per bed area (A) at maximum, indicating the minimum importance of the vertical variations in stem projected area in drag prediction.

The input parameters of the *Rhizophora* root model are basically DBH of individual trees (in Eq. (5.9)–(5.10)) and tree density, n_{tree} (in Eq. (5.3)), in the area to predict drag. These are basic information collected for forest inventories and are easy to measure in the field; these can be even estimated from remotely sensed data such as airborne LiDAR and UAV optical imagery (Jucker et al., 2017; Fatoyinbo et al., 2018; Zhu et al., 2019). Therefore, we expect that simulating the flows in mangrove forests using hydrodynamic models through the implementation of the drag model Eq. (5.1) is now feasible.

Some considerations should be noted when using the *Rhizophora* root model, especially on its parameter settings. First, the scaling parameters of root systems (Table 5.1) are site- or species-specific (Yoshikai et al., 2021a, b), thus applying the model to a forest without available information on the scaling relationship requires a field survey (see Yoshikai et al., 2021a or Note S5.3 for the methods in obtaining the scaling relationship in the field with reduced workload). Next, the value of the critical height HR_{min} should be also properly defined for the site, therefore we suggest the measurement of the minimum root heights in the field to find a representative value of HR_{min}. Lastly, the root angle of the approximated linear root shape in Eq. (5.11), θ_l, seems to vary depending on the site or species (Fig. S5.4). The use of the root angle determined for the other mangrove forest, which is 7.5° steeper than at our study site, affected the prediction of the a and the drag to some extent as shown in Fig. 5.10c–d. The θ_l was determined from the relationship between the number of roots and root projected

area, $n_{root,i}(z)$ and $a_{root0,i}(z)$, and both parameters are labor-intensive to obtain in the field. Hence, we suggest to take the response of the predicted drag with a different setting of θ_l provided in Fig. 5.10 as model uncertainty when applying the value to other *Rhizophora* mangrove forests. Nevertheless, the drag can still be predicted with reasonable accuracy using estimates of θ_l from other mangrove forests (Fig. 5.10c–d), thus highlighting the significance of this work in contributing to a better prediction of drag in mangrove forests.

5.5 Conclusions

This study presents the drag force and drag coefficient estimated from a 17-year-old planted *Rhizophora* mangrove forest based on comprehensive hydrodynamics and vegetation morphology data collected in the field. We found much higher values of the vegetation projected area density, a, in the field than the conditions assumed in previous flume experiments mainly due to root branching and high tree density. Despite the difference in the vegetation complexity, we confirmed the adherence of drag in the *Rhizophora* mangrove forest to the quadratic drag law as in the flume experiments. The derived drag coefficient, C_D, also showed comparable values to the ones derived for model-mangroves in previous flume experiments. Thus, the drag model proposed by laboratory-based studies can be applied to *Rhizophora* mangrove forests having high morphological complexity. However, the results presented are for the planted *Rhizophora* mangrove forests with uniform tree distribution and size; the applicability of results to other sites, specifically to natural *Rhizophora* mangrove forests needs to be addressed in future studies. We also showed that a can be predicted from stem diameter and tree density, which can be easily measured in the field, using an empirical *Rhizophora* root model that employs site/species specific scaling parameters. While drag prediction using the predicted a showed good accuracy, it also showed relatively high sensitivity to θ_l (root angle of approximated linear root shape) – a labor-intensive parameter to obtain in the field. This should be taken as model uncertainty when applying the parameter setting to other *Rhizophora* mangrove forests. These results provide a way to use the drag model in hydrodynamic models by incorporating realistic values of the drag coefficient and spatially variable vegetation projected area density for representing mangrove drag effects, overall contributing to a better understanding of flow, transport, and geomorphic dynamics in *Rhizophora* mangrove forests.

5.6 References

Adame, M. F., Neil, D., Wright, S. F., & Lovelock, C. E. (2010). Sedimentation within and among mangrove forests along a gradient of geomorphological settings. Estuarine, Coastal and Shelf Science, 86(1), 21–30.

Best, Ü. S., van der Wegen, M., Dijkstra, J., Reyns, J., van Prooijen, B. C., & Roelvink, D. (2022). Wave attenuation potential, sediment properties and mangrove growth dynamics data over Guyana's intertidal mudflats: assessing the potential of mangrove restoration works. Earth System Science Data, 14(5), 2445–2462.

Biron, P. M., Robson, C., Lapointe, M. F., & Gaskin, S. J. (2004). Comparing different methods of bed shear stress estimates in simple and complex flow fields. Earth Surface Processes and Landforms: The Journal of the British Geomorphological Research Group, 29(11), 1403–1415.

Bryan, K. R., Nardin, W., Mullarney, J. C., & Fagherazzi, S. (2017). The role of cross-shore tidal dynamics in controlling intertidal sediment exchange in mangroves in Cù Lao Dung, Vietnam. Continental Shelf Research, 147, 128–143.

Cao, Z., Zhang, Y., Wolfram, P. J., Brus, S. R., Rowland, J. C., Xu, C., ... & Petersen, M. R. (2021). Effects of different vegetation drag parameterizations on the tidal propagation in coastal marshlands. Journal of Hydrology, 603, 126775.

Chen, Y., Li, Y., Cai, T., Thompson, C., & Li, Y. (2016). A comparison of biohydrodynamic interaction within mangrove and saltmarsh boundaries. Earth Surface Processes and Landforms, 41(13), 1967–1979.

Chen, Y., Li, Y., Thompson, C., Wang, X., Cai, T., & Chang, Y. (2018). Differential sediment trapping abilities of mangrove and saltmarsh vegetation in a subtropical estuary. Geomorphology, 318, 270–282.

Chen, Z., Ortiz, A., Zong, L., & Nepf, H. (2012). The wake structure behind a porous obstruction and its implications for deposition near a finite patch of emergent vegetation. Water Resources Research, 48(9).

Donato, D. C., Kauffman, J. B., Murdiyarso, D., Kurnianto, S., Stidham, M., & Kanninen, M. (2011). Mangroves among the most carbon-rich forests in the tropics. Nature geoscience, 4(5), 293–297.

Ezcurra, P., Ezcurra, E., Garcillán, P. P., Costa, M. T., & Aburto-Oropeza, O. (2016). Coastal landforms and accumulation of mangrove peat increase carbon sequestration and storage. Proceedings of the National Academy of Sciences, 113(16), 4404–4409.

Fatoyinbo, T., Feliciano, E. A., Lagomasino, D., Lee, S. K., & Trettin, C. (2018). Estimating mangrove aboveground biomass from airborne LiDAR data: a case study from the Zambezi River delta. Environmental Research Letters, 13(2), 025012.

Friess, D. A., Rogers, K., Lovelock, C. E., Krauss, K. W., Hamilton, S. E., Lee, S. Y., ... & Shi, S. (2019). The state of the world's mangrove forests: past, present, and future. Annual Review of Environment and Resources, 44, 89–115.

Furukawa, K., Wolanski, E., & Mueller, H. (1997). Currents and sediment transport in mangrove forests. Estuarine, Coastal and Shelf Science, 44(3), 301–310.

Gijón Mancheño, A., Jansen, W., Winterwerp, J.C., & Uijttewaal, W. S. J. (2021). Predictive model of bulk drag coefficient for a nature-based structure exposed to currents. Scientific reports, 11, 3517. https://doi.org/10.1038/s41598-021-83035-0

Gijsman, R., Horstman, E. M., van der Wal, D., Friess, D. A., Swales, A., & Wijnberg, K. M. (2021). Nature-based engineering: a review on reducing coastal flood risk with mangroves. Frontiers in Marine Science, 8, 825.

Giri, C., Ochieng, E., Tieszen, L. L., Zhu, Z., Singh, A., Loveland, T., ... & Duke, N. (2011). Status and distribution of mangrove forests of the world using earth observation satellite data. Global Ecology and Biogeography, 20(1), 154–159.

Horstman, E. M., Bryan, K. R., & Mullarney, J. C. (2021). Drag variations, tidal asymmetry and tidal range changes in a mangrove creek system. Earth Surface Processes and Landforms.

Horstman, E. M., Dohmen-Janssen, C. M., Bouma, T. J., & Hulscher, S. J. (2015). Tidal-scale flow routing and sedimentation in mangrove forests: Combining field data and numerical modelling. Geomorphology, 228, 244–262.

Horstman, E. M., Dohmen-Janssen, C. M., Narra, P. M. F., Van den Berg, N. J. F., Siemerink, M., & Hulscher, S. J. (2014). Wave attenuation in mangroves: A quantitative approach to field observations. Coastal engineering, 94, 47–62.

Jucker, T., Caspersen, J., Chave, J., Antin, C., Barbier, N., Bongers, F., ... & Coomes, D. A. (2017). Allometric equations for integrating remote sensing imagery into forest monitoring programmes. Global change biology, 23(1), 177–190.

Kalra, T. S., Aretxabaleta, A., Seshadri, P., Ganju, N. K., & Beudin, A. (2017). Sensitivity analysis of a coupled hydrodynamic-vegetation model using the effectively subsampled quadratures method (ESQM v5. 2). Geoscientific Model Development, 10(12), 4511–4523.

Krauss, K. W., McKee, K. L., Lovelock, C. E., Cahoon, D. R., Saintilan, N., Reef, R., & Chen, L. (2014). How mangrove forests adjust to rising sea level. New Phytologist, 202(1), 19–34.

Lentz, S. J., Davis, K. A., Churchill, J. H., & DeCarlo, T. M. (2017). Coral reef drag coefficients–water depth dependence. Journal of Physical Oceanography, 47(5), 1061–1075.

Li, L., Wang, X. H., Andutta, F., & Williams, D. (2014). Effects of mangroves and tidal flats on suspended-sediment dynamics: Observational and numerical study of Darwin Harbour, Australia. Journal of Geophysical Research: Oceans, 119(9), 5854–5873.

Li, L., Wang, X. H., Williams, D., Sidhu, H., & Song, D. (2012). Numerical study of the effects of mangrove areas and tidal flats on tides: A case study of Darwin Harbour, Australia. Journal of Geophysical Research: Oceans, 117(C6).

Liénard, J., Lynn, K., Strigul, N., Norris, B. K., Gatziolis, D., Mullarney, J. C., ... & Henderson, S. M. (2016). Efficient three-dimensional reconstruction of aquatic vegetation geometry: Estimating morphological parameters influencing hydrodynamic drag. Estuarine, Coastal and Shelf Science, 178, 77–85.

Lightbody, A. F., & Nepf, H. M. (2006). Prediction of velocity profiles and longitudinal dispersion in salt marsh vegetation. Limnology and oceanography, 51(1), 218–228.

Liu, M. Y., Huai, W. X., Yang, Z. H., & Zeng, Y. H. (2020). A genetic programming-based model for drag coefficient of emergent vegetation in open channel flows. Advances in Water Resources, 140, 103582.

Macreadie, P. I., Robertson, A. I., Spinks, B., Adams, M. P., Atchison, J. M., Bell-James, J., ... & Rogers, K. (2022). Operationalizing marketable blue carbon. One Earth, 5(5), 485–492.

Maza, M., Adler, K., Ramos, D., Garcia, A. M., & Nepf, H. (2017). Velocity and drag evolution from the leading edge of a model mangrove forest. Journal of Geophysical Research: Oceans, 122(11), 9144–9159.

Mazda, Y., Wolanski, E., King, B., Sase, A., Ohtsuka, D., & Magi, M. (1997). Drag force due to vegetation in mangrove swamps. Mangroves and salt marshes, 1(3), 193–199.

Méndez-Alonzo, R., Moctezuma, C., Ordoñez, V. R., Angeles, G., Martínez, A. J., & López-Portillo, J. (2015). Root biomechanics in *Rhizophora mangle*: anatomy, morphology and ecology of mangrove's flying buttresses. Annals of Botany, 115(5), 833–840.

Menéndez, P., Losada, I. J., Beck, M. W., Torres-Ortega, S., Espejo, A., Narayan, S., ... & Lange, G. M. (2018). Valuing the protection services of mangroves at national scale: The Philippines. Ecosystem services, 34, 24–36.

Menéndez, P., Losada, I. J., Torres-Ortega, S., Narayan, S., & Beck, M. W. (2020). The global flood protection benefits of mangroves. Scientific reports, 10(1), 1–11.

Moki, H., Taguchi, K., Nakagawa, Y., Montani, S., & Kuwae, T. (2020). Spatial and seasonal impacts of submerged aquatic vegetation (SAV) drag force on hydrodynamics in shallow waters. Journal of Marine Systems, 209, 103373.

Monismith, S. G., Hirsh, H., Batista, N., Francis, H., Egan, G., & Dunbar, R. B. (2019). Flow and drag in a seagrass bed. Journal of Geophysical Research: Oceans, 124(3), 2153–2163.

Mullarney, J. C., Henderson, S. M., Reyns, J. A., Norris, B. K., & Bryan, K. R. (2017). Spatially varying drag within a wave-exposed mangrove forest and on the adjacent tidal flat. Continental Shelf Research, 147, 102–113.

Nepf, H. M. (1999). Drag, turbulence, and diffusion in flow through emergent vegetation. Water resources research, 35(2), 479–489.

Nepf, H. M. (2012). Flow and transport in regions with aquatic vegetation. Annual review of fluid mechanics, 44, 123–142.

Norris, B. K., Mullarney, J. C., Bryan, K. R., & Henderson, S. M. (2017). The effect of pneumatophore density on turbulence: a field study in a *Sonneratia*-dominated mangrove forest, Vietnam. Continental Shelf Research, 147, 114–127.

Ohira, W., Honda, K., Nagai, M., & Ratanasuwan, A. (2013). Mangrove stilt root morphology modeling for estimating hydraulic drag in tsunami inundation simulation. Trees, 27(1), 141–148.

Ong, J. E., Gong, W. K., & Wong, C. H. (2004). Allometry and partitioning of the mangrove, *Rhizophora apiculata*. Forest Ecology and Management, 188(1-3), 395–408.

Pope, N. D., Widdows, J., & Brinsley, M. D. (2006). Estimation of bed shear stress using the turbulent kinetic energy approach—A comparison of annular flume and field data. Continental Shelf Research, 26(8), 959–970.

Primavera, J. H., & Esteban, J. M. A. (2008). A review of mangrove rehabilitation in the Philippines: successes, failures and future prospects. Wetlands Ecology and Management, 16(5), 345–358.

Rogers, K., Saintilan, N., & Woodroffe, C. D. (2014). Surface elevation change and vegetation distribution dynamics in a subtropical coastal wetland: Implications for coastal wetland response to climate change. Estuarine, Coastal and Shelf Science, 149, 46–56.

Saintilan, N., Khan, N. S., Ashe, E., Kelleway, J. J., Rogers, K., Woodroffe, C. D., & Horton, B. P. (2020). Thresholds of mangrove survival under rapid sea level rise. Science, 368(6495), 1118–1121.

Sasmito, S. D., Kuzyakov, Y., Lubis, A. A., Murdiyarso, D., Hutley, L. B., Bachri, S., ... & Borchard, N. (2020). Organic carbon burial and sources in soils of coastal mudflat and mangrove ecosystems. Catena, 187, 104414.

Shan, Y., Liu, C., & Nepf, H. (2019). Comparison of drag and velocity in model mangrove forests with random and in-line tree distributions. Journal of Hydrology, 568, 735–746.

Sharma, S., MacKenzie, R. A., Tieng, T., Soben, K., Tulyasuwan, N., Resanond, A., ... & Litton, C. M. (2020). The impacts of degradation, deforestation and restoration on mangrove ecosystem carbon stocks across Cambodia. Science of the Total Environment, 706, 135416.

Suello, R. H., Hernandez, S. L., Bouillon, S., Belliard, J. P., Dominguez-Granda, L., Van de Broek, M., ... & Temmerman, S. (2022). Mangrove sediment organic carbon storage and sources in relation to forest age and position along a deltaic salinity gradient. Biogeosciences, 19(5), 1571–1585.

Suwa, R., Rollon, R., Sharma, S., Yoshikai, M., Albano, G. M. G., Ono, K., ... & Nadaoka, K. (2021). Mangrove biomass estimation using canopy height and wood density in the South East and East Asian regions. Estuarine, Coastal and Shelf Science, 248, 106937.

Taillardat, P., Friess, D. A., & Lupascu, M. (2018). Mangrove blue carbon strategies for climate change mitigation are most effective at the national scale. Biology Letters, 14(10), 20180251.

Tanino, Y., & Nepf, H. M. (2008). Laboratory investigation of mean drag in a random array of rigid, emergent cylinders. Journal of Hydraulic Engineering, 134(1), 34–41.

Tomlinson, P.B., 2016. The Botany of Mangroves. Cambridge University Press, Cambridge.

Willemsen, P. W. J. M., Horstman, E. M., Borsje, B. W., Friess, D. A., & Dohmen-Janssen, C. M. (2016). Sensitivity of the sediment trapping capacity of an estuarine mangrove forest. Geomorphology, 273, 189–201.

Xie, D., Schwarz, C., Brückner, M. Z., Kleinhans, M. G., Urrego, D. H., Zhou, Z., & Van Maanen, B. (2020). Mangrove diversity loss under sea-level rise triggered by bio-morphodynamic feedbacks and anthropogenic pressures. Environmental Research Letters, 15(11), 114033.

Xu, Y., & Nepf, H. (2020). Measured and predicted turbulent kinetic energy in flow through emergent vegetation with real plant morphology. Water Resources Research, 56(12), e2020WR027892.

Xu, Y., & Nepf, H. (2021). Suspended sediment concentration profile in a *Typha latifolia* canopy. Water Resources Research, 57(9), e2021WR029902.

Yoshikai, M. (2021). Data for field measurement and prediction of drag in a planted *Rhizophora* mangrove forest [Dataset]. Zenodo. https://doi.org/10.5281/zenodo.5760343.

Yoshikai, M., Nakamura, T., Suwa, R., Argamosa, R., Okamoto, T., Rollon, R., ... & Nadaoka, K. (2021a). Scaling relations and substrate conditions controlling the complexity of *Rhizophora* prop root system. Estuarine, Coastal and Shelf Science, 248, 107014.

Yoshikai, M., Nakamura, T., Suwa, R., Rollon, R., & Nadaoka, K. (2021b). Measurement and modeling of above-ground root systems as attributes of flow and wave attenuation function of mangroves, in: Mangroves: Ecology, Biodiversity and Management, edited by: Rastogi RP, Phulwaria M, Gupta DK, Springer Singapore, Singapore, pp 279–303.

Yoshikai, M., Nakamura, T., Suwa, R., Sharma, S., Rollon, R., Yasuoka, J., Egawa, R., & Nadaoka, K. (2022). Predicting mangrove forest dynamics across a soil salinity gradient using an individual-based vegetation model linked with plant hydraulics. Biogeosciences, 19, 1813–1832, https://doi.org/10.5194/bg-19-1813-2022, 2022.

Zhang, X., Chua, V. P., & Cheong, H. F. (2015). Hydrodynamics in mangrove prop roots and their physical properties. Journal of hydro-environment research, 9(2), 281–294.

Zhang, K., Liu, H., Li, Y., Xu, H., Shen, J., Rhome, J., & Smith III, T. J. (2012). The role of mangroves in attenuating storm surges. Estuarine, Coastal and Shelf Science, 102, 11–23.

Zhu, X., Hou, Y., Weng, Q., & Chen, L. (2019). Integrating UAV optical imagery and LiDAR data for assessing the spatial relationship between mangrove and inundation across a subtropical estuarine wetland. ISPRS Journal of Photogrammetry and Remote Sensing, 149, 146–156.

Supporting Information for Chapter 5

Note S5.1. Particle tracking velocimetry survey

A particle tracking velocimetry (PTV) survey was conducted on March 20, 2019, during spring tide, to examine the flow field around a reference tree (Fig. 5.1c). Four downward-looking digital video cameras (RICOH WG-5) were attached on the stem of the reference tree and oriented in such a way that the different camera views covered the entire root system. A pressure sensor was deployed near the reference tree to monitor water depth. Floating particles (represented by leaves of *Moringa oleifera Lam*, 1 cm dimension in average) were prepared prior to the survey. The PTV was conducted twice at different water depths during flood tide (22:00 and 22:40 on March 20, 2019; Fig. S5.2c). Before releasing the particles, a square scale with known dimension was placed on the water surface seen by each camera view; this was used for image rectification and scaling. The particles were then released, and the movement of particles around the reference tree was monitored by the four video cameras with a rate of 30 frames per second. After the particle release, velocity profiling using an electro-magnetic current meter (AEM213-DA sensor) was conducted at four locations (P1–P4), as performed in the drag survey described in the manuscript. However, note that profiling was not done when the water depth was shallow for the profiling (22:40 on March 20, 2019).

The trajectories of particles were analyzed for each video data using the open-source PTV software TracTrac developed by Heyman (2019). The video data with particle trajectories were rectified and projected to real-world coordinates with a homography matrix determined based on the square scale (Patalano et al., 2017). The projected data from each camera were combined to make one mosaic image with trajectories that covers the entire root system of the tree. The image was partitioned into 10 cm × 10 cm grids, and in each grid, particle displacements per 10 frames ($dt \approx 0.33$ second) were extracted for all particles as displacement samples. The mean particle displacement per dt was calculated by averaging all the displacement samples in a grid, and the mean velocity in the grid was derived from the mean displacement (Fig. S5.2a–b).

The mean velocities in the grids were spatially averaged, and the major axis component of the averaged velocity was represented as the stream-wise spatially averaged velocity at the water surface, $\langle u \rangle$. The mean velocities of regions where velocity profiling was conducted were also extracted (P1–P4; Fig. S5.2a–b), and the surface stream-wise velocity averaged for the four locations $\langle u_{p1–4} \rangle$ were likewise derived. The $\langle u_{p1–4} \rangle$ was also estimated from the surface velocities measured by the AEM213-DA sensor. The $\langle u_{p1–4} \rangle$ was then

compared with $\langle u \rangle$ to examine the validity of the assumption that the average of the velocities at the four locations, $\langle u_{p1-4} \rangle$, represents the spatial average in the area, $\langle u \rangle$.

The results showed that the $\langle u_{p1-4} \rangle$ derived from PTV and current meter sensor are comparable with values 6.3 cm s^{-1} and 6.6 cm s^{-1}, respectively (Fig. S5.2d), which ensures a certain accuracy of the PTV-derived velocity field. The comparison with $\langle u \rangle$ showed 10% to 20% deviation of $\langle u_{p1-4} \rangle$ from $\langle u \rangle$. The values of deviation were referred to as errors of estimating the spatially averaged velocity from velocities at the four locations.

Note S5.2. Acoustic Doppler Velocimeter (ADV) data processing

The instantaneous velocity data collected by the ADV were despiked using the phase-space method described in Mori et al. (2007). The despiked velocities (eastward, northward, and vertical) were rotated to give the velocities along the *x*, *y*, and *z*-axes, where the instrument tilt was corrected to make the averaged vertical velocity zero (Lee et al., 2004). Bed drag (F_{bed}, m^2 s^{-2}) was then determined from Reynolds stress, $(-\overline{u'w'})$, where *u*' and *w*' are the velocity fluctuations of *x*- and *z*-axis components (m s^{-1}), respectively, and the overbar denotes the time average (note that velocities in the equations in the manuscript denote time-averaged values without the overbars).

As shown in Figs. 5.5b and 5.5f, the velocity measured by ADV during the flood tides largely deviated from the EM-measured velocity and $\langle U_{ref} \rangle$, possibly due to the local influence of nearby roots (Fig. 5.2c). Thus, the Reynolds stress measured during flood tides might have been affected by the wakes generated by the roots aside from the bottom friction. In this regard, we excluded the data during flood tides when estimating the bed drag coefficient.

The estimated drag coefficient, C_{bed}, was 4.2×10^{-3} (Fig. S5.3). This value is higher but in the same order of magnitude as the drag coefficient observed in muddy tidal environment (e.g., 2.5×10^{-3} in Mariotti and Fagherazzi, 2012).

Note S5.3. A simple field measurement method for the derivation of scaling parameters for the root system

In this study we used two scaling relations in the *Rhizophora* root system – the DBH–*S* relationship using parameters β and β_1, and the DBH–HR_{max} relationship using parameters α and α_1 as described in Section 5.2.6. We used the values reported in Yoshikai et al. (2021a) for our study site (Table 5.1). In that work, the heights of all roots (*HR*) were measured for a tree, then the vertical distribution of the number of roots was derived from height data. The

value of S for a tree was then determined so that the modeled vertical distribution of roots provided in Eq. (5.8) constrained by HR_{min} fits the measured one.

While the DBH–HR_{max} relationship can be easily obtained in the field, obtaining DBH–S relationship by measuring the heights of all roots could be labor-intensive. In this regard, Yoshikai et al. (2021a) proposed a simple method for the derivation of the value of S based on the following equation, which is a rearrangement of Eq. (5.10)

$$\log S = \frac{\log HR_{min} - \log HR_{max}}{t-1} \quad \text{(S5.1)}$$

From this equation, the value of S for a tree can be estimated by measuring the maximum and minimum root heights (HR_{max} and HR_{min}, respectively) and the total number of roots (t) of the tree. While the height measurement of 30 roots by two persons would take around 10 minutes, the measurement of HR_{max} and HR_{min} and counting of roots can be done within 3 minutes. This simplification greatly reduces the amount of field work needed to obtain the site/species-specific scaling parameters.

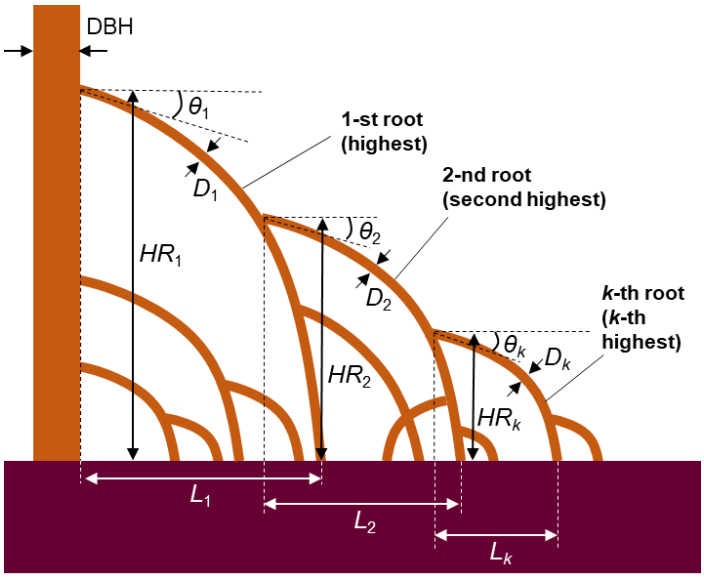

Figure S5.1. Numbering of roots and measured geometric parameters of roots (HR_k: height, L_k: horizontal distance, θ_k: angle, D_k, diameter of k-th root) and stem (DBH: diameter at breast height). Modified from Yoshikai et al. (2021a).

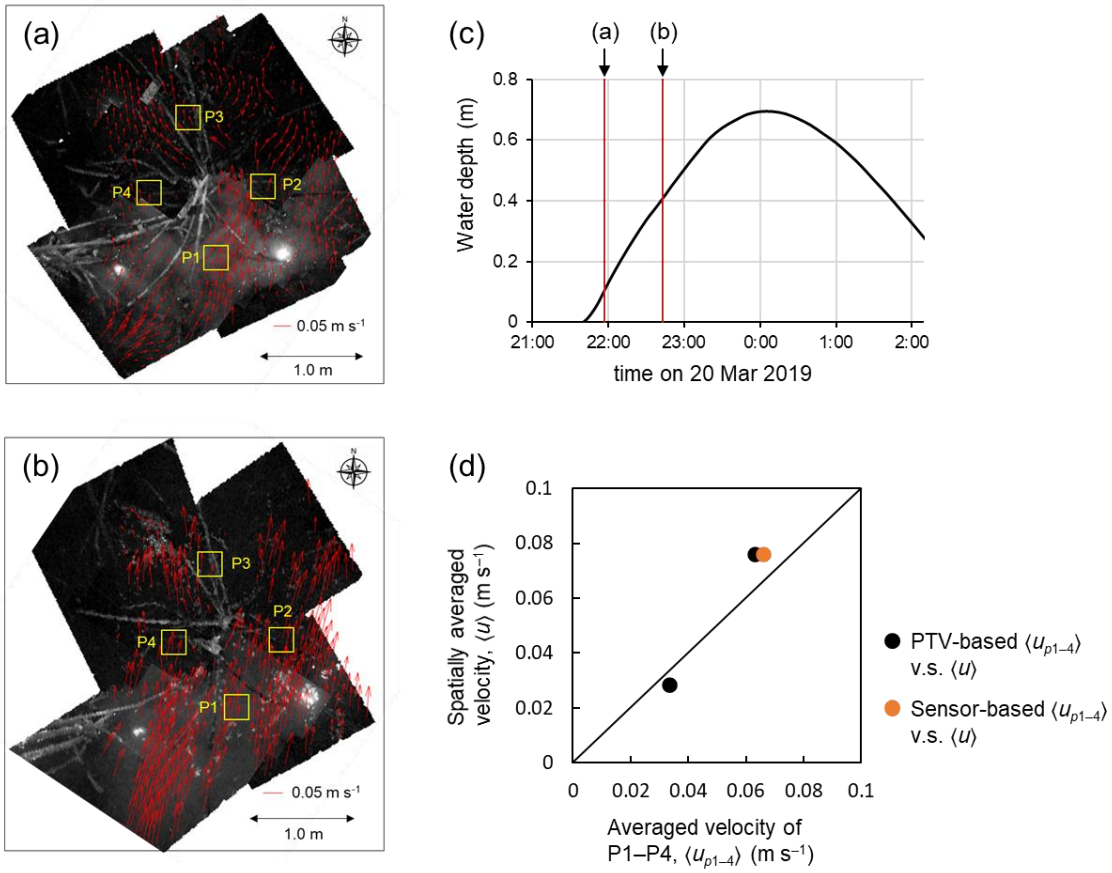

Figure S5.2. Mean velocity fields around the reference tree at (a) 22:00 and (b) 22:40 on March 20, 2019; (c) time-series data of water depth near the reference tree (the timing when the particles were released are indicated by the red lines); and (d) comparison between $\langle u_{p1-4} \rangle$ and $\langle u \rangle$.

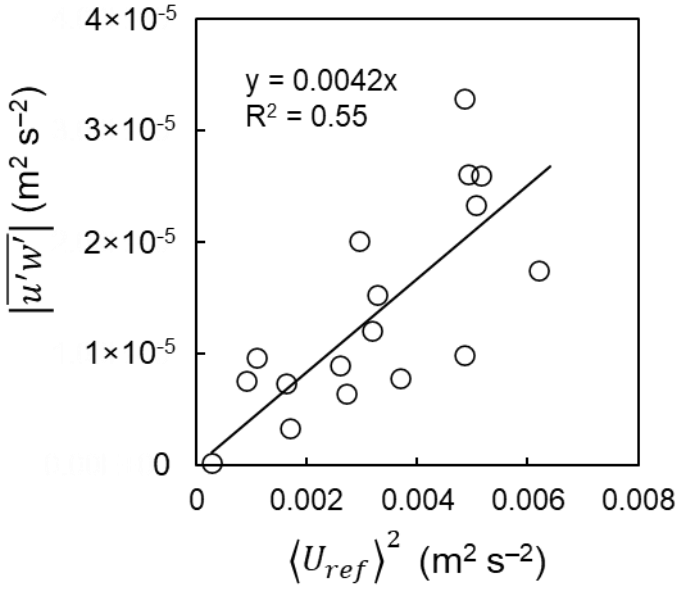

Figure S5.3. Relationship between $\langle U_{ref} \rangle^2$ and Reynolds stress $\left|\overline{u'w'}\right|$. The slope of the fitted line represents the bed drag coefficient.

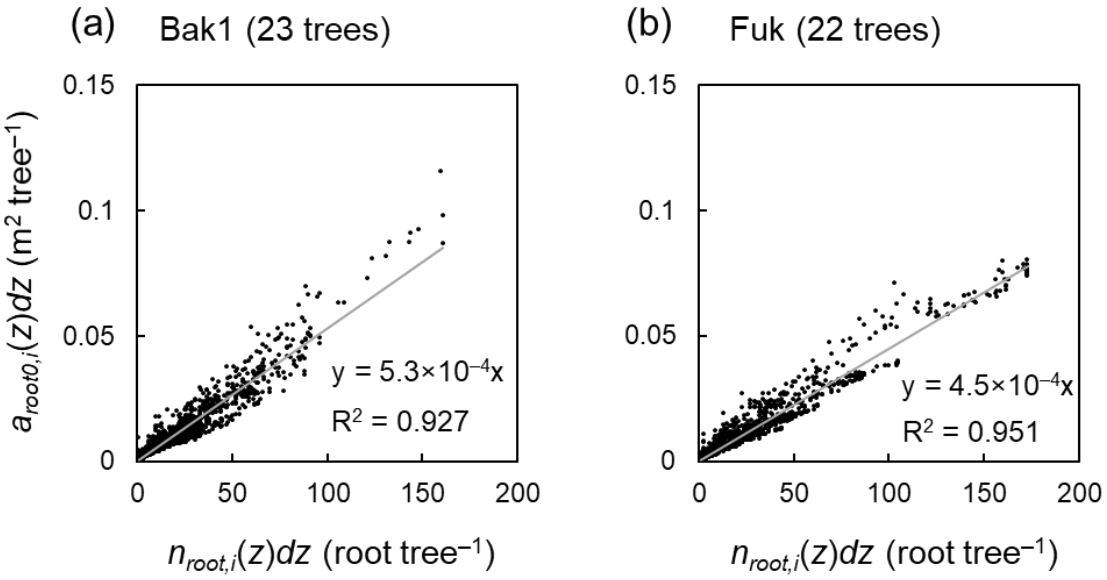

Figure S5.4. Comparison of number of roots per *dz* per tree, $n_{root,i}(z)$ (root m^{-1} tree^{-1}), and root projected area with zero azimuth angles per *dz* per tree, $a_{root0,i}(z)$ (m tree^{-1}), for (a) our study site for drag measurement (referred to as Bak1 in Yoshikai et al., 2021) and (b) Fukido mangrove forest in Ishigaki Island, Japan (Fuk in Yoshikai et al., 2021). A 0.01-m vertical height interval, *dz*, was used to compute the vertical profiles. Data from 23 trees in Bak1 and 22 trees in Fuk were plotted, respectively.

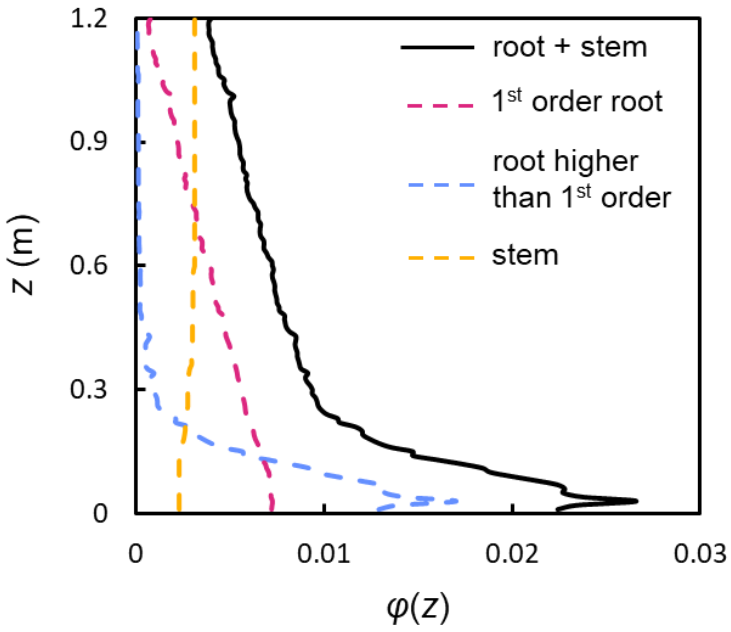

Figure S5.5. Vertical profile of solid volume fraction (φ, dimensionless), where the values of φ were calculated with 0.01-m vertical resolution. The black solid line shows the solid volume fraction of total vegetation while the red, blue, and yellow dashed lines show the contributions of 1st order root, higher order root, and stem to φ, respectively.

References for the Supporting Information

Heyman, J. (2019). TracTrac: A fast multi-object tracking algorithm for motion estimation. Computers & Geosciences, 128, 11–18.

Lee, X., Massman, W., & Law, B. (2004). Handbook of Micrometeorology: A Guide for Surface Flux Measurement and Analysis. Lee, X., Massman, W., & Law, B. Eds., Atmospheric and Oceanographic Sciences Library, Vol. 29, Kluwer, 250 pp., doi:10.1007/1-4020-2265-4.

Mariotti, G., & Fagherazzi, S. (2012). Channels-tidal flat sediment exchange: The channel spillover mechanism. Journal of Geophysical Research: Oceans, 117(C3).

Mori, N., Suzuki, T., & Kakuno, S. (2007). Noise of acoustic Doppler velocimeter data in bubbly flows. Journal of engineering mechanics, 133(1), 122–125.

Patalano, A., García, C. M., & Rodríguez, A. (2017). Rectification of Image Velocity Results (RIVeR): A simple and user-friendly toolbox for large scale water surface Particle Image Velocimetry (PIV) and Particle Tracking Velocimetry (PTV). Computers & Geosciences, 109, 323–330.

Chapter 6: Representing the impact of *Rhizophora* mangroves on flow in a hydrodynamic model: the importance of three-dimensional root system structures

6.1.1 Abstract

Coastal wetland vegetations modulate water flow by exerting drag which has an important implication on sediment transport and geomorphic dynamics. This vegetation effect on flow is commonly represented in hydrodynamic models by approximating the vegetations as an array of vertical cylinders or increased bed roughness. However, this simple approximation may not be valid in the case of *Rhizophora* mangroves that have complicated three-dimensional root structures. Here, we present a new model to represent the impacts of *Rhizophora* mangroves on flow in hydrodynamic models. The model explicitly accounts for the effects of the three-dimensional root structures on mean flow and turbulence, as well as the effects of two different length scales of vegetation-generated turbulence characterized by stem diameter and root diameter. The model employs an empirical model for the *Rhizophora* root structures that can be applied using basic vegetation parameters (mean stem diameter and tree density) without rigorous measurements of the root structures. We tested the model against the flows measured in a model mangrove forest in the laboratory and an actual mangrove forest in the field from previous studies. We show that compared to the conventional approximation using an array of cylinders or increased bed roughness, the new model significantly improves the predictability of velocity, turbulent kinetic energy, and bed shear stress in the *Rhizophora* mangrove forests. Overall, the presented new model offers a more realistic but feasible framework for simulating flows in *Rhizophora* mangrove forests with complex root structures using hydrodynamic models.

6.1.2 Introduction

Mangroves are one of the coastal wetland habitats that grow in intertidal areas in tropical and subtropical regions (Hamilton and Casey, 2016). They have characteristic aboveground root systems with varying morphological structures among genera, such as pneumatophores or “pencil roots” of *Avicennia* and *Sonneratia*, and prop roots of *Rhizophora* (Krauss et al., 2014). Especially due to the presence of aboveground root systems, mangroves exert drag against water flow that lowers flow velocity. This creates conditions preferable for the deposition and retention of tidally and fluvially transported sediments (Furukawa et al., 1997; Krauss et al., 2003; Horstman et al., 2015; Chen et al., 2016, 2018; Willemsen et al., 2016; Best et al., 2022) similar to other wetland habitats such as salt marshes (Temmerman et al., 2005; Bouma et al., 2007; Mudd et al., 2010; Weisscher et al., 2022). The flow-vegetation interactions coupled with sediment transport play a major role in driving the long-term geomorphic evolution of wetland habitats (Mariotti and Fagherazzi, 2010; Mariotti and Canestrelli, 2017; Brückner et al., 2019; Kalra et al., 2022; Willemsen et al., 2022). This further determines the persistence of mangroves amidst threats due to sea-level rise (Fagherazzi et al., 2012, 2020; Lovelock et al., 2015; Kirwan et al., 2016).

Representing the effect of vegetation on flow (vegetation drag) in hydrodynamic models is important to advance our understanding of hydrodynamics in coastal wetlands with implications on sediment transport and geomorphic dynamics (Temmerman et al., 2005; Nardin et al., 2016; Lokhorst et al., 2018). Several modeling studies have shown that depending on the magnitude of vegetation drag, the resulting geomorphic evolution can vary dramatically, and correspondingly, the ecosystems’ fate in response to sea-level rise (Boechat Albernaz et al., 2020; Xie et al., 2020). The vegetation drag in salt marshes and seagrass beds is commonly represented in hydrodynamic models by an array of vertical cylinders (cylinder drag model; Ashall et al., 2016; Zhu et al., 2020), the drag effect of which has been well studied both for emergent and submerged cases (e.g., Nepf, 1999, 2012). Although fewer compared to studies on salt marshes, some studies have incorporated the drag effects of mangroves in hydrodynamic models to evaluate their role in controlling flow and sediment transport (van Maanen et al., 2015; Bryan et al., 2017; Mullarney et al., 2017; Rodríguez et al., 2017; Xie et al., 2020). However, most of them are limited to *Avicennia* or *Sonneratia*-dominated mangrove forests whose aboveground roots (pencil roots) are geometrically simple and resemble that of a cylinder array.

In contrast, the root system of *Rhizophora* genus (prop root system) has three-dimensionally complicated structures that cannot simply be approximated by the array of vertical cylinders. Consequently, the representation of drag by *Rhizophora* mangroves in hydrodynamic models remains to be established despite the worldwide occurrences of this mangrove genus (Friess et al., 2019). This knowledge gap can be seen in the studies that

have approximated the drag by *Rhizophora* mangroves with arbitrarily increased bed roughness (Zhang et al., 2012) or cylinder arrays with arbitrary cylinder density (Xie et al., 2020) without much theoretical and experimental support (reviewed in Le Minor et al., 2021). One exception is a modeling study by Horstman et al. (2015) that approximated the root structures of *Rhizophora* mangroves using a cylinder array with vertically variable cylinder densities. However, their method requires an exhausting field survey of the root structures as a requirement for proper model application, which may not be feasible for a forest-scale simulation.

In addition to flow velocity, vegetation affects turbulence (Nepf, 2012; Xu and Nepf, 2020), which is also relevant to the transport of substances (e.g., sediment and solutes) through turbulent diffusion (Tanino and Nepf, 2008; Xu and Nepf, 2021). While several hydrodynamic models can account for vegetation-generated turbulence (e.g., Temmerman et al., 2005, Marsooli et al., 2016), so far, no model has been established to predict the turbulence structures in *Rhizophora* mangrove forests. A rigorous, but feasible representation of the impact of *Rhizophora* mangroves on flow velocity and turbulence in a hydrodynamic model is thus needed.

One of the challenges in modeling the flow in *Rhizophora* mangroves is the quantification of the complex root structures that can be labor-intensive when applied to a forest scale. Recently, an empirical model to predict the structures of *Rhizophora* root systems from stem diameter was proposed by Yoshikai et al. (2021). The model's general applicability to the root structures of various tree sizes has been extensively confirmed (Yoshikai et al., 2021). This empirical *Rhizophora* root model (hereafter denoted as *Rh*-root model) offers the possibility to feasibly simulate the flow in the forest scale once it is implemented in the hydrodynamic model.

In order to contribute to realistic but feasible simulations of hydrodynamics in *Rhizophora* mangrove forests, here, we implement a new drag and turbulence model coupled with the *Rh*-root model to represent the impacts of *Rhizophora* mangroves in a three-dimensional hydrodynamic model–the Regional Ocean Modeling System (ROMS; Shchepetkin and McWilliams, 2005) of the model framework COAWST (Coupled Ocean–Atmosphere–Wave–Sediment Transport Modeling System; Warner et al., 2010). The impact of the vertically varying projected area of roots on flow velocity and turbulence is specifically taken into consideration by the new model. Furthermore, the new model accounts for two different length scales of turbulence generated by *Rhizophora* mangroves–stem diameter and root diameter–as characterized by a flume experiment by Maza et al. (2017). Here, we aim to examine the following: (a) how does the consideration of the three-dimensional root structures of *Rhizophora* mangroves in the hydrodynamic model improve the predictability of flow velocity

and turbulence compared to the conventional drag approximation using cylinder arrays or increased bed roughness? (b) how can the new model be effectively applied to *Rhizophora* mangrove forests in the field with limited known root parameters?

6.2 Materials and Methods

6.2.1 Model description

A proposed framework for modeling the flow in *Rhizophora* mangrove forests is presented in Fig. 6.1. We used a three-dimensional hydrodynamic model, ROMS, in the model framework COAWST. The vegetation module has been added by Beudin et al. (2017) to account for the drag by vegetation (such as seagrasses and salt marshes) in the momentum equations in ROMS. The equations added by Beudin et al. (2017) are basically in the same form as the cylinder drag model (see Note S6.1 in the Supporting Information). We modified these equations to make them suitable for representing the impact of *Rhizophora* mangroves on flow; these equations are described below (Sections 6.2.1.1 and 6.2.1.2). We added a new module in COAWST–the *Rhizophora* root module–that provides the vertical profile of the projected area density of root systems from stem diameter and tree density in each model grid (Fig. 6.1; Section 6.2.1.3).

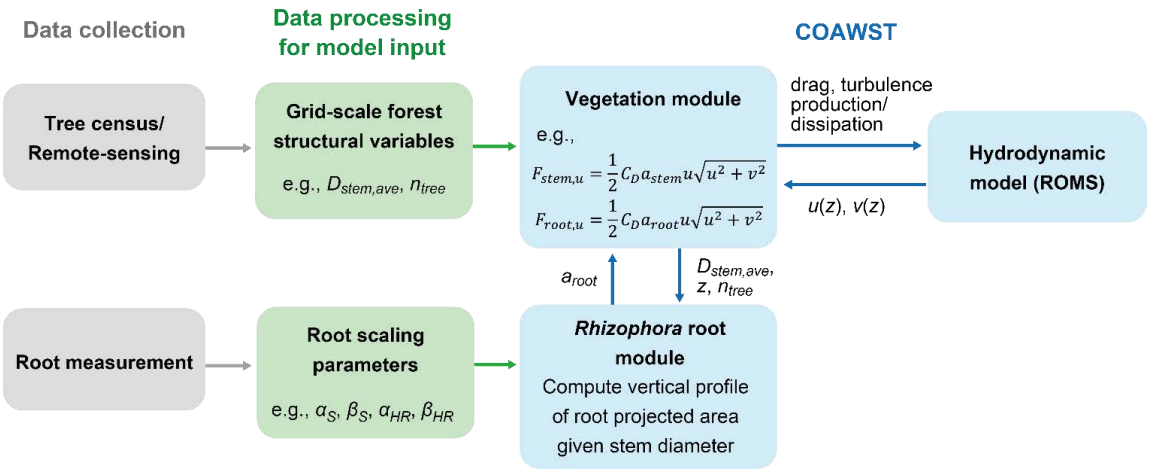

Figure 6.1. The proposed framework of modeling flow in *Rhizophora* mangrove forests using COAWST. $D_{stem,ave}$ and n_{tree} are the mean stem diameter and tree density, respectively, to be given in each grid, a_{stem} and a_{root} are the stem and root projected area density, where a_{stem} is a product of $D_{stem,ave}$ and n_{tree}. $F_{stem,u}$ and $F_{root,u}$ are the drag forces exerted on the *u*-component of flow by the stem and root, respectively. See Note S6.3 and Table S6.1 for explanations of the root scaling parameters.

This manuscript considers velocities as temporally averaged unless specified. We did not consider the subgrid-scale spatial heterogeneity of velocity generated by vegetation as in other modeling studies (e.g., King et al., 2012; Marsooli et al., 2016). The Reynolds number (*Re*) defined using the root diameter as length scale could be higher than the value ensuring fully turbulent structures of root-generated wakes (*Re* > 120; Shan et al., 2019) even for weak currents (~1 cm s^{-1}) that could diminish the dependence of drag coefficient (C_D) on *Re*. Thus, we treat C_D as a constant as in Beudin et al. (2017). For simplicity, we present equations in the two-dimensional form on the *x*-*z* plane (zero velocity in *y*-direction) while the equations implemented in ROMS are three-dimensional (*x*-*y*-*z*), where *x*-*y* represents the horizontal plane and *z* represents the vertical direction.

6.2.1.1 Drag force

In *Rhizophora* mangrove forests, the stem and roots are the main components that exert drag in tidal flows. We partition the drag by *Rhizophora* mangroves (vegetation drag) into the contributions by stems and roots and calculated it using the quadratic drag law as

$$F_{veg}(z) = F_{stem}(z) + F_{root}(z) = \frac{1}{2} C_D n_{tree} D_{stem,ave} u(z)^2 + \frac{1}{2} C_D a_{root}(z) u(z)^2 \qquad (6.1)$$

where F_{veg} is the spatially-averaged vegetation drag (m s^{-2}), z is the height from bed (m), F_{stem} and F_{root} are the contributions by stems and roots to F_{veg}, respectively, C_D is the drag coefficient, n_{tree} is the tree density (m^{-2}), $D_{stem,ave}$ is the mean stem diameter (m), a_{root} is the spatially-averaged projected area density of roots (m^{-1}), and u is the flow velocity (m s^{-1}). We represented stems as cylindrical shapes with vertically uniform diameter (Maza et al., 2017) and then calculated the F_{stem} using the cylinder drag model–the same equations introduced by Beudin et al. (2017) (Note S6.1 and Table 6.1). Here, we assumed the vertically constant and uniform drag coefficient (C_D) for stems and roots.

6.2.1.2 Turbulence

In ROMS, the generic length scale (GLS) model is implemented as the turbulence closure, where the equations can represent several two-equation closure models such as *k*–*ε* and *k*–*ω* models by adjusting the model parameters (Umlauf and Burchard, 2003; Warner et al., 2005). In this manuscript, we present equations in the form of the *k*–*ε* model for reference purposes as this is the most studied two-equation closure model for flows in vegetated areas (López and García, 2001; Katul et al., 2004; Defina and Bixio, 2005; King et al., 2012). Beudin et al. (2017) have included an additional term for wake production due to vegetation (P_w) in the equation for turbulence kinetic energy (TKE) as

$$\frac{\partial k}{\partial t} + u\frac{\partial k}{\partial x} = \frac{\partial}{\partial z}\left(\frac{\upsilon_t}{\sigma_k}\frac{\partial k}{\partial z}\right) + P_s + B + P_w - \varepsilon \quad (6.2)$$

where k is TKE ($m^2\ s^{-2}$), v_t is the eddy viscosity ($m^2\ s^{-1}$), σ_k is the turbulent Schmidt number for k (1.0), P_s, B, and P_w represent the production of k by shear, buoyancy, and wakes generated by vegetation ($m^2\ s^{-3}$), respectively, and ε is the turbulent dissipation ($m^2\ s^{-3}$). Similarly, they included an additional term (D_w) in the equation for ε as

$$\frac{\partial \varepsilon}{\partial t} + u\frac{\partial \varepsilon}{\partial x} = \frac{\partial}{\partial z}\left(\frac{\upsilon_t}{\sigma_\varepsilon}\frac{\partial k}{\partial z}\right) + \frac{\varepsilon}{k}(c_1 P_s + c_3 B - c_2\varepsilon) + D_w \quad (6.3)$$

where σ_ε is the turbulent Schmidt number for ε (1.3), c_1 (1.44), c_2 (1.92), and c_3 are the model constants, where the value of c_3 varies depending on the stratification state (Warner et al., 2005), and D_w is the dissipation rate of wakes ($m^2\ s^{-4}$). The wake production rate (P_w) is typically considered equal to the rate of work done by the flow against vegetation drag, i.e., $P_w = F_{veg}u$ (Nepf, 2012). In contrast, the turbulence dissipation rate largely depends on the turbulence length scale in addition to the TKE, which requires a prior knowledge of the turbulence length scale of wakes for correctly predicting the D_w (King et al., 2012; Liu et al., 2017; Li and Busari, 2019).

Previous flume studies for flow through vegetated areas have shown that the stem diameter (or leaf width) is the plausible turbulence length scale of wakes (Tanino and Nepf, 2008; King et al., 2012). In the case of flow in *Rhizophora* mangrove forests, however, there are two potential length scale: stem diameter and root diameter–that could significantly differ from each other (Maza et al., 2017). This variation makes it challenging to parameterize them into one representative length scale of wakes (L in Eq. S6.6 in Note S6.2). To resolve this, we partitioned the P_w and D_w into the terms for wakes generated by stems and roots, respectively, as

$$P_w = P_{w,stem} + P_{w,root} = F_{stem}u + F_{root}u \quad (6.4)$$

$$D_w = D_{w,stem} + D_{w,root} = c_2\frac{P_{w,stem}}{\tau_{stem}} + c_2\frac{P_{w,root}}{\tau_{root}} \quad (6.5)$$

where $P_{w,stem}$ and $P_{w,root}$ ($m^2\ s^{-3}$) are the production of k by stem- and root-generated wakes, $D_{w,stem}$ and $D_{w,root}$ ($m^2\ s^{-4}$) are the dissipation rate of stem- and root-generated wakes, and τ_{stem} and τ_{root} (s) are the time-scale of stem- and root-generated wakes, respectively; these are given by

$$\tau_{stem} = \left(\frac{{L_{stem}}^2}{{c_w}^2 P_{w,stem}}\right)^{1/3} \quad (6.6a)$$

$$\tau_{root} = \left(\frac{{L_{root}}^2}{{c_w}^2 P_{w,root}}\right)^{1/3} \quad (6.6b)$$

where L_{stem} and L_{root} (m) are the length scale of stem- and root-generated wakes, respectively, and c_w is the model constant. Here, we set mean stem diameter ($D_{stem,ave}$) and root diameter ($D_{root,ave}$) as L_{stem} and L_{root}, respectively.

We considered c_w in Eq. (6.6) as a calibration parameter whereas Beudin et al. (2017) gave a value of 0.09. Tanino and Nepf (2008) predicted the TKE for a flow through an array of emergent cylinders with cylinder projected area density, a, and cylinder diameter, d, using $k = \gamma \left(\frac{1}{2} C_D a d\right)^{2/3} u^2$, where γ is the scale coefficient that needs to be empirically determined. We can relate c_w with γ as $c_w = \gamma^{-3/2}$ by applying the k–ε model to a limiting case of a steady, uniform, and neutrally-stratified flow through homogeneous emergent vegetation such that all the terms in Eqs. (6.2–6.3) except for k, ε, P_w, and D_w can be neglected (King et al., 2012; Liu et al., 2017). We adjusted the value of c_w so that the corresponding γ value falls within a reported range (0.8–1.6; King et al., 2012; Xu and Nepf, 2020).

6.2.1.3 Root projected area density

We used the empirical *Rhizophora* root model (*Rh*-root model) developed by Yoshikai et al. (2021) as a predictor of the root projected area density (a_{root}) in Eq. (6.1). Based on allometric relationships characterized by some site- and species-specific root scaling parameters (α_S, β_S, α_{HR}, β_{HR} in Eq. S6.7 in Note S6.3), the *Rh*-root model predicts the vertical profile of root projected area per vertical interval (dz; 0.05 m in this study) for a tree "i" ($A_{root,i}(z)$ (m^2)) from the stem diameter of the tree ($D_{stem,i}$), where the subscript "i" represents the tree index. In short, $A_{root,i}(z)$ is expressed as $A_{root,i}(z) = f(D_{stem,i})$, where f represents a function of the *Rh*-root model (see Note S6.3 for the details).

The vertical profile of spatially-averaged projected area density of roots in each grid can be calculated as $a_{root}(z) = n_{tree} \sum_{i=1}^{N_{tree}} f(D_{stem,i}) / (N_{tree} dz)$, where n_{tree} is the tree density (m^{-2}) and N_{tree} is the number of trees in each grid. While some variations in tree sizes (i.e., $D_{stem,i}$), and thereby, $f(D_{stem,i})$ within a grid are expected, it would be convenient if the subgrid-scale variations can be parameterized using a grid-scale parameter for modeling purposes. In this study, we propose that the mean stem diameter ($D_{stem,ave}$) can be used for the parameterization as $\sum_{i=1}^{N_{tree}} f(D_{stem,i}) / N_{tree} \approx f(D_{stem,ave})$, so that $a_{root} \approx n_{tree} f(D_{stem,ave}) / dz$.

We investigated the above assumption using tree census data collected from three sites (Bak1, Bak2, and Fuk; see Fig. S6.1 and Note S6.4 in the Supporting Information for the map and description of the sites). Using the *Rh*-root model, we computed the vertical distribution of the mean projected area of individuals in the tree census plots, $\sum_{i=1}^{N_{tree}} f(D_{stem,i}) / N_{tree}$, and its representation using the mean stem diameter, $f(D_{stem,ave})$, and compared them (Fig. 6.2). The results demonstrate that the use of $D_{stem,ave}$ can well represent the mean projected area density of individuals for all the three sites regardless of the

differences in the forest structures (e.g., stem diameter distribution, tree density) and root scaling parameters (Table S6.1).

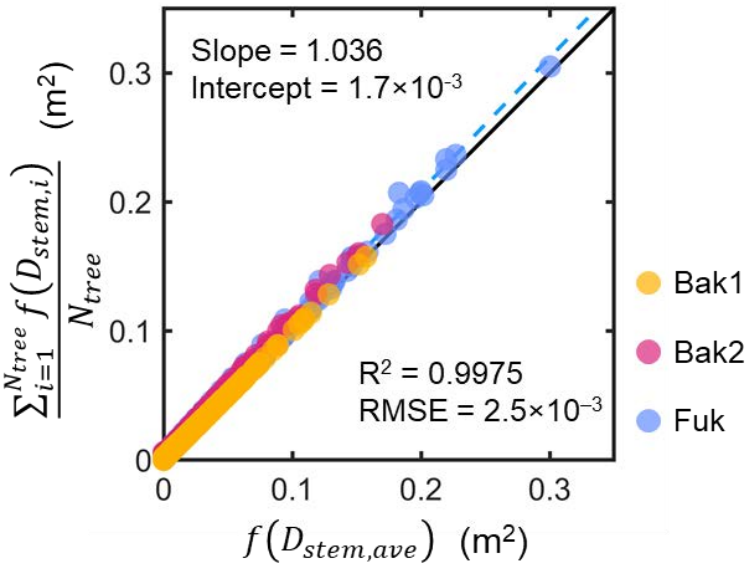

Figure 6.2. Comparison of the vertical profiles of mean projected area per vertical height interval (*dz*; 0.05 m) of individuals in tree census plots from three sites (Bak1, Bak2, and Fuk), $\sum_{i=1}^{N_{tree}} f(D_{stem,i})/N_{tree}$, and its representation using the mean stem diameter, $f(D_{stem,ave})$, where N_{tree} is the number of *Rhizophora* trees in a plot, $D_{stem,ave}$ is the mean stem diameter of *Rhizophora* trees in the plot, the subscript "*i*" represents the tree index, and *f* represents the function of the *Rhizophora* root model that gives the vertical profile of the root projected area of individuals. The black line indicates the 1:1 line and the blue dashed line indicates the best-fitting line.

6.2.2 Model testing

We tested the new model implemented in the COAWST against the measurements of flow in a laboratory model of the *Rhizophora* mangrove forest by Maza et al. (2017) and in a planted *Rhizophora* mangrove forest in the field by Yoshikai et al. (2022a). Note S6.5 provides some descriptions of the implementation of the new model to the COAWST. Both studies have provided detailed information on vegetation and hydrodynamic parameters that allow us to evaluate the model's performance. Specifically, the mangrove forests in both studies have spatially uniform vegetation distribution due to the uniformly sized and evenly distributed trees (approximately, in the case of the real mangrove forest in Yoshikai et al., 2022a). Moreover, both studies have measured flow structures at a location where the flow is well developed, which eliminates the dependence of flow structures on the proximity to the forest leading edge.

Given these conditions, we tested the model using a model grid assuming a schematized mangrove forest with uniform bed elevation and vegetation variables described below, and not with a grid representing the actual geometric/topographic conditions of the flume/field. Table S6.3 summarizes the measured hydrodynamic variables in Maza et al. (2017) and Yoshikai et al. (2022a), the variables controlled in the model, and the target variables to reproduce for each test case.

We created an orthogonal computational grid of 200 m × 200 m area with a 5-m horizontal resolution for the model runs (Fig. S6.2). We set 15 vertical layers with approximately uniform layer thickness to be applied to the laboratory-based study of Maza et al. (2017). For the field-based study (Yoshikai et al., 2022a), the number of vertical layers was reduced to 5 because of the shallow water depths. To create a unidirectional flow in the model, we set the eastern and western boundaries of the model domain closed (no water fluxes) and the northern and southern boundaries open (Fig. S6.2). Then we imposed water level differences between the northern and southern boundaries to drive the flow based on the pressure gradient, where the water fluxes through the boundaries are given to equate the local pressure gradient and the drag force (bed + vegetation). The model was run without wind in the simulation. When the steady state of flow was attained in the simulation, we compared the flow condition at the center of the model domain with the measured values (Fig. S6.2). This means that the actual time-series of the flow during the tidal cycle was not reproduced when the model was applied to the field mangrove forest; rather, steady states of flow were created for each flow measurement. Table 6.1 summarizes the key vegetation and hydrodynamic parameters for each test case.

We set different objectives for the applications of the model to laboratory- and field-based studies. The main objective of applying the model to a laboratory-based study is to examine the effectiveness of the formulations for the drag and turbulence terms (Eq. (6.1)–(6.6)), which were newly implemented in the COAWST to predict the flow structures in the *Rhizophora* mangrove forest, compared to the ones predicted by the cylinder drag model. Here, we consider the vegetation frontal area density (a) as a known parameter. In contrast, the parameter a is usually unknown and needs to be predicted in the case of mangrove forests in the field. Hence, the main objective of the application to the field-based study is to examine the effectiveness of the proposed framework (Fig. 6.1) that includes the *Rh*-root model – the predictor of a – in the COAWST, compared to the drag parameterizations proposed in previous studies. Table 6.2 summarizes the different model configurations tested to represent the impact of *Rhizophora* mangroves for applications to the laboratory- and field-based studies. Below we describe an overview of the measurements by Maza et al. (2017) and Yoshikai et al. (2022a) and the model settings.

Table 6.1. Vegetation and hydrodynamic parameter settings for model testing against flume experiments (Exp 1 and 2) in Maza et al. (2017) and field measurement in Yoshikai et al. (2022a). Figure S6.3 shows the location where the values of vegetation and hydrodynamic variables in the table were derived in Yoshikai et al. (2022a). Note that the values of vegetation and hydrodynamic variables in the flume in Maza et al. (2017) were converted to the real scale. The row for γ shows the values that best fit the measurements within the range of 0.8–1.6.

Parameter	Exp 1	Exp 2	Field
Stem diameter (D_{stem}, m)	0.2	0.2	0.066 [a]
Root diameter (D_{root}, m)	0.038	0.038	0.030 [a]
Maximum root height (HR_{max}, m)	2.01	2.01	1.10 [a]
Tree density (n_{tree}, m^{-2})	0.072	0.072	0.36
Drag coefficient (C_D)	0.8	0.8	1.0
Water depth (h, m)	3.0	1.79	0.14–0.53 [b]
Cross-sectional mean velocity (U, m s^{-1})	0.31	0.58	[c]
Scale coefficient (γ)	1.5	0.9	0.8

[a] Mean value at the measurement site.
[b] Water depth varies depending on the tidal phase (see Fig. 6.6a, e).
[c] One of the target parameters for model prediction.

Table 6.2. Tested model configurations to represent the impact of *Rhizophora* mangroves against flume experiments (Exp1 and 2) in Maza et al. (2017) and field measurement in Yoshikai et al. (2022a). n_{tree}: tree density; n_v: cylinder density; $D_{stem,ave}$: mean stem diameter; b_v: cylinder density; a_{root}: root projected area density; $D_{root,ave}$: mean root diameter; z_0: bed roughness length; N_{layer}: number of vertical layers of model grid.

Test case	Model configuration	Parameter settings					
		n_{tree} or n_v (m^{-2})	$D_{stem,ave}$ or b_v (m)	a_{root} (m^{-1})	$D_{root,ave}$ (m)	z_0 (m)	N_{layer}
Flume experiment	*Rh* model	0.072 (n_{tree})	0.2 ($D_{stem,ave}$)	Measured value [a]	0.038	0.5×10^{-3} [e]	15
	Cylinder model for Exp1	1.22 (n_v)	0.038 (b_v)	-	-	0.5×10^{-3} [e]	15
	Cylinder model for Exp2	1.76 (n_v)	0.038 (b_v)	-	-	0.5×10^{-3} [e]	15

Field measurement	*Rh* model with actual a_{root}	0.36 (n_{tree})	0.066 ($D_{stem,ave}$)	Measured value [b]	0.030	0.5×10^{-3}	5
	Rh model with modeled a_{root}	0.36 (n_{tree})	0.066 ($D_{stem,ave}$)	Modeled value [c]	0.030	0.5×10^{-3}	5
	Cylinder model (sparse)	13.5 (n_v)	0.030 (b_v)	-	-	0.5×10^{-3}	5
	Cylinder model (dense)	32.3 (n_v)	0.030 (b_v)	-	-	0.5×10^{-3}	5
	Generic root model	0.36 (n_{tree})	0.066 ($D_{stem,ave}$)	Eq. (S6.11) [d]	0.010	0.5×10^{-3}	5
	Increased z_0	-	-	-	-	0.02	3
	No vegetation	-	-	-	-	0.5×10^{-3}	5

[a] Corresponds to the value of black markers minus $n_{tree}D_{stem,ave}$ in Fig. 6.3a.
[b] Corresponds to the value of black markers minus $n_{tree}D_{stem,ave}$ in Fig. 6.3b.
[c] Corresponds to the value of blue markers minus $n_{tree}D_{stem,ave}$ in Fig. 6.3b.
[d] Corresponds to the value of light green markers minus $n_{tree}D_{stem,ave}$ in Fig. 6.3b.
[e] Assumed value.

6.2.2.1 Application to a laboratory-based study

The model *Rhizophora* mangrove forest created in the flume by Maza et al. (2017) was 1/12th, while we ran our model in a real scale, i.e., we converted the velocities in the flume to the real scale by keeping the Froude number (Table 6.1). The real-scale vertical profile of vegetation projected area density (a) is shown in Fig. 6.3a. Maza et al. (2017) fabricated the root systems based on the data in Ohira et al. (2013) and distributed the model trees in-line in the flume. Maza et al. (2017) created two flow conditions by varying the water depth (h) and cross-sectional mean velocity (U) (Exp 1 and 2; Table 6.1) and measured the vertical profiles of velocities and TKE at five lateral positions in the model forest, at which flows were fully developed (Table S6.3). We averaged the data taken at the five positions to estimate the spatial average of the velocity and TKE to be compared with the model output.

We imposed the real-scale vertical profile of a examined in Maza et al. (2017) (black markers in Fig. 6.3a) over the model domain. This means that the *Rh*-root module that predicts a_{root} was not applied for the simulations performed here. We optimized the water levels at the boundaries to create the same flow conditions (h and U) at the center of the model domain as the ones in Exp 1 and 2, respectively.

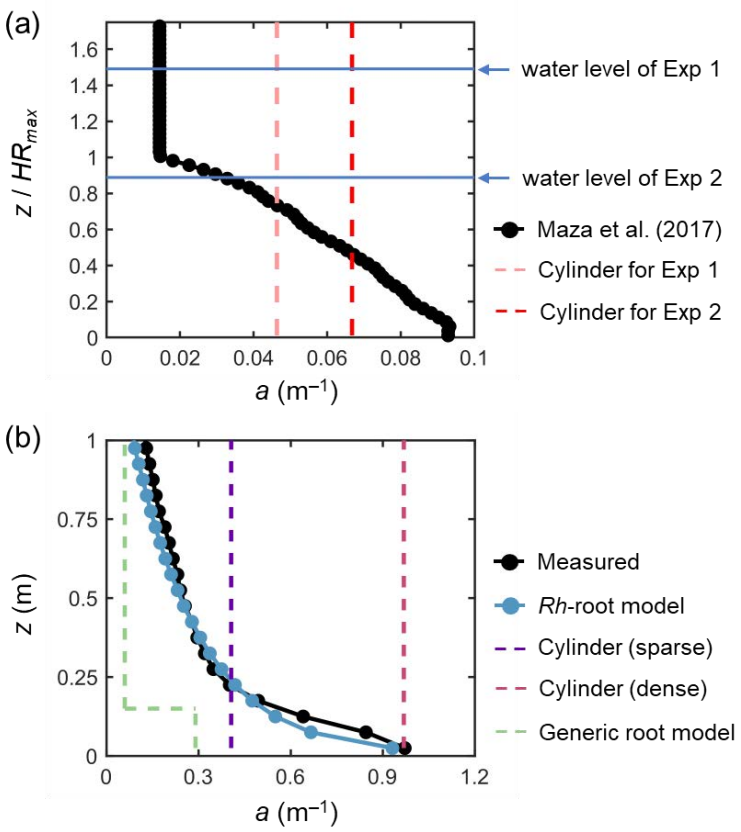

Figure 6.3. Vertical profiles of vegetation projected area density, ***a***, in (a) a model *Rhizophora* mangrove forest examined by Maza et al. (2017) and (b) a real *Rhizophora* mangrove forest examined by Yoshikai et al. (2022a), where the values were calculated with ***dz*** = 0.05 m vertical interval (markers). HR_{max} is the maximum root height (2.01 m in Maza et al. (2017); Table 6.1). The modeled ***a*** using the *Rh*-root model in panel "b" is given by the *Rhizophora* root module using the parameters shown in Tables 6.1 and S6.1 (for Bak2). The projected area density of cylinder arrays (in panels "a" and "b") as well as the ***a*** predicted using the generic mangrove root model (in panel "b"), which were used for comparison with the new model to represent the impacts of *Rhizophora* mangroves, is also shown (dashed lines).

We used a value of 0.8 for the drag coefficient (C_D) in the model (Table 6.1), the value of which was derived in fully developed flows with high Reynolds numbers (> 230) by Maza et al. (2017). The value of the bottom roughness (z_0) in the flume is unknown; hence we gave 0.5 mm to z_0, which is the value derived in the field-based study (see Section 6.2.2.2). Due to the uncertainty of the bottom roughness, we did not include the modeled near-bed velocity and TKE for comparison with the measurements, above which the velocity and TKE were insensitive to the bottom roughness. Another unknown parameter is the scale coefficient in the turbulence closure, γ (= $c_w^{2/3}$; see Section 6.2.1.2). We run the model by varying γ in a reported range (0.8–1.6) with an interval of 0.1 to seek a value that produced the best fit with

the measurement, mostly for the TKE profile. Figure S6.4 provides the model sensitivity to the varying γ for the prediction of TKE profiles.

In addition to the simulation using the actual a (black markers in Fig. 6.3a), referred to as the "*Rh* model", we tested the use of the cylinder drag model, referred to as the "cylinder model" (Table 6.2). We defined the cylinder array for Exp 1 and 2, respectively, where the cylinder projected area density was set equal to the depth-average of the actual a for each case (dashed lines in Fig. 6.3a); we set the cylinder diameter equal to the root diameter of the model *Rhizophora* trees (0.038 m; Table 6.1). Cylinder height was set well higher than the water level to create the condition that cylinders span the entire water column – this also applies to the cylinder drag model examined in the next section.

6.2.2.2 Application to a field-based study

Yoshikai et al. (2022a) measured vegetation and hydrodynamic parameters at 17-year-old planted stands of *Rhizophora apiculata* in a mangrove forest locally known as Bakhwan Ecopark in Aklan, Philippines (Fig. S6.3). The site corresponds to Bak2 in Fig. 6.2. Like in the flume condition of Maza et al. (2017), approximately uniformly sized trees are evenly distributed. The measured spatially averaged vegetation projected area density (a) at the site is shown in Fig. 6.3b. Due to the higher complexity of the root systems and higher tree density (Table 6.1), the a near the bed showed almost 10 times higher value than the one in Maza et al. (2017) (Fig. 6.3). Yoshikai et al. (2022a) conducted hydrodynamic measurements during ebb tides on September 10 and 11, 2018 that corresponded to spring tide conditions. The measured parameters were water depth, spatially averaged velocity profile (based on measurements at four locations), water surface slope along a major flow direction, and bed shear stress (Table S6.3). The flow at the site is considered fully developed.

We imposed the measured water surface slope at the boundaries to drive the flow, where the water depths at the boundaries were adjusted to realize the same water depth at the center of the model domain as the measurement. We used a value of 1.0 for the drag coefficient (C_D) and 0.5 mm for the bottom roughness (z_0) based on the results in Yoshikai et al. (2022a) (Table 6.1). As in the previous section, we changed the value of γ in a reported range (0.8–1.6) with an interval of 0.1 to seek a value that produced the best fit with the measured velocity profile. Note that the TKE profile has not been measured in the field, thus it could not be validated.

We tested seven different model configurations (Table 6.2): *Rh* model using the measured values for a_{root} (actual a; black markers in Fig. 6.3b), *Rh* model using the modeled a_{root} (blue markers in Fig. 6.3b), cylinder model using two different cylinder densities (sparse

and dense; purple and red dashed lines in Fig. 6.3b), use of the other predictive model for *Rhizophora* root structures used in Xie et al. (2020) as the predictor of a_{root} in Eq. (6.1) (termed as generic root model; green dashed line in Fig. 6.3b), increased bed roughness (z_0), and a case without imposing the vegetation drag (no vegetation). Among these, the proposed framework (Fig. 6.1) was used for the case *Rh* model using the modeled a_{root} (the *Rhizophora* root module provided the a_{root} in the simulation) with input parameters of measured mean stem diameter ($D_{stem,ave}$) and tree density (n_{tree}). We set the sparse cylinder case based on Horstman et al. (2013) who suggested the use of vegetation geometry measured at a height of around 0.25 m for cylinder array approximation. We set the dense cylinder array to produce an equivalent resistance to Manning's coefficient of 0.14 at a water depth of 0.5 m, a value often used to represent the drag by mangroves (e.g., Zhang et al., 2012; Menéndez et al., 2020). The generic root model used in Xie et al. (2020) predicts the mangrove root structure (a_{root}) as an array of vertical cylinders with a fixed diameter (D_{root}) and height (H_{root}) from a given stem diameter and tree density (see Note S6.6 for the model details). We use the term "generic" because Xie et al. (2020) used this model to represent root structures of several different mangrove genera including *Rhizophora*. Here, we used the same parameter values for D_{root} and H_{root} as the ones used in Xie et al. (2020) for *Rhizophora* root structures: D_{root} = 0.01 m and H_{root} = 0.15 m. The vegetation frontal area (stem + root) predicted by the generic root model using measured mean stem diameter ($D_{stem,ave}$ = 0.066 m) and tree density (n_{tree} = 0.36 m^{-2}) is shown in Fig. 6.3b. Here, the predicted a_{root} is used for calculating the drag by roots in Eq. (6.1). In addition, $D_{stem,ave}$ = 0.066 m and D_{root} = 0.01 m were applied for L_{stem} and L_{root} in the turbulence dissipation term of Eq. (6.6) (Table 6.2). For the case of increased z_0, we reduced the number of vertical layers from 5 to 3 and set z_0 = 0.02 m (Table 6.2; see Note S6.7 for the details of bed shear stress calculation and the choice of the value). We note that the z_0 value equivalent to Manning's coefficient of 0.14 at 0.5 m water depth is z_0 = 0.22 m, but we were able to increase the value up to 0.02 m due to the numerical limitation of the logarithmic velocity profile assumption implemented in the COAWST (Eq. (S6.13)). For the case without vegetation, z_0 is kept as 0.5×10^{-3} m, the same as the other vegetated cases. In the increased z_0 and the no vegetation cases, the bed shear stress is the main force to equate with the imposed pressure gradient.

6.3 Results

6.3.1 Comparison with a laboratory-based study

Figure 6.4 shows a comparison of the modeled and measured vertical profiles of velocity (u) and TKE (k) normalized by cross-sectional mean velocity (U) for Exp 1 and 2, the conditions examined by Maza et al. (2017). The profile of normalized velocity was reasonably predicted by the *Rh* model (Fig. 6.4a, c), especially at the lower part of the root system (i.e., $z/HR_{max} < 0.6$) in Exp 1 where the velocity was greatly attenuated compared to the upper part or above the root system (Fig. 6.4a). The higher values of the γ lead to more homogeneous velocity profiles because of the enhanced vertical momentum exchange by the elevated TKE, while the sensitivity to the varying γ was not significant. The *Rh* model also predicted well the overall trend of the normalized TKE profile measured by Maza et al. (2017) for both Exp 1 and 2 by adjusting the value of γ (Fig. 6.4b, d). Notably, the *Rh* model captured well the distinct vertical variations in TKE observed in Exp 1 when $\gamma = 1.5$ (Fig. 6.4b), while for Exp 2, the best fit was obtained when $\gamma = 0.9$ (Fig. 6.4d). Overall, $\gamma = 1.2$ produced the smallest total error of Exp 1 and 2 between the model and measured values (Fig. S6.4). It under- and overestimated the TKE averaged over the measurement section by about 20 and 40 % for Exp 1 and 2, respectively (Fig. 6.4b and d), which is generally a fairly good agreement for predicting TKE.

In contrast to the *Rh* model, the cylinder model predicted the nearly uniform vertical profile of velocity except for the region close to the bed both for Exp 1 and 2 and largely deviated from the measurements (Fig. 6.4a and c). The TKE predicted by the cylinder model also showed a nearly uniform vertical profile (Fig. 6.4b and d). While the cylinder model showed comparable TKE with the *Rh* model at the lower part of the root system (i.e., $z/HR_{max} < 0.4$) for both cases, it showed a significantly smaller TKE at the upper region from the *Rh* model and the measurement.

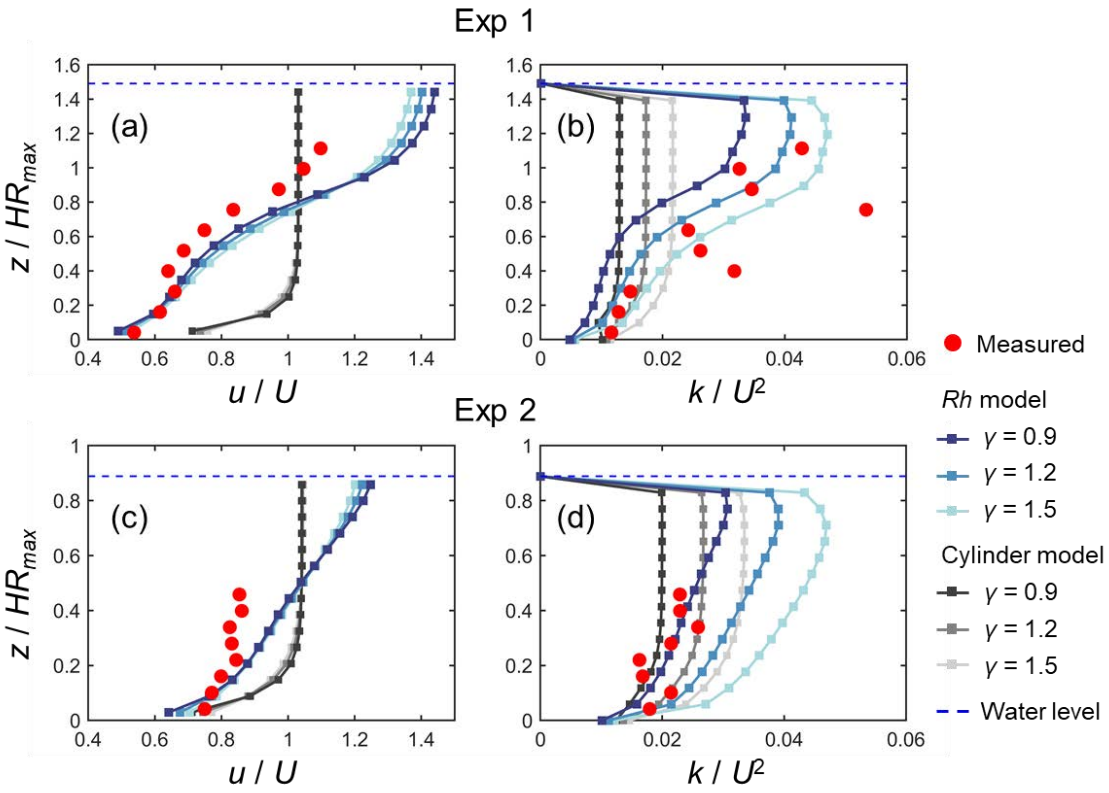

Figure 6.4. Comparison of the vertical profiles of (temporally and spatially averaged) velocity (u) and turbulent kinetic energy (k) normalized by the cross-sectional mean velocity (U) predicted by the COAWST with different model configurations (*Rh* model and cylinder model) and with different γ values, and measurement by Maza et al. (2017) for (a, b) Exp 1 and (c, d) Exp 2. HR_{max} is the maximum root height. Data on the measured values are provided in Table S6.4.

6.3.2 Comparison with a field-based study

Figure 6.5 shows the comparison of modeled velocity profiles with measurements by Yoshikai et al. (2022a) for some selected tidal phases in a *Rhizophora* mangrove forest (Bakhawan Ecopark). The *Rh* model using the measured profile of root projected area density (actual a_{root}) predicted well the overall trend of measured velocity profiles in various tidal phases (Fig. 6.5a). However, the model seemed to have underestimated the velocity attenuation from the surface to the bottom, which resulted in slightly higher near-bottom velocity and/or lower near-surface velocity compared to the measurement. Here, the value of γ was chosen as 0.8 from the range 0.8–1.6 (Table 6.2), which produced the best fit with the measured velocity profile. The *Rh* model using the modeled a_{root} provided by the *Rhizophora* root module showed comparable performance with the use of actual a_{root} in predicting the

velocity profile (Fig. 6.5a). However, although not significant, the use of modeled a_{root} tended to further underestimate the velocity attenuation from the surface to the bottom due to the underestimation of a_{root} near the bed by the *Rh*-root model (Fig. 6.3b).

The cylinder model with sparse arrays showed comparable velocities with measurements near the water surface, but significantly overestimated the velocities near the bed (Fig. 6.5b). Alternatively, the dense arrays showed comparable velocities near the bed, but significantly underestimated the velocities near the water surface (Fig. 6.5c). The use of generic root model as a predictor of a_{root} in Eq. (6.1) led to significant overestimation of velocities over the depths (Fig. 6.5d) due to the significantly underestimated vegetation projected area density (Fig. 6.3b). The approximation of mangrove drag in the z_0 (increased bed roughness case) predicted the significant attenuation of flow velocity from the surface to the bottom due to the large bottom friction, which did not well represent the actual conditions of velocity profile in the *Rhizophora* mangrove forest (Fig. 6.5e). The condition without imposing vegetation drag effects led to a large overestimation of the velocities, approximately 3–4 times larger than the measurements (Fig. 6.5f).

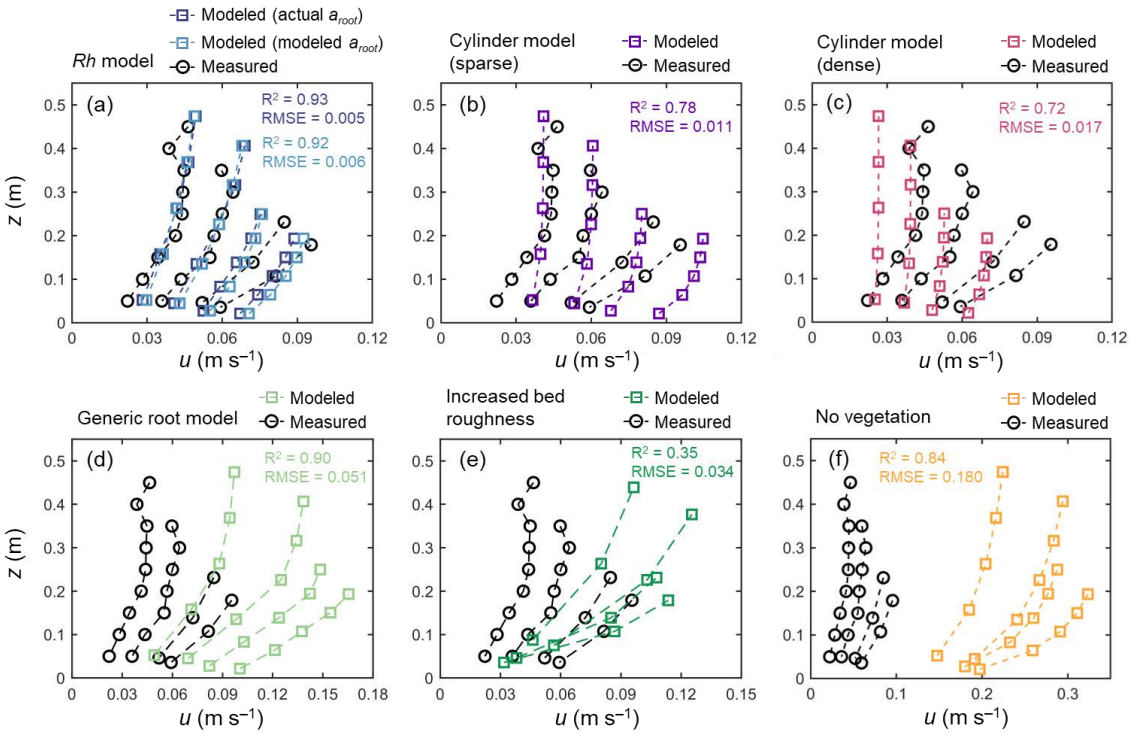

Figure 6.5. Comparison of the vertical profiles of velocity (u) predicted by the COAWST employing (a) *Rh* model using actual and modeled root projected area density profile (a_{root}), (b) cylinder model with sparse and (c) dense array, (d) generic root model, (e) increased bed roughness as an approximation of vegetation drag, and (f) without imposing vegetation drag (no vegetation), and measurement by Yoshikai et al. (2022a) for some selected tidal phases

during the measurement period. The root mean square error (RMSE) and R^2 values of the modeled *u* against the measured data are also shown, for which computation of the predicted value at the height of the measurement point was obtained by the interpolation of *u* computed at adjacent vertical layers. Data on the measured values are provided in Table S6.5.

A fairly good reproduction of tidal flows by the *Rh* model can also be seen in agreement with the measurement for the time-series of channel-mean velocity (*U*), (spatially averaged) velocity at z = 0.05 m (u_{bottom}), and bed shear stress (τ_{bed}) during the 2-days measurement period (Fig. 6.6). Note that we estimated the model prediction of velocity at z = 0.05 m from linear interpolation of velocities computed at adjacent vertical layers. The u_{bottom} was generally overestimated by about 15 % (Fig. 6.6c, g), as also seen in Fig. 6.5a. As a result, the τ_{bed} was overestimated by about 30 % by the model, which is still a reasonable agreement (Fig. 6.6d, h). As demonstrated in Fig. 6.5a, the *Rh* model employing the modeled a_{root} also showed a comparable performance for the time-series data (Fig. 6.6).

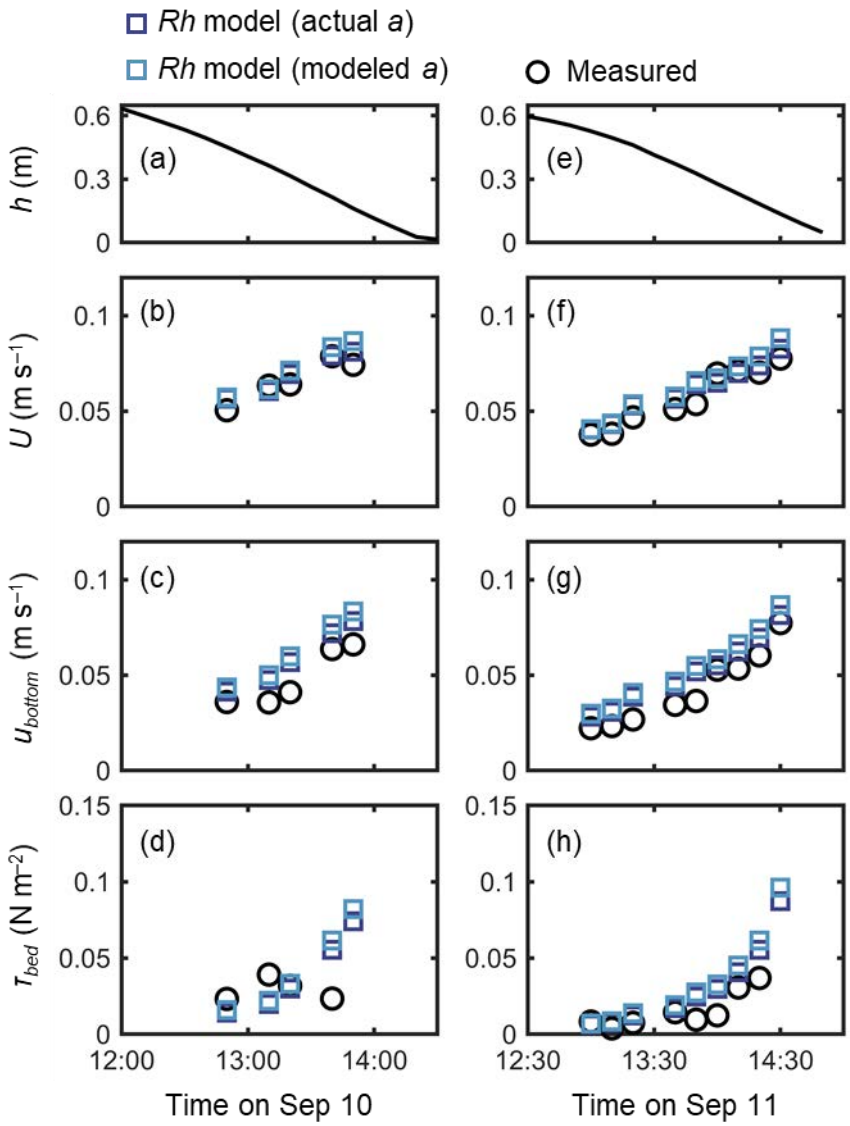

Figure 6.6. Time-series of (a, e) measured water depth (h), measured and predicted (b, f) cross-sectional mean velocity (U), (c, g) (spatially averaged) velocity at z = 0.05 m, and (d, h) bed shear stress (τ_{bed}) during the two-days measurement in Bakhawan Ecopark. The measured values are from Yoshikai et al. (2022a) and the predicted values are obtained through the COAWST employing the *Rh* model using actual and modeled root projected area density profile (a_{root}). Data on the measured values are provided in Table S6.6.

The cylinder model with a sparse array led to a significant overestimation trend of the U, u_{bottom}, and τ_{bed} over the tidal phases especially when the water depth decreased (Fig. 6.7). The cylinder model with a dense array led to the underestimation of U in most of the tidal phases but showed an agreement with the measurement for u_{bottom} and τ_{bed} (Fig. 6.7). The use of generic root model resulted in consistently higher U, u_{bottom}, and τ_{bed} compared to the measured values (Fig. 6.8), similar to the trend seen in Fig. 6.5d. Although the case using the

increased z_0 showed a large overestimation of flow velocities as much as the case using the generic root model when the water depth is relatively high (e.g., h > 0.3 m), it approached the measured values with decreasing water depth (Fig. 6.8); we will discuss these contrasting results in the following section. Because the bed drag is the main force to counteract the imposed pressure gradient in the increased z_0 case, the τ_{bed} showed a large overestimation over the tidal phases as expected (Fig. 6.8c, f). The model without imposing vegetation drag led to a large overestimation of these parameters over the tidal phases (Fig. S6.5), similar to the result shown in Fig. 6.5f.

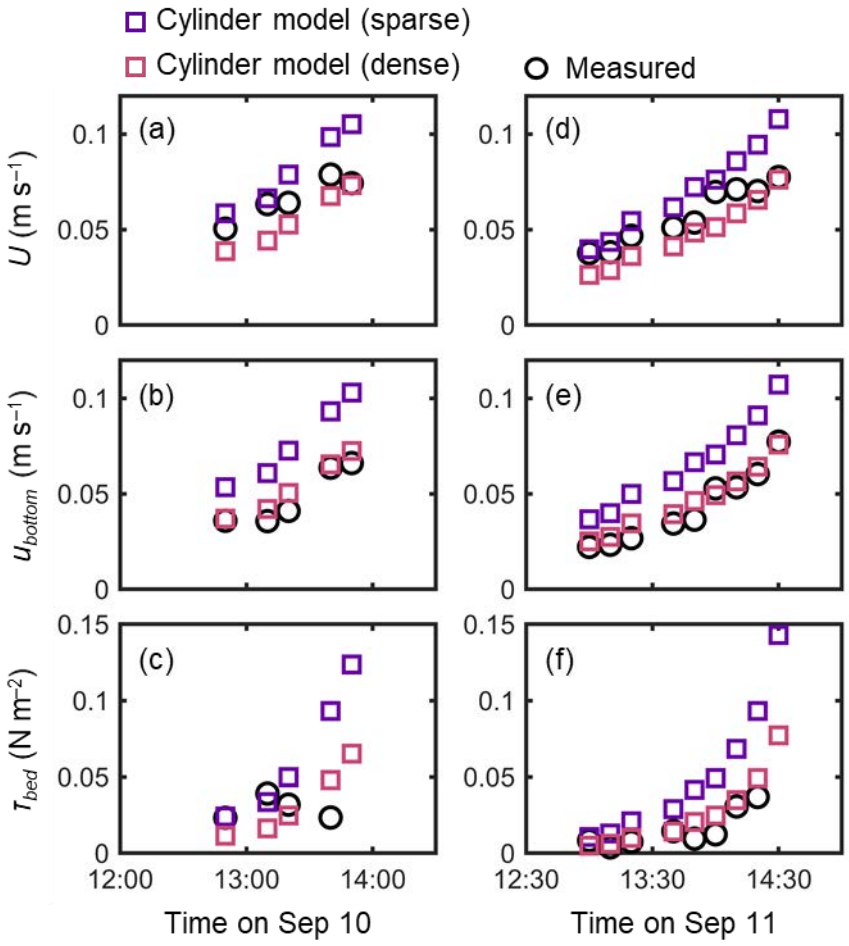

Figure 6.7. Time-series of measured and predicted (a, d) cross-sectional mean velocity (U), (b, e) (spatially averaged) velocity at z = 0.05 m, and (c, f) bed shear stress (τ_{bed}) during the two-days measurement in Bakhawan Ecopark. The measured values are from Yoshikai et al. (2022a) and the predicted values are obtained through the COAWST employing the cylinder model with sparse and dense arrays.

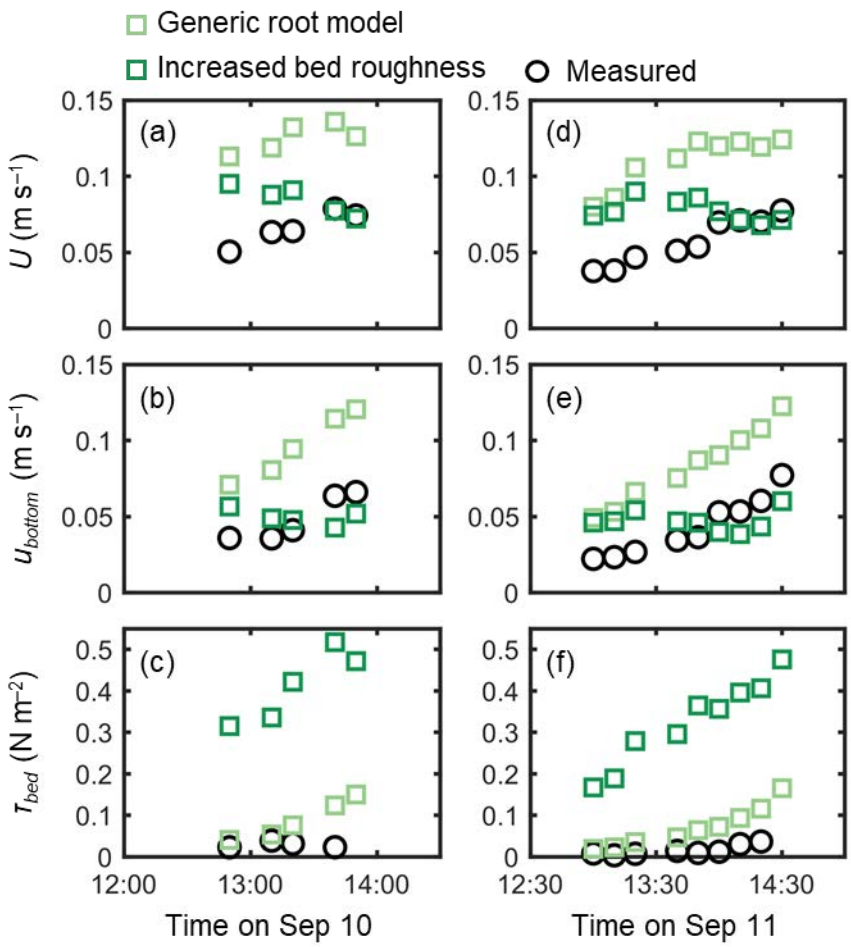

Figure 6.8. Time-series of measured and predicted (a, d) cross-sectional mean velocity (U), (b, e) (spatially averaged) velocity at z = 0.05 m, and (c, f) bed shear stress (τ_{bed}) during the two-days measurement in Bakhawan Ecopark. The measured values are from Yoshikai et al. (2022a) and the predicted values are obtained through the COAWST employing the generic root model and the increased bed roughness as an approximation of drag by mangroves, respectively.

6.4 Discussion

6.4.1 Performance of the previously proposed drag parameterization

Due to the general lack of information on the vertically varying projected area of the complicated root systems, the drag by *Rhizophora* mangroves has been represented by the increased Manning's roughness coefficient values (e.g., Zhang et al., 2012) or an array of

cylinders with arbitrary cylinder density (Horstman et al., 2013; Xie et al., 2020) in hydrodynamic models with 2D configuration. We evaluated these drag parameterizations using the cylinder array or increased bed roughness approximation in 3D configuration (dashed lines in Fig. 6.3 for the cylinder arrays). Consistent with previous studies (Liu et al., 2008; King et al., 2012), the cylinder array approximations showed the vertically uniform velocity and TKE profile except near the bed, which largely deviated from the measurements (Figs. 6.4 and 6.5). Moreover, for the tidal flows with changing water depth, the two different cylinder array configurations (sparse and dense) failed to capture the velocity changes over the tidal phases (Fig. 6.7) due to the inability to capture the changes in submerged vegetation projected area of *Rhizophora* mangroves.

The generic mangrove root model used in Xie et al. (2020) predicts the *Rhizophora* root system as an array of vertical cylinders having a fixed height and diameter. However, the root system structures of *Rhizophora* mangroves cannot be simply approximated as the array of vertical cylinders as shown in Fig. 6.3b. Although the shape of the velocity vertical profiles predicted using the generic root model resembles that of observed profiles as indicated by the high R^2 value in Fig. 6.5d, the model failed to predict the absolute values as indicated by the high RMSE due to the significant underestimation of the a (Fig. 6.3b). Because the shape of a predicted by the generic root model is similar to those of submerged vegetations, it is expected that the velocity inflection at the top of the root zone ($z = H_{root}$) will form as the projected area density of roots (a_{root}) further increases (e.g., King et al., 2012; Nepf 2012), which would further deviate the results from the actual velocity profiles.

Unlike the cylinder array approximations including the generic root model where the total projected area of submerged cylinders changes with the water depth, the approximation with increased bed roughness inherently assumes the invariant area of obstructions to flows. This means that the impact of bed roughness on flow velocity becomes more significant as the water depth decreases. This effect can be seen in the prediction of cross-mean flow velocity (U) at different tidal phases where the predicted U, which was largely overestimated under the relatively high water depth (h > 0.3 m), approached the measured values as the water depth decreases, unlike the case using the generic root model (Fig. 6.8b, e). The approximation with increased bed roughness leads to the large overestimation of τ_{bed} (Fig. 6.8c, f), hence making it not suitable for applications to sediment transport modeling in mangrove forests. Overall, none of the previously proposed drag parameterization captured well the flow structures in the *Rhizophora* mangrove forests examined in this study.

6.4.2 Performance of the new model

We proposed a new drag and turbulence model for flows in *Rhizophora* mangrove forests that works on the 3D hydrodynamic model, ROMS, and implemented in the COAWST. The model explicitly accounts for the vertically varying projected area of the root systems for drag force and TKE production in 3D configuration. In addition, the model accounts for the two different length-scales of wakes (roots- and stem-generated wakes) in the turbulence closure model (k–ε model in this study), an aspect none of the modeling studies has examined yet (e.g., López and García, 2001; King et al., 2012). With the relatively simple modifications made to the equations introduced by Beudin et al. (2017) (Eqs. 6.1, 6.4–6.6), our results showed significantly improved reproducibility of ROMS for the vertical profiles of velocity and TKE, and velocity changes over the tidal phases in *Rhizophora* mangrove forests (Figs. 6.4, 6.5, and 6.6). The new model also reasonably predicted the bed shear stress together with these parameters (Fig. 6.6d and h). Although some studies have accounted for the vertically varying vegetation projected area in hydrodynamic models for salt marshes (Temmerman et al., 2005) or mangrove forests with *Rhizophora* stands (Horstman et al., 2013, 2015), the efficacy of accounting for the vegetation 3D structures in the model has not been demonstrated. Overall, this is the first modeling study to introduce the realistic representation of the influences of *Rhizophora* mangrove morphological structures on the flow that was validated with existing data. The good performance of the model in both the model- and real-*Rhizophora* mangrove forests suggests the model's applicability to forests having the vegetation density a in the range of 0.09–0.9 m^{-1} near the bed (Fig. 6.3) and an in-line tree distribution like planted mangrove forests. However, the applicability to forests having a > 0.9 m^{-1} and/or heterogeneous tree sizes and distribution, a condition often observed in natural mangrove forests, needs further investigation in future studies.

The laboratory-based study of Maza et al. (2017) provided valuable data for evaluating the new model for TKE in a *Rhizophora* mangrove forest, which is currently unavailable from field-based studies. They observed the elevated TKE at the upper root zone and above the root zone (z/HR_{max} > 0.5; Fig. 6.4b). Maza et al. (2017) discussed the TKE production by shear (P_s in Eq. 6.2) as one of the main reasons for the elevated TKE. However, we found that the different dominance of the root- and stem-generated wakes over the depth can explain these observations. For instance, the lower root zone that is dominated by root-generated wakes with length-scale set as root diameter (0.038 m; Table 6.2) resulted in a higher dissipation rate (Eq. 6.6a), thereby lower TKE (Fig. 6.4b). On the other hand, the higher root zone dominated by stem-generated wakes with length-scale set as stem diameter (0.2 m; Table 6.2) resulted in a lower dissipation rate (Eq. 6.6b), thereby higher TKE (Fig. 6.4b). This result is similar to the observation by Xu and Nepf (2020) that found vertically varying turbulence integral length-scale in a canopy of a salt marsh plant *Typha*. Without accounting for the two different length

scales, the model failed to reproduce the TKE profile while the velocity profile remained similar, suggesting the minor importance of shear production in reproducing the TKE (Fig. S6.6). The model also predicted the gradually increasing TKE upwards in the lower root zone (z/HR_{max} < 0.5), which is consistent with the measurements (Fig. 6.4b, d). While the model showed good reproducibility of the TKE profile, it should be noted that different γ values produced the best fit with the measurement for Exp1 and Exp2 (Fig. 6.4b, d). At this moment, the exact explanation for this observation is yet to be determined, whether it can be attributed to measurement uncertainty or processes that were not represented in the model. Further research on the turbulence structures in *Rhizophora* mangrove forests is needed. Unlike the TKE profiles predicted for the model mangrove forest, the TKE predicted for the field mangrove forest (Bakhawan Ecopark) having much higher vegetation complexity (higher a; Fig. 6.3) showed nearly uniform vertical profiles (Fig. S6.7); these results cannot be validated at this moment due to lack of necessary data. Field studies on turbulence structures are likewise needed in this sense.

From the results shown, we highlighted the importance of accounting for the vertically varying projected area of the root systems with 3D configuration for capturing the flow structures (Figs. 6.4–6.8). The model predictability is therefore dependent on the root projected area, which is typically unknown and labor-intensive to measure (Yoshikai et al., 2021). For the practical use of the model, we implemented in COAWST an empirical model for the *Rhizophora* root system (*Rh*-root model; Fig. 6.1) with parameterization of subgrid-scale tree variations (Fig. 6.2) that enables the model application without rigorous measurements of root structures. The simulation for flows in Bakhawan Ecopark using the modeled a_{root} provided by the *Rhizophora* root module showed almost identical results to the one using the measured a_{root} in the field (Figs. 6.5 and 6.6). This indicates the applicability of the model framework for predicting the flows in real *Rhizophora* mangrove forests. The grid-scale parameters required are mean stem diameter ($D_{stem,ave}$) and tree density (n_{tree}), which are basic information collected during tree census surveys (Simard et al., 2019; Suwa et al., 2021). Although the process of collecting these spatial data exceeds the scope of the study, we expect that even remotely sensed data such as airborne LiDAR (Jucker et al., 2017; Dai et al., 2018) or UAV optical imagery (Otero et al., 2018), which can detect basic tree features (e.g., tree height and crown width) that have a strong relationship with stem diameter (Jucker et al., 2017; Azman et al., 2021), can provide such information effectively. Obtaining the root scaling parameters requires field surveys (Fig. 6.1); however, these parameters can be relatively easily obtained by sampling 10–20 trees at the site (see Yoshikai et al., 2021, 2022a for the procedure). The collection of these data is far less exhaustive than extensively measuring the vertical profile of a_{root} in the area of interest as done by Horstman et al. (2015).

Therefore, the model presented in this study may achieve a realistic forest-scale numerical modeling of flows in *Rhizophora* mangrove forests in the field.

6.4.3 Further model improvement

In order to extend the application of the presented model to sediment transport modeling, an accurate representation of vegetation impacts on both mean flow and turbulence structures that control sediment horizontal flux, retention/erosion, and turbulent mixing, is of primary importance (Nardin and Edmonds, 2014; Xu et al., 2022). Specifically, the greatly reduced near-bed velocity compared to the upper region that may significantly contribute to the sediment retention function of *Rhizophora* mangroves may be a key factor for the sediment transport modeling in this kind of forest, which was captured by the new model only (*Rh*-model in Figs. 6.4–6.5). While we expect the improved prediction of the sediment transport process in *Rhizophora* mangrove forests given the improved prediction of overall flow structures using the presented new model, future studies on model application and validation with the field data on sedimentary processes are needed.

Several recent laboratory-based studies have shown that the turbulence generated by vegetation could contribute to sediment erosion, and in that case, TKE may be a better predictor of erosion rate than bed shear stress (Tinoco and Coco, 2016; Yang and Nepf, 2018; Liu et al., 2021). Currently, most numerical models evaluate sediment erosion based on bed shear stress even for the region with vegetations (e.g., Zhu et al., 2020; Breda et al., 2021; Zhang et al., 2022). Accounting for the impact of vegetation-generated turbulence on the sediment erosion in the model may be the next step to better represent the sediment transport process in *Rhizophora* mangrove forests, where the presented model has the potential to contribute to it. Yet, the insights into the effects of turbulence on sediment erosion in *Rhizophora* mangrove forests are very limited at present, necessitating further laboratory- and field-based studies.

In order to predict the long-term geomorphic evolution of mangrove forests, the interactive feedback of vegetation-flow-sediment needs to be precisely simulated (van Maanen et al., 2015; Rodríguez et al., 2017; Xie et al., 2020). This process involves dynamic vegetation models that can capture long-term changes in root structure complexity in accordance with forest growth/development (e.g., Xie et al., 2020)–a process poorly represented in previous studies in the case of *Rhizophora* mangrove forests. An advantage of the proposed model is that the root structures of *Rhizophora* mangroves are allometrically predicted in the hydrodynamic model from the basic forest structural variables–mean stem diameter and tree density, of which long-term dynamics can now be predicted using dynamic

vegetation models for mangroves (e.g., Yoshikai et al., 2022b). The coupling of the hydrodynamic-sediment transport model and the dynamic vegetation model is one of the next challenges that will advance our understanding of the long-term geomorphic evolution in mangrove forests.

6.5 Concluding remarks

Modeling flow in *Rhizophora* mangroves has been challenging due to their complex root structures. This manuscript presents a new model to represent the impacts of *Rhizophora* mangroves on flow implemented in the COAWST model framework toward a better understanding of hydrodynamics in mangrove forests. The new model explicitly accounts for the effect of the three-dimensional root structures on drag and turbulence as well as the two potential length scales of vegetation-generated turbulence. We showed that the new model significantly improves the prediction of velocity and TKE in *Rhizophora* mangrove forests compared to the conventional approximations of the impact of *Rhizophora* mangroves using cylinder array or increased bed roughness. Specifically, the greatly attenuated near-bed velocity and the consequently lowered bed shear stress due to the high root density at the lower portion of the root systems are captured by the new model only. This has an important implication when expanding the model to simulate sediment transport. Thus, accounting for the realistic morphological structures of *Rhizophora* mangroves in the hydrodynamic model with a three-dimensional configuration is important. While obtaining information on root structures in the field could be challenging, the new model is now feasible in its application due to the incorporation of the empirical model for *Rhizophora* root structures to the COAWST. The model developed here may thus serve as a fundamental tool to advance our understanding of the hydrodynamics and related transport processes in *Rhizophora* mangrove forests with complex root structures.

6.6 References

Ashall, L. M., Mulligan, R. P., van Proosdij, D., and Poirier, E.: Application and validation of a three-dimensional hydrodynamic model of a macrotidal salt marsh. Coastal Engineering, 114, 35–46. https://doi.org/10.1016/j.coastaleng.2016.04.005, 2016.

Azman, M. S., Sharma, S., Shaharudin, M. A. M., Hamzah, M. L., Adibah, S. N., Zakaria, R. M., and MacKenzie, R. A.: Stand structure, biomass and dynamics of naturally

regenerated and restored mangroves in Malaysia. Forest Ecology and Management, 482, 118852. https://doi.org/10.1016/j.foreco.2020.118852, 2021.

Best, Ü. S., van der Wegen, M., Dijkstra, J., Reyns, J., van Prooijen, B. C., and Roelvink, D.: Wave attenuation potential, sediment properties and mangrove growth dynamics data over Guyana's intertidal mudflats: assessing the potential of mangrove restoration works. Earth System Science Data, 14(5), 2445–2462. https://doi.org/10.5194/essd-14-2445-2022, 2022.

Beudin, A., Kalra, T. S., Ganju, N. K., and Warner, J. C.: Development of a coupled wave-flow-vegetation interaction model. Computers & Geosciences, 100, 76–86. https://doi.org/10.1016/j.cageo.2016.12.010, 2017.

Boechat Albernaz, M., Roelofs, L., Pierik, H. J., and Kleinhans, M. G.: Natural levee evolution in vegetated fluvial-tidal environments. Earth surface processes and landforms, 45(15), 3824–3841. https://doi.org/10.1002/esp.5003, 2020.

Bouma, T. J., Van Duren, L. A., Temmerman, S., Claverie, T., Blanco-Garcia, A., Ysebaert, T., and Herman, P. M. J.: Spatial flow and sedimentation patterns within patches of epibenthic structures: Combining field, flume and modelling experiments. Continental Shelf Research, 27(8), 1020–1045. https://doi.org/10.1016/j.csr.2005.12.019, 2007.

Breda, A., Saco, P. M., Sandi, S. G., Saintilan, N., Riccardi, G., and Rodríguez, J. F.: Accretion, retreat and transgression of coastal wetlands experiencing sea-level rise. Hydrology and Earth System Sciences, 25(2), 769–786. https://doi.org/10.5194/hess-25-769-2021, 2021.

Brückner, M. Z., Schwarz, C., van Dijk, W. M., van Oorschot, M., Douma, H., and Kleinhans, M. G.: Salt marsh establishment and eco-engineering effects in dynamic estuaries determined by species growth and mortality. Journal of Geophysical Research: Earth Surface, 124(12), 2962–2986. https://doi.org/10.1029/2019JF005092, 2019.

Bryan, K. R., Nardin, W., Mullarney, J. C., and Fagherazzi, S.: The role of cross-shore tidal dynamics in controlling intertidal sediment exchange in mangroves in Cù Lao Dung, Vietnam. Continental Shelf Research, 147, 128–143. https://doi.org/10.1016/j.csr.2017.06.014, 2017.

Chen, Y., Li, Y., Cai, T., Thompson, C., and Li, Y.: A comparison of biohydrodynamic interaction within mangrove and saltmarsh boundaries. Earth Surface Processes and Landforms, 41(13), 1967–1979. https://doi.org/10.1002/esp.3964, 2016.

Chen, Y., Li, Y., Thompson, C., Wang, X., Cai, T., and Chang, Y.: Differential sediment trapping abilities of mangrove and saltmarsh vegetation in a subtropical estuary. Geomorphology, 318, 270–282. https://doi.org/10.1016/j.geomorph.2018.06.018, 2018.

Dai, W., Yang, B., Dong, Z., and Shaker, A.: A new method for 3D individual tree extraction using multispectral airborne LiDAR point clouds. ISPRS journal of photogrammetry and remote sensing, 144, 400–411. https://doi.org/10.1016/j.isprsjprs.2018.08.010, 2018.

Defina, A. and Bixio, A. C.: Mean flow and turbulence in vegetated open channel flow. Water Resources Research, 41(7). https://doi.org/10.1029/2004WR003475, 2005.

Fagherazzi, S., Kirwan, M. L., Mudd, S. M., Guntenspergen, G. R., Temmerman, S., D'Alpaos, A., van de Koppel, J., Rybczyk, J. M, Reyes, E., Craft, C., and Clough, J.: Numerical models of salt marsh evolution: Ecological, geomorphic, and climatic factors. Reviews of Geophysics, 50(1). https://doi.org/10.1029/2011RG000359, 2012.

Fagherazzi, S., Mariotti, G., Leonardi, N., Canestrelli, A., Nardin, W., and Kearney, W. S.: Salt marsh dynamics in a period of accelerated sea level rise. Journal of Geophysical Research: Earth Surface, 125, e2019JF005200. https://doi.org/10.1029/2019JF005200, 2020.

Friess, D. A., Rogers, K., Lovelock, C. E., Krauss, K. W., Hamilton, S. E., Lee, S. Y., Lucas, R., Primavera, J., Rajkaran, R., and Shi, S.: The state of the world's mangrove forests: past, present, and future. Annu. Rev. Environ. Resour, 44(1), 89–115. https://doi.org/10.1146/annurev-environ-101718-033302, 2019.

Furukawa, K., Wolanski, E., and Mueller, H.: Currents and sediment transport in mangrove forests. Estuarine, Coastal and Shelf Science, 44(3), 301–310. https://doi.org/10.1006/ecss.1996.0120, 1997.

Hamilton, S. E. and Casey, D.: Creation of a high spatio-temporal resolution global database of continuous mangrove forest cover for the 21st century (CGMFC-21). Global Ecology and Biogeography, 25(6), 729–738. https://doi.org/10.1111/geb.12449, 2016.

Horstman, E. M., Dohmen-Janssen, C. M., Bouma, T. J., and Hulscher, S. J.: Tidal-scale flow routing and sedimentation in mangrove forests: Combining field data and numerical modelling. Geomorphology, 228, 244–262. https://doi.org/10.1016/j.geomorph.2014.08.011, 2015.

Horstman, E., Dohmen-Janssen, M., and Hulscher, S. J. M. H.: Modeling tidal dynamics in a mangrove creek catchment in Delft3D. Coastal Dynamics Arcachon, France, 833–844, 24–28 June 2013.

Jucker, T., Caspersen, J., Chave, J., Antin, C., Barbier, N., Bongers, F., Dalponte, M., van Ewijk, K. Y., Forrester, D. I., Haeni, M., Higgins, S. I., Holdaway, R. J., Iida, Y., Lorimer, C., Marshall, P. L., Momo, S., Moncrieff, G. R., Ploton, P., Poorter, L., Rahman, K. A., Schlund, M., Sonké, B., Sterck, F. J., Trugman, A. T., Usoltsev, V. A., Vanderwel, M. C., Waldner, P., Wedeux, B. M. M., Wirth, C., Wöll, H., Woods, M., Xiang, W.,

Zimmermann, N. E., and Coomes, D. A.: Allometric equations for integrating remote sensing imagery into forest monitoring programmes. Global change biology, 23(1), 177–190. https://doi.org/10.1111/gcb.13388, 2017.

Kalra, T. S., Ganju, N. K., Aretxabaleta, A. L., Carr, J. A., Defne, Z., and Moriarty, J. M.: Modeling marsh dynamics using a 3-D coupled wave-flow-sediment model. Front. Mar. Sci. 8. doi: 10.3389/fmars.2021.740921, 2022.

Katul, G. G., Mahrt, L., Poggi, D., and Sanz, C.: One-and two-equation models for canopy turbulence. Boundary-layer meteorology, 113(1), 81–109. https://doi.org/10.1023/B:BOUN.0000037333.48760.e5, 2004.

King, A. T., Tinoco, R. O., and Cowen, E. A.: A k–ε turbulence model based on the scales of vertical shear and stem wakes valid for emergent and submerged vegetated flows. Journal of Fluid Mechanics, 701, 1–39. https://doi.org/10.1017/jfm.2012.113, 2012.

Kirwan, M. L., Temmerman, S., Skeehan, E. E., Guntenspergen, G. R., and Fagherazzi, S.: Overestimation of marsh vulnerability to sea level rise. Nature Climate Change, 6(3), 253–260. https://doi.org/10.1038/nclimate2909, 2016.

Krauss, K. W., Allen, J. A., and Cahoon, D. R.: Differential rates of vertical accretion and elevation change among aerial root types in Micronesian mangrove forests. Estuarine, Coastal and Shelf Science, 56(2), 251–259. https://doi.org/10.1016/S0272-7714(02)00184-1, 2003.

Krauss, K. W., McKee, K. L., Lovelock, C. E., Cahoon, D. R., Saintilan, N., Reef, R., and Chen, L.: How mangrove forests adjust to rising sea level. New Phytologist, 202(1), 19–34. https://doi.org/10.1111/nph.12605, 2014.

Le Minor, M., Zimmer, M., Helfer, V., Gillis, L. G., Huhn, K.: Flow and sediment dynamics around structures in mangrove ecosystems—a modeling perspective, in: Dynamic Sedimentary Environments of Mangrove Coasts, edited by Sidik, F. and Friess, D. A., Elsevier, 83–120, https://doi.org/10.1016/B978-0-12-816437-2.00012-4, 2021.

Li, C. W. and Busari, A. O.: Hybrid modeling of flows over submerged prismatic vegetation with different areal densities. Engineering Applications of Computational Fluid Mechanics, 13(1), 493–505. https://doi.org/10.1080/19942060.2019.1610501, 2019.

Liu, C., Shan, Y., and Nepf, H.: Impact of stem size on turbulence and sediment resuspension under unidirectional flow. Water Resources Research, 57(3), e2020WR028620. https://doi.org/10.1029/2020WR028620, 2021.

Liu, D., Diplas, P., Fairbanks, J. D., and Hodges, C. C.: An experimental study of flow through rigid vegetation, J. Geophys. Res., 113, F04015, doi:10.1029/2008JF001042, 2008.

Liu, Z., Chen, Y., Wu, Y., Wang, W., and Li, L.: Simulation of exchange flow between open water and floating vegetation using a modified RNG k-ε turbulence model. Environ Fluid Mech 17, 355–372. https://doi.org/10.1007/s10652-016-9489-5, 2017.

Lokhorst, I. R., Braat, L., Leuven, J. R., Baar, A. W., Van Oorschot, M., Selaković, S., and Kleinhans, M. G.: Morphological effects of vegetation on the tidal–fluvial transition in Holocene estuaries. Earth Surface Dynamics, 6(4), 883–901. https://doi.org/10.5194/esurf-6-883-2018, 2018.

López, F. and García, M. H.: Mean flow and turbulence structure of open-channel flow through non-emergent vegetation. Journal of Hydraulic Engineering, 127(5), 392–402. https://doi.org/10.1061/(ASCE)0733-9429(2001)127:5(392), 2001.

Lovelock, C. E., Cahoon, D. R., Friess, D. A., Guntenspergen, G. R., Krauss, K. W., Reef, R., Rogers, K., Saunders, M. L., Sidik, F., Swales, A., Saintilan, N., Thuyen, L. X, and Triet, T.: The vulnerability of Indo-Pacific mangrove forests to sea-level rise. Nature, 526(7574), 559–563. https://doi.org/10.1038/nature15538, 2015.

Mariotti, G. and Canestrelli, A.: Long-term morphodynamics of muddy backbarrier basins: Fill in or empty out?. Water Resources Research, 53(8), 7029–7054. https://doi.org/10.1002/2017WR020461, 2017.

Mariotti, G. and Fagherazzi, S.: A numerical model for the coupled long-term evolution of salt marshes and tidal flats. Journal of Geophysical Research: Earth Surface, 115(F1). https://doi.org/10.1029/2009JF001326, 2010.

Marsooli, R., Orton, P. M., Georgas, N., and Blumberg, A. F.: Three-dimensional hydrodynamic modeling of coastal flood mitigation by wetlands. Coastal Engineering, 111, 83–94. https://doi.org/10.1016/j.coastaleng.2016.01.012, 2016.

Maza, M., Adler, K., Ramos, D., Garcia, A. M., and Nepf, H.: Velocity and drag evolution from the leading edge of a model mangrove forest. Journal of Geophysical Research: Oceans, 122(11), 9144–9159. https://doi.org/10.1002/2017JC012945, 2017.

Menéndez, P., Losada, I. J., Torres-Ortega, S., Narayan, S., and Beck, M. W.: The global flood protection benefits of mangroves. Scientific reports, 10(1), 1–11. https://doi.org/10.1038/s41598-020-61136-6, 2020.

Mori, N., Chang, C. W., Inoue, T., Akaji, Y., Hinokidani, K., Baba, S., Takagi, M., Mori, S., Koike, H., Miyauchi, M., Suganuma, R., Sabunas, A., Miyashita, T., and Shimura, T.: Parameterization of mangrove root structure of *Rhizophora stylosa* in coastal hydrodynamic model. Frontiers in Built Environment, 7, 782219. https://doi.org/10.3389/fbuil.2021.782219, 2022.

Mudd, S. M., D'Alpaos, A., and Morris, J. T.: How does vegetation affect sedimentation on tidal marshes? Investigating particle capture and hydrodynamic controls on biologically

mediated sedimentation. Journal of Geophysical Research: Earth Surface, 115(F3). https://doi.org/10.1029/2009JF001566, 2010.

Mullarney, J. C., Henderson, S. M., Reyns, J. A., Norris, B. K., and Bryan, K. R.: Spatially varying drag within a wave-exposed mangrove forest and on the adjacent tidal flat. Continental Shelf Research, 147, 102-113. https://doi.org/10.1016/j.csr.2017.06.019, 2017.

Nardin, W. and Edmonds, D. A.: Optimum vegetation height and density for inorganic sedimentation in deltaic marshes. Nature Geoscience, 7(10), 722–726. https://doi.org/10.1038/ngeo2233, 2014.

Nardin, W., Edmonds, D. A., and Fagherazzi, S.: Influence of vegetation on spatial patterns of sediment deposition in deltaic islands during flood. Advances in Water Resources, 93, 236–248. https://doi.org/10.1016/j.advwatres.2016.01.001, 2016.

Nepf, H. M.: Drag, turbulence, and diffusion in flow through emergent vegetation. Water resources research, 35(2), 479–489. https://doi.org/10.1029/1998WR900069, 1999.

Nepf, H. M.: Flow and transport in regions with aquatic vegetation. Annual review of fluid mechanics, 44, 123–142. https://doi.org/10.1146/annurev-fluid-120710-101048, 2012.

Ohira, W., Honda, K., Nagai, M., and Ratanasuwan, A.: Mangrove stilt root morphology modeling for estimating hydraulic drag in tsunami inundation simulation. Trees, 27(1), 141–148. https://doi.org/10.1007/s00468-012-0782-8, 2013.

Otero, V., Van De Kerchove, R., Satyanarayana, B., Martínez-Espinosa, C., Fisol, M. A. B., Ibrahim, M. R. B., Sulong, I., Mohd-Lokman, H., Lucas, R., and Dahdouh-Guebas, F.: Managing mangrove forests from the sky: Forest inventory using field data and Unmanned Aerial Vehicle (UAV) imagery in the Matang Mangrove Forest Reserve, peninsular Malaysia. Forest Ecology and Management, 411, 35–45. https://doi.org/10.1016/j.foreco.2017.12.049, 2018.

Rodríguez, J. F., Saco, P. M., Sandi, S., Saintilan, N., and Riccardi, G.: Potential increase in coastal wetland vulnerability to sea-level rise suggested by considering hydrodynamic attenuation effects. Nature communications, 8(1), 1–12. https://doi.org/10.1038/ncomms16094, 2017.

Shan, Y., Liu, C., and Nepf, H.: Comparison of drag and velocity in model mangrove forests with random and in-line tree distributions. Journal of Hydrology, 568, 735–746. https://doi.org/10.1016/j.jhydrol.2018.10.077, 2019.

Shchepetkin, A. F. and McWilliams, J. C.: The regional oceanic modeling system (ROMS): a split-explicit, free-surface, topography-following-coordinate oceanic model. Ocean modelling, 9(4), 347–404. https://doi.org/10.1016/j.ocemod.2004.08.002, 2005.

Simard, M., Fatoyinbo, L., Smetanka, C., Rivera-Monroy, V. H., Castañeda-Moya, E., Thomas, N., and Van der Stocken, T.: Mangrove canopy height globally related to precipitation, temperature and cyclone frequency. Nature Geoscience, 12(1), 40–45. https://doi.org/10.1038/s41561-018-0279-1, 2019.

Suwa, R., Rollon, R., Sharma, S., Yoshikai, M., Albano, G. M. G., Ono, K., Adi, N. S., Ati, R. N. A., Kusumaningtyas, M. A., Kepel, T. L., Maliao, R. J., Primavera-Tirol, Y. H., Blanco, A. C., and Nadaoka, K.: Mangrove biomass estimation using canopy height and wood density in the South East and East Asian regions. Estur. Coast. Shelf S., 248, 106937, 2021.

Tanino, Y. and Nepf, H. M.: Lateral dispersion in random cylinder arrays at high Reynolds number. Journal of Fluid Mechanics, 600, 339–371. https://doi.org/10.1017/S0022112008000505, 2008.

Temmerman, S., Bouma, T. J., Govers, G., Wang, Z. B., De Vries, M. B., and Herman, P. M. J.: Impact of vegetation on flow routing and sedimentation patterns: Three-dimensional modeling for a tidal marsh. Journal of Geophysical Research: Earth Surface, 110(F4). https://doi.org/10.1029/2005JF000301, 2005.

Tinoco, R. O. and Coco, G.: A laboratory study on sediment resuspension within arrays of rigid cylinders. Advances in Water Resources, 92, 1–9. https://doi.org/10.1016/j.advwatres.2016.04.003, 2016.

Umlauf, L. and Burchard, H.: A generic length-scale equation for geophysical turbulence models. Journal of Marine Research, 61(2), 235–265. https://doi.org/10.1357/002224003322005087, 2003.

van Maanen, B., Coco, G., and Bryan, K. R.: On the ecogeomorphological feedbacks that control tidal channel network evolution in a sandy mangrove setting. Proceedings of the Royal Society A: Mathematical, Physical and Engineering Sciences, 471(2180), 20150115. https://doi.org/10.1098/rspa.2015.0115, 2015.

Warner, J. C., Armstrong, B., He, R., and Zambon, J. B.: Development of a coupled ocean–atmosphere–wave–sediment transport (COAWST) modeling system. Ocean modelling, 35(3), 230–244. https://doi.org/10.1016/j.ocemod.2010.07.010, 2010.

Warner, J. C., Sherwood, C. R., Arango, H. G., and Signell, R. P.: Performance of four turbulence closure models implemented using a generic length scale method. Ocean Modelling, 8(1-2), 81–113. https://doi.org/10.1016/j.ocemod.2003.12.003, 2005.

Weisscher, S. A. H., Van den Hoven, K., Pierik, H. J., and Kleinhans, M.: Building and raising land: mud and vegetation effects in infilling estuaries. Journal of Geophysical Research: Earth Surface, 127(1). https://doi.org/10.1029/2021JF006298, 2022.

Willemsen, P. W. J. M., Horstman, E. M., Borsje, B. W., Friess, D. A., and Dohmen-Janssen, C. M.: Sensitivity of the sediment trapping capacity of an estuarine mangrove forest. Geomorphology, 273, 189–201. https://doi.org/10.1016/j.geomorph.2016.07.038, 2016.

Willemsen, P. W. J. M., Smits, B. P., Borsje, B. W., Herman, P. M. J., Dijkstra, J. T., Bouma, T. J., and Hulscher, S. J. M. H.: Modeling decadal salt marsh development: variability of the salt marsh edge under influence of waves and sediment availability. Water resources research, 58(1), e2020WR028962. https://doi.org/10.1029/2020WR028962, 2022.

Xie, D., Schwarz, C., Brückner, M. Z., Kleinhans, M. G., Urrego, D. H., Zhou, Z., and Van Maanen, B.: Mangrove diversity loss under sea-level rise triggered by bio-morphodynamic feedbacks and anthropogenic pressures. Environmental Research Letters, 15(11), 114033. https://doi.org/10.1088/1748-9326/abc122, 2020.

Xu, Y., Esposito, C. R., Beltrán-Burgos, M., and Nepf, H. M.: Competing effects of vegetation density on sedimentation in deltaic marshes. Nature communications, 13(1), 1–10. https://doi.org/10.1038/s41467-022-32270-8, 2022.

Xu, Y. and Nepf, H.: Measured and predicted turbulent kinetic energy in flow through emergent vegetation with real plant morphology. Water Resources Research, 56(12), e2020WR027892. https://doi.org/10.1029/2020WR027892, 2020.

Xu, Y. and Nepf, H.: Suspended sediment concentration profile in a *Typha latifolia* canopy. Water Resources Research, 57(9), e2021WR029902. https://doi.org/10.1029/2021WR029902, 2021.

Yang, J. Q. and Nepf, H. M.: A turbulence-based bed-load transport model for bare and vegetated channels. Geophysical Research Letters, 45(19), 10–428. https://doi.org/10.1029/2018GL079319, 2018.

Yoshikai, M., Nakamura, T., Suwa, R., Argamosa, R., Okamoto, T., Rollon, R., Basina, R., Primavera-Tirol, Y. H., Blanco, A. C., Adi, N. S., and Nadaoka, K.: Scaling relations and substrate conditions controlling the complexity of *Rhizophora* prop root system. Estur. Coast. Shelf S., 248, 107014, 2021.

Yoshikai, M., Nakamura, T., Bautista, D. M., Herrera, E. C., Baloloy, A., Suwa, R., Basina, R., Primavera-Tirol, Y. H., Blanco, A.C., and Nadaoka, K.: Field measurement and prediction of drag in a planted *Rhizophora* mangrove forest. Journal of Geophysical Research: Oceans, 127, e2021JC018320. https://doi.org/10.1029/2021JC018320, 2022a.

Yoshikai, M., Nakamura, T., Suwa, R., Sharma, S., Rollon, R., Yasuoka, J., Egawa, R., and Nadaoka, K.: Predicting mangrove forest dynamics across a soil salinity gradient using

an individual-based vegetation model linked with plant hydraulics. Biogeosciences, 19(6), 1813–1832. https://doi.org/10.5194/bg-19-1813-2022, 2022b.

Zhang, K., Liu, H., Li, Y., Xu, H., Shen, J., Rhome, J., and Smith III, T. J.: The role of mangroves in attenuating storm surges. Estuarine, Coastal and Shelf Science, 102, 11–23. https://doi.org/10.1016/j.ecss.2012.02.021, 2012.

Zhang, X., Chua, V. P., and Cheong, H. F.: Hydrodynamics in mangrove prop roots and their physical properties. Journal of hydro-environment research, 9(2), 281–294. https://doi.org/10.1016/j.jher.2014.07.010, 2015.

Zhang, Y., Svyatsky, D., Rowland, J. C., Moulton, J. D., Cao, Z., Wolfram, P. J., Xu, C., and Pasqualini, D. (2022). Impact of coastal marsh eco-geomorphologic change on saltwater intrusion under future sea level rise. Water Resources Research, e2021WR030333. https://doi.org/10.1029/2021WR030333.

Zhu, Q., Wiberg, P. L., and Reidenbach, M. A.: Quantifying Seasonal Seagrass Effects on Flow and Sediment Dynamics in a Back-Barrier Bay. Journal of Geophysical Research: Oceans, 126(2), e2020JC016547. https://doi.org/10.1029/2020JC016547, 2021.

Supporting Information for Chapter 6

Note S6.1. Vegetation module implemented by Beudin et al. (2017)

As in the main text, we describe the equations in the two-dimensional form (*x*-*z* plane; zero velocity in *y*-direction) for convenience, while the equations implemented in ROM are three-dimensional; see Beudin et al. (2017) for the complete equations. The vegetation module implemented by Beudin et al. (2017) is for seagrasses/marshes that were represented by the cylinder drag model. They implemented the vegetation impacts not only on flows but also on wave damping. They also included additional functions of leaf bending considering the flexibility of submerged vegetations. Here we only describe the equations for impacts of rigid vegetation (no bending) on flow; these equations were used for comparison with the newly implemented drag and turbulence model for *Rhizophora* mangrove forests.

The drag by vegetation is calculated using the quadratic drag law as

$$F_{veg}(z) = \frac{1}{2} C_D n_v b_v u(z)^2 \quad \text{(S6.1)}$$

where F_{veg} is the spatially-averaged vegetation drag (m s^{-2}), z is the height from bed (m), C_D is the drag coefficient, n_v is the number of plants (stems or leaves) per unit area (m^{-2}), b_v is the stem or leaf width (m), and u is the flow velocity (m s^{-1}).

The production of turbulence kinetic energy (TKE) by vegetation drag is expressed as

$$P_w = F_{veg} u \quad \text{(S6.2)}$$

where P_w is the production of TKE by vegetation-generated wakes (m^2 s^{-3}). The dissipation rate of wakes is expressed as

$$D_w = c_2 \frac{P_w}{\tau_{eff}} = c_2 \frac{P_w}{min(\tau_{free}, \tau_{veg})} \quad \text{(S6.3)}$$

where D_w is the wake dissipation rate (m^2 s^{-4}), c_2 (1.92) is the constant of the k–ε model, and τ_{eff} (s) are the effective time-scale of wakes, which takes the minimum of time-scale of free turbulence (τ_{free}) and time-scale regulated by spaces between the nearest-neighbor plants (τ_{veg}). These are described as

$$\tau_{free} = \frac{k}{\varepsilon} \quad \text{(S6.4a)}$$

$$\tau_{veg} = \left(\frac{L^2}{{c_w}^2 P_w}\right)^{1/3} = \left(\frac{s^2}{{c_w}^2 P_w}\right)^{1/3} \quad \text{(S6.4b)}$$

where k is the TKE (m^2 s^{-2}), ε is the turbulent dissipation (m^2 s^{-3}), c_w is the model constant, which was set as 0.09 in Beudin et al. (2017), and L (m) is the length-scale of wakes, which

was set as the mean spacing of nearest-neighbor plants (s) in Beudin et al. (2017) where s is calculated from the density, width, and thickness of stem/leaf.

Note S6.2. Minor modifications of k–ε model introduced by Beudin et al. (2017)

In Beudin et al. (2017), the time-scale of wakes (τ_{eff}) was defined by the minimum of τ_{free} and τ_{veg} as described in Eq. (S6.3) in S1. However, we noticed the minimum function used for τ_{eff} yields complicated results. This may be because of the interactive feedback between τ_{free} and τ_{veg}, such that a case of $\tau_{eff} = \tau_{veg}$ in Eq. (S6.3) at one moment affects τ_{free} at the next moment through the equations for k (Eq. 6.2) and ε (Eq. 6.3); these in turn will affect τ_{eff} in Eq. (S6.3). As a result, the original model by Beudin et al. (2017) predicted TKE significantly smaller than the model predictions using the time-scale set as either of τ_{free} and τ_{veg}, which are difficult to interpret (results not shown). This minimum function for the time-scale of wake turbulence has not been well supported by previous theoretical and experimental works. As such, we avoided the use of the minimum function for τ_{eff} in our analysis.

The use of τ_{free} for τ_{eff} corresponds to the time-scale used such as in López and García (2001), Defina and Bixio (2005), and Baptist et al. (2007). However, King et al. (2012) and Liu et al. (2017) found that the use of τ_{veg} for τ_{eff}, which explicitly specifies the length-scale of wakes (L in Eq. S6.4b), would produce much better results than the use of τ_{free} for τ_{eff}.

For τ_{veg}, the use of s for the length-scale, L, in Eq. (S6.4b) inherently assumes the conditions $s < d$, where d is the cylinder diameter, which is equal to b_v for the seagrasses/marshes, where otherwise d should be applied for L (Tanino and Nepf, 2008; Nepf, 2012). In our analysis performed in the main text, the cylinder approximations (Fig. 6.3) did not satisfy the conditions $s < d$, thus the d (= b_v) would be appropriate for L.

Based on these, we modified Eqs. (S6.3–6.4) as

$$D_w = c_2 \frac{P_w}{\tau_{veg}} \tag{S6.5}$$

$$\tau_{veg} = \left(\frac{L^2}{{c_w}^2 P_w}\right)^{1/3} = \left(\frac{{b_v}^2}{{c_w}^2 P_w}\right)^{1/3} \tag{S6.6}$$

These modified equations were used for the model analysis using the cylinder array approximations in the main text.

Note S6.3. *Rhizophora* root model

The vertical profile of root projected area density (a_{root}) was computed using the empirical model for *Rhizophora* root structures (*Rh*-root model) proposed by Yoshikai et al. (2021); the procedure is summarized below.

The model was designed to predict the structure of the individual root system. It predicts the vertical profile of the number of roots of a tree using two parameters–*S* (scaling factor) and HR_{max} (maximum root height). The *S* and HR_{max} are strongly related to tree size represented by the stem diameter measured at 1.3-m height (D_{stem}). The k^{th} highest root in a root system can be then expressed as

$$HR_k = HR_{max} S^{(k-1)} \geq HR_{min} \quad \text{(S6.7a)}$$

$$S = 1 - \beta_S {D_{stem,i}}^{\alpha_S} \quad \text{(S6.7b)}$$

$$HR_{max} = \alpha_{HR} D_{stem,i} + \beta_{HR} \quad \text{(S6.7c)}$$

where HR_{min} in Eq. (S6.7a) is a model parameter (critical root height) that limits the minimum root height of a tree, $D_{stem,i}$ is the stem diameter (m) where the subscript "*i*" represents tree index, and α_S, β_S, α_{HR}, β_{HR} are the scaling parameters for *S* and HR_{max}, respectively. The α_S, β_S, α_{HR}, β_{HR} are considered site- and species-specific parameters, thus the values need to be derived through a field survey. See Yoshikai et al. (2021) or (2022a) for the procedure to obtain these parameter values in the field with reduced workload. The value of HR_{min} also needs to be determined for a site through a field survey.

From Eq. (S6.7), the heights of all roots of a tree can be predicted. Yoshikai et al. (2022a) suggested that the individual roots can be approximated as a linear shape to estimate the projected area of roots. The linear shape of a root projected from the direction along the *x*-axis can be expressed as

$$z = (tan\theta_l)\left(\frac{y}{cos\psi}\right) + HR \qquad \text{where } 0 < z < HR \quad \text{(S6.8)}$$

where *y* and *z* represent the horizontal and vertical coordinate of a point, where $y = 0$ at the location where a root emerges from the stem or another root and $z = 0$ at the ground, *HR* is the height of a root (m), θ_l is the angle of the approximated linear shape relative to the horizontal axis, and ψ is the azimuth root angle around the *z*-axis relative to the *x*-axis. The value of θ_l was empirically determined in Yoshikai et al. (2022a). The projected area of a root can be calculated by multiplying the root length provided by Eq. (S6.8) and the mean root diameter ($D_{root,ave}$). Then, by summing up the projected areas of all the roots per vertical height interval, *dz* (0.05 m in this study), the vertical profile of root projected area per *dz* of a tree "*i*" ($A_{root,i}(z)$ (m^2)) can be calculated. Here, because the root azimuth angle in Eq. (6.8), ψ, is unknown, Yoshikai et al. (2022a) employed random numbers to ψ and estimated $A_{root,i}$ from the ensemble approach. Based on the ensemble computations, we found that the $A_{root,i}$ computed using random numbers for ψ is approximately 80 % of the $A_{root,i}$ computed using the

zero value for ψ for all the roots, which is referred to as $A_{root0,i}$ below. Hence, we calculated the $A_{root,i}$ as

$$A_{root,i}(z) = 0.8 \times A_{root0,i}(z) \quad \text{(S6.9)}$$

where the multiplication by 0.8 represents the effects of random azimuth angle on the projected area. This approach (Eq. S6.9) does not require the ensemble approach to estimate $A_{root,i}$, which is convenient for implementation to the numerical model.

Note S6.4. Tree census data

We used tree census data collected from three sites–two from Bakhawan Ecopark, Aklan, Philippines (11° 43' N, 122° 23' E; Suwa et al., unpublished data), and one from Fukido River mangrove forest, Ishigaki, Japan (24° 20' N, 124° 15' E; Suwa et al., 2021)–to investigate the validity of the proposed parameterization of tree size variations (see Section 6.2.1.3). We refer to the two sites of Bakhawan Ecopark as Bak1 and Bak2, respectively, and Fukido River mangrove forest as Fuk.

The sites Bak1 and Bak2 are 30-year-old and 17-year-old planted stands, respectively, of *Rhizophora apiculata*; Bak2 includes the site where the vegetation and hydrodynamic data were collected by Yoshikai et al. (2022a), which were used for model evaluation in this study. The site Fuk is a natural mangrove forest vegetated by *Rhizophora stylosa* and *Buruguiera gymnorrhiza*. Along with the soil salinity gradient, a notable change in the forest structural variables (stem diameter, tree height, species composition) was observed at this forest (Yoshikai et al., 2022b). As described in Suwa et al. (2021), a 7-m radius circular plot was established and the stem diameter at 1.3-m height (D_{stem}) was measured for all the trees. The number of plots for the tree census is 6 for Bak1, 6 for Bak2, and 15 for Fuk, respectively. We did not use the data of 10 plots out of a total of 24 plots in Fuk collected in Suwa et al. (2021) because of the absence of *R. stylosa* trees.

The root structures of *R. apiculata* and *R. stylosa* at these three sites were investigated in Yoshikai et al. (2021) and the values of the *Rh*-root model parameters were derived (Table S6.1). These parameter values were used for the computation of the vertical profile of root projected area per *dz* of a tree, $A_{root,i}(z)$, for each site using the *Rh*-root model; these are shown in Fig. 6.2.

Table S6.1. *Rhizophora* root model parameters for three tree census sites.

Parameter	Bak1	Bak2	Fuk
Scaling parameter for S (α_S)	–0.91	–2.04	–1.76

Scaling parameter for S (β_S)	$10^{-2.00}$	$10^{-3.59}$	$10^{-3.18}$
Scaling parameter for S (α_{HR})	2.06	15.38	2.71
Scaling parameter for S (β_{HR})	0.82	0.08	0.50
Critical root height (HR_{min}, m)	0.01[a]	0.01	0.01[a]
Root angle of approximated linear root shape (θ_l, degree)	–34.5[a]	–34.5	–41.9
Mean root diameter ($D_{root,ave}$, m)	0.03[a]	0.03	0.03

[a] Value determined for Bak2 was used.

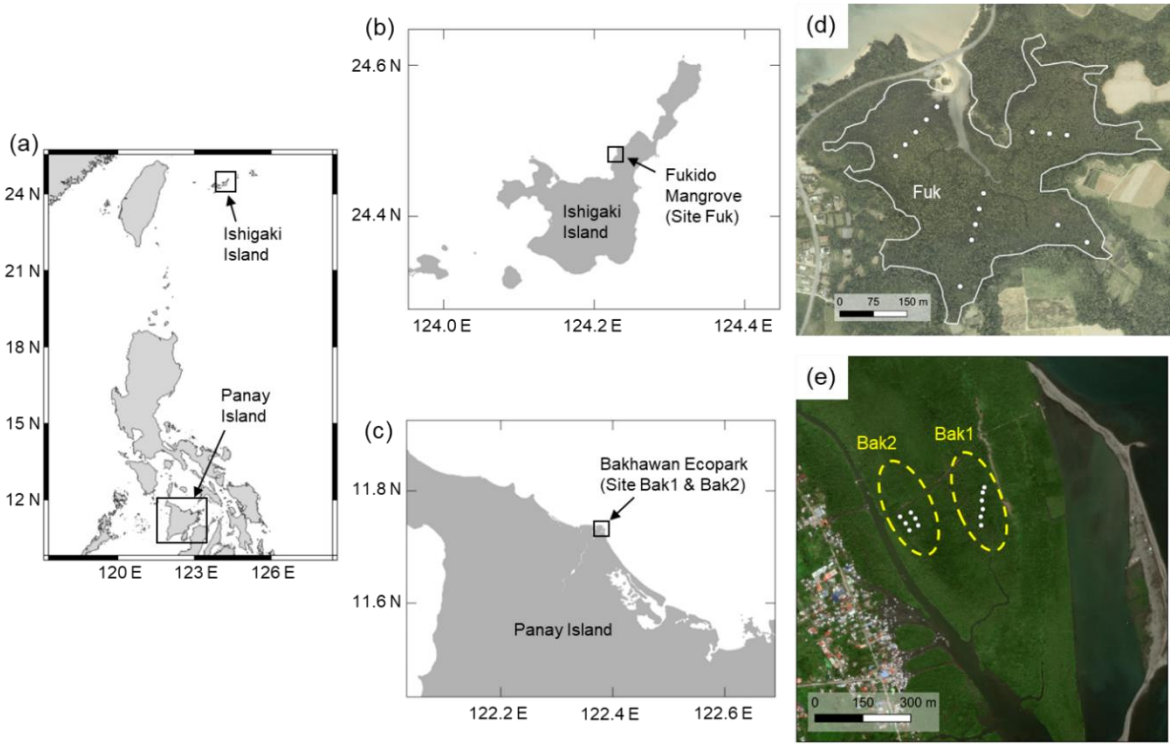

Figure S6.1. Map of the sites (Bak1, Bak2, and Fuk) indicated in Fig. 6.2. The white dots in panels “d” and “e” represent the tree census stations from which data are used in Fig. 6.2. In panel “e”, the approximate locations of the 30-year-old (Bak1) and 17-year-old (Bak2) planted stands are also indicated. Shorelines in panel “a–c” are from the Global Self-consistent, Hierarchical, High-resolution Geography (GSHHG) database. The aerial photo in panel “d” is from Asia Air Survey Co. Ltd., Japan, and the satellite image in panel “e” is from © Google Earth.

Note S6.5. Implementation of the new model to the COAWST

We replaced the equations for drag force and turbulence introduced by Beudin et al. (2017) with the ones presented in Sections 6.2.1.1–6.2.1.2 (Eqs. (6.1)–(6.6)) in the COAWST. The *Rhizophora* root module that gives $a_{root}(z)$ from n_{tree} and $D_{stem,ave}$ using the *Rh*-root model was newly added in the COAWST (Fig. 6.1). Table S6.2 shows the grid-explicit input parameters related to this study. Parameters related to root structures are inputted to the model as universal parameters (not grid-explicit; Table S6.1). We introduced a new input parameter, species index (*spe*), that identifies the vegetation as *Rhizophora* species (*spe* = 1) or seagrass/marsh species (*spe* = 0). Depending on *spe*, the model interpretation of the inputted parameters varies (Table S6.2). If *spe* = 1, the vegetation module interacts with the *Rhizophora* root module for a_{root} (Fig. 6.1) to compute the drag by the roots (F_{root} in Eq. (6.1)) and the TKE production and dissipation of the root-generated wakes ($P_{w,root}$ and $D_{w,root}$ in Eqs. (6.4)–(6.6)). Otherwise (*spe* = 0), zero value is given to a_{root}, which vanishes all the root-related terms in Eqs. (6.1), (6.4)–(6.6), making them identical to the ones introduced by Beudin et al. (2017) and thus applying the cylinder drag model (however, see S2 for the modification of the equations of Beudin et al. (2017)). This means that the equations presented can be used both for *Rhizophora* mangroves and seagrasses/marshes by switching the value of *spe*.

Table S6.2. Grid-explicit input parameters. Symbols used in Beudin et al. (2017) are also shown. Parameters absent in the column of Beudin et al. (2017) are the ones newly added in this study. Mean tree height (H_{ave}) is only relevant for some extreme conditions when the water level becomes higher than H_{ave}.

Symbol		Unit	Interpretation by the model	
This study	Beudin et al. (2017)		Case *spe* = 1	Case *spe* = 0
spe		-	*Rhizophora* species	Seagrass/marsh
$D_{stem,ave}$	b_v	m	Mean stem diameter	Leaf width or stem diameter
n_{ree}	n_v	m^{-2}	Tree density	Leaf or stem density
H_{ave}	l_v	m	Mean tree height	Leaf or stem length

Note S6.6. Generic mangrove root model used in Xie et al. (2020)

We examined the use of the mangrove root model used in Xie et al. (2020) (termed as generic root model in the main text) as a predictor of a_{root} in Eq. (6.1). In Xie et al. (2020), the

shape of roots was simplified to cylindrical objects with a fixed diameter and height, hence to the array of vertical cylinders. The number of roots of a tree is given by the function of stem diameter as:

$$n_{root,ind} = n_{root,max} \frac{1}{1+exp\left[f_{root}\left(\frac{D_{stem,max}}{2} - D_{stem}\right)\times 100\right]} \quad \text{(S6.10)}$$

where $n_{root,ind}$ is the number of roots of a tree having a stem diameter of D_{stem} (m), $n_{root,max}$ is the maximum number of roots of a tree, f_{root} = 0.1 is a constant describing the rate of increase of roots with D_{stem}, $D_{stem,max}$ is the maximum stem diameter (m), and the factor 100 is for the unit conversion of stem diameter from meter to centimeter. In Xie et al. (2020), the parameters are set as $n_{root,max}$ = 5000, $D_{stem,max}$ = 1.0 (m) for *Rhizophora* trees. In addition, Xie et al. (2020) gave the root diameter (D_{root}) and height (H_{root}) values as D_{root} = 0.01 m and H_{root} = 0.15 m, respectively.

We applied the generic root model to the field mangrove setting of Bakhawan Ecopark. We used the measured mean stem diameter $D_{stem,ave}$ = 0.066 m (Table 6.1) for D_{stem} in Eq. (S6.10), then calculated the $n_{root,ind}$ with the same parameter setting as Xie et al. (2020). The a_{root}, which is used for calculating the drag by the roots in Eq. (6.1), is then given as:

$$a_{root} = n_{tree} n_{root,ind} D_{root} \quad \text{for } z \le H_{root} \quad \text{(S6.11a)}$$

$$a_{root} = 0 \quad \text{for } z > H_{root} \quad \text{(S6.11b)}$$

Note S6.7. Calculation of bed shear stress in the COAWST and the choice of bed roughness value for the case of increased z_0

In the COAWST, bed shear stress is computed based on quadratic law using the velocities at the bottom computational cell as (Warner et al., 2008):

$$\tau_{bed} = \rho_w C_{bed} u^2 \quad \text{(S6.12)}$$

where τ_{bed} is the bed shear stress (N m^{-2}), ρ_w is the water density (kg m^{-3}), C_{bed} is the bed drag coefficient, and u is the flow velocity (m s^{-1}) computed at the bottom cell. It assumes that the flow in the bottom boundary layer has the classic vertical logarithmic profile as:

$$|u| = \frac{u_*}{\kappa} \ln\left(\frac{z_{bottom}}{z_0}\right) \quad \text{(S6.13)}$$

where u_* is the friction velocity, $\sqrt{\tau_{bed}}$, κ = 0.41 is the von Kármán constant, z_{bottom} is the elevation of the middle point of the bottom computational cell above the bed (m), and z_0 is the bed roughness length (m). From Eqs. (S6.12)–(S6.13), the C_{bed} is calculated using z_0 as:

$$C_{bed} = \kappa^2 \left[\ln\left(\frac{z_{bottom}}{z_0}\right)\right]^{-2} \quad \text{(S6.14)}$$

The value of z_0 or C_{bed} can be related to the Manning's coefficient ($n_{manning}$) considering turbulent open channel flow as follows. In an open channel flow with depth-averaged velocity

U_{mean}, water depth h, and bed slope S_0, the U_{mean} can be described using the Manning's coefficient as:

$$U_{mean} = \frac{1}{n_{manning}} h^{2/3} {S_0}^{1/2} \quad \text{(S6.15)}$$

Assuming a steady flow where the momentum balance can be reduced to an equilibrium between the bed shear stress τ_{bed} and the gravitational (or pressure) forces driving the flow, the bed shear stress can be expressed as (Crompton et al., 2020):

$$\tau_{bed} = \rho_w g h S_0 \quad \text{(S6.16)}$$

where g is the gravitational acceleration (m s^{-2}). From Eq. (S6.15)–(S6.16) and assuming that the depth-averaged form of Eq. (S6.12), $\tau_{bed} = \rho_w C_{bed,mean} U_{mean}^2$, is valid, the Manning's coefficient can be expressed as:

$$n_{manning} = h^{1/6} \sqrt{\frac{C_{bed,mean}}{g}} \quad \text{(S6.17)}$$

where $C_{bed,mean}$ is the bed drag coefficient which is used for computing τ_{bed} using the U_{mean}. Also, by relating the depth-averaged form of Eq. (S6.14), $C_{bed,mean}$ can be expressed using z_0 as (Lenz et al., 2017):

$$C_{bed,mean} = \kappa^2 \left[\ln\left(\frac{h}{z_0}\right) \right]^{-2} \quad \text{(S6.18)}$$

Considering the Manning's coefficient of 0.14, which is a value typically used for approximating the drag by mangroves (e.g., Zhang et al., 2012), and a water depth of 0.5 m, based on Eqs. (S6.17)–(S6.18), the equivalent bed roughness z_0 is 0.22 m.

The application of Eqs. (6.12)–(6.14) needs the condition $z_0 < z_{bottom}$, which limits the applicable z_0 value for representing the mangrove drag depending on the water depth or thickness of the bottom cell. In the application to the field-based study, the lowest water depth for examination was around 0.15 m (Fig. 6.6; Table S6.6), where the z_{bottom} is decreased down to 0.015 m. In order to increase the applicable z_0 value in our analysis, we reduced the number of vertical layers from 5 to 3 (Table 6.2), which increased the minimum z_{bottom} up to 0.025 m. We then conducted the analysis using z_0 = 0.02 m as a case of increased z_0. However, this value is considered generally lower compared to the typical Manning's coefficient value of 0.14 (of which the equivalent value is z_0 = 0.22 m under the water depth 0.5 m).

Table S6.3. Measured flow variables in the model and field mangrove forest by Maza et al. (2017) and Yoshikai et al. (2022a), respectively, the variables controlled in the model, and target variables to reproduce for application to the respective mangrove forest.

	Model mangrove forest in Maza et al. (2017)	Field mangrove forest in Yoshikai et al. (2022a)
Measured flow variables	h, U, $u(z)$, $k(z)$	h, $\Delta\eta$, $u(z)$, U, τ_{bed}

Controlled variables in the model	h, U	h, $\Delta\eta$
Target variables to reproduce	$u(z)$, $k(z)$	$u(z)$, U, τ_{bed}

Table S6.4. Data from the flume experiments of Maza et al. (2017) that were used for the model validation in Figure 6.4. The values of geometric and flow parameters were converted from the scale in the flume to the real scale. The velocity (u) and turbulent kinetic energy (k) were taken by averaging the measurements at five lateral positions (ADV3p1–p5; see Fig. 6.5 of Maza et al., 2017) in the model mangrove forest where the flows were fully developed, which were taken as spatially-averaged values in the mangrove forest. HR_{max}: maximum root height, h: water depth, U: cross-sectional mean velocity, z: height above the bed.

Experiment #	HR_{max} (m)	h (m)	U (m s^{-1})	z (m)	u/U	k/U^2
Exp 1	2.016	3.0	0.31	0.08	0.54	0.012
				0.32	0.62	0.013
				0.56	0.66	0.015
				0.80	0.64	0.032
				1.04	0.69	0.026
				1.28	0.75	0.024
				1.52	0.84	0.053
				1.76	0.97	0.035
				2.00	1.05	0.033
				2.24	1.10	0.043
Exp 2	2.016	1.79	0.58	0.08	0.75	0.018
				0.20	0.77	0.021
				0.32	0.80	0.017
				0.44	0.84	0.016
				0.56	0.83	0.021
				0.68	0.83	0.026
				0.80	0.86	0.023
				0.92	0.85	0.023

Table S6.5. Data from field measurements of Yoshikai et al. (2022a) that were used for the model validation in Figure 6.5. Velocity (u) was obtained by averaging the measurements at four locations around the reference tree shown in Fig. S6.3c which was taken as spatially-averaged values in the mangrove forest.

Local time	h (m)	z (m)	u (m s^{-1})
2018/9/10 12:50	0.45	0.35	0.060
		0.30	0.064
		0.25	0.060
		0.20	0.057
		0.15	0.055
		0.10	0.044

		0.05	0.036
2018/9/10 13:40	0.21	0.18	0.096
		0.11	0.082
		0.04	0.059
2018/9/11 13:00	0.53	0.45	0.046
		0.40	0.039
		0.35	0.045
		0.30	0.044
		0.25	0.044
		0.20	0.041
		0.15	0.034
		0.10	0.028
		0.05	0.022
2018/9/11 14:00	0.28	0.23	0.085
		0.14	0.072
		0.05	0.052

Table S6.6. Data from field measurements of Yoshikai et al. (2022a) that were used for the model forcing and validation in Figures 6.6–6.8. The $\Delta\eta$ is the water level difference imposed across the open boundaries in the model (see Fig. S6.2), h is the water depth, U is the cross-sectional mean flow velocity, u_{bottom} is the spatially-averaged velocity at z = 0.05 m, and τ_{bed} is the bed shear stress.

Local time	$\Delta\eta$ (m)	h (m)	U (m s^{-1})	u_{bottom} (m s^{-1})	τ_{bed} (N m^{-2})
2018/09/10 12:50	0.0143	0.45	0.050	0.036	0.023
2018/09/10 13:10	0.0189	0.36	0.063	0.036	0.039
2018/09/10 13:20	0.0273	0.32	0.064	0.041	0.032
2018/09/10 13:40	0.0462	0.21	0.079	0.064	0.023
2018/09/10 13:50	0.0572	0.16	0.074	0.066	-
2018/09/11 13:00	0.0065	0.53	0.038	0.022	0.008
2018/09/11 13:10	0.0078	0.50	0.038	0.023	0.004
2018/09/11 13:20	0.0124	0.46	0.047	0.027	0.008
2018/09/11 13:40	0.0163	0.37	0.051	0.034	0.014
2018/09/11 13:50	0.0228	0.33	0.054	0.036	0.010
2018/09/11 14:00	0.0260	0.28	0.070	0.053	0.012
2018/09/11 14:10	0.0345	0.23	0.071	0.053	0.031
2018/09/11 14:20	0.0449	0.18	0.070	0.060	0.037
2018/09/11 14:30	0.0585	0.14	0.078	0.077	-

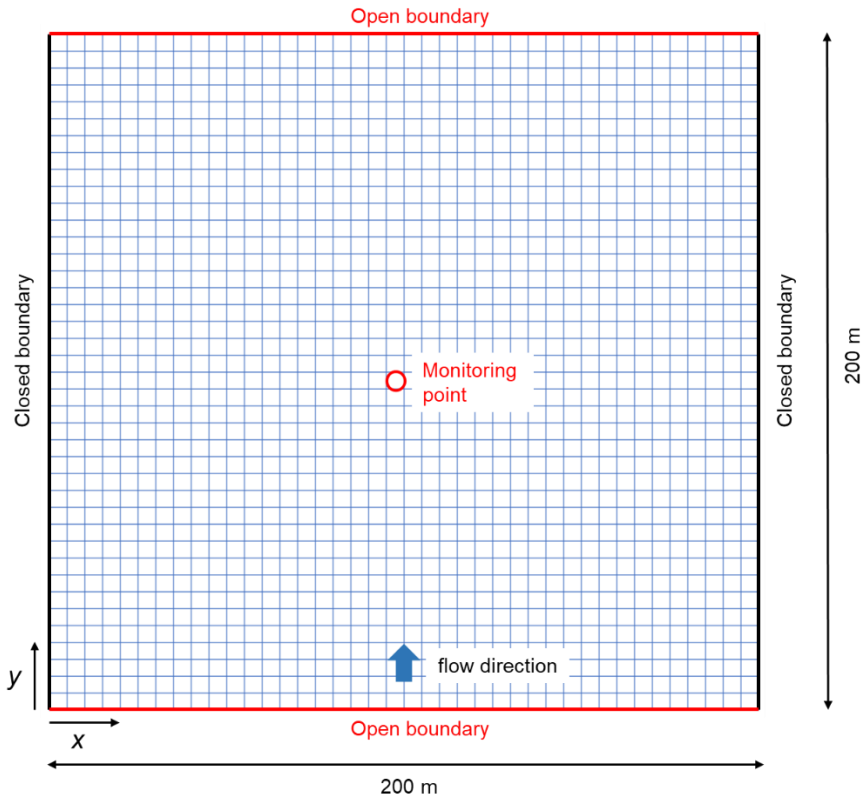

Figure S6.2. Model grid (40 × 40 with 5 m horizontal resolution) used for testing the model against laboratory-based and field-based studies. The red circle indicates the location of the monitoring point at which the simulated flow variables were compared with the measured data.

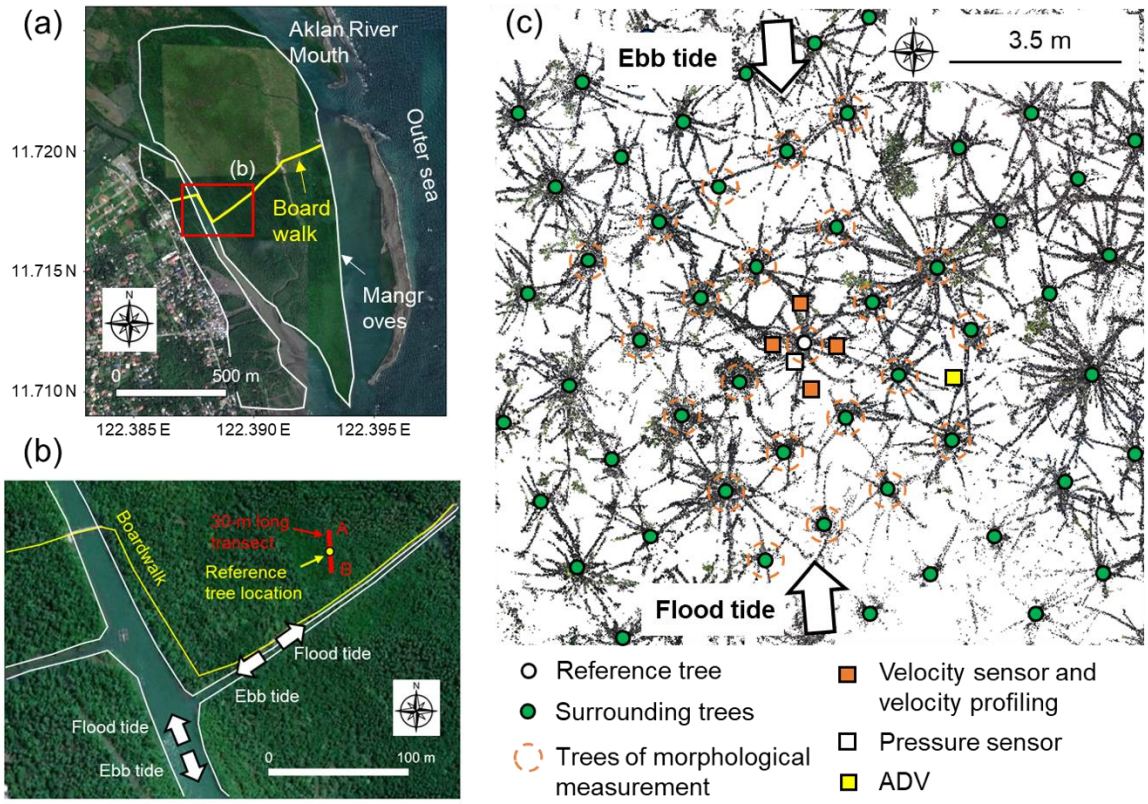

Figure S6.3. (a) Satellite image (© Google Earth) of the study site of Yoshikai et al. (2022a) – Bakhawan Ecopark (red box indicates the area of panel "b"), (b) locations of transect A–B across which the water level gradient was measured together with the hydrodynamic parameters around the reference tree (the satellite image is from © Google Earth), (c) top view of LiDAR point clouds around the reference tree with information on the locations of trees whose morphological structures were measured, where velocity profiling was conducted, and where sensors were deployed (velocity sensor: electromagnetic velocity meter deployed near the bottom; ADV: Acoustic Doppler Velocimeter deployed to estimate the bed shear stress). It has been shown in Yoshikai et al. (2022a) that the average of the velocity measured at the four locations represents well the spatially-averaged values. The point clouds shown were cropped at heights between 0.1–1.7 m for better visualization of the root systems. Figures are modified from Yoshikai et al. (2022a).

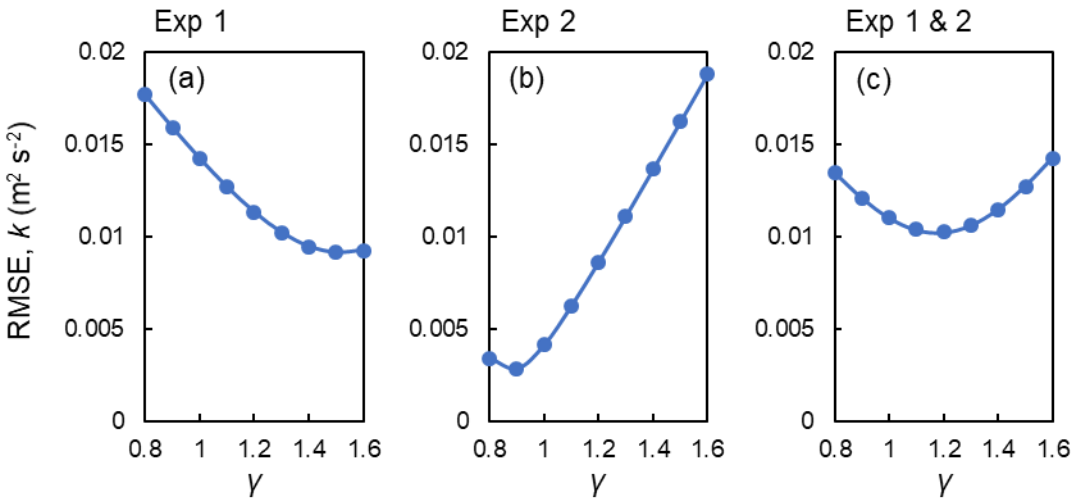

Figure S6.4. Root mean square error (RMSE) of modeled turbulent kinetic energy (k) against the measured data in (a) Exp 1, (b) Exp2, and (c) both Exp 1 and 2 of the flume experiment, by varying the value of scale coefficient (γ), for which the computation of the predicted value at the height of the measurement point was obtained by the interpolation of k computed at adjacent vertical layers.

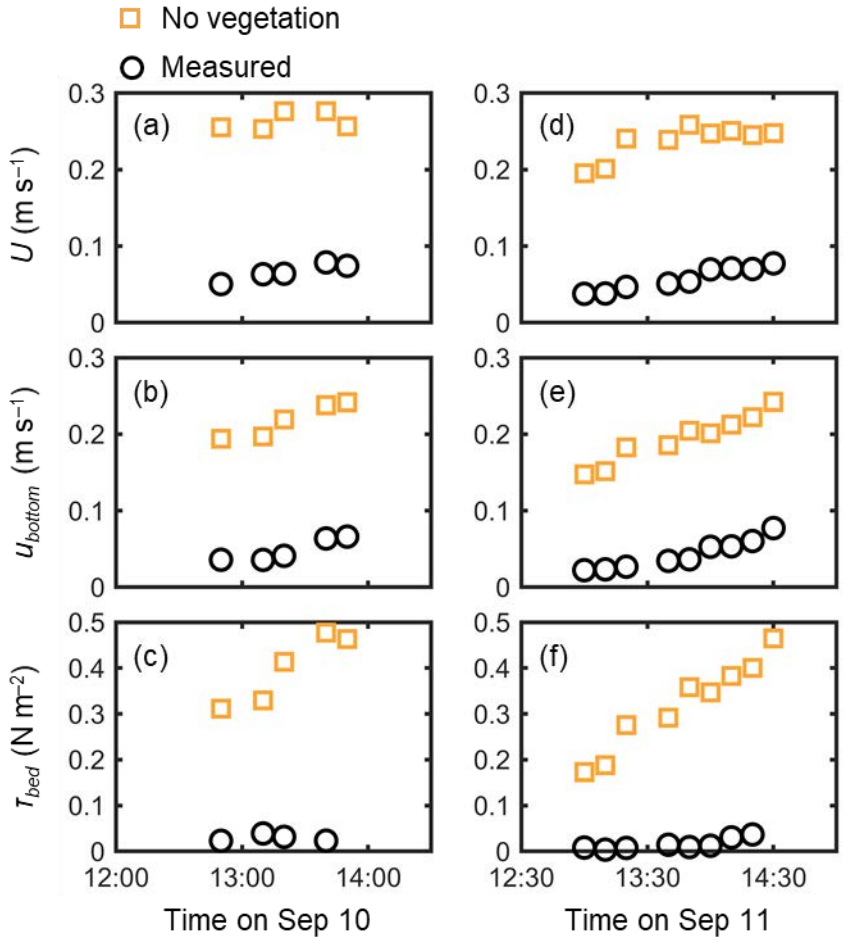

Figure S6.5. Time-series of measured and predicted (a, d) cross-sectional mean velocity (U), (b, e) (spatially averaged) velocity at z = 0.05 m, and (c, f) bed shear stress (τ_{bed}) during the two-days measurement in Bakhawan Ecopark. The measured values are from Yoshikai et al. (2022a) and the predicted values are obtained through the COAWST without imposing vegetation drag (no vegetation).

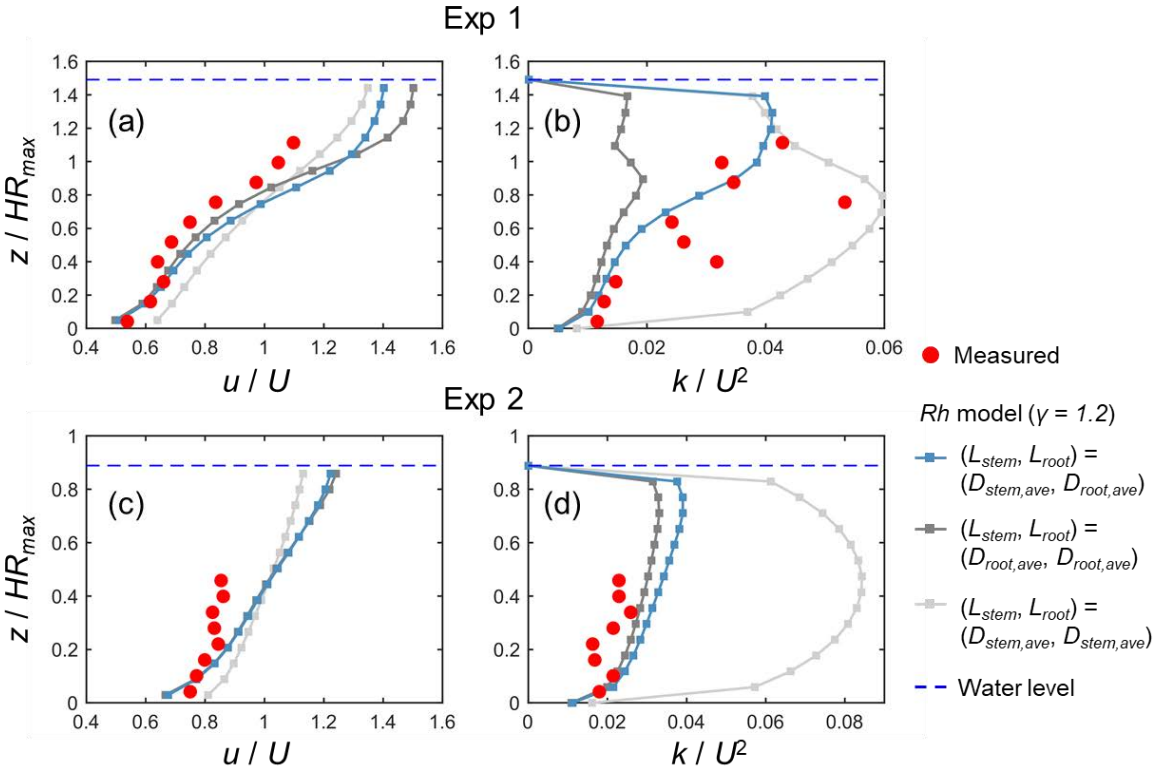

Figure S6.6. Comparison of the vertical profiles of (temporally and spatially averaged) velocity (u) and turbulent kinetic energy (k) normalized by the cross-sectional mean velocity (U) measured by Maza et al. (2017) and predicted by the COAWST using the *Rh* model with different length-scales of stem- and root-generated wakes (L_{stem} and L_{root}, respectively) defined – blue markers: L_{stem} and L_{root} set to the stem diameter ($D_{stem,ave}$) and root diameter ($D_{root,ave}$), respectively; dark-gray markers: L_{stem} and L_{root} both set to $D_{root,ave}$; light-gray markers: L_{stem} and L_{root} both set to $D_{stem,ave}$. The scale coefficient (γ) was set to 1.2 for all the cases.

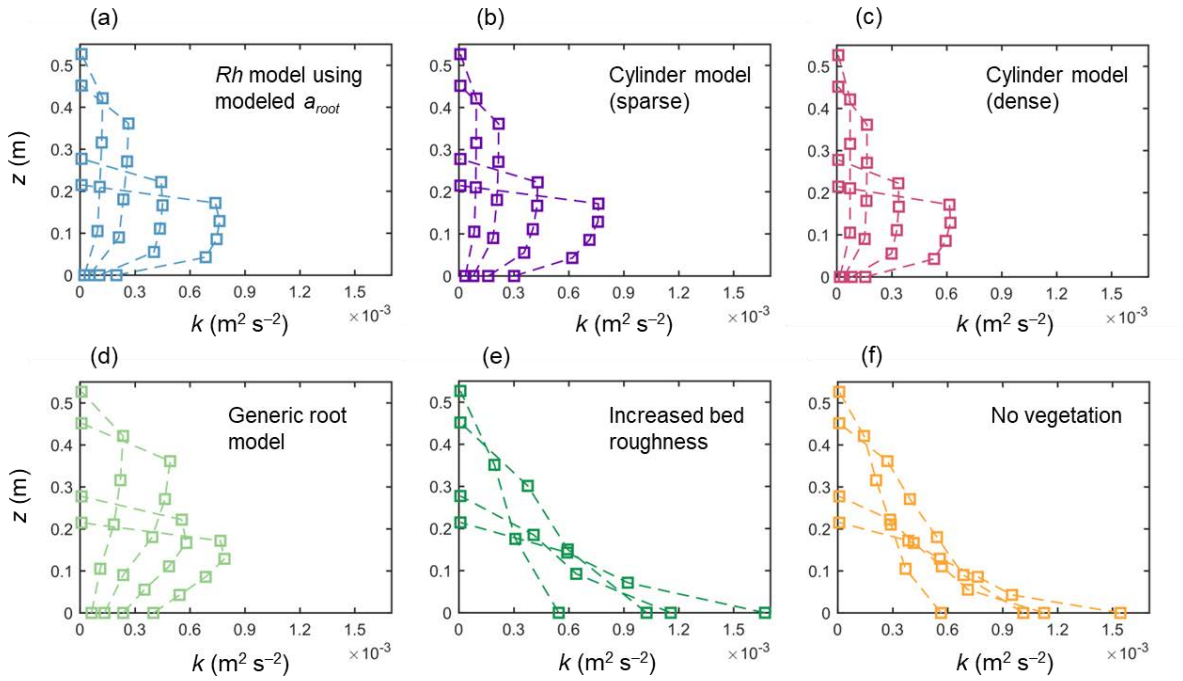

Figure S6.7. Vertical profiles of turbulent kinetic energy (k) predicted by the COAWST employing (a) *Rh* model using modeled root projected area density profile (a_{root}), (b) cylinder model with sparse and (c) dense arrays, (d) generic root model, (e) increased bed roughness as an approximation of vegetation drag, and (f) without imposing vegetation drag (no vegetation) for some tidal phases corresponding to the ones shown in Fig. 6.5.

References for the Supporting Information

Baptist, M. J., Babovic, V., Rodríguez Uthurburu, J., Keijzer, M., Uittenbogaard, R. E., Mynett, A., and Verwey, A.: On inducing equations for vegetation resistance. Journal of Hydraulic Research, 45(4), 435–450. https://doi.org/10.1080/00221686.2007.9521778, 2007.

Beudin, A., Kalra, T. S., Ganju, N. K., and Warner, J. C.: Development of a coupled wave-flow-vegetation interaction model. Computers & Geosciences, 100, 76–86. https://doi.org/10.1016/j.cageo.2016.12.010, 2017.

Crompton, O., Katul, G. G., and Thompson, S.: Resistance formulations in shallow overland flow along a hillslope covered with patchy vegetation. Water Resources Research, 56, e2020WR027194. https://doi.org/10.1029/2020WR027194, 2020.

Defina, A. and Bixio, A. C.: Mean flow and turbulence in vegetated open channel flow. Water Resources Research, 41(7). https://doi.org/10.1029/2004WR003475, 2005.

King, A. T., Tinoco, R. O., and Cowen, E. A.: A k–ε turbulence model based on the scales of vertical shear and stem wakes valid for emergent and submerged vegetated flows. Journal of Fluid Mechanics, 701, 1–39. https://doi.org/10.1017/jfm.2012.113, 2012.

Lentz, S. J., Davis, K. A., Churchill, J. H., and DeCarlo, T. M.: Coral reef drag coefficients-water depth dependence. Journal of Physical Oceanography, 47(5), 1061–1075. https://doi.org/10.1175/jpo-d-16-0248.1, 2017.

Liu, Z., Chen, Y., Wu, Y., Wang, W., and Li, L.: Simulation of exchange flow between open water and floating vegetation using a modified RNG k-ε turbulence model. Environ Fluid Mech 17, 355–372. https://doi.org/10.1007/s10652-016-9489-5, 2017.

López, F. and García, M. H.: Mean flow and turbulence structure of open-channel flow through non-emergent vegetation. Journal of Hydraulic Engineering, 127(5), 392–402. https://doi.org/10.1061/(ASCE)0733-9429(2001)127:5(392), 2001.

Nepf, H. M.: Flow and transport in regions with aquatic vegetation. Annual review of fluid mechanics, 44, 123–142. https://doi.org/10.1146/annurev-fluid-120710-101048, 2012.

Suwa, R., Rollon, R., Sharma, S., Yoshikai, M., Albano, G. M. G., Ono, K., Adi, N. S., Ati, R. N. A., Kusumaningtyas, M. A., Kepel, T. L., Maliao, R. J., Primavera-Tirol, Y. H., Blanco, A. C., and Nadaoka, K.: Mangrove biomass estimation using canopy height and wood density in the South East and East Asian regions. Estur. Coast. Shelf S., 248, 106937, 2021.

Tanino, Y. and Nepf, H. M.: Lateral dispersion in random cylinder arrays at high Reynolds number. Journal of Fluid Mechanics, 600, 339–371. https://doi.org/10.1017/S0022112008000505, 2008.

Warner, J. C., Sherwood, C. R., Signell, R. P., Harris, C. K., and Arango, H. G.: Development of a three-dimensional, regional, coupled wave, current, and sediment-transport model. Computers & geosciences, 34(10), 1284–1306. https://doi.org/10.1016/j.cageo.2008.02.012, 2008.

Xie, D., Schwarz, C., Brückner, M. Z., Kleinhans, M. G., Urrego, D. H., Zhou, Z., and Van Maanen, B.: Mangrove diversity loss under sea-level rise triggered by bio-morphodynamic feedbacks and anthropogenic pressures. Environmental Research Letters, 15(11), 114033. https://doi.org/10.1088/1748-9326/abc122, 2020.

Yoshikai, M., Nakamura, T., Suwa, R., Argamosa, R., Okamoto, T., Rollon, R., Basina, R., Primavera-Tirol, Y. H., Blanco, A. C., Adi, N. S., and Nadaoka, K.: Scaling relations and substrate conditions controlling the complexity of *Rhizophora* prop root system. Estur. Coast. Shelf S., 248, 107014. https://doi.org/10.1016/j.ecss.2020.107014, 2021.

Yoshikai, M., Nakamura, T., Bautista, D. M., Herrera, E. C., Baloloy, A., Suwa, R., Basina, R., Primavera-Tirol, Y. H., Blanco, A.C., and Nadaoka, K.: Field measurement and

prediction of drag in a planted *Rhizophora* mangrove forest. Journal of Geophysical Research: Oceans, 127, e2021JC018320. https://doi.org/10.1029/2021JC018320, 2022a.

Yoshikai, M., Nakamura, T., Suwa, R., Sharma, S., Rollon, R., Yasuoka, J., Egawa, R., and Nadaoka, K.: Predicting mangrove forest dynamics across a soil salinity gradient using an individual-based vegetation model linked with plant hydraulics. Biogeosciences, 19(6), 1813–1832. https://doi.org/10.5194/bg-19-1813-2022, 2022b.

Zhang, K., Liu, H., Li, Y., Xu, H., Shen, J., Rhome, J., and Smith III, T. J.: The role of mangroves in attenuating storm surges. Estuarine, Coastal and Shelf Science, 102, 11–23. https://doi.org/10.1016/j.ecss.2012.02.021, 2012.

Chapter 7: Modeling flow and sediment transport in an estuarine mangrove forest and adjacent areas

7.1.1 Abstract

Mangroves, a coastal wetland ecosystem with complex above-ground root systems, are known to modulate flow and sediment transport and promote sedimentation – processes that could drive the sequestration of allochthonous organic carbon and the long-term geomorphic evolution of mangrove forests. However, insights on how and to what extent mangrove forests impact the sediment transport in the forest and their adjacent areas are limited. This study aims to address these challenges by using a hydrodynamic-sediment transport model. A new model incorporating the impacts of species-specific three-dimensional root structures (e.g., “prop roots” of *Rhizophora* species and “pencil roots” of *Avicennia* and *Sonneratia* species) on flow and sediment transport was applied to a restored riverine mangrove forest in the Philippines influenced by tidal and fluvial processes. The model suggested the significant impact of the mangrove forest reducing the flow velocity coming into the forest and regulating sediment resuspension. The model also suggested a threshold-like response of sedimentation rate in mangrove forest to the river runoff events such that the rise of water level in the adjacent channel brought by the increase in the river runoff could initiate the overland flow on the mangrove forest and supply a significant amount of fluvial sediments to the mangrove forest, facilitating sedimentation. Simulations without imposing the impact of mangroves on flow showed a significant increase in flow velocity and a significant amount of sediment loss in the mangrove forest due to sediment erosion. The increase in the river discharge further increases the sediment loss amount, contrary to the trends observed in the simulations with imposing the mangrove impact. These results highlight the vital role of mangroves in retaining the sediments and thus soil organic carbon, which may significantly contribute to the mangroves’ carbon sequestration function.

7.1.2 Introduction

Mangroves are known as biogeomorphic ecosystems that interact with hydrodynamics-sedimentary processes and affect landform (Krauss et al., 2014; Woodroffe et al., 2016; Rodríguez et al., 2017; Xie et al., 2020; Temmink et al., 2022). Especially due to the presence of above-ground roots, they exert drag and slow down the water flow (Furukawa et al., 1997; Horstman et al., 2015; Chen et al., 2016, 2018; Willemsen et al., 2016; Mullarney et al., 2017; Best et al., 2022). This creates favorable conditions for sediment deposition, which is known as the mangroves' "sediment trapping" function. Because some of the sediments are in the form of particulate organic matter transported from outer systems, this biogeomorphic feedback could significantly contribute to the carbon sequestration in mangrove forests (Sasmito et al., 2020; Suello et al., 2022). However, the control of biogeomorphic feedback on the carbon sequestration in mangrove forests is largely unknown. The evaluation of the biogeomorphic feedback in the mangrove forests is challenging because it is influenced by the mangroves' complicated root system structures.

The sequestration of allochthonous carbon in a mangrove forest depends also on its geomorphological settings, such as the presence of a river that transports the land-derived organic carbon to the mangrove forest (Lovelock et al., 2015; Sidik et al., 2016). Because of the strong dependence on the geomorphological settings, the evaluation of the geomorphic feedback requires the understanding of the flow and sediment transport in a large-scale that could include the whole mangrove forest and the adjacent creeks/river. This further makes the evaluation of geomorphic feedback challenging because the mangrove forest could have significant spatial heterogeneity in the vegetation morphological structures affecting flow and sediment transport, attributed to the spatial heterogeneity in the species composition, tree sizes, and tree density.

It is generally considered that the sequestration of allochthonous carbon is determined by the two factors – effectiveness with which mangroves trap sediments transported from rivers, and the amount of supply of the fluvially transported sediments to the mangrove forest. Therefore, the allochthonous carbon sequestration should be significantly influenced by the amount of river discharge aside from the vegetation structures. Yet, many modeling studies have used constant river discharge rate for evaluating the sedimentation in coastal vegetation habitats subject to river-influences (e.g., Nardin and Edmonds, 2014; Nardin et al., 2016; Baar et al., 2022). If the above-mentioned factors nonlinearly change with the changes in river discharge, it yields a significant uncertainty in the prediction of the allochthonous carbon sequestration or sedimentation in the river-influenced mangrove forests.

This study aims to explore how mangroves affect flow and sediment transport and contribute to the sedimentation of fluvial sediments, which is considered as a primary process of the biogeomorphic feedback. We also aim to examine the dependence of sedimentation

rate in the mangrove forest on river discharge. We address these aims by a large-scale modeling of flow and sediment transport in a riverine mangrove forest and its adjacent area in the Philippines. We specifically take into account the spatially-explicit impacts of mangroves on the flow and sediment transport, which has not been achieved by previous studies. Here, we leverage the newly developed hydrodynamic model (COAWST_rh v1.0; Yoshikai et al., 2023), remotely-sensed data, and field data to achieve this large-scale modeling.

7.2 Materials and Methods

7.2.1 Study site

We selected a planted riverine mangrove forest (locally known as Bakhawan Ecopark) at the mouth of Aklan River located in the Aklan province, Panay Island, Philippines (Fig. 7.1). The large amount of sediment discharge from the Aklan River formed tidal flat down the river. The plantation of *Rhizophora apiculata* took place in the early 1990s in a mudflat. Subsequent plantations were periodically conducted, producing zones characterized by *R. apiculata* stands with different ages (e.g., ~10 years old, ~20 years old, and ~30 years old). Additionally, natural recruitment of other species such as *Avicennia marina* and *Sonneratia alba* took place on the mud bank (Ray et al., 2023). Over the years, this mangrove forest has shown expansion of its area, mainly following river runoff events that may have supplied a large amount of sediments as a base of mangrove development. The baseflow of Aklan River in wet season is considered around 100 m^3 s^{-1}. However, at an extreme condition, the river discharge of ~10,000 m^3 s^{-1} has been reported when Typhoon Fengshen approached in 2008. The tide is semi-diurnal with the highest amplitude of 2.0 m.

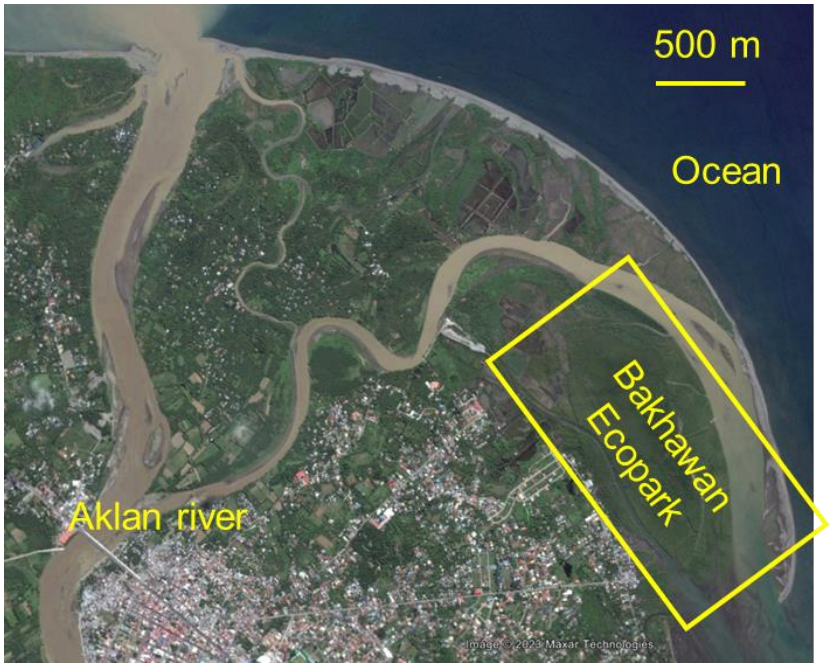

Figure 7.1. Satellite image (Google Earth) of the study site – downstream of Aklan River including Bakhawan Ecopark.

7.2.2 Field data collection

7.2.2.1 Ground elevation and bathymetry data

The spatial measurement of the ground elevations in the mangrove forest were conducted in October 2022. We derived the ground elevation by measuring the water depth at high tides assuming a uniform water level in the forest at these conditions. The measurement was conducted at the plots of tree census along four transect established for natural *Avicennia* and *Sonneratia* stands, and ~30 years old, ~20 years old, and ~10 years old planted stands of *R. apiculata* (Suwa et al., unpublished). In total, data on the 22 stations were taken (Fig. 7.2).

The bathymetry of Aklan River downstream and some creeks in the Bakhawan Ecopark was measured using single-beam echosounder in February 2022.

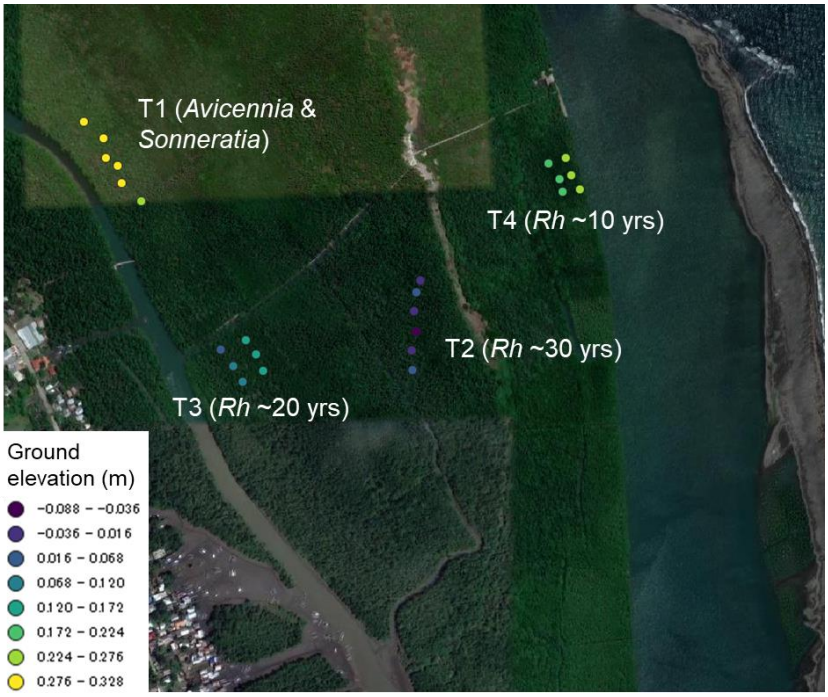

Figure 7.2. Measured ground elevation in the mangrove forest along the four transect (T1–T4).

7.2.2.2 Vegetation data

In each plot shown in Fig. 7.2, tree census measurement was conducted in 2018 (Suwa et al., unpublished data).

Aside from the usual tree census data, we collected the data on above-ground root structures in some selected sites. Especially, we measured the prop root systems of Rhizophora mangroves at the 20 years old and 30 years old stands (Yoshikai et al., 2021). In addition, we measured the geometry of pneumatophores of *Avicennia* and *Sonneratia* mangroves at some stations. Specifically, we randomly established 0.25 cm × 0.25 cm quadrats at each station, and we measured the height and the diameter at the middle height of all pneumatophores in the quadrat. We also calculated the density of pneumatophores (root density) in each quadrat. Assuming the cylindrical shape of the pneumatophores and using tree density data (Zanne et al., 2009), we calculated pneumatophore biomass in each quadrat. We average the calculated pneumatophore biomass values in the quadrats in a plot as a representative value of the plot.

We calculated the above-ground biomass (AGB, kg m^{-2}) and pneumatophore biomass per species in the plots where the data were collected, and compared them. Figure 7.3 shows the measured diameter, height, and AGB-pneumatophore biomass relationships for *A. marina* and *S. alba*. The data shows the variations of diameter and height of pneumatophore are

relatively small (Fig. 7.3). It also shows the high correlation between the AGB and pneumatophore biomass.

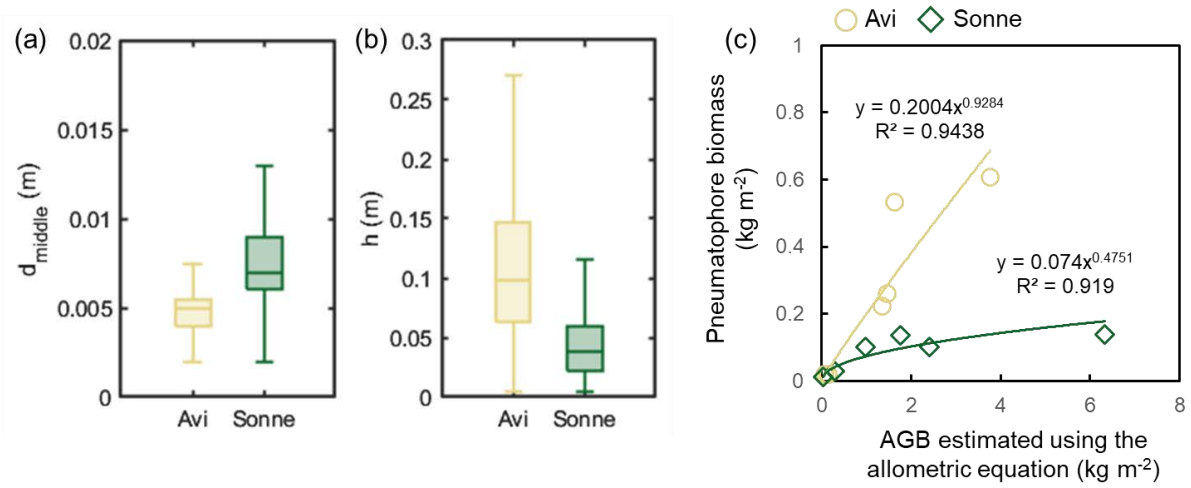

Figure 7.3. (a) Measured pneumatophore diameter at the middle height (d_{middle}), (b) height of pneumatophores (h), and (c) the relationship of above-ground biomass (AGB) and pneumatophore biomass for *Avicennia marina* and *Sonneratia alba*. The number of measured pneumatophores is 701 for *A. marina* and 319 for *S. alba*, respectively.

7.2.3 Mapping ground elevation and vegetation parameters

We used LiDAR data obtained in 2014 by the Phil-LIDAR Project for mapping the ground elevation and vegetation parameters in the study site. For the ground elevation, we generated a digital elevation model (DEM) that reflects the ground elevation and a digital surface model (DSM) that reflects the canopy top elevation with a 10-m horizontal resolution. We derived the canopy height model (CHM) by subtracting the DSM from DEM. We then compared the DEM with the measured ground elevation data (Fig. 7.4). The comparison suggested that the LiDAR-derived DEM can well represent the ground elevation in the mangrove forest in our study site, despite the differences in the year when the data were taken (2014 for the LiDAR data and 2022 for the ground elevation measurement).

We also found that the LiDAR-derived CHM compares well with the measured mean tree heights in the plots (Fig. 7.5). However, the LiDAR-derived CHM showed generally higher values than the measured mean tree height. This may be because the LiDAR-derived CHM may reflect the information of the height of the highest tree in the area, while the data is for the mean tree height.

We used the LiDAR-derived DEM as the present-day ground elevation in the Bakhawan Ecopark based on the result shown in Fig. 7.4. We mapped the mean tree height

using the LiDAR-derived CHM based on the relationship shown in Fig. 7.5. Additionally, we obtained the spatial variation of the mean stem diameter and tree density based on some allometric relations.

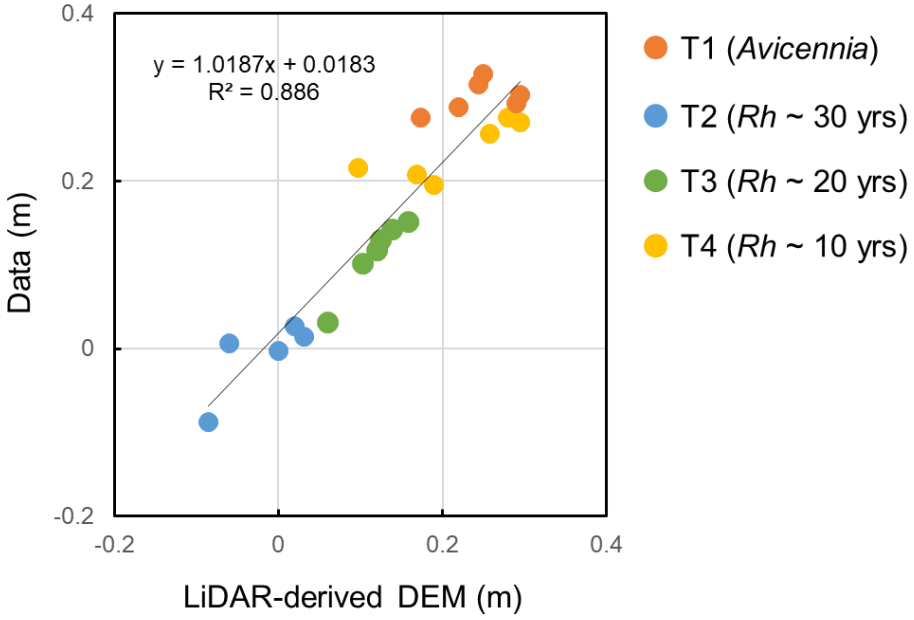

Figure 7.4. Comparison of the LiDAR-derived DEM and the measured ground elevation in the Bakhawan Ecopark.

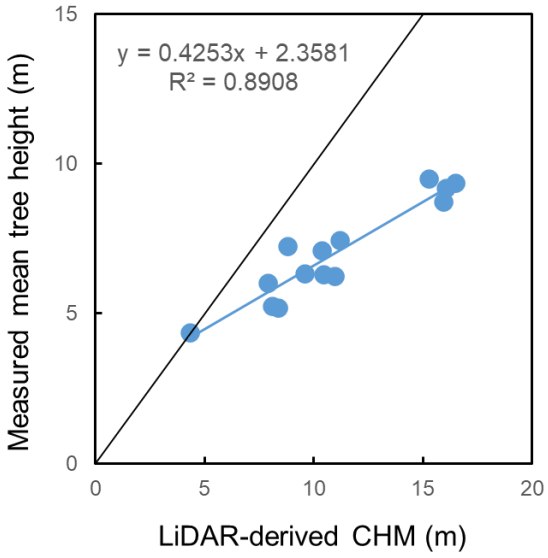

Figure 7.5. Comparison of the LiDAR-derived CHM and the measured mean tree height in the Bakhawan Ecopark. The black line indicates the 1:1 relationship and the blue line indicates the best linear fit.

7.2.4 Update of the COAWST mangrove root module

In the Bakhawan Ecopark, *A. marina* and *S. alba* stands dominate at some areas, aside from the *Rhizophora* stands. Therefore, it is important to model the above-ground root structures of *A. marina* and *S. alba* (pneumatophores) for modeling the hydrodynamics and sediment transport in this forest. We have added a new model in the mangrove root module in COAWST representing the *Avicennia* and *Sonneratia* roots (Fig. 7.6). The model of the *Avicennia* and *Sonneratia* roots is based on the allometric relationship shown in Fig. 7.3c, and estimate the projected area of roots from stem diameter and tree density by assuming a constant root diameter and height which are shown in Fig 7.3a and b, respectively.

The linkage of the vegetation structures of *Avicennia* and *Sonneratia* mangroves with the hydrodynamics is same as the generic mangrove root model presented in Chapter 6.

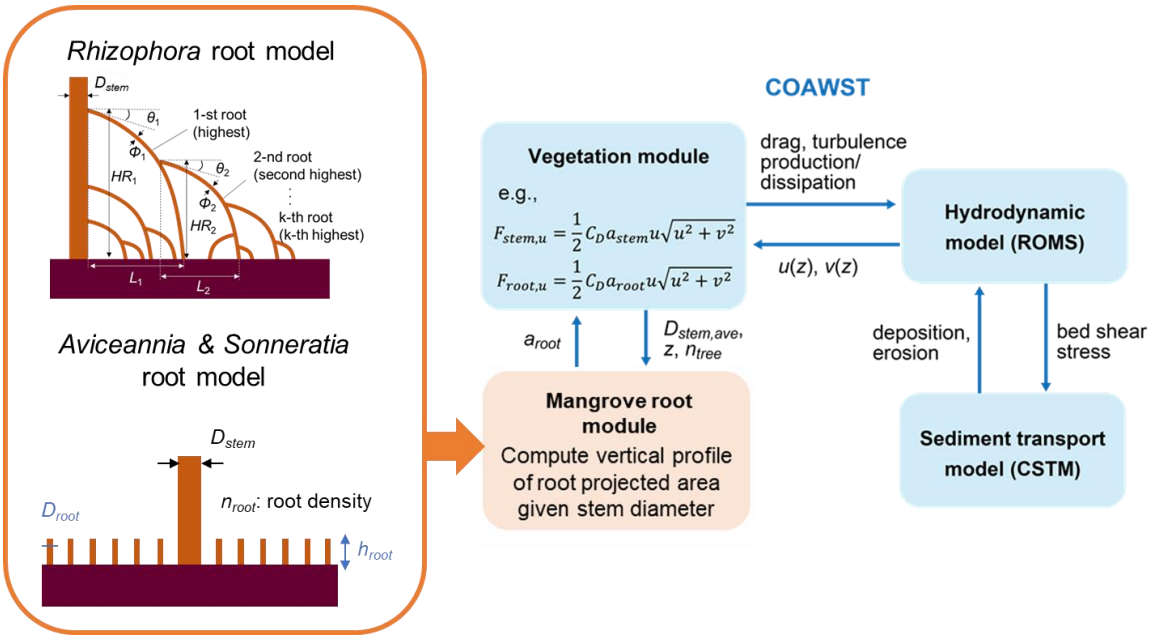

Figure 7.6. Updated COAWST incorporating the model for *Avicennia* and *Sonneratia* roots (pneumatophores).

7.2.5 Model set up

We generated a model grid for the Aklan River downstream covering the mangrove forest (Bakhawan Ecopark) and its adjacent area and some part of the outer sea (Fig. 7.7). The horizontal grid resolution is about 33 m. The vertical layers were partitioned into four layers with approximately same layer thickness for the three-dimensional simulation. The initial and boundary conditions were given from a larger-scale model (offline nesting).

To incorporate the mangrove drag effects on hydrodynamics, we also inputted the spatially-explicit vegetation information such as species composition, mean tree height, and tree density (Fig. 7.8a and b). The species composition is based on the map provided by Dr.

Rene Rollon (unpublished data). Using the updated COAWST incorporating the models for the *Rhizophora* prop root systems and the *Avicennia* and *Sonneratia* pneumatophores (Fig. 7.6), the horizontally and vertically variable vegetation structures were given to the model simulation (Fig. 7.8c–f). Here, due to the lack of information, we assumed the even tree density of *A. marina* and *S. alba* stands in the mixed stands of these species.

In this study, the sediment module (CSTM) was also activated (Fig. 7.6). We inputted a sediment type with a median sediment grain diameter of 0.012 mm representing muddy sediments. The particle settling velocity was set as 0.1 mm s^{-1}. In the COAWST, the sediment resuspension (erosion) flux is calculated (E, kg m^{-2} s^{-1}) as

$$E = \max\left(E_0\left(\frac{\tau}{\tau_{cr}}\right) - 1{,}0\right) \quad (7.1)$$

where, E_0 is a surface erosion rate which was set as 10^{-4} kg m^{-2} s^{-1}, τ is the bottom shear stress (N m^{-2}) and the τ_{cr} is the critical shear stress for erosion (Warner et al., 2008). Here we gave 0.1 N m^{-2} to τ_{cr}, following previous modeling study (Horstman et al., 2015). Because the sediments in the river channel are usually coarser than those in mangrove forests due to the high flow energy, we imposed the initial condition of these muddy sediments only in the mangrove forests (zero-sediment thickness outside the mangrove forest). Note that even with the zero-sediment thickness, the model accepts the sedimentation at these areas. The module calculating the morphological change following sediment deposition/erosion was not activated in this study.

We conducted two simulations – a wet season baseflow simulation and a flood event simulation. We tested the model configurations using and without using the vegetation module for both simulations to examine how mangroves could affect hydrodynamics and sediment transport in and around the mangrove forest.

For the baseflow simulation, we run the model for about two weeks to cover both neap and spring tides. Here, an estimated baseflow of 100 m^3 s^{-1} of Aklan River was constantly given to the model as point source. We gave a constant suspended sediment concentration (SSC) of 70 mg L^{-1} as the river discharge. A spin-up simulation for about one-week period was run prior to the actual simulation to make the steady-state conditions of the SSC.

For the flood event simulations, we examined the impact of the short-term river runoff on sediment transport. We examined the river runoff of 200, 400, 600, 800, 1000, 2000, 3000, 4000, 5000, and 6000 m^3 s^{-1}. The given suspended concentrations were linearly increased corresponding to the increase in the river runoff, which are 140, 280, 420, 560, 700, 1400, 2100, 2800, 3500, and 4200 mg L^{-1}, respectively. We gave these river runoff conditions for one day during a neap tide condition. Between the runoff period, we gave a smooth transition from and to the baseflow for six hours.

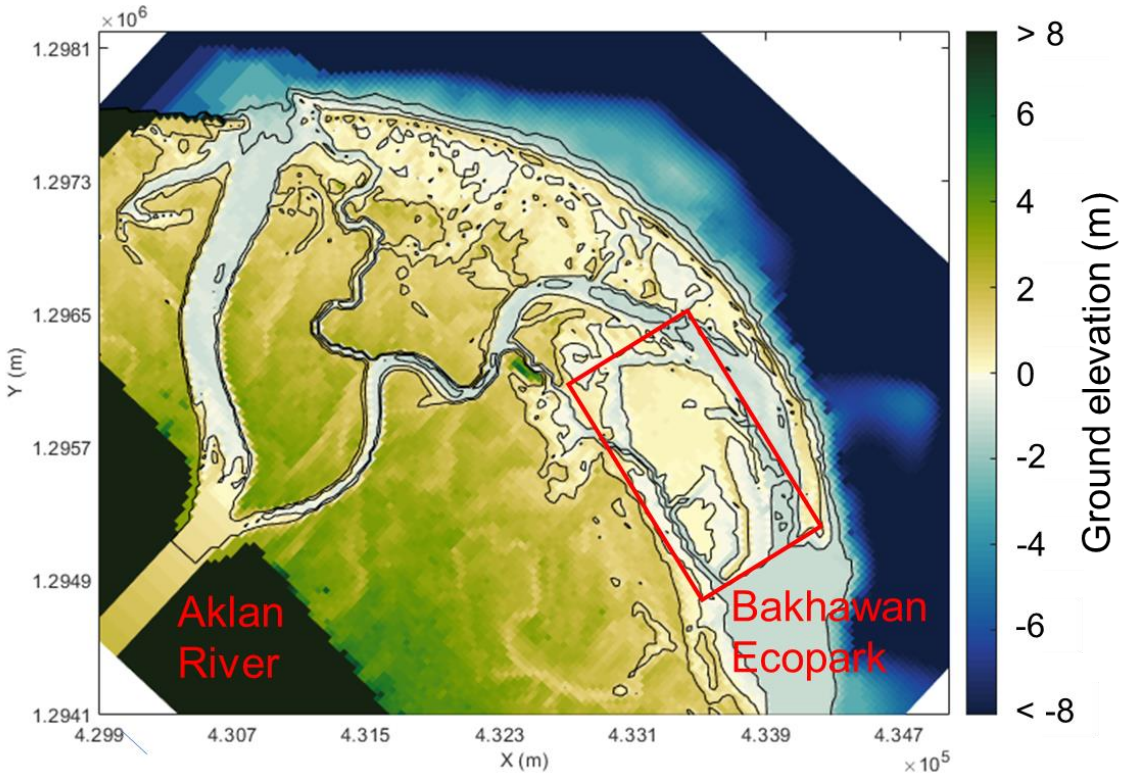

Figure 7.7. Model grid. Some parts of the grid are not shown because they are out of the frame.

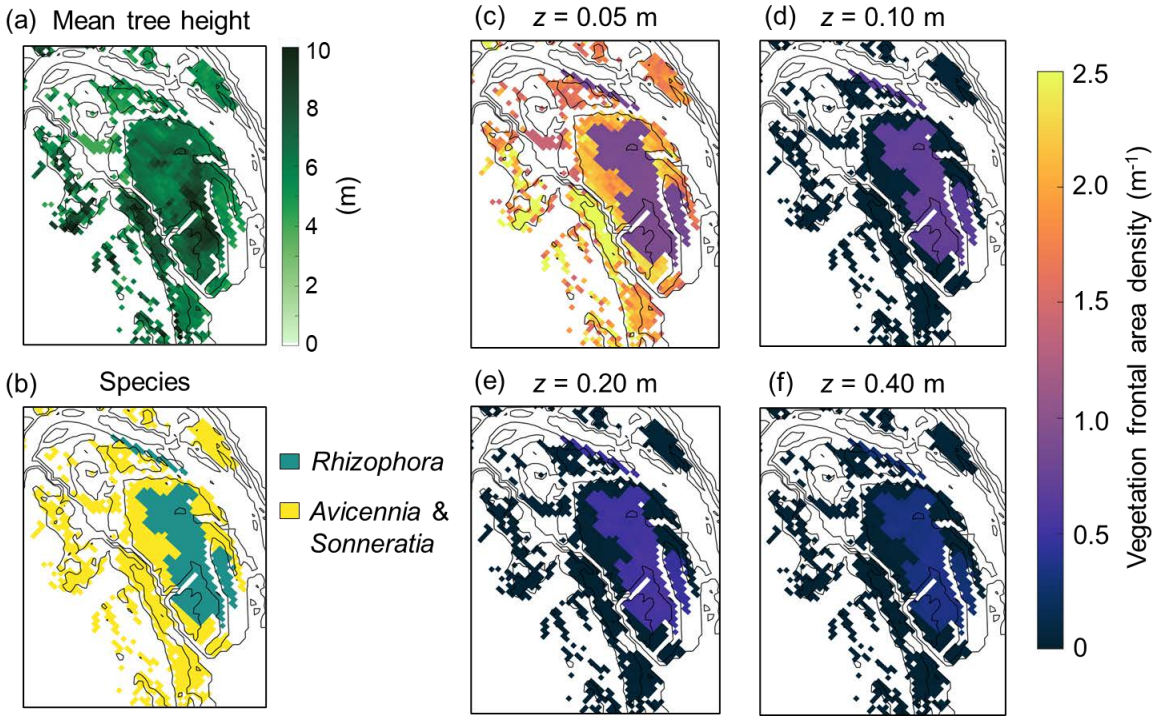

Figure 7.8. Inputted (a) mean tree height and (b) species composition, and modeled vegetation frontal area density at (c) z = 0.05 m, (d) z = 0.10 m, (e) z = 0.20 m, and (f) z = 0.40 m around the Bakhawan Ecopark which was given by the COAWST mangrove root module.

7.3 Results and Discussion

7.3.1 Baseflow simulation

The simulated SSC at low and high tides during a neap and a spring tide condition are shown in Fig. 7.9. During the flood tide, the seawaters come into the river mouth connecting to the channel adjacent to the mangrove forest (Bakawan Ecopark) while the seawater intrusion is not observed for the other river mouth (Fig. 7.9a and c). Specifically, at the channel beside the mangrove forest, the water is influenced both by the seawater intrusion during the flood tide and the river discharge mainly during the ebb tide. The results also show that the flow velocity and SSC in the mangrove forest are greatly lower than those in the adjacent channel (Fig. 7.9).

The tidal stage plots showed the similar trends (Fig. 7.10). At the channel, the SSC increases when water level is going down, but decreases after the low tide. Notably, the SSC is significantly low, at the level of the negligible river-influence, when the increasing water level crosses the ground level of the adjacent mangrove forest (Fig. 7.10b). This indicates that the most of the fluvial sediments are discharged to the ocean, and almost negligible amount of sediments go into the mangrove forest during the baseflow conditions. As shown in the Fig. 7.10c, the flow velocity in the mangrove forest is greatly attenuated from the channel, and the SSC is very low throughout the tidal phase.

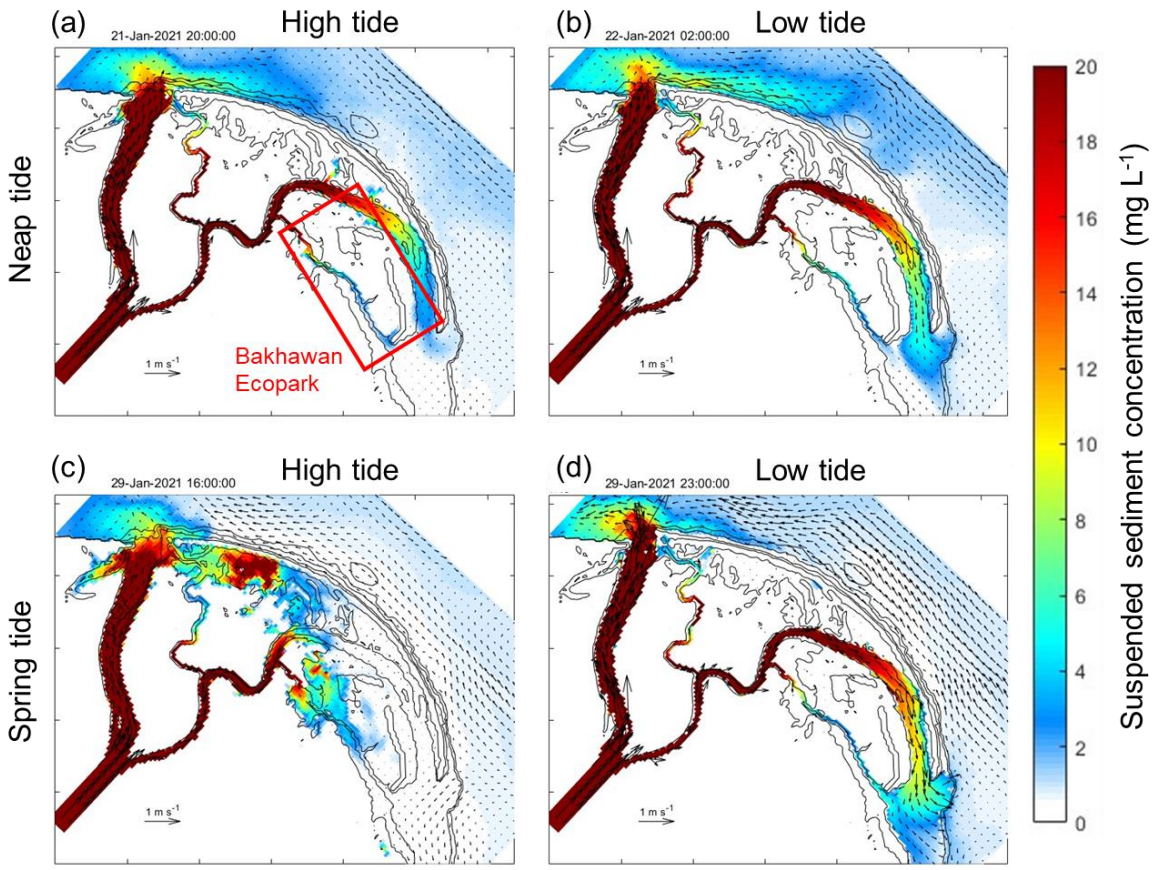

Figure 7.9. Simulated suspended sediment concentrations in the Aklan River downstream at (a) high tide and (b) low tide during a neap tide condition and at (c) high tide and (d) low tide during a spring tide condition. The arrows indicate flow direction and velocity magnitude (reference vector for 1 m s^{-1} is provided in the maps). The location of Bakhawan Ecopark is indicated in the panel "a".

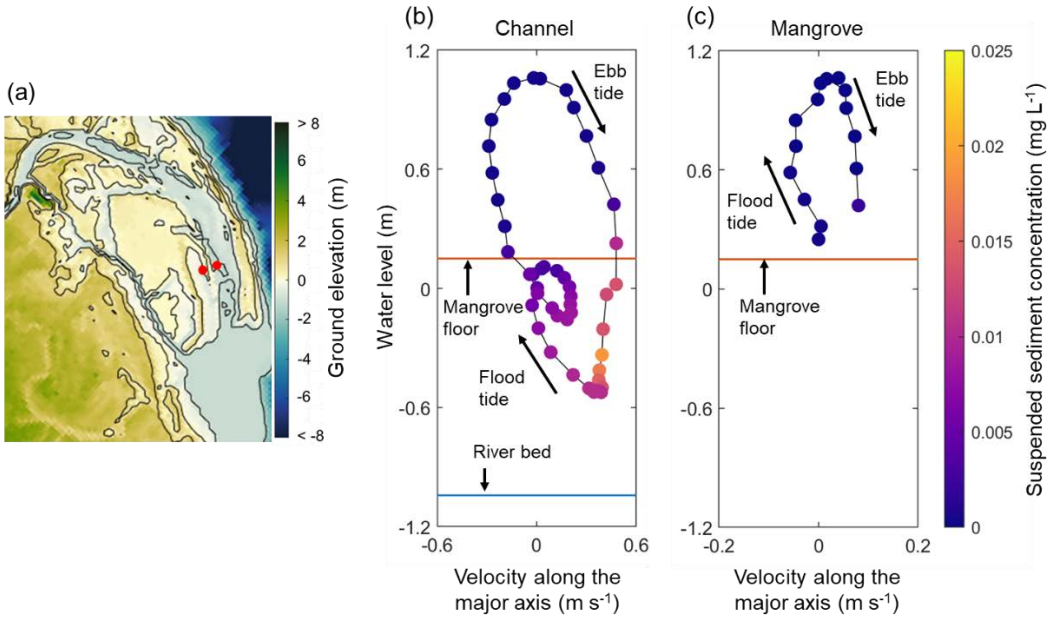

Figure 7.10. (a) Locations of the channel and the adjacent mangrove stations (red circles) for analysis of tidal stage plots; Tidal stage plots for the simulated flow velocity along the major axis during a spring tide condition for (b) the channel and (c) the adjacent mangrove stations. The color of the markers indicates the simulated suspended sediment concentrations.

Figure 7.11 compares the flow velocity and SSC at a peak flow condition (during a flood tide) simulated with and without the effect of mangroves on flow. The result clearly demonstrated the significance of the mangrove impact on flow and sediment transport. Because of the drag by mangrove forest, the flow is concentrated on the channel (Fig. 7.11a), and the flow velocity inside the mangrove forest is low (< 0.1 m s^{-1}), similar to results of modeling studies on salt marshes (e.g., Temmerman et al., 2005; Oliver et al., 2020). As a result, the bed shear stress inside the forest remained relatively low and did not cause sediment resuspension, as indicated by the very low SSC inside the forest (Fig. 7.11b). However, if the effect of mangroves is turned off in the simulation, the flow velocity inside the forest is significantly elevated to the level of > 0.2 m s^{-1}, and instead, the flow velocity in the channel is lowered, compared to the case with the effect of mangroves (Fig. 7.11c). Consequently, the bed shear stress inside the forest exceeded the critical value (τ_{cr}), and caused sediment resuspension as indicated by the high SSC (Fig. 7.11d).

Figure 7.12 shows the averaged sedimentation rate both for the case with and without the mangrove effects. The model suggested near-zero sedimentation rates inside the mangrove forest in the case with mangrove effects, consistent with the result implying the very small fluvial sediment inputs to the forest (Fig. 7.10) and the sediment resuspension (Fig. 7.11b). Without the mangroves, however, the large part of the mangrove forest showed negative sedimentation rate indicating the loss of sediments, due to the elevated flow velocity and bed shear stress (Fig. 7.12b). Note that some part of the mangrove forest showed the positive sedimentation rate due to the redistribution of the resuspended sediments in the adjacent areas. These results clearly showed that the mangroves are efficient in attenuating the flow velocity and retain sediments inside the forest. However, the river-influence on sedimentation in the forest seems negligible during the baseflow condition.

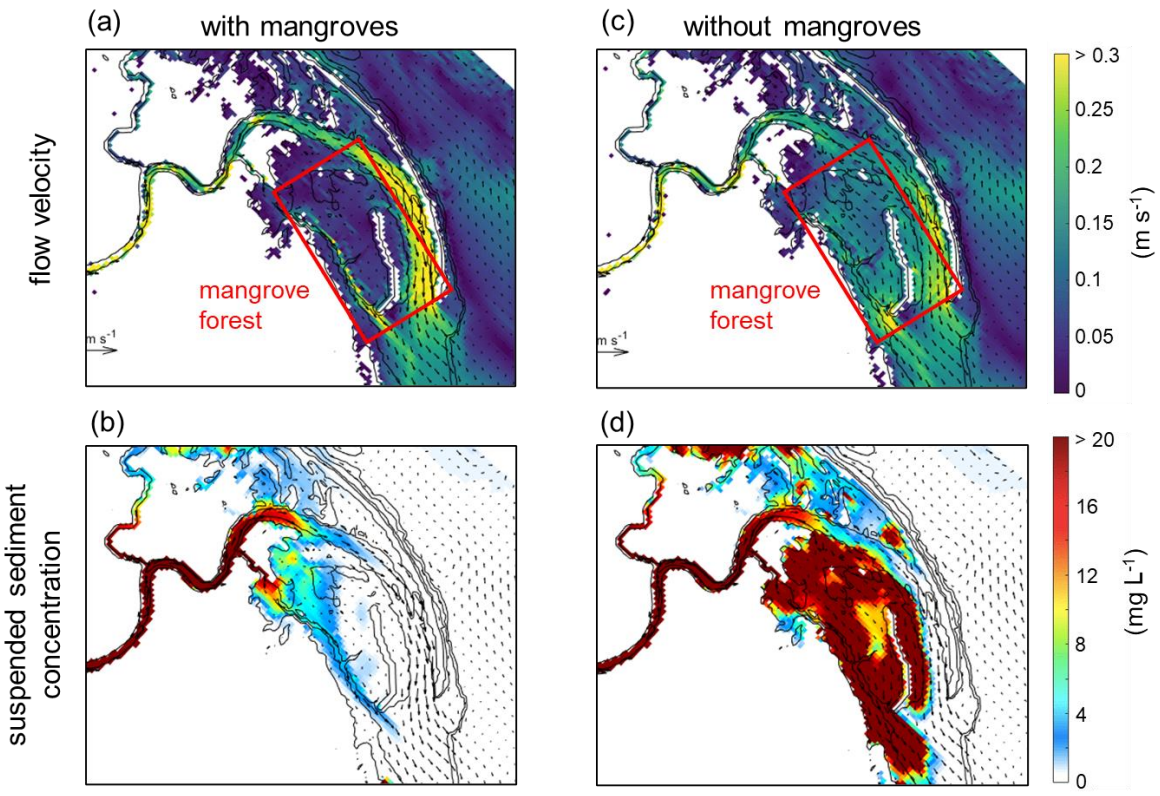

Figure 7.11. Snapshot of the simulated (a) flow velocity and (b) suspended sediment concentrations when the overall flow velocity is peaked during a spring tide condition (flood tide) with imposing the impact of mangroves on flow, and (c-d) without imposing the impact of mangroves. The arrows indicate the direction and magnitude of flow velocity.

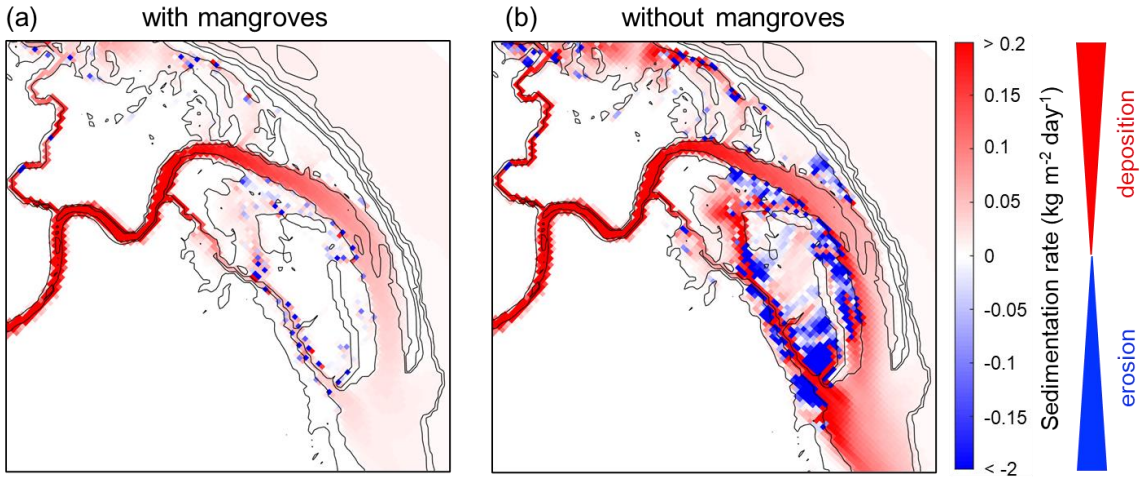

Figure 7.12. Averaged sedimentation rate for the two-weeks wet season baseflow simulation (a) with imposing and (b) without imposing the mangrove impact on flow.

7.3.2 Flood event simulation

Figure 7.13 shows the flow velocity, SSC, and sediment mass change from flood event simulations using the river discharge of 600 m^3 s^{-1}, 1000 m^3 s^{-1}, 2000 m^3 s^{-1}, 4000 m^3 s^{-1}. As shown in Section 7.3.1, the hydraulic resistance of mangrove forest lowered flow velocity inside the forest and increased the flow velocity in the adjacent channel. When the river discharge is 600 m s^{-1} or 1000 m s^{-1}, although the amount of fluvially-transported sediments is greatly increased compared to the baseflow conditions, the supply of fluvial sediments to the mangrove forest is still quite small. This is because the water level at the adjacent channel is lower than the ground level of the mangrove forest, and also the water flux to the forest is very small due to the greatly attenuated flow velocity. Consequently, the model suggested nearly zero sedimentation in the mangrove forest.

When the river discharge further increased to 2000 m^3 s^{-1} or 4000 m^3 s^{-1}, the water level in the channel elevated to higher than the ground level of the adjacent mangrove areas, which caused the overland flow from the channel to the mangrove forest (Fig. 7.13g–l). This led the supply of a significant amount of fluvial sediments to the mangrove forest. The accretion of sediments is more pronounced in the areas near the channel compared to the interior areas (Fig. 7.13i and l). The dependence of sedimentation on the water level increase by the increased river discharge can be seen in the comparison of the changes in the sedimentation amount and the water depth in the mangrove forest against the river discharge (Fig. 7.14). We also estimated the amount of organic carbon deposition in the mangrove forest by a flood event using the simulated amount of sediment deposition. Due to the lack of data on the particulate organic carbon concentration in the river, we used a mean value of the particulate organic carbon fraction in suspended sediment concentration in rivers in Asian region (1.23 weight %) reported in Kandasamy & Nagender Nath (2016). The result showed that the organic carbon deposition in the mangrove forest by one flood event could be the same level as the one-year carbon accumulation rate in the 20 years old planted stands in Bakhawan Ecopark estimated by Ray et al. (2023) when the river discharge is 6000 m^3 s^{-1} (Fig. 7.15). This suggests the significance of the sedimentation of river-originated sediments in the carbon sequestration in riverine mangrove forests. The model also suggested the significant amount of sedimentation at the front of mangrove forest, of which accreted sediment may provide mangroves with a base for establishment. This is consistent with the recent trend of this mangrove area showing the areal expansion towards the further downstream following flood events.

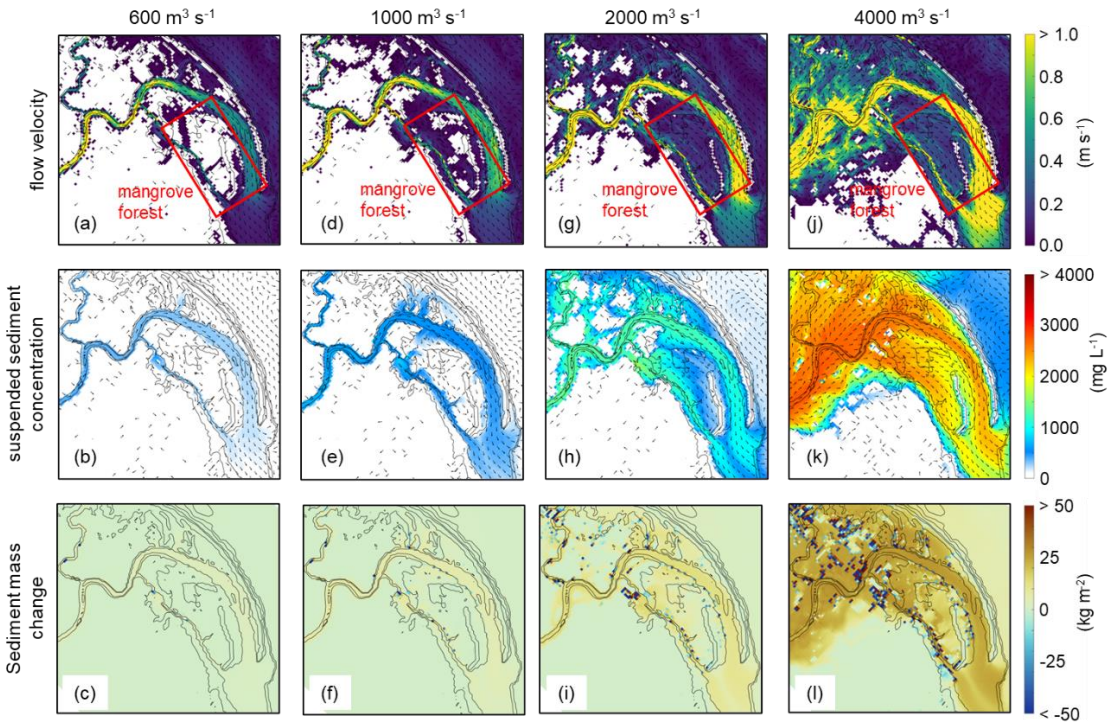

Figure 7.13. Flow velocity, suspended sediment concentration, and sediment mass change from the flood event simulations with river discharge of (a–c) 600 m^3 s^{-1}, (d–f) 1000 m^3 s^{-1}, (g–i) 2000 m^3 s^{-1}, (j–l) 4000 m^3 s^{-1}. The flow velocity and suspended sediment concentration are snapshots during an ebb tide when the offshore water level crossed 0 m mean sea level. The sediment mass change is the difference of the amount of sediments before and after the one-day flood event. The arrows indicate flow velocity magnitude and direction.

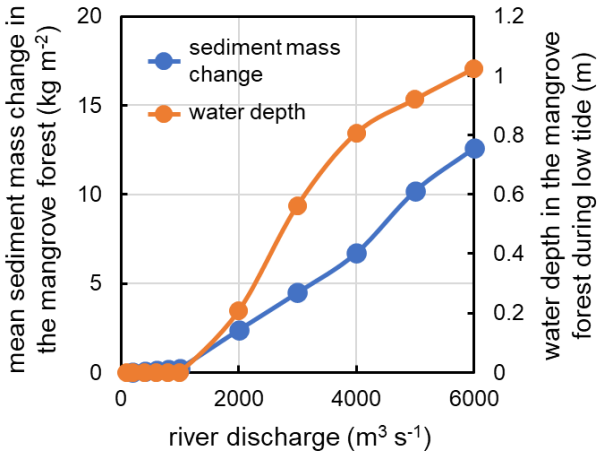

Figure 7.14. Responses of the mean sediment mass change in the mangrove forest during the flood event and water depth in the mangrove forest during the low tide to the river discharge in the flood event simulation.

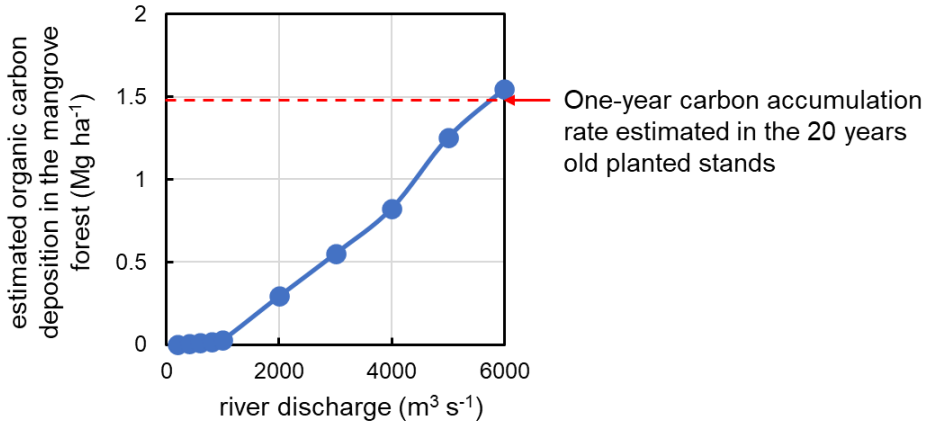

Figure 7.15. Estimated amount of organic carbon deposition in the mangrove forest by a flood event as a function of river discharge. The red dashed line indicates the one-year carbon accumulation rate in the 20 years old planted stands in Bakhawan Ecopark estimated by Ray et al. (2023).

Figure 7.16 compares the results of simulations with imposing and without imposing the impact of mangroves on flow with the river discharge 4000 m^3 s^{-1}. Without imposing the mangrove impact, however, the flow velocity in the mangrove forest is not well decelerated and showed flow velocity around 0.6 m s^{-1} (Fig. 7.16d). The high bed shear stress attributed to the high flow velocity then induced sediment resuspension in wide area of the mangrove forest as suggested by the much higher SSC than the case with the mangrove impact, of which resuspended sediments are flowing away to the offshore (Fig. 7.16b and e). As a result, the entire mangrove forest showed large loss of sediments (Fig. 7.16f). Figure 7.17 shows the response of the mean sediment mass change in the mangrove forest to the river discharge both for the simulation cases with and without imposing the mangrove impact on flow. In the case with imposing the mangrove impact, a threshold-like notable increase in the sediment deposition is observed at the river discharge of 2000 m^3 s^{-1}, probably due to the elevated water level in the channel that initiated the overland flows in the mangrove forest (Fig. 7.14). In contrast, the case without imposing the mangrove impact showed the nonlinearly increased loss of sediments as river discharge increased. This may be because of the increased flow velocity magnitude in the forest by the increase in the river discharge, which elevated bed shear stress and induced sediment resuspension. Notably, the effect of switching-off the mangrove impact is far more significant than the effect of changes in the river discharge on sedimentation with the impact of mangroves. These results clearly demonstrated the function of mangroves to effectively retain sediments. If mangroves are cleared by deforestation, the mangroves' sediment retention function is lost. It is likely that this causes erosion and loss of a significant amount of the sediment, thereby soil organic carbon, from the mangrove forest.

These results suggest that soil organic carbon stored in mangrove forests is retained by the mangroves' function to attenuate the flow energy coming into the mangrove forest.

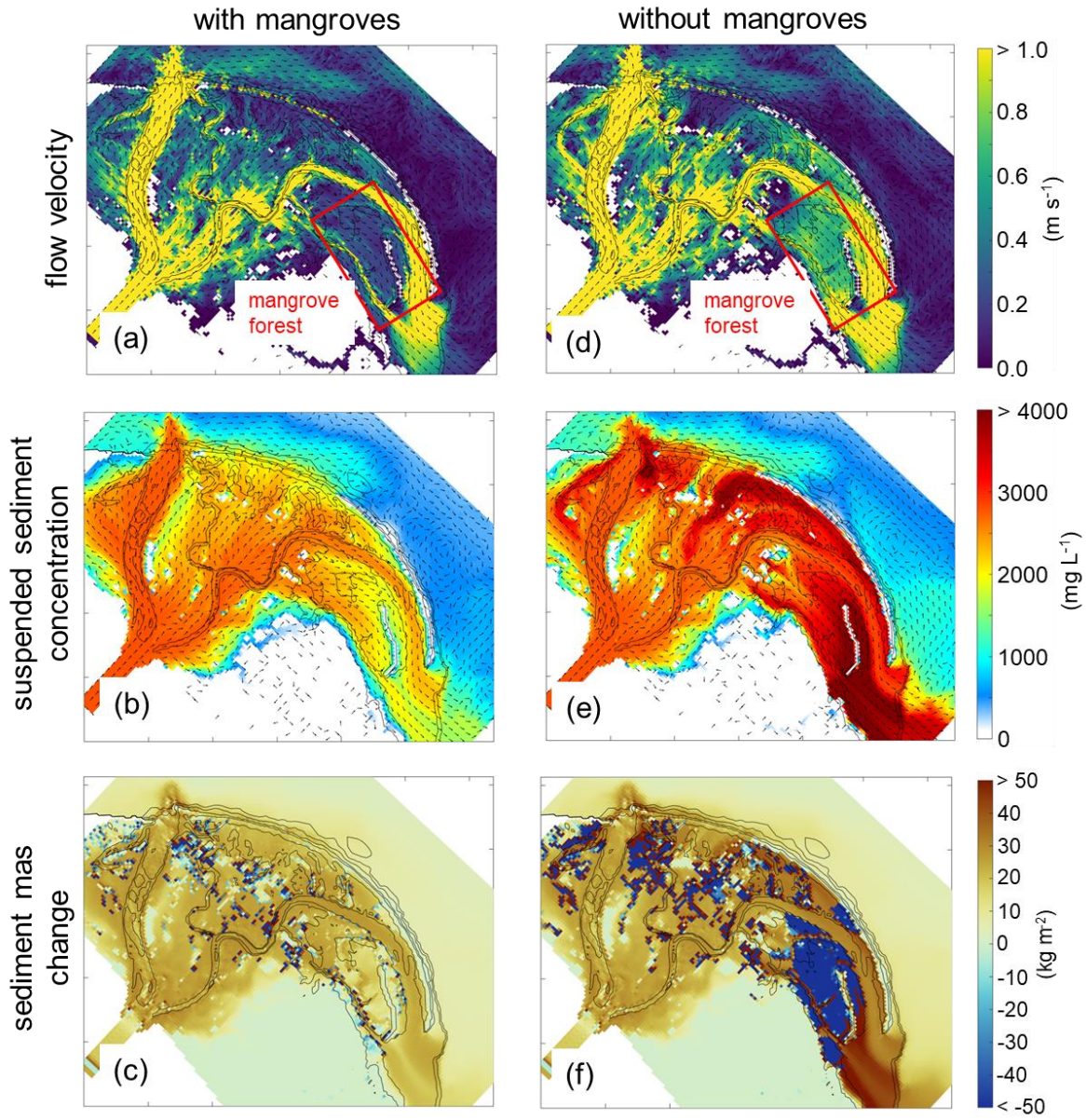

Figure 7.16. Flow velocity, suspended sediment concentration, and sediment mass change from the flood event simulations with river discharge of 4000 m^3 s^{-1} (a–c) with imposing and (d–f) without imposing the impact of mangroves on flow. The flow velocity and suspended sediment concentration are snapshots during an ebb tide when the offshore water level crossed 0 m mean sea level. The sediment mass change is the difference of the amount of sediments before and after the one-day flood event. The arrows indicate flow velocity magnitude and direction. The panels "a"–"c" are same as Fig. 7.13j–l.

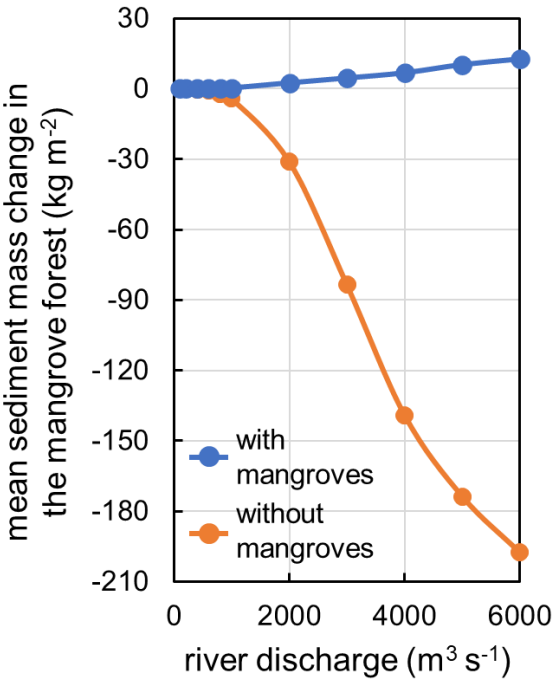

Figure 7.17. Response of the mean sediment mass change in the mangrove forest to the river discharge in the flood event simulation with and without imposing the impact of mangroves on flow.

7.4 Conclusions

This study investigated the sediment transport processes in a riverine mangrove forest through a model analysis. Notably, the impact of spatially-variable mangrove morphological structures was implemented in a forest-scale flow simulation for the first time. The model showed that the mangroves significantly reduce the flow velocity coming into the forest and regulate sediment resuspension through the lowered bed shear stress. Alternatively, the model suggested negligibly small sedimentation rates in the mangrove forest when the river discharge is in baseflow conditions. This is because the fluvial sediments are pushed by the flooding tides further upstream than the site facing the mangrove forest when the water level reaches the ground level of the forest. Through the flood event simulations, the model suggested that the increased river runoff could rise the water level in the channel which causes overland flow on the mangrove forest. This overland flow supplies a significant amount of fluvial sediments to the mangrove forest, facilitating sedimentation. Simulations without imposing the impact of mangroves on flow showed significantly increased flow velocity compared to the case with imposing the mangrove impact. A significant amount of sediment loss in the mangrove forest occurs due to resuspension caused by the increased flow velocity.

The increase in the river discharge further increased the sediment loss amount, contrary to the trends observed in the simulations with imposing the mangrove impact. These results underscore the vital role of mangroves in retaining the sediments and thus soil organic carbon, which may significantly contribute to the mangroves' carbon sequestration function.

7.5 References

Baar, A.W., Braat, L. & Parsons, D.R. (2023) Control of river discharge on large-scale estuary morphology. Earth Surface Processes and Landforms, 48(3), 489–503. https://doi.org/10.1002/esp.5498.

Best, Ü. S., van der Wegen, M., Dijkstra, J., Reyns, J., van Prooijen, B. C., & Roelvink, D. (2022). Wave attenuation potential, sediment properties and mangrove growth dynamics data over Guyana's intertidal mudflats: assessing the potential of mangrove restoration works. Earth System Science Data, 14(5), 2445–2462. https://doi.org/10.5194/essd-14-2445-2022.

Chen, Y., Li, Y., Cai, T., Thompson, C., & Li, Y. (2016). A comparison of biohydrodynamic interaction within mangrove and saltmarsh boundaries. Earth Surface Processes and Landforms, 41(13), 1967–1979. https://doi.org/10.1002/esp.3964.

Chen, Y., Li, Y., Thompson, C., Wang, X., Cai, T., & Chang, Y. (2018). Differential sediment trapping abilities of mangrove and saltmarsh vegetation in a subtropical estuary. Geomorphology, 318, 270–282. https://doi.org/10.1016/j.geomorph.2018.06.018.

Furukawa, K., Wolanski, E., & Mueller, H. (1997). Currents and sediment transport in mangrove forests. Estuarine, Coastal and Shelf Science, 44(3), 301–310. https://doi.org/10.1006/ecss.1996.0120.

Horstman, E. M., Dohmen-Janssen, C. M., Bouma, T. J., & Hulscher, S. J. (2015). Tidal-scale flow routing and sedimentation in mangrove forests: Combining field data and numerical modelling. Geomorphology, 228, 244–262. https://doi.org/10.1016/j.geomorph.2014.08.011.

Kandasamy, S., & Nagender Nath, B. (2016). Perspectives on the terrestrial organic matter transport and burial along the land-deep sea continuum: caveats in our understanding of biogeochemical processes and future needs. Frontiers in Marine Science, 3, 259. https://doi.org/10.3389/fmars.2016.00259.

Krauss, K. W., McKee, K. L., Lovelock, C. E., Cahoon, D. R., Saintilan, N., Reef, R., & Chen, L. (2014). How mangrove forests adjust to rising sea level. New Phytologist, 202(1), 19-34. https://doi.org/10.1111/nph.12605.

Lovelock, C. E., Cahoon, D. R., Friess, D. A., Guntenspergen, G. R., Krauss, K. W., Reef, R., ... & Triet, T. (2015). The vulnerability of Indo-Pacific mangrove forests to sea-level rise. Nature, 526(7574), 559-563. https://doi.org/10.1038/nature15538.

Mullarney, J. C., Henderson, S. M., Reyns, J. A., Norris, B. K., and Bryan, K. R. (2017) Spatially varying drag within a wave-exposed mangrove forest and on the adjacent tidal flat. Continental Shelf Research, 147, 102-113. https://doi.org/10.1016/j.csr.2017.06.019.

Nardin, W., & Edmonds, D. A. (2014). Optimum vegetation height and density for inorganic sedimentation in deltaic marshes. Nature Geoscience, 7(10), 722–726. https://doi.org/10.1038/ngeo2233.

Nardin, W., Edmonds, D. A., & Fagherazzi, S. (2016). Influence of vegetation on spatial patterns of sediment deposition in deltaic islands during flood. Advances in Water Resources, 93, 236–248. https://doi.org/10.1016/j.advwatres.2016.01.001.

Olliver, E. A., Edmonds, D. A., & Shaw, J. B. (2020). Influence of floods, tides, and vegetation on sediment retention in Wax Lake Delta, Louisiana, USA. Journal of Geophysical Research: Earth Surface, 125(1), e2019JF005316. https://doi.org/10.1029/2019JF005316.

Ray, R., Suwa, R., Miyajima, T., Munar, J., Yoshikai, M., San Diego-McGlone, M. L., and Nadaoka, K. (2023). Sedimentary blue carbon dynamics based on chronosequential observations in a tropical restored mangrove forest, Biogeosciences, 20, 911–928. https://doi.org/10.5194/bg-20-911-2023.

Rodríguez, J. F., Saco, P. M., Sandi, S., Saintilan, N., & Riccardi, G. (2017). Potential increase in coastal wetland vulnerability to sea-level rise suggested by considering hydrodynamic attenuation effects. Nature communications, 8(1), 1–12. https://doi.org/10.1038/ncomms16094.

Sasmito, S. D., Kuzyakov, Y., Lubis, A. A., Murdiyarso, D., Hutley, L. B., Bachri, S., ... & Borchard, N. (2020). Organic carbon burial and sources in soils of coastal mudflat and mangrove ecosystems. Catena, 187, 104414. https://doi.org/10.1016/j.catena.2019.104414.

Sidik, F., Neil, D., & Lovelock, C. E. (2016). Effect of high sedimentation rates on surface sediment dynamics and mangrove growth in the Porong River, Indonesia. Marine Pollution Bulletin, 107(1), 355-363. https://doi.org/10.1016/j.marpolbul.2016.02.048.

Suello, R. H., Hernandez, S. L., Bouillon, S., Belliard, J. P., Dominguez-Granda, L., Van de Broek, M., ... & Temmerman, S. (2022). Mangrove sediment organic carbon storage and sources in relation to forest age and position along a deltaic salinity gradient. Biogeosciences, 19(5), 1571–1585. https://doi.org/10.5194/bg-19-1571-2022.

Temmerman, S., Bouma, T. J., Govers, G., Wang, Z. B., De Vries, M. B., & Herman, P. M. J. (2005). Impact of vegetation on flow routing and sedimentation patterns: Three-dimensional modeling for a tidal marsh. Journal of Geophysical Research: Earth Surface, 110(F4). https://doi.org/10.1029/2005JF000301.

Temmink, R. J., Lamers, L. P., Angelini, C., Bouma, T. J., Fritz, C., van de Koppel, J., ... & van der Heide, T. (2022). Recovering wetland biogeomorphic feedbacks to restore the world's biotic carbon hotspots. Science, 376(6593), eabn1479. https://doi.org/10.1126/science.abn1479.

Warner, J. C., Sherwood, C. R., Signell, R. P., Harris, C. K., & Arango, H. G. (2008). Development of a three-dimensional, regional, coupled wave, current, and sediment-transport model. Computers & geosciences, 34(10), 1284–1306. https://doi.org/10.1016/j.cageo.2008.02.012.

Willemsen, P. W. J. M., Horstman, E. M., Borsje, B. W., Friess, D. A., & Dohmen-Janssen, C. M. (2016). Sensitivity of the sediment trapping capacity of an estuarine mangrove forest. Geomorphology, 273, 189–201. https://doi.org/10.1016/j.geomorph.2016.07.038.

Woodroffe, C. D., Rogers, K., McKee, K. L., Lovelock, C. E., Mendelssohn, I. A., & Saintilan, N. 529 (2016). Mangrove Sedimentation and Response to Relative Sea-Level Rise. Annual Review of Marine Science, 8(1), 243–266. https://doi.org/10.1146/annurev-marine-122414-034025.

Xie, D., Schwarz, C., Brückner, M. Z., Kleinhans, M. G., Urrego, D. H., Zhou, Z., & Van Maanen, B. (2020). Mangrove diversity loss under sea-level rise triggered by bio-morphodynamic feedbacks and anthropogenic pressures. Environmental Research Letters, 15(11), 114033. https://doi.org/10.1088/1748-9326/abc122.

Yoshikai, M., Nakamura, T., Herrera, E. C., Suwa, R., Rollon, R., Ray, R., Furukawa, K., and Nadaoka, K. (2023) Representing the impact of *Rhizophora* mangroves on flow in a hydrodynamic model (COAWST_rh v1.0): the importance of three-dimensional root system structures. Geoscientific Model Development, 16, 5847–5863, https://doi.org/10.5194/gmd-16-5847-2023.

Yoshikai, M., Nakamura, T., Suwa, R., Argamosa, R., Okamoto, T., Rollon, R., ... & Nadaoka, K. (2021). Scaling relations and substrate conditions controlling the complexity of *Rhizophora* prop root system. Estuarine, Coastal and Shelf Science, 248, 107014. https://doi.org/10.1016/j.ecss.2020.107014.

Zanne, A. E., Lopez-Gonzalez, G., Coomes, Ilic, J., Jansen, S., D. A., Lewis, S. L., Miller, R. B., Swenson, N. G., Wiemann, M. C., and Chave, J. (2009). Data from: Towards a worldwide wood economics spectrum, https://doi.org/10.5061/dryad.234,2009.

Supporting Information for Chapter 7

Note S7.1. Consideration on modifying the horizontal mixing terms in ROMS for flows in mangrove forests

In Chapter 6, the effect of *Rhizophora* mangroves on turbulence has been implemented in *k*–*ε* model of the ROMS. This effect is considered in the ROMS as vertical mixing of momentum in the momentum equations (e.g., second term in the right-and side of Eq. S7.1 below) and of scalars in the advective-diffusive equations. Alternatively, the effect of *Rhizophora* mangroves on horizontal mixing of momentum and scalars have not been considered in the model yet. This effect might be relevant in the case of simulations for spatially heterogeneous flow field, which is examined in this chapter.

The momentum equation in the *x*-direction in ROMS can be written as

$$\frac{\partial u}{\partial t} + u\frac{\partial u}{\partial x} + u\frac{\partial v}{\partial y} + u\frac{\partial w}{\partial z} - fv = -\frac{1}{\rho_0}\frac{\partial P}{\partial x} - \frac{\partial}{\partial z}\left(\overline{u'w'} - \upsilon\frac{\partial u}{\partial z}\right) + F_u + D_u \quad \text{(S7.1)}$$

where u, v, w are the velocities in the x-, y-, and z-directions, f is the Coriolis parameter, ρ_0 is the reference density of seawater, P is the pressure, v is the molecular viscosity, F_u is the external force in the x-direction, and the D_u is the horizontal mixing of momentum, where an overbar indicates a time average, and a prime (‘) indicates a fluctuating turbulent quantity (Warner et al., 2005, 2008).

The horizontal mixing term can be written as

$$D_u = \frac{\partial \tau_{xx}}{\partial x} + \frac{\partial \tau_{xy}}{\partial y} \quad \text{(S7.2)}$$

$$\tau_{xx} = 2A_M\frac{\partial u}{\partial x},\ \tau_{xy} = 2A_M\left(\frac{\partial u}{\partial y} + \frac{\partial v}{\partial x}\right) \quad \text{(S7.3)}$$

where, A_M is the eddy viscosity (Mellor, 2002). This term represents the mixing of momentum by eddies of which scale is smaller than grid size, the effect which cannot be resolved by the model grid. And hence, the eddy viscosity to be given depends on the grid size, which is estimated using the Smagorinsky model as

$$A_M = C_M\Delta x\Delta y\sqrt{\left(\frac{\partial u}{\partial x}\right)^2 + \left(\frac{\partial v}{\partial y}\right)^2 + \left(\frac{\partial v}{\partial x} + \frac{\partial u}{\partial y}\right)^2/2} \quad \text{(S7.4)}$$

where C_M is the constant (= 0.1) Δx and Δy are the grid sizes of x- and y-directions (Klingbeil et al., 2018).

However, in the mangrove forests, the size of the largest eddies may be regulated by plant-related parameters such as spacing of individual trees (Tanino and Nepf, 2008), which could be significantly smaller than grid size. For example, the tree spacing in the 20 years old planted stands in the Bakhwan Ecopark is estimated as 1.66 m by assuming a uniform tree

distribution while the grid size used in this study is 33.3 m. This suggests that the model may overestimate the subgrid-scale eddy size in the mangrove forest, and hence overestimate the horizontal mixing term (D_u in Eq. S7.1).

In order to see how significantly the horizontal mixing occurs in the model, we extracted the velocity distribution across the river-mangrove interface where it is considered that the largest horizontal mixing occurs (Fig. S7.1a). The result shows that the velocity at a mangrove grid adjacent to the channel is somewhat elevated compared to the grid in the interior forest possibly because of the horizontal mixing, while in the grids further inside the mangrove forest, the velocity is almost constant, indicating the negligible impact of horizontal mixing (Fig. S7.1b). This suggests that the mangrove areas that are affected significantly by the horizontal mixing in the model are limited to the grids adjacent to the channel even though the model may significantly overestimate the horizontal mixing term in the mangrove forest.

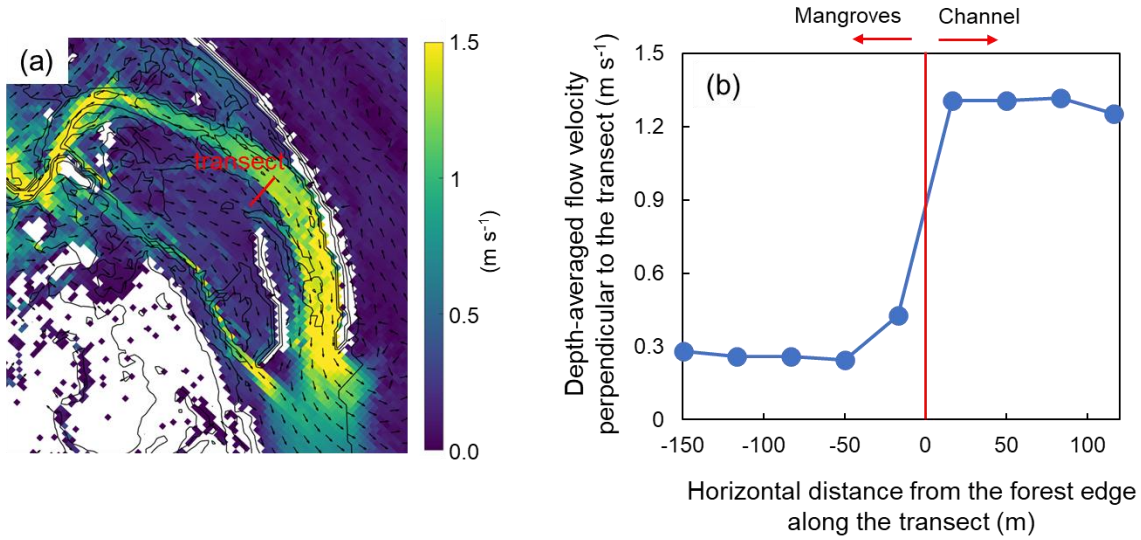

Figure S7.1. (a) Flow velocity from the flood event simulation with river discharge of 4000 m^3 s^{-1} indicating the transect set from the river to the mangrove forest in the perpendicular direction to the river flow, and (b) the depth-averaged flow velocity along the transect during the peak flow velocity condition.

We also set up another model assuming a schematic mangrove forest with a channel for investigating the impact of the horizontal mixing term (Fig. S7.2a). The grid size was set as 10 m while the vegetation parameters were set as the same as the model set for Bakhawan Ecopark. The results showed that the mangrove grid adjacent to the channel is slightly elevated compared to the grid in the interior forest, while the velocities in the grids further inside the forest are almost constant (Fig. S7.2b). The stress by the horizontal mixing term is elevated to the level of the vegetation drag term at the grid adjacent to the channel while in the further inside the forest, the stress by the horizontal mixing term is almost zero (Fig. S7.2c).

These results suggest that the significant impact of horizontal mixing is limited to the grid adjacent to the channel in this case as well.

As a conclusion, it is considered that the significant impact of the horizontal mixing is limited only to the grids adjacent to the channel or river even though the grid size is significantly larger than the tree spacing and therefore it is considered that the model overestimates the horizontal mixing term in mangrove forests. However, the model may overestimate the flow velocity at grids adjacent to the creek/river, due to the overestimated horizontal mixing with the momentum in the creek/river. The modification of the Smagorinsky model (Eq. S7.4) for mangrove forests may be required depending on the aim of study. The present model may be able to reasonably predict the overall flow and sediment transport patterns in mangrove forests because the impact of horizontal mixing term is limited to the grids adjacent to creek/river only. However, the present model may somewhat overestimate the flow velocity at the grids adjacent to the creek/river due to the overestimated horizontal mixing, which may cause significant errors in long-term geomorphic dynamics simulations, hence requiring further model modification for mangrove forests. Further research is needed for obtaining the insights into the horizontal eddy size and horizontal momentum mixing in mangrove forests, and how to implement the effects of regulated eddy size in mangrove forests into the model.

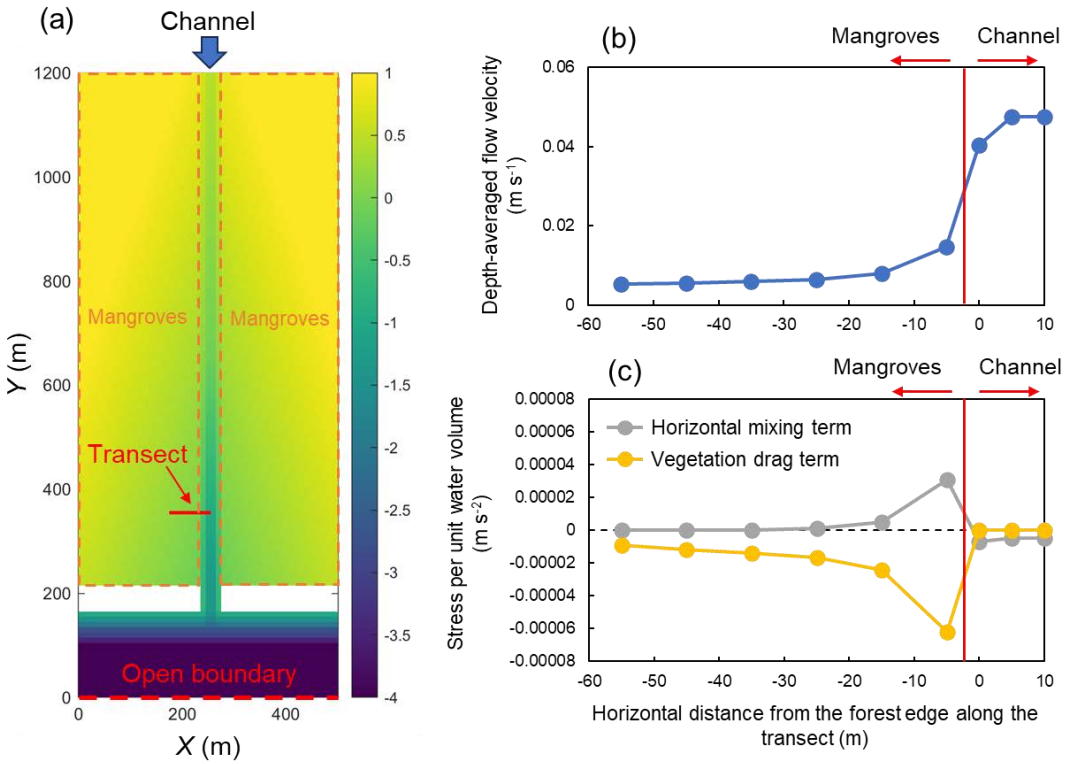

Figure S7.2. (a) Model grid for a schematic mangrove forest with a channel for investigating the impact of the horizontal mixing term indicating the transect set from the channel to the

mangrove forest in the perpendicular direction to the channel flow, (b) depth-averaged flow velocity along the transect during a flood tide condition, and (c) a comparison of the horizontal mixing term and the vegetation drag term along the transect.

References for the Supporting Information

Klingbeil, K., Lemarié, F., Debreu, L., & Burchard, H. (2018). The numerics of hydrostatic structured-grid coastal ocean models: State of the art and future perspectives. Ocean Modelling, 125, 80-105.

Mellor, G. L. (1998). Users guide for a three-dimensional, primitive equation, numerical ocean model. Princeton, NJ: Program in Atmospheric and Oceanic Sciences, Princeton University.

Tanino, Yukie, and Heidi M. Nepf. "Lateral dispersion in random cylinder arrays at high Reynolds number." Journal of Fluid Mechanics 600 (2008): 339-371.

Warner, J. C., Sherwood, C. R., Arango, H. G., & Signell, R. P. (2005). Performance of four turbulence closure models implemented using a generic length scale method. Ocean Modelling, 8(1-2), 81-113.

Warner, J. C., Sherwood, C. R., Signell, R. P., Harris, C. K., and Arango, H. G.: Development of a three-dimensional, regional, coupled wave, current, and sediment-transport model. Computers & geosciences, 34(10), 1284–1306. https://doi.org/10.1016/j.cageo.2008.02.012, 2008.

Chapter 8: Assessment of the impact of typhoon events on wave and sediment erosion in a fringing mangrove forest

8.1.1 Abstract

Mangroves protect coasts by attenuating wave and flow energy, contributing to the retention of sediments and soil organic carbon in mangrove forests. However, the insights into at what extent and degree mangrove forests would attenuate flow and wave energy and protect sediments from erosion and loss. This study aims to assess the impact of extreme conditions – high waves and storm surges induced by typhoons – on the potential sediment erosion and loss in a fringing-type mangrove forest through a model analysis. We incorporated the mangroves' wave damping effects into a wave model and conduct flow-wave simulations in a schematized pseudo 1-D fringing mangrove forest. We varied typhoon intensity in the simulation up to a level of future-intensified super typhoons projected for 2100. We showed that the mangroves significantly attenuate the wave height within the mangrove forests. However, the forest-averaged sediment erosion rate nonlinearly increase as the typhoon intensity increases, due to the amplified and less attenuated wave heights propagating from reef flat to the mangrove forest. Alternatively, the clearance of the mangrove forest induces much higher sediment erosion rate than the increase in typhoon intensity. This suggests that the loss of mangroves by typhoon impacts or deforestation may drastically increase the sediment loss even during regular typhoon conditions, while the mangroves effectively reduce the amount of sediment and soil organic carbon loss. These results stress the need for management and restoration efforts of mangrove forests under the impact of climate change.

8.1.2 Introduction

Mangroves are known to protect coasts from waves and surges by attenuating wave and flow energy (Temmerman et al., 2023). This mangroves' coastal protection function also retains the sediments in the mangrove forest effectively and contributes significantly to the mangroves' carbon sequestration function by reducing the sediment erosion potential against

incoming high flow and wave energy. However, it is unknown at what extent and degree mangrove forests would attenuate flow and wave energy and protect their sediments and the sequestered soil organic carbon from erosion and loss. This study concerns the impact of extreme conditions – typhoon-induced storm surges and high waves – on sediment loss from a mangrove forest. Specifically, we focus on the impact on fringing-type mangrove forests which are subject to the impact of waves coming from offshore.

In November of 2013, a super Typhoon Haiyan hit central Philippines. While the mangrove forests in the wide area of the central Philippines have been damaged by Typhoon Haiyan, specifically mangroves in Eastern Samar and Western Samar showed the greatest damage in terms of extent and severity (Long et al., 2016; Villamayor et al., 2016). The fringing mangrove forests in Hernani in Eastern Samar are such sites where mangroves were severely damaged (Long et al., 2016; Fig. 8.1). The typhoon cleared some part of the mangrove forests (Fig. 8.1c). Although the mangroves show some recovery, the damages still remain even in 2021 (Fig. 8.1d). As well as the damages to mangroves themselves, trace of sediment erosion probably due to high waves and storm surge brought by Typhoon Haiyan has been observed. This implies that a large amount of organic carbon stored in mangrove sediments could be lost by typhoons. Furthermore, in the phase of climate change, it is expected that the typhoon intensity will be enhanced in the future (Mei et al., 2015). Therefore, it is important to assess how the potential amount of sediment loss would increase with the increasing intensity of typhoons.

This study aims to assess the impacts of waves and storm surges induced by typhoons on the sediment erosion in fringing mangrove forests through a model analysis. We incorporate the mangroves' wave damping effect into the wave model of COAWST, and enable to account for the mangrove impacts on both flow and waves for the first time. We set up a schematized mangrove forest model for the analysis and assessed the sediment erosion in the mangrove forest during typhoon conditions through a flow-wave simulation. Specifically, we varied the typhoon intensity in the model up to a level of future-intensified super typhoons projected for 2100 (Mei et al., 2015).

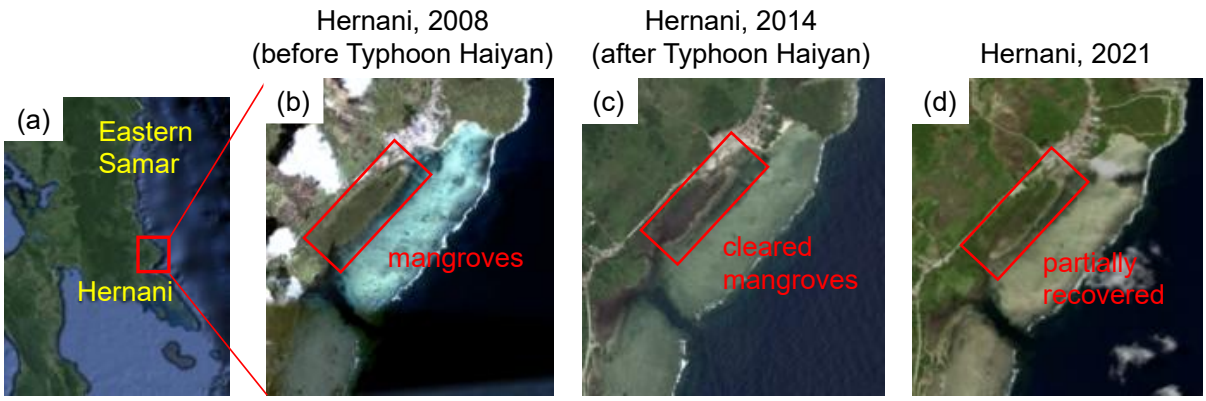

Figure 8.1. (a) Location of Hernani, Eastern Samar, in the Philippines, satellite images of a fringing mangrove forest in (b) 2008 (before the impact of Typhoon Haiyan in 2013), (c) 2014 (after the impact of Typhoon Haiyan), and (d) 2021 (Google Earth).

8.2 Materials and Methods

8.2.1 Inclusion of mangroves' wave damping effect in the COAWST

We have implemented the effects of mangroves on wave damping in the ROMS-SWAN coupled model under the model framework COAWST. The effect of cylinder-type vegetation on wave damping has been implemented by Suzuki et al. (2011) based on the model of Dalrymple et al. (1984), which has been formulated as

$$S_{ds,veg} = \sqrt{\frac{2}{\pi}} g^2 C_D b_v N_v \left(\frac{k}{\sigma}\right)^3 \frac{\sinh^3 kh_v + 3\sinh kh_v}{3k\cosh^3 kh} \sqrt{E_{tot}} E(\sigma,\theta) \qquad (8.1)$$

where $S_{ds,veg}$ is wave energy dissipation by vegetation (m^2 s), g is the gravity acceleration (m s^{-2}), C_D is the vegetation drag coefficient, b_v is the plant (stem) diameter (m), N_v is the plant density (m^{-2}), h_v is the vegetation height (m), k is the wave number (m^{-1}), σ is the wave frequency (s^{-1}), E_{tot} is the total wave energy (m^2), and E is the variance density 2D spectrum (m^2 s). Note that the actual equation implemented by Suzuki et al. (2011) can account for the vertically variable vegetation parameters (e.g., b_v, N_v) by adapting the Eq. (8.1) for multiple layers; however, we do not consider this multiple layer-approach for our analysis as described below.

A laboratory study of Maza et al. (2019) investigated wave attenuation in a *Rhizophora* mangrove forest. They derived the wave damping coefficient of the Rhizophora mangrove forest for random waves which can be described as

$$\frac{H_{rms}(x)}{H_{rms,i}} = \frac{1}{1+\beta x} \quad (8.2)$$

where x is the horizontal position along the forest (m), H_{rms} is the root mean square wave height for random waves (m), $H_{rms,i}$ is the root mean square of incident wave heights (m), and β is the wave damping coefficient. From Eqs. (8.1) and (8.2), the drag coefficient for the cylinder-type vegetations can be described using the wave damping coefficient as (Maza et al., 2019)

$$C_D = \frac{3\sqrt{\pi}}{N_v b_v H_{rms,i} k} \frac{(\sinh 2kh + 2kh)\sinh kh}{\sinh^3 kh_v + 3\sinh kh_v} \beta \quad (8.3)$$

Maza et al. (2019) modified Eq. (8.3) to estimate the drag coefficient for *Rhizophora* mangroves to account for the vertically variable vegetation structures of Rhizophora mangroves as

$$C_D = \frac{3\sqrt{\pi}}{A_{veg} H_{rms,i} k} \frac{(\sinh 2kh + 2kh)\sinh kh}{\sinh^3 kh + 3\sinh kh} \beta \quad (8.4)$$

where A_{veg} is the vertically averaged submerged vegetation frontal area density of the mangroves (m^{-1}). Using Eq. (8.4), Maza et al. (2019) found a nearly constant C_D value of 1.0 for the *Rhizophora* mangrove forest for variable wave conditions. This indicates that by using the vertically averaged vegetation parameter represented by A_{veg}, the wave damping effect of *Rhizophora* mangroves can be reasonably estimated. Based on these, we modified Eq. (8.1) for *Rhizophora mangroves* as

$$S_{ds,veg} = \sqrt{\frac{2}{\pi}} g^2 C_D A_{veg} \left(\frac{k}{\sigma}\right)^3 \frac{\sinh^3 kh + 3\sinh kh}{3k\cosh^3 kh} \sqrt{E_{tot}} E(\sigma,\theta) \quad (8.5)$$

We implemented this equation in the SWAN (Simulating Waves Nearshore; Booij et al., 1999) under the framework COAWST (Fig. 8.2). The parameter A_{veg} is provided by the mangrove root module implemented in Yoshikai et al. (2023). This framework enables the ROMS-SWAN coupled model in mangrove forests.

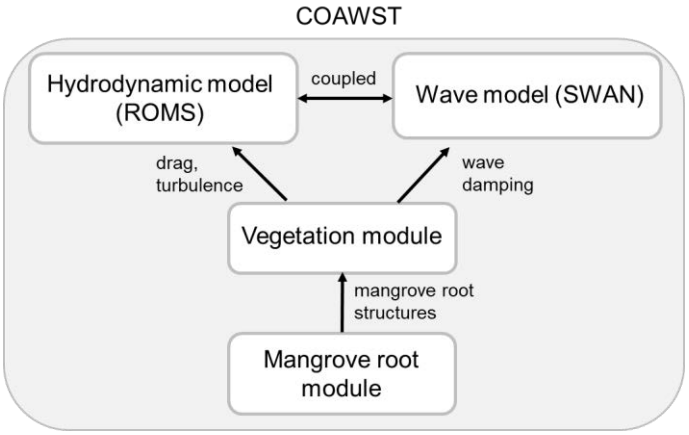

Figure 8.2. Model system incorporating the impact of mangroves on flow and waves.

8.2.2 Testing the implemented mangroves' wave damping effect

We tested the implemented mangroves' wave damping effect using a simple model grid having a uniform *Rhizophora* mangrove forest area as shown in Fig. 8.3. The model grid is adapted from the one used in Beudin et al. (2017) which was used for testing the implemented cylinder-type vegetation effects. The model domain 10 km × 10 km with 100 m horizontal grid resolution and has uniform water depth of 1.0 m. We assumed a 1 km × 1 km spatially uniform *Rhizophora* mangrove forest located at the center of the model grid (Fig. 8.3). For tree parameters (stem diameter, tree density) and the root scaling parameters, the values derived in a planted Rhizophora mangrove forest in Aklan, Philippines (Bakhawan Ecopark) by Yoshikai et al., (2022) were used. We used a constant value of 1.0 for the drag coefficient based on the results of Maza et al. (2019)

Figure 8.4 shows the tree density imposed in the model and the H_{rms} along a transect established perpendicular to the open boundary crossing the center of the model grid, and the wave decay in the *Rhizophora* mangrove forest represented by $H_{rms}/H_{rms,i}$. The model showed the significant wave decay from the edge of the forest compared to the non-vegetated area (Fig. 8.4a and b). We also estimated the wave decay analytically using the Eqs. (8.4)–(8.5), and found a nearly exact agreement with the results from the model (Fig. 8.4c). This confirms that the effect of mangroves' wave damping has been properly implemented in the COAWST.

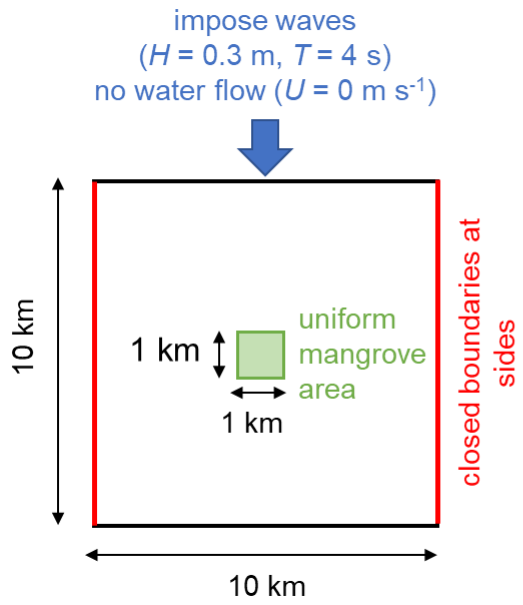

Model grid

Parameter	Unit	Value
Grid dimension	-	100 × 100
Grid horizontal resolution	m	100
Number of vertical layers	-	10
Water depth (h)	m	1.0

Vegetation parameters

Parameter	Unit	Value
Species	-	*Rhizophora* species
Tree density (n_{tree})	m^{-2}	0.36
Mean stem diameter (D_{stem})	m	0.066
Root scaling parameters	-	same as Bak2 in Yoshikai et al. (2022)

Figure 8.3. Model grid used for testing the *Rhizophora* mangroves' wave damping effect in the COAWST. The information on the imposed boundary conditions for waves, and the model grid and vegetation parameters are also provided.

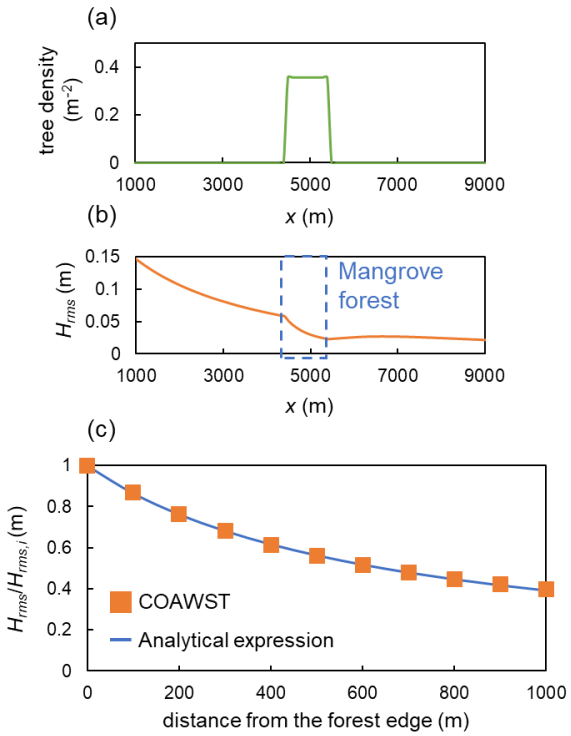

Figure 8.4. (a) Tree density imposed in the model, (b) simulated root mean square wave height (H_{rms}) along the transect perpendicular to the open boundary crossing the center of the model grid, and (c) simulated H_{rms} normalized by the incident value at the forest edge ($H_{rms,i}$). The estimated wave attenuation from an analytical model is also shown in the panel "c".

Model grid used for testing the *Rhizophora* mangroves' wave damping effect in the COAWST. The information on the imposed boundary conditions for waves, and the model grid and vegetation parameters are also provided.

8.2.3 Assessment of the impact of typhoon events on sediment loss

We assessed the impact of typhoon events on sediment loss in fringing-type mangrove forests using the model described in Section 8.2.2. Based on the mangrove forest in Hernani, Eeastern Samar as a typical fringing-type mangrove forest formed on reef flat (Fig. 8.5a), we generated a model grid representing a schematized fringing mangrove forest (Fig. 8.5b). The grid dimension is 102 in the cross-shore direction and 50 in the along-shore direction with the grid resolution of 50 m. However, because we set uniform condition in the along-shore direction for the topography and vegetation parameters, the model can be basically regarded as one-dimensional model. The model domain includes a mangrove forest, reef flat, reef slope, and some part of offshore (Fig. 8.5b) We set the topography of -0.5 m relative to the mean sea level (MSL) for the reef flat and from -0.5 m to 1.0 m relative to MSL for the mangrove forest. We assumed a uniform *Rhizophora* mangrove forest having a ground level slope of 0.001 based on the data on a fringing mangrove forest from Montgomery et al. (2019). We set the same vegetation parameters used in Section 8.2.2 (Fig. 8.3) for this analysis.

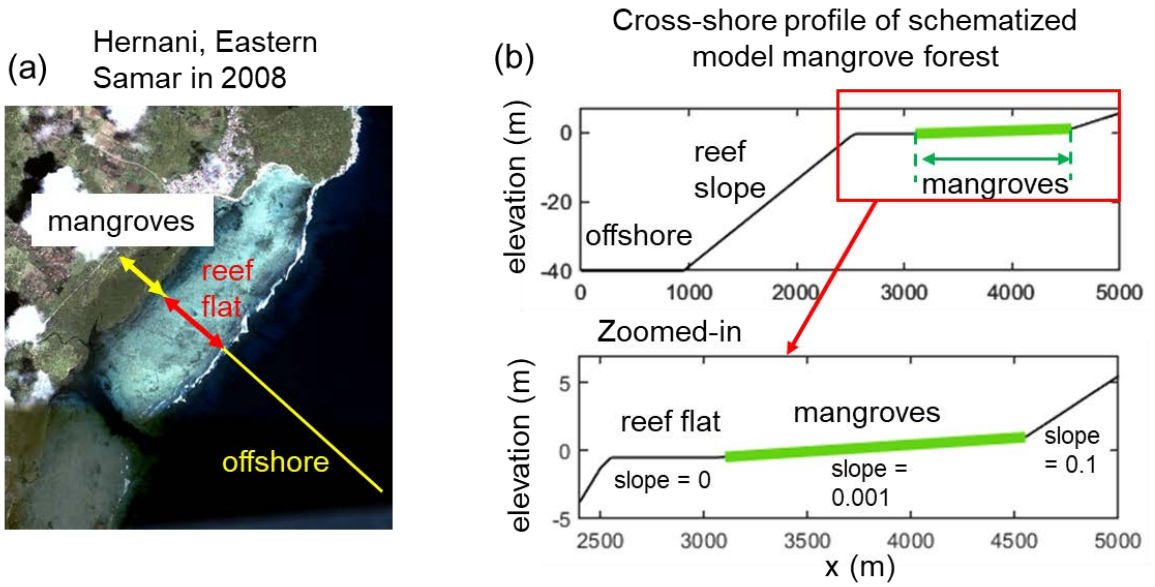

Figure 8.5. (a) Satellite image of a mangrove frorest in Hernani, Eastern Samar in 2008 (Google Earth) as a typical fringing type mangrove forest, and (b) a cross-shore profile of a schematized fringing-type mangrove forest for a model analysis.

Because the scale of the model domain is much smaller than the scale where high waves and storm surge are generated by typhoons, we gave the high wave and storm surge conditions to the model as boundary conditions. As such, we gave wave height and the water level to the offshore boundary, and a cyclic boundary condition to the across-shore boundaries. Because of the 1-D nature of the model grid, we cannot simulate the strong flows by storm surges. Therefore, the storm surge is represented only by the elevated water level imposed at the boundary, and zero flow velocity was given to the boundary. Here, we did not consider tidal variations in water levels and flows, and assumed a condition when the 0 m tide level relative to MSL (with absence of the storm surge). In addition, we gave zero wind speed in the model because wind is not significant on waves and storm surges in the scale of the model grid considered in this study. In this study, the wave height and wave period for the boundary at a given wind speed (U_w, m s^{-1}) was given as (Bethel et al., 2021)

$$\frac{H_{wave}}{H_{wave,0}} = \left(\frac{U_w}{U_{w,0}}\right)^2 \tag{8.6}$$

$$\frac{T_{wave}}{T_{wave,0}} = \frac{H_{wave}}{U_w} \times \frac{U_{w,0}}{H_{wave,0}} \tag{8.7}$$

where H_{wave} (m) and T_{wave} (s) is the wave height and wave period at a given wind speed U_w (m), and $H_{wave,0}$ (m) and $T_{wave,0}$ (s) is the wave height a at a reference wind speed $U_{w,0}$. We estimated the maximum wind speed at a given typhoon central air pressure (P_c, hPa) using the empirical typhoon wind field model of Holland (1980) and use this value as U_w. We estimated the maximum wind speed of a typhoon of which P_c is 900 hPa – a level observed for Typhoon Haiyan – and use it as the reference wind speed ($U_{w,0}$) in Eqs. (8.6)–(8.7). We gave the reference wave height ($H_{wave,0}$) 12 m and reference wave period ($T_{wave,0}$) 15 s, respectively, based on a numerical wave simulation for Eastern Samar region during the period of Typhoon Haiyan by Bautista et al. (unpublished). Storm surge occurs mainly due to the two processes – the atmospheric pressure effect and the wind effect. In general, water level rises for about 1 m with 100 hPa difference with the ambient atmospheric pressure. The contribution of the wind effect to the rise of water level ($\Delta\eta$, m) was estimated assuming a momentum balance of wind stress and pressure gradient as

$$\Delta\eta = \int_0^l \frac{\rho_a C_{D,air} {U_w}^2}{\rho_a g h(x)} dx \tag{8.8}$$

where $\Delta\eta$ is the rise of water level (m), ρ_a is the air density (kg m^{-3}), $C_{D,air}$ is the drag coefficient for wind stress, ρ_w is the water density (kg m^{-3}), $h(x)$ is the local water depth at a position x (m), and l is the cross-shore length subject to the impact of wind (m). Equation (8.8) requires

information on the offshore topography represented by the $h(x)$ and l, which is not included in the model. In this study, we gave 75 km to l, and set h assuming a constant slope of 0.0017 from water depth of 30 m at the model's offshore boundary ($h(x=0)$), assuming a typical continental shelf.

The sediment resuspension flux is calculated by the COAWST as

$$E = \max\left(E_0\left(\frac{\tau}{\tau_{cr}}\right) - 1{,}0\right) \quad (8.9)$$

where E_0 is a surface erosion rate which was set as 10^{-4} kg m^{-2} s^{-1}, τ is the bottom shear stress (N m^{-2}) and the τ_{cr} is the critical shear stress for erosion (Warner et al., 2008). We gave 0.2 N m^{-2} to τ_{cr}, following a previous modeling study on fringing mangrove forest (Xie et al., 2020). In this study, because of the one-dimensional nature of the model simulation, flows associated with storm surge do not occur, and hence the eroded sediments is not flushed out from the mangrove forest. This means that the model cannot directly evaluate the sediment loss from the mangrove forest. Therefore, we calculated the forest-mean sediment erosion rate and used as a indicator of sediment loss amount during the typhoon event.

We conducted the wave simulation during the typhoon conditions by varying the central pressure of the typhoon from 860 hPa to 1000 hPa with 20 hPa intervals. Currently, the minimum typhoon pressure is around 900 hPa; therefore, the conditions with 860 hPa and 880 hPa assumes intensified super typhoons by the climate change in the future. Note that we gave constant wave and surge conditions and did not consider the temporal change in these parameters during the typhoon conditions. The model result was retrieved when the model simulation reached a steady state.

8.3 Results and Discussion

Figure 8.6 shows the simulated mean water level, wave height, bed shear stress, and the sediment resuspension flux under the different typhoon intensity. The water level rises as the typhoon intensity increases, up to about 4 m when the typhoon central pressure is 860 hPa (Fig. 8.6a). The waves break at the reef slope-flat transition, but the increased water level weakens the wave breaking effects of the reef flat. As a result, higher waves (up to about 2.2 m when the central pressure is 860 hPa) propagate through the reef flat towards the mangrove forest (Fig. 8.6b). The model showed a notable wave attenuation within the mangrove forest (Fig. 8.6b). However, as expected, the wave heights in the mangrove forest are higher throughout the forest as the incoming wave height increases. The higher waves induce higher bed shear stress through wave excursion over the bed. The model showed from 1.5 N m^{-2} to 5 N m^{-2} bed shear stress at the forest edge as the typhoon intensity increases from 980 hPa

to 860 hPa (Fig. 8.6c), which is significantly higher than the critical shear stress for erosion for the mangrove sediments (0.2 N m^{-2}). Note that these values are only by waves, and the potential contribution of storm surge currents are not considered in this study as described in Section 8.2.3. Hence, the bed shear stress may become higher than those simulated values in actual conditions. The model showed that the increased bed shear stress induced by the higher waves increases the sediment erosion (resuspension flux; Fig. 8.6d). On the other hand, the attenuation of bed shear stress within the forest affected the area where the substantial erosion occurs, suggesting the effectiveness of mangroves in reducing the impact of typhoons on sediment loss (Fig. 8.6d).

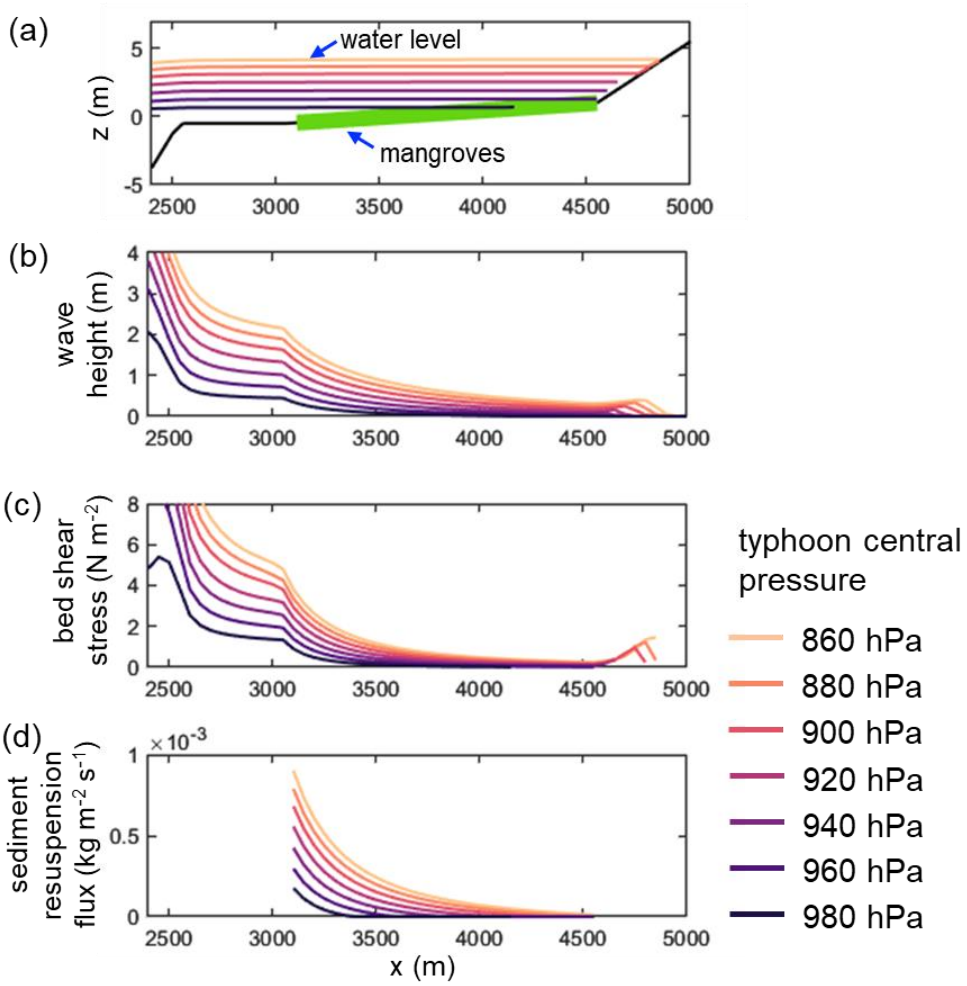

Figure 8.6. Simulated (a) mean water level, (b) wave height, (c) bed shear stress, and (d) sediment resuspension flux along the cross-shore profile under the different typhoon intensity from 860 hPa to 980 hPa with 20 hPa intervals. The region where the mangrove forest is imposed is indicated in the panel “a”. Note that the sediment resuspension flux is shown only for the mangrove forest in the panel “d”.

Figure 8.7 compares the results from simulations with and without imposing the mangroves' wave damping effect under the typhoon intensity of 960 hPa. It highlights the role of mangroves in attenuating the waves and lower bed shear stress significantly within the forest (Fig. 8.7b–c), resulting in the limited sediment erosion rate compared to the case without mangrove effects (Fig. 8.7d).

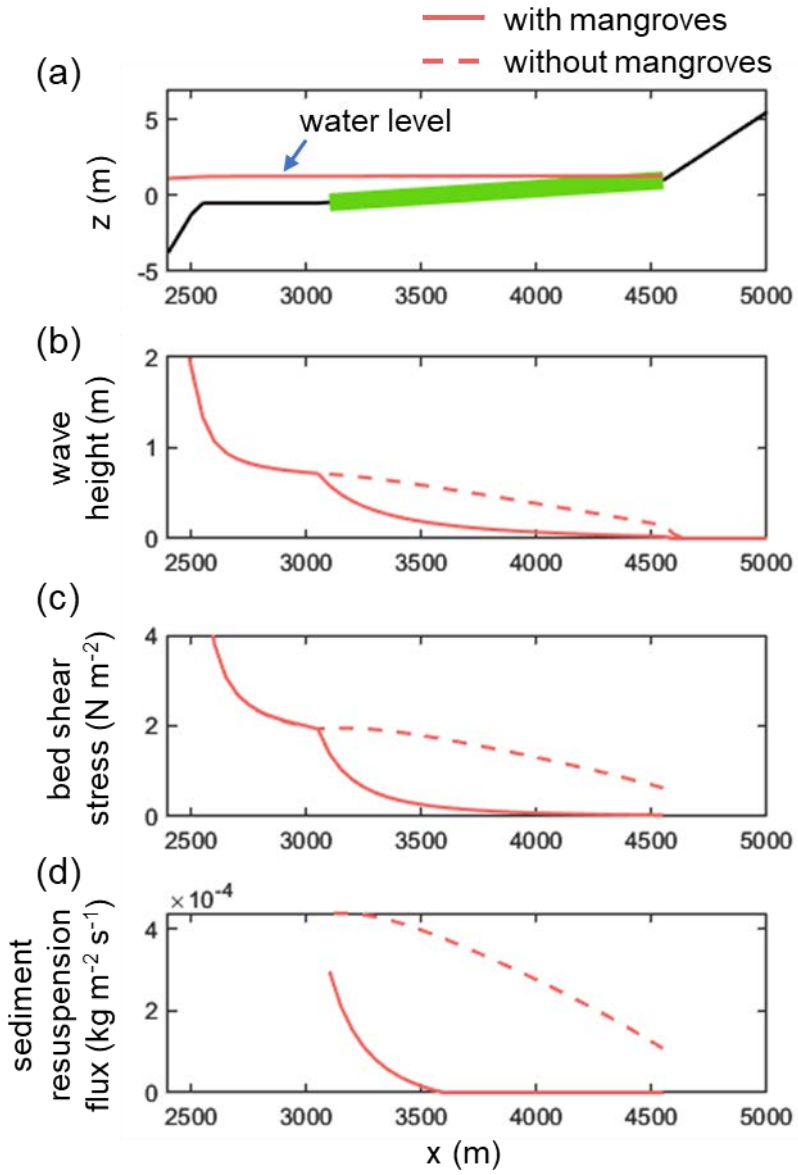

Figure 8.7. Simulated (a) mean water level, (b) wave height, (c) bed shear stress, and (d) sediment resuspension flux along the cross-shore profile under the typhoon intensity of 960 hPa with and without imposing the effect of mangroves.

When compared the forest-averaged sediment resuspension flux with typhoon intensity represented by the maximum wind speed, a nonlinear relationship emerged (Fig. 8.8). This nonlinear increase is because of the higher sediment erosion rate at a given forest

position and the larger area where the sediment erosion occurs within the forest (Fig. 8.6d), which are both amplified by the higher incoming waves and elevated mean water level (Fig. 8.6a, b). This indicates that the sediment loss potential from the mangrove forest, thus mangrove soil organic carbon loss potential would further increase nonlinearly with the future increase in typhoon intensity, suggesting the need to account for such increased episodic loss of blue carbon for management action in the future.

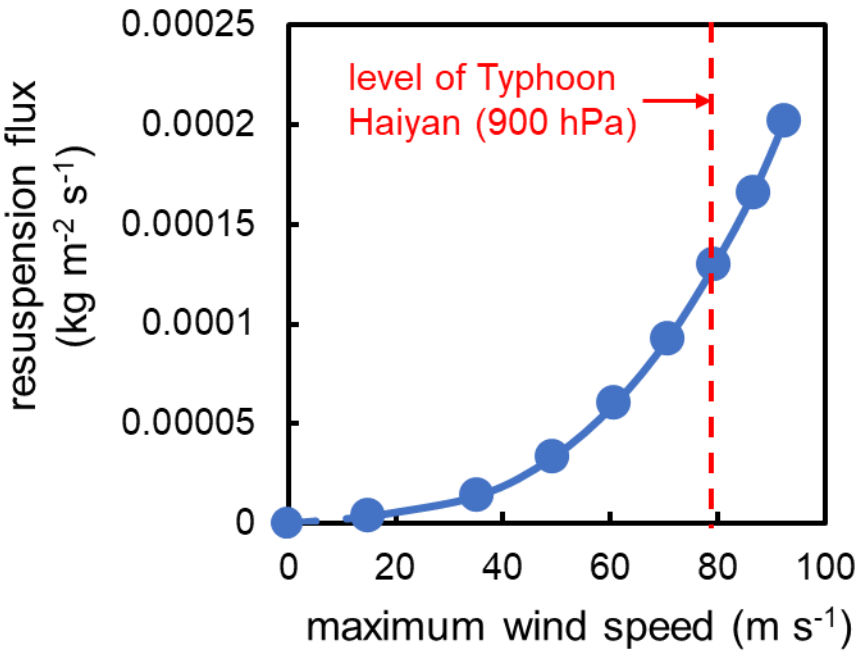

Figure 8.8. Response of the simulated forest-averaged sediment resuspension flux against the typhoon's maximum wind speed. The level of Typhoon Haiyan's maximum wind speed is also indicated.

However, when compared with the results from the simulation without imposing the mangroves' wave damping effects, we found far greater resuspension flux than the simulation with the mangrove effects (Fig. 8.9). Notably, the model suggested that the effect of clearance of the mangrove forest (disappearance of the mangroves' wave damping effect) on the sediment loss from the mangrove forest (represented by the forest-averaged sediment resuspension flux) is more significant than the effect of increase in wind speed. For example, the resuspension flux in a mangrove forest under the wind speed 80 m s^{-1} is generated with the wind speed less than 40 m s^{-1} if there are no mangroves. This suggests that the loss of mangroves may drastically increase the sediment loss even during regular typhoon conditions. Hence, it will be critical for mangrove soil organic carbon loss if another typhoon hit the damaged and unrecovered (e.g., Fig. 8.1d), or deforested mangrove forests, urging the management and restoration efforts of mangroves under the changing climate. Alternatively,

the results suggested that the wave damping by mangroves effectively reduce the amount of sediment and soil organic carbon loss from high waves during typhoon condition.

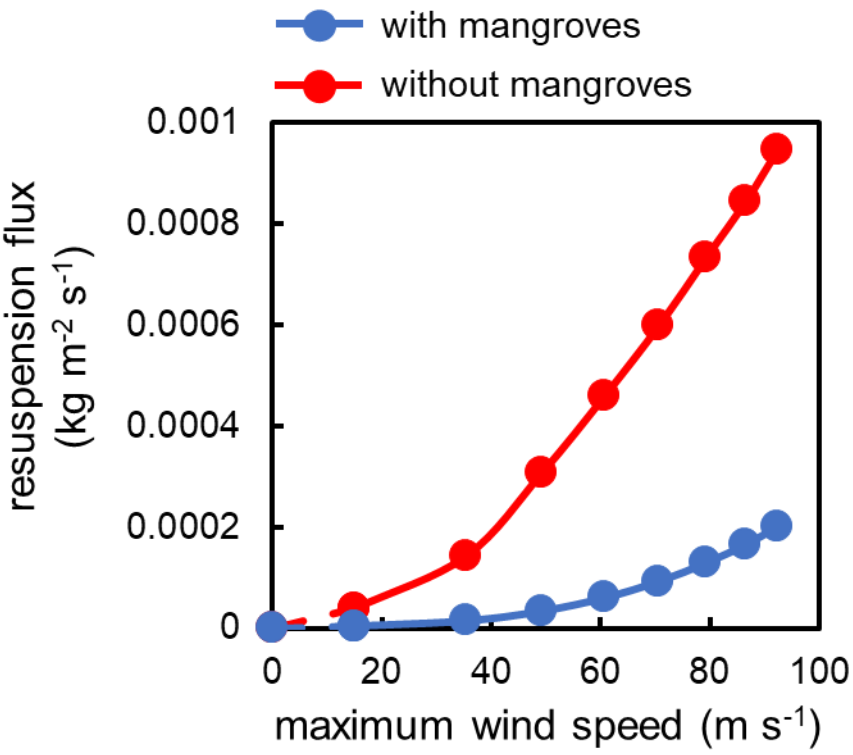

Figure 8.9. Comparison of the responses of simulated forest-averaged sediment resuspension flux with and without imposing the mangrove impact against the typhoon's maximum wind speed.

This study assessed the impact of typhoons on sediment loss from a mangrove forest using a new model incorporating the impact of mangroves on flow and waves. However, there are some aspects that need to address further for more reliable estimates. For example, Roeber and Bricker (2015) showed that the wave heights could be amplified in the fringing reef due to the presence of infragravity waves, and such phenomenon was observed in Hernani (Roeber and Bricker, 2015). This process requires a phase-resolving model to account for, while the SWAN used in this study is a phase-averaged model. Recently, Olabarrieta et al. (2023) introduced an infragravity wave driver to the COAWST, and implementing the mangrove impact in it is one of the future topic to address. The sediment resuspension largely depends on the critical bed shear stress (τ_{cr} in Eq. (8.9)); however, the insights into this parameter for mangrove forests are very limited. Furthermore, when the mangroves are cleared or damaged, it is expected that the fine root's soil-holding capacity is eventually lost which may also affect the critical shear stress. These knowledge gaps need to be addressed in future studies. This study used a pseudo 1-D schematized model domain

which does not generated storm surge currents in the simulation. While it is expected that the strong storm surge currents would induce the soil erosion further, some studies suggested that the strong currents of storm surges transport sediments to salt marshes promoting sedimentation (e.g., Pannozzo et al., 2022, 2023), which may depend on local topographic conditions. Application of the model to an actual mangrove forest condition to investigate the wave and storm surge impacts on the mangrove sediment loss potential is also one of the topics to address in the future studies. Lastly, not only the typhoon intensity but also the typhoon frequency should be accounted for the assessment of the impact of future increase in the typhoon intensity on sediment loss from mangrove forests.

8.4 Conclusions

This study incorporated the mangrove wave damping effect in the wave model of the COAWST to enable it to account for the mangrove impacts on both flow and waves for the first time. Using the model, we assessed the impact of typhoons on sediment loss in a fringing-type mangrove forest associated with the waves and storm surges. The mode suggested the significant role of mangroves in attenuating the wave height within the forest. As the typhoon intensity increases, both the offshore water level and wave height increase. This increases the wave heights propagating to the mangrove forest, leading to the increase in both the sediment erosion rate and the area where the substantial erosion occurs. As a result, the forest-averaged sediment erosion rate showed a nonlinear increase against the increase in typhoon maximum wind speed. This alarms a significant future increase in the sediment loss potential from mangrove forests due to the future increase in typhoon intensity. However, the clearance of the mangrove forest induces much higher sediment erosion rate than the increase in typhoon intensity. These results highlight the role of mangroves in reducing the amount of sediment and soil organic carbon loss during typhoon conditions and the importance of management and restoration efforts of mangroves under the changing climate.

8.5 References

Bethel, B. J., Dong, C., & Wang, J. (2021). An Empirical Wind-Wave Model for Hurricane-Forced Wind Waves in the Caribbean Sea. Earth and Space Science, 8(12), e2021EA001956. https://doi.org/10.1029/2021EA001956.

Beudin, A., Kalra, T. S., Ganju, N. K., and Warner, J. C.: Development of a coupled wave-flow-vegetation interaction model. Computers & Geosciences, 100, 76–86. https://doi.org/10.1016/j.cageo.2016.12.010, 2017.

Booij, N. R. R. C., Ris, R. C., & Holthuijsen, L. H. (1999). A third-generation wave model for coastal regions: 1. Model description and validation. Journal of geophysical research: Oceans, 104(C4), 7649-7666. https://doi.org/10.1029/98JC02622.

Dalrymple, R. A., Kirby, J. T., Hwang, P. A., 1984. Wave diffraction due to areas of energy dissipation. J. Waterw. Port Coast. Ocean Eng. 110, 67–79.

Holland, G. J. (1980). An analytic model of the wind and pressure profiles in hurricanes. Monthly Weather Review, 108(8), 1212–1218. https://doi.org/10.1175/1520-0493(1980)108<1212:AAMOTW>2.0.CO;2.

Long J, Giri C, Primavera J, and Trivedi M (2016) Damage and recovery assessment of the Philippines' mangroves following Super Typhoon Haiyan. Marine pollution bulletin, 109(2), 734-743. Long, J., Giri, C., Primavera, J., & Trivedi, M. (2016). Damage and recovery assessment of the Philippines' mangroves following Super Typhoon Haiyan. Marine pollution bulletin, 109(2), 734-743. https://doi.org/10.1016/j.marpolbul.2016.06.080.

Maza, M., Lara, J. L., & Losada, I. J. (2019). Experimental analysis of wave attenuation and drag forces in a realistic fringe *Rhizophora* mangrove forest. Advances in Water Resources, 131, 103376. https://doi.org/10.1016/j.advwatres.2019.07.006.

Mei, W., Xie, S. P., Primeau, F., McWilliams, J. C., & Pasquero, C. (2015). Northwestern Pacific typhoon intensity controlled by changes in ocean temperatures. Science advances, 1(4), e1500014. https://doi.org/10.1126/sciadv.150001.

Montgomery, J. M., Bryan, K. R., Mullarney, J. C., & Horstman, E. M. (2019). Attenuation of storm surges by coastal mangroves. Geophysical Research Letters, 46(5), 2680-2689. https://doi.org/10.1029/2018GL081636.

Olabarrieta, M., Warner, J. C., & Hegermiller, C. A. (2023). Development and application of an infragravity wave (InWave) driver to simulate nearshore processes. Journal of Advances in Modeling Earth Systems, 15(6), e2022MS003205. https://doi.org/10.1029/2022MS003205.

Pannozzo, N., Leonardi, N., Carnacina, I., & Smedley, R. (2021). Salt marsh resilience to sea-level rise and increased storm intensity. Geomorphology, 389, 107825. https://doi.org/10.1016/j.geomorph.2021.107825.

Pannozzo, N., Leonardi, N., Carnacina, I., & Smedley, R. K. (2023). Storm sediment contribution to salt marsh accretion and expansion. Geomorphology, 430, 108670. https://doi.org/10.1016/j.geomorph.2023.108670.

Roeber, V., & Bricker, J. D. (2015). Destructive tsunami-like wave generated by surf beat over a coral reef during Typhoon Haiyan. Nature communications, 6(1), 7854. https://doi.org/10.1038/ncomms8854.

Suzuki, T., Zijlema, M., Burger, B., Meijer, M. C., & Narayan, S. (2012). Wave dissipation by vegetation with layer schematization in SWAN. Coastal Engineering, 59(1), 64-71. https://doi.org/10.1016/j.coastaleng.2011.07.006.

Temmerman, S., Horstman, E. M., Krauss, K. W., Mullarney, J. C., Pelckmans, I., & Schoutens, K. (2023). Marshes and mangroves as nature-based coastal storm buffers. Annual Review of Marine Science, 15, 95-118. https://doi.org/10.1146/annurev-marine-040422-092951.

Villamayor BMR, Rollon RN, Samson MS, Albano GMG, and Primavera JH (2016) Impact of Haiyan on Philippine mangroves: Implications to the fate of the widespread monospecific *Rhizophora* plantations against strong typhoons. Ocean & Coastal Management, 132, 1-14. https://doi.org/10.1016/j.ocecoaman.2016.07.011.

Warner, J. C., Sherwood, C. R., Signell, R. P., Harris, C. K., & Arango, H. G. (2008). Development of a three-dimensional, regional, coupled wave, current, and sediment-transport model. Computers & geosciences, 34(10), 1284–1306. https://doi.org/10.1016/j.cageo.2008.02.012.

Xie, D., Schwarz, C., Brückner, M. Z., Kleinhans, M. G., Urrego, D. H., Zhou, Z., & Van Maanen, B. (2020). Mangrove diversity loss under sea-level rise triggered by bio-morphodynamic feedbacks and anthropogenic pressures. Environmental Research Letters, 15(11), 114033. https://doi.org/10.1088/1748-9326/abc122.

Yoshikai, M., Nakamura, T., Herrera, E. C., Suwa, R., Rollon, R., Ray, R., Furukawa, K., and Nadaoka, K. (2023) Representing the impact of *Rhizophora* mangroves on flow in a hydrodynamic model (COAWST_rh v1.0): the importance of three-dimensional root system structures. Geoscientific Model Development, 16, 5847–5863, https://doi.org/10.5194/gmd-16-5847-2023.

Yoshikai, M., Nakamura, T., Bautista, D. M., Herrera, E. C., Baloloy, A., Suwa, R., Basina, R., Primavera-Tirol, Y. H., Blanco, A.C., and Nadaoka, K. (2022) Field measurement and prediction of drag in a planted *Rhizophora* mangrove forest. Journal of Geophysical Research: Oceans, 127, e2021JC018320. https://doi.org/10.1029/2021JC018320.

Chapter 9: Conclusions

Biomass dynamics and hydrodynamics-sediment transport are key processes governing blue carbon dynamics, yet our understanding of these processes in the blue carbon ecosystems are limited. This thesis presented modeling works towards a better understanding of the ecological and physical processes shaping the blue carbon dynamics.

Chapters 2–3 addressed a better understanding of biomass dynamics of seagrass meadows and mangrove forests. In Chapter 2, a new seagrass growth model driven by a coupled hydrodynamic-biogeochemical model was introduced. This model was applied to a seagrass meadow in the Philippines, which has been impacted by the unregulated mariculture activities in adjacent areas. The model successfully reproduced the distribution of above-ground seagrass biomass for two co-existing species. It highlighted the impact of high nutrient loads on underwater light and seagrass growth rates and a potential of recovery of seagrass meadows through mariculture regulation. In Chapter 3, a new mangrove growth model was developed and applied to a mangrove forest in Japan. This model incorporates a plant hydraulic module to consider the soil salinity control on plant water uptake and its linkage to photosynthesis and nutrient uptake. The model showed a remarkable performance in predicting the patterns in forest structures composed of two co-existing species across the soil salinity gradient. It unveiled the roles of salinity and tree competition in shaping the forest structures, and identified crucial plant traits.

Chapters 4–6 addressed a better understanding of hydrodynamics-sediment transport in mangrove forests, with a specific focus on the flow-vegetation interaction of *Rhizophora* mangroves, characterized by their complicated above-ground root structures (prop root systems). In Chapter 4, the morphological structures of the prop root systems were extensively investigated by collecting data from 156 trees in Indonesia, the Philippines, and Japan. This research established an allometric relationship between root structures and stem diameter and develops an empirical model for predicting *Rhizophora* root structures, demonstrating an excellent fit with the collected data. In Chapter 5, a detailed measurement of hydrodynamics in a planted *Rhizophora* mangrove forest was presented. This included quantifying the drag force exerted by the mangroves and estimating the drag coefficient of *Rhizophora* mangroves in the field for the first time. This research demonstrated a reasonable prediction of drag using the obtained drag coefficient and the empirical *Rhizophora* root model. In Chapter 6, the impact of *Rhizophora* mangroves on flow was formulated and implemented into a hydrodynamic model. It incorporates the empirical *Rhizophora* root model, which enables the forest-scale simulation of hydrodynamics without rigorous measurements of root structures.

The model's reasonable performance in predicting mean flow and turbulence in *Rhizophora* mangrove forests was verified using data from previous studies.

Chapters 7–8 featured two case studies applying the developed hydrodynamic model to investigate sediment transport processes in mangrove forests. In Chapter 7, the model was applied to a riverine mangrove forest in the Philippines. The results revealed that the increased hydraulic resistance of the mangrove forest significantly attenuates flow within the forest, leading to retention of sediments. When the effect of mangroves on flow was deactivated in the model, a substantial loss of sediments occurred due to soil erosion. In Chapter 8, the model was extended to consider the effect of mangroves on wave damping. It assessed the impact of typhoon events on sediment loss in a mangrove forest. The model demonstrated that mangroves effectively dissipate wave energy, regulating sediment loss. It also suggested that as typhoon intensity rises, sediment loss increases nonlinearly. However, the loss of mangroves has a far more significant impact on sediment erosion than an increase in typhoon intensity. These results underscore the vital role of mangrove forests in retaining sediments and thus soil organic carbon. Altogether, this thesis advances our understanding of ecological and physical processes in blue carbon ecosystems, providing a solid foundation for modeling the blue carbon dynamics under the impacts of climate change.

Future research should address the coupling of those ecological and physical models. Although there still are many challenges and knowledge gaps to achieve it, this coupled model enables the evaluation of coastal vegetation ecosystems' fate under the impact of climate change, which would provide valuable information for managing the ecosystems. Furthermore, modeling of biogeochemical aspects in the blue carbon dynamics needs to be addressed and integrated with those models to finally achieve the evaluation of blue carbon dynamics.